



A Review of Different Synthesis Approaches to Nanoparticles: Bibliometric Profile

Oluwaseun Jacob Ajala^{1,2*} , **Damian Onwudiwe**³ , **Samuel Ogunniyi**⁴ ,
Setyo Budi Kurniawan⁵ , **Olumide Esan**¹ , **Oluwole Samuel Aremu**⁶ 

¹Department of Pure and Applied Chemistry, Ladoké Akintola University of Technology, P. M. B. 4000, Ogbomoso, Nigeria.

²Department of Chemistry, Federal University of Technology, P. M. B. 65, Bosso Campus, Minna, Niger State, Nigeria.

³Department of Chemistry, Faculty of Natural and Agricultural Science, North-West University (Mafikeng Campus), Private Bag X2046, Mmabatho 2735, South Africa.

⁴Department of Chemical Engineering, University of Ilorin, P. M. B 1515, Ilorin, Nigeria.

⁵Department of Chemical Engineering and Process Engineering, Faculty of Engineering and Built Environment, Universiti Kebangsaan Malaysia, 43600 UKM Bangi, Selangor, Malaysia.

⁶Department of Chemistry and Biochemistry, University of Windsor – Ontario Canada 401 Sunset Avenue Windsor, Canada.

Abstract: Nanomaterials are currently one of the most popular emerging materials used in different applications such as drug delivery, water treatment, cancer treatment, electronic, food preservations, and production of pesticide. This is due to their interesting features including size-dependent properties, lightweight, biocompatibility, amphiphilicity and biodegradability. They offer wide possibilities for modification and are used in multiple functions with enormous possibilities. Some of them are medically suitable which has opened new opportunities for medical improvement especially for human health. These characteristics also make nanomaterials one of the pioneers in green materials for various needs, especially in environmental engineering and energy sectors. In this review, several synthesis approaches for nanoparticles mainly physical, chemical, and biological have been discussed extensively. Furthermore, bibliometric analysis on the synthesis of nanoparticles was evaluated. About 117,162 publications were considered, of which 92% are journal publications. RSC Advances is the most published outlet on the synthesis of nanoparticles and China has the highest number of researchers engaged in the synthesis of nanoparticles. It was noted in the evaluation of synthesis approach that biological approach is the savest method but with a low yield, while the chemical approach offers a high yield with some level of hazardous effect. Also, the bibliometric analysis revealed that the field of nanotechnology is a trending and hot ground for research.

Keywords: Nanoparticle, Chemical, Physical, Biological, Bibliometric analysis.

Submitted: November 14, 2023. **Accepted:** August 9, 2024.

Cite this: Ajala, OJ, Onwudiwe D, Ogunniyi S, Kurniawan SB, Esan O, Aremu OS. A Review of Different Synthesis Approaches to Nanoparticles: Bibliometric Profile. JOTCSA. 2024;11(4):1329-68.

DOI: <https://doi.org/10.18596/jotcsa.1389331>

***Corresponding author's E-mail:** oluwaseun_ajala81@yahoo.com

1. INTRODUCTION

Nanomaterials are currently one of the most popular emerging materials used in various applications (1). The fascinating optical, structural and morphological properties of materials as they approach the nanometric domain have increased the research attention on these materials. Other properties of note include lightweight, biocomp-atibility, amphiphilicity and biodegradability (2). Nanomaterials are known

to be used for multiple functions with enormous possibilities in modification (3). The biocompatibility of some nanomaterials, especially with the human system, has open new opportunities for medical improvement (4). These characteristics also make nanomaterials one of the pioneers in green materials for various needs, especially in environmental engineering and energy sectors.

Application of nanomaterials is mostly medical (5), electronic (6), absorbent (7-13) and membrane technologies (14). Medical application of nanomaterials includes the delivery of drugs, heat, or other substance to a specific targeted cell (15). They are also used in devices such as sensors to provide fast results of disease diagnostic (16), antibacterial compounds (17), purifier in water treatment (7, 18), wound healing treatment (19), as cell reparation agents (20), and in nano-electronic technology. The improved optical and electronic properties has been utilized in display productions, such as organic light-emitting diodes (21), as support in the wireless technology and internet of things (22), as well as in nano-communication in which medical devices could transmit information inside the human body for medical purposes (23). In the membrane sectors, various types of nanomaterials such as carbon, graphene and fullerene are currently widely used (14, 24).

Due to the wide array of benefits and utilization, the current study focuses on highlighting the different synthesis approaches of nanomaterials. Synthesis of nanomaterials can be conducted via various methods including the solid phase (25), liquid phase (26), and thermal methods (27). The solid phase syntheses involve synthesis methods without the use of solvents. The liquid phase syntheses include the solvent dissolution and sol-gel process, while the thermal methods include synthesis at elevated temperatures such as microwave irradiation, plasma, magnesio-thermic reduction, solar energy, and neutron irradiation methods. This paper is aimed to explore and highlight the different synthesis route of nanomaterials via the 3 broad physical, chemical, and biological routes. The bibliometric analysis of these various synthesis approaches is discussed. This review paper will enhance the knowledge on the synthesis route of nanomaterials and the utilization of the synthesized materials for different applications.

2. TECHNIQUES FOR SYNTHESIZING NANOMATERIALS

The two broad categories of synthesis routes are bottom-up and top-down approaches. Physical methods are used in top-down approaches, whereas chemical and biological methods are used in bottom-up approaches. Other synthesis methods falls under these two categories and are discussed in this section.

2.1 Physical Methods of Nanomaterial Synthesis

In this method, electric current is used to generate electron from the initial material to produce the required electron (Ionic Species) which further converted into atomic material and develop into nanoparticle (NPs) (28). Physical methods have the advantages of high speed (29), none use of toxic chemicals (30), uniform size (2), purity (31), and shape (3). Their disadvantages include high cost (32), less productivity (33), radiation exposure (34), high temperature (35), energy intensive (30), high pressure (36), less thermal stability (37), complex

shape and size tenability (38), and less stability (39, 40). This synthesis approach could alter the physicochemical and surface chemistry of nanoparticles, making it unsuitable for producing nanoparticles in standard sizes and forms (41). Physical techniques such as ball milling (42), evaporation-condensation (43), sputtering (44), laser ablation (45), and arc discharge methods are examples of this process (46). The use of physical techniques in the synthesis of metal-nanoparticles have recently aroused the interest of researchers, owing to the adjustable parameters utilized in reactions (47). Unlike chemical or biological techniques, physical methods do not require reagents or solvents that can contaminate the samples (48, 49).

In addition, the homogeneity of nanomaterial is potentially high when created via physical techniques (5). However, the requirement for huge and expensive equipment, the long duration of synthesis time are the present challenges (50, 51).

2.1.1 Laser ablation

The laser-induced ablation approach has drawn increased attention among other physical methods because of its eco-friendliness, simplicity and ability to offer nanoparticles with even sizes (52). In synthesizing diverse kinds of NPs by laser ablation, a high-power pulsed laser is a critical and coherent need for ablation on the sample's surface (53). Adjusting parameters such as wavelength, pulse width, repetition rate of the laser source, temperature and ablation time, the production of nanoparticles with chosen morphological characteristics is attainable (54). This is the most prevalent technique for metallic alloy-NPs production among the physical procedures (50). In this approach, a solid substance is irradiate via a laser to produce particles of nano-size (55). This technique involves creating nanoparticle in a liquid environment by obtaining colloidal solution of nanoparticle from solid target material in a variety of solvent (56). A solid target material is abraded using a laser beam as the energy source, resulting in the vaporization to atoms and clusters (57). The NPs are progressively formed in ambient media (58). The settings specified before the experimental setup may impact the final concentration and condition of the nanoparticle solution (39, 59) as it is depicted in Fig 1. The approach offers several notable benefits in particle production. The first is the ability to produce several particles in a single operation, and the second is the laser source's capacity to generate various colloidal solution concentrations in accordance with the chosen parameters (47). The primary issue, despite the solution's promise, continues to be the large, expensive equipment needed (60). The analysis duration is longer than the chemical procedures, and the process is more difficult (49).

Strong laser pulses are centered on metal's target contained in a liquid (61) and NPs might be produced using laser ablation of metallic bulk materials in solution (62). The size of the NPs formed by alcohol based materials depends on its chain length (63). C-3 (Prop-) to C-5 (Pent-) long alcohol chain had more

stable particles than short-chains; ethanol and methanol (64). The features of the metal-NPs generated are determined by various factors such as ablation time (65) which increases, as the amount of metal-NPs increase till ablation time optimum value is reached. Increasing surfactant content may also yield smaller metal-NPs (66). According to reported studies, metal-NPs produced by femtosecond laser pulses have a narrower size distribution than those produced by nanosecond laser pulses (67). After the ablation, the liquid environment exclusively includes metal-NPs without other chemicals, and ions.

Laser ablation facilitates the production of nanoparticles with regulated shapes and sizes, resulting in better long-term stability and high yields (55). The *in-situ* conjugation of bio-molecules with gold nanoparticles is one of the biomedical applications of the laser ablation technique, and it is possible since the synthesis is flexible and can be done in both aqueous and organic solvents (64). This strategy has consequently shown to be more successful than traditional procedures through minimizing waste production, manual operation and refining size control of nanoparticle (68).

The studies by Islam, Shohag (47) is a notable example of this technology, ZnO NPs was synthesized via laser ablation in a NaOH solution (particle size from 80.76 - 102.54 nm) and spherical shape which refined size control of the nanoparticles compared to other methods. Singh, Nayak (69), produced ZnO NPs by laser ablation from a mixture of zinc, methanol, and deionized water solution with sizes of the particles range from 1 - 30 nm. Similarly, Mintcheva, Yamaguchi (70) reported the synthesis of laser-ablated rod-shaped ZnO NPs

with an average width of 30 nm and a length in the range 40 to 110 nm. Menazea and Ahmed (71), prepared Ag NPs using various liquid media, including distilled water, deionized water, tetrahydrofuran, and dimethylformamide. The study indicated that Ag NPs generated in deionized water had more significant ablation, antibacterial efficiency and stability than other media. Zhang, Gokce (72), employed laser beam irradiation with focused and unfocused laser beams at 12 and 900 mJ/cm², respectively. They showed that the diameter of the NP decreased with the reduction in laser wavelength, going from 29 - 12 nm.

The pulsed laser approach may also be utilized for synthesizing metal-organic frameworks (MOF) and inorganic metal complexes or the surface modification of nanomaterials, including nanoparticles coated with organic compounds that can be quickly produced using a single process (73). No by-products and hazardous agents are required for the process. Hence, the pulsed laser synthesis processes are ecologically favourable (54). Fig. 1 depicts this method.

Laser ablation industry is now undergoing fast change. The current advancement in the usage of new lasers with various modes of operation and wavelengths, as well as equipment, are leading to promising outcomes in terms of treatment selectivity, among other developing solutions and advances that are remarkable (74). Laser ablation is evolving into a viable surgical in the medical field (75). Its overarching objectives are to lessen the pain associated with particular cancers and to enhance outcomes (20).

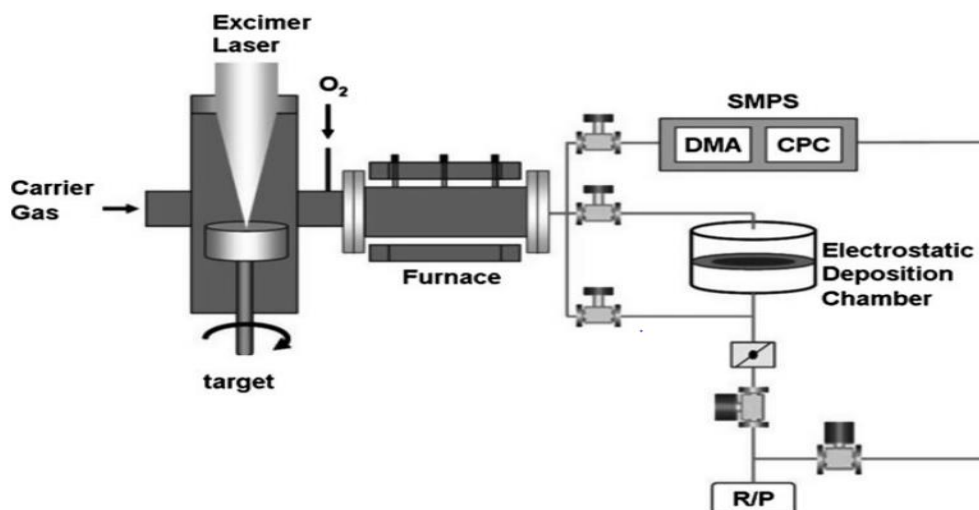


Figure 1: A picture of a laser system connected to a particle analyser (76).

2.1.2. Ball milling

Ball milling is a mechanical process used to generate nanoparticles (77). It started in 1970, and the technology is employed today mainly for ceramic, metallic, and nanoparticles (1). Its key benefits are connected to the cheap cost, the tiny size of particles created, the capacity to handle refractory materials and their purity since no chemical reagents or solvents are required (50). This approach involves

the application of a solid force to activate electrons from the material's crystals and electrons from the inner structure (78). High energy is released throughout the operation due to the velocity differential between the rotating balls and the grinding jars (63). The high temperature required to begin chemical synthesis will rise due to the frequent collisions depicted in Figure 2. This procedure produces nanoparticles or doped nanoparticles as a

result of the high temperature's crucial role in atom diffusion (79). The downsides of this approach include the potential for environmental or milling ball contamination and the creation of irregular-shaped NPs (1). Compared with a more significant temperature of 1000 °C, this approach can mill the material better (56). Different variables, including time, milling speed, process control agent, atmosphere, ball-to-powder ratio, temperature, and the size distribution, affect the quality of products produced by ball milling (80).

According to an earlier reported study, ball milling is also suitable for the environmentally friendly synthesis of silver, a process that has been extensively researched in recent years (56, 81). Nicolae-Maranciuc, Chicea (50), used silver nitrate in the presence of two naturally occurring compounds acting as reducing agents while using the ball milling procedure. Eggshell membranes and *Origanum vulgare L.* were added to the silver precursor solution as reducing agents. The results suggested that both biocompatible chemicals, with certain variations, might be employed as reducing agents in this procedure which are used to convert ionic species into atomic material which develops into NPs. The TEM analysis revealed that the particle diameters of *Origanum vulgare L.* are lower. The plant's optical and antibacterial characteristics seem superior to those of the eggshell membrane (82). Fine metal NPs were prepared using the high-energy

ball milling approach in an elevated shaker mill (68). Its primary benefit is the capacity to concurrently create enormous volumes of material (47). According to Abdullah, Bakar (83), a high-energy ball milling was employed to produce ZnO NPs with a mean particle size of 0.8 nm. Through milling, particles with ultimate sizes ranging from 200 to 400 nm were produced. Similarly, Raha and Ahmaruzzaman (84) developed a high-energy ball milling method to create rod-shaped ZnO NPs in the 20 – 90 nm range. A high-intensity ball milling process was adopted to generate ZnO NPs from ZnO microcrystalline powder by Prasad, Kumar (85). The samples were processed in a ball mill for 2, 20, and 50 h. According to the findings, the particle size varied over time. The duration of the ball milling process increases with decreasing particle size. Spherical ZnO-NPs with around 30 nm particle sizes were detected in the milled sample. Khayati (86), showed the production of Ag NPs graphite as a reducing agent utilizing a mill. The resulting Ag NPs had a size of 14 nm in the presence of process control agents. Alam and Hossain (87), synthesized rod-shaped ZnO NPs using a high-energy milling technique in the range of 20 to 90 nm. The higher the ball milling duration, the lesser the particle size. After 50 hours of milling, the material revealed spherically formed ZnO-NPs with particle sizes of roughly 30 nm. High-energy ball milling is a handy approach to generating nanosized particles. A typical example of ball mill is shown in Figure 2a & b.

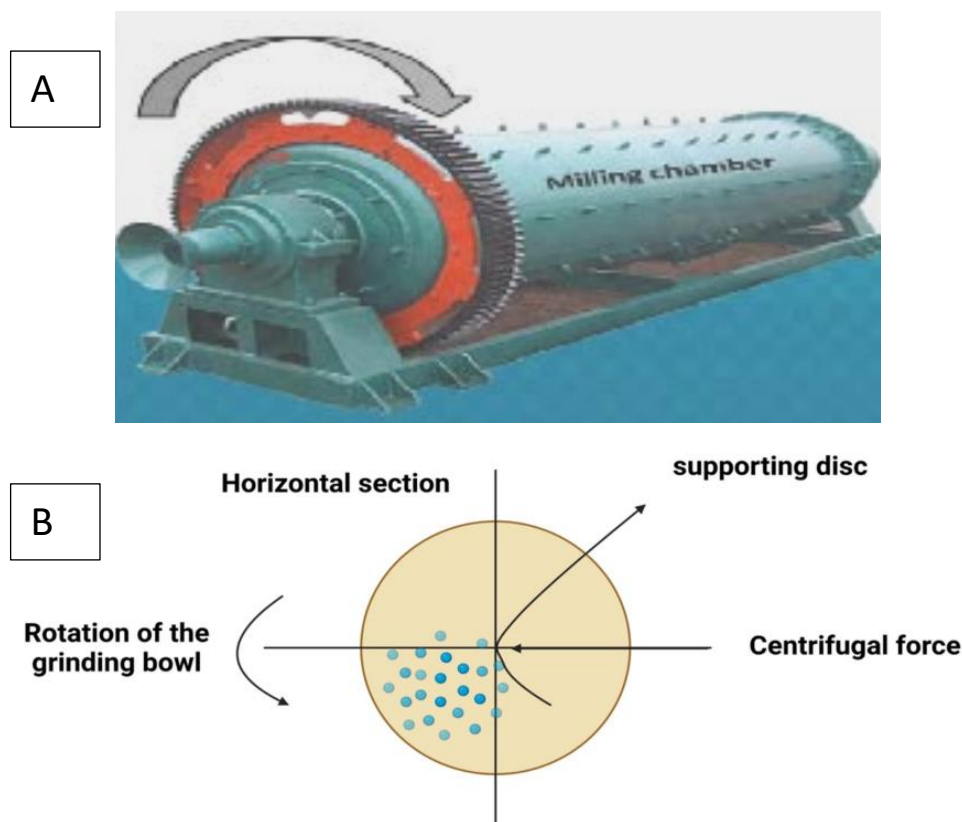


Figure 2: (a) A rock tumbler Ball mills (88), and (b) Illustration of the steps needed to create metallic nanoparticles using high-energy ball milling techniques (47).

2.1.3. Evaporation – Condensation

Evaporation-condensation can be used to synthesize NPs using an air pressure tube furnace/tiny ceramic heater (4). This approach is often used to generate

metal-based NPs. There are three primary phases in the evaporation-condensation process: (1) the material is sublimated or evaporated to produce a gaseous phase; (2) the substrate receives material

from the source via condensation, and (3) films or particles are generated by nucleation and subsequently followed by growth (89). Rapid cooling of the vapour results in significant concentrations of tiny NPs (90). Additionally, this approach requires a specified kilowatt of electricity from a standard furnace and a given time to attain a steady temperature (91). Radiation was utilized as a reducing agent in this process to produce NPs due to its ability to generate ionic species which further converted to atomic material for the production of NPs (92). This technique was used to assemble nanospheres from different metal components. The downsides of evaporation-condensation are the lengthy process time, and the huge amount of energy needed (93).

Sharma and Kumar (94), Evaporation- condensation process comprises heating of a combination of AgNO_3 and CH_3COONa in a tube furnace. This led to the liquid mixture being converted into a gas, which was then condensed into Ag-NPs after cooling. The produced Ag-NPs ranged from 3 - 50 nm. Ong and Nyam (95), used the inert gas helium to demonstrate the evaporation-condensation approach for synthesizing Ag NPs spherical Ag NPs of 9 to 32 nm, with few agglomerations, were formed at a lower inert gas pressure and evaporation temperature. A

ceramic heater with a maximum temperature of 1500 °C was used by Lee and Jun (96) to produce Ag-NPs using the evaporation-condensation method. Poly-dispersed Ag-NPs were produced from a heater surface with a constant temperature. The Ag-NPs generated were in the size range of 6.2 - 21.5 nm. Similarly, Hara, Fukuoka (97), produced Ag-NPs using temperatures ranging from 1300 to 1400 °C in a furnace, and the vapour was diluted with N_2 gas. Ag-NPs of 50, 90, and 130 nm were generated at various synthesis temperatures.

However, the synthesis of mainly metallic alloy NPs through evaporation-condensation in a tube furnace has some limitations. The tube furnace has a big volume, uses significant amount of energy to increase the temperature of the metal supply's environment, and has to be maintained for a longer time to retain its thermal stability (98). One of the most appealing nanomaterials for commercial uses is Ag-NPs (99). They have been widely employed in a variety of environmental applications, including textile coatings, food storage, anti-bacterial treatments in the health sector, and electronic goods (100). Ag-NPs were employed as anti-bacterial agents for a variety of purposes, including water treatment, cleaning and disinfection of medical equipment (101).

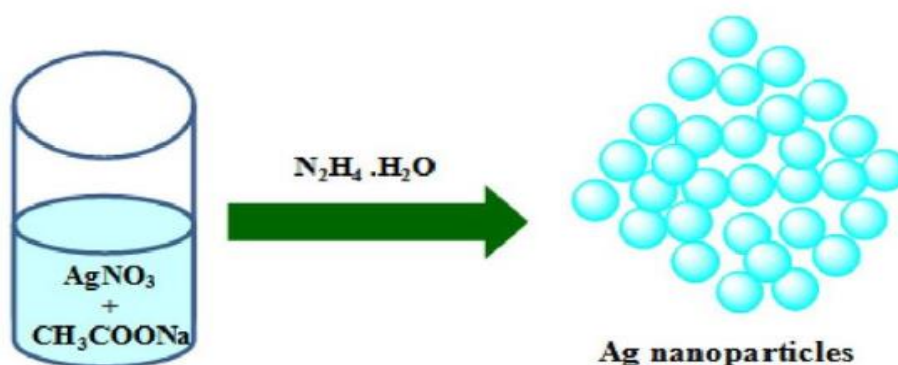


Figure 3: Synthesis of silver nanoparticles by evaporation-condensation method.

2.1.4. Arc discharge method

Due to its ease of apparatus setup and capacity for high production rate, the arc discharge technique has attracted much attention for producing nanoparticles (76). This approach has been used to successfully create a variety of nanoparticles. One of the most studied nanomaterials prepared with this process is carbon nanotubes (CNTs). In this method, a direct current (DC) arc discharge was utilized (102) (Figure 4). The process of producing carbon nano-tubes (CNTs) involves applying a current arc voltage across two graphite electrodes, which causes carbon to evaporate while a catalyst is immersed in an inert gas (103).

The arc discharge approach may be used to synthesize nanoparticles in either continuous or pulsed mode (104). High-purity graphite is employed as an electrode in the production of MWNTs and SWNTs, and arc discharge may be performed in

helium or hydrogen gas (105). The arc discharge technique needs vacuum equipment with an effective cooling system. Then the precursor is introduced and heated by the thermal plasma, which creates the ideal environment for the induction of processes that result in super-saturation and particle nucleation (40). It breaks down into radicals, atoms, and ions in the presence of thermal plasma to create an ionized gas at high temperature (106). The plasma arc's high temperatures and dense concentration of species cause a diffusion mechanism that quickly quenches gas species. This condense to form particles during this process after cooling down by combining with a cold gas or being enlarged by a nozzle (107).

Koushika, Shanmugavelayutham (108), created Fe_3O_4 -NPs from mild steel scrap via transferred arc plasma approach. Similarly, Si-NPs was created by using a radio-frequency thermal plasma technique to recycle silicon waste (Lee, Kim, (109)). Several

metals, alloys, and metal oxides NPs have been synthesized effectively using plasma methods (46). The composition, size, and shape of NPs may be readily adjusted by altering some parameters such as raw material composition, applied voltage and current, gas type and concentration within the reaction chamber, and reaction type (110). Helium, argon, nitrogen, air, and hydrogen are the most common gasses for producing thermal plasma (111).

Typically, experimental factors are changed to improve the arc discharge process, including

current/voltage, buffer gas, catalysts, carbon sources, electrode morphologies, external fields, etc. (112). In essence, the experimental parameters determine the plasma characteristics, the spatial distribution, and the nucleation and development of carbon in the space and time domains (113). In most situations, nanoparticles generated via the arc discharge process are exposed to high cooling rates. The homogeneity of the nanoparticles created using this process often degrades due to uneven cooling. Thus, regulating particle nucleation and development requires attention (114).

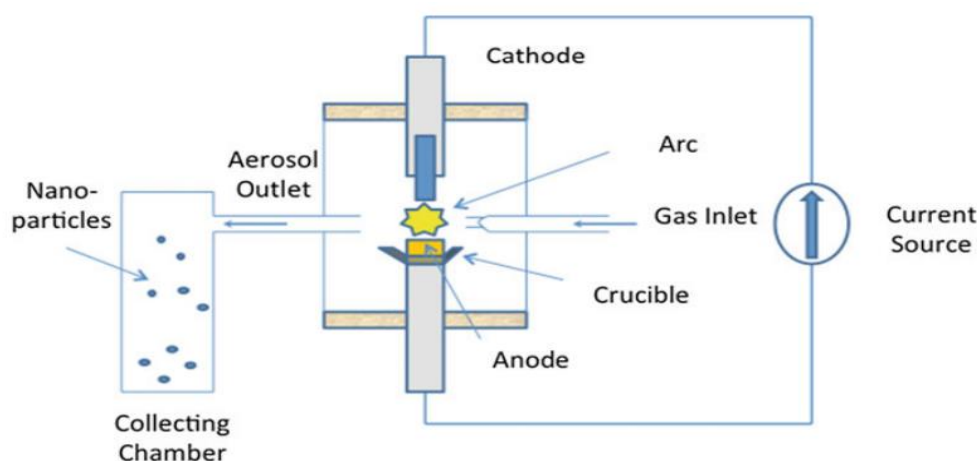


Figure 4: Schematic representation of the experimental configuration for arc discharge in gas chamber (115).

2.1.5. Sputtering

Sputtering involves depositing a thin layer of nanoparticles, which are formed through an annealing process (116). This approach is known as physical vapour deposition, and its efficiency is primarily determined by parameters such as layer thickness, temperature, substrate type, and annealing time (117). All these factors directly impact the nanoparticles' shapes and sizes (118). Ion sputtering is a physical process for depositing substrates that employ high-energy equipment and an ionized plasma (119, 120). The method relies on injecting argon gas, which when exposed to a powerful electric field creates a plasma inside the cavitate and causes the ions to move as an intensely focused ion beam from the anode to the cathode (49). In most circumstances, the concentrated ion beams are sputtered on a selected substance as an adhering film. Since this is a top-down method, a high vacuum is necessary in order to accelerate the gas ions and finish the deposition (121).

In order to better monitor the changes in single molecule analysis techniques like surface-enhanced Raman spectroscopy, López-Lorente, Picca (122), utilized ion beam sputtering to deposit nanocomposites using variable proportions of Ag and TiO_x/ZnO on silica surfaces (SERS). Three samples were created: an Ag- TiO_x composite made with two co-sputtering targets, Ag-NPs deposited on ZnO, and Ag-NPs deposited on TiO_x . The results of the study showed that the substrate's sensitivity can be

increased by adding silver and ceramics, allowing for the collection of more detailed information via vibrational spectroscopy. The samples made of Ag/ TiO_x increased the SERS while also functioning as photocatalytic materials. The study showed that, in addition to their antibacterial effects, Ag-NPs also possess exceptional chemistry and surface functionalization abilities; hence, using Ag-NPs as spectroscopic substrates is a feasible strategy for further research (50). Also, Zhao, Zhang (123), reported the preparation of Sn-NiO films via simple one-step magnetron sputtering process for a superior electrochromic performance. The amount of Sn in the Sn-NiO films was controlled by adjusting the sputtering power of the SnO_2 target. The optimized Sn-NiO film was used as an anodic electrochromic layer to prepare inorganic all solid-state electrochromic device (ECD) and the ECD displayed excellent electrochromic performance. The strategy of preparing NiO modified by Sn^{4+} ion presents an innovative direction to obtain high performance electrochromic materials for energy saving smart windows. Wang, Qu (124), reported the preparation of Cu-doped Ag thin films via magnetron co-sputtering method which was successfully fabricated on SiO_2 substrate. He discovered that the peak value of 36.8 dB is the highest shielding effectiveness at an optimal concentration of 2 mol%. This exceptional property make Cu-doped Ag films highly valuable and applicable for electromagnetic shielding in transparent windows which is as a result of Co-sputtering method.

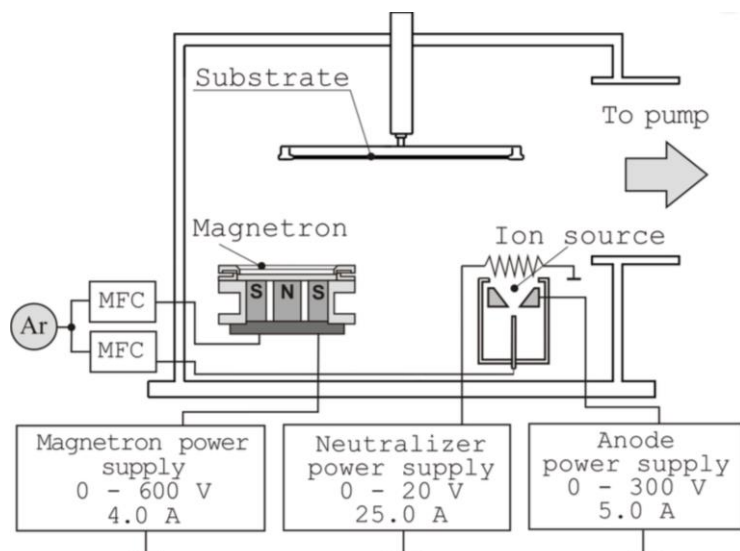


Figure 5: Schematic representation of the experimental configuration for sputtering (124).

2.2. Biological Methods of Synthesizing Nanomaterials

Green synthesis of nanoparticles by various physiochemical processes necessitates considerable energy consumption, harsh reaction conditions, costs, and the usage of harmful substances (125). Synthetic ways of producing nanoparticles also generates some hazardous by-products that are harmful to the environment and living things (126). Biological synthesis commonly referred to as "green synthesis", is an alternative route to the production of nanoparticles. Green synthesis of nanoparticles is a new topic in nanoscience that includes the efficient preparation of functional nanoparticles utilizing plant extracts, bacteria, and fungi (127). Biological pathways are beneficial in various fields since they are simple, safe, biocompatible, and harmless to living things and the environment (128, 129). The green synthesis process is not only dependable, economical, and time-saving, but it also reduces the creation of hazardous waste (130, 131). The green strategy for the synthesis of nanoparticles is the preferable technology since it does not involve significant energy consumption, such as high pressure or temperature. In contrast to the other synthesis methods, it employs moderate reaction conditions and nontoxic precursors (132).

The use of plants and microorganisms to synthesize metal nanoparticles has excited lots of research interests (133, 134). Numerous metallic nanoparticles have recently been created using a green method and are widely employed in the pharmaceutical and biological industries (135). However, biologically synthesized nanoparticles play an essential role in the environmental and biomedical domains due to their high yield, enhanced stability, excellent biocompatibility, and lower bio-toxicity (136). Furthermore, as interest in sustainable development grows, so does interest in biological synthesis, since it conserves raw resources and decreases the use of dangerous chemicals (137). Plant components such as seeds, leaves, peels, fruits, and flowers are high in phytochemicals including terpenoids, phenols, etc which function as reducing agents (137-140). The production of NPs by

microorganisms and plants has several benefits, including mono-dispersity, the absence of harmful compounds, effective, fast, and eco-friendly process (1). The synthesis of NPs depends critically on factors like pH, incubation period, and temperature (141). Metal-alloy NPs (MNP), which were generated biologically, showed superior biocompatibility than metal alloy NPs manufactured using diverse physicochemical approaches (142). Biologically produced MNPs have been widely employed to address difficulties or to boost process efficiency in industries and biomedical sciences (143-145).

2.2.1. Green synthesis using microorganism

Microbes offer enormous potentials for producing ecologically friendly metallic nanoparticles (MNPs) without the need for traditional physical or chemical methods (146). Microbes are everywhere, and they may swiftly adapt to their surroundings and develop tolerance to hazardous metals (147). Enzymes in physiological and biological functions enable microorganisms to create metallic alloy NPs. The proteins, enzymes, and functional groups are all known for their ability to decrease ions (148). Two fundamental strategies underlie microbial resistance to hazardous metals. Nanoparticles (NPs) may be produced by microbes both intracellularly and extracellularly. Microbes may generate materials of various sizes and morphologies at the nanoscale by bio-mineralizing inorganic minerals intracellularly or extracellularly (147, 149). The transfer of metal ions into the microorganism causes the intracellular synthesis of metallic alloy NPs (137). In contrast, the extracellular approach also involves the metal ion concentration at the cell surface (150). In a nutshell, for the extracellular approach, the specific microorganism is cultivated for 1-2 days in a rotary shaker, the biomass is separated through centrifugation, while the supernatant is collected (50). MNPs are created by combining a specific ratio of cell-free culture supernatant and filter-sterilized metallic salt solution, then incubating the mixture at the ideal temperature (151, 152).

In contrast to generated intracellular MNPs, the microbial biomass is centrifuged and thoroughly

washed with sterile water (125). The biomass is then dissolved in a metallic salt solution that has been sterilized. The combination is incubated as a visible colour change is monitored (153). The biomass is removed by centrifugation after several cycles of sonication, and the produced MNPs are then quantified using a UV spectrophotometer (145, 154). The microbial cell wall/membrane is broken down by ultrasonication, allowing the MNPs to exit the cell (142). Because it does not need the same processing steps as intracellular production and recovery of MNPs, such as centrifugation, sonication, and washing, extracellular synthesis of MNPs is regarded as a low-cost, fast, and scalable technique (155). Diverse fungal metabolites with improved oxidation/reduction potential and increased bioaccumulation potential have been used to study the mycosynthesis of MNPs using simple, environmentally safe methods (156). Three different phenomena, including electron shuttle quinones, nitrate reductase activity, and their interactions, have been characterized for the myco-mediated generation of MNPs (157). For the production of various MNPs, many enzymes have been identified, including NADPH-dependent reductases in the case of *Fusariumoxysporum* and nitrate reductase in the case of *Penicillium sp* (59). Few studies have demonstrated how *actinomycetes* contribute to the development of MNPs (158). *Actinomycetes* have the

potential to be used in the synthesis of stable, mono-dispersed MNPs, but further studies are needed (159).

Kalpna and Devi Rajeswari (149), synthesized ZnO NPs from Vitexnegundo plant extract using zinc nitrate hexahydrate as a precursor. Bio-synthesised ZnO nanoparticles with size of 40.5-20.8 nm exhibited antibacterial properties against *Staphylococcus aureus* and *Escherichia coli*. Undabarrena, Ugalde (160) reported that the reductase enzyme from *Streptomyces sp.* has been used to synthesize zinc with 11.84-24.82 nm size, copper with 6.93 nm size, and silver NPs with 5.62 nm size and MNPs. Yeast has been utilized to synthesize MNPs by downstream techniques AbdelRahim, Mahmoud (161). Capsids of genetically modified viruses has also been utilized as bio-templates to create titanium nanostructures and quantum dot nano-wires (156, 157). Semiconductor nanoparticles have also been synthesized by using some biological molecules including polyphosphates, amino acids, and fatty acids as templates. Other biological techniques for green nanostructure synthesis include protein cages (162), DNA (163), bio-lipid cylinders (164), multi-cellular superstructures (165), and viroid capsules (166), which have been used for template-mediated MNP production (167). This process is represented in Fig. 6.



Figure 6: Green synthesis of nanoparticles by various microorganisms (168).

2.2.2. Green synthesis using plants

Plants contain a variety of molecular functions, naturally occurring compounds, secondary metabolites, or phytochemicals, which may be exploited as efficient biological factories to deal with environmental toxins caused by industrial wastes (169). Synthesis via the use of plant extracts allow a considerably easier approach to creating nanoparticles in more significant quantities than microbe-mediated synthesis (15). The solvent, pressure, temperature, and pH conditions in green synthesis approaches are all essential considerations (150). Numerous plant extracts, particularly those from the leaves, have been thoroughly studied for NPs production because they contain a variety of useful phyto-chemicals like flavones, terpenoids, ketones, phenols, amides, aldehydes, carboxylic

acids, and ascorbic acids (1). These bio-molecules can transform metal salts into metal nanoparticles, which have been explored for diagnostic and anti-microbial applications (170).

Plants also offer several potential uses in biomedicine due to the presence of biologically active substances such as flavonoids, alkaloids, terpenoids, saponins, polyphenols, co-enzymes, carbohydrates, vitamins and proteins (171). In Ayurvedic, Thai, and Chinese traditional medicine, plants have been extensively used to treat various illnesses, including skin conditions, rheumatism, venereal infections, and beriberi (169). The biological effects of plants have been found to include antimycotic, antibacterial, antiviral, free radical scavenging, anticancer, and anti-inflammatory properties (172).

Therefore, a replacement option for producing nanoparticles is by employing plants and their components. Because they are non-toxic, naturally capable of capping ends, reduce metal ions, and can accumulate heavy metals in their cells. Synthesis of nanoparticles with plants involves a simple, energy-free, quick, and affordable approach (173). Nanoparticles produced from plants or their components have the requisite size and form, are non-toxic, biocompatible, stable, have enhanced activity, and have a solid capacity to penetrate (174). Plant and its component include numerous biochemicals that play a vital role in reducing, capping and stabilizing metal ions to nanoparticles (135, 175). Recently, scientists have been focusing on plants to biosynthesize biocompatible nanoparticles. Secondary plant metabolites may play a vital and critical function as reducers, and stabilizing agents for biosynthesizing nanoparticles (150).

Additionally, phytochemicals' surface adsorption results in biocompatible nanoparticles' formation (176). Instead of using nanoparticles that are produced routinely, they might additionally improve the biological properties of nanoparticles. The use of plants in the synthesis of nanoparticles offers a number of advantages since it are dependable, simple, economical, easy to scale up, and ecologically friendly (177). Plants are also preferable to microbial synthesis methods for the green production of nanoparticles since they need less

time, are safe, and do not require complex laboratory infrastructure (178).

Ijaz, Shahid (179), reported the fabrication of CuO-NPs using *Abutilon indicum* leaves aqueous extract and described A one-port synthesis of ZnO and Cu-doped ZnO nanoparticles using aqueous leaf extracts of *Abutilon indicum* and *Clerodendrum infortunatum* has been described Khan and Lee (180). Several components, including fruits, leaves, fruit peels, roots, and seeds, have been used to prepare Au nanoparticle, Ag nanoparticle, Pd nanoparticle, Pd/Fe₃O₄ nanoparticle, and Pd/CuO nanoparticle, respectively (127). The initial stage in producing nanoparticles by plants is collecting desirable plant parts, such as leaves, fruits, and roots followed by cleaning and drying as shown in Figure 7. The dried material is then grinded and heated for an extended period at the ideal temperature. Plant solid waste is filtered using plant extract. Metal salt solution and aqueous plant extract are heated at optimal temperature conditions. The nanoparticle synthesis production may be determined by visual examination (130, 181). Plants produce nanoparticles by reducing metal ions into NPs through redox reactions such as the enol-to-keto-transformation, which are electron-rich phytochemical molecular functions found in sugars, polyphenols, and flavonoids in plant extract (182, 183). Saponins, alkaloids, terpenoids, co-enzymes, and proteins in plant extracts capped and stabilized the nanoparticles (180).

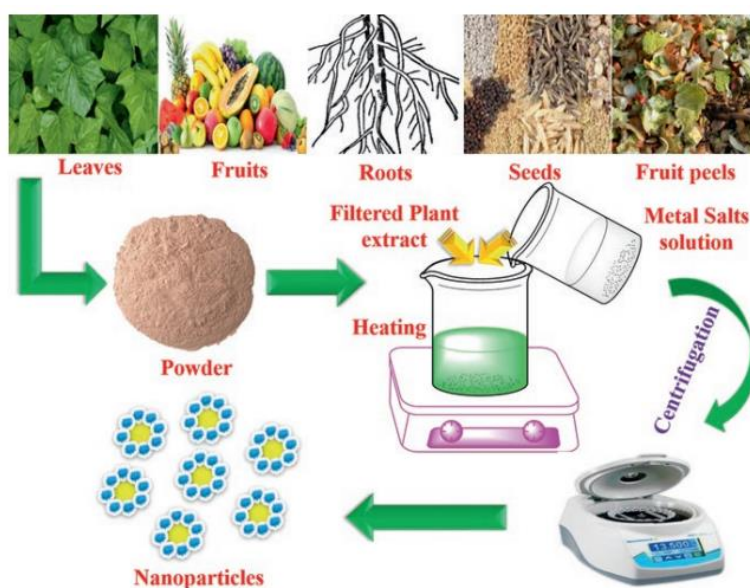


Figure 7: Green nanoparticle synthesis using various plant components, such as leaves, fruits peel, fruits, roots, and seeds (180).

2.3. Chemical Methods of Synthesis of Various Nanoparticles

This section detailed numerous chemical techniques for the preparation of various nanomaterials. This highlights the significance and comparative merit of one strategy over the others.

2.3.1. Hydrothermal method

This method involves preparing nanoparticles in an aqueous medium under high temperature and pressure. Different studies have examined the use of hydrothermal method to prepare various nanoparticles, including titanium oxide and graphene oxide among others (184). Even while hydrothermal technology is regarded as cost-effective and environmentally beneficial, it frequently involves high temperatures (185). An autoclave has a temperature range of 160 to 180 °C (87). However, there are several limitations, such as the inability to

clearly see the crystal material growing in autoclave and the expensive nature of the equipment. When the temperature in the autoclave exceeds the boiling point of water, the pressure reaches saturation with vapour. The autoclave's temperature and the volume of solution supplied directly affect how much internal pressure is generated (186). Synthesis of zinc oxide was reported by Bulcha, Leta Tesfaye (187) which was synthesized using hydrothermal method. He reported successful production of zinc oxide

synthesis. Jubeer, Manthrammel (188), also reported the synthesis of ZnS nanoparticle through the hydrothermal method which was found successful. Chen, Liu (189) and Khan, Usman (190) synthesis Ce-doped SnO₂ hollow spheres and CuAl₂O₄/rGO nanocomposites respectively using one-pot hydrothermal method and from there finding the synthesis was successful. Figure 8 is an example of hydrothermal synthesis method of nanoparticle showing the synthesis of GO nanoparticle.

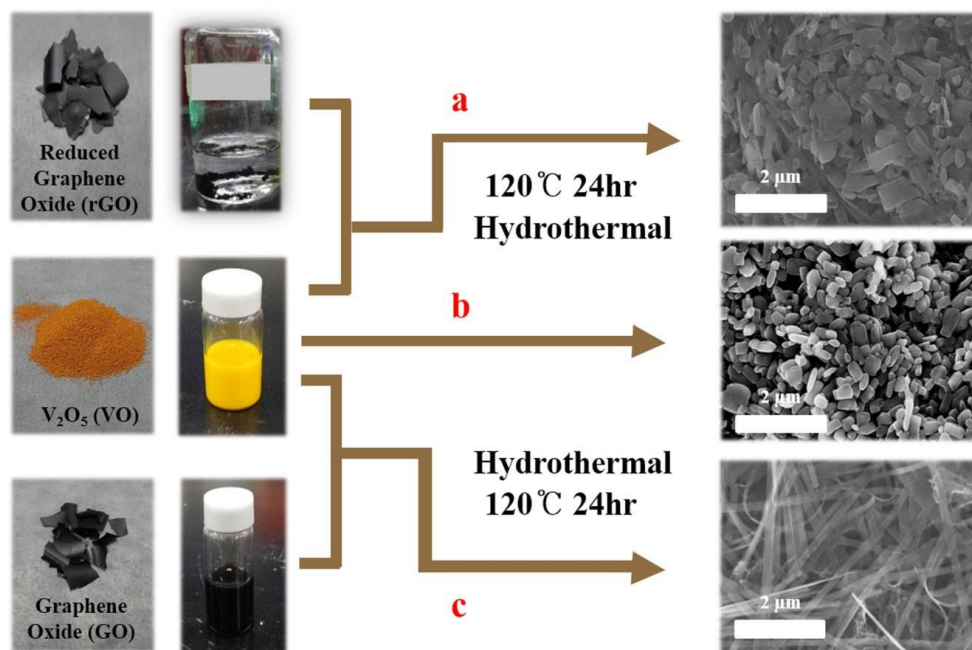


Figure 8: Synthesis of GO nanoparticle using Hydrothermal Method (24).

2.3.2. Solvothermal method

This method involves the application of non-aqueous solution (precursor and non-aqueous solvent) at high temperature and pressure to produce various nanoparticles. Both synthesis in alkaline environments and in the presence of organic molecule precursors fall under the solvo-thermal technology which involves the reaction between precursor(s) in a solvent in a close system (191). The use of a solvothermal method to create nanoparticles offers a number of benefits, including economical, and releasing nearly no by-products throughout the reaction (192). For instance, Perumal, MonikandaPrabu (193), demonstrated a solvothermal method for producing TiO₂ nanoparticles, using toluene and titanium tetra isopropoxide as the solvent. The solution underwent thermal treatment in a stainless steel autoclave at 250 °C for 5 hours at a rate of 20 °C/min, followed by two hours of calcinations at 550 °C. The XRD measurement showed the synthesis of pure anatase TiO₂ nanoparticles with a particle size of 20 nm, in contrast to the SEM images that showed particles with irregular shapes and an average size in the range of 7–14 nm. Similarly, ammonium citratoperotitanate and polyvinyl alcohol (PVA) were

used to create anatase TiO₂ nanoparticles Uematsu, Baba (194). The PVA was mixed with the titanium precursor, which was then micro-waved to evaporation. Kløve, Philippot (195), reported the synthesis of pure-phase tetragonal ZrO₂ nanoparticle via simple solvothermal synthesis. Different types of Alcohol were used for condition variation as solvent and studies using in-situ scattering. The variation of tetragonal or monoclinic phase ratios within the produced powders was directly correlated with the amount of in-situ generated water from solvent dehydration during the syntheses. Zhang, Feng (196), reported the synthesis of hollow CoS_x@CdS polyhedron constructed by ZIF-67 via one-pot solvothermal route. It was discovered that the photocurrent responses of the CoS_x@CdS-modified ITO electrodes could be specifically turned on by Hg²⁺, in contrast to these of the CoS_x or CdS-modified ones showing no significant Hg²⁺ induced photocurrent. Under visible light irradiation, herein, the synergetic combination of CoS_x and CdS components could improve the carriers transferring of photoelectrochemical system. Figure 9 summarized solvothermal synthesis method of nanoparticles.



Figure 9: Synthesis of Nanoparticle using Solvothermal Method (24).

2.3.3. Co-precipitation Method

This entails the co-precipitation of metal cations from several sources, including hydroxides, citrates, carbonates, and oxalates (197). At the suitable temperature, these precipitates are transformed into powders because the demerit of this method is that product co-precipitates with unwanted contaminants as well as the analyte (198). By producing inclusion and occlusion (when a contaminant generates a frame site in the transporter's crystal structure, which is about a crystallographic fault), re-precipitating the analyte can correct this imperfection (when an adsorbed contamination becomes physically surrounded inside the crystal) Priyadharshini, Shobika (199), Nickel ferrite nanoparticles was prepared using the co-precipitation process with starting materials such as;

$\text{Ni}(\text{NO}_3)_2 \cdot 6\text{H}_2\text{O}$ and $\text{Fe}(\text{NO}_3)_3 \cdot 9\text{H}_2\text{O}$ before annealing the samples at various temperatures (500 °C, 700 °C, and 900 °C). According to the XRD study, a highly crystalline ferrite phase was formed, with average crystallite sizes ranging from 9 to 21 nm, depending on the annealing temperature. Priyadharshini, Shobika (199), also used a co-precipitation technique to create NiFe_2O_4 nanoparticles. The creation of the cubic spinal phase of NiFe_2O_4 was confirmed by XRD analysis, and SEM analysis revealed the formation of spherical particles with an average particle size of 28 nm. Although this approach is difficult and expensive, co-precipitation produces nanoparticles whose shapes are unpredictable, necessitating more deliberate efforts to achieve the desired particle size and form. Figure 10 presents the synthesis procedure.

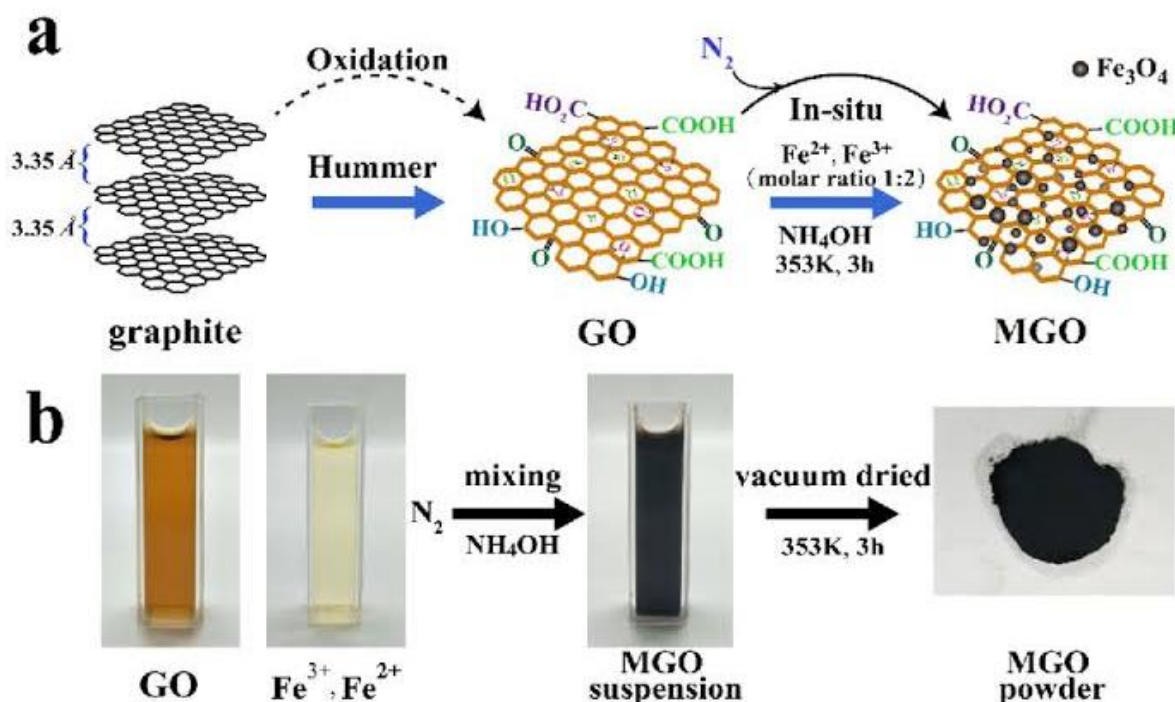


Figure 10: Synthesis of Nanoparticle using Co-precipitation Method (197).

2.3.4. Sol-gel method

This is a straightforward and affordable wet-chemical approach used to create composite materials with exceptional control over size. With this method, the solution (sol) progressively develops into a gel-like substance that is composed of both liquid and solid

phase (18, 200). Non-aqueous and aqueous sol-gel syntheses are the two types of sol-gel methods. The initial stage in creating a rational synthesis for non-aqueous sol-gel creation of metal oxide nanoparticles is to elaborate the chemical formation mechanism alongside investigations on the crystallization process (201). However, in order to verify that this technique yields comprehensive results, it is

necessary to explore many characterizations qualities, including crystallographic and microscopy.

In contrast, the hydrolysis of metal alkoxides occurs very fast in aqueous conditions when using the sol-gel method, complicating the ability to control reaction rate. When using the non-aqueous sol-gel approach, the carbon-oxygen bond may be applied with moderate reactivity at a low reaction temperature, which causes the nanoparticle to have a high crystallinity. The right solvent must be selected because it has a significant impact on how nanoparticles develop. For instance, Ahmed, Aly (202), used the sol gel approach to create titanium dioxide (TiO_2) nanoparticles by combining ethanol and titanium chloride (TiCl_4). The created TiO_2 nanoparticles were calcined for two hours at various temperatures between 200 and 800 °C. Up to 400

°C, these materials demonstrated good thermal resilience.

Polyacrylic acid (PAA) was used as a chelating agent in the sol-gel process to create spinel nickel ferrite nanoparticles. NiFe_2O_4 nanoparticles' size, specific surface area, and crystallinity were all influenced by the molar ratios of PAA to total metal ions and the calcination temperature (203). Using glycine gels made from metal nitrate and glycine solutions, Liu, Guo (204), adapted the sol-gel combustion process to create ultrafine barium ferrite ($\text{BaFe}_{12}\text{O}_{19}$) nanoparticles with sizes ranging from 55 to 110 nm. Furthermore, Zakir, Iqbal (205), used the sol-gel auto combustion approach to create spinel nickel ferrite (NiFe_2O_4) nanoparticles. Figure 11 summarized sol-gel synthesis method of nanoparticle.

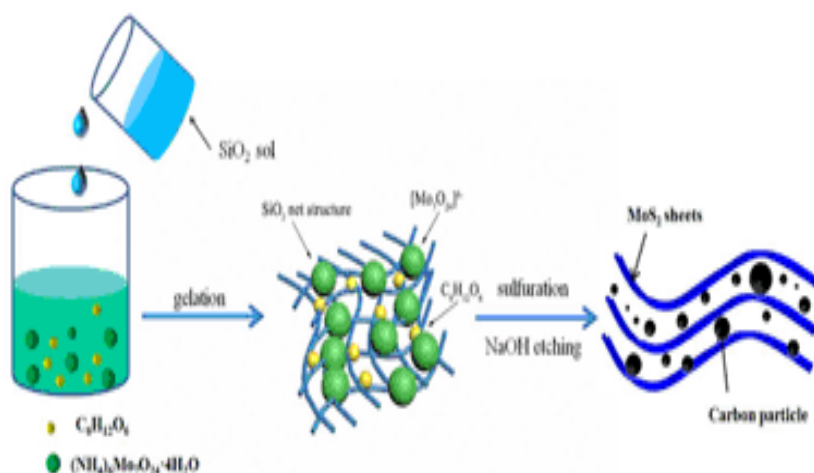


Figure 11: Synthesis of nanoparticles using Sol-gel Method (200).

2.3.5. Solution mixing method

The fundamental method for mixing solutions is in a solvent system. This method uses electrospinning to combine two distinct nanoparticles in a solution. Since there is no chemical connection between the new substance and the base, the main disadvantage is the potential leaching of the added material. For instance, the synthesis of Zinc doped Iron oxide/GO/Polymer ternary nanocomposites using solution mixing approach was explored by Suneetha, Selvi (206). The impedance study showed that the modified electrode made of nanoparticle had an excellent capacitance with a bond phase angle of 87° and was a promising candidate for use in super

capacitors. Zeng, Teng (207), used ultrasonic techniques to create Al-graphene oxide composites, and they discovered that the materials had a 255 MPa tensile strength. The creation of graphene oxide metal oxide/metal nanocomposites has been shown to improve mechanical qualities and address a variety of energy and environmental-related problems. An effective method for producing graphene- TiO_2 nanomaterials by photocatalyzing the reduction of graphene oxide in solution has been reported Nawaz, Moztahida (208), Figure 12 depicts a simplified solution mixing synthesis process for nanoparticles.

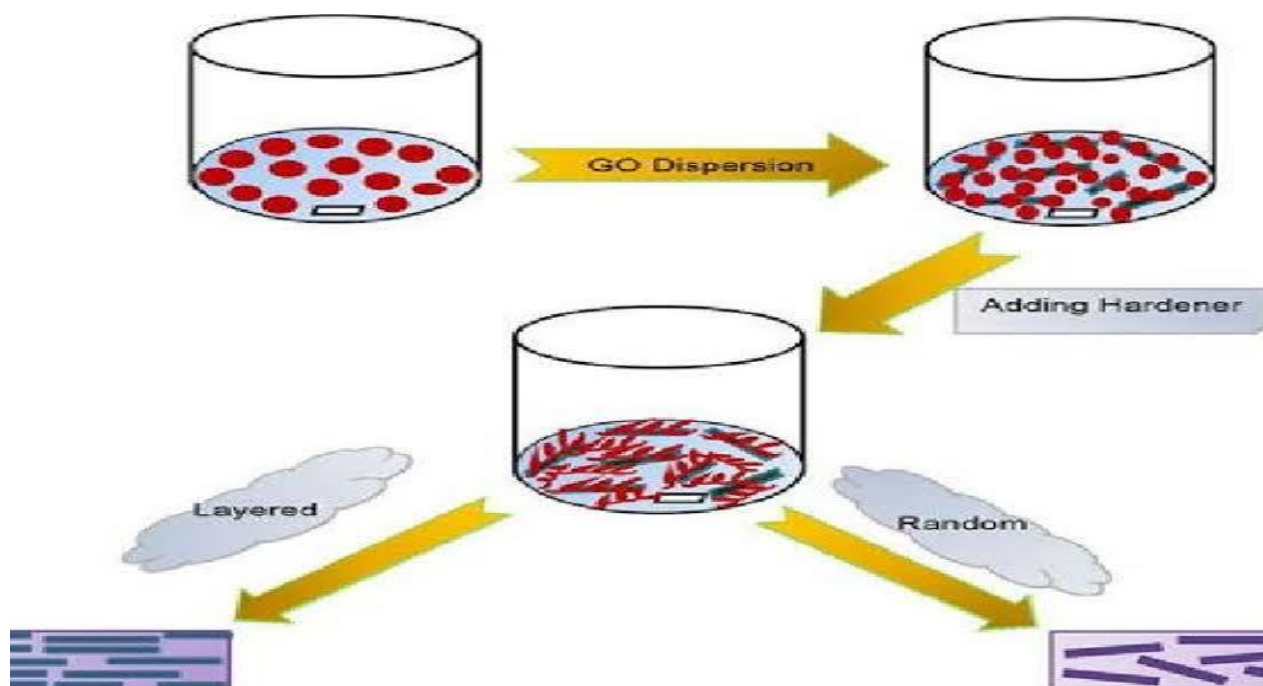


Figure 12: Synthesis of GO nanoparticles using Solution Mixing Method (208).

2.3.6. Chemical vapour deposition (CVD)

Chemical vapour deposition (CVD) is a method which involves the deposition of solid materials from a chemical reaction through the production of vapour or vicinity of a normally heated substrate surface. This is an example of vapour-solid reaction which is normally used in the production of thin films in the semiconductor industry. In this method, vapour phase precursors are brought into a hot wall reactor under conditions that favour nucleation of particles in the vapour phase rather than deposition of a film on the wall. It is called chemical vapour synthesis or chemical vapour condensation in analogy to the chemical vapour deposition processes used to deposit thin solid films on surfaces. This method has tremendous flexibility in producing a wide range of materials. Hong, Liu (209), reported the synthesis of

layered two-dimensional MoSi_2N_4 material via chemical vapour deposition. The monolayer was built up by septuple atomic layers of N-Si-N-Mo-N-Si-N which can be viewed as a MoN_2 layer sandwiched between two Si-N bilayers. Xu, Zhang (210), reported the synthesis of graphene on thin metal films using chemical vapour deposition which was successfully produced. Thin metal films are usually made by depositing metals on various substrates such as single-crystal sapphire which serves as catalytic substrates for high quality graphene growth. Table 1 is the summary of different synthesis routes to nanoparticles such as chemical, physical, and biological for different applications, such as optical communication, membrane, adsorbents, sensor, electronic, and antimicrobial.

Table 1: Overview on the synthesis of different nanomaterials.

Nanomaterials	Synthesis routes	Synthesis methods	Applications	Ref.
Aramid	Chemical	In-situ	Membrane	(211)
Rubidium chloride doped magnesium oxide	Chemical	Green	Optical communication	(212)
Polyacrylamide hydrogels	Physical	Thermal	Membrane	(213)
Hyperbranched polyethyleneimine	Chemical	Facile	Adsorbent	(214)
Ru-poly(amindoamine)	Chemical	Ionic liquid	Electronic	(215)
MXenes	Chemical	Triple carbides and nitrides MAX	Membrane	(216)
Amine functionalized mesoporous silica	Chemical	Etching and polymerization	Adsorbent	(217)
Carbon dots-based covalent	Chemical	Schiff-base reaction	Food additive and adsorbent	(218)
ZnO	Physical Chemical	Carbon microspheres	Sensor and adsorbent	(219)
Graphite flakes and carbon-based nanomaterials	Physical	Thermal	-	(220)
In_2O_3	Physical	Hydrothermal and calcination	Sensor	(221)
$\text{TiO}_2/\text{WO}_{3-x}$ hybrid	Chemical	Ethanoic acid	Nanowire	(222)

Nanomaterials	Synthesis routes	Synthesis methods	Applications	Ref.
Tungsten oxide	Physical Chemical	Hydrothermal and Dissolution	Electronic	(223)
One-dimensional α -MoO ₃	Physical	Hydrothermal	Sensor	(224)
BaLa ₂ ZnO ₅ :Dy ³⁺	Physical	Dissolution and thermal processes	Solar cell	(225)
Nano-Fe ₃ O ₄ @TiO ₂ -Pr-2AB@Cu	Chemical	Coprecipitation	Cosmetic	(226)
Ag/ZnO	Chemical	Facile	Antibacterial	(227)
CoNi ₂ S ₄	Physical Chemical	Dissolution and calcination	Adsorbent	(228)
MgFe ₂ O ₄	Physical	Microwave solution combustion	Dye degrader	(229)
Pd-dopedCeO ₂	Physical	Hydrothermal	Sensor	(230)
Ba ₂ YAlO ₅ :Dy ³⁺	Physical	Propellant combustion	Electronic	(231)
AgNPs	Biological Chemical	Plant extraction	Antimicrobial	(232)
CNMs	Physical Chemical	Surface activation and heating	Membrane	(233)
Sn-SnO ₂ -C	Physical	Monte-Carlo reaction	Electronic	(234)
MoO _x /Nb ₂ O ₅	Physical	Calcination	Medical	(235)
GO-MgO	Biological	Plant extraction	Adsorbent	(236)
Silica nanoparticles, graphene nanosheets and graphene oxide nanosheets	Physical	Ambient fiery and furnace	Medical	(237)
TiO ₂ /Ag	Chemical	Sterilization and purification	Electronic	(238)
Mg(OH) ₂	Biological	Seaweed extraction	Anti- mycobacterial	(239)
Tris(selenobenzoato)antimony(III), tris(selenobenzoato)bismuth(III) and bis(selenobenzoato)dibutyltin(IV)	Chemical	One pot process	Electronic	(240)
NaBH ₄ and FeCl ₃ ·6H ₂ O	Chemical	In-situ	Algae harvesting	(241)
Metal ion dopedZnO	Physical	Combustion	Adsorbent	(242)
Porous TiO ₂	Biological	Biomass assistance	Electronic	(243)
CaO	Biological Physical	Fruit extraction and furnace	Antimicrobial	(244)
Bimetallic Cu-Ni hybrid	Biological Chemical	Plant extraction and dissolution	Antimicrobial	(245)
α -MnS	Chemical	Dissolution	Electronic	(246)
Ca ₃ MgAl ₁₀ O ₁₇	Chemical	Facile	Sensor	(247)
SWCNT-hybrid	Chemical	Subphthalocyanine substitution	Electronic	(248)
FeFe ₂ O ₄	Chemical	Facile	Adsorbent	(249)
Biogenicgold	Chemical	Dissolution	Electronic	(250)
Zn-F co-dopedTiO ₂	Physical	Sol-gel and coprecipitation	Electronic	(251)
2-methyl-6-nitroquinoline	Chemical	Cyclization reaction	Medical	(252)
CuFe ₂ O ₄	Biological	Waste eggshell extraction	Adsorbent and antibacterial	(253)
ZnO _x S _{1-x}	Chemical	Facile	Adsorbent	(254)
Zn _x Fe _{3-x} O ₄ redox	Chemical	Dissolution	Adsorbent	(255)
Gd doped α -Sb ₂ O ₄	Physical	Washing and calcinations	Electronic	(256)

3. METHODOLOGY

Scopus Database was chosen for data collection of the current study primarily due to the broad range of data covered, in-depth coverage of various publications (especially with regard to citation by source), and the system that ensures rigorous peer review(257). The data were searched and collated on the 30th December, 2022, with the search scope being inclusive of all sorts of articles available in the WoS database to ensure that the current study covered all potentially relevant publications. Important search terms were encapsulated in double quote marks to produce the best results, and related terms were split using the OR operator to produce a wider range of results. Examples of keywords include Title-ABS-KEY [synthesis AND nanoparticle] and Title-ABS-KEY [synthesis AND nanoparticle]. As an alternative, TITLE-ABS-KEY [nanomaterial] and TITLE-ABS-KEY [synthesis] were chosen to search for recent papers between 2010 and 2023, which will ultimately help recognize and study various research topics with a higher number of publications.

The WoS website also generated citation statistics so users could see the year-by-year trend of documents published and the frequency with which they were cited. In order to determine the quantity of publications relative to various authors, nations, affiliations, research areas, publishers, and journals, the WoS website was also examined. Lastly, the downloaded data were imported into the VOSviewer 1.6.18.0 programme to plot co-occurrence maps of author keywords used in the articles as well as

network maps showing relationships between authors and nations.

In order to create network maps with respect to various parameters such as author, citation, organization, country, and keyword co-occurrence, Ludo Waltman and Nees Jan van Eck created the free-to-use scientometric programme VOS viewer (Visualisation of Similarities). The dataset was also sorted using the three metrics of total link strength, document count, and citation count using the VOSviewer software. According to the data, a frame's dominance in network maps increases with frame size, and a frame's networking power increases with the number of lines that originate from it (a line serves as a connection between two frames). When it comes to keyword co-occurrence maps, the larger the frame size, the more frequently a keyword is used. Various applications were assessed by examining the most recent, pertinent, and highly referenced publications found on the WoS website, in addition to the various network mapping and trend studies, and mechanistic insights were presented for each nanoparticle synthesis.

4. RESULTS AND DISCUSSION

4.1. Primary Details and Publication Patterns

117,162 publications of the total documents from more than 15,568 sources had more than 19000 keywords in addition to the author's own keywords with an average of 15 citations per document and more than 2000 authors. In Figure 13, the analyzed papers span the period of January 2010 to December 2022, indicating that research is progressing to improve synthesis of different nanoparticles.

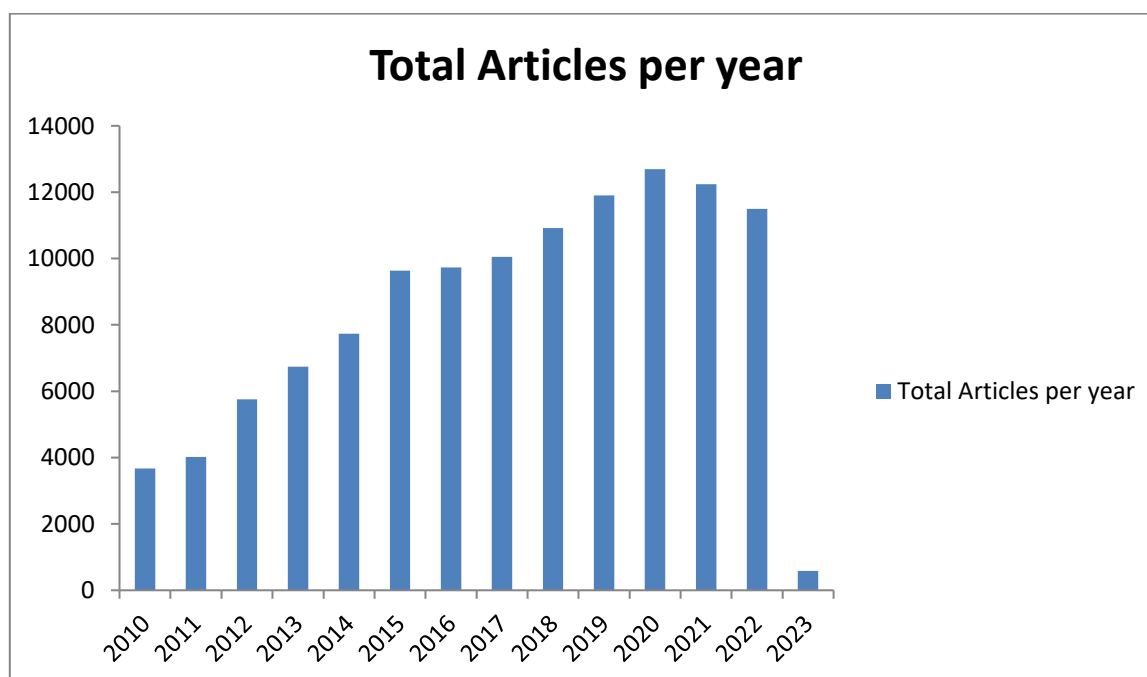


Figure 13: General patterns of the publications per year.

Between 2007 and 2020, the overall number of annual publications grew gradually. The chart, however, demonstrates that following the available information on Scopus whereby there was low publication between 1985 and 2009. The lack of

research papers during those years can be linked to a lack of understanding of the application of nanotechnology which ultimately led to an increase in publication output starting in 2010. With 12,691 and 12,237 documents for 2020 and 2021

respectively reported the largest publication production. The reason why 2020 was the largest yearly publication was because researchers concentrate much on research due to Covid-19 pandemics lockdown.

4.2. Performance of Various Journals

About 111,553 journals in total have published studies on the synthesis of nanoparticles. Table 2 highlights the h-index and other performance metrics-based lists of the 20 most relevant journals.

The top 20 journals generated more than 25 % of the total papers related to synthesis of nanoparticles over the course of the 13 years, indicating both a widespread distribution of these publications and a general interest in these devices. 2638, 2138, 1712, 1599 and 1577 articles are the five most prominent journals by total number of publications (TNP) are RSC Advances, Journal of Colloid and Interface Science, Journal of Nanoparticle Research, ACS Applied Materials and Interfaces and chemical Communication respectively.

Table 2: Top 20 most published Journals.

Rank	Sources	Documents	IF
1	RSC Advances	2628	4.036
2	Journal of Colloid and Interface Science	2138	9.965
3	Journal of Nanoparticle Research	1712	2.533
4	ACS Applied Materials and Interfaces	1599	10.383
5	Chemical Communications	1577	6.065
6	New Journal of Chemistry	1574	3.925
7	Journal of Alloys and Compounds	1551	6.371
8	Colloids and Surfaces A Physicochemical And Engineering Aspects	1507	5.518
9	Journal of Materials Science Materials in Electronics	1359	2.779
10	Materials Letters	1357	3.574
11	Applied Surface Science	1282	7.392
12	Ceramics International	1242	5.532
13	Nanoscale	1214	8.307
14	Materials Today Proceedings	1213	-
15	Journal of The American Chemical Society	1123	16.383
16	Colloids and Surfaces B Biointerfaces	1122	5.999
17	International Journal of Biological Macromolecules	1040	8.025
18	Materials Chemistry and Physics	923	4.094
19	Journal of Nanoscience and Nanotechnology	872	4.849
20	Langmuir	848	4.331

4.3. Authors' Characteristics

4.3.1. Performances of authors

The research on synthesis of nanoparticles was written by more than 1650 authors. Table 3 depicts the top ten most prolific authors in terms of publication, together with their total number of publications. The first author in the top ten most productive authors has the most articles published (196), while the tenth author has the fewest (85).

More than half of these writers are from the top ten most productive countries, implying that they are more productive in the field of research. Prof. Salavati-Niasari has the most published articles (196), indicating that he has a good academic performance with scientific quality and that the majority of his works are well known. Prof. Rajeshkumar is the second-most prolific author in terms of publication, with 137 papers.

Table 3: Top 20 most published authors.

Ranks	Authors	Documents
1	Salavati-Niasari, M	196
2	Rajeshkumar, S	137
3	Asiri, A.M	129
4	Baykal, A.	112
5	Chen, S.M	105
6	Nasrollahzadeh, M	99
7	Ghaedi, M	89
8	Maaza, M	87
9	Darroudi, M	86
10	Morsali, A	85

4.3.2. Most cited articles

The top most cited publications for the examined period (2010–2023) were also concerned about the first authors' countries, the journal's name, and the number of TCs. Differences in the number of citations or references received in a given year can be used to quantify the impact of publications and the authors' influence. As shown in Figure 13, most prolific authors are from China, India, United States, and Iran. The article, titled "porphyrin-sensitized solar cells with cobalt (II/III)-based redox electrolyte exceed 12 percent efficiency" was published in science in 2011 with 5475 total citations. The article, titled "MoS₂ nanoparticles grown on graphene: an

advanced catalyst for the hydrogen evolution reaction" which appeared in journal of the American chemical society in 2011 and received 4150 total citations, is the second-most referenced article overall. This article provides a general overview of nanostructures, discusses their significance, and reviews current developments in nanostructured on graphene while the article, titled "principles of nanoparticle design for overcoming biological barriers to drug delivery" is the third most cited article. It had 3737 TCs when it was published in Nature Biotechnology in 2015. The research described the principles of nanoparticle design for overcoming biological barriers to drug delivery.

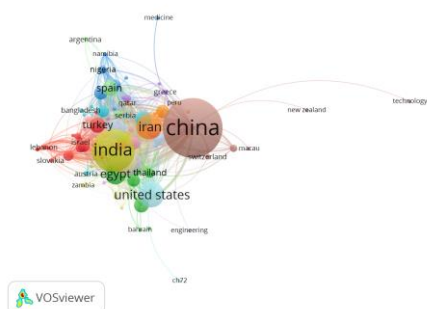


Figure 14: The Map of top 20 countries in terms of academic cooperation for Nanoparticle synthesis. *Colour caption: The colour size indicate the percentage quantities of nanoparticle synthesized countries with their collaborator.*

5. CONCLUSION

In this review, different synthesis methods of several nanoparticles such as chemical, physical and biological techniques were discussed. The co-precipitation approach is a chemical synthesis route and it is the simplest of all techniques while green synthesis produces non-toxic compounds but it has very low yields compared to other techniques. There are many other factors that are associated with these synthesis approaches which are very important such as cost, simplicity, and percentage yield. The character of the products is largely influenced by the specifics of the preparation. The huge specific surface area, quick charge transfers, and the shape of the materials are features that determine the performance of the nanoparticles.

Since various applications of nanoparticles have emerged, bibliometric examination of the evolution of literary works connected to synthesis of nanoparticles has been examined. Between 2010 and December 2022, about 117,162 publications on synthesis of nanoparticles were identified using bibliometric analysis in the Scopus database, and 92% of them were journal articles. The study demonstrates that in the period under evaluation, the literature on synthesis of nanoparticles has advanced significantly. Research publications about synthesis of nanoparticles were published in over 139 sources. The top five journals with more than 30% contributions to the subject field are RSC Advances, Journal of Colloid and Interface Science, Journal of Nanoparticle Research, ACS Applied Materials and Interfaces, and Chemical Communication. The top five most productive nations are as follows: South Korea, China, India, and the United States, with China being the most prolific across all references, indicating its leadership position in nanoparticle synthesis research. The most productive institution is Ministry of Education China with 5,356 articles, followed by Chinese Academy of Sciences with 4,472 articles and CNRS Centre National de la Recherche Scientifique with 1419 articles. The top 10 institutions all have positive international inter-institutional relationships. The bibliometric analysis also identifies the most popular terms, which point to the most popular subject areas. The future of synthesis of nanoparticles lies in the basic development of composite materials from various types of preparations in order to overcome their drawbacks. The bibliometric studies, in our opinion, will motivate academics to further investigate the previously highlighted areas and promote future cooperation.

6. ACKNOWLEDGMENT

The authors Acknowledged African-German Network of Excellences for 2023 AGNES Intra-Africa Mobility grants for the sponsorship.

7. REFERENCES

1. Rupesh Kumar M, Ranjith S, Balu H, Bharathi DR, Chandan K, Ahmed SS. Role of nanotechnology in biomedical applications: an updated review. UPI J

Pharm Med Heal Sci [Internet]. 2022 Nov 8;5(2):39-43. Available from: [<URL>](#).

2. Sadeghi-Aghbash M, Rahimnejad M. Zinc phosphate nanoparticles: A review on physical, chemical, and biological synthesis and their applications. Curr Pharm Biotechnol [Internet]. 2022 Aug 16;23(10):1228-44. Available from: [<URL>](#).

3. MubarakAli D, Kim H, Venkatesh PS, Kim JW, Lee SY. A systemic review on the synthesis, characterization, and applications of palladium nanoparticles in biomedicine. Appl Biochem Biotechnol [Internet]. 2023 Jun 29;195(6):3699-718. Available from: [<URL>](#).

4. Naganthran A, Verasoundarapandian G, Khalid FE, Masarudin MJ, Zulkharnain A, Nawawi NM, et al. Synthesis, characterization and biomedical application of silver nanoparticles. Materials [Internet]. 2022 Jan 6;15(2):427. Available from: [<URL>](#).

5. Phan TTV, Huynh TC, Manivasagan P, Mondal S, Oh J. An up-to-date review on biomedical applications of palladium nanoparticles. Nanomaterials [Internet]. 2019 Dec 27;10(1):66. Available from: [<URL>](#).

6. Pandey P. Role of Nanotechnology in Electronics: A review of recent developments and patents. Recent Pat Nanotechnol [Internet]. 2022 Mar 26;16(1):45-66. Available from: [<URL>](#).

7. Ajala OJ, Tijani JO, Bankole MT, Abdulkareem AS. Wastewater treatment technologies. In: Environmental footprints and eco-design of products and processes [Internet]. Springer, Singapore; 2022. p. 1-28. Available from: [<URL>](#).

8. Ajala OJ, Khadir A, Ighalo JO, Umenweke GC. Cellulose-based nano-biosorbents in water purification. In: Nano-biosorbents for decontamination of water, air, and soil pollution [Internet]. Elsevier; 2022. p. 395-415. Available from: [<URL>](#).

9. Ajala OJ, Nwosu FO, Ahmed RK. Adsorption of atrazine from aqueous solution using unmodified and modified bentonite clays. Appl Water Sci [Internet]. 2018 Nov 30;8(7):214. Available from: [<URL>](#).

10. Nwosu FO, Ajala OJ, Okeola FO, Adebayo SA, Olanlokun OK, Eletta AO. Adsorption of chlorotriazine herbicide onto unmodified and modified kaolinite: Equilibrium, kinetic and thermodynamic studies. Egypt J Aquat Res [Internet]. 2019 Jun 1;45(2):99-107. Available from: [<URL>](#).

11. Nwosu FO, Ajala OJ, Owoyemi RM, Raheem BG. Preparation and characterization of adsorbents derived from bentonite and kaolin clays. Appl Water Sci [Internet]. 2018 Nov 10;8(7):195. Available from: [<URL>](#).

12. Abdullahi A, Ighalo J, Ajala O, Ayika S. Physicochemical analysis and heavy metals remediation of pharmaceutical industry effluent using bentonite clay modified by H₂SO₄ and HCl. J

Turkish Chem Soc Sect A Chem [Internet]. 2020 Oct 30;7(3):727–44. Available from: [<URL>](#).

13. Ighalo JO, Tijani IO, Ajala OJ, Ayandele FO, Eletta OAA, Adeniyi AG. Competitive biosorption of Pb(II) and Cu(II) by functionalised *Micropogonias undulates* scales. *Recent Innov Chem Eng* [Internet]. 2021 Jan 21;13(5):425–36. Available from: [<URL>](#).

14. Libralato G, Volpi Ghirardini A, Avezzù F. Toxicity removal efficiency of decentralised sequencing batch reactor and ultra-filtration membrane bioreactors. *Water Res* [Internet]. 2010 Aug 1;44(15):4437–50. Available from: [<URL>](#).

15. Verma N, Kumar N. Synthesis and Biomedical Applications of copper oxide nanoparticles: An expanding horizon. *ACS Biomater Sci Eng* [Internet]. 2019 Mar 11;5(3):1170–88. Available from: [<URL>](#).

16. Song Y, Rampley CPN, Chen X, Du F, Thompson IP, Huang WE. Application of bacterial whole-cell biosensors in health. In: *Handbook of cell biosensors* [Internet]. Cham: Springer International Publishing; 2022. p. 945–61. Available from: [<URL>](#).

17. Shafiei F, Ashnagar A, Ghavami-Lahiji M, Najafi F, Amin Marashi SM. Evaluation of antibacterial properties of dental adhesives containing metal nanoparticles. *J Dent Biomater* [Internet]. 2018 Mar 4;5(1):510–9. Available from: [<URL>](#).

18. Ighalo JO, Sagboye PA, Umenweke G, Ajala OJ, Omoarukhe FO, Adeyanju CA, et al. CuO nanoparticles (CuO NPs) for water treatment: A review of recent advances. *Environ Nanotechnology, Monit Manag* [Internet]. 2021 May 1;15:100443. Available from: [<URL>](#).

19. Ali NH, Amin MCIM, Ng SF. Sodium carboxymethyl cellulose hydrogels containing reduced graphene oxide (rGO) as a functional antibiofilm wound dressing. *J Biomater Sci Polym Ed* [Internet]. 2019 May 24;30(8):629–45. Available from: [<URL>](#).

20. Chugh H, Sood D, Chandra I, Tomar V, Dhawan G, Chandra R. Role of gold and silver nanoparticles in cancer nano-medicine. *Artif Cells, Nanomedicine, Biotechnol* [Internet]. 2018 Oct 31;46(sup1):1210–20. Available from: [<URL>](#).

21. Su M, Zhang T, Su J, Wang Z, Hu Y, Gao Y, et al. Homogeneous ZnO nanowire arrays p-n junction for blue light-emitting diode applications. *Opt Express* [Internet]. 2019 Aug 5;27(16):A1207–15. Available from: [<URL>](#).

22. Nayyar A, Puri V, Le DN. Internet of nano things (IoNT): Next evolutionary step in nanotechnology. *nanosci nanotechnol* [Internet]. 2017;7(1):4–8. Available from: [<URL>](#).

23. Hamza EK, Jaafar SN. Nanotechnology application for wireless communication system. In: *Materials horizons: From nature to nanomaterials* [Internet]. Springer, Singapore; 2022. p. 115–30. Available from: [<URL>](#).

24. Ajala OJ, Tijani JO, Bankole MT, Abdulkareem AS. A critical review on graphene oxide nanostructured material: Properties, synthesis, characterization and application in water and wastewater treatment. *Environ Nanotechnology, Monit Manag* [Internet]. 2022 Dec 1;18:100673. Available from: [<URL>](#).

25. Rawtani D, Khatri N, Tyagi S, Pandey G. Nanotechnology-based recent approaches for sensing and remediation of pesticides. *J Environ Manage* [Internet]. 2018 Jan 15;206:749–62. Available from: [<URL>](#).

26. Li H, Zhu Y. Liquid-Phase synthesis of iron oxide nanostructured materials and their applications. *Chem – A Eur J* [Internet]. 2020 Jul 27;26(42):9180–205. Available from: [<URL>](#).

27. Alam SN, Sharma N, Kumar L. Synthesis of graphene oxide (GO) by modified hummers method and its thermal reduction to obtain reduced graphene oxide (rGO)*. *Graphene* [Internet]. 2017 Jan 10;6(1):1–18. Available from: [<URL>](#).

28. Krishnia L, Thakur P, Thakur A. Synthesis of nanoparticles by physical route. In: *Synthesis and applications of nanoparticles* [Internet]. Singapore: Springer Nature Singapore; 2022. p. 45–59. Available from: [<URL>](#).

29. Chen L, Hong M. Functional nonlinear optical nanoparticles synthesized by laser ablation. *Opto-Electronic Sci* [Internet]. 2022;1(5):210007. Available from: [<URL>](#).

30. Muddapur UM, Alshehri S, Ghoneim MM, Mahnashi MH, Alshahrani MA, Khan AA, et al. Plant-based synthesis of gold nanoparticles and theranostic applications: A review. *Molecules* [Internet]. 2022 Feb 18;27(4):1391. Available from: [<URL>](#).

31. Chandrakala V, Aruna V, Angajala G. Review on metal nanoparticles as nanocarriers: current challenges and perspectives in drug delivery systems. *Emergent Mater* [Internet]. 2022 Dec 4;5(6):1593–615. Available from: [<URL>](#).

32. Nazneen H, Rather GA, Ali A, Chakravorty A. The role of plant-mediated biosynthesised nanoparticles in agriculture. In: *Sustainable agriculture* [Internet]. Cham: Springer International Publishing; 2022. p. 97–117. Available from: [<URL>](#).

33. Ying S, Guan Z, Ofoegbu PC, Clubb P, Rico C, He F, et al. Green synthesis of nanoparticles: Current developments and limitations. *Environ Technol Innov* [Internet]. 2022 May 1;26:102336. Available from: [<URL>](#).

34. Jeevanandam J, Krishnan S, Hii YS, Pan S, Chan YS, Acquah C, et al. Synthesis approach-dependent antiviral properties of silver nanoparticles and nanocomposites. *J Nanostructure Chem* [Internet]. 2022 Oct 15;12(5):809–31. Available from: [<URL>](#).

35. Ndaba B, Roopnarain A, Rama H, Maaza M. Biosynthesized metallic nanoparticles as fertilizers: An emerging precision agriculture strategy. *J Integr*

Agric [Internet]. 2022 May 1;21(5):1225–42. Available from: [<URL>](#).

36. Chong WJ, Shen S, Li Y, Trinchi A, Pejak D, (Louis) Kyratzis I, et al. Additive manufacturing of antibacterial PLA-ZnO nanocomposites: Benefits, limitations and open challenges. J Mater Sci Technol [Internet]. 2022 Jun 1;111:120–51. Available from: [<URL>](#).

37. Rakib-Uz-Zaman SM, Hoque Apu E, Muntasir MN, Mowna SA, Khanom MG, Jahan SS, et al. Biosynthesis of silver nanoparticles from *Cymbopogon citratus* leaf extract and evaluation of their antimicrobial properties. Challenges [Internet]. 2022 May 5;13(1):18. Available from: [<URL>](#).

38. Ahmad W, Chandra Bhatt S, Verma M, Kumar V, Kim H. A review on current trends in the green synthesis of nickel oxide nanoparticles, characterizations, and their applications. Environ Nanotechnology, Monit Manag [Internet]. 2022 Dec 1;18:100674. Available from: [<URL>](#).

39. Harish V, Tewari D, Gaur M, Yadav AB, Swaroop S, Bechelany M, et al. Review on nanoparticles and nanostructured materials: Bioimaging, biosensing, drug delivery, tissue engineering, antimicrobial, and agro-food applications. nanomaterials [Internet]. 2022 Jan 28;12(3):457. Available from: [<URL>](#).

40. Kumar VB, Porat Z, Gedanken A. Synthesis of doped/hybrid carbon dots and their biomedical application. Nanomaterials [Internet]. 2022 Mar 8;12(6):898. Available from: [<URL>](#).

41. Aldeen TS, Ahmed Mohamed HE, Maaza M. ZnO nanoparticles prepared via a green synthesis approach: Physical properties, photocatalytic and antibacterial activity. J Phys Chem Solids [Internet]. 2022 Jan 1;160:110313. Available from: [<URL>](#).

42. Das RP, Pradhan AK. An introduction to different methods of nanoparticles synthesis. In: Bio-nano interface [Internet]. Singapore: Springer Singapore; 2022. p. 21–34. Available from: [<URL>](#).

43. Sehgal S, Kumar J, Nishtha. Involvement of gold and silver nanoparticles in lung cancer nanomedicines: A review. Mater Today Proc [Internet]. 2022 Jan 1;62(P12):6468–76. Available from: [<URL>](#).

44. Koohestani H, Salmaniannezhad H, Salmaniannezhad H, Khai MR. Synthesis and characterization of MgF₂/Cu coating on aluminum produced by sputtering technique. Mech Adv Compos Struct [Internet]. 2022 Nov 1;9(2):297–302. Available from: [<URL>](#).

45. Alshammari FH. Physical characterization and dielectric properties of chitosan incorporated by zinc oxide and graphene oxide nanoparticles prepared via laser ablation route. J Mater Res Technol [Internet]. 2022 Sep 1;20:740–7. Available from: [<URL>](#).

46. Sivakumar S, Kumaresan L, Bertilla DMS, Dhanabal MHV, Shanmugavelayutham G, Zhu J. Synthesis of magnetic and superhydrophobic nickel

nanoparticles by plasma arc discharge method, application for efficient recoverable and repeatable oil separation from oily-water. Appl Phys A [Internet]. 2022 Jan 5;128(1):5. Available from: [<URL>](#).

47. Islam F, Shohag S, Uddin MJ, Islam MR, Nafady MH, Akter A, et al. Exploring the journey of zinc oxide nanoparticles (ZnO-NPs) toward biomedical applications. Materials [Internet]. 2022 Mar 15;15(6):2160. Available from: [<URL>](#).

48. Biswas MC, Chowdhury A, Hossain MM, Hossain MK. Applications, drawbacks, and future scope of nanoparticle-based polymer composites. In: Nanoparticle-Based Polymer Composites [Internet]. Elsevier; 2022. p. 243–75. Available from: [<URL>](#).

49. Lee KX, Shameli K, Yew YP, Teow SY, Jahangirian H, Rafiee-Moghaddam R, et al. Recent developments in the facile bio-synthesis of gold nanoparticles (AuNPs) and their biomedical applications. Int J Nanomedicine [Internet]. 2020 Jan;Volume 15:275–300. Available from: [<URL>](#).

50. Nicolae-Maranciuc A, Chicea D, Chicea LM. Ag Nanoparticles for biomedical applications—synthesis and characterization—A review. Int J Mol Sci [Internet]. 2022 May 21;23(10):5778. Available from: [<URL>](#).

51. Gomaa EZ. Microbial mediated synthesis of zinc oxide nanoparticles, characterization and multifaceted applications. J Inorg Organomet Polym Mater [Internet]. 2022 Nov 7;32(11):4114–32. Available from: [<URL>](#).

52. Subhan A, Mourad AHI, Das S. Pulsed laser synthesis of Bi-metallic nanoparticles for biomedical applications: A review. In: 2022 Advances in Science and Engineering Technology International Conferences (ASET) [Internet]. IEEE; 2022. p. 1–7. Available from: [<URL>](#).

53. Tikhonowski G V., Popov AA, Zelepukin I, Popova-Kuznetsova E, Dombrovskaya YI, Deev SM, et al. Laser synthesis of nanomaterials for nuclear nanomedicine. In: Kabashin A V., Farsari M, Mahjouri-Samani M, editors. Nanoscale and Quantum Materials: From Synthesis and Laser Processing to Applications 2022 [Internet]. SPIE; 2022. p. 22. Available from: [<URL>](#).

54. Pastukhov AI, Belyaev IB, Bulmahn JC, Zelepukin I V., Popov AA, Zavestovskaya IN, et al. Laser-ablative aqueous synthesis and characterization of elemental boron nanoparticles for biomedical applications. Sci Rep [Internet]. 2022 Jun 1;12(1):9129. Available from: [<URL>](#).

55. Popov AA, Swiatkowska-Warkocka Z, Marszalek M, Tselikov G, Zelepukin I V., Al-Kattan A, et al. Laser-ablative synthesis of ultrapure magneto-plasmonic core-satellite nanocomposites for biomedical applications. Nanomaterials [Internet]. 2022 Feb 1;12(4):649. Available from: [<URL>](#).

56. Ielo I, Rando G, Giacobello F, Sfameni S, Castellano A, Galletta M, et al. Synthesis, chemical-

physical characterization, and biomedical applications of functional gold nanoparticles: A review. *Molecules* [Internet]. 2021 Sep 26;26(19):5823. Available from: [<URL>](#).

57. AlMalki FA, Khashan KS, Jabir MS, Hadi AA, Sulaiman GM, Abdulameer FA, et al. Eco-friendly synthesis of carbon nanoparticles by laser ablation in water and evaluation of their antibacterial activity. Tan B, editor. *J Nanomater* [Internet]. 2022 Jan 7;2022(1):7927447. Available from: [<URL>](#).

58. Le TD, Phan H, Kwon S, Park S, Jung Y, Min J, et al. Recent Advances in laser induced graphene: Mechanism, fabrication, properties, and applications in flexible electronics. *Adv Funct Mater* [Internet]. 2022 Nov 7;32(48):2205158. Available from: [<URL>](#).

59. Wasim M, Mushtaq M, Khan SU, Farooq A, Naeem MA, Khan MR, et al. Development of bacterial cellulose nanocomposites: An overview of the synthesis of bacterial cellulose nanocomposites with metallic and metallic-oxide nanoparticles by different methods and techniques for biomedical applications. *J Ind Text* [Internet]. 2022 Jun 13;51(2S):1886S-1915S. Available from: [<URL>](#).

60. Kannan K, Radhika D, Sadasivuni KK, Reddy KR, Raghu A V. Nanostructured metal oxides and its hybrids for photocatalytic and biomedical applications. *Adv Colloid Interface Sci* [Internet]. 2020 Jul 1;281:102178. Available from: [<URL>](#).

61. Naser H, Hassan Z, Mohammad SM, Shanshool HM, Al-Hazeem NZ. Parameters influencing the absorbance of gold-silver alloy nanomaterials using the pulsed laser ablation in liquid (plal) approach: A review. *Brazilian J Phys* [Internet]. 2022 Jun 18;52(3):100. Available from: [<URL>](#).

62. Popov A, Tikhonowski G, Shakhov P, Popova-Kuznetsova E, Tselikov G, Romanov R, et al. Synthesis of titanium nitride nanoparticles by pulsed laser ablation in different aqueous and organic solutions. *Nanomaterials* [Internet]. 2022 May 13;12(10):1672. Available from: [<URL>](#).

63. Elahi N, Kamali M, Baghersad MH. Recent biomedical applications of gold nanoparticles: A review. *Talanta* [Internet]. 2018 Jul 1;184:537–56. Available from: [<URL>](#).

64. Fronya AA, Antonenko S V., Karpov N V., Pokryshkin NS, Eremina AS, Yakunin VG, et al. Germanium nanoparticles prepared by laser ablation in low pressure helium and nitrogen atmosphere for biophotonic applications. *Materials* [Internet]. 2022 Aug 2;15(15):5308. Available from: [<URL>](#).

65. Tarasenko N, Kornev V, Ramanenka A, Li R, Tarasenko N. Photoluminescent neodymium-doped ZnO nanocrystals prepared by laser ablation in solution for NIR-II fluorescence bioimaging. *Heliyon* [Internet]. 2022 Jun 1;8(6):e09554. Available from: [<URL>](#).

66. Mat Isa SZ, Zainon R, Tamal M. State of the Art in Gold Nanoparticle synthesis via pulsed laser

ablation in liquid and its characterisation for molecular imaging: A review. *Materials* [Internet]. 2022 Jan 24;15(3):875. Available from: [<URL>](#).

67. Pattanayak S, Mollick MMR, Maity D, Chakraborty S, Dash SK, Chattopadhyay S, et al. Butea monosperma bark extract mediated green synthesis of silver nanoparticles: Characterization and biomedical applications. *J Saudi Chem Soc* [Internet]. 2017 Sep 1;21(6):673–84. Available from: [<URL>](#).

68. Medina Cruz D, Mostafavi E, Vernet-Crua A, Barabadi H, Shah V, Cholula-Díaz JL, et al. Green nanotechnology-based zinc oxide (ZnO) nanomaterials for biomedical applications: A review. *J Phys Mater* [Internet]. 2020 Jul 1;3(3):034005. Available from: [<URL>](#).

69. Singh KR, Nayak V, Singh J, Singh AK, Singh RP. Potentialities of bioinspired metal and metal oxide nanoparticles in biomedical sciences. *RSC Adv* [Internet]. 2021 Jul 15;11(40):24722–46. Available from: [<URL>](#).

70. Mintcheva N, Yamaguchi S, Kulinich SA. Hybrid TiO₂-ZnO nanomaterials prepared using laser ablation in liquid. *Materials* [Internet]. 2020 Feb 5;13(3):719. Available from: [<URL>](#).

71. Menazea AA, Ahmed MK. Synthesis and antibacterial activity of graphene oxide decorated by silver and copper oxide nanoparticles. *J Mol Struct* [Internet]. 2020 Oct 15;1218:128536. Available from: [<URL>](#).

72. Zhang D, Gökce B, Barcikowski S. Laser synthesis and processing of colloids: Fundamentals and applications. *Chem Rev* [Internet]. 2017 Mar 8;117(5):3990–4103. Available from: [<URL>](#).

73. Theerthagiri J, Karuppasamy K, Lee SJ, Shwetharani R, Kim HS, Pasha SKK, et al. Fundamentals and comprehensive insights on pulsed laser synthesis of advanced materials for diverse photo- and electrocatalytic applications. *Light Sci Appl* [Internet]. 2022 Aug 10;11(1):250. Available from: [<URL>](#).

74. Schena E, Saccomandi P, Fong Y. Laser ablation for cancer: Past, present and future. *J Funct Biomater* [Internet]. 2017 Jun 14;8(2):19. Available from: [<URL>](#).

75. Sadrolhosseini AR, Mahdi MA, Alizadeh F, Rashid SA. Laser technology and its applications. In: *Laser technology and its applications* [Internet]. IntechOpen; 2019. p. 63–81. Available from: [<URL>](#).

76. Su SS, Chang I. Review of production routes of nanomaterials. In: *Commercialization of nanotechnologies—A case study approach* [Internet]. Cham: Springer International Publishing; 2018. p. 15–29. Available from: [<URL>](#).

77. He Y, Yi C, Zhang X, Zhao W, Yu D. Magnetic graphene oxide: Synthesis approaches, physicochemical characteristics, and biomedical

applications. *TrAC Trends Anal Chem* [Internet]. 2021 Mar 1;136:116191. Available from: [<URL>](#).

78. Makvandi P, Wang C, Zare EN, Borzacchiello A, Niu L, Tay FR. Metal-Based nanomaterials in biomedical applications: Antimicrobial activity and cytotoxicity aspects. *Adv Funct Mater* [Internet]. 2020 May 17;30(22):1910021. Available from: [<URL>](#).

79. Pradeep NB, Hegde MMR, Rajendrachari S, Surendranathan AO. Investigation of microstructure and mechanical properties of microwave consolidated TiMgSr alloy prepared by high energy ball milling. *Powder Technol* [Internet]. 2022 Aug 1;408:117715. Available from: [<URL>](#).

80. Wallyn J, Anton N, Vandamme TF. Synthesis, principles, and properties of magnetite nanoparticles for in vivo imaging applications—A review. *Pharmaceutics* [Internet]. 2019 Nov 12;11(11):601. Available from: [<URL>](#).

81. Baláž M, Tkáčiková L, Stahorský M, Casas-Luna M, Dutková E, Čelko L, et al. Ternary and quaternary nanocrystalline Cu-based sulfides as perspective antibacterial materials mechanochemically synthesized in a scalable fashion. *ACS Omega* [Internet]. 2022 Aug 9;7(31):27164–71. Available from: [<URL>](#).

82. Kotcherlakota R, Das S, Patra CR. Therapeutic applications of green-synthesized silver nanoparticles. In: *Green synthesis, characterization and applications of nanoparticles* [Internet]. Elsevier; 2019. p. 389–428. Available from: [<URL>](#).

83. Abdullah FH, Bakar NHHA, Bakar MA. Current advancements on the fabrication, modification, and industrial application of zinc oxide as photocatalyst in the removal of organic and inorganic contaminants in aquatic systems. *J Hazard Mater* [Internet]. 2022 Feb 15;424:127416. Available from: [<URL>](#).

84. Raha S, Ahmaruzzaman M. ZnO nanostructured materials and their potential applications: progress, challenges and perspectives. *Nanoscale Adv* [Internet]. 2022 Apr 12;4(8):1868–925. Available from: [<URL>](#).

85. Prasad S, Kumar V, Kirubanandam S, Barhoum A. Engineered nanomaterials: nanofabrication and surface functionalization. In: *Emerging Applications of Nanoparticles and Architecture Nanostructures* [Internet]. Elsevier; 2018. p. 305–40. Available from: [<URL>](#).

86. Shafaei A, Khayati GR. A predictive model on size of silver nanoparticles prepared by green synthesis method using hybrid artificial neural network-particle swarm optimization algorithm. *Measurement* [Internet]. 2020 Feb 1;151:107199. Available from: [<URL>](#).

87. Alam S, Hossain MZ. A Simple hydrothermal protocol for the synthesis of zinc oxide nanorods. *Jagannath Univ J Sci* [Internet]. 2021;7(2):75–80. Available from: [<URL>](#).

88. Ghorbani HR. A review of methods for synthesis of Al nanoparticles. *Orient J Chem* [Internet]. 2014 Dec 31;30(4):1941–9. Available from: [<URL>](#).

89. Khan ZUH, Khan A, Chen Y, Shah NS, Muhammad N, Khan AU, et al. Biomedical applications of green synthesized Nobel metal nanoparticles. *J Photochem Photobiol B Biol* [Internet]. 2017 Aug 1;173:150–64. Available from: [<URL>](#).

90. Thakur AK, Sathyamurthy R, Velraj R, Lynch I. Development of a novel cellulose foam augmented with candle-soot derived carbon nanoparticles for solar-powered desalination of brackish water. *Environ Sci Nano* [Internet]. 2022 Apr 14;9(4):1247–70. Available from: [<URL>](#).

91. Jeyaraj M, Gurunathan S, Qasim M, Kang MH, Kim JH. A Comprehensive review on the synthesis, characterization, and biomedical application of platinum nanoparticles. *nanomaterials* [Internet]. 2019 Dec 2;9(12):1719. Available from: [<URL>](#).

92. Jin SE, Jin HE. Synthesis, characterization, and three-dimensional structure generation of zinc oxide-based nanomedicine for biomedical applications. *Pharmaceutics* [Internet]. 2019 Nov 4;11(11):575. Available from: [<URL>](#).

93. Ehsan M, Waheed A, Ullah A, Kazmi A, Ali A, Raja NI, et al. Plant-based bimetallic Silver-Zinc Oxide nanoparticles: A comprehensive perspective of synthesis, biomedical applications, and future trends. Kim BS, editor. *Biomed Res Int* [Internet]. 2022 Apr 30;2022(1):215183. Available from: [<URL>](#).

94. Sharma A, Kumar S. Synthesis and green synthesis of silver nanoparticles. In: *Engineering materials* [Internet]. Springer, Cham; 2021. p. 25–64. Available from: [<URL>](#).

95. Ong WTJ, Nyam KL. Evaluation of silver nanoparticles in cosmeceutical and potential biosafety complications. *Saudi J Biol Sci* [Internet]. 2022 Apr 1;29(4):2085–94. Available from: [<URL>](#).

96. Lee SH, Jun BH. Silver nanoparticles: synthesis and application for nanomedicine. *Int J Mol Sci* [Internet]. 2019 Feb 17;20(4):865. Available from: [<URL>](#).

97. Hara R, Fukuoka T, Takahashi R, Utsumi Y, Yamaguchi A. Surface-enhanced raman spectroscopy using a coffee-ring-type three-dimensional silver nanostructure. *RSC Adv* [Internet]. 2015 Dec 1;5(2):1378–84. Available from: [<URL>](#).

98. Abdullah AH, Jasim AH, Eltayef EM. The medical applications of silver nanoparticles. *Int J Pharmacogn Life Sci* [Internet]. 2022 Jan 1;3(1):1–6. Available from: [<URL>](#).

99. Natsuki J, Natsuki T, Hashimoto Y. A review of silver nanoparticles: Synthesis methods, properties and applications. *Int J Mater Sci Appl* [Internet]. 2015;4(5):325–32. Available from: [<URL>](#).

100. Rashidi S, Mahian O, Languri EM. Applications of nanofluids in condensing and evaporating systems. *J Therm Anal Calorim* [Internet]. 2018 Mar 2;131(3):2027–39. Available from: [<URL>](#).
101. Ramanathan S, Gopinath SCB, Arshad MKM, Poopalan P, Perumal V. Nanoparticle synthetic methods: strength and limitations. In: *Nanoparticles in analytical and medical devices* [Internet]. Elsevier; 2021. p. 31–43. Available from: [<URL>](#).
102. Tharchanaa SB, Priyanka K, Preethi K, Shanmugavelayutham G. Facile synthesis of Cu and CuO nanoparticles from copper scrap using plasma arc discharge method and evaluation of antibacterial activity. *Mater Technol* [Internet]. 2021 Jan 28;36(2):97–104. Available from: [<URL>](#).
103. Haider A, Kang IK. Preparation of silver nanoparticles and their industrial and biomedical applications: A comprehensive review. *Adv Mater Sci Eng* [Internet]. 2015 Jan 1;2015(1):65257. Available from: [<URL>](#).
104. Corbella C, Portal S, Zolotukhin DB, Martinez L, Lin L, Kundrapu MN, et al. Pulsed anodic arc discharge for the synthesis of carbon nanomaterials. *Plasma Sources Sci Technol* [Internet]. 2019 Apr 29;28(4):045016. Available from: [<URL>](#).
105. Corbella C, Portal S, Rao J, Kundrapu MN, Keidar M. Tracking nanoparticle growth in pulsed carbon arc discharge. *J Appl Phys* [Internet]. 2020 Jun 28;127(24):243301. Available from: [<URL>](#).
106. Ge G, Li L, Wang D, Chen M, Zeng Z, Xiong W, et al. Carbon dots: synthesis, properties and biomedical applications. *J Mater Chem B* [Internet]. 2021 Aug 25;9(33):6553–75. Available from: [<URL>](#).
107. Chaitoglou S, Sanaee MR, Aguiló-Aguayo N, Bertran E. Arc-Discharge synthesis of iron encapsulated in carbon nanoparticles for biomedical applications. Soni A, editor. *J Nanomater* [Internet]. 2014 Jan 13;2014(1):178524. Available from: [<URL>](#).
108. Koushika EM, Shanmugavelayutham G, Saravanan P, Balasubramanian C. Rapid synthesis of nano-magnetite by thermal plasma route and its magnetic properties. *Mater Manuf Process* [Internet]. 2018 Nov 18;33(15):1701–7. Available from: [<URL>](#).
109. Lee S, Kim TH, Kim DW, Park DW. Preparation of silicon nanopowder by recycling silicon wafer waste in radio-frequency thermal plasma process. *Plasma Chem Plasma Process* [Internet]. 2017 Jul 27;37(4):967–78. Available from: [<URL>](#).
110. Luo F, Tang Z, Xiao S, Xiang Y. Study on properties of copper-containing austenitic antibacterial stainless steel. *Mater Technol* [Internet]. 2019 Jul 29;34(9):525–33. Available from: [<URL>](#).
111. Corbella C, Portal S, Kundrapu MN, Keidar M. Nanosynthesis by atmospheric arc discharges excited with pulsed-DC power: A review. *Nanotechnology* [Internet]. 2022 Aug 20;33(34):342001. Available from: [<URL>](#).
112. Zhang D, Ye K, Yao Y, Liang F, Qu T, Ma W, et al. Controllable synthesis of carbon nanomaterials by direct current arc discharge from the inner wall of the chamber. *Carbon N Y* [Internet]. 2019 Feb 1;142:278–84. Available from: [<URL>](#).
113. Putri AC, Anwar M, Iftadi I, Ramelan A, Adrianto F, Saraswati TE. Plasma characteristics of underwater arc discharge in nanoparticle fabrication. *J Electr Electron Information, Commun Technol* [Internet]. 2022 May 30;4(1):11–5. Available from: [<URL>](#).
114. Borand G, Akçamlı N, Uzunsoy D. Structural characterization of graphene nanostructures produced via arc discharge method. *Ceram Int* [Internet]. 2021 Mar 15;47(6):8044–52. Available from: [<URL>](#).
115. Wang C, Sun L, Sun Q, Zhang Z, Xia W, Xia W. Experimental observations of constricted and diffuse anode attachment in a magnetically rotating arc at atmospheric pressure. *Plasma Chem Plasma Process* [Internet]. 2019 Mar 21;39(2):407–21. Available from: [<URL>](#).
116. Rane AV, Kanny K, Abitha VK, Thomas S. Methods for synthesis of nanoparticles and fabrication of nanocomposites. In: *Synthesis of inorganic nanomaterials* [Internet]. Elsevier; 2018. p. 121–39. Available from: [<URL>](#).
117. Ghribi F, El Mir L, Omri K, Djessas K. Sputtered ZnS thin film from nanoparticles synthesized by hydrothermal route. *Optik* [Internet]. 2016 Apr 1;127(7):3688–92. Available from: [<URL>](#).
118. Shahidi S, Dalalsharifi S, Ghoranneviss M, Mongkholrattanasit R. In situ deposition of magnetic nanoparticles on glass mat using plasma sputtering method. *J Text Inst* [Internet]. 2022 Mar 4;113(3):349–59. Available from: [<URL>](#).
119. Tulinski M, Jurczyk M. Nanomaterials Synthesis Methods. In: *Metrology and standardization of nanotechnology* [Internet]. Wiley; 2017. p. 75–98. Available from: [<URL>](#).
120. Nattah AM, Mohaisen AH. An overview of titanium oxide nanoparticles, chareacterisation, synthesis and potential applications. *J Univ Babylon Eng Sci* [Internet]. 2022;30(1):72–85. Available from: [<URL>](#).
121. Palmer RE, Cai R, Vernieres J. Synthesis without Solvents: The cluster (nanoparticle) beam route to catalysts and sensors. *Acc Chem Res* [Internet]. 2018 Sep 18;51(9):2296–304. Available from: [<URL>](#).
122. López-Lorente AI, Picca RA, Izquierdo J, Kranz C, Mizaikoff B, Di Franco C, et al. Ion beam sputtering deposition of silver nanoparticles and TiO_x/ZnO nanocomposites for use in surface enhanced vibrational spectroscopy (SERS and SEIRAS).

Microchim Acta [Internet]. 2018 Feb 2;185(2):153. Available from: [<URL>](#).

123. Zhao Y, Zhang X, Chen X, Li W, Wang L, Li Z, et al. Preparation of Sn-NiO films and all-solid-state devices with enhanced electrochromic properties by magnetron sputtering method. Electrochim Acta [Internet]. 2021 Jan 20;367:137457. Available from: [<URL>](#).

124. Wang D, Qu Z, Wang Y, Cheng E, Wang Q. Role of Cu-doping concentration in the synthesis, microstructure and properties of Ag thin films via magnetron co-sputtering method. Vacuum [Internet]. 2023 Oct 1;216:112437. Available from: [<URL>](#).

125. Brar KK, Magdoui S, Othmani A, Ghanei J, Narisetty V, Sindhu R, et al. Green route for recycling of low-cost waste resources for the biosynthesis of nanoparticles (NPs) and nanomaterials (NMs)-A review. Environ Res [Internet]. 2022 May 1;207:112202. Available from: [<URL>](#).

126. Zambonino MC, Quizhpe EM, Jaramillo FE, Rahman A, Santiago Vispo N, Jeffries C, et al. Green synthesis of selenium and tellurium nanoparticles: Current trends, biological properties and biomedical applications. Int J Mol Sci [Internet]. 2021 Jan 20;22(3):989. Available from: [<URL>](#).

127. Rónavári A, Igaz N, Adamecz DI, Szerencsés B, Molnar C, Kónya Z, et al. Green silver and gold nanoparticles: Biological synthesis approaches and potentials for biomedical applications. Molecules [Internet]. 2021 Feb 5;26(4):844. Available from: [<URL>](#).

128. Razavi M, Salahinejad E, Fahmy M, Yazdimamaghani M, Vashae D, Tayebi L. Green chemical and biological synthesis of nanoparticles and their biomedical applications. In: Green processes for nanotechnology [Internet]. Cham: Springer International Publishing; 2015. p. 207–35. Available from: [<URL>](#).

129. Mondal S, Hoang G, Manivasagan P, Moorthy MS, Kim HH, Vy Phan TT, et al. Comparative characterization of biogenic and chemical synthesized hydroxyapatite biomaterials for potential biomedical application. Mater Chem Phys [Internet]. 2019 Apr 15;228:344–56. Available from: [<URL>](#).

130. Waris A, Din M, Ali A, Ali M, Afridi S, Baset A, et al. A comprehensive review of green synthesis of copper oxide nanoparticles and their diverse biomedical applications. Inorg Chem Commun [Internet]. 2021 Jan 1;123:108369. Available from: [<URL>](#).

131. Tauseef A, Hisam F, Hussain T, Caruso A, Hussain K, Châtel A, et al. Nanomicrobiology: Emerging trends in microbial synthesis of nanomaterials and their applications. J Clust Sci [Internet]. 2023 Mar 4;34(2):639–64. Available from: [<URL>](#).

132. Lateef A, Elegbede JA, Akinola PO, Ajayi VA. Biomedical applications of green synthesized-

metallic nanoparticles: A review. Pan African J Life Sci [Internet]. 2019 Nov 1;3(1):157–82. Available from: [<URL>](#).

133. Adeyemi JO, Oriola AO, Onwudiwe DC, Oyedeji AO. Plant extracts mediated metal-based nanoparticles: Synthesis and biological applications. Biomolecules [Internet]. 2022 Apr 24;12(5):627. Available from: [<URL>](#).

134. Katata-Seru L, Moremedi T, Aremu OS, Bahadur I. Green synthesis of iron nanoparticles using *Moringa oleifera* extracts and their applications: Removal of nitrate from water and antibacterial activity against *Escherichia coli*. J Mol Liq [Internet]. 2018 Apr 15;256:296–304. Available from: [<URL>](#).

135. Habeeb Rahuman HB, Dhandapani R, Narayanan S, Palanivel V, Paramasivam R, Subbarayalu R, et al. Medicinal plants mediated the green synthesis of silver nanoparticles and their biomedical applications. IET Nanobiotechnology [Internet]. 2022 Jun 15;16(4):115–44. Available from: [<URL>](#).

136. Aisida SO, Akpa PA, Ahmad I, Zhao T kai, Maaza M, Ezema FI. Bio-inspired encapsulation and functionalization of iron oxide nanoparticles for biomedical applications. Eur Polym J [Internet]. 2020 Jan 5;122:109371. Available from: [<URL>](#).

137. Nayak V, Singh KR, Verma R, Pandey MD, Singh J, Pratap Singh R. Recent advancements of biogenic iron nanoparticles in cancer theranostics. Mater Lett [Internet]. 2022 Apr 15;313:131769. Available from: [<URL>](#).

138. Menazea AA, Ismail AM, Awwad NS, Ibrahim HA. Physical characterization and antibacterial activity of PVA/Chitosan matrix doped by selenium nanoparticles prepared via one-pot laser ablation route. J Mater Res Technol [Internet]. 2020 Sep 1;9(5):9598–606. Available from: [<URL>](#).

139. Yang B, Chen Y, Shi J. Mesoporous silica/organosilica nanoparticles: Synthesis, biological effect and biomedical application. Mater Sci Eng R Reports [Internet]. 2019 Jul 1;137:66–105. Available from: [<URL>](#).

140. Aremu OS, Qwebani-Ogunleye T, Katata-Seru L, Mkhize Z, Trant JF. Synergistic broad-spectrum antibacterial activity of *Hypoxis hemerocallidea*-derived silver nanoparticles and streptomycin against respiratory pathobionts. Sci Rep [Internet]. 2021 Jul 27;11(1):15222. Available from: [<URL>](#).

141. von Baeckmann C, Guillet-Nicolas R, Renfer D, Kählig H, Kleitz F. A Toolbox for the synthesis of multifunctionalized mesoporous silica nanoparticles for biomedical applications. ACS Omega [Internet]. 2018 Dec 31;3(12):17496–510. Available from: [<URL>](#).

142. Li X, Shan J, Zhang W, Su S, Yuwen L, Wang L. Recent advances in synthesis and biomedical applications of two-dimensional transition metal dichalcogenide nanosheets. Small [Internet]. 2017 Feb 16;13(5):1602660. Available from: [<URL>](#).

143. Shanmuganathan R, Karuppusamy I, Saravanan M, Muthukumar H, Ponnuchamy K, Ramkumar VS, et al. Synthesis of silver nanoparticles and their biomedical applications - A comprehensive review. *Curr Pharm Des* [Internet]. 2019 Oct 3;25(24):2650–60. Available from: [<URL>](#).
144. Mirzaei H, Darroudi M. Zinc oxide nanoparticles: Biological synthesis and biomedical applications. *Ceram Int* [Internet]. 2017 Jan 1;43(1):907–14. Available from: [<URL>](#).
145. Cardoso VF, Francesko A, Ribeiro C, Bañobre-López M, Martins P, Lanceros-Mendez S. Advances in magnetic nanoparticles for biomedical applications. *Adv Healthc Mater* [Internet]. 2018 Mar 27;7(5):1700845. Available from: [<URL>](#).
146. Sharma NK, Vishwakarma J, Rai S, Alomar TS, AlMasoud N, Bhattarai A. Green Route Synthesis and characterization techniques of silver nanoparticles and their biological adeptness. *ACS Omega* [Internet]. 2022 Aug 9;7(31):27004–20. Available from: [<URL>](#).
147. Ganapathe LS, Mohamed MA, Mohamad Yunus R, Berhanuddin DD. Magnetite (Fe₃O₄) nanoparticles in biomedical application: from synthesis to surface functionalisation. *magnetochemistry* [Internet]. 2020 Dec 3;6(4):68. Available from: [<URL>](#).
148. Verma R, Pathak S, Srivastava AK, Prawer S, Tomljenovic-Hanic S. ZnO nanomaterials: Green synthesis, toxicity evaluation and new insights in biomedical applications. *J Alloys Compd* [Internet]. 2021 Sep 25;876:160175. Available from: [<URL>](#).
149. Kalpana VN, Devi Rajeswari V. A review on green synthesis, biomedical applications, and toxicity studies of ZnO NPs. *Bioinorg Chem Appl* [Internet]. 2018 Aug 1;2018(1):569758. Available from: [<URL>](#).
150. Tran T Van, Nguyen DTC, Kumar PS, Din ATM, Jalil AA, Vo DVN. Green synthesis of ZrO₂ nanoparticles and nanocomposites for biomedical and environmental applications: a review. *Environ Chem Lett* [Internet]. 2022 Apr 8;20(2):1309–31. Available from: [<URL>](#).
151. Woźniak A, Malankowska A, Nowaczyk G, Grześkowiak BF, Tuśnio K, Słomski R, et al. Size and shape-dependent cytotoxicity profile of gold nanoparticles for biomedical applications. *J Mater Sci Mater Med* [Internet]. 2017 Jun 11;28(6):92. Available from: [<URL>](#).
152. Zhu S, Gong L, Xie J, Gu Z, Zhao Y. Design, synthesis, and surface modification of materials based on transition-metal dichalcogenides for biomedical applications. *Small Methods* [Internet]. 2017 Dec 20;1(12):1700220. Available from: [<URL>](#).
153. Jeevanandam J, Kiew SF, Boakye-Ansah S, Lau SY, Barhoum A, Danquah MK, et al. Green approaches for the synthesis of metal and metal oxide nanoparticles using microbial and plant extracts. *Nanoscale* [Internet]. 2022 Feb 17;14(7):2534–71. Available from: [<URL>](#).
154. Andrade RGD, Veloso SRS, Castanheira EMS. Shape anisotropic iron oxide-based magnetic nanoparticles: Synthesis and biomedical applications. *Int J Mol Sci* [Internet]. 2020 Apr 1;21(7):2455. Available from: [<URL>](#).
155. Hameed S, Khalil AT, Ali M, Numan M, Khamlich S, Shinwari ZK, et al. Greener synthesis of ZnO and Ag-ZnO nanoparticles using *Silybum Marianum* for diverse biomedical applications. *Nanomedicine* [Internet]. 2019 Mar 4;14(6):655–73. Available from: [<URL>](#).
156. Li R, Liu Y, Seidi F, Deng C, Liang F, Xiao H. Design and construction of fluorescent cellulose nanocrystals for biomedical applications. *Adv Mater Interfaces* [Internet]. 2022 Apr 6;9(11):2101293. Available from: [<URL>](#).
157. Ahmad B, Hafeez N, Bashir S, Rauf A, Mujeeb-ur-Rehman. Phytofabricated gold nanoparticles and their biomedical applications. *Biomed Pharmacother* [Internet]. 2017 May 1;89:414–25. Available from: [<URL>](#).
158. Croissant JG, Fatieiev Y, Almalik A, Khashab NM. Mesoporous silica and organosilica nanoparticles: Physical chemistry, biosafety, delivery strategies, and biomedical applications. *Adv Healthc Mater* [Internet]. 2018 Feb;7(4):1700831. Available from: [<URL>](#).
159. Rajivgandhi G, Mythili Gnanamangai B, Heela Prabha T, Poornima S, Maruthupandy M, Alharbi NS, et al. Biosynthesized zinc oxide nanoparticles (ZnO NPs) using actinomycetes enhance the anti-bacterial efficacy against *K. Pneumoniae*. *J King Saud Univ - Sci* [Internet]. 2022 Jan 1;34(1):101731. Available from: [<URL>](#).
160. Undabarrena A, Ugalde JA, Seeger M, Cámara B. -Genomic data mining of the marine actinobacteria *Streptomyces* sp. H-KF8 unveils insights into multi-stress related genes and metabolic pathways involved in antimicrobial synthesis. *PeerJ* [Internet]. 2017 Feb 14;5(2):e2912. Available from: [<URL>](#).
161. AbdelRahim K, Mahmoud SY, Ali AM, Almaary KS, Mustafa AEZMA, Hussein SM. Extracellular biosynthesis of silver nanoparticles using *Rhizopus stolonifer*. *Saudi J Biol Sci* [Internet]. 2017 Jan 1;24(1):208–16. Available from: [<URL>](#).
162. Kianfar E. Protein nanoparticles in drug delivery: animal protein, plant proteins and protein cages, albumin nanoparticles. *J Nanobiotechnology* [Internet]. 2021 May 29;19(1):159. Available from: [<URL>](#).
163. Willem de Vries J, Schnichels S, Hurst J, Strudel L, Gruszka A, Kwak M, et al. DNA nanoparticles for ophthalmic drug delivery. *Biomaterials* [Internet]. 2018 Mar 1;157:98–106. Available from: [<URL>](#).

164. Talebi S, Ramezani F, Ramezani M. Biosynthesis of metal nanoparticles by microorganism. *Nanocon* [Internet]. 2010;10:12–4. Available from: [<URL>](#).
165. Li HJ, Du JZ, Liu J, Du XJ, Shen S, Zhu YH, et al. Smart Superstructures with Ultrahigh pH-sensitivity for targeting acidic tumor microenvironment: Instantaneous size switching and improved tumor penetration. *ACS Nano* [Internet]. 2016 Jul 26;10(7):6753–61. Available from: [<URL>](#).
166. Chowdhury NK, Choudhury R, Gogoi B, Chang CM, Pandey RP. Microbial synthesis of gold nanoparticles and their application. *Curr Drug Targets* [Internet]. 2022 Jul 28;23(7):752–60. Available from: [<URL>](#).
167. Ahmad F, Ashraf N, Ashraf T, Zhou RB, Yin DC. Biological synthesis of metallic nanoparticles (MNPs) by plants and microbes: their cellular uptake, biocompatibility, and biomedical applications. *Appl Microbiol Biotechnol* [Internet]. 2019 Apr 18;103(7):2913–35. Available from: [<URL>](#).
168. Gahlawat G, Choudhury AR. A review on the biosynthesis of metal and metal salt nanoparticles by microbes. *RSC Adv* [Internet]. 2019 Apr 26;9(23):12944–67. Available from: [<URL>](#).
169. De Matteis V, Cascione M, Toma CC, Leporatti S. Silver nanoparticles: Synthetic routes, in vitro toxicity and theranostic applications for cancer disease. *Nanomaterials* [Internet]. 2018 May 10;8(5):319. Available from: [<URL>](#).
170. Sagadevan S, Lett JA, Fatimah I, Lokanathan Y, Léonard E, Oh WC, et al. Current trends in the green syntheses of tin oxide nanoparticles and their biomedical applications. *Mater Res Express* [Internet]. 2021 Aug 1;8(8):082001. Available from: [<URL>](#).
171. Kiani BH, Haq I ul, Alhodaib A, Basheer S, Fatima H, Naz I, et al. Comparative evaluation of biomedical applications of zinc nanoparticles synthesized by using *Withania somnifera* plant extracts. *Plants* [Internet]. 2022 Jun 7;11(12):1525. Available from: [<URL>](#).
172. Khan S, Ul-Islam M, Ullah MW, Zhu Y, Narayanan KB, Han SS, et al. Fabrication strategies and biomedical applications of three-dimensional bacterial cellulose-based scaffolds: A review. *Int J Biol Macromol* [Internet]. 2022 Jun 1;209:9–30. Available from: [<URL>](#).
173. Asad S, Anwar N, Shah M, Anwar Z, Arif M, Rauf M, et al. Biological synthesis of silver nanoparticles by *Amaryllis vittata* (L.) Herit: From antimicrobial to biomedical applications. *Materials* [Internet]. 2022 Aug 9;15(16):5478. Available from: [<URL>](#).
174. Poudel DK, Niraula P, Aryal H, Budhathoki B, Phuyal S, Marahatha R, et al. Plant-mediated green synthesis of Ag NPs and their possible applications: A critical review. Kumar B, editor. *J Nanotechnol* [Internet]. 2022 Mar 16;2022(1):779237. Available from: [<URL>](#).
175. Pandit C, Roy A, Ghotekar S, Khusro A, Islam MN, Emran T Bin, et al. Biological agents for synthesis of nanoparticles and their applications. *J King Saud Univ - Sci* [Internet]. 2022 Apr 1;34(3):101869. Available from: [<URL>](#).
176. Kiani BH, Ikram F, Fatima H, Alhodaib A, Haq I ul, Ur-Rehman T, et al. Comparative evaluation of biomedical and phytochemical applications of zinc nanoparticles by using *Fagonia cretica* extracts. *Sci Rep* [Internet]. 2022 Jun 15;12(1):10024. Available from: [<URL>](#).
177. Danish MSS, Estrella-Pajulas LL, Alemaida IM, Grilli ML, Mikhaylov A, Senjyu T. Green synthesis of silver oxide nanoparticles for photocatalytic environmental remediation and biomedical applications. *Metals* [Internet]. 2022 Apr 29;12(5):769. Available from: [<URL>](#).
178. Nahari MH, Al Ali A, Asiri A, Mahnashi MH, Shaikh IA, Shettar AK, et al. Green synthesis and characterization of iron nanoparticles synthesized from aqueous leaf extract of *Vitex leucoxydon* and its biomedical applications. *Nanomaterials* [Internet]. 2022 Jul 14;12(14):2404. Available from: [<URL>](#).
179. Ijaz F, Shahid S, Khan SA, Ahmad W, Zaman S. Green synthesis of copper oxide nanoparticles using *Abutilon indicum* leaf extract: Antimicrobial, antioxidant and photocatalytic dye degradation activities. *Trop J Pharm Res* [Internet]. 2017 May 4;16(4):743–53. Available from: [<URL>](#).
180. Khan SA, Lee CS. Green Biological synthesis of nanoparticles and their biomedical applications. In: *Nanotechnology in the life sciences* [Internet]. Springer, Cham; 2020. p. 247–80. Available from: [<URL>](#).
181. Soni M, Mehta P, Soni A, Goswami GK. Green nanoparticles: Synthesis and applications. *IOSR J Biotechnol Biochem* [Internet]. 2018;4(3):78–83. Available from: [<URL>](#).
182. Khan T, Ullah N, Khan MA, Mashwani Z ur R, Nadhman A. Plant-based gold nanoparticles; a comprehensive review of the decade-long research on synthesis, mechanistic aspects and diverse applications. *Adv Colloid Interface Sci* [Internet]. 2019 Oct 1;272:102017. Available from: [<URL>](#).
183. Happy Agarwal, Soumya Menon, Venkat Kumar S, Rajeshkumar S. Mechanistic study on antibacterial action of zinc oxide nanoparticles synthesized using green route. *Chem Biol Interact* [Internet]. 2018 Apr 25;286:60–70. Available from: [<URL>](#).
184. Kigozi M, Ezealigo BN, Onwualu AP, Dzade NY. Hydrothermal synthesis of metal oxide composite cathode materials for high energy application. In: *Chemically deposited nanocrystalline metal oxide thin films* [Internet]. Cham: Springer International Publishing; 2021. p. 489–508. Available from: [<URL>](#).
185. Hu J, Li H, Muhammad S, Wu Q, Zhao Y, Jiao Q. Surfactant-assisted hydrothermal synthesis of TiO₂/reduced graphene oxide nanocomposites and

their photocatalytic performances. *J Solid State Chem* [Internet]. 2017 Sep 1;253:113–20. Available from: [<URL>](#).

186. Malekshahi Byranvand M, Kharat AN, Fatholahi L, Malekshahi Beiranvand Z. A Review on synthesis of Nano-TiO₂ via different methods. *J Nanostructures* [Internet]. 2013;3:1–9. Available from: [<URL>](#).

187. Bulcha B, Leta Tesfaye J, Anatol D, Shanmugam R, Dwarampudi LP, Nagaprasad N, et al. Synthesis of zinc oxide nanoparticles by hydrothermal methods and spectroscopic investigation of ultraviolet radiation protective properties. R L, editor. *J Nanomater* [Internet]. 2021 Sep 22;2021(1):617290. Available from: [<URL>](#).

188. Jubeer EM, Manthrammel MA, Subha PA, Shkir M, Biju KP, AlFaify SA. Defect engineering for enhanced optical and photocatalytic properties of ZnS nanoparticles synthesized by hydrothermal method. *Sci Rep* [Internet]. 2023 Oct 5;13(1):16820. Available from: [<URL>](#).

189. Chen N, Liu B, Zhang P, Wang C, Du Y, Chang W, et al. Enhanced photocatalytic performance of Ce-doped SnO₂ hollow spheres by a one-pot hydrothermal method. *Inorg Chem Commun* [Internet]. 2021 Oct 1;132:108848. Available from: [<URL>](#).

190. Khan S, Usman M, Abdullah M, Suleman Waheed M, Faheem Ashiq M, Ishfaq Ahmad M, et al. Facile synthesis of CuAl₂O₄/rGO nanocomposite via the hydrothermal method for supercapacitor applications. *Fuel* [Internet]. 2024 Feb 1;357:129688. Available from: [<URL>](#).

191. Soares CPP, Baptista R de L, Cesar DV. Solvothermal reduction of graphite oxide using alcohols. *Mater Res* [Internet]. 2017 Dec 18;21(1):e20170726. Available from: [<URL>](#).

192. Yuan R, Wen H, Zeng L, Li X, Liu X, Zhang C. Supercritical CO₂ assisted solvothermal preparation of CoO/Graphene nanocomposites for high performance lithium-ion batteries. *Nanomaterials* [Internet]. 2021 Mar 10;11(3):694. Available from: [<URL>](#).

193. Perumal S, Monikandaprabu K, Sambandam CG, Mohamed AP. Synthesis and characterization studies of solvothermally synthesized undoped and Ag-doped TiO₂ nanoparticles using toluene as a solvent. *J Eng Res Appl* [Internet]. 2014;4(7):184–7. Available from: [<URL>](#).

194. Uematsu T, Baba M, Oshima Y, Tsuda T, Torimoto T, Kuwabata S. Atomic resolution imaging of gold nanoparticle generation and growth in ionic liquids. *J Am Chem Soc* [Internet]. 2014 Oct 1;136(39):13789–97. Available from: [<URL>](#).

195. Kløve M, Philippot G, Auxéméry A, Aymonier C, Iversen BB. Stabilizing tetragonal ZrO₂ nanocrystallites in solvothermal synthesis. *Nanoscale* [Internet]. 2024 Feb 8;16(6):3185–90. Available from: [<URL>](#).

196. Zhang L, Feng L, Li P, Chen X, Jiang J, Zhang S, et al. Direct Z-scheme photocatalyst of hollow CoS_x@CdS polyhedron constructed by ZIF-67-templated one-pot solvothermal route: A signal-on photoelectrochemical sensor for mercury(II). *Chem Eng J* [Internet]. 2020 Sep 1;395:125072. Available from: [<URL>](#).

197. Revathi J, Abel MJ, Archana V, Sumithra T, Thiruneelakandan R, Joseph prince J. Synthesis and characterization of CoFe₂O₄ and Ni-doped CoFe₂O₄ nanoparticles by chemical Co-precipitation technique for photo-degradation of organic dyestuffs under direct sunlight. *Phys B Condens Matter* [Internet]. 2020 Jun 15;587:412136. Available from: [<URL>](#).

198. Pu S, Xue S, Yang Z, Hou Y, Zhu R, Chu W. In situ co-precipitation preparation of a superparamagnetic graphene oxide/Fe₃O₄ nanocomposite as an adsorbent for wastewater purification: synthesis, characterization, kinetics, and isotherm studies. *Environ Sci Pollut Res* [Internet]. 2018 Jun 13;25(18):17310–20. Available from: [<URL>](#).

199. Priyadharshini P, Shobika PA, Monisha P, Gomathi SS, Pushpanathan K. Nickel ferrite magnetic nanoparticles: evidence for superparamagnetism in smaller size particles. *J Aust Ceram Soc* [Internet]. 2022 Dec 5;58(5):1455–80. Available from: [<URL>](#).

200. Arya S, Mahajan P, Mahajan S, Khosla A, Datt R, Gupta V, et al. Review—influence of processing parameters to control morphology and optical properties of sol-gel synthesized ZnO nanoparticles. *ECS J Solid State Sci Technol* [Internet]. 2021 Feb 1;10(2):023002. Available from: [<URL>](#).

201. Tadic M, Panjan M, Tadic BV, Lazovic J, Damjanovic V, Kopani M, et al. Magnetic properties of hematite (α-Fe₂O₃) nanoparticles synthesized by sol-gel synthesis method: The influence of particle size and particle size distribution. *J Electr Eng* [Internet]. 2019 Dec 1;70(7):71–6. Available from: [<URL>](#).

202. Youssef F, Farghaly U, Abd El-Baky RM, Waly N. Comparative study of antibacterial effects of titanium dioxide nanoparticles alone and in combination with antibiotics on MDR *Pseudomonas aeruginosa* Strains. *Int J Nanomedicine* [Internet]. 2020 May;Volume 15:3393–404. Available from: [<URL>](#).

203. Arkaban H, Khajeh Ebrahimi A, Yarahmadi A, Zarrintaj P, Barani M. Development of a multifunctional system based on CoFe₂O₄ @polyacrylic acid NPs conjugated to folic acid and loaded with doxorubicin for cancer theranostics. *Nanotechnology* [Internet]. 2021 Jul 23;32(30):305101. Available from: [<URL>](#).

204. Liu J, Guo C, Zhang Y. Research of crystal changing of barium hexaferrite prepared by citric acid sol-gel method. *Funct Mater Lett* [Internet]. 2017 Apr 3;10(02):1750001. Available from: [<URL>](#).

205. Zakir R, Iqbal SS, Rehman AU, Nosheen S, Ahmad TS, Ehsan N, et al. Spectral, electrical, and dielectric characterization of Ce-doped Co-Mg-Cd spinel nano-ferrites synthesized by the sol-gel auto combustion method. *Ceram Int* [Internet]. 2021 Oct 15;47(20):28575–83. Available from: [<URL>](#).
206. Suneetha RB, Selvi P, Vedhi C. Synthesis, structural and electrochemical characterization of Zn doped iron oxide/grapheneoxide/chitosan nanocomposite for supercapacitor application. *Vacuum* [Internet]. 2019 Jun 1;164:396–404. Available from: [<URL>](#).
207. Zeng X, Teng J, Yu J gang, Tan A shuang, Fu D fa, Zhang H. Fabrication of homogeneously dispersed graphene/Al composites by solution mixing and powder metallurgy. *Int J Miner Metall Mater* [Internet]. 2018 Jan 3;25(1):102–9. Available from: [<URL>](#).
208. Nawaz M, Moztahida M, Kim J, Shahzad A, Jang J, Miran W, et al. Photodegradation of microcystin-LR using graphene-TiO₂/sodium alginate aerogels. *Carbohydr Polym* [Internet]. 2018 Nov 1;199:109–18. Available from: [<URL>](#).
209. Hong YL, Liu Z, Wang L, Zhou T, Ma W, Xu C, et al. Chemical vapor deposition of layered two-dimensional MoSi₂N₄ materials. *Science* [Internet]. 2020 Aug 7;369(6504):670–4. Available from: [<URL>](#).
210. Xu S, Zhang L, Wang B, Ruoff RS. Chemical vapor deposition of graphene on thin-metal films. *Cell Reports Phys Sci* [Internet]. 2021 Mar 24;2(3):100372. Available from: [<URL>](#).
211. Wu Y, Zhao Z, Sun C, Ji C, Zhang Y, Qu R, et al. In-situ synthesis of PPTA nanomaterials in PS matrix and their enhanced performances in PS-based nanocomposite. *Eur Polym J* [Internet]. 2022 Oct 5;179:111535. Available from: [<URL>](#).
212. Suba A, Selvarajan P, Jebaraj Devadasan J. Rubidium chloride doped magnesium oxide nanomaterial by using green synthesis and its characterization. *Chem Phys Lett* [Internet]. 2022 Apr 16;793:139463. Available from: [<URL>](#).
213. Amparo SZS do, Vasconcelos CKB de, Almeida AIAR, Sena LEB, Lima MCF, Medeiros FS, et al. Microwave-assisted synthesis of PAM preformed particle gels reinforced with carbon nanomaterials for conformance control in oil recovery. *Fuel* [Internet]. 2022 Dec 15;330:125650. Available from: [<URL>](#).
214. Zhang J, Tian X, Cui X, Zheng A, Li J, Bai Y, et al. Facile synthesis of hyperbranched magnetic nanomaterials for selective adsorption of proteins. *Talanta* [Internet]. 2023 Jan 15;252:123895. Available from: [<URL>](#).
215. Hammond OS, Mudring AV. Ionic liquids and deep eutectics as a transformative platform for the synthesis of nanomaterials. *Chem Commun* [Internet]. 2022 Mar 22;58(24):3865–92. Available from: [<URL>](#).
216. Siwal SS, Sheoran K, Mishra K, Kaur H, Saini AK, Saini V, et al. Novel synthesis methods and applications of MXene-based nanomaterials (MBNs) for hazardous pollutants degradation: Future perspectives. *Chemosphere* [Internet]. 2022 Apr 1;293:133542. Available from: [<URL>](#).
217. Shingdilwar S, Kumar D, Sahu B, Banerjee S. Straightforward synthesis of multifunctional porous polymer nanomaterials for CO₂ capture and removal of contaminants. *Polym Chem* [Internet]. 2022 Apr 12;13(15):2165–72. Available from: [<URL>](#).
218. Fu Y, Li Z, Hu C, Li Q, Chen Z. Synthesis of carbon dots-based covalent organic nanomaterial as stationary phase for open tubular capillary electrochromatography. *J Chromatogr A* [Internet]. 2022 Aug 16;1678:463343. Available from: [<URL>](#).
219. Li Q, Cui Y, Lin J, Zhao C, Ding L. Synthesis of carbon microsphere-assisted snowflake-like ZnO nanomaterials for selective detection of NO₂ at room temperature. *J Ind Eng Chem* [Internet]. 2022 Jun 25;110:542–51. Available from: [<URL>](#).
220. Hussain SA, Ali S, Islam ZU, Khan M. Low-temperature synthesis of graphite flakes and carbon-based nanomaterials from banana peels using hydrothermal process for photoelectrochemical water-splitting. *Phys E Low-dimensional Syst Nanostructures* [Internet]. 2022 Jul 1;141:115231. Available from: [<URL>](#).
221. Li Q, Huang N, Cui Y, Lin J, Zhao C, Ding L. Synthesis of porous rod-like In₂O₃ nanomaterials and its selective detection of NO at room temperature. *J Alloys Compd* [Internet]. 2022 May 5;902:163632. Available from: [<URL>](#).
222. Wang BB, Zhong XX, Zhu J, Wang Y, Zhang Y, Cvelbar U, et al. Single-step synthesis of TiO₂/WO₃-hybrid nanomaterials in ethanoic acid: Structure and photoluminescence properties. *Appl Surf Sci* [Internet]. 2021 Oct 1;562:150180. Available from: [<URL>](#).
223. Mohan V V., Anjana PM, Rakhi RB. One pot synthesis of tungsten oxide nanomaterial and application in the field of flexible symmetric supercapacitor energy storage device. *Mater Today Proc* [Internet]. 2022 Jan 1;62:848–51. Available from: [<URL>](#).
224. Xu H, Liu C, Srinivasakannan C, Chen M, Wang Q, Li L, et al. Hydrothermal synthesis of one-dimensional α-MoO₃ nanomaterials and its unique sensing mechanism for ethanol. *Arab J Chem* [Internet]. 2022 Sep 1;15(9):104083. Available from: [<URL>](#).
225. Sehrawat P, Malik RK, Punia R, Maken S, Kumari N. Ecofriendly synthesis and white light-emitting properties of BaLa₂ZnO₅:Dy³⁺ nanomaterials for lighting application in NUV-WLEDs and solar cells. *Chem Phys Lett* [Internet]. 2022 Apr 1;792:139399. Available from: [<URL>](#).
226. Najahi Mohammadzadeh Z, Hamidinasab M, Ahadi N, Bodaghifard MA. A novel hybrid organic-

- inorganic nanomaterial: Preparation, characterization and application in synthesis of diverse heterocycles. Polycycl Aromat Compd [Internet]. 2022 Apr 21;42(4):1282–301. Available from: [<URL>](#).
227. Khan MJ, Tahir K, El-Zahhar AA, Arooj A, AL-Abdulkarim HA, Saleh EAM, et al. Facile synthesis of silver modified zinc oxide nanocomposite: An efficient visible light active nanomaterial for bacterial inhibition and dye degradation. Photodiagnosis Photodyn Ther [Internet]. 2021 Dec 1;36:102619. Available from: [<URL>](#).
228. Chowdhury A, Kumari S, Khan AA, Hussain S. Synthesis of mixed phase crystalline CoNi_2S_4 nanomaterial and selective mechanism for adsorption of Congo red from aqueous solution. J Environ Chem Eng [Internet]. 2021 Dec 1;9(6):106554. Available from: [<URL>](#).
229. Jarariya R, Suresh K. Spinel ferrite nanomaterials - MgFe_2O_4 - Synthesis by appropriate microwave solution combustion (Msc) method of visible light-responsive photocatalyst for Rb21 dye degradation. Mater Today Proc [Internet]. 2023 Jan 1;72:2618–29. Available from: [<URL>](#).
230. Liu H, Zhu Y, Ma J, Chen C, Cheng P, Zhang S. Hydrothermal synthesis of Pd-doped CeO_2 nanomaterials and electrochemical detection for phenol. J Cryst Growth [Internet]. 2022 May 15;586:126626. Available from: [<URL>](#).
231. Sehrawat P, Malik RK, Punia R, Sheoran M, Singh S, Kumar M. New $\text{Ba}_2\text{YAlO}_5:\text{Dy}^{3+}$ nanomaterials for WLEDs: Propellant combustion synthesis and photometric features for enhanced emission of cool-white light under NUV excitation. Chem Phys Lett [Internet]. 2021 Oct 16;781:138985. Available from: [<URL>](#).
232. Vijay R, Drisya VM, Selta DRF, Rathi MA, Gopalakrishnan V, Alkhalifah DHM, et al. Synthesis and characterization of silver nanomaterial from aqueous extract of *Commelina forskoalii* and its potential antimicrobial activity against Gram negative pathogens. J King Saud Univ - Sci [Internet]. 2023 Jan 1;35(1):102373. Available from: [<URL>](#).
233. Acauan LH, Kaiser AL, Wardle BL. Direct synthesis of carbon nanomaterials via surface activation of bulk copper. Carbon N Y [Internet]. 2021 Jun 15;177:1–10. Available from: [<URL>](#).
234. Zaikovskii A, Yudin I, Kozlachkov D, Nartova A, Fedorovskaya E. Gas pressure control of electric arc synthesis of composite $\text{Sn-SnO}_2\text{-C}$ nanomaterials. Vacuum [Internet]. 2022 Jan 1;195:110694. Available from: [<URL>](#).
235. Singh N, Kalbande PN, Umbarkar S, Sudarsanam P. Efficient cascade C-N coupling reactions catalyzed by a recyclable $\text{MoO}_x/\text{Nb}_2\text{O}_5$ nanomaterial for valuable N-heterocycles synthesis. Mol Catal [Internet]. 2022 Nov 1;532:112742. Available from: [<URL>](#).
236. Sahoo SK, Panigrahi GK, Sahu MK, Arzoo A, Sahoo JK, Sahoo A, et al. Biological synthesis of GO-MgO nanomaterial using *Azadirachta indica* leaf extract: A potential bio-adsorbent for removing Cr(VI) ions from aqueous media. Biochem Eng J [Internet]. 2022 Jan 1;177:108272. Available from: [<URL>](#).
237. Sharma SK, Sharma G, Sharma A, Bhardwaj K, Preeti K, Singh K, et al. Synthesis of silica and carbon-based nanomaterials from rice husk ash by ambient fiery and furnace sweltering using a chemical method. Appl Surf Sci Adv [Internet]. 2022 Apr 1;8:100225. Available from: [<URL>](#).
238. Rajangam K, Amuthameena S, Thangavel S, Sanjanadevi VS, Balraj B. Synthesis and characterisation of Ag incorporated TiO_2 nanomaterials for supercapacitor applications. J Mol Struct [Internet]. 2020 Nov 5;1219:128661. Available from: [<URL>](#).
239. Govindaraju K, Anand KV, Anbarasu S, Theerthagiri J, Revathy S, Krupakar P, et al. Seaweed (*Turbinaria ornata*)-assisted green synthesis of magnesium hydroxide [$\text{Mg}(\text{OH})_2$] nanomaterials and their anti-mycobacterial activity. Mater Chem Phys [Internet]. 2020 Jan 1;239:122007. Available from: [<URL>](#).
240. Khan MD, Aamir M, Akhtar J, Malik MA, Revaprasadu N. Metal selenobenzoate complexes: Novel single source precursors for the synthesis of metal selenide semiconductor nanomaterials. Mater Today Proc [Internet]. 2019 Jan 1;10:66–74. Available from: [<URL>](#).
241. Liu PR, Yang ZY, Hong Y, Hou YL. An in situ method for synthesis of magnetic nanomaterials and efficient harvesting for oleaginous microalgae in algal culture. Algal Res [Internet]. 2018 Apr 1;31:173–82. Available from: [<URL>](#).
242. Kaynar UH, Çam Kaynar S, Ekdal Karali E, Ayvacikli M, Can N. Adsorption of thorium(IV) ions by metal ion doped ZnO nanomaterial prepared with combustion synthesis: Empirical modelling and process optimization by response surface methodology (RSM). Appl Radiat Isot [Internet]. 2021 Dec 1;178:109955. Available from: [<URL>](#).
243. Li X, Zhang F, Zhai B, Wang X, Zhao J, Wang Z. Facile synthesis of porous anatase TiO_2 nanomaterials with the assistance of biomass resource for lithium ion batteries with high-rate performance. J Phys Chem Solids [Internet]. 2020 Oct 1;145:109552. Available from: [<URL>](#).
244. Sinha S, Kr. Aman A, Kr. Singh R, Kr N, Shivani K. Calcium oxide(CaO) nanomaterial (Kukutanda twak Bhasma) from egg shell: Green synthesis, physical properties and antimicrobial behaviour. Mater Today Proc [Internet]. 2021 Jan 1;43:3414–9. Available from: [<URL>](#).
245. Abdullah, Hussain T, Faisal S, Rizwan M, Saira, Zaman N, et al. Green synthesis and characterization of copper and nickel hybrid nanomaterials: Investigation of their biological and photocatalytic

- potential for the removal of organic crystal violet dye. *J Saudi Chem Soc* [Internet]. 2022 Jul 1;26(4):101486. Available from: [<URL>](#).
246. Tigwera GA, Khan MD, Nyamen LD, Aboud AA, Moyo T, Dlamini ST, et al. Molecular precursor route for the phase selective synthesis of α -MnS or metastable γ -MnS nanomaterials for magnetic studies and deposition of thin films by AACVD. *Mater Sci Semicond Process* [Internet]. 2022 Mar 1;139:106330. Available from: [<URL>](#).
247. Vasudha M, Khan AA, Bhumika KM, Gayathri D, Nagaswarupa HP, Shashi shekhar TR, et al. Facile chemical synthesis of $\text{Ca}_3\text{MgAl}_{10}\text{O}_{17}$ nanomaterials for photocatalytic and non-enzymatic sensor applications. *Sensors Int* [Internet]. 2021 Jan 1;2:100082. Available from: [<URL>](#).
248. K ksoy B, Aky z D,  enocak A, Durmu  M, Demirba  E. Novel SWCNT-hybrid nanomaterial functionalized with subphthalocyanine substituted asymmetrical zinc (II) phthalocyanine conjugate: Design, synthesis, characterization and sensor properties for pesticides. *Sensors Actuators B Chem* [Internet]. 2021 Feb 15;329:129198. Available from: [<URL>](#).
249. Dinh VP, Tran NQ, Le NQT, Tran QH, Nguyen TD, Le VT. Facile synthesis of FeFe_2O_4 magnetic nanomaterial for removing methylene blue from aqueous solution. *Prog Nat Sci Mater Int* [Internet]. 2019 Dec 1;29(6):648–54. Available from: [<URL>](#).
250. Vel zquez-Hern ndez I, Est vez M, Vergara-Casta eda H, Guerra-Balc zar M,  lvarez-Contreras L, Luna-B rcenas G, et al. Synthesis and application of biogenic gold nanomaterials with {100} facets for crude glycerol electro-oxidation. *Fuel* [Internet]. 2020 Nov 1;279:118505. Available from: [<URL>](#).
251. Bayan EM, Lupeiko TG, Pustovaya LE, Volkova MG, Butova VV, Guda AA. Zn–F co-doped TiO_2 nanomaterials: Synthesis, structure and photocatalytic activity. *J Alloys Compd* [Internet]. 2020 May 5;822:153662. Available from: [<URL>](#).
252. Chandrappa M, Swathi K, Girish Kumar S, Pullela PK. Nanomaterial assisted bulk scale synthesis of 2-methyl-6-nitroquinoline. *Mater Today Proc* [Internet]. 2021 Jan 1;37(Part 2):1469–74. Available from: [<URL>](#).
253. Zhang Y, Chen Y, Kang ZW, Gao X, Zeng X, Liu M, et al. Waste eggshell membrane-assisted synthesis of magnetic CuFe_2O_4 nanomaterials with multifunctional properties (adsorptive, catalytic, antibacterial) for water remediation. *Colloids Surfaces A Physicochem Eng Asp* [Internet]. 2021 Mar 5;612:125874. Available from: [<URL>](#).
254. Uppal H, Chawla S, Joshi AG, Haranath D, Vijayan N, Singh N. Facile chemical synthesis and novel application of zinc oxysulfide nanomaterial for instant and superior adsorption of arsenic from water. *J Clean Prod* [Internet]. 2019 Jan 20;208:458–69. Available from: [<URL>](#).
255. Al-Anazi A, Abdelraheem WH, Scheckel K, Nadagouda MN, O’Shea K, Dionysiou DD. Novel franklinite-like synthetic zinc-ferrite redox nanomaterial: synthesis, and evaluation for degradation of diclofenac in water. *Appl Catal B Environ* [Internet]. 2020 Oct 15;275:119098. Available from: [<URL>](#).
256. Adimule V, Yallur BC, Challa M, Joshi RS. Synthesis of hierarchical structured Gd doped α - Sb_2O_4 as an advanced nanomaterial for high performance energy storage devices. *Heliyon* [Internet]. 2021 Dec 1;7(12):e08541. Available from: [<URL>](#).
257. Bello IT, Adio SA, Oladipo AO, Adedokun O, Mathevula LE, Dhlamini MS. Molybdenum sulfide-based supercapacitors: From synthetic, bibliometric, and qualitative perspectives. *Int J Energy Res* [Internet]. 2021 Jul 11;45(9):12665–92. Available from: [<URL>](#).



Molecular Interaction of Dextran and Sodium Hydroxide through Ultrasonic Investigation

Subhrraj Panda¹

¹Centurion University of Technology and Management, Odisha, India.

Abstract: Studies were conducted to analyze the intermolecular interactions between dextran solute and 1M sodium hydroxide solvent in aqueous solutions at different temperatures and concentrations. This involved measuring ultrasonic speed (U), density (ρ), and viscosity (η). Various acoustic parameters such as free volume (V_f), internal pressure (Π), Rao's constant (R), and Wada's constant (W) were calculated at a constant frequency using the experimentally obtained values of density (ρ), viscosity (η), and ultrasonic speed (U) of the solutions. The results provide insight into the temperature and concentration dependence of these parameters and the intermolecular interactions within the system. This investigation offers valuable information about the interaction type between solute and solvent, structural rearrangement, and the extent of molecular interaction in liquid solutions.

Keywords: Aqueous dextran, Ultrasonic speed, Density, Viscosity, Molecular interactions.

Submitted: August 17, 2023. **Accepted:** August 5, 2024.

Cite this: Panda S. Molecular Interaction of Dextran and Sodium Hydroxide through Ultrasonic Investigation. JOTCSA. 2024;11(4): 1369-76.

DOI: <https://doi.org/10.18596/jotcsa.1345350>

***Corresponding author's E-mail:** subhrraj4u@gmail.com

1. INTRODUCTION

The study of molecular interactions is crucial to comprehending the composition and properties of liquids. Several studies have been carried out on the interaction in liquid mixtures using various techniques, including infrared spectroscopy, nuclear magnetic resonance spectroscopy, and ultrasonic research. These methods have proven to be practical tools for obtaining information about liquid systems' physical and chemical properties (1). The approach of researching molecular interactions using knowledge of thermodynamic parameter fluctuation with composition and temperature provides insight into the molecular process. Industry demands a broad spectrum of chemical and physical properties of liquid solutions.

Researchers have used ultrasonic methods to study polymer structures from various perspectives (2-4). Researching acoustic characteristics is a convenient approach for investigating liquid structures, particularly dilute polymer solutions. Using basic procedures, it provides a strong understanding of the potential structure of the polymer and solvent molecules at various concentrations and some information about the amount of connection (5). In previous years, the most popular and cost-effective

technique for determining density (ρ), viscosity (η), and ultrasonic speed (U) was to use a specific gravity bottle, a capillary viscometer, and an ultrasonic interferometer (6-10). To anticipate the solute-solvent, ion-solvent, and solvent-solvent interactions in aqueous solutions, including electrolytes, ultrasonic speed measurements are beneficial in the field of study.

Since ultrasonic speed is essentially connected to the binding forces between the medium's constituents, it is very sensitive to the structure and interactions seen in liquid systems. The intermolecular free path length in a solution determines the ultrasonic speed. The presence of ultrasonic waves stirs the molecules in the solution. The medium is flexible, allowing disrupted molecules to return to their equilibrium positions. The molecules of a solute attract the molecules of a solvent when they are introduced together. This phenomenon is referred to as restricted compressibility and compression. Aggregation of solvent molecules around solute molecules strengthens solvent-solute interactions. Solvent-solute interactions result in a considerable alteration of the solute's structure (11).

Utilizing a through transmission approach at a frequency of 5 MHz, ultrasonic investigations were

carried out to measure longitudinal and shear wave velocities and attenuation across a temperature range of 300 to 700 K (12). Using the through transmission technique, ultrasonic velocities and attenuation for $\text{La}_{1-x}\text{Ca}_x\text{MnO}_3$ samples were evaluated using a high-power ultrasonic pulser receiver and recorded via a 1 GHz digital storage oscilloscope. 5 MHz X- and Y-cut transducers produced longitudinal and shear waves, and a programmable temperature controller was used to regulate the heating rate, which allowed for measurements to be made between 300 and 600 K at a rate of 0.5 K/min. The recorded ultrasonic velocities and densities were used to determine elastic constants that took temperature variations into account, such as bulk, longitudinal, shear, and Poisson's moduli and Young's modulus (13). According to in situ ultrasonic experiments, NLSMO's Curie temperature was lower than BLSMO's and continued to drop as the Sr concentration increased. Furthermore, the extensive transitions seen in the NLSMO samples indicated that the usual phase transition from ferromagnetic to paramagnetic (FM to PM) was absent (14).

If ionic solvents are present in solutions, then the interaction is purely ion-dipole interaction, which depends on the ion size and polarity of the solute (15-17). After adding the solute to the solvent, the ion and solute molecule interact, which causes volume contraction (18,19). Several researchers have determined the ultrasonic speed and related parameters (20-23). From the literature review, it is found that studies have been made for various univalent and bivalent electrolytes, biomolecules, heterocyclic compounds, drugs, and different solvent systems like CH_3OH , ethylene glycol propanol, and other proteins.

The values of the relevant thermodynamic and acoustic parameters, as well as ρ , η , and U , have been determined in this article at temperatures of "303K, 308K, 313K, 318K, and 323K" in 1MHz frequency, of dextran 0.1, 0.25, 0.50, 0.75, and 1 percent concentrations in 1(M) sodium hydroxide solution. The various acoustic parameters like free volume (V_f), internal pressure (Π_i), Rao's constant (R), and Wada's constant (W) have been calculated at constant frequency in different temperatures and concentrations (24-26). Dextran has broad industrial applicability, particularly in the pharmaceutical industry, so we chose it for our study. Dextran is water soluble. Dextran, initially utilized to convert human red blood cells into synthetic blood-volume expanders to enhance the degree of polymerization, is now being employed in clinical applications and pharmaceutical industry tablet studies (27-29).

Ultrasonic techniques are widely utilized in engineering and many other fields to study molecular interactions in liquids. These techniques use the propagation of ultrasonic waves through liquids to gather information on the properties, compositions, and behaviors of molecules. It is possible to use ultrasonic interferometry to determine conformational changes in the molecules. Understanding the underlying chemical mechanisms

and how the structure of molecules changes during binding may be gained from this. Using ultrasonic techniques, phase shifts and the solidification of liquids are detected. Changes in ultrasonic wave properties, which can be utilized to detect changes in molecular interactions during cooling or heating, aid in the understanding of the freezing and melting processes.

2. EXPERIMENTAL MATERIALS & METHODS

For studies, 1(M) sodium hydroxide AR (analytical reagent) grade with a minimum assay of 99.9% and the polymer dextran with a molecular weight of 70,000 Da manufactured by HI Media Laboratories Private Limited, India. The NaOH solution was made from freshly distilled water. The solute, dextran 70,000 Da, was utilized, and its concentrations varied throughout distinct (w/v) percentage ranges (30,31).

2.1. Measurements

The mass of a known volume of the solution was measured, and density was calculated using a Pycnometer (specific gravity bottle). Using a conventional equation and a 25mL specific gravity bottle (Figure 1), the density (32-34) of the solution is calculated with an accuracy of $0.1 \text{ kg}\cdot\text{m}^{-3}$. Utilizing a specific gravity bottle, the thickness was measured with an error of 0.04%.



Figure 1: Specific gravity bottle.

$$\rho_2 = \frac{w_2}{w_1} \rho_1 \quad (1)$$

Where w_1 and w_2 denote the weight, ρ_1 and ρ_2 denote the density of distilled water and the experimental solution, respectively

Viscosity was measured by timing the flow of the solution through the viscometer capillary at controlled temperature conditions. The viscosity (32-34) of the polymer solution was assessed using a pre-calibrated Ostwald's viscometer (Figure 2) with an error range of 0.067% (Figure 2). The flow time of the solutions used for the inquiry is used to calculate the viscosity, with an inaccuracy of up to 0.01 seconds. The equation was used to calculate the values at the specified temperatures.

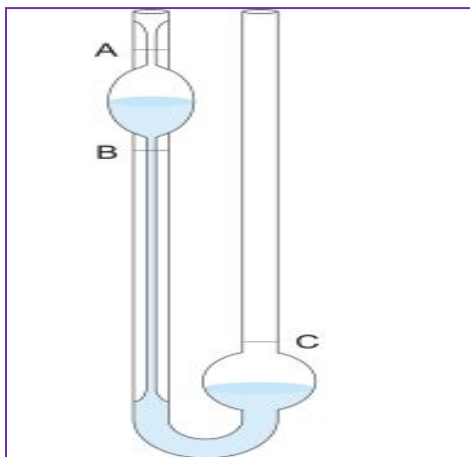


Figure 2: Ostwald's viscometer.

$$\eta_2 = \eta_1 \left(\frac{t_2}{t_1} \right) \left(\frac{\rho_2}{\rho_1} \right) \quad (2)$$

where η_1 and η_2 are the viscosities, and t_1 and t_2 are the times of flow of distilled water and the experimental solution, respectively.

Using an ultrasonic interferometer (Figure 3) having uncertainty within the order of ± 0.056 , The ultrasonic wave's speed in solution was measured using 11 distinct frequency bands (35). The interferometer measuring cell is a specially created double-walled vessel with a temperature constant configuration. Water was circulated through the outer jacket of the double-walled estimation cell containing the test solution using an electronically controlled advanced steady temperature shower that functioned in the temperature range of -10°C to 85°C with an accuracy of 0.1 K . All measurements were made in a water bath with a flowing medium that had a 0.10°C uncertainty. Measurements were taken at multiple frequencies (1 MHz, 5 MHz, 9 MHz, and 12 MHz). The sample was placed in the interferometer, and ultrasonic velocity was recorded at each frequency.



Figure 3: Ultrasonic interferometer.

3. THEORETICAL ASPECT

The calculated thermodynamic and acoustic parameters (36)

Free volume:

"Free volume (V_f) in terms of ultrasonic velocity (U) and the viscosity (η)" of the liquid is as follows:

$$V_f = \left(\frac{M_{\text{eff}} U}{K \eta} \right)^2 \quad (3)$$

Where M_{eff} is the solution's effective molecular weight, and K is the temperature-independent constant, which is 4.281×10^9 for all liquids.

Internal pressure:

It can be calculated using the relation given below

$$\pi_i = bRT \left(\frac{K\eta}{U} \right)^{3/2} \left(\frac{\rho^{2/3}}{M_{\text{eff}}^{7/6}} \right) \quad (4)$$

Where b stands for cubic packing, which is assumed to be 2 for all liquids, T is the absolute temperature in Kelvin, and R is the universal gas constant.

Rao's constant:

Rao has demonstrated the empirical relationship between molecular weight, density, and ultrasonic velocity of liquids.

$$R = \frac{M_{\text{eff}}}{\rho} U^{1/3} \quad (5)$$

This equation is called Rao's rule, and R is also called the molar sound velocity. Rao provided a theoretical explanation of his formula based on the phase rule and kinetic theory of liquids.

Wada's constant:

Wada explored how molar compressibility changed with a concentration in a variety of liquid systems. He came up with the empirical relationship,

$$W = \frac{M_{\text{eff}}}{\rho} \beta^{-1/7} \quad (6)$$

4. RESULTS AND DISCUSSION

The experimental values of density (ρ), viscosity (η), and ultrasonic speed (U), the derived parameters free volume (V_f), internal pressure (Π_i), Rao's constant (R), and Wada's constant (W) of dextran in H_2O - NaOH are given in Table 1-3 and displayed in Figure 4 to 10.

Table 1: Ultrasonic speed (U) and free volume (V_f).

T (K)	(U) m/s					$(V_f) (\times 10^{-3} \text{m}^3 \cdot \text{mol}^{-1})$				
	0.10%	0.25%	0.50%	0.75%	1%	0.10%	0.25%	0.50%	0.75%	1%
303	1587.0	1589.0	1590.0	1591.0	1593.0	7.437	7.348	7.156	6.887	6.671
308	1594.0	1596.0	1597.0	1598.0	1599.0	8.870	8.621	8.381	8.157	7.784
313	1600.0	1601.0	1603.0	1604.0	1606.0	10.759	10.098	9.946	9.509	9.032
318	1606.0	1607.0	1608.0	1610.0	1612.0	11.641	11.054	10.882	10.712	10.212
323	1611.0	1613.0	1614.0	1615.0	1618.0	13.232	12.988	12.545	11.914	11.312

Table 2: Internal pressure (Π_i).

T (K)	$\Pi_i(\times 10^3 \text{ N}\cdot\text{m}^{-2})$				
	0.10%	0.25%	0.50%	0.75%	1%
303	122.65	123.17	124.33	125.96	127.44
308	117.41	118.62	119.80	120.92	122.99
313	111.74	114.19	114.86	116.62	118.83
318	110.40	112.42	113.04	113.72	115.74
323	107.24	107.97	109.29	111.30	113.40

Table 3: Rao’s constant (R) and Wada’s constant(W).

T (K)	(R) ($\text{m}^3/\text{mole})(\text{m}/\text{s})^{1/3}(10^{-3})$)					(W) ($\text{m}^3/\text{mole})(\text{N}/\text{m}^2)^{1/7}(10^{-3})$)				
	0.10%	0.25%	0.50%	0.75%	1%	0.10%	0.25%	0.50%	0.75%	1%
303	1.126	1.126	1.126	1.125	1.124	0.0797	0.0797	0.0797	0.0796	0.0796
308	1.130	1.129	1.129	1.128	1.126	0.0799	0.0799	0.0798	0.0798	0.0797
313	1.134	1.133	1.132	1.132	1.130	0.0801	0.0801	0.0800	0.0800	0.0799
318	1.138	1.137	1.136	1.135	1.133	0.0804	0.0803	0.0803	0.0802	0.0801
323	1.142	1.142	1.141	1.140	1.138	0.0807	0.0806	0.0806	0.0805	0.0804

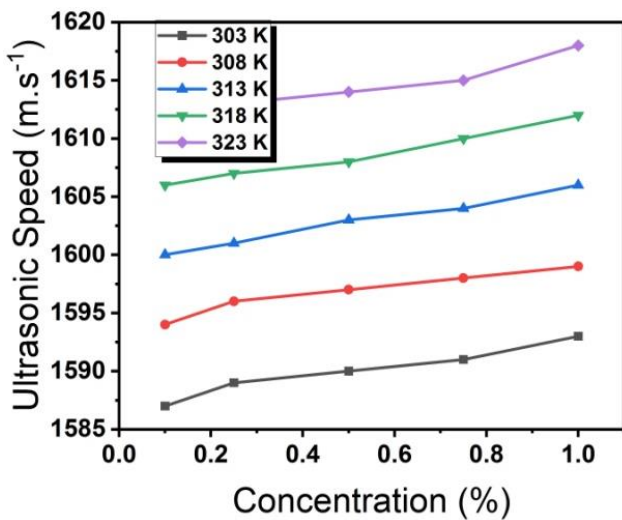


Figure 4: Ultrasonic speed vs concentration.

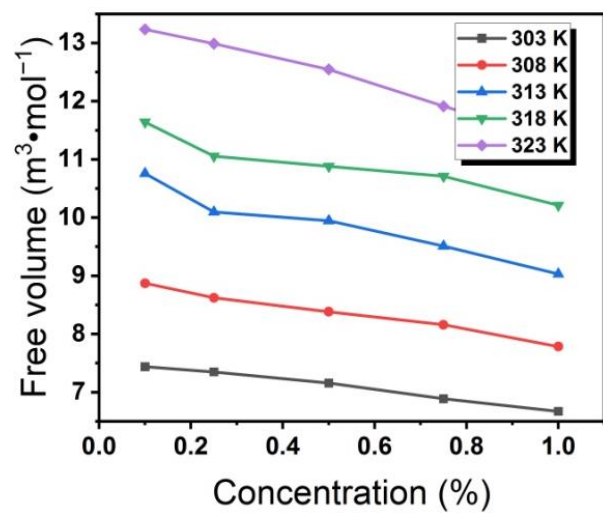


Figure 6: Free volume vs concentration.

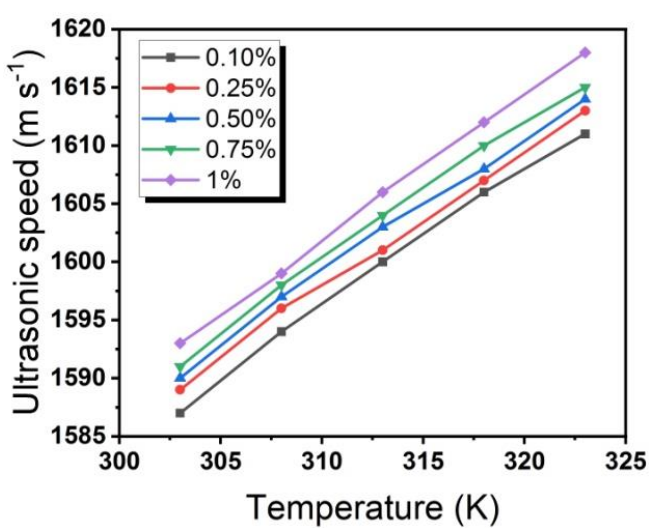


Figure 5: Ultrasonic speed vs temperature.

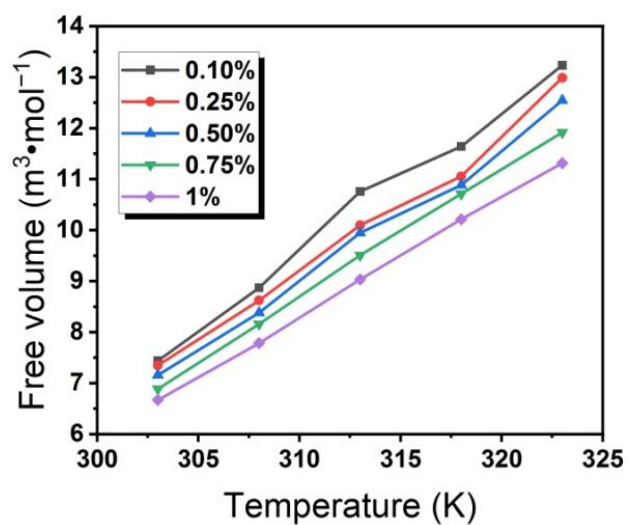


Figure 7: Free volume vs temperature.

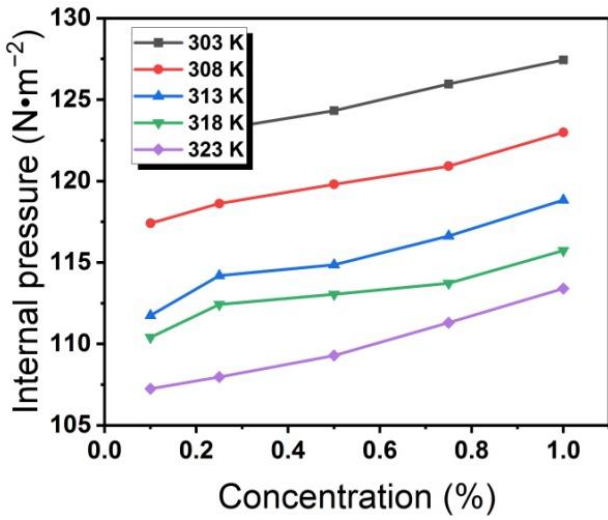


Figure 8: Internal pressure vs concentration.

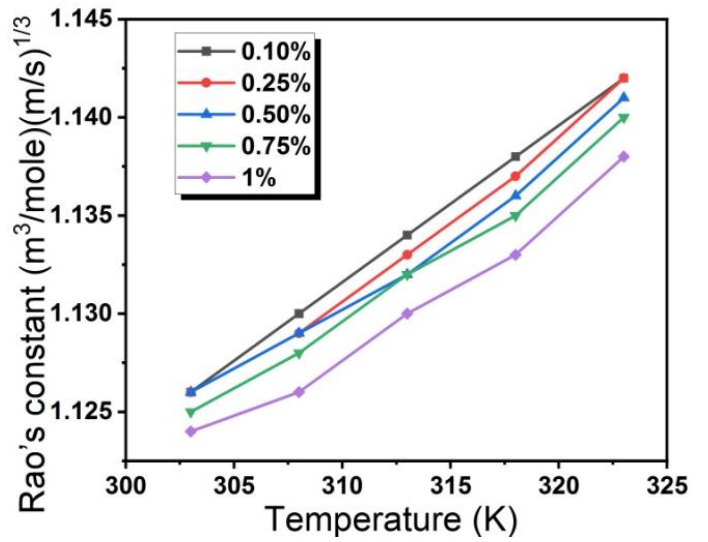


Figure 11: Rao's constant vs temperature.

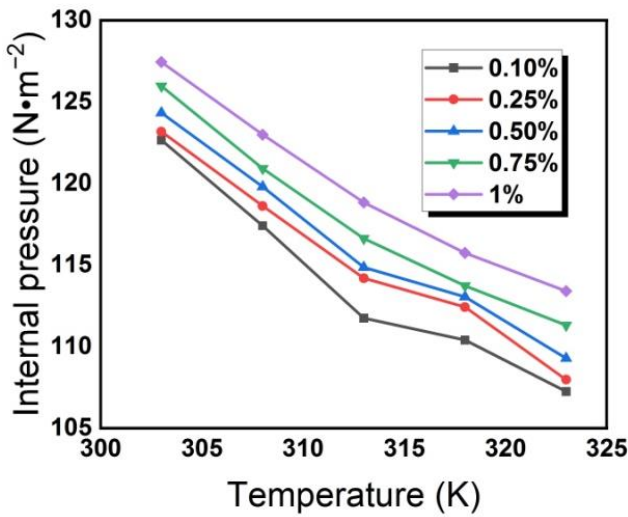


Figure 9: Internal pressure vs temperature.

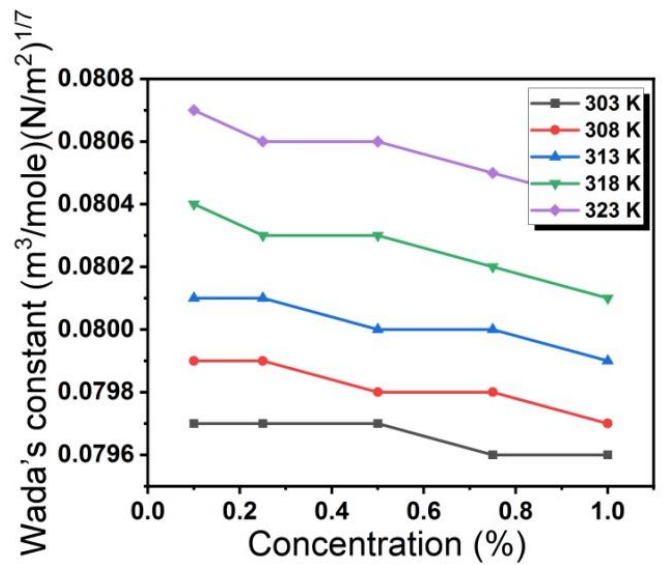


Figure 12: Wada's constant vs with concentration.

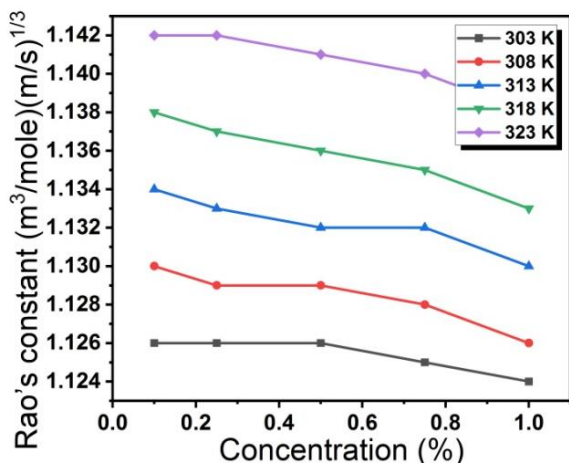


Figure 10: Rao's constant vs concentration.

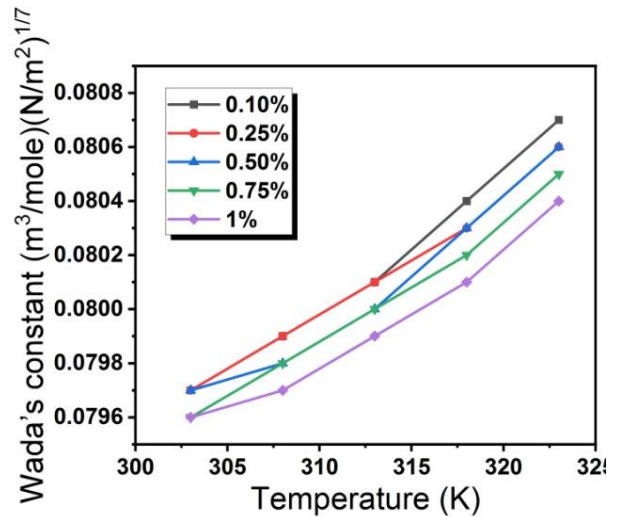


Figure 13: Wada's constant vs temperature.

5. DISCUSSION

The number of molecules in the medium rises as the concentration of dextran increases, making the medium denser and increasing sound speed. The rise in speed (Figure 4) might be owing to cohesive forces, implying that the observed values are due to molecular attachment (37,38). This suggests a molecular connection, which may be brought about by hydrogen or dipole-hydrogen bonds between NaOH and water. The relationship between sodium hydroxide (Na^+) and water molecules rather than between sodium hydroxide (Na^+) and dextran molecules is caused by ion-dipole interaction. The variation in speed may be caused by the solvent particles' self-relationship and concentration-dependent dipole-induced dipole cooperation between the segment atoms. At the mixture's saturation area, there is a slight shift in speed, indicating that the dispersive force outweighs the dipole-induced dipole force, and the molecular association comes to an end. This is so because the dextran molecule is larger than the water molecule. Therefore, the polarizability will increase with size and may result in substantial contact forces. With increased temperature, ultrasonic speed increases (Figure 5), indicating that molecular association takes place in the solution (39-42).

The free volume is a practical volume in which the core molecules can move within the solution due to the attraction of nearby molecules. The reduction in free volume (Figure 6) and temperature increase (Figure 7) with increasing concentration and temperature validate the ion-solvent interactions. As the concentration (vol.%) of dextran in NaOH increases, it is seen that the free volume (V_f) falls and the internal pressure (π_i) rises, indicating interaction in the molecules of the component liquids. The fact that the free volume reduces as the concentration increases shows that the molecules have arranged themselves so that less vacant space is accessible, indicating a reduction in compressibility (43,44).

The internal pressure is observed in the opposite trend, which is accepted. It is seen from Figure 8 that internal pressure increases with an increase in concentration because, with the addition of more solute, ion-solvent interaction increases. The internal pressure (45) drops as the temperature rises because increased thermal energy causes thermal agitation of ions, which limits the likelihood of contacts and lessens cohesive forces, resulting in a decrease in the internal pressure (Figure 9). The space a molecule has to travel in a hypothetical unit cell is called the free volume. The system's increased free volume demonstrates how the intensity of the interaction steadily grows as the solute concentration rises. It suggests that there is just minimal contact between the solvent molecules and the solute. Internal pressure is a more general term and a measurement of all the forces (dispersion, ionic, and dipolar) at work in the liquid system, contributing to its overall cohesion and adhesion. Figures 11 and 13 illustrate Rao's and Wada's constant rise as the temperature rises. The increasing trends of Rao's

constant and Wada's constant (46,47) with concentration imply that more components are available in a given location, resulting in a close packing of the medium and increasing interactions.

6. CONCLUSION

The impact of temperatures and concentrations on thermoacoustic parameters has been researched. The investigations above have revealed the characteristics of molecular forces, such as hydrogen bonds, charge transfer complexes, hydrogen bond breaking, and complexes. Intermolecular forces, also referred to as electrostatic forces, are weak between charged particles of a permanent dipole and an induced dipole molecule. Due to the different sizes and shapes of the molecules, the geometric fitting of one molecule into another results in the components' structural features. Depending on the chemical makeup of the polymer fragment, its polarity, and its solubility parameter, forces of attraction or dispersion start to develop between them when introduced to a solvent. When the solvent-solute interaction outweighs the solute-solute attraction, the troops holding the polymer coil in place weaken. As a result, the solvent molecules penetrate the spaces between the segments and disrupt their interaction. They encircle and make contact with each piece individually. The segments release or unfurl from their tightly coiled structure during this process. To put it another way, the combined segments without a solvent are now solvated.

7. CONFLICT OF INTEREST

The authors declare that there is no conflict of interest regarding the publication of this paper.

8. ACKNOWLEDGMENTS

The author expresses gratitude to the department's staff at ABIT Cuttack for their assistance.

9. REFERENCES

1. Fort RJ, Moore WR. Viscosities of binary liquid mixtures. *Trans Faraday Soc* [Internet]. 1966 Jan 1;62:1112-9. Available from: [<URL>](#).
2. Panda S. Thermo-acoustic Parameters of Polymer Dextran with Aqueous Sodium Hydroxide: An Ultrasonic Study. *Curr Mater Sci* [Internet]. 2022 Aug 18;16(2):217-24. Available from: [<URL>](#).
3. Panda S. Analysis of Aqueous Dextran: An Ultrasonic Study. *Curr Microw Chem* [Internet]. 2022 Mar 25;9(1):30-6. Available from: [<URL>](#).
4. Pawar NR, Chimankar OP. Ultrasonic absorption and excess absorption study of polar and non-polar binary liquid mixtures. *J Pure Appl Ultrason* [Internet]. 2015;37(4):83-90. Available from: [<URL>](#).
5. Nath G, Sahu S, Paikaray R. Effect of frequency on acoustic parameters in a binary mixture of polar liquids. *Indian J Phys* [Internet]. 2009 Dec 11;83(11):1567-74. Available from: [<URL>](#).
6. Mehra R, Gaur AK. Study of a Binary Liquid Mixture of Diethylamine and 1-Decanol and Validation of Theoretical

- Approaches of Sound Speed at Different Temperatures. *J Chem Eng Data* [Internet]. 2008 Mar;53(3):863–6. Available from: [<URL>](#).
7. Beebi S, Nayeem SM, Rambabu C. Investigation of molecular interactions in binary mixture of dimethyl carbonate + N-methylformamide at T = (303.15, 308.15, 313.15 and 318.15) K: Thermo-physical and spectroscopic study. *J Therm Anal Calorim* [Internet]. 2019 Mar 30;135(6):3387–99. Available from: [<URL>](#).
8. Panda S, Mahapatra AP. Molecular interaction studies of aqueous Dextran solution through ultrasonic measurement at 313K with different concentration and frequency. *Arch Phys Res* [Internet]. 2015;6(2):6–12. Available from: [<URL>](#).
9. Palani R, Geetha A, Swara RK. Ultrasonic studies on molecular interaction and physico-chemical behaviour of some divalent transition metal sulphates in aqueous propylene glycol at 303.15 K. *Rasayan J Chem* [Internet]. 2009;2(3):602–8. Available from: [<URL>](#).
10. Pandey JD, Dey R, Datt Bhatt B. Estimation of molecular radius of liquids and liquid mixtures from sound velocity. *J Mol Liq* [Internet]. 2004 Apr;111(1–3):67–71. Available from: [<URL>](#).
11. Panda R, Panda S, Biswal SK. A Review of Ultrasonic Wave Propagation through Liquid Solutions. *Curr Microw Chem* [Internet]. 2024 Mar 18;11(1):2–15. Available from: [<URL>](#).
12. Arunachalam M, Thamilmaran P, Sankarrajan S, Sakthipandi K. Study of high temperature metal-insulator phase transition in $\text{La}_{1-x}\text{Ca}_x\text{MnO}_3$ employing in-situ ultrasonic studies. *Phys B Condens Matter* [Internet]. 2015 Jan 1;456:118–24. Available from: [<URL>](#).
13. Sakthipandi K, Rajendran V. Metal insulator transition of bulk and nanocrystalline $\text{La}_{1-x}\text{Ca}_x\text{MnO}_3$ perovskite manganite materials through in-situ ultrasonic measurements. *Mater Charact* [Internet]. 2013 Mar 1;77:70–80. Available from: [<URL>](#).
14. Sakthipandi K, Rajendran V, Jayakumar T. Phase transitions of bulk and nanocrystalline $\text{La}_{1-x}\text{Sr}_x\text{MnO}_3$ ($x=0.35$ and 0.37) perovskite manganite materials using in situ ultrasonic studies. *Mater Res Bull* [Internet]. 2013 Apr 1;48(4):1651–9. Available from: [<URL>](#).
15. Panda R, Panda S, Biswal SK. Acoustic behavior of electrolytes in aqueous dimethyl sulphoxide as a solvent at different temperatures. *J Therm Anal Calorim* [Internet]. 2024 May 1;149(10):4839–53. Available from: [<URL>](#).
16. Das N, Kumar Praharaj M, Panda S. Exploring ultrasonic wave transmission in liquids and liquid mixtures: A comprehensive overview. *J Mol Liq* [Internet]. 2024 Jun 1;403:124841. Available from: [<URL>](#).
17. Panda S. Acoustical Analysis of Dextran+urea: Insights into Molecular Interactions. *Recent Innov Chem Eng (Formerly Recent Patents Chem Eng)* [Internet]. 2023 Dec 19;17(1):44–54. Available from: [<URL>](#).
18. Panda S. Molecular interaction of novel polymer dextran with 1(N) sodium hydroxide solution: Ultrasonic studies. *Asia-Pacific J Sci Technol* [Internet]. 2022;27(6):APST 270603. Available from: [<URL>](#).
19. Panda S. Molecular Interaction of Polymer Dextran in Sodium Hydroxide through Evaluation of Thermo Acoustic Parameters. *Indian J Pharm Educ Res* [Vol] [Internet]. 2020;54(3):630–6. Available from: [<URL>](#).
20. Zolkiflee NF, Affandi MMRMM, Majeed ABA. Molecular dynamics and related solution chemistry of lovastatin in aqueous solution of arginine: Viscometric analysis. *J Mol Liq* [Internet]. 2019 Apr 1;279:386–91. Available from: [<URL>](#).
21. Ali A, Nain AK, Abida. Ultrasonic and Volumetric Studies of Molecular Interactions in Acetonitrile + 1-Alkanol (C₆, C₈, C₁₀) Binary Liquid Mixtures at Different Temperatures. *J Chinese Chem Soc* [Internet]. 2004 Jun 1;51(3):477–85. Available from: [<URL>](#).
22. Sonar AN, Pawar NS, Khairnar MD. Ultrasonic studies on molecular interaction of substituted heterocyclic compounds in acetone-water mixture at 303K. *Int J Appl Biol Pharm Technol* [Internet]. 2011;3(2):291–5. Available from: [<URL>](#).
23. Thirumaran S, Sabu J. Ultrasonic investigation of amino acids in aqueous sodium acetate medium. *Indian J Pure Appl Phys* [Internet]. 2009;47:87–96. Available from: [<URL>](#).
24. Das M, Das S, Pattanaik AK. Acoustical Behaviour of Sodium Nitroprusside in Aquo-Organic Solvent Media at 308.15 K. Prabhakar YS, editor. *J Chem* [Internet]. 2013 Jan 7;2013(1):942430. Available from: [<URL>](#).
25. Panda S, Mahapatra AP. Study of acoustical parameters of dextran in 2 (M) glycine using ultrasonic technique at different frequencies. *J Pure Appl Ultrason* [Internet]. 2017;39:83–7. Available from: [<URL>](#).
26. Panda S. Ultrasonic Study of Novel Polymer Dextran in Aqueous Media at 12 MHz. *Curr Microw Chem* [Internet]. 2023 Sep 11;10(2):237–43. Available from: [<URL>](#).
27. Panda S, Mahapatra AP. Intermolecular interaction of aqueous dextran with urea. *Int J Innov Technol Explor Eng* [Internet]. 2019;8(11):742–8. Available from: [<URL>](#).
28. Gil EC, Colarte AI, El Ghzaoui A, Durand D, Delarbre JL, Bataille B. A sugar cane native dextran as an innovative functional excipient for the development of pharmaceutical tablets. *Eur J Pharm Biopharm* [Internet]. 2008 Feb 1;68(2):319–29. Available from: [<URL>](#).
29. Jeanes A, Haynes WC, Wilham CA, Rankin JC, Melvin EH, Austin MJ, et al. Characterization and Classification of Dextrans from Ninety-six Strains of Bacteria 1b. *J Am Chem Soc* [Internet]. 1954 Oct 1;76(20):5041–52. Available from: [<URL>](#).
30. Panda S. Thermoacoustical parameters of dextran polymer in sodium hydroxide solutions. *Artic Songklanakarin J Sci Technol* [Internet]. 2022;44(4):1125–30. Available from: [<URL>](#).
31. Panda S, Mahapatra AP. Molecular Interaction of Dextran with Urea Through Ultrasonic Technique. *Clay Res* [Internet]. 2019;38(1):35–42. Available from: [<URL>](#).
32. Panda S, Mahapatra AP. Acoustic and Ultrasonic Studies of Dextran in 2(M) Glycine-Variation with Frequencies and Concentrations. *Int J Pure Appl Phys* [Internet]. 2016;12(1):71–9. Available from: [<URL>](#).
33. Panda S, Mahapatra AP. Study of Acoustic and Thermodynamic Properties of Aqueous Solution of Dextran at Different Concentration and Temperature through Ultrasonic Technique. *Int J Sci Res* [Internet]. 2013;503–8. Available from: [<URL>](#).
34. Bhandakkar VD, Chimankar O, Ramdin Pawar N. Ultrasonic study of molecular interactions in some bio-

liquids. J Chem Pharm Res [Internet]. 2010;2(4):873-7. Available from: [<URL>](#).

35. Ali A, Akhtar Y, Hyder S. Ultrasonic and volumetric studies of glycine in aqueous electrolytic solutions. J pure Appl Ultrason. 2003;25(1):13-8.

36. Panda S. Molecular Interaction Study of Binary Liquid Solution Using Ultrasonic Technique. Recent Innov Chem Eng (Formerly Recent Patents Chem Eng [Internet]. 2022 Apr 7;15(2):138-46. Available from: [<URL>](#).

37. Palani R, Balakrishnan S. Acoustical properties of ternary mixtures of 1-alkanols in di-isopropyl ether and 2,2,2-trifluoroethanol mixed solvent. Indian J Pure Appl Phys [Internet]. 2010;48:644-50. Available from: [<URL>](#).

38. Jyothirmai G, Nayeem SM, Khan I, Anjaneyulu C. Thermo-physicochemical investigation of molecular interactions in binary combination (dimethyl carbonate + methyl benzoate). J Therm Anal Calorim [Internet]. 2018 Apr 22;132(1):693-707. Available from: [<URL>](#).

39. Singla M, Jindal R, Kumar H. Volumetric, acoustic, and UV absorption studies on solute-solvent interactions of dipeptides of glycine with aqueous amoxicillin solutions. Thermochim Acta [Internet]. 2014 Sep 10;591:140-51. Available from: [<URL>](#).

40. Godhani DR, Dobariya PB, Sanghani AM, Mehta JP. Thermodynamic properties of binary mixtures of 1,3,4-oxadiazole derivative with chloroform, N, N -dimethyl formamide at 303, 308 and 313 K and atmospheric pressure. Arab J Chem [Internet]. 2017 Feb 1;10:S422-30. Available from: [<URL>](#).

41. Pal A, Kumar H, Kumar B, Gaba R. Density and speed of sound for binary mixtures of 1,4-dioxane with propanol and butanol isomers at different temperatures. J Mol Liq [Internet]. 2013 Nov 1;187:278-86. Available from: [<URL>](#).

42. Takaya H, Nii S, Kawaizumi F, Takahashi K. Enrichment of surfactant from its aqueous solution using ultrasonic atomization. Ultrason Sonochem [Internet]. 2005 Aug 1;12(6):483-7. Available from: [<URL>](#).

43. Patil KC, Dudhe CM. Acoustical and viscometric studies of Gentamicin sulphate in aqueous medium. Der Pharma Chem [Internet]. 2016;8(20):227-33. Available from: [<URL>](#).

44. Akhtar Y, Ibrahim SF. Ultrasonic and thermodynamic studies of glycine in aqueous electrolytes solutions at 303K. Arab J Chem [Internet]. 2011 Oct 1;4(4):487-90. Available from: [<URL>](#).

45. Panda S. Thermoacoustical Analysis of Polymer Dextran at Different Frequencies Subhraraj Panda. Bulg J Phys [Internet]. 2022 Apr 20;49(2):136-44. Available from: [<URL>](#).

46. Wada Y. On the Relation between Compressibility and Molal Volume of Organic Liquids. J Phys Soc Japan [Internet]. 1949 Jul 15;4(4-6):280-3. Available from: [<URL>](#).

47. Panda S. Acoustic and thermodynamics study of aqueous dextran: an ultrasonic analysis. Rom J Biophys [Internet]. 2023;33(3):105-18. Available from: [<URL>](#).



Biological Activities of Extracts and Isolated Calotropin from *Gomphocarpus purpurascens* Leaves: A Computational and Experimental Study

Tsegu Kiros^{1*} , Seid Mohammed² , Aman Dekebo^{3,4*} , Yadessa Melaku^{3,4*} 

¹Haramaya University, Chemistry Department, Dire Dawa, P.O.Box. 138, Ethiopia.

²Adama Science and Technology University, Department of Applied Biology, Adama, P.O.Box. 1888, Ethiopia.

³Adama Science and Technology University, Department of Applied Chemistry, Adama, P.O.Box. 1888, Ethiopia.

⁴Adama Science and Technology University, Institute of Pharmaceutical Sciences, Ethiopia.

Abstract: *Gomphocarpus purpurascens* A.Richs. (sub-family: Asclepiadaceae, family: Apocynaceae) is an endemic plant in Ethiopia and Eritrea. The chromatographic fractionation of the chloroform:methanol (1:1) leaf extract resulted in the isolation of a cardenolide-type compound named calotropin. Its structure was confirmed based on the 1D-NMR (¹H, ¹³C, and DEPT-135) spectral data along with reported work. This is the first report on the isolation of calotropin from the leaves of *G. purpurascens*. The *n*-hexane extract displayed better antibacterial activity against *E. coli* and *P. aeruginosa* (8.1 ± 0.0 to 10.8 ± 0.1 mm) up to 12,500 µg/mL concentration. Generally, all the extracts and the isolated compound, calotropin, showed better antibacterial activity against the *P. aeruginosa* strain than chloramphenicol (7.1 ± 0.2 to 7.3 ± 0.5 mm). The tested chloroform: methanol (1:1) extract indicated a weak antifungal activity against *C. albicans* compared to ketoconazole 10 µg/disc (17.67 ± 2.52 mm). On the contrary, all the extracts were found to have a good DPPH radical scavenging activity (IC₅₀ values, 1.1-2.7 µg/mL) comparable to ascorbic acid (1.0 µg/mL). The isolated calotropin exhibited a stronger binding capacity (-10.3 kcal/mol) against the *P. aeruginosa* PqsA (5OE3) protein model than chloramphenicol (-7.0 kcal/mol). This compound was also found to violate Lipinski's rules of five (with a molecular weight > 500 g/mol) and showed immunotoxicity and cytotoxicity properties. Given that this is a preliminary report, further biochemical investigations would be needed on this *G. purpurascens* plant to identify additional phytoconstituents with superior efficacy.

Keywords: *Gomphocarpus purpurascens*, Asclepiadaceae, Apocynaceae, Calotropin, Biological activities, Docking analysis.

Submitted: March 7, 2024. **Accepted:** August 14, 2024.

Cite this: Kiros T, Mohammed S, Dekebo A, Melaku Y. Biological Activities of Extracts and Isolated Calotropin from *Gomphocarpus purpurascens* Leaves: A Computational and Experimental Study. JOTCSA. 2024;11(4): 1377-86.

DOI: <https://doi.org/10.18596/jotcsa.1393500>

***Corresponding author's E-mail:** kirosorg@gmail.com; amandekab@gmail.com; yadessamelaku2010@gmail.com

1. INTRODUCTION

Gomphocarpus purpurascens A.Richs. (Syn. *Asclepias purpurascens* and *Gomphocarpus fruticosus*) is a member of the sub-family Asclepiadaceae of the family Apocynaceae. It is locally known as "Tefreina" (in Amharic) (1) and "Ari-Yuyo" (in Oromifa) (2). *G. purpurascens* grows as an annual shrub on open, rocky ground and in disturbed areas. It occurs in most Ethiopian regions and is endemic to the highland regions of Ethiopia and Eritrea (1). In

the prehistoric Harla town of eastern Ethiopia, the leaves of *G. purpurascens* are used for the treatment of itching skin and evil eyes (2). Currently, there is a claim that the itchy skin has potentially been caused by the methicillin-resistant *Staphylococcus aureus* (3). In Ethiopia, people also use *G. purpurascens* for the treatment of wounds and wart diseases (4). Besides, extracts prepared from the roots and leaves of the plant have traditionally been used as anti-inflammatory and analgesic agents in the Tigray, Amhara, and southern regions of Ethiopia (5).

Regarding the experimental-based biological activity of the plant, to our knowledge, only a few reports were found in the literature. For example, to our knowledge, only one study (6) was reported about the antimicrobial activity of the leaves of *G. purpurascens*. According to this report, three concentrations (150, 300, and 600 mg/mL) of the ethanol and methanol leaf extracts of *G. purpurascens* were tested against some bacterial pathogens and the *C. albicans* fungal strain. These extracts scored respective inhibition zone values of 6.09 ± 0.18 to 6.90 ± 0.40 mm and 9.19 ± 0.07 to 13.20 ± 0.1 mm against *E. coli*; 9.51 ± 0.1 to 12.7 ± 0.15 mm and 7.1 ± 0.01 to 8.2 ± 0.01 mm against *S. aureus*; 9.01 ± 0.01 to 9.77 ± 0.15 mm and 9.8 ± 0.01 to 13.8 ± 0.10 mm against *P. aeruginosa*; and 6.34 ± 0.04 to 6.64 ± 0.04 mm and 8.01 ± 0.01 to 13.79 ± 0.01 mm against *C. albicans*. The reported result was compared with the tetracycline (13.09 – 25.65 mm at 0.025 mg/mL) and ketoconazole (7.87 ± 2.18 mm at 25 mg/mL) standard drugs. Asfaw et al. (7) also reported the antibacterial activity, against only the *E. coli* bacterium, of acetone and methanol extracts of the leaves and stems of *G. purpurascens* with inhibition values of 55 mm and 60 mm, respectively (concentration was not mentioned). Another study reported by Ayanaw et al. (5) indicated that 80% of methanol extracts from the leaves and roots of this plant showed a dose-reliant anti-inflammatory and analgesic effect. The same authors (5) also reported the presence of some classes of phytochemicals, such as terpenoids, flavonoids, alkaloids, and phenolics. Different plant species of the family Asclepiadaceae were claimed for their anticancer and antioxidant potentials (8). However, according to our information, no reports were found on the antioxidant activity of the *G. purpurascens* species. Few compounds were previously reported from some species of the genus *Gomphocarpus*. Three triterpenoids (3β -taraxerol acetate, 13α -methyl, 27 -norolean- 14 -en- 3β -ol (3β -taraxerol and betulinic acid), a pregnane glycoside ((lineolon- 3 - O - β -D-cymaropyranosyl-(1 - 4)- β -D-cymaropyranosyl-(1 - 4)- β -D-oleandropyranose)) and a cardenolide glycoside (gomphoside) were reported from the aerial parts of *Gomphocarpus fruticosus* (9). Besides, two other cardenolide compounds named uzarigenin and calotropin were isolated both from *G. fruticosus* and *G. sinaicus* (9, 10). However, based on our best search, no chemical constituents were reported from the species *G. purpurascens*. The limited antimicrobial activity reports, the absence of any report on the antioxidant activity study and isolated chemical constituents, and the claimed traditional medicinal uses against itchy skin and wound diseases (caused by common bacteria like *Staphylococcus aureus*, *Pseudomonas aeruginosa*, and *Escherichia coli*) of *G. purpurascens* leaves initiated us to do the present work. If not, no biological and phytochemical studies conducted on this *G. purpurascens* species have initiated us to do the present work. This study reported, for the first time, the isolation of the cardenolide compound, calotropin, and its *in vitro* and *in silico* antibacterial and antioxidant activities from the leaves of *G. purpurascens*. Also, the *in vitro* antimicrobial and

antioxidant effects of crude leaf extracts of this plant were reported herein.

2. MATERIALS AND METHODS

2.1. Plant Material

The leaves of *Gomphocarpus purpurascens* (Figure 1) were collected from the prehistoric Harla town and surrounding villages, Dire Dawa, Eastern Ethiopia (latitude $9^{\circ}27'$ and $9^{\circ}39'N$, longitude $41^{\circ}38'$ and $42^{\circ}20'E$, 950-2260 m asl) during October 2022. The plant was identified by Dr. Anteneh Belayneh, Haramaya University, Ethiopia, and a voucher specimen (voucher number AHU126) was deposited in the herbarium of the mentioned University. Collected fresh samples were washed with tap water and then dried at room temperature under shade. The dried samples were coarsely powdered and sieved using an electrical blender. Powdered samples were packed in a tightly sealed glass bottle and stored in a refrigerator ($4^{\circ}C$) for later experimental work.



Figure 1: Photo of *Gomphocarpus purpurascens* plant (photo by Tsegu K., 2022).

2.2. Test Microbial Cultures

Three human standard bacterial pathogens, viz., *Staphylococcus aureus* (*S. aureus*, ATCC 25923), *Escherichia coli* (*E. coli*, ATCC 25922), and *Pseudomonas aeruginosa* (*P. aeruginosa*, ATCC 27853), and a fungal strain, *Candida albicans* (*C. albicans*, ATCC 10231), were obtained from the Ethiopian Public Health Institute (EPHI).

2.3. Chemicals, Apparatuses and Instruments

Chemicals

Chemicals such as methanol, ethanol, *n*-hexane, ethyl acetate, chloroform, dichloromethane, acetic acid, acetone, and 230-400 mesh size silica gel were used for extraction, chromatographic separation, and TLC analysis purposes. Iodine vapor was used and served as a TLC-detecting agent. Ferric chloride, potassium ferricyanide, 0.2 M potassium phosphate buffer, and trichloroacetic acid were consumed for the study of potassium ferric ion reduction antioxidant power (PFRAP), and DPPH free radical was used for the DPPH antioxidant assay. Mueller Hinton agar (MHA) and Potato Dextrose agar (PDA) media were used for antibacterial and antifungal activity evaluation, respectively, using DMSO as a positive control. Chloramphenicol, ketoconazole, and

ascorbic acid were used and served as reference drugs for the antibacterial, antifungal, and antioxidant activity assays, respectively.

Apparatuses and Instruments: An electrical laboratory blender (Torrington, CT., USA), orbital shaker (Hy-5A, Movel Scientific Instrument CO. Ltd., China), a suction filtration apparatus, and a rotary evaporator (rotary vacuum, Jainsons, India) were used for plant sample grinding, extraction, filtration, and solvent evaporation, respectively. Silica gel 60 F₂₅₄ pre-coated aluminum TLC sheet (Merck), TLC chamber, and capillary tube were used for TLC analysis. A UV-lamp cabinet (254 and 365 nm, UVP Chromato-Vue C-70G, Analytik Jena, USA) was used and served as a non-destructive TLC-detecting tool. The PTLC and glass column were used for fractionation of the extract and isolation of the compound. A Petri dish, an incubator (Binder B28, Germany), and an autoclave (Tuttnauer 3150EL, Israel) were used for the evaluation of antimicrobial activity. A UV-Vis spectrophotometer (Cecil CE4001 UV/VIS, Cambridge, England) was employed for absorbance measurement during the antioxidant activity assay. 1D-NMR (¹H, ¹³C, and DEPT-135) (BRUKER ACQ 400 AVANCE) spectroscopic instrument was employed for the structural identification of the isolated compound.

2.4. Extraction and Chromatographic Fractionation

The commonly applied successive organic solvent extraction protocol (11) was used in this study. That is, P powdered leaves (500 g) were macerated in *n*-hexane (3x, 2.5 L) by shaking overnight and then followed by filtration and concentration, resulting in a dark yellow dry extract (18 g). The remaining residue, after *n*-hexane extraction, was re-extracted successively with chloroform, chloroform: methanol (1:1), ethanol, and methanol using the same technique. The extract solutions were filtered and concentrated to yield corresponding dry extracts of 6 g, 53 g, 27 g, and 43 g. Then, the chloroform: methanol (1:1) extract, after TLC examination, was submitted to silica gel chromatographic fractionation. That is, green crude extract (30 g) was reconstituted in chloroform: methanol (1:1, 150 mL), adsorbed on normal silica gel (40 g), and concentrated. The adsorbed powder was then applied over a glass column packed with silica gel (200 g) and eluted with *n*-hexane/CHCl₃/EtOAc/MeOH of different polarity ratios. A total of three hundred seventy-six fractions (20-50 mL) were collected, and those with similar TLC profiles were combined. Among the combined fractions, Fr. 85-92 (dark gel, 100 mg) was repacked over the same normal silica gel-packed column (30 g) to give sixty sub-fractions after being eluted with CHCl₃/EtOAc in different polarity ratios. Finally, the sub-fr.11-25 (30 mg) was reapplied on a PTLC plate and run using an *n*-hexane/EtOAc/AcOH (3:1:0.1) solvent system, resulting in the isolation of calotropin (12 mg).

The chemical structure of the isolated calotropin (Figure 1) was identified using a 1D- NMR (¹H, ¹³C, and DEPT-135) spectroscopic instrument in comparison with the reported data. The 1D-NMR (¹H,

¹³C, and DEPT-135) analysis was performed on a BRUKER ACQ 400 AVANCE spectrometer with 400 MHz for ¹H and 100 MHz for ¹³C, and DEPT-135. The instrument was equipped with a 5 mm proton probe and operated at a temperature of 298 K with topspin software (version 2.1). Tetramethyl silane (TMS) was used as an internal standard to measure the chemical shifts (δ_{ppm}) of the acquired spectra. Finally, the generated spectra were further processed using the software MestReNova (Mestrelab Research S.L., version 12).

2.5. In Vitro Antimicrobial Activity Evaluation

2.5.1. Antibacterial activity assay

The antibacterial activity of both crude extracts and the isolated compound was evaluated against three standard human pathogens, namely, *Staphylococcus aureus* (*S. aureus*, ATCC 25923), *Escherichia coli* (*E. coli*, ATCC 25922), and *Pseudomonas aeruginosa* (*P. aeruginosa*, ATCC 27853) bacterial strains. Experimental activity was conducted at the Microbiology Laboratory of the School of Medical Laboratory, Haramaya University. The agar medium disc-diffusion technique was followed to evaluate the antibacterial effectiveness of the extracts and isolated compound using the standard protocols of the Clinical and Laboratory Standards Institute (CLSI) (12, 13). A stock solution of each extract (200 mg in 2 mL) and isolated compound (5 mg in 5 mL) was prepared in 4% DMSO. Then, three concentrations (50,000, 25,000, and 12,500 μ g/mL) of each extract and four various dilutions (500, 300, 100, and 50 μ g/mL) of the isolated compound were prepared from corresponding stock solutions using the two-fold serial dilution method (14,15). Chloramphenicol-impregnated standard disc (30 μ g) and DMSO solvent were used and served as positive and negative controls, respectively. The remaining detailed experimental procedures applied in this study were similar to those stated in (15, 16). Each experiment was done in duplicate, and results were presented as mean \pm standard deviation after statistical analysis with SPSS software (version 20).

2.5.2. Antifungal activity assay

The chloroform: methanol (1:1) extract of *G. purpurascens* leaves was assessed for its antifungal activity against *Candida albicans* ATCC 10231 using the disc diffusion method. A PDA medium was prepared as per the manufacturer's instructions. The PDA-containing plate was then inoculated with *Candida albicans* suspension by streaking it with a sterilized swab very well. Similar to the antibacterial activity experiment, four concentrations (12,500, 25,000, 50,000, and 100,000 μ g/mL) of the chloroform:methanol extract was prepared in DMSO, and 100 μ L amount of each concentration was loaded onto a sterile Whatman filter paper disc (6 mm). The impregnated discs were placed on the surface of the inoculated agar plates using sterile forceps. Commercial ketoconazole/Tilt disc (10 μ g/disc) was used as a reference drug. Then, the PDA plates were sealed with Parafilm and incubated at 27 °C for 3-5 days for fungal growth. After incubation, the diameters of the zones of inhibition around each disc were measured using a caliper (in mm). Experiments

were conducted in duplicate, and the results were expressed in as the mean and standard deviation.

2.6. In Vitro Antioxidant Activity Examination

The *in vitro* antioxidative effect of extracts and isolated compounds was evaluated against DPPH free radicals using six different concentrations (500, 250, 150, 100, 50, and 25 µg/mL) prepared from corresponding stock solutions (1 mg/mL in MeOH). Ascorbic acid (AA) was used as a standard antioxidant agent at similar concentrations. The assaying experiment was done following the procedures described previously (15-17). The antioxidant potential of each extract and isolated calotropin was evaluated in terms of percentage scavenging activity calculated using the following formula (1):

$$\text{DPPH scavenging activity (\%)} = \left(1 - \frac{A}{A_0}\right) \times 100 \quad (1)$$

where A and A₀ are the absorbances of samples with DPPH and the negative control (DPPH solution, 0.004% w/v in MeOH), respectively, the DPPH free radical trapping power of the extracts and the compound was also expressed in terms of IC₅₀ (the concentration needed to scavenge the total DPPH radicals by 50%). This IC₅₀ value was obtained from the regression equation derived from the percentage scavenging activity versus the concentration graph of each tested sample. The experimental activity was done in triplicate, and the results were expressed as the mean ± standard deviation.

2.7. In Silico Molecular Modeling Study

The molecular binding capacity of the isolated compound, calotropin, was studied by docking against the *P. aeruginosa* PqsA (5OE3) enzyme model. The molecular docking analysis was performed using the AutoDock Vina tools (version 4.2). All the necessary protocols were adjusted during the computational analysis, as stated previously (16). The conformation with the best-scored pose between the protein model and the isolated compound with the lowest binding energy was considered for the binding capacity. The molecular docking results were analyzed based on the binding energy (kcal/mol) and number of binding interactions between potential amino acid residues and the studied compound. The drug-likeness, ADME, and toxicity properties predictions of the isolated compound were also computed by SwissADME, PreADMET, and OSIRIS/Pro Tox-II property explorer software.

3. RESULTS AND DISCUSSION

In this study, the phytochemical investigation of the leaves of *G. purpurascens* resulted in the isolation of a cardenolide compound, calotropin (Figure 1). The *in silico* and *in vitro* antibacterial activity of this isolated compound was also evaluated herein. Besides, extracts of the leaves of *G. purpurascens* were assessed for their potential antibacterial, antifungal, and antioxidant effects against microbial strains and oxidants.

3.1. Structural Identification of Isolated Compound

Isolated compound (Calotropin, Figure 2): Black gel (12 mg); R_f 0.4 (*n*-hexane/EtOAc/AcOH, 3:1:0.1); See Table 1 for ¹H, ¹³C and DEPT-135 NMR spectral data.

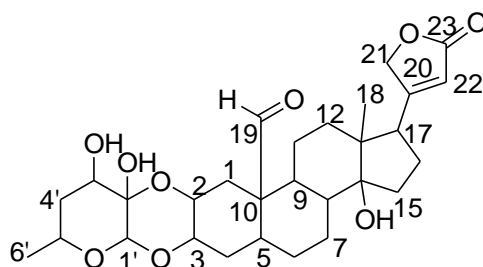
In the ¹H NMR spectrum (Figure S1) of the isolated compound, a deshielded singlet signal at δ_H 10.05 (1H, H-19) is due to the aldehydic proton. In contrast, a doublet signal at δ_H 5.93 (1H, H-22, d, J = 7.35) is due to an olefinic methine proton. Moreover, a broad singlet signal was observed at δ_H 4.72 (1H, H-1'), suggestive of oxygenated methine proton (-O-CH-O-). In addition, a broad doublet signal (integrated for two protons) was observed at δ_H 4.53 (2H, H-21, br d, J = 24.52) which underlined the occurrence of methylenoxy methylene protons (-CH₂-O-). The ¹H spectrum also confirmed the presence of three additional oxygenated methine protons, which appeared as a broad doublet at δ_H 4.0 (1H, H-2, br d, J = 6.06) and multiplets at δ_H 3.89 (1H, H-3) and 3.45 (1H, H-5'). A hydroxylated methine proton (-CH-OH) was also found as a multiplet signal at δ_H 3.64 (1H, H-3'). In the aliphatic region, a doublet of doublet signal appeared at δ_H 2.85 (1H, H-17, dd, J = 10.2, 6.4), implying the presence of a methine proton attached to a tertiary carbon adjacent to a quaternary olefinic carbon. Moreover, a doublet at δ_H 0.94 (3H, H-6', d, J = 7.1) and singlet at δ_H 0.83 (3H, H-18) signals were observed to confirm the presence of two methyl groups positioned at oxygenated tertiary and quaternary carbon, respectively. In the aliphatic region, additional twelve multiplet signals were shown at δ_H 2.47 which ascribed to nine different methylene (18H, H-1, H-4, H-6, H-7, H-11, H-12, H-15, H-16 and H-4') and three methine (3H, H-5, H-8 and H-9) groups.

The corresponding ¹³C and DEPT-135 spectra (Figures S2 and S3) presented twenty-nine unsymmetrical recognizable signals, which attributed to seven quaternary, one hydroxylated methine (-CH-OH), four oxygenated methine (-O-CH-O-), one oxygenated methylene (-CH₂-O-), one olefinic methine (=CH-), four aliphatic methine (-CH-), nine aliphatic methylene (-CH₂-) and two methyl (-CH₃) groups. Two of the seven quaternary signals appeared at δ_C 208.0 (C-19) and 175.9 (C-23 overlapped), corresponding to the aldehyde and furan carbonyl carbons, respectively. The remaining five belonged to two aliphatic carbons at δ_C 52.6 (C-10) and 49.0 (C-13), two hydroxylated carbons at δ_C 90.4 (C-2') and 84.4 (C-14), and one olefinic carbon at δ_C 175.9 (C-20 overlapped). The signal at δ_C 116.6 (C-22) was ascribed to the olefinic methine carbon, and the one at δ_C 71.9 (C-3') belonging to the hydroxylated methine carbon. The signal resonated at δ_C 73.9 (C-21), representing the oxygenated methylene carbon. The overall spectral data (Table 1) is in agreement with the reported data in the literature (10) for calotropin (Figure 2).

Table 1: ^1H , ^{13}C , and DEPT-135 NMR (CD_3OD) data of calotropin.

Attribution	Isolated compound			Calotropin (10) in $\text{CDCl}_3:\text{CD}_3\text{OD}$ (4:1)	
	δ_{H}	δ_{C}	DEPT-135	δ_{H}	δ_{C}
1	2.47 (m)	30.2	-CH ₂ -	*	34.2
2	4.0 (br d, $J = 6.06$)	70.5	-CH-O-	4.00 (dd, $J = 12.5, 4.0$)	68.1
3	3.89 (m)	77.9	-CH-O-	3.85 (m)	71.2
4	1.68 (m)	33.0	-CH ₂ -	*	32.6
5	1.68 (m)	43.0	-CH-	*	44.1
6	1.41 (m)	28.7	-CH ₂ -	*	28.9
7	1.41 (m)	27.4	-CH ₂ -	*	27.2
8	1.26 (m)	38.8	-CH-	*	42.9
9	1.68 (m)	49.3	-CH-	*	49.9
10	-	52.6	Q	-	52.4
11	1.41 (m)	24.2	-CH ₂ -	*	21.4
12	1.26 (m)	33.4	-CH ₂ -	*	38.5
13	-	49.0	Q	-	49.2
14	-	84.4	Q	-	83.9
15	2.12 (m)	36.8	-CH ₂ -	*	38.7
16	1.68 (m)	26.5	-CH ₂ -	*	26.3
17	2.85 (dd, $J = 10.2, 6.4$)	50.4	-CH-	2.69 (dd, $J = 9.0, 4.5$)	50.1
18	0.83 (s)	14.8	-CH ₃	0.89 (s)	15.1
19	10.05 (s)	208.0	Q (C=O)	*	207.7
20	-	175.9	Q	-	175.7
21	4.53 (br d, $J = 24.52$)	73.9	-CH ₂ -O-	4.63 (dd, $J = 18.0, 1.0$)	73.5
22	5.93 (d, $J = 7.35$)	116.6	=CH-	5.69 (br s)	116.8
23	-	175.9	Q (C=O)	-	175.5
1'	4.72 (br s)	94.1	-O-CH-O-	4.78 (s)	95.5
2'	-	90.4	Q	-	90.9
3'	3.64 (m)	71.9	-CH-OH	3.72 (m)	72.3
4'	2.37 (m)	35.4	-CH ₂ -	*	37.8
5'	3.45 (m)	66.3	-CH-O-	3.38 (m)	67.8
6'	0.94 (d, $J = 7.1$)	19.9	-CH ₃	1.02 (d, $J = 6.0$)	20.4
OHS	2.05 (s)	-	-	*	-

* Values not reported

**Figure 2:** Structure of calotropin isolated from *G. purpurascens* leaves.

3.2. In Vitro Antimicrobial Activity Evaluation

3.2.1. Antibacterial activity assay

The antibacterial inhibition zone diameters, expressed as mean \pm standard deviation, recorded by five extracts of *G. purpurascens* leaves against three standard human bacterial pathogens are reported in Table 2. As can be shown in Table 2, all the tested concentrations of all extracts indicated positive activities against all strains, except the lowest concentrations (12,500 and 25,000 $\mu\text{g}/\text{mL}$) of chloroform (against *S. aureus*), chloroform:methanol (against *P. aeruginosa*), methanol (against *E. coli*), and ethanol (against *S. aureus*) extracts, which were found inactive (< 7 mm inhibition zone). The highest inhibitory value (10.1 ± 0.1 mm) against *E. coli* at the highest concentration (100,000 $\mu\text{g}/\text{mL}$)

was scored by *n*-hexane extract and then followed by 1:1 of chloroform:methanol (9.4 ± 0.0 mm) and chloroform (9.1 ± 0.3 mm) extracts. The lowest concentration (12,500 $\mu\text{g}/\text{mL}$) of the four extracts also inhibited the growth of *E. coli* (7.1 ± 0.1 to 8.1 ± 0.0 mm). The *S. aureus* bacterium was found to be sensitive to all extracts at the maximum concentration (100,000 $\mu\text{g}/\text{mL}$), with the larger diameter of the zone of inhibition value (9.1 ± 0.2 mm) recorded by the methanol extract. The *P. aeruginosa* was also found to be more susceptible to *n*-hexane extract (10.8 ± 0.1 mm) at the highest dose (100,000 $\mu\text{g}/\text{mL}$). Thus far, one similar study was reported by (6), aiming to evaluate the antibacterial activity of ethanol and methanol leaf extracts of *G. purpurascens* against the same

standard bacteria mentioned above. However, the tested concentrations (150, 300, and 600 mg/mL) in the reported study were far higher than the ones tested in the present work. According to the report, the ethanol and methanol leaf extracts scored respective inhibition zone values of 6.09 ± 0.18 to 6.90 ± 0.40 mm and 9.19 ± 0.07 to 13.20 ± 0.1 mm

against *E. coli*; 9.51 ± 0.1 to 12.7 ± 0.15 mm and 7.1 ± 0.01 to 8.2 ± 0.01 mm against *S. aureus*; and 9.01 ± 0.01 to 9.77 ± 0.15 mm and 9.8 ± 0.01 to 13.8 ± 0.10 mm against *P. aeruginosa*. In essence, our result was comparable to this report, regardless of the huge concentration difference.

Table 2: Antibacterial inhibition zone diameter (mean \pm sd) of leaf extracts of *G. purpurascens* against the *E. coli*, *S. aureus*, and *P. aeruginosa* standard bacterial strains.

Bacterial strains	Concentration ($\mu\text{g/mL}$)	Diameter of zone of inhibition (mean \pm sd, mm) of extracts					
		<i>n</i> -Hexane	CHCl_3	CHCl_3 :MeOH (1:1)	MeOH	EtOH	Chloramphenicol (30 μg)
<i>E. coli</i>	12,500	8.1 ± 0.0	7.8 ± 0.2	7.9 ± 0.3	6.8 ± 0.0	7.1 ± 0.1	24.3 \pm 0.8
	25,000	9.2 ± 0.2	8.4 ± 0.4	9.0 ± 0.1	6.9 ± 0.1	7.9 ± 0.4	
	50,000	9.8 ± 0.0	8.7 ± 0.0	9.4 ± 0.0	7.1 ± 0.1	8.4 ± 0.1	
	100,000	10.1 ± 0.1	9.1 ± 0.3	9.4 ± 0.0	7.2 ± 0.0	8.7 ± 0.1	
<i>S. aureus</i>	12,500	7.0 ± 0.0	0.0	7.0 ± 0.8	7.1 ± 0.4	6.3 ± 0.0	19.4 \pm 1.8
	25,000	7.6 ± 1.2	6.9 ± 0.0	7.2 ± 0.7	8.3 ± 0.0	6.6 ± 0.0	
	50,000	8.1 ± 0.0	7.5 ± 0.0	7.4 ± 0.7	8.8 ± 0.5	7.0 ± 0.0	
	100,000	8.8 ± 0.5	8.0 ± 0.1	8.1 ± 0.2	9.1 ± 0.1	7.2 ± 0.0	
<i>P. aeruginosa</i>	12,500	9.1 ± 0.1	7.1 ± 0.0	6.5 ± 0.3	7.8 ± 0.0	7.5 ± 0.1	7.1 \pm 0.2
	25,000	9.2 ± 0.0	7.9 ± 0.0	7.7 ± 0.2	8.2 ± 0.2	8.1 ± 0.4	
	50,000	9.7 ± 0.2	8.1 ± 0.2	8.0 ± 0.1	8.6 ± 0.0	8.5 ± 0.0	
	100,000	10.8 ± 0.1	8.8 ± 0.0	8.6 ± 0.0	9.2 ± 0.0	9.0 ± 0.1	

The isolated compound, calotropin, showed an inhibitory effect against *P. aeruginosa* at all concentrations, with a higher diameter of the zone of inhibition value of 8.8 ± 0.1 mm recorded at 1000 $\mu\text{g/mL}$ concentration (Table 3). This compound also

attempted to inhibit the growth of *E. coli* up to 300 $\mu\text{g/mL}$ dose (7.7 ± 0.7 mm), whereas it was found to have no activity against the methicillin-resistant *S. aureus* (MRSA) bacterium at all concentrations.

Table 3: Antibacterial activity of the isolated compound (calotropin) against the *E. coli*, *S. aureus* and *P. aeruginosa* bacterial strains.

Concentrations ($\mu\text{g/mL}$)	Diameter of zone of inhibition (mean \pm sd, mm) of calotropin		
	<i>E. coli</i>	<i>S. aureus</i>	<i>P. aeruginosa</i>
50	6.3 ± 0.0	0.0	7.4 ± 0.2
100	6.8 ± 0.1	0.0	7.8 ± 0.1
300	7.7 ± 0.7	0.0	7.9 ± 0.1
500	8.1 ± 0.3	0.0	8.6 ± 0.1
1000	8.8 ± 0.0	0.0	8.8 ± 0.1
Chloramphenicol (30 $\mu\text{g/disc}$)	25.3 ± 0.8	19.2 ± 1.6	7.3 ± 0.5

3.2.2. Antifungal activity assay

The chloroform:methanol (1:1) extract of *Gomphocarpus purpurascens* leaves was assessed for its potential antifungal activity against *C. albicans* ATCC 10231. The obtained result indicated that the extract displayed a slight activity only at the maximum concentration of 100,000 $\mu\text{g/mL}$ with a diameter of the zone of inhibition value of 11.00 ± 1.00 mm.

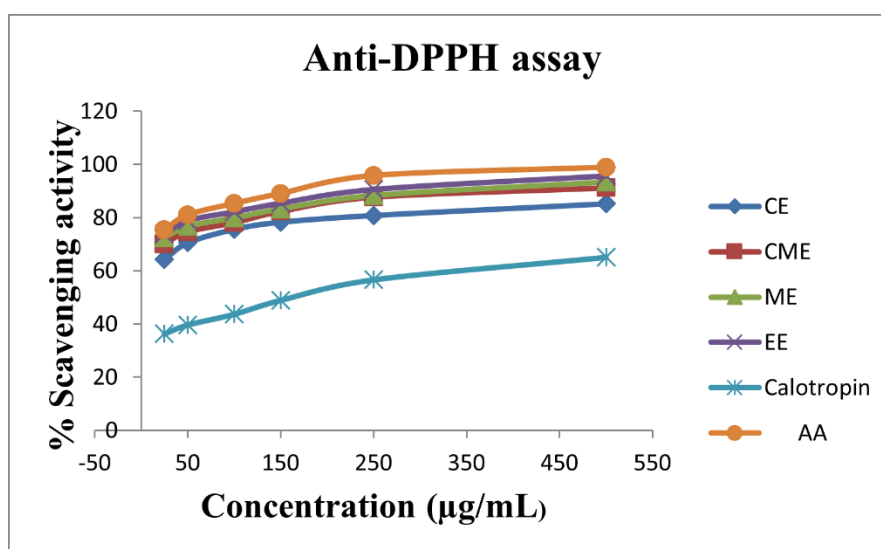
However, this extract was found to be totally inactive up to 12,500 $\mu\text{g/mL}$. It was generally found to be weak compared to the standard antifungal drug ketoconazole 10 $\mu\text{g/disc}$ (17.67 ± 2.52 mm).

3.3. In Vitro Antioxidant Potential Examination

As presented in Table 4 and depicted in Figure 3, an auspicious anti-DPPH free radical inhibitory effect was observed in all extracts with higher scavenging percentage values (95.7 ± 0.00 and 93.5 ± 0.00 , respectively) recorded by the ethanol and methanol extracts at 500 $\mu\text{g/mL}$, with each having an IC_{50} value of 1.1 $\mu\text{g/mL}$. The chloroform: methanol (1:1) and chloroform extracts also displayed good DPPH radical scavenging percentage values of 91.2 ± 0.00 (IC_{50} value of 1.7 $\mu\text{g/mL}$) and 85.2 ± 0.00 (IC_{50} value of 2.7 $\mu\text{g/mL}$). The isolated compound, calotropin, exhibited far less DPPH scavenging percentage (65.09 ± 0.04) at the higher concentration (500 $\mu\text{g/mL}$) with a higher IC_{50} value of 134.0 $\mu\text{g/mL}$.

Table 4: DPPH scavenging activity percentage of *G. purpurascens* leaf extracts and the isolated calotropin.

Concentration (µg/mL)	% Scavenging activity (mean ± sd) against DPPH free radical					
	CHCl ₃	CHCl ₃ : MeOH	MeOH	EtOH	Calotropin	Ascorbic acid
25	64.30 ± 0.00	70.1 ± 0.00	72.53 ± 0.15	73.7 ± 0.00	36.3 ± 0.00	75.45 ± 0.07
50	70.6 ± 0.00	74.6 ± 0.00	76.83 ± 0.15	78.87 ± 0.06	39.64 ± 0.03	80.99 ± 0.10
100	75.60 ± 0.00	78.07 ± 0.00	79.97 ± 0.06	82.2 ± 0.00	43.7 ± 0.03	85.29 ± 0.07
150	78.30 ± 0.20	82.3 ± 0.00	83.3 ± 0.00	85.43 ± 0.06	48.92 ± 0.07	89.01 ± 0.00
250	80.83 ± 0.06	87.7 ± 0.00	88.4 ± 0.00	90.6 ± 0.00	56.64 ± 0.04	95.79 ± 0.03
500	85.2 ± 0.00	91.2 ± 0.00	93.5 ± 0.00	95.7 ± 0.00	65.09 ± 0.04	98.89 ± 0.00
IC ₅₀ (µg/mL)	2.7	1.7	1.1	1.1	134.0	1.0

**Figure 3:** DPPH radical scavenging activity percentage versus concentration (µg/mL) of *G. purpurascens* leaf extracts and the isolated calotropin.

3.4. In Silico Molecular Modeling Study

The docking analysis output revealed that the isolated compound, calotropin, formed some interactions with the amino acid residues of the *P. aeruginosa* PqsA (5OE3) enzyme (Figure 4). This compound recorded a docking score of -10.3 kcal/mol, which was found to be higher than that of chloramphenicol (-7.0 kcal/mol) (Figure 5). It established six hydrogen bonds with Gly-169, Lys-172, Arg-397, Ala-170, Thr-380, and Thr-164 amino acid residues of the protein model 5OE3. This compound also formed a π -cation interaction with Arg-333 and six Van der Waals interactions with Thr-164, Thr-304, Gly-302, Ala-303, Glu-305, and Gln-369 amino residues (Figure 4).

The drug-likeness property prediction report indicated that this calotropin was found to violate one of Lipinski's rules of five (with a molecular weight > 500 g/mol). The ADME property prediction report showed that the compound scored a higher skin permeation value (logP) of -8.89 cm/s. It also exhibited high gastro-intestinal absorption and was found to be non-blood brain barrier (BBB) permeable. Besides, the compound showed an inhibitory interaction with the P-glycoprotein (P-gp) enzyme, whereas it was observed as a non-inhibitor of all the cytochrome-P (CYP) enzymes. The toxicity property prediction report revealed that this calotropin compound was found within the toxicity class of two with an LD₅₀ value of 8 mg/kg. It displayed immunotoxicity and cytotoxicity properties. However, it was found to be a non-

hepatotoxic, non-carcinogenic, and non-mutagenic isolate.

4. CONCLUSION

The present study reported, for the first time, the combined antimicrobial and antioxidant activities of various extracts of the leaves of *G. purpurascens*. Besides, a cardenolide compound, known as calotropin, was isolated from the leaves of the plant and reported herein, along with its binding capacity against the *P. aeruginosa* PqsA (5OE3) enzyme. This compound showed a strong binding capacity with a docking score of -10.3 kcal/mol against the target enzyme, which supported the obtained *in vitro* antibacterial activity. The various extracts of the leaves of *G. purpurascens* displayed good antibacterial activity against all tested bacterial strains, which supported the claimed traditional medicinal uses of the plant. Besides, all the leaf extracts exhibited promising DPPH radical scavenging activity comparable to that of ascorbic acid (1.0 µg/mL) at the same concentrations, and this may give a clue for the anticancer potential of the plant and the isolation of potential antioxidant compounds. Since this is a preliminary report, we believe that further biochemical investigations would be needed on this *G. purpurascens* plant species to increase the chance of obtaining additional phytochemicals with modified biological activity.

Further, it was higher than that of chloramphenicol (-7.0 kcal/mol). On the leaves of *G. purpurascens*,

they led to the isolation of a cardenolide compound called calotropin. All the extracts and isolated compound, calotropin, displayed better antibacterial activity against *P. aeruginosa* strain than chloramphenicol (7.1 ± 0.2 to 7.3 ± 0.5 mm) at all tested concentrations. However, the tested chloroform: methanol (1:1) extract was found to have negligible antifungal activity against *C. albicans* compared to the standard ketoconazole $10 \mu\text{g}/\text{disc}$ (17.67 ± 2.52 mm). All the leaf extracts exhibited promising DPPH radical scavenging activity with IC_{50} values ranging from 1.1-2.7 $\mu\text{g}/\text{mL}$ equivalence to ascorbic acid (1.0 $\mu\text{g}/\text{mL}$) at the same tested concentrations. The molecular docking result revealed that the isolated compound, calotropin,

showed a good binding capacity against *P. aeruginosa* PqsA (5OE3) with a docking score of -10.3 kcal/mol, which was higher than that of the chloramphenicol (-7.0 kcal/mol). The drug-likeness candidacy and the pharmacokinetic property result showed that the isolated calotropin violated one of Lipinski's rules of five (with molecular weight > 500 g/mol) and was found to be an immunotoxic and cytotoxic isolate. Since this is a preliminary report, further biochemical investigations would be needed on this *G. purpurascens* plant species to increase the chance of obtaining additional phytochemicals with modified biological activity.

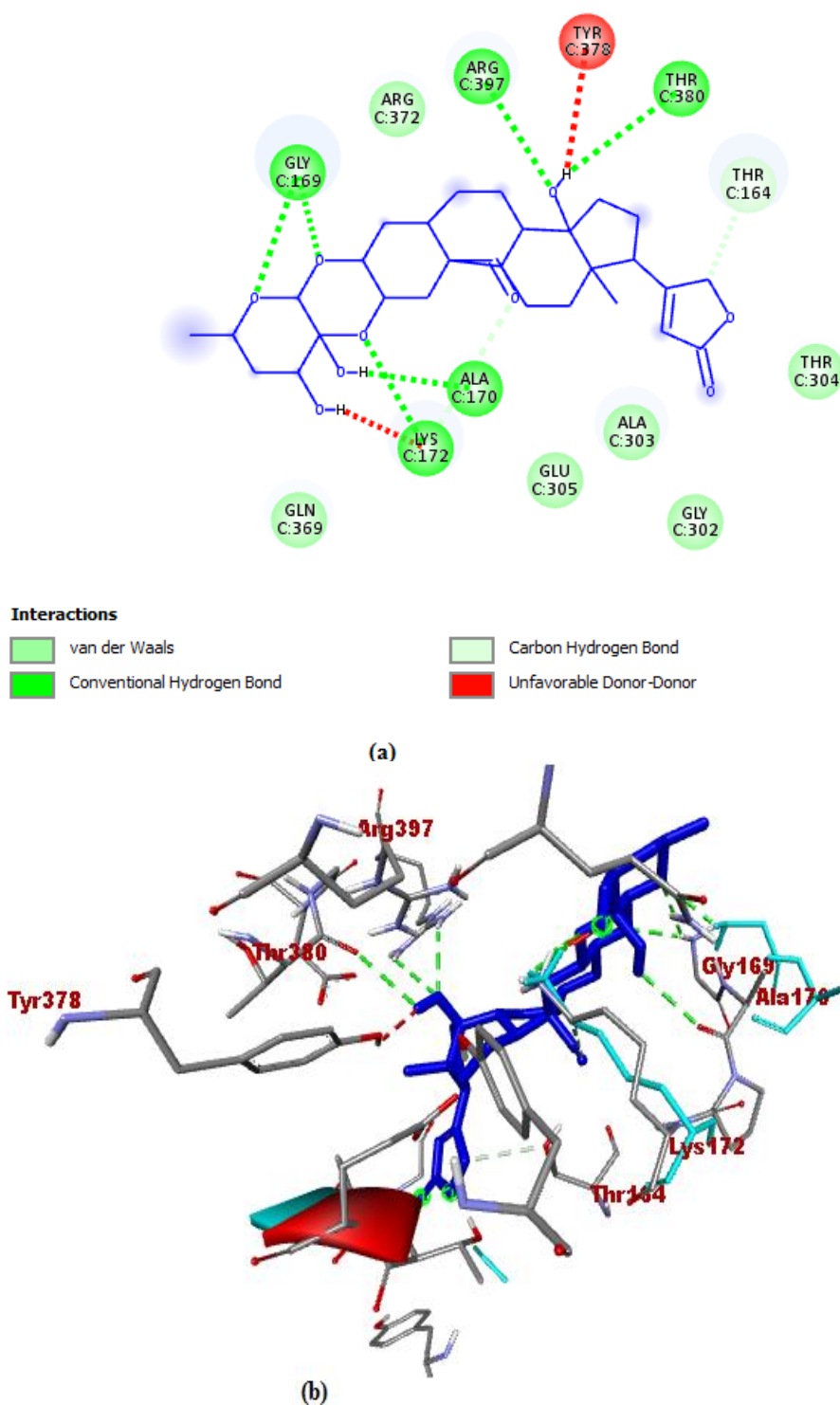
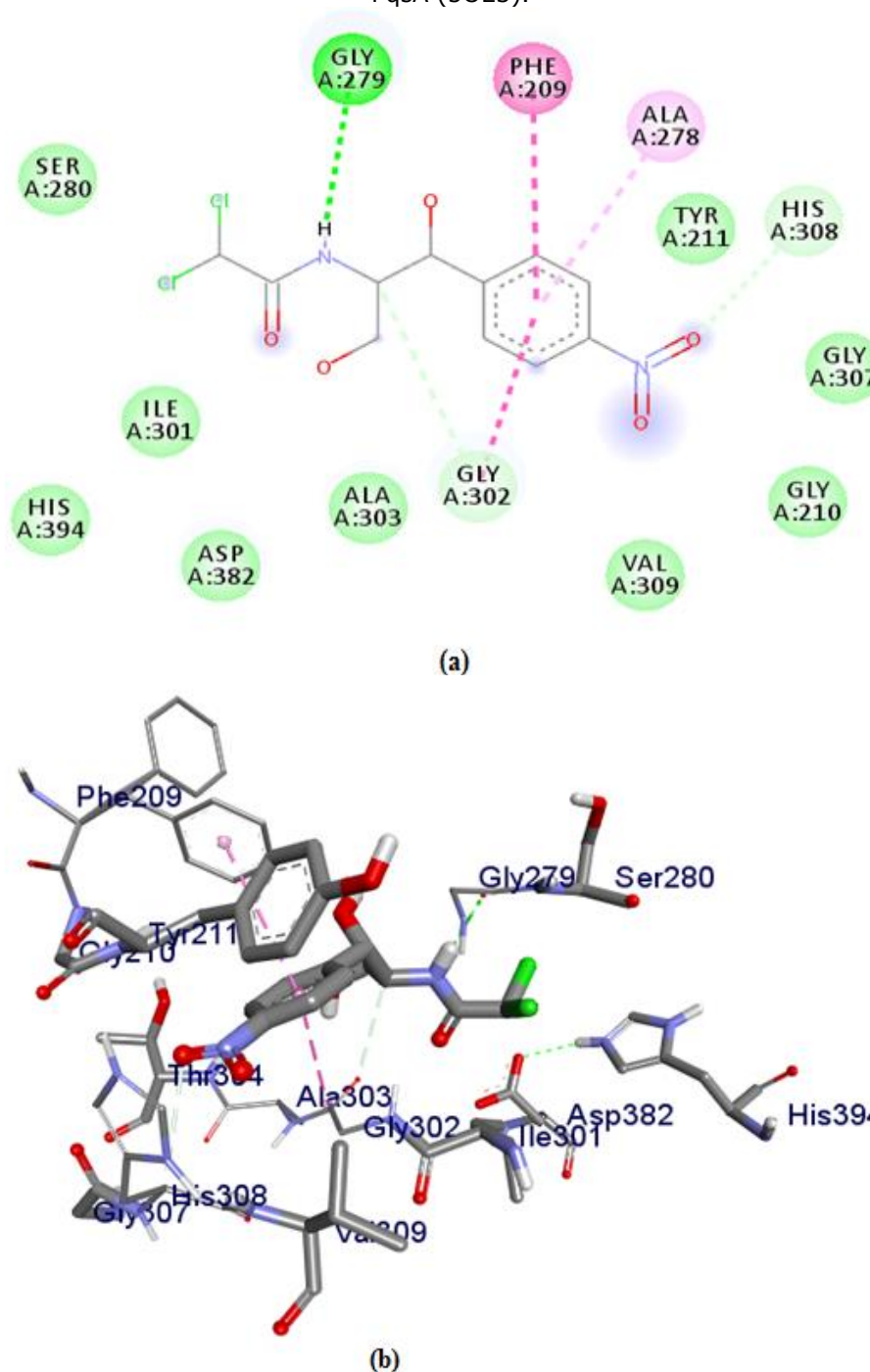


Figure 4: Ligand-protein interaction **(a)** and 3D representation **(b)** between calotropin and *P. aeruginosa* PqsA (5OE3).**Figure 5:** Ligand-protein interaction **(a)** and 3D representation **(b)** between chloramphenicol and *P. aeruginosa* PqsA (5OE3).

5. CONFLICT OF INTEREST

The authors declared no conflict of interest.

6. ACKNOWLEDGMENTS

This research was funded by Adama Science and Technology University [grant number ASTU/AS-R/003/2020], the World Academy of Sciences (TWAS), and the United Nations Educational, Scientific and Cultural Organization (UNESCO) [TWAS Research grant number RGA No. 20-274 RG/CHE/AF/AC_G - FR3240314163].

7. SUPPLEMENTARY MATERIALS

¹H, ¹³C, and DEPT-135 NMR spectra of isolated compounds (calotropin) are available online.





8. REFERENCES

- Hedberg I. Flora of ethiopia and eritrea. In: The Biodiversity of african plants [Internet]. Dordrecht: Springer Netherlands; 1996. p. 802-4. Available from: [<URL>](#).

2. Belayneh A, Bussa NF. Ethnomedicinal plants used to treat human ailments in the prehistoric place of Harla and Dengego valleys, eastern Ethiopia. *J Ethnobiol Ethnomed* [Internet]. 2014 Dec 5;10(1):18. Available from: [<URL>](#).
3. Deng L, Costa F, Blake KJ, Choi S, Chandrabalan A, Yousuf MS, et al. *S. aureus* drives itch and scratch-induced skin damage through a V8 protease-PAR1 axis. *Cell* [Internet]. 2023 Nov 22;186(24):5375-5393.e25. Available from: [<URL>](#).
4. Asfaw M, Mulaw A. Evaluation of topical antifungal activity of *Gomphocarpus purpurascens* A. rich leaves and stems extracts against epizootic lymphangitis. *Int J Microbiol Res* [Internet]. 2018;9(2):19–25. Available from: [<URL>](#).
5. Ayanaw MA, Yesuf JS, Birru EM. Evaluation of analgesic and anti-inflammatory activities of methanolic leaf and root extracts of *Gomphocarpus purpurascens* A. Rich (Asclepiadaceae) in mice. *J Exp Pharmacol* [Internet]. 2023 Jan 1;Volume 15:1–11. Available from: [<URL>](#).
6. Miseganaw D, Sahile Samuel, Negash W. In vitro antimicrobial effects of *Gomphocarpus purpurascens* a. rich against standard and clinically isolated microorganisms. *Glob Sci Journals* [Internet]. 2019;7(6):121–36. Available from: [<URL>](#).
7. Asfaw M, Mitku F, Mulaw A. Laboratory evaluation of antibacterial activity of *Gomphocarpus purpurascens* A. Rich leaves and stems extracts against *Escherichia coli*. *Int J Microbiol Res* [Internet]. 2018;9(1):16–8. Available from: [<URL>](#).
8. Gammatantrawet N, Nguyễn CT, Susawaengsup C, Ramli ANM, Tongkoom K, Chatsungnoen T, et al. Phytochemistry of medicinal herbs belongs to asclepiadaceae family for therapeutic applications: A critical review. *Mol Biotechnol* [Internet]. 2024 Mar 20;Article in Press:1–25. Available from: [<URL>](#).
9. Marzouk AM, Osman SM, Gohar AA. A new pregnane glycoside from *Gomphocarpus fruticosus* growing in Egypt. *Nat Prod Res* [Internet]. 2016 May 2;30(9):1060–7. Available from: [<URL>](#).
10. Green PWC, Veitch NC, Stevenson PC, Simmonds MSJ. Cardenolides from *Gomphocarpus sinaicus* and *Pergularia tomentosa* (Apocynaceae: Asclepiadoideae) deter the feeding of *Spodoptera littoralis*. *Arthropod Plant Interact* [Internet]. 2011 Sep 6;5(3):219–25. Available from: [<URL>](#).
11. Latif Z, Gray A. Natural products isolation. Second edition. Totowa, New Jersey: Humana Press inc.; 2006.
12. Singh VK. Selected Indian Folk medicinal claims and their relevance in primary health care programme. *Glimpses Plant Res.* 1993;10:147–52.
13. Kunert O, Rao BVA, Babu GS, Padmavathi M, Kumar BR, Alex RM, et al. Novel steroidal glycosides from two Indian *Caralluma* species, *C. stalagmifera* and *C. indica*. *Helv Chim Acta* [Internet]. 2006 Feb 21;89(2):201–9. Available from: [<URL>](#).
14. McCartney JE, Collee JG, Mackie TJ. Practical medical microbiology. Charchil Livingstone; 1989.
15. Kiros T, Eswaramoorthy R, Mohammed S, Dekebo A, Melaku Y. Compounds with antibacterial and antioxidant activities from *Cadia purpurea*. *Nat Prod Res* [Internet]. 2023 Aug 18;37(16):2672–80. Available from: [<URL>](#).
16. Kiros T, Eswaramoorthy R, Melaku Y, Dekebo A. In vitro antibacterial and antioxidant activities and molecular docking analysis of phytochemicals from *Cadia purpurea* roots. Mu J, editor. *J Trop Med* [Internet]. 2022 Feb 24;2022(1):1–13. Available from: [<URL>](#).
17. Khorasani Esmaili A, Mat Taha R, Mohajer S, Banisalam B. Antioxidant activity and total phenolic and flavonoid content of various solvent extracts from *in vivo* and *in vitro* grown *Trifolium pratense* L. (Red Clover). *Biomed Res Int* [Internet]. 2015 Jan 1;2015(1):1–11. Available from: [<URL>](#).



Enhancing Skincare Formulas with Olive Oil-Infused Citrus Peel Extracts: A Comprehensive Study

Mebarka Imane Benguechoua^{1,2*} , Madjda Benguechoua² , Khedidja Benarous^{1,2*} ,
Alaeddine Kaouka¹ , Mohamed Yousfi² 

¹Applied Sciences and Didactics laboratory, Higher Normal School, Laghouat, Algeria.

²Fundamental Sciences Laboratory, Amar Telidji University, Laghouat, Algeria.

Abstract: The increasing global demand for natural and organic ingredients in cosmetics has spurred a surge in research exploring innovative formulations. This study delves into the utilization of citrus fruit peels and seeds macerated in olive oil as a foundation for novel ointments. Through the analysis of extracts from a variety of citrus sources, including orange, lemon, tangerine, grapefruit, and citron peels, as well as lemon and tangerine seeds, their physicochemical properties and antioxidant activity were meticulously examined using thin-layer chromatography (TLC). A groundbreaking aspect of this research is the revelation of the *in vitro* antioxidant potential of DMSO extracts obtained from these citrus-infused olive oils. Chemical assays unequivocally confirmed the presence of phenols and flavonoids, renowned for their robust antioxidant properties, across all extracts. These significant findings not only reinforce the well-documented benefits of citrus fruits in combating premature aging and diseases but also underscore the untapped potential of citrus by-products as valuable natural cosmetic ingredients. This preliminary investigation serves as a beacon illuminating the promising prospects of integrating citrus fruit remnants into cosmetic formulations. The imperative for further exploration in this realm is evident, aiming to refine formulations and advocate for the sustainable exploitation of citrus resources within the cosmetics sector. By embarking on deeper research endeavors, an inclusive comprehension of leveraging the inherent potency of citrus fruits for the creation of cutting-edge and efficacious natural cosmetic products can be achieved.

Keywords: Citrus by-products, Infused olive oil, Cosmetic formulations, Antioxidant, Skincare.

Submitted: June 1, 2024. **Accepted:** July 30, 2024.

Cite this: Benguechoua MI, Benguechoua M, Benarous K, Kaouka A, Yousfi M. Enhancing Skincare Formulas with Olive Oil-Infused Citrus Peel Extracts: A Comprehensive Study. JOTCSA. 2024;11(4): 1387-96.

DOI: <https://doi.org/10.18596/jotcsa.1492998>

***Corresponding author's E-mail:** m.benkechoua@ens-lagh.dz; k.benarous@lagh-univ.dz

1. INTRODUCTION

Olive oil plays a crucial role in the Mediterranean diet (1,2), with extensive research conducted to showcase its numerous health benefits. In particular, olive oil contains more than 30 different types of phenolic compounds, which are powerful antioxidants that help protect the body from free radicals (3). Extra Virgin Olive Oil (EVOO), renowned for being the highest quality among all categories of olive oils, is one of the most extensively studied food sources of antioxidants. This is attributed to the presence of various antioxidant compounds in EVOO (4). Their potent bioactive components exhibit robust cardio-protective attributes, aiding in the reduction of blood pressure and the prevention of atherosclerosis (5,6).

In recent times, there has been a growing trend to incorporate aromatic herbs, spices, and vegetables into extra virgin olive oil (EVOO) to create flavored oils. This practice aims to improve the sensory qualities, nutritional value, health benefits, and shelf life of the oil (7,8).

Among the natural flavors used with olive oil is *Citrus*, which is a genus belonging to the Rutaceae family of trees and shrubs, including oranges, lemons, grapefruits, tangerines, and limes (9). The citrus fruits were the second most produced fruits worldwide in 2021, accounting for 161.8 million tons produced in more than 10.2 million hectares (10). Therefore, Citrus by-products are immense and can be classified into peels (flavedo and albedo), seeds, and pulp residues, where the flavedo is the outer colored part of the bark that contains the oil sacs. In

contrast, the albedo is the white inner part of the bark, which is rich in pectin (9). In addition, peels are also high in sugars and have a high concentration of D-limonene, a potent antimicrobial compound (11-13). The residual pulp consists of the membranes and partitions of the segments that once contained the juice. As for the seeds, they are mainly composed of non-nitrogenous extracts, fats, crude proteins, and fibers (14).

Citrus peels, typically discarded as waste, are abundant in beneficial compounds such as Vitamin C, fiber, phenolics, and flavonoids, providing antioxidant, anticarcinogenic, and anti-inflammatory properties. Citrus fruits, thanks to their content of ascorbic acid, antiseptics, and antioxidants, are an effective natural weapon against acne. They help regulate sebum production, eliminate bacteria, and protect the skin from free radical damage (15,16). These criteria make it the best choice to be incorporated in organic and natural ointments, which are semi-solid and greasy preparations for external application to the skin, rectum, or nasal mucosa (17). The use of synthetic ointments encompasses the risk of skin irritation and allergic reactions triggered by specific cosmetic chemicals, such as formaldehyde-releasing preservatives, which can lead to skin problems. Additionally, these ointments may contain harmful components like petrolatum, propylene glycol, and synthetic colors, which have the potential to induce various health problems. Nowadays, the use of organic ointments possesses a considerable advantage thanks to the progressive discovery of the applications of plant oils in health care and in areas of economic interest, and they are also cheaper and without adverse effects. Recently,

homemade medicines such as ointments have gained popularity without having been tested for compliance with standards. Therefore, the objective of this study is to develop natural citrus-based ointments incorporated in extra virgin olive oil (EVOO) and to evaluate the quality attributes of natural citrus ointment on the basis of various physicochemical characteristics.

2. MATERIAL AND METHODS

2.1. Chemicals and Reagents

1,1-diphenyl-2-picrylhydrazyl radical (DPPH), quercetin, catechine, and rutin were purchased from Sigma Aldrich; all other chemicals and solvents used were of analytical grade investigations.

2.2. Materials

Citrus fruits were purchased directly from the market; citron was obtained from a farm in Laghouat Province, South of Algeria. After air-drying in shaded areas at room temperature for a week, citrus peels and seeds were coarsely powdered using a dry grinder. Subsequently, the resulting powder was stored in airtight bags under dark conditions until further utilization.

For the maceration procedure, EVOO was purchased from a local certified producer. Beeswax, one of the natural raw materials employed in the ointment formulations, was purchased from a local beekeeper.

2.3. Preparation of Olive Oil-Infused Citrus Peels and Seeds

We have outlined the protocol for preparing EVOO-infused citrus peels and seeds, detailed in Figure 1.

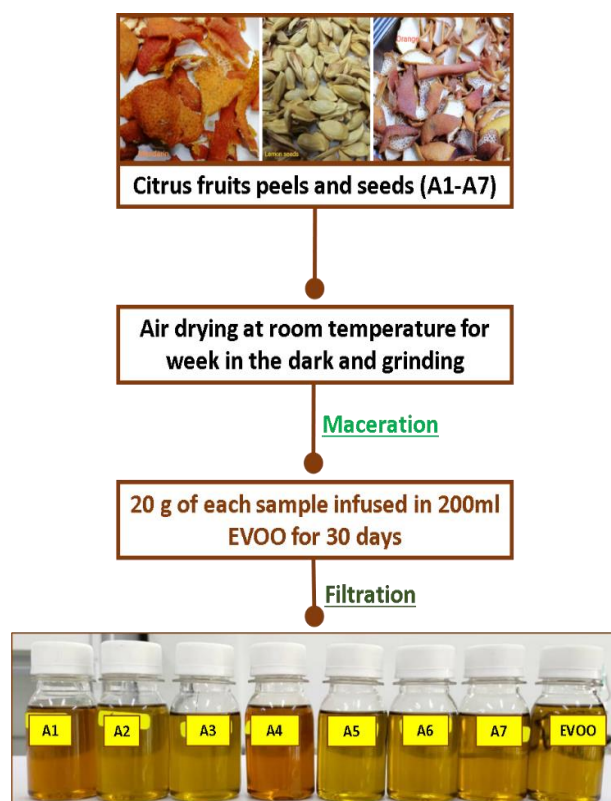


Figure 1: Description of the process for extracting citrus peels and seeds with EVOO through maceration. **A1:** Orange peels, **A2:** Lemon Peels, **A3:** Lemon Seeds, **A4:** Mandarine Peels, **A5:** Mandarine Seeds, **A6:** Grapefruits Peels, **A7:** Citron Peels, **EVOO:** Extra Virgin Olive Oil

The EVOO infused with citrus peels and seeds, displaying varying colors and fragrances, has been carefully preserved in bottles within a dark environment at room temperature until ready for use.

2.3.1 Physical analysis of the oil samples (Refractive Index)

Measurement of the refractive index of the infused samples was done by means of a refractometer according to the method of AOAC (2000) (17).

2.4. Phytochemical Tests

2.4.1. Extraction with DMSO

An extract solution was prepared using the methodology outlined by Erdal Eroglu et al. (2021) (18), with some modifications. Initially, a precise volume of DMSO, combined with double the volume of citrus peels and seeds-infused EVOO, was mixed in a beaker. This mixture was then subjected to gentle stirring on a hot plate at 37°C for 2 hours. Subsequently, the amalgam was allowed to rest undisturbed in darkness for 1 hour until a clear phase separation between the DMSO and the citrus-infused EVOO occurred. Following phase separation, the DMSO fraction was carefully transferred into a glass tube. Simultaneously, a control test tube containing solely EVOO was subjected to the same extraction protocol for comparative purposes. All DMSO-dissolved extracts were promptly stored in a refrigerated environment for subsequent utilization. The major families of secondary metabolites were elucidated through tube-colored reactions employing conventional characterization methods (19).

2.4.2. Phenolic compounds test

The total phenolic contents of all DMSO extracts were quantified utilizing the Folin-Ciocalteu test (20), as per preliminary assessments. Following the established protocol, 100 µL of extract samples were mixed with 250 µL of Folin-Ciocalteu reagent in a test tube and allowed to incubate for 2 minutes at room temperature. Subsequently, 1000 µL of sodium carbonate (Na₂CO₃) was added to the same tube, and the samples were further incubated for 30 min at room temperature in darkness. The emergence of a blue coloration signified the presence of total phenolic compounds.

2.4.3. Flavonoids test

The flavonoid contents of DMSO extracts were determined by the AlCl₃ test (21). 500 µL of an AlCl₃ solution (10%) is taken with 500 µL of each sample in test tubes. The whole was incubated for 15 min at room temperature. The appearance of the yellow color indicates the presence of flavonoids.

2.4.4. Thin-layer chromatography analysis (TLC)

TLC was performed on silica gel 60 f 254, 20X10 cm HPTLC plates (Merck, Darmstadt, Germany) with ethyl acetate : methanol : water (10:1.35:1) (v/v/v) as a mobile phase (22).

Standards, solutions such as quercetin, catechin, and Rutin (2.5 mg/mL each) were applied with DMSO extracts to the plates in the form of strips. After development, the plates were dried with a flow of

cold air using a hair dryer; the plates were documented under ultraviolet (UV) light 254 and 366 nm lamp by a camera device. Then, the plate was immersed in iodine (I₂) as a developer. The areas of the molecules appeared as brown spots, so another plate that was prepared with the same protocol was sprayed in the DPPH solution at one mM and dried quickly with a dryer. Next, antioxidant activity was visualized on the basis of trapping the stable artificial radical molecule (DPPH). The zones with an antioxidant effect appeared as yellow spots on the dark purple background and were photographed by a professional camera in visible light after the plates were dried (23,24). All retention factor values were calculated as described in different literature sources (23,24).

2.5. Ointments Preparation

To formulate the citrus-infused EVOO ointments, the following process was followed:

- 2 g of beeswax were melted over low heat until the temperature reached 60-70°C.
- 10 mL of the EVOO infused with the various citrus fruit peels was then added to the melted beeswax.
- The mixture was simmered until a homogeneous oily solution was obtained.
- The mixture was allowed to cool, resulting in the formation of an ointment with a desirable consistency.
- The prepared ointments were then transferred into storage containers for future use.

This straightforward yet effective method enabled the successful incorporation of the citrus-infused EVOO into a stable and well-textured ointment formulation. The controlled heating and cooling process ensured the homogeneity and appropriate consistency of the final ointment products.

2.5.1. Testing of Physical Properties of Ointments

Based on the search results, the key points regarding the evaluation of the physical properties of the citrus-based semi-solid ointments are organoleptic properties, homogeneity, pH, water resistance, skin absorption, and skin sensitivity. By thoroughly evaluating these physical properties, we will be able to assess the quality, stability, and suitability of the citrus-based semi-solid ointment formulations for topical application.

2.5.2. Organoleptic properties

The ointments were assessed for their appearance, color, odor, and texture to ensure they met the desired sensory characteristics.

2.5.3. Homogeneity test

The ointments were evaluated for their homogeneity, ensuring the active ingredients and excipients were uniformly distributed throughout the formulation. A 0.5 g of formulated ointments was placed on the skin and then leveled and observed based on color uniformity and the absence of lumps and granules.

2.5.4. pH test

The pH of the ointments was measured to confirm they were within the acceptable range for topical application, typically close to the skin's natural pH.

Using the pH paper, a thin layer of the ointment was applied, and it was then given some time to stand. The pH level was then determined by comparing it to a color chart.

2.5.5. Water resistance test

The ointments were tested for their ability to resist water and maintain their integrity when exposed to moisture, an important property for topical products. On glass plates, a thin layer of ointment was spread, then a drop of water was added. If they are non-miscible, this means that ointments are resistant to water.

2.5.6. Skin absorption

The ointments were evaluated for their ability to be absorbed into the skin, which is crucial for delivering the active ingredients to the target site. A small amount of ointment was applied to a specific area of the hand; we made circular movements, and then the time taken to absorb the ointment was recorded. Each type of ointment was repeated three times.

2.5.7. Topical Sensitivity Test

The ointments were tested for any potential skin irritation or sensitization reactions to ensure they were well-tolerated when applied topically. All ointments were tested for their skin sensitivity tests by applying them to the skin for a week and observing the side effects, if any, as a set of parameters like skin inflammation, skin irritation, reddening of the skin (allergic reactions) ...etc.

3. RESULTS AND DISCUSSION

3.1. DMSO Extraction of EVOO-Infused Citrus Peels and Seeds

The analysis of phytochemicals in plant-based products, particularly in oil seed plant extracts with complex compositions, continues to be a major challenge. Previous research has commonly used methanol as the preferred solvent to extract bioactive compounds from plants infused oil to perform phytochemical characterization (25,26).

This study used DMSO for the first time to extract bioactive compounds from EVOO—citrus peels and seeds. The extraction of bioactive components of infused EVOO—citrus peels was successfully obtained. The transparent color of DMSO has become different according to the color of each sample. This study specifically selected EVOO for the preparation, adhering to a traditional medicine recipe.

Extractive conditions such as incubation time, darkness, and temperature decrease the rate of oxidation, which alters the organoleptic properties of the oil compared to other studies (18).

3.2. Qualitative Phytochemical Screening

Preliminary phytochemical screening of DMSO extracts revealed the presence of various bioactive components, including phenolics and flavonoids (Figure 2). The current study found that DMSO-citrus peel olive oil extracts show a positive test (+++++) for phenols and flavonoids with the exception of A1 and A3 (++) , which could be attributed to the improved solubility of the active compounds in organic solvents.

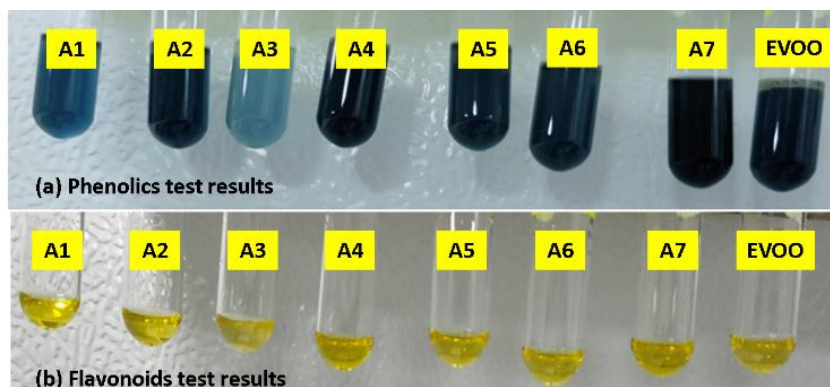


Figure 2: Phytochemical Screening of phenolics and flavonoids.

3.3. Thin-Layer Chromatography Analysis

To avoid false positive results when using TLC-DPPH to analyze antioxidant compounds, it is recommended to dry the chromatograms and shoot them directly under white light after spraying with the DPPH solution. This procedure helps to ensure the stability of the resulting coloring.

The UV detection of the spots showing the antioxidant effect can also be significant since they are visible at 366 nm but not at 254 nm (Figures 3A and 3B).

The iodine developer plate has areas of the molecules in the form of brown spots (Figure 3C). From this

plate, Rf is calculated for quercetin, catechine, and rutin (Rf values of 0.86, 0.78, and 0.24, respectively) where quantified in all the TLC plates (Table 1). Among the compounds available as standards, quercetin, and catechine were present in all DMSO-citrus peels and seeds-EVOO extracts. Visualization of the plate in UV light over time wavelength (366 nm) indicates the presence of multiple spots with varying degrees of Polarization and coloration in all extracts. The iodine developer plate (Figure 3C) revealed the presence of various phenolic compounds with differing polarities. These compounds appeared as multiple spots with Rf values ranging from 0.28 to 0.95, which were not readily apparent under short-wavelength UV light (254 nm),

as shown in Figure 3A. In iodine plat, all DMSO- citrus - EVOO extracts revealed four spots except the DMSO- Grap fruits Peels - EVOO (A6) and DMSO-Citron Peels - EVOO (A7) extracts have five spots at $R_f = 0.94, 0.88, 0.8, 0.74, 0.34$ of A6 and $R_f = 1, 0.86, 0.857, 0.73, 0.34$ of A7.

Monitoring the transformation of the purple DPPH solution to a yellow color identified the presence of positive antioxidant activity. The TLC-DPPH analysis of the DMSO-Citrus-EVOO and DMSO-EVOO extracts revealed several characteristic antioxidant zones. DMSO-Orange peels-EVOO (A1), DMSO-

Lemon Seeds-EVOO (A3), and DMSO-Grapefruit Peels-EVOO (A6) extracts displayed weak antioxidant activity.

Previous works assessed the DPPH radical scavenging ability of different citrus species and indicated that the antioxidant activity and phenolic content are strongly affected by the species and extraction solvent (27,28). However, it should be noted that no published work has been done on thin-layer chromatography analysis of DPPH in Citrus peels infused olive oil.

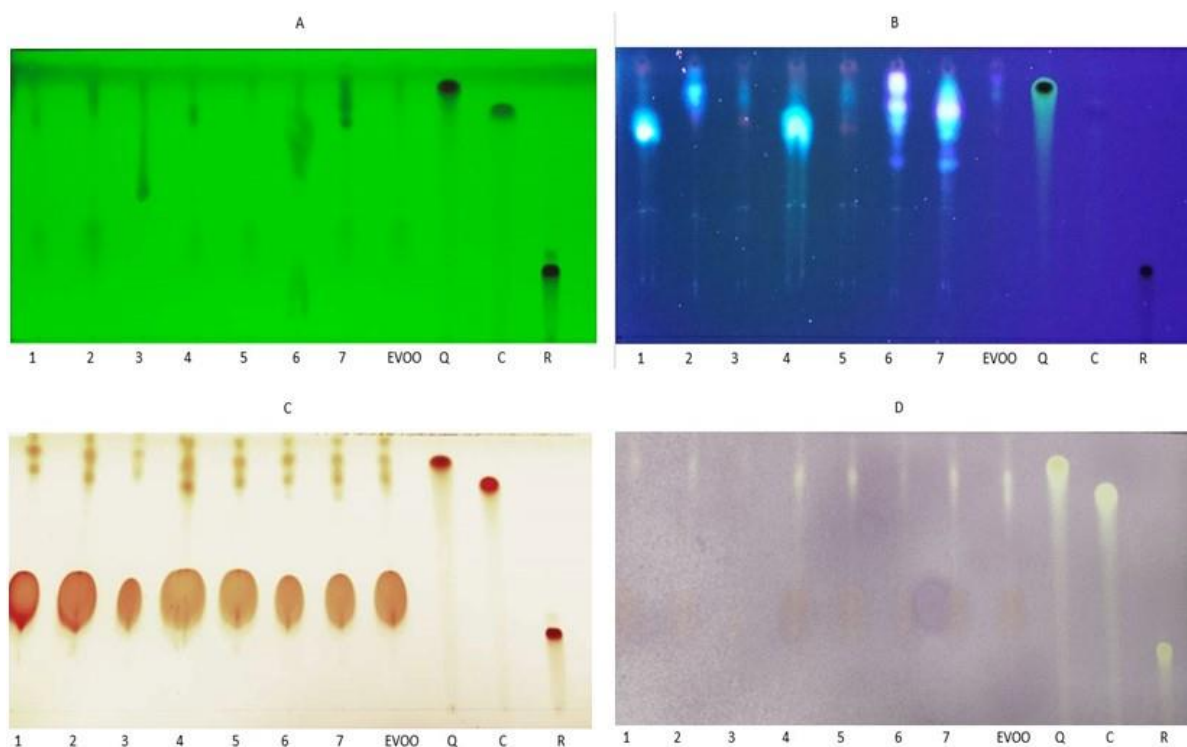


Figure 3: TLC chromatograms of DMSO-Citrus-EVOO, DMSO-EVOO extracts, and standards at 254 nm (A), at 366 nm (B), iodine (C), and at white light after DPPH assay (D).

A1: Orange peels, **A2:** Lemon Peels, **A3:** Lemon Seeds, **A4:** Mandarin Peels, **A5:** Mandarin Seeds, **A6:** Grapefruits Peels, **A7:** Citron Peels, **EVOO:** Extra Virgin Olive Oil, **Q:** Quercetin, **C:** catechin, **R:** rutin

Table 1: R_f values of DMSO-Citrus-EVOO, DMSO -EVOO and standards extracts.

Compounds	R_f
A1	0.95 /0.86 /0.79 /0.3
A2	0.94 /0.88 /0.82 /0.32
A3	0.93 /0.86 /0.8 /0.28
A4	0.94 /0.89 /0.82 /0.32
A5	0.93 /0.86 /0.79 /0.34
A6	0.94 /0.88 /0.8 /0.73 /0.34
A7	0.93 /0.86 /0.8 /0.73 /0.34
EVOO	0.94 /0.87 /0.81 /0.33
Quercetin	0.86
Catechin	0.78
Rutin	0.24

3.4. Physical Analysis of the Infused-EVOO Samples

Table 2 shows the refractive index of EVOO-infused citrus peels and seeds. The values of all oil samples

ranged from 1.4659 to 1.4669. The results are within the limits set by Codex Alimentarius (2017) standards for olive oils (29).

Table 2: Refractive index of EVOO-infused citrus peels and seeds.

The oil samples	Refractive index at 23 C°
A1	1.4662
A2	1.4663
A3	1.4665
A4	1.466
A5	1.4665
A6	1.4669
A7	1.4662
EVOO	1.4659

3.5. Testing of Physical Properties of Ointment

3.5.1. Organoleptic test

Organoleptic characteristics refer to the sensory properties of a product, including its appearance, smell, taste, and texture. For EVOO-infused Citrus Peel-derived ointments, the organoleptic characteristics are primarily influenced by the type of citrus fruit used and the quality of the olive oil. The color and appearance of the formulated ointment vary depending on the kind of citrus peels and seeds

used. Lemon peel-infused olive oil ointment has a lighter color compared to orange and tangerine peel-infused olive oil ointment (Figure 4). The aroma is typically a pleasant combination of the citrus fruit and the olive oil, with the citrus notes being more prominent. The taste is a balance of the citrus and olive oil flavors, with the citrus peel adding a slightly sweet and tangy taste. The texture is smooth and creamy, with the ointment being easily spreadable.

**Figure 4:** Formulated ointments.

A1: Orange peels, **A2:** Lemon Peels, **A3:** Lemon Seeds, **A4:** Mandarin Peels
A5: Mandarin Seeds, **A6:** Grapefruits Peels, **A7:** Citron Peels, **HO:** EVOO

3.5.2. Homogeneity test

A homogeneity test is performed to analyze whether the basic materials have been mixed homogeneously during the ointment's synthesis process. The ointment's dosage is visually observed based on color

uniformity and the absence of lumps and granules. The results of this test showed that all formulated ointments from EVOO-infused citrus peels and seeds present homogeneity before and after application to the skin (Figure 5).



Before application



After application

Figure 5: Homogeneity test.

3.5.3. pH test

Monitoring the pH value of ointments is essential for ensuring their stability, efficacy, and safety. It is an important aspect of quality control and regulatory compliance. The pH value of the skin is typically between 5 and 6 (30), and maintaining this pH level is crucial for the skin's barrier function, which helps prevent the entry of harmful microbes and other substances. Changes in the skin's pH level, particularly if it becomes more alkaline, can lead to impaired barrier function, dryness, and irritation. The pH value of ointments can also affect their physical

properties, such as their viscosity and spreadability. Changes in pH can lead to changes in the ointment's consistency, which can affect its application and effectiveness. The pH values of all formulated ointments fall within the range of 5 to 6 (Figure 6). This aligns well with the average skin surface pH. Therefore, our results can be considered acceptable, minimizing the risk of irritation upon application.

3.5.4. Water resistance

All formulated ointments are anhydrous in nature and composed of water-insoluble components. They

exhibit a non-miscible and non-absorbent relationship with water, presenting an almost spherical shape (Figure 7). They tend to be more water-resistant compared to water-based emulsions. Therefore, they remain on the skin surface for a long time without drying out. When applied topically, they form a barrier on the skin's surface, which helps restrict the evaporation of water naturally present in the skin, ultimately increasing its hydration levels.

3.5.5. Skin Absorption

The absorption of ointments by the skin is an essential factor in the effectiveness of topical medications. Ointments are a common formulation for dermatological drugs due to their ability to enhance drug penetration and absorption into the skin. The factors affecting the absorption of ointments by the skin include the cornified layer, medication particle size, degree of skin hydration, contact time, skin temperature, and epidermal damage. The cornified layer, the top layer of the epidermis, is crucial in determining the absorption of ointments (31). Moistening the skin can enhance the absorption of medication by softening the cornified layer, allowing the ointment to penetrate more effectively. The size of the medication particles is also an essential factor; solutions such as olive oil or lanolin base have greater absorption (32). Table 3 demonstrates that all ointment formulations exhibited a short absorption duration. This trend suggests a direct relationship between the active ingredient percentage and the absorption duration.

All formulations contain a considerable proportion of oils and are greasier, thereby facilitating faster absorption rates into the skin.



Figure 6: pH of formulated ointments.

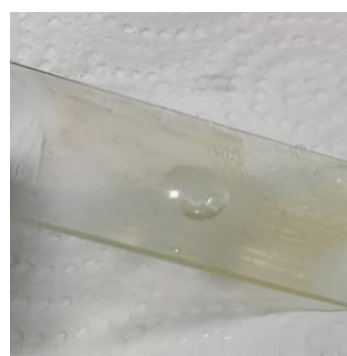


Figure 7: Water resistance test of ointments.

Table 3: Duration of absorption by the skin.

Sample	Duration of absorption by skin (s) per 1 cm
A1	33.93 ±2.04
A2	33.04±2.42
A3	30.06±0.55
A4	29.68±1.39
A5	30.16±0.97
A6	34.1±2.27
A7	34.65±3.86
EVOO	30.94±0.67

3.5.6. Topical sensitivity test

No side effects were observed, such as skin inflammation, irritation, or reddening of the skin (allergic reaction); i.e., these formulations did not produce any skin irritation for about a week when applied to the skin.

4. CONCLUSION

The study conclusively demonstrates the significant antioxidant properties of citrus extracts infused in extra virgin olive oil (EVOO), highlighting their ability to trap DPPH radicals and reduce oxidative potency effectively. This innovative approach underscores the potential of utilizing citrus fruit peels and seeds, often considered waste, as valuable resources in combating oxidative stress-related diseases, enhancing food products, and formulating natural cosmetic products. By integrating these citrus-infused oils into ointments, the research not only showcases their antioxidant benefits but also emphasizes their favorable physicochemical

properties, such as optimal pH, water resistance, and efficient skin absorption, making them suitable for topical applications. The detailed documentation of the methodologies, including the novel use of DMSO for bioactive compound extraction, ensures reproducibility and serves as a solid foundation for future research. This study paves the way for further exploration into optimizing formulations, understanding the individual roles of bioactive compounds, and expanding the use of other natural oils for infusion, thereby contributing to the development of effective, sustainable, and environmentally friendly natural products.

5. ACKNOWLEDGMENT

Declared none.

6. REFERENCES









1. Trichopoulou A, Martínez-González MA, Tong TY, Forouhi NG, Khandelwal S, Prabhakaran D, et al.

- Definitions and potential health benefits of the Mediterranean diet: views from experts around the world. *BMC Med* [Internet]. 2014 Dec 24;12(1):112. Available from: [<URL>](#).
2. Schwingshackl L, Hoffmann G. Does a mediterranean-type diet reduce cancer risk? *Curr Nutr Rep* [Internet]. 2016 Mar 23;5(1):9-17. Available from: [<URL>](#).
3. Rafehi H, Ververis K, Karagiannis TC. Mechanisms of action of phenolic compounds in olive. *J Diet Suppl* [Internet]. 2012 May 17;9(2):96-109. Available from: [<URL>](#).
4. Schwingshackl L, Christoph M, Hoffmann G. Effects of olive oil on markers of inflammation and endothelial function—A systematic review and meta-analysis. *Nutrients* [Internet]. 2015 Sep 11;7(9):7651-75. Available from: [<URL>](#).
5. Bulotta S, Celano M, Lepore SM, Montalcini T, Pujia A, Russo D. Beneficial effects of the olive oil phenolic components oleuropein and hydroxytyrosol: focus on protection against cardiovascular and metabolic diseases. *J Transl Med* [Internet]. 2014 Dec 3;12(1):219. Available from: [<URL>](#).
6. Antoun N, Tsimidou M. Gourmet olive oils: Stability and consumer acceptability studies. *Food Res Int* [Internet]. 1997 Mar;30(2):131-6. Available from: [<URL>](#).
7. Gambacorta G, Faccia M, Pati S, Lamacchia C, Baiano A, La Notte E. Changes in the chemical and sensory profile of extra virgin olive oils flavored with herbs and spices during storage. *J Food Lipids* [Internet]. 2007 Jun 26;14(2):202-15. Available from: [<URL>](#).
8. Choi IS, Lee YG, Khanal SK, Park BJ, Bae HJ. A low-energy, cost-effective approach to fruit and citrus peel waste processing for bioethanol production. *Appl Energy* [Internet]. 2015 Feb;140:65-74. Available from: [<URL>](#).
9. Sharma K, Mahato N, Cho MH, Lee YR. Converting citrus wastes into value-added products: Economic and environment friendly approaches. *Nutrition* [Internet]. 2017 Feb;34:29-46. Available from: [<URL>](#).
10. FAOSTAT. FAO statistical databases (FAO, 2023) [Internet]. [cited 2024 Aug 26]. Available from: [<URL>](#).
11. Wu GA, Terol J, Ibanez V, López-García A, Pérez-Román E, Borredá C, et al. Genomics of the origin and evolution of citrus. *Nature* [Internet]. 2018 Feb 7;554(7692):311-6. Available from: [<URL>](#).
12. Sengupta S, Pradhan A, Biswas S, Bhattacharya M. Exploring the antimicrobial properties of lemon: A comparative analysis of peel, seed, and pulp. *Microbiol Res J Int* [Internet]. 2024 Aug 21;34(9):10-24. Available from: [<URL>](#).
13. Ladaniya MS. Citrus fruit: Biology, technology and evaluation [Internet]. Elsevier; 2008. Available from: [<URL>](#).
14. Singh B, Singh JP, Kaur A, Singh N. Phenolic composition, antioxidant potential and health benefits of citrus peel. *Food Res Int* [Internet]. 2020 Jun;132:109114. Available from: [<URL>](#).
15. Liew SS, Ho WY, Yeap SK, Sharifudin SA Bin. Phytochemical composition and in vitro antioxidant activities of *Citrus sinensis* peel extracts. *PeerJ* [Internet]. 2018 Aug 3;6:e5331. Available from: [<URL>](#).
16. Andrade MA, Barbosa CH, Shah MA, Ahmad N, Vilarinho F, Khwaldia K, et al. Citrus by-products: Valuable source of bioactive compounds for food applications. *Antioxidants* [Internet]. 2022 Dec 25;12(1):38. Available from: [<URL>](#).
17. Osei YG. Developing suitable pharmaceutical dosage forms for G-REA herbal powder [Internet]. 2013. Available from: [<URL>](#).
18. Eroglu E, Girgin SN. A unique phenolic extraction method from olive oil macerate of *Hypericum perforatum* using DMSO: Assessment of in vitro anticancer activity, LC-MS/MS profile, total phenolic content and antioxidant capacity. *South African J Bot* [Internet]. 2021 Jul;139:6-11. Available from: [<URL>](#).
19. Houghton PJ, Raman A. Laboratory handbook for the fractionation of natural extracts [Internet]. Boston, MA: Springer US; 1998. Available from: [<URL>](#).
20. Maiga A, Houngnimassoun HMA, Attindehou S, Houinato M, Salifou S. Effet vermicide *in vitro* de l'extrait aqueux des feuilles de *Chenopodium ambrosioides* L. 1753 sur *Haemonchus contortus* et *Oesophagostomum colombianum* parasites gastro-intestinaux des petits ruminants. *J Anim Plant Sci* [Internet]. 2020;43(3):7501-12. Available from: [<URL>](#).
21. Dirar AI, Alsaadi DHM, Wada M, Mohamed MA, Watanabe T, Devkota HP. Effects of extraction solvents on total phenolic and flavonoid contents and biological activities of extracts from Sudanese medicinal plants. *South African J Bot* [Internet]. 2019 Jan;120:261-7. Available from: [<URL>](#).
22. Benarous K, Bombarda I, Iriepa I, Moraleda I, Gaetan H, Linani A, et al. Harmaline and hispidin from *Peganum harmala* and *Inonotus hispidus* with binding affinity to *Candida rugosa* lipase: In silico and in vitro studies. *Bioorg Chem* [Internet]. 2015 Oct;62:1-7. Available from: [<URL>](#).
23. Wagner H, Bladt S. Plant drug analysis [Internet]. Berlin, Heidelberg: Springer Berlin Heidelberg; 1996. Available from: [<URL>](#).
24. Maleš Ž, Plazibat M, Vundać V, Žuntar I, Pilepić K. Thin-layer chromatographic analysis of flavonoids, phenolic acids, and amino acids in some Croatian *Hypericum* taxa. *J Planar Chromatogr – Mod TLC*

- [Internet]. 2004 Aug;17(4):280–5. Available from: [<URL>](#).
25. Heinrich M, Daniels R, Stintzing FC, Kammerer DR. Comprehensive phytochemical characterization of St. John's wort (*Hypericum perforatum* L.) oil macerates obtained by different extraction protocols via analytical tools applicable in routine control. Pharmazie [Internet]. 2017;72(3):131–8. Available from: [<URL>](#).
26. Orhan IE, Kartal M, Gülpinar AR, Cos P, Matheussen A, Maes L, et al. Assessment of antimicrobial and antiprotozoal activity of the olive oil macerate samples of *Hypericum perforatum* and their LC–DAD–MS analyses. Food Chem [Internet]. 2013 Jun;138(2–3):870–5. Available from: [<URL>](#).
27. Saleem M, Durani AI, Asari A, Ahmed M, Ahmad M, Yousaf N, et al. Investigation of antioxidant and antibacterial effects of citrus fruits peels extracts using different extracting agents: Phytochemical analysis with in silico studies. Heliyon [Internet]. 2023 Apr;9(4):e15433. Available from: [<URL>](#).
28. Ashraf H, Iahtisham-Ul-Haq, Butt MS, Nayik GA, Ramniwas S, Damto T, et al. Phytochemical and antioxidant profile of citrus peel extracts in relation to different extraction parameters. Int J Food Prop [Internet]. 2024 Dec 31;27(1):286–99. Available from: [<URL>](#).
29. Codex Alimentarius. Codex standard for vegetable oils with specific name. Codex STAN 210-1999. 2017;
30. Souto EB, Fangueiro JF, Fernandes AR, Cano A, Sanchez-Lopez E, Garcia ML, et al. Physicochemical and biopharmaceutical aspects influencing skin permeation and role of SLN and NLC for skin drug delivery. Heliyon [Internet]. 2022 Feb;8(2):e08938. Available from: [<URL>](#).
31. Lambers H, Piessens S, Bloem A, Pronk H, Finkel P. Natural skin surface pH is on average below 5, which is beneficial for its resident flora. Int J Cosmet Sci [Internet]. 2006 Oct 19;28(5):359–70. Available from: [<URL>](#).
32. Günther C, Kowal K, Schmidt T, Jambrecina A, Toner F, Nave R. Comparison of in vitro and in vivo percutaneous absorption across human skin using bay1003803 formulated as ointment and cream. Clin Pharmacol Drug Dev [Internet]. 2020 Jul 24;9(5):582–92. Available from: [<URL>](#).



Phoenix Dactylifera Hydrochar as a Green Modification Material Based on Glassy Carbon Electrodes for the Detection of Methylene Blue

Mohamed Bendany¹ , Khalid Ait Ben Brahim¹ , Youssef El Hamdouni² ,
Hajar Oumoussa¹ , Zineb Hammi¹ , Nouhaila Gadda¹ , Najoua Labjar^{1*} ,
Abdelouahed Dahrouch², Souad El Hajjaji² 

¹Laboratory of Molecular Spectroscopy Modelling, Materials, Nanomaterials, Water and Environment, CERNE2D, ENSAM, Mohammed V University in Rabat, Morocco.

²Laboratory of Molecular Spectroscopy Modelling, Materials, Nanomaterials, Water and Environment, CERNE2D, Faculty of Science, Mohammed V University in Rabat, Morocco.

Abstract: A novel electrochemically sensitive sensor has been developed based on Hydrochar derived from Phoenix dactylifera was prepared for the detection of Methylene Blue (MB). These hydrochar (HC) have been used for the modification of the glassy carbon electrode (GCE). This electrode was characterized by scanning electron microscopy (SEM). The electrochemical properties of MB in the modified electrode (HC/GCE) were studied by square-wave voltammetry (SWV) and cyclic voltammetry (CV) under optimized conditions. Owing to a synergistic effect, the HC/GCE exhibited an obvious electrocatalytic effect on positively charged MB. The influence of experimental variables (accumulation time, supporting electrolyte, pH) was studied. Under optimized conditions, the constructed sensor illustrated a linear voltammetric curve for the MB in the concentration interval from 10^{-4} M to 10^{-10} M, with a detection limit of 0.2nM. A study of the effect of interference on sensor functionality was carried out, as well as an analysis of MB recovery in real wastewater samples. The modified electrode offers numerous advantages, including easy preparation, low detection limit, high sensitivity, good repeatability, short response time and an effective detection platform for MB in wastewater.

Keywords: Biomass, Methylene Blue, Glassy Carbon electrode, Electrochemical detection.

Submitted: December 29, 2023. **Accepted:** July 16, 2024.

Cite this: Bendany M, Brahim KAB, El Hamdouni Y, Oumoussa H, Hammi Z, Gadda N, Labjar N, Dahrouch A, El Hajjaji S. Phoenix Dactylifera Hydrochar as a Green Modification Material Based on Glassy Carbon Electrodes for the Detection of Methylene Blue. JOTCSA. 2024;11(4): 1397-406.

DOI: <https://doi.org/10.18596/jotcsa.1351638>

***Corresponding author's E-mail:** najoua.labjar@ensam.um5.ac.ma

1. INTRODUCTION

Methylene blue (MB) dye is an indicator used in various diagnostic tests and has several important aspects. MB is classified as a thiazine dye, characterized by its dark blue or bluish-green color. When it presents in alcoholic or aqueous media, it turns dark blue. It is odorless and has an air stability (1-3). In medicine, MB is used as a dye and indicator to visualize blood vessels (4,5). MB was initially proposed for sentinel node detection in various malignancies, including breast cancer (6). In the human body, it activates reductase enzymes that reduce MB to leukomethylene blue, which in turn converts methemoglobin to hemoglobin (7). Methemoglobinemia (MetHb) can develop when there is an excess of methylene blue (MB) in the

body through the oxidation of hemoglobin (8). Although its applications are numerous across multiple disciplines, MB has been identified like an extremely toxic dye for newborns, causing different problems such as hyperbilirubinemia, renal failure, hemolytic anemia, hypertension, nausea, headaches, mental confusion, deep sweating and precordial pain (9-13). In addition, MB has a strong inhibitory effect on sperm motility in healthy individuals (14).

MB is commonly used in the textile, leather, cosmetics and other additional fields for various applications. Typically, residues of MB are released into various water sources, resulting in undesirable colored water that causes environmental pollution (15,16). The presence of dyes modifies the

characteristics of water such as color, taste, odor, pH, and density. Dyes cause water to become highly opaque, limiting the penetration of light and consequently reducing the levels of dissolved oxygen, thereby negatively impacting aquatic ecosystems (17). Therefore, it is essential to develop an effective technique for the detection and elimination of MB to ensure the safety of treated liquid effluent discharges. Some of the frequently employed analytical methods for MB detection include capillary electrophoresis (18), UV-Vis spectroscopy (19,20), electrochemical and surface enhanced raman spectroscopy (21) and liquid chromatography coupled to tandem mass spectrometry (8).

Despite their high sensitivity and selectivity, these methods are often difficult to implement due to their higher cost, the difficulty of sample pretreatment and the time required to perform the analysis.

Such problems can be solved by using electrochemical techniques which are relatively simple, cost-effective, accessible methods with high selectivity and sensitivity (22-25).

MB detection was performed using a gold electrode (26), a carbon paste electrode modified with thiol-functionalized clay (27), a gold nanoparticle-based glassy carbon electrode (28) and a MWCNTs-modified glassy carbon electrode (29).

Biomass is a renewable form of organic substance derived from plant and animal waste, which is used as a raw material (30). A multitude of biomasses with a porous structure and a variety of components can be carbonized to form porous biomass-derived carbon products (31,32).

In the last few years, biomass-derived products (PCs) have received considerable attention because of their special characteristics. These include excellent chemical stability, high surface area, economical precursors and a simple, environmentally-friendly preparation process (33). Biomass has been used in a number of studies for electrochemical applications. For example, Chen and his team (34) developed an activated carbon from banana stalks as a precursor material, to be used in an electrochemical application as a nitrite (NO_2^-) sensor. The three-dimensional porous structure elaborated from the kenaf stem is proving to be an excellent support for a biosensing platform (35). In addition, a hierarchical meso-macropore pore carbon derived from seaweed has been effectively applied to quantify H_2O_2 concentrations in human urine samples (36). This research shows that functional porous carbons obtained from biomass sources have great potential as innovative electrode materials.

Hydrothermal carbonization is a thermochemical conversion method that transforms biomass into hydrocarbon (37). This process, carried out in the presence of water under autogenous pressure at relatively low temperatures (generally between 150 and 300°C), has great potential as a treatment

solution for biodegradable waste (38). The resulting end product, known as hydrochar, manifests itself as a solid material rich in oxygenated functional groups, consisting mainly of carbon. The particularly attractive characteristics of hydrochar are generating considerable interest in its potential applications as a substitute for carbon materials (35,39).

This article presents the modification of a glassy carbon electrode by hydrochar (HC/GCE) for MB detection. The hydrochar was created by hydrothermal carbonization of Phoenix dactylifera biomass. The chemical properties of this hydrochar give it remarkable electrocatalytic activity for MB detection. The electrode exhibited a great performance with many advantages like, easy preparation, rapid response time, high sensitivity and selectivity with LOD of 0.2 nM. In conclusion, this approach has been used effectively to identify MB concentration in wastewater samples, with promising results.

2. EXPERIMENTAL

2.1. Instrumentation

The voltammetric tests were all done with a BIOLOGIC Sciences VMP3 potentiostat/galvanostat, model (SP: 50). The ECLAB data acquisition software was utilized to oversee and track the experiments. The surface morphology of the modifier was examined using the FEI-Quanta 650 scanning electron microscope with energy dispersive X-ray spectroscopy (SEM-EDX).

2.2. Chemicals and Reagents

The GCE was procured from Lorraine ltd (Shanghai, Chine). The counter-electrode and reference electrode were obtained from Metrohm AG (Herisau, Switzerland). Potassium dihydrogen Phosphate, Potassium Chloride, Sodium Acetate, Sodium Hydroxide, dipotassium Hydrogen Phosphate, Alumina oxide, N,N-Dimethylformamide (DMF), Methylene blue, Methanol and Hydrochloric Acid were supplied by Fluka Chemika (Sébastien Brant, France). All solutions were produced with distilled water. All materials utilized were of analytical grade and employed without undergoing additional purification procedures. A 0.1 M phosphate buffered solution (PBS) was obtained by combining 0.1 M NaH_2PO_4 and 0.1 M Na_2HPO_4 . To adjust the pH of PBS solutions (pH 4-8), (0.1M) HCl and (0.1M) NaOH solutions were employed during the preparation process.

2.3. Hydrochar Preparation

Hydrochar has been prepared by the hydrothermal carbonization (HTC) process. Phoenix dactylifera kernels were washed using distilled water, then dried at 80°C for a week. It was then ground and sieved to obtain a 50 μm powder. 5g of the biomass obtained was mixed with 25 ml of distilled water. This mixture was ultrasonicated for one hour, then placed in an oven at 200°C for 24 hours. Finally, the black powder obtained was filtered. The resulting solid product, called hydrochar (HC).

2.4. Modified Electrode Preparation

Firstly, the GCE surface was refined using alumina powder with sizes of 0.05 μm and 0.3 μm . Then, it was carefully washed many times using distilled water and methanol using an ultrasonic bath. After this, the GCE was air-dried at room temperature. Next, 1 mg of biomass was dissolved in 1mL DMF. This solution was placed in an ultrasonic bath for 24 hours, to form a stable suspension. The purpose of this step was also to release protons from the hydroxyl groups to facilitate interaction between the modifier and methylene blue. Finally, 5 μl of suspension was dropped on the surface of the electrode and the electrode (HC/GCE) was dried under an infrared lamp to evaporate any residual solvent and firmly fix the modifier to the electrode surface.

2.5. Electrochemical Measurements

The setup for the experiment consisted of a three-electrode device. It includes HC/GCE electrode as working electrode, a platinum wire as a counter-

electrode and a saturated calomel electrode as the reference electrode. The unmodified and modified electrodes were analyzed by the CV method for electrochemical characterization. Furthermore, the detection tests for MB were conducted using the SWV technique. A 10^{-4} M solution of MB in different buffer solutions (0.1M) was prepared.

3. RESULTS AND DISCUSSION

3.1. Biomass and Hydrochar Characterization

Figure 1 shows that the surface morphology changed significantly as a result of the HTC process. SEM analysis of the hydrochar revealed the formation of a porous surface, coarser and rougher than that of the initial biomass prior to HTC treatment. In addition, an increase in particle size and pore volume was observed. The presence of cavities, pores and rough surfaces on the hydrochar testifies to the creation of an interconnected porous structure.

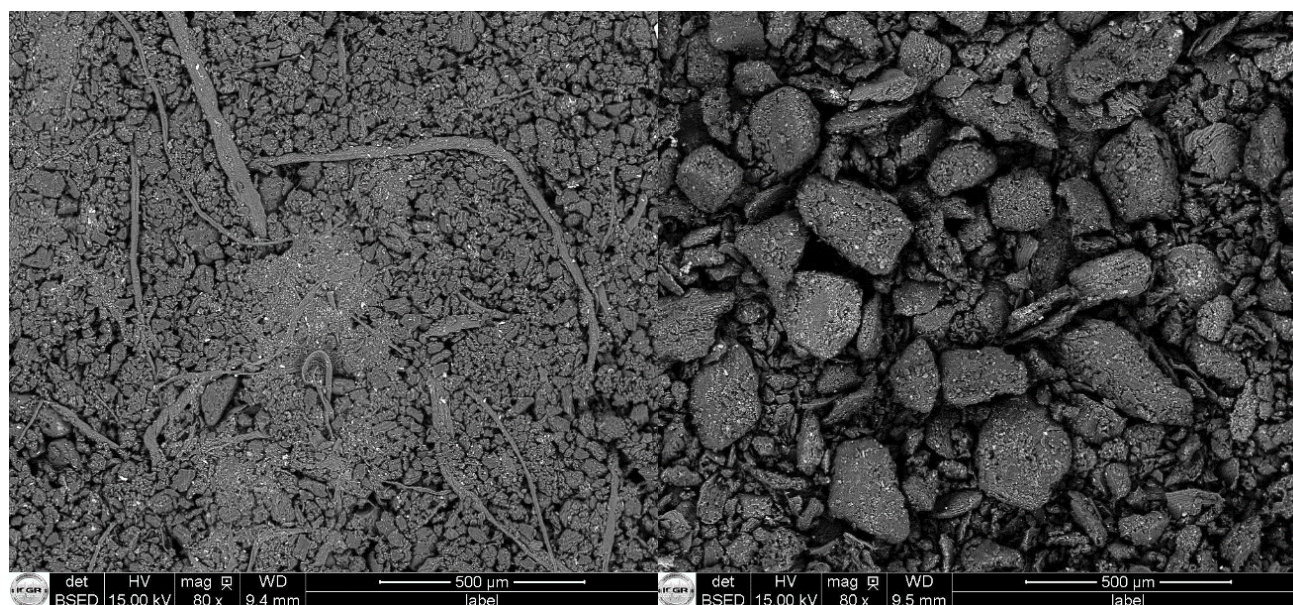


Figure 1: SEM images of Biomass (left) and Hydrochar (right).

3.2. Voltammetric Analysis

SWV is an electroanalytical technique known for its sensitivity and quick response, offering excellent resolution for analyzing the signal of the analyte. In this study, the voltammetric behavior of the MB dye was investigated using both unmodified and modified electrodes in a 0.1 M, PBS (pH=6)

solution. The potential range for the analysis was set from -0.5 V to 0.2 V. At the unmodified electrode, the oxidation of the MB dye occurred at -0.21 V, accompanied by a peak current reaching a maximum of 50 μA . The electrode modified with HA/GCE showed an increase in MB response current to 325 μA , as shown in Figure 2.

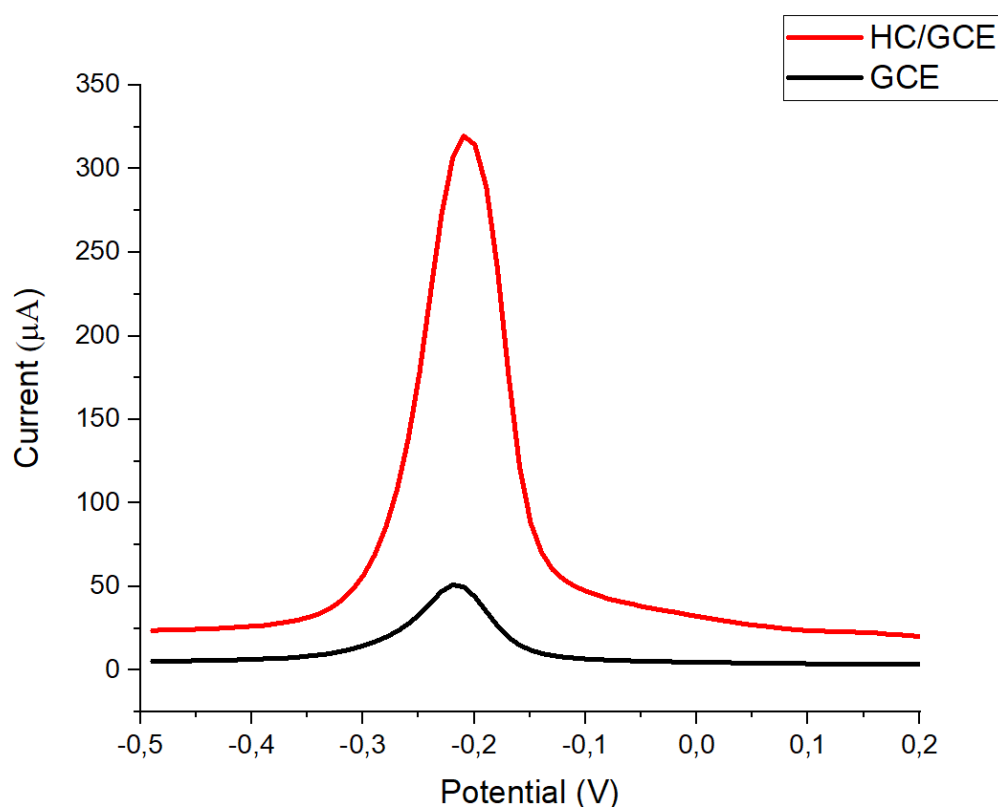


Figure 2: Comparative SWVs of (10^{-4}M) MB at the unmodified and modified electrodes in a potential range of -0.5 to 0.2 with an accumulation time of 60s in PBS (pH=6).

This increase is due to the presence of hydrochar, characterized by its porous structure offering a large surface area. This characteristic increases the active surface of the electrode, enhancing the adsorption and electrochemical reactions of the species concerned (40). This increase in specific surface area improves MB detection sensitivity. This increase is also due to the presence of negatively

charged deprotonated hydroxyl groups on the surface of the modified electrode, facilitating interaction with the positively charged MB.

Figure 3 illustrates the suggested mechanism for the oxidation of MB, which involves the transfer of two protons and two electrons (29,41,42).

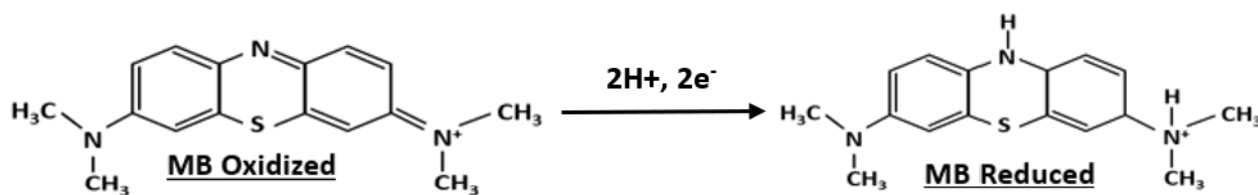


Figure 3: Suggested oxidation mechanism for MB at HC/GCE.

3.3. Influence of the Scan Rate

Cyclic voltammetry experiments were conducted to evaluate the impact of scan rate on MB dye peak current, varying scan rates from 10 to 250 mV/s as seen in (Fig.4a). The objective was to identify if the electrochemical reactions were controlled by adsorption or diffusion processes by examining the correlation between signal strength and scan speed, The objective was to identify if the electrochemical reactions were controlled by adsorption or diffusion processes by examining the correlation between

signal strength and scan speed. The curve of $I = f(V)$ with a linear plot in (Fig.4b) indicates that adsorption controls the reaction process and the curve of $I = f(V^{1/2})$ with a linear plot in (Fig.4c) suggests that the reaction is controlled by diffusion. $\log(I_p) = f(\log(V))$ with a slope of 0.58, as shown in (Fig.4d), indicates the presence of adsorption and diffusion processes in the reaction. The dominance of the diffusion process is evident as the R^2 of the curve $I = f(V)$ in (Fig.4b) is lower than the R^2 of the curve $I = f(V^{1/2})$ in (Fig.4c).

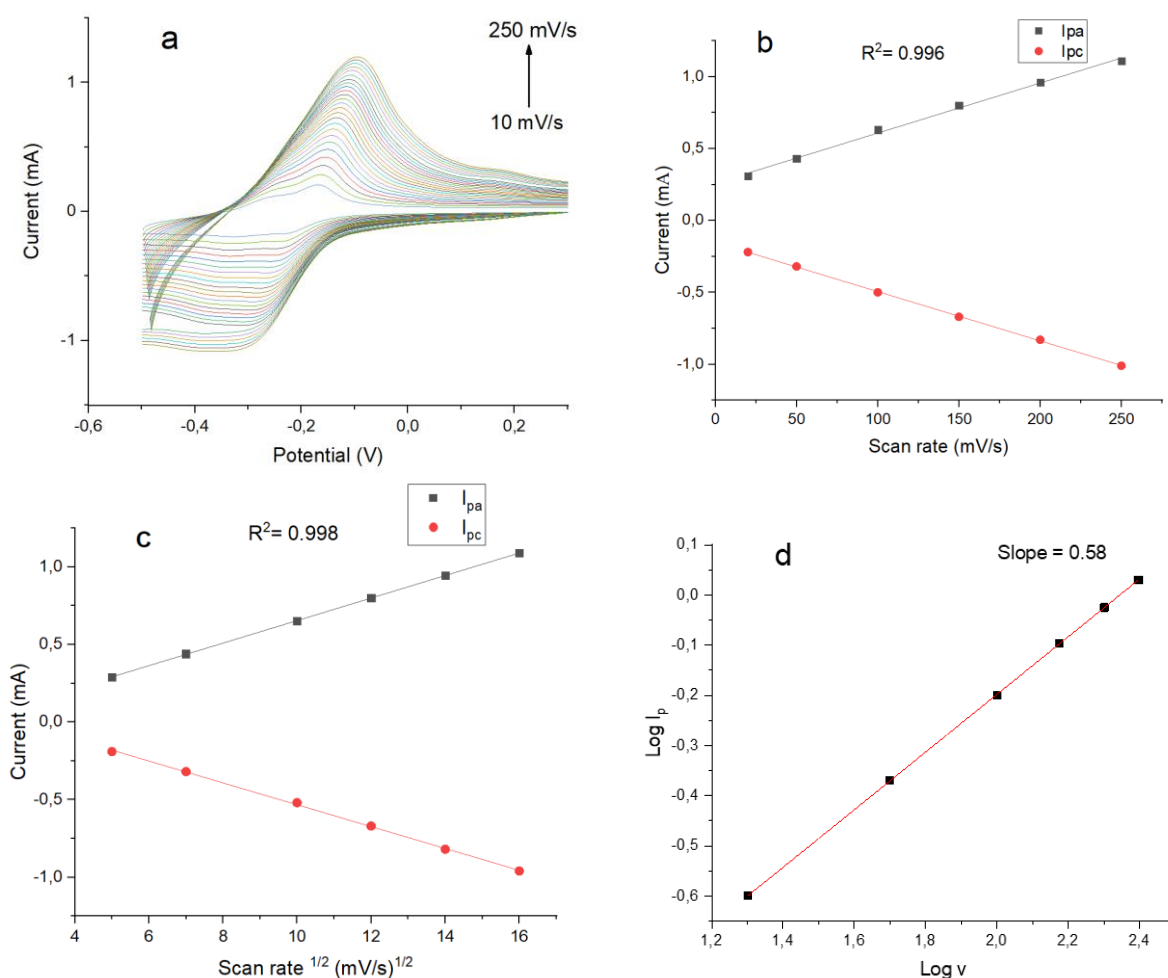


Figure 4: (a) CV of (10^{-4} M) MB at different scan rates, (b) influence of the evolution of v on the intensity of the redox current, (c) influence of the evolution of $v^{1/2}$ on the intensity of the redox current and (d) Plot of the log of the oxidative peak current vs log of scan rate in PBS (pH=6).

3.4. Experimental Parameters Optimization

Various parameters have been optimized to maximize the current response of the MB by the use of the co-doped electrode. The choice of electrolyte is crucial to achieve a robust and strong signal of the target analyte. Therefore, various supporting electrolytes were investigated: PBS, KCl, HCl, and acetate at pH 7.0 with a concentration of 0.1 M.

PBS proved to be the most suitable supporting electrolyte, where the analyte showed oxidation with a maximum current response and a definite peak relative to other electrolytes. The bar graph in (Fig.5a) illustrates that PBS is the optimal supporting electrolyte for MB detection.

The impact of pH was studied using PBS solutions with pH ranging from 4 to 8. As shown in (Fig.5b), the strongest signal was obtained at pH 6.0. In an acidic electrolyte medium, the presence of a high concentration of H^+ ions result in a reduction of the oxidation peak of MB. This phenomenon can be attributed by the fact that the hydroxyl groups of the hydrochar, being already negatively charged, tend to attract protons from the solution instead of the MB molecule, which reduces the response of the oxidation peak.

As the pH of the solution increases, the competition between cationic MB and H^+ ions decrease due to a decrease in the concentration of H^+ ions in the medium. This leads to a greater interaction between the modifier and MB molecules, promoting their preconcentration at the electrode surface. When the pH of the solution exceeds 6, the presence of a high concentration of OH^- ions can prevent the access of cationic MB molecules to the electrode surface. Consequently, a decrease in the intensity of the MB current peak is observed. Hence, the pH value of 6 was identified as the optimal pH for PBS.

The effect of the accumulation time of MB on the surface of the modified electrode was examined in the range of 5 seconds to 120 seconds (Fig.5c). A rise in the current intensity is observed with an increase in the accumulation time from 5 seconds to 60 seconds. After a duration of 60 seconds, a decline in intensity values is observed, suggesting saturation of the binding sites required for MB attachment to the electrode surface. Therefore, 60s is the optimal accumulation time. Examining the accumulation potential, we found no significant change.

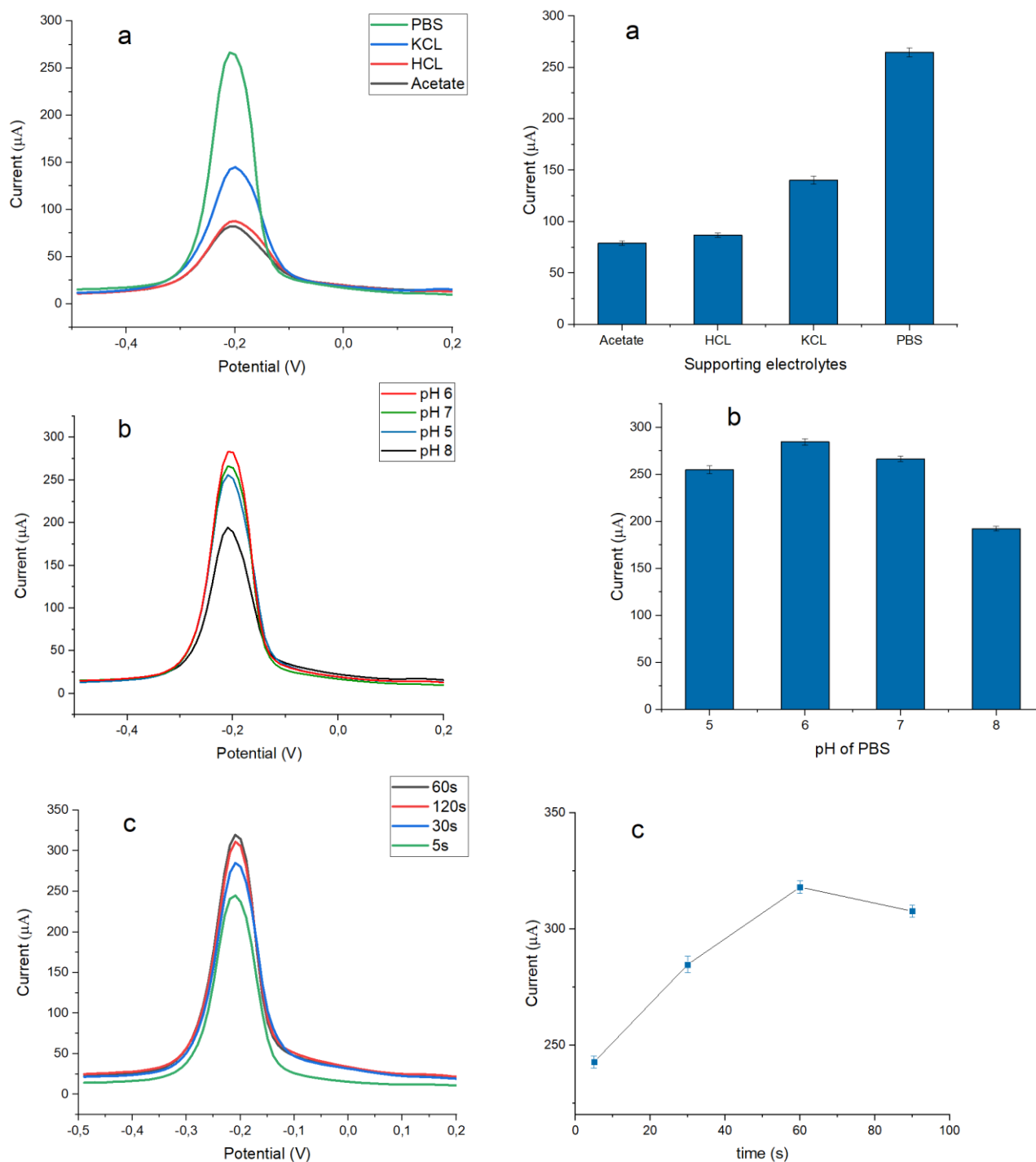


Figure 5: Variation of experimental parameters (a) electrolyte, (b) Electrolyte pH, (c) Accumulation time on the response of the HC/GCE in presence of 10^{-4}M (MB).

3.5. Calibration Study

The SWV was employed to evaluate the detection capability of the co-doped electrode that was prepared with the previously mentioned optimal physicochemical parameters. Different concentrations of MB were examined and the results are illustrated in (Fig.6a).

(Fig.6b) displays a linear correlation between peak current and MB concentration, ranging from 10^{-4} M to 10^{-10} M. A calibration curve demonstrating the

linearity between peak current and concentration (10^{-4} M to 10^{-10} M) is represented in (Fig.6b).

The limit of quantification ($LOQ = 10 \sigma/m$) and detection ($LOD = 3 \sigma/m$) for the target analyte were determined based on the calibration curve, following the guidelines set by IUPAC (43). The calculated LOD and LOQ of MB are $2 \times 10^{-10}\text{M}$ and $4 \times 10^{-10}\text{M}$ respectively. Table 1 compares different modified electrodes for MB determination.

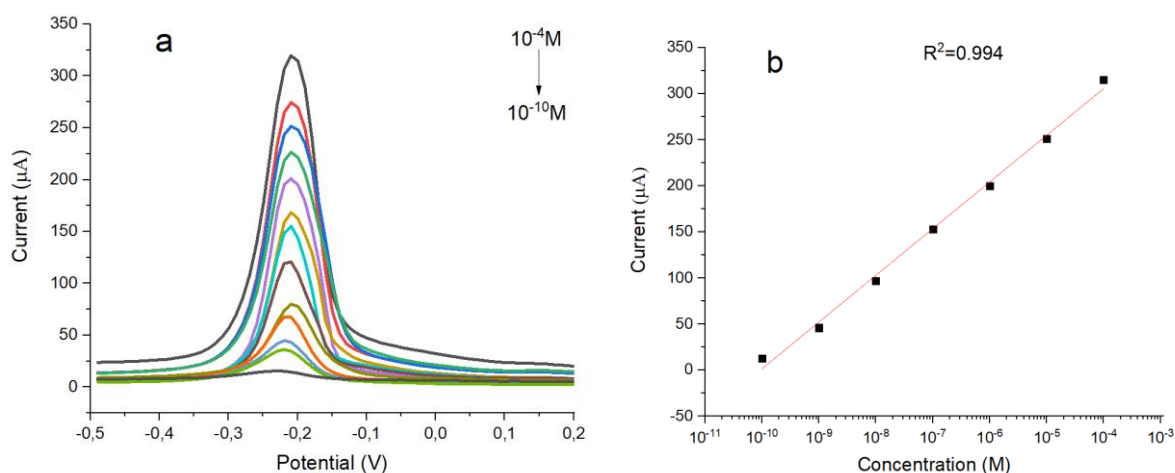


Figure 6: (a) SWV of MB detection on the HC/GCE for various concentrations under optimal conditions, (b) calibration curves of MB in PBS (pH=6).

Table 1: Comparison of the HC/GCE detection limits with other modified electrodes.

Methylene Blue	Electrode Modifier	LOD (nM)	Reference
Oxidation	Self-doped TiO ₂ nanotubes	475	(44)
Oxidation	Thiol functionalized Clay	400	(27)
Oxidation	Ibu-AuNps	3.9	(28)
Oxidation	NH ₂ -fMWCNTs	0.21	(29)
Oxidation	HC/GCE	0.2	This Work

3.6. Interference Study

The interference generated by other substances present in the actual sample plays a central role in determining a sensor's selectivity. Table 2 shows various substances and dyes for their interference on the MB dye current signal using the modified sensor. Each interferant was combined in a 1:1 ratio with the MB dye solution. Positive values indicate an increase in the actual response of (10⁻⁴M) MB.

According to the data in the table, ions such as Mg²⁺, Mn²⁺, Remazol Red, Remazol Yellow and Methyl Orange produced no interference effect, while the other components showed a positive interference effect. According to the data obtained, the influence of interference remains well within the tolerable limit of ±5%. This means that the sensor developed is selective for the detection of MB in real samples containing other substances.

Table 2: Effect of interference (%) in MB determination by other compounds.

Compound	Interference (%)	Compound	Interference (%)
Mg ²⁺	0.0	Pb ²⁺	+3.0
Mn ²⁺	0.0	Remazol Yellow	0.0
Zn ²⁺	+1.5	Blue Patent	+1.0
Cu ²⁺	+2.0	Remazol Red	0.0
-	-	Methyl Orange	0.0

4. RECOVERY OF MB IN WASTEWATER SAMPLES

The applicability of HC/GCE was tested for the determination of MB in wastewater samples recovered from Rabat area. The wastewater was first filtered and different concentration of MB were

added. Recovery rates ranged from 92% to 96% (table 3). In addition, the relative standard deviation of five parallel determinations using electrodes from different batches proved to be less than 5%. This indicates that HC/GCE exhibits remarkable reproducibility, making it suitable for analytical determinations in real sample matrices.

Table 3: Determination of MB in wastewater.

Conc. added (M)	Conc. Found (M)	Recovery (%)	RSD% (n=5)
5.5 × 10 ⁻⁵	5.2 × 10 ⁻⁵	94.5%	3.5
1.35 × 10 ⁻⁵	1.25 × 10 ⁻⁵	92.6%	2.3
5.5 × 10 ⁻⁶	5.3 × 10 ⁻⁶	96%	4.1

5. CONCLUSION

In this work, we successfully developed a novel electrochemical sensor by modifying a glassy carbon electrode with hydrochar derived from *Phoenix dactylifera*. This modified electrode (HC/GCE) demonstrated exceptional electrocatalytic activity for the detection of Methylene Blue (MB). The hydrochar was prepared through hydrothermal carbonization of the biomass, resulting in a porous structure with excellent electrochemical properties. The sensor's performance was extensively evaluated through various experiments. Cyclic voltammetry and square wave voltammetry analyses indicated a significant increase in the response current of positively charged MB at the HC/GCE compared to an unmodified electrode.

In conclusion, the hydrochar-modified glassy carbon electrode (HC/GCE) presented a highly sensitive, selective, and efficient platform for the electrochemical detection of Methylene Blue. This sensor holds great promise for practical applications in wastewater analysis, environmental monitoring, and related fields.

6. REFERENCES

- Hossain MA, Mahbbat Ali M, Islam TSA. Comparative adsorption of Methylene blue on different low cost adsorbents by continuous column process. *Int Lett Chem Phys Astron* [Internet]. 2018 Jan;77:26–34. Available from: [<URL>](#).
- Kim KH, Ihm SK. Heterogeneous catalytic wet air oxidation of refractory organic pollutants in industrial wastewaters: A review. *J Hazard Mater* [Internet]. 2011 Feb;186(1):16–34. Available from: [<URL>](#).
- H. A. dyes. J. W. & S. Berneth. In *Ullmann's Encyclopedia of Industrial Chemistry*. 2011.
- Carole M, Mathelin C, Croce S, Brasse D, Gairard B, Gharbi M, et al. Methylene blue dye, an accurate dye for sentinel lymph node identification in early breast cancer. *Anticancer Res* [Internet]. 2009;29:4119–26. Available from: [<URL>](#).
- Chen W, Chen L, Yang S, Chen Z, Qian G, Zhang S, et al. A novel technique for localization of small pulmonary nodules. *Chest* [Internet]. 2007 May;131(5):1526–31. Available from: [<URL>](#).
- Giuliano AE, Kirgan DM, Guenther JM, Morton DL. Lymphatic mapping and sentinel lymphadenectomy for breast cancer. *Ann Surg* [Internet]. 1994 Sep;220(3):391–401. Available from: [<URL>](#).
- Bélaz-David N, Decosterd LA, Appenzeller M, Ruetsch YA, Chioléro R, Buclin T, et al. Spectrophotometric determination of methylene blue in biological fluids after ion-pair extraction and evidence of its adsorption on plastic polymers. *Eur J Pharm Sci* [Internet]. 1997 Nov 1;5(6):335–45. Available from: [<URL>](#).
- Xu J, Dai L, Wu B, Ding T, Zhu J, Lin H, et al. Determination of methylene blue residues in aquatic products by liquid chromatography-tandem mass spectrometry. *J Sep Sci* [Internet]. 2009 Dec 11;32(23–24):4193–9. Available from: [<URL>](#).
- Peter C, Hongwan D, K pfer A, Lauterburg BH. Pharmacokinetics and organ distribution of intravenous and oral methylene blue. *Eur J Clin Pharmacol* [Internet]. 2000 Jun 19;56(3):247–50. Available from: [<URL>](#).
- Salhab M, Al sarakbi W, Mokbel K. Skin and fat necrosis of the breast following methylene blue dye injection for sentinel node biopsy in a patient with breast cancer. *Int Semin Surg Oncol* [Internet]. 2005 Dec 28;2(1):26. Available from: [<URL>](#).
- Bai SW, Huh EH, Jung DJ, Park JH, Rha KH, Kim SK, et al. Urinary tract injuries during pelvic surgery: Incidence rates and predisposing factors. *Int Urogynecol J* [Internet]. 2006 Aug 30;17(4):360–4. Available from: [<URL>](#).
- Lipskikh OI, Korotkova EI, Khristunova YP, Berek J, Kratochvil B. Sensors for voltammetric determination of food azo dyes - A critical review. *Electrochim Acta* [Internet]. 2018 Jan;260:974–85. Available from: [<URL>](#).
- Albert M, Lessin MS, Gilchrist BF. Methylene blue: Dangerous dye for neonates. *J Pediatr Surg* [Internet]. 2003 Aug;38(8):1244–5. Available from: [<URL>](#).
- Sheynkin YR, Starr C, Li PS, Goldstein M. Effect of methylene blue, indigo carmine, and renografin on human sperm motility. *Urology* [Internet]. 1999 Jan;53(1):214–7. Available from: [<URL>](#).
- Hassan SS, Sirajuddin, Solangi AR, Agheem MH, Junejo Y, Kalwar NH, et al. Ultra-fast catalytic reduction of dyes by ionic liquid recoverable and reusable mafenamic acid derived gold nanoparticles. *J Hazard Mater* [Internet]. 2011 Jun;190(1–3):1030–6. Available from: [<URL>](#).
- Veisi H, Razeghi S, Mohammadi P, Hemmati S. Silver nanoparticles decorated on thiol-modified magnetite nanoparticles (Fe₃O₄/SiO₂-Pr-S-Ag) as a recyclable nanocatalyst for degradation of organic dyes. *Mater Sci Eng C* [Internet]. 2019 Apr;97:624–31. Available from: [<URL>](#).
- Singh J, Kumar V, Kim KH, Rawat M. Biogenic synthesis of copper oxide nanoparticles using plant extract and its prodigious potential for photocatalytic degradation of dyes. *Environ Res* [Internet]. 2019 Oct;177:108569. Available from: [<URL>](#).
- Borwitzky H, Haefeli WE, Burhenne J. Analysis of methylene blue in human urine by capillary electrophoresis. *J Chromatogr B* [Internet]. 2005 Nov 5;826(1–2):244–51. Available from: [<URL>](#).
- Disanto AR, Wagner JG. Pharmacokinetics of highly ionized drugs I: Methylene blue—whole blood, urine, and tissue assays. *J Pharm Sci* [Internet]. 1972 Apr;61(4):598–602. Available from: [<URL>](#).

20. Disanto AR, Wagner JG. Pharmacokinetics of highly ionized drugs II: Methylene blue—absorption, metabolism, and excretion in man and dog after oral administration. *J Pharm Sci* [Internet]. 1972 Jul;61(7):1086–90. Available from: [<URL>](#).
21. Nicolai SH de A, Rodrigues PR., Agostinho SM., Rubim JC. Electrochemical and spectroelectrochemical (SERS) studies of the reduction of methylene blue on a silver electrode. *J Electroanal Chem* [Internet]. 2002 May;527(1–2):103–11. Available from: [<URL>](#).
22. Amini N, Shamsipur M, Gholivand MB, Barati A. A glassy carbon electrode modified with carbon quantum dots and polyalizarin yellow R dyes for enhanced electrocatalytic oxidation and nanomolar detection of l-cysteine. *Microchem J* [Internet]. 2017 Mar;131:9–14. Available from: [<URL>](#).
23. Mahmoudi-Moghaddam H, Tajik S, Beitollahi H. A new electrochemical DNA biosensor based on modified carbon paste electrode using graphene quantum dots and ionic liquid for determination of topotecan. *Microchem J* [Internet]. 2019 Nov;150:104085. Available from: [<URL>](#).
24. Pedrozo-Penafiel MJ, Miranda-Andrades JR, Gutierrez-Beleño LM, Larrudé DG, Aucelio RQ. Indirect voltammetric determination of thiomersal in influenza vaccine using photo-degradation and graphene quantum dots modified glassy carbon electrode. *Talanta* [Internet]. 2020 Aug;215:120938. Available from: [<URL>](#).
25. Hasanzadeh M, Hashemzadeh N, Shadjou N, Eivazi-Ziaei J, Khoubnasabjafari M, Jouyban A. Sensing of doxorubicin hydrochloride using graphene quantum dot modified glassy carbon electrode. *J Mol Liq* [Internet]. 2016 Sep;221:354–7. Available from: [<URL>](#).
26. Li J, Zhao F, Zhao J, Zeng B. Adsorptive and stripping behavior of methylene blue at gold electrodes in the presence of cationic gemini surfactants. *Electrochim Acta* [Internet]. 2005 Oct;51(2):297–303. Available from: [<URL>](#).
27. Tonlé IK, Ngameni E, Tcheumi HL, Tchiéda V, Carteret C, Walcarius A. Sorption of methylene blue on an organoclay bearing thiol groups and application to electrochemical sensing of the dye. *Talanta* [Internet]. 2008 Jan 15;74(4):489–97. Available from: [<URL>](#).
28. Hassan SS, Nafady A, Sirajuddin, Solangi AR, Kalhoro MS, Abro MI, et al. Ultra-trace level electrochemical sensor for methylene blue dye based on nafion stabilized ibuprofen derived gold nanoparticles. *Sensors Actuators B Chem* [Internet]. 2015 Mar;208:320–6. Available from: [<URL>](#).
29. Hayat M, Shah A, Nisar J, Shah I, Haleem A, Ashiq MN. A novel electrochemical sensing platform for the sensitive detection and degradation monitoring of methylene blue. *Catalysts* [Internet]. 2022 Mar 8;12(3):306. Available from: [<URL>](#).
30. Abioye AM, Ani FN. Recent development in the production of activated carbon electrodes from agricultural waste biomass for supercapacitors: A review. *Renew Sustain Energy Rev* [Internet]. 2015 Dec;52:1282–93. Available from: [<URL>](#).
31. Yang S, Wang S, Liu X, Li L. Biomass derived interconnected hierarchical micro-meso-macroporous carbon with ultrahigh capacitance for supercapacitors. *Carbon N Y* [Internet]. 2019 Jun;147:540–9. Available from: [<URL>](#).
32. Xiao K, Liu H, Li Y, Yi L, Zhang X, Hu H, et al. Correlations between hydrochar properties and chemical constitution of orange peel waste during hydrothermal carbonization. *Bioresour Technol* [Internet]. 2018 Oct;265:432–6. Available from: [<URL>](#).
33. Sevilla M, Fuertes AB, Mokaya R. High density hydrogen storage in superactivated carbons from hydrothermally carbonized renewable organic materials. *Energy Environ Sci* [Internet]. 2011;4(4):1400–10. Available from: [<URL>](#).
34. Madhu R, Veeramani V, Chen SM. Heteroatom-enriched and renewable banana-stem-derived porous carbon for the electrochemical determination of nitrite in various water samples. *Sci Rep* [Internet]. 2014 Apr 23;4(1):4679. Available from: [<URL>](#).
35. Wang L, Zhang Q, Chen S, Xu F, Chen S, Jia J, et al. Electrochemical sensing and biosensing platform based on biomass-derived macroporous carbon materials. *Anal Chem* [Internet]. 2014 Feb 4;86(3):1414–21. Available from: [<URL>](#).
36. Hei Y, Li X, Zhou X, Liu J, Sun M, Sha T, et al. Electrochemical sensing platform based on kelp-derived hierarchical meso-macroporous carbons. *Anal Chim Acta* [Internet]. 2018 Mar;1003:16–25. Available from: [<URL>](#).
37. Espro C, Satira A, Mauriello F, Anajafi Z, Moulaei K, Iannazzo D, et al. Orange peels-derived hydrochar for chemical sensing applications. *Sensors Actuators B Chem* [Internet]. 2021 Aug;341:130016. Available from: [<URL>](#).
38. Fang J, Zhan L, Ok YS, Gao B. Minireview of potential applications of hydrochar derived from hydrothermal carbonization of biomass. *J Ind Eng Chem* [Internet]. 2018 Jan;57:15–21. Available from: [<URL>](#).
39. Pistone A, Espro C. Current trends on turning biomass wastes into carbon materials for electrochemical sensing and rechargeable battery applications. *Curr Opin Green Sustain Chem* [Internet]. 2020 Dec;26:100374. Available from: [<URL>](#).
40. Cancelliere R, Cianciaruso M, Carbone K, Micheli L. Biochar: A sustainable alternative in the development of electrochemical printed platforms. *Chemosensors* [Internet]. 2022 Aug 22;10(8):344. Available from: [<URL>](#).

41. Solangi AG, Tahira A, Bhatti MA, Hulio AA, Chang AS, Solangi ZA, et al. Facile synthesis of NiCo₂O₄ nanostructures with abundant surface oxygen vacancies, and reduced content of Co and Ni valence states for the efficient and bifunctional electrochemical and photocatalytic oxidation of methylene blue. *Microchem J* [Internet]. 2024 Apr;199:110046. Available from: [<URL>](#).
42. Gong J, Guo Y, Lu J, Cheng Y, Wang H. TEMPO oxidized nanofiber carbon quantum dots/TiO₂ composites with enhanced photocatalytic activity for degradation of methylene blue. *Chem Phys Lett* [Internet]. 2022 Feb;788:139297. Available from: [<URL>](#).
43. Belter M, Sajnóg A, Barańkiewicz D. Over a century of detection and quantification capabilities in analytical chemistry – Historical overview and trends. *Talanta* [Internet]. 2014 Nov;129:606–16. Available from: [<URL>](#).
44. Soto PC, Salamanca-Neto CAR, Moraes JT, Sartori ER, Bessegato GG, Lopes F, et al. A novel sensing platform based on self-doped TiO₂ nanotubes for methylene blue dye electrochemical monitoring during its electro-Fenton degradation. *J Solid State Electrochem* [Internet]. 2020 Aug 28;24(8):1951–9. Available from: [<URL>](#).



A Statistical Study Comparing Experimental and Theoretical Yields of Activated Carbon Prepared from Pomegranate (*Punica granatum*) Peels via Chemical Treatment

Semaa I. Khaleel^{1*} , Ammar A.H.AL-Khazraji², Emad A.S.AL-Hyali²

¹Department of Petroleum and Refining Engineering, College of Petroleum and Mining Engineering, University of Mosul, 41001, Mosul, Iraq.

²Department of Chemistry, College of Education for pure science, University of Mosul, 41001, Mosul, Iraq.

Abstract: Due to the great importance that activated carbon has gained through its use in combating pollution, removing dyes components, and other uses, it has been prepared in different ways. In this research, a statistical study was conducted to compare the practical and theoretical values of activated carbon yield prepared from pomegranate peels with some additives (Novolak resin and Beji asphalt) in order to improve its specifications. Since the preparation of activated carbon is controlled by a group of variables, a number of matters were tested for the possibility of finding a linear relationship based on the effect of the amount of the iodine number, density, ash content, and humidity on the yield of all prepared types of activated carbon, and considering the possibility of achieving the relationship through additional additives that can be obtained through it on carbon with a homogeneous surface and specifications. Also, finding a general mathematical relationship that brings together all the types prepared from pomegranate peels after adding new variables representing the percentages of adding asphalt to them and novolak resin used in preparation and activation. This equation makes it possible to control the proportions of the resulting yield before trying to measure, test and evaluate any of the practically calculated values such as the iodine number, density, ash content and humidity using the mathematical equation and calculating them for unknown values if the other characteristics are known. This achieves a shortening of the time period. The success of this method is evidenced by the high experimental R² values, the low SE, and the logical variation of the variable coefficients.

Keywords: Activated carbon, Pomegranate peels, Yield, Statistical study.

Submitted: January 7, 2024. **Accepted:** August 5, 2024.

Cite this: Khaleel SI, AL-Khazraji AAH, AL-Hyali EAS. A Statistical Study Comparing Experimental and Theoretical Yields of Activated Carbon Prepared from Pomegranate (*Punica granatum*) Peels via Chemical Treatment. JOTCSA. 2024;11(4): 1407-16.

DOI: <https://doi.org/10.18596/jotcsa.1416075>

***Corresponding author's E-mail:** semaabraheem@uomosul.edu.iq

1. INTRODUCTION

Activated carbon is known as a porous solid material that has a large internal surface area and a developed porous structure. Possessing these characteristics of activated carbon makes it a material with a high adsorption capacity for many chemicals both gaseous and liquid (1). The ability of activated carbon to remove colored substances from aqueous solutions has been known since the fifteenth century when it was used in the sugar industry in Britain to shorten the colors. It was then used on a large scale in the manufacture of masks to protect against toxic gases during first world war and its areas of use expanded to include various

industrial and chemical processes (2). Activated carbon was prepared at the beginning of the twentieth century from coconut shells but the increased demand for it and the limited quantities available of these shells prompted manufacturers to try to manufacture it from other organic materials. They used coal, coal tar, different types of wood, polymers, and asphalt materials in addition to other materials various others (3).

Activated carbon is characterized by unique properties and cheap prices, which is why it has no competitor in the global market compared to zeolite (as an inorganic adsorbent). Also, the pores and surface area are distributed in a very wide and

indefinite manner compared to zeolite and this is what made carbon one of the most important adsorbent materials even though more than 30% of Carbon research specializes in developing activated carbon in terms of obtaining new sources, modern manufacturing processes, and searching for future applications (4). The global demand for activated carbon is increasing as a result of environmental problems especially in the field of water and air purification. However, the raw materials used to produce activated carbon are not renewable and despite the great influence of natural raw materials on the specifications of the final product the search for cheap adsorbent materials with less impact and toxicity on the environment, it has led to the use of by-products of agricultural products, oil waste, the use of newspapers, old tires, and any remaining carbon materials from industrial processes and various treatments to prepare activated carbon (5).

Activated carbon is a complex product that is difficult to classify based on its behavior, surface area, and method of preparation. However, it has been classified based on its physical properties into: Powdered activated carbon it has a particle size of less than 1.0 mm, an average diameter of 0.15-0.25 mm, and a large internal surface area. This type is used in gravity filters (6). Granulated activated carbon size of particles of this type is relatively larger and the external surface area is smaller when compared to activated carbon in powder form, as the size of its particles ranges between (1.5-2.5 mm). These carbon particles are used to treat water, remove odors, separate components of the flow system, and adsorption of gaseous substances and vapors (6, 7). Extruded activated carbon is made by extruding a quantity of activated carbon in powder form into a cylindrical shape, producing a mass of activated carbon with a diameter ranging between (0.8-130 mm), it is used in gas phase adsorption applications. Polymer coated activated carbon prepared by coating porous activated carbon with polymeric materials to give a smooth, permeable cover and cover that does not allow the pores to become clogged, it is used in filtration processes (6). Activated carbon in the form of molecular sieve it has a structure in the form of molecular sieves, and contains a high percentage of small pore sizes compared to other pores. Also is used to separate gases, such as separating nitrogen and oxygen at room temperature (8). Activated carbon fibers prepared by developing the non-crystalline structure of the primary material such as rayon, bitumen, polymers, phenolic resins at a temperature (800°C), followed by a steam activation process at (800-1000) °C, thus obtaining a very high surface area of up to (2500 cm²/g), activated carbon fibers have a number of advantages over granular activated carbon in that they have porous structures and a large physical surface area (6, 9).

There are many methods and materials used in preparing activated carbon, and some of them are as follows: Al-Ghannam *et al.* (10) were able to prepare activated carbon from *Morus Nigra* using an excess of potassium hydroxide at (25±550)°C for

three hours. Aweed (11) was able to prepare several models of activated carbon using some plant wastes (coconut shells, date pits, sunflower peels, and harvest waste) by reacting them with an excess of potassium hydroxide KOH[1:2] (plant waste: base) at (25±550)°C for three hours. Hamdoon *et al.* (12) were able to prepare activated carbon from coconut shells using different percentages of Baiji asphalt as an additive and using the chemical activation method. The effect of adding different percentages of Baiji asphalt on the properties of the activated carbon prepared from coconut shells was observed. Saleh *et al.* (13) were able to prepare activated carbon from Iraqi reed material by carbonizing it at a temperature of 450 °C. It was found that the prepared carbon was characterized by density (0.451 g/cm³), ash content (9.4%), moisture content (4.8%), and using X-rays was found to lack a crystal structure with less graphite and silica.

Ramakrishnan *et al.* (14) were able to prepare types of activated carbon from *Jatropha* husk peels, biodiesel fuel, the seeds of which are used as fuel for cars, industrial and agricultural solid waste by chemically activating them using (H₃PO₄, HNO₃, HCl, H₂SO₄, NaOH, ZnCl₂). The physical and chemical properties were studied it was found that the prepared types of activated carbon are low cost and are used to remove organic and inorganic substances from water. Ragan *et al.* (15) were able to prepare activated carbon from the renewable resource cellulose-lignin, which contains 66% carbon by weight, by carbonizing it at a temperature of 950°C for 5 minutes. It was found that the prepared samples possess good adsorptive properties. Zengin *et al.* (16) were able to prepare activated carbon from the pyrolysis of melamine waste (coated chipboard) by carbonizing it at a temperature of (600-800)°C and then chemically activating it with NaOH. It was found that the prepared activated carbon had a higher surface area at a temperature of 600°C and a concentration of 50% by weight of sodium hydroxide, it was also found that its outer surfaces have an amorphous and heterogeneous composition.

Al-Badran (17) prepared activated carbon from local raw materials by treating bomber cores with concentrated phosphoric acid in a ratio of [1:1], then heat-treated them at 500°C for one hour. The internal surface area of the activated carbon prepared by the nitrogen escape method (BET) was calculated and was found to be 886.697 m²/g it was found to have a high adsorption capacity. Abechi *et al.* (18) studied the preparation of activated carbon by chemically activating palm kernel shells with KOH at 800°C for 45 minutes it was found to have a high adsorption capacity. Salman (19) studied the preparation of activated carbon from pomegranate tree branches (BP) through physicochemical activation by treatment with potassium hydroxide and carbon dioxide. The effect of activation temperature, activation time, and percentage of chemical impregnation of carbon with methylene blue dye (MB) and its removal from its aqueous solution was studied. The best activation

temperature was 620°C, activation time was 1.4 hours, and the yield was 16%, the removal percentage for methylene blue dye was 92.5%.

Njewa *et al.* (20) were able to prepare activated carbon from rice peels and potato peels by chemical activation with 40% phosphoric acid H_3PO_4 the effect of the carbonization temperature and impregnation rate was studied using the continuous activation period, also studied physical, chemical properties such as (surface shape, surface charge), and amines aromatics, other functional groups were detected. This is excellent for adsorption through surface chemistry studies. Islam *et al.* (21) prepared activated carbon from jute sticks by chemical activation using H_2SO_4 , H_3PO_4 , and $ZnCl_2$ the activating factors and carbonization temperatures were studied, which ranged between 300-350°C. The carbon atoms were identified by iodine absorption and the method of infrared spectroscopy (FT-IR).

In this research, a statistical study was conducted to compare the experimental and theoretical values of the yield of activated carbon prepared from (pomegranate peels as a raw material with additions of polymeric residues and petroleum residues). here able to control the percentages of the resulting yield before trying, testing and evaluating any of the experimentally calculated values such as the iodine number, density, content, Ash and humidity. The success of this method is evidenced by the high experimental R^2 values, the low SE, and the logical variation of the variable coefficients.

2. EXPERIMENTAL SECTION

2.1. Preparation of Activated Carbon

The raw material is prepared by taking the peels of pomegranate in their natural dry form then grinding them and turning them into powder. Then comes the primary carbonation stage, where the prepared raw material is placed in a stainless steel bowl coated with a layer of nickel and mixed with potassium hydroxide in proportions ranging between [(1:0.5) - (1:3)] [pomegranate peels: KOH]. An increase of 0.5% by weight of potassium hydroxide for each reaction. The mixture was homogenized by adding (5-10)mL (milliliters) of distilled water and then heated to a temperature of 350°C with continuous stirring for three hours until the release of gases stopped. Then transfer the mixture to final carbonization and activation. Heat the mixture to a temperature (25±550)°C for two hours in order to complete the activation process, the samples were then left to cool to room temperature.

Finally, purification of activated carbon was completed, prepared and contaminated with the base and metal components, the samples were washed with distilled water several times for the purpose of removing unreacted potassium hydroxide and ensuring that the product of the washing process was neutral. Then the resulting carbon was treated with a solution of (10%)

hydrochloric acid and using a thermal sublimation process for two hours to remove any trace of ions and to reduce Mineral components to a minimum. Then, it was washed with distilled water several times, and the resulting carbon samples were dried at 110-120°C for 24 hours, sieved using 20-40 mesh sieves, and stored in a dehydrator, isolated from air and moisture.

2.2. Preparing Activated Carbon Samples from Mixtures

Activated carbon was prepared from a mixture of (pomegranate peels with asphalt), where the pomegranate peels were mixed with Baiji asphalt in proportions ranging between (5-25)% by weight of the asphalt material, with an increase of 5% by weight of the asphalt for each sample. Activated carbon was prepared from a mixture of pomegranate peels and novolak resin, where the pomegranate peels were mixed with thermally crushed novolac resin (the novolak resin, represented by the waste of this material used in the manufacture of home cooking utensils, was cut into small pieces and placed in a covered ceramic crucible). With aluminum foil, then heated the lid in an electric oven at 400°C for one hour. After that, the material was taken out and left to cool to room temperature, then it was crushed into a fine powder using a mortar. In proportions ranging from (5-25)% by weight with an increase of 5% by weight of novolak resin for each sample. Activated carbon was prepared from a mixture of (pomegranate peels with asphalt and novolak resin): Pomegranate peels were mixed with a mixture of (asphalt: novolak resin) [1:1] in proportions ranging from (5-25)% by weight with an increase of 5% by weight of the mixture in every addition.

Repeated the processes mentioned in section (2.1) on the mixtures prepared in the above, and using a fixed ratio of potassium hydroxide [1:2.5] [pomegranate peels: KOH] as the best ratio used to prepare activated carbon from pomegranate peels (22, 23).

2.3. Conducting some Measuring on Prepared Activated Carbon Samples

2.3.1. Measuring internal surface area of activated carbon by adsorption iodine

This method is one of the well-known and common methods used to determine the internal surface area of activated carbon, and it represents the number of milligrams of iodine adsorbed from the solution by one gram of activated carbon. One gram of activated carbon was weighed and placed in a 250 mL conical flask. 10 mL of 5% HCl was added to it. The contents of the flask were heated to the boiling point for half a minute and then cooled to laboratory temperature. After that, 100 mL of 0.1 M iodine solution was added to it. The mixture was shaken for half an hour, then filtered, discarding 20 mL at the beginning of the filtration process, and collecting 50 mL to titrate it with a 0.1 M solution of aqueous sodium thiosulfate. Using starch as detector the volume of sodium thiosulfate used was calculated from the buret and then the weight of

iodine adsorbed by the activated carbon was calculated (24).

2.3.2. *Measuring of density*

A certain amount of activated carbon was placed in a volumetric bottle with a capacity of 5 mL so that the activated carbon occupies its volume, while making sure that the carbon particles were at one level at the mark. After that, the carbon in the volumetric bottle was weighed using a sensitive balance and the density was calculated as follows:(25)

$$\text{Density (g/cm}^3\text{)} = \text{mass / volume}$$

2.3.3. *Measuring of ash content percentage*

Weigh (1 g) of activated carbon and place it in Porcelain Crucible. The Porcelain Crucible is placed in an electric oven at (1000°C) for three hours. Then it was left to cool, then it was weighed using a sensitive balance, then the weight of the remaining ash was calculated for each of the prepared activated carbon models, then the percentage of ash in each sample was calculated (26).

2.3.4. *Measuring of humidity percentage*

Weigh (1 g) of the sample accurately and place it in an oven at 150°C for three hours, then cool it and weigh it accurately and quickly, and from the difference in weights, the humidity content is calculated in the form of a percentage (27).

2.4. **Conducting a Statistical Study**

This study was conducted using a statistical program, SPSS where the version number is 19 and the release date is 2010.

3. RESULTS AND DISCUSSION

The statistical study is complementary to practical studies, and through it the effect of a group of independent variables (x) on a dependent variable (y) can be tested through an equation called the multivariate linear regression analysis equation, which can be represented by the following relationship:

$$y = b + a_1x_1 + a_2x_2 + \dots + a_nx_n \tag{1}$$

Through this equation it is possible to estimate the extent of the influence of a group of independent variables (x₁, x₂,...x_n) on the dependent variable (y) from the magnitude of its coefficients (a₁, a₂,...a_n) respectively. While the value of b is a fixed magnitude for a reference value. The success of the linear relationship is usually evaluated through two criteria: the correlation coefficient R² whose values are limited to (0-1), and the relationship is linear whenever the value of R² approaches one. The other criterion is the value of the standard deviation SE which represents the amount of deviation of the experimental value from the theoretically calculated value which should at best not exceed 5% of the experimental value. The values of the coefficients of a(x) indicate the amount of slope in the straight line, or in other words, the extent to which the value of x affects y while the sign of a indicates the nature of the relationship whether inverse or direct.

The statistical study will be conducted on the activated carbon prepared from the peels of pomegranate (Pp). Tables 1-4 show the specifications of the prepared activated carbon (22, 23).

Table 1: The properties of the activated carbon prepared from Pp.

S	RM : KOH	ION	Dy	ASC	HYC	Yd
C _n	1:0	339.420	0.397	3.21	9.07	21.705
1	1:0.5	654.959	0.383	3.19	8.13	20.401
2	1:1	674.507	0.306	3.17	10.55	18.810
3	1:1.5	710.808	0.292	3.14	10.76	16.528
4	1:2	780.620	0.273	3.08	10.88	14.904
5	1:2.5	822.507	0.261	3.02	11.87	13.327
6	1:3	788.997	0.281	4.00	7.03	8.800
B.D.H.*	-	908	0.345	3.200	0.80	-

S: samples , RM: Raw material, ION : Iodine Number (mg/g) , Dy: Density (g/cm³), ASC: Ash Content%, HYC: Humidity Content%, Yd: Yield% , B.D.H.*: Commercial carbon

Table 2: Properties of activated carbon prepared from mixture (Pp with BAs) using [1:2.5] [RM:KOH].

S	BAs	ION	Dy	ASC	HYC	Yd
7	5	830.884	0.256	3.01	11.89	14.105
8	10	864.394	0.218	2.94	11.42	15.232
9	15	881.149	0.178	2.82	12.01	16.034
10	20	900.696	0.118	1.75	12.20	17.691
11	25	925.828	0.080	1.68	12.38	21.631
B.D.H.*	-	908	0.345	3.200	0.80	-

BAs: Beji Asphalt%

Table 3: Properties of activated carbon prepared from mixture (Pp with REN) using [1:2.5] [RM:KOH]

S	REN %	ION	Dy	ASC	HYC	Yd
12	5	836.469	0.221	2.98	11.93	14.831
13	10	892.318	0.210	2.92	11.47	16.243
14	15	945.375	0.196	2.54	12.41	18.284
15	20	976.092	0.106	1.87	12.29	20.072
16	25	1004.017	0.075	1.23	13.71	22.471
B.D.H.*	-	908	0.345	3.200	0.80	-

REN: Resin Novolak

Table 4: Properties of activated carbon prepared from mixture (Pp with the Asphalt and the REN) using [1:2.5] [RM:KOH]

S	Mixed(Asphalt, REN)%	ION	Dy	ASC	HYC	Yd
17	5	864.394	0.220	2.86	11.98	14.907
18	10	981.677	0.186	2.75	11.59	18.071
19	15	995.639	0.144	2.08	12.61	19.231
20	20	1017.979	0.104	1.72	12.74	27.580
21	25	1129.677	0.064	1.79	13.92	34.410
B.D.H.*	-	908	0.345	3.200	0.80	-

In order to complete this study, we conducted the following:

First, the relationship between the different variables whether y or x values was evaluated which represented the basis for this study, which are the values of the yield of the prepared activated carbon, the iodine number, density, ash content,

and humidity by applying the simple linear relationship of the straight line which are:

$$y = b + ax \tag{2}$$

The relationship between these variables was evaluated by calculating the R² values for each of them with each other. The results obtained were included in Tables 5-8.

Table 5: Results of statistical analysis of data taken from Table 1.

	Yd y	ION x ₁	Dy x ₂	ASC x ₃	HYC x ₄
Yd (y)	1				
ION (x ₁)	0.716	1			
Dy (x ₂)	0.506	0.698	1		
ASC (x ₃)	0.454	0.039	0.004	1	
HYC (x ₄)	0.051	0.052	0.237	0.684	1

Table 6: Results of statistical analysis of data taken from Table 2.

	Yd y	ION x ₁	Dy x ₂	ASC x ₃	HYC x ₄
Yd (y)	1				
ION (x ₁)	0.878	1			
Dy (x ₂)	0.893	0.969	1		
ASC (x ₃)	0.781	0.776	0.892	1	
HYC (x ₄)	0.571	0.473	0.613	0.639	1

Table 7: Results of statistical analysis of data taken from Table 3.

	Yd y	ION x ₁	Dy x ₂	ASC x ₃	HYC x ₄
Yd (y)	1				
ION (x ₁)	0.947	1			
Dy (x ₂)	0.904	0.788	1		
ASC (x ₃)	0.957	0.827	0.967	1	
HYC (x ₄)	0.755	0.580	0.654	0.805	1

Table 8: Results of statistical analysis of data taken from Table 4.

	Yd y	ION x₁	Dy x₂	ASC x₃	HYC x₄
Yd (y)	1				
ION (x ₁)	0.837	1			
Dy (x ₂)	0.929	0.882	1		
ASC (x ₃)	0.716	0.628	0.885	1	
HYC (x ₄)	0.815	0.671	0.821	0.680	1

The second step to complete this study included performing a multivariate regression analysis for each of the Tables 1-4 separately which included the preparation of activated carbon with different methods and additives. Three variables were chosen for the purpose of analysis: the iodine

number, density, and ash content as the best variables based on the preliminary study in first step due to the lack of degrees of freedom in the statistical analysis due to the small number of observations. The results of the regression analysis obtained are listed in the following Tables 9-12.

Table 9: Results of regression analysis of data taken from Table 1.

Variables	Variables Coefficient	Fixed value	
ION	-0.035		R ² = 0.994
Dy	18.634	b= 56.004	SE= ±0.507
ASC	-6.226		
Observation Number = 6			

Table 10: Results of regression analysis of data taken from Table 2.

Variables	Variables Coefficient	Fixed value	
ION	0.026		R ² = 0.895
Dy	-23.453	b= -1.089	SE= ±1.901
ASC	-0.277		
Observation Number = 5			

Table 11: Results of regression analysis of data taken from Table 3.

Variables	Variables Coefficient	Fixed value	
ION	0.021		R ² = 0.999
Dy	11.265	b= 4.018	SE= ±0.142
ASC	-3.205		
Observation Number = 5			

Table 12: Results of regression analysis of data taken from Table 4.

Variables	Variables Coefficient	Fixed value	
ION	-0.071		R ² = 0.992
Dy	-366.840	b= 106.495	SE= ±1.385
ASC	17.667		
Observation Number = 5			

When the results obtained from the regression analysis were used to calculate the yield theoretically and compare it with the experimental

values, the results were as listed in Tables 13 and 14.

Table 13: Comparison between the experimental and calculated results of the activated carbon yield prepared from the data of Tables 1 and 2 respectively.

Results Table (1)				Results Table (2)			
S	Exp. val	Cal. val	diff	S	Exp. val	Cal. val	diff
1	20.401	20.356	0.045	1	14.105	13.676	0.429
2	18.810	18.362	0.448	2	15.232	15.458	-0.226
3	16.528	17.017	-0.489	3	16.034	16.865	-0.831
4	14.904	14.593	0.311	4	17.691	19.077	-1.386
5	13.327	13.277	0.050	5	21.631	20.641	0.990
6	8.800	8.721	0.079				

Exp. val: Experimental value, Cal. val: Calculated value
diff.: difference, S : Sequence

Table 14: Comparison between the experimental and calculated results of the activated carbon yield prepared from the data of Tables 3 and 4 respectively.

Results Table (3)				Results Table (4)			
S	Exp. val	Cal. Val	diff	S	Exp. val	Cal. val	diff
1	14.831	14.523	0.308	1	14.907	14.946	-0.039
2	16.243	15.764	0.479	2	18.071	17.148	0.923
3	18.284	17.938	0.346	3	19.231	19.727	-0.496
4	20.072	19.717	0.355	4	27.580	26.454	1.126
5	22.471	22.005	0.466	5	34.410	34.434	-0.024

Observing the results obtained from the tables above, we note that there is a linear relationship with a good correlation coefficient and a low standard deviation. In addition, there is a correspondence in the practical values and the values calculated from the results obtained from the regression analysis. This result encouraged us to

complete this study and try to find one general equation that combines all Methods By introducing new variables including adding humidity content as well as the proportions of additives in the preparation of KOH, asphalt and novolak resin the data used in the regression analysis are listed in Table 15.

Table 15: Data used in regression analysis to find a general equation.

Yd	ION	Dy	ASC	HYC	%KOH	%Asp	%Nov	%Mix
20.401	654.959	0.383	3.190	8.130	0.5	0	0	0
18.810	674.507	0.306	3.170	10.550	1	0	0	0
16.528	710.808	0.292	3.140	10.760	1.5	0	0	0
14.904	780.620	0.273	3.080	10.880	2	0	0	0
8.800	788.997	0.281	4.000	7.030	3	0	0	0
14.105	830.884	0.256	3.010	11.890	2.5	5	0	0
15.232	864.394	0.218	2.940	11.420	2.5	10	0	0
16.034	881.149	0.178	2.820	12.010	2.5	15	0	0
17.691	900.696	0.118	1.750	12.200	2.5	20	0	0
21.631	925.828	0.080	1.680	12.380	2.5	25	0	0
14.831	836.469	0.221	2.980	11.930	2.5	0	5	0
16.243	892.318	0.210	2.920	11.470	2.5	0	10	0
18.284	945.375	0.196	2.540	12.410	2.5	0	15	0
20.072	976.092	0.106	1.870	12.290	2.5	0	20	0
22.471	1004.017	0.075	1.230	13.710	2.5	0	25	0
14.907	864.394	0.220	2.860	11.980	2.5	0	0	5
18.071	981.677	0.186	2.750	11.590	2.5	0	0	10
27.580	1017.979	0.104	1.720	12.740	2.5	0	0	20

Asp : Asphalt , Nov : Novolak

The results of the regression analysis obtained from the data listed in Table 15 were as follows:

Table 16: Results of regression analysis of the data in Table 15.

Variables	variables Coefficient	
ION	-0.014	
Dy	3.016	b= 28.818
ASC	-0.378	R ² = 0.978
HYC	0.318	SE= ±0.830
%KOH	-3.460	
%Asphalt	0.506	
%Novolak	0.881	
Observation Number = 18		

The results listed in Table 16 can be formulated in the form of a mathematical equation and written as follows:

$$yield = 28.818 - 0.014 \times Iod. + 3.016 \times Density \quad (3)$$

When using above equation to theoretically calculate the yield ratio values and compare them with the experimental values it was found that there is a large correspondence between the calculated values and the experimental values with an error rate not exceeding 5% as shown in Table 17.

Table 17: Comparison between the experimental and theoretical results of the prepared activated carbon yield From the data in Table 14.

Seq	Y _{exp.}	Y _{calc.}	Y _{exp.} - Y _{calc.}
1	20.401	20.453	-0.052
2	18.810	18.994	-0.184
3	16.528	16.792	-0.264
4	14.904	14.088	0.816
5	8.800	8.963	-0.163
6	14.105	13.881	0.224
7	15.232	15.104	0.128
8	16.034	16.912	-0.878
9	17.691	18.852	-1.161
10	21.631	20.399	1.232
11	14.831	14.321	0.510
12	16.243	15.913	0.330
13	18.284	18.100	0.184
14	20.072	20.144	-0.072
15	22.471	22.883	-0.412
16	14.907	15.864	-0.957
17	18.071	18.442	-0.371
18	27.580	27.251	0.329

4. CONCLUSIONS

From the results of this study, it was concluded that the yield of prepared activated carbon can be calculated by knowing the percentage of ash, humidity, density, and iodine number. Any of these variables can also be calculated with an unknown substance if the value of the other variables is available. The values of the parameters of the variables indicate that the yield percentage is directly proportional to the density and to the humidity content, and this is logical, as increasing the density increases the yield percentage of the activated carbon, and increasing the yield of the prepared activated carbon increases the amount of humidity adsorbed on its surface. Increasing the base percentage reduces the yield because the user

burns it to prepare in the catalysis process and increases the ash content percentage. Increasing asphalt or novolak resin increases the yield of the prepared carbon because increasing these materials increases the carbon content of the materials used in preparing the activated carbon. There is a large correspondence between the percentage of calculated and experimental results with a percentage that does not exceed the percentage of experimental error which is inferred from the percentage of standard deviation.

5. CONFLICT OF INTEREST

The author have no conflicts of interest.

6. ACKNOWLEDGMENTS

I thank the university of mosul in Iraq for supported me to complete this work.

7. REFERENCES

- Jabit NB. The production and characterization of activated carbon using local agricultural waste through chemical activation process [Internet]. 2007. Available from: [<URL>](#).
- Al-Dabouni AA. Introduction to petrochemicals. University of Mosul; 1991. 307–322 p.
- Alhamed Y. Activated carbon from dates' stone by ZnCl₂ activation. J King Abdulaziz Univ Sci [Internet]. 2006;17(2):75–98. Available from: [<URL>](#).
- De Ridder DJ. Adsorption of organic micropollutants onto activated carbon and zeolites. Water Manag Acad Press [Internet]. 2012;7–14. Available from: [<URL>](#).
- Lozano-Castelló D, Lillo-Ródenas MA, Cazorla-Amorós D, Linares-Solano A. Preparation of activated carbons from Spanish anthracite. Carbon N Y [Internet]. 2001 Apr 1;39(5):741–9. Available from: [<URL>](#).
- Pradhan S. Production and characterization of Activated carbon produced from asuitable Industrial Sludge [Internet]. National Institute of Technology; 2011. Available from: [<URL>](#).
- Shahbeik H, Bagheri N, Ghorbanian SA, Hallajisani A, Pourkarimi S. A new adsorption isotherm model of aqueous solutions on granular activated carbon. World J Model Simul [Internet]. 2013;9(4):243–54. Available from: [<URL>](#).
- Inagaki M. New carbons - control of structure and functions [Internet]. Elsevier; 2000. Available from: [<URL>](#).
- Gottipati R. Preparation and characterization of microporous activated carbon from biomass and its application in the removal of Chromium(VI) from aqueous phase. National Institute of Technology Rourkela; 2012.
- AL Ghannam KA, Aweed KA, Hamdoon AA. Preparation of activated from Morus nigra by chemical treatment. Natl J Chem. 2004;13:26–33.
- Aweed KA. Production of activated carbon from some agricultural wastes by chemical treatment. Natl J Chem [Internet]. 2005;17:138–42. Available from: [<URL>](#).
- Hamdon AA, Abdul Aziz AN, Ali MH. Study the effect of the structural modifications on the properties of the activated carbon prepared from coconut-shell by chemical treatment. Tikrit J Pure Sci [Internet]. 2008;13(3):278–82. Available from: [<URL>](#).
- Saleh NJ, Ismaeel MI, Ibrahim RI, Zablouk MA, Amer A. Preparation activated carbon of from Iraqi reed. Eng Technol J [Internet]. 2008 Mar 28 [cited 2024 Aug 28];26(3):291–304. Available from: [<URL>](#).
- Ramakrishnan K, Namasivayam C. Development and characteristic of activated carbons from Jatropha husk, an agro industrial solid waste, by chemical activation methods. J Environ Eng Manag [Internet]. 2009;19(3):173–8. Available from: [<URL>](#).
- Ragan S, Megonnell N. Activated carbon from renewable resources-lignin. Cellul Chem Technol [Internet]. 2011;45(8):527–31. Available from: [<URL>](#).
- Zengin A, Akalin MK, Tekin K, Erdem M, Tay T, Karagoz S. Preparation and characterization of activated carbons from waste melamine coated chipboard by NaOH activation. Ekoloji [Internet]. 2012 Dec 31;21(85):123–8. Available from: [<URL>](#).
- Al-Badran SFJ. Preparation of activated carbon by chemical activation with phosphoric acid using Cordia myxa fruits nuclei as raw material. J Basrah Res [Internet]. 2013;39(4B):98–106. Available from: [<URL>](#).
- Abechi SE, Gimba CE, Uzairu A, Dallatu YA. Preparation and characterization of activated carbon from palm kernel shell by chemical activation. Res J Chem Sci [Internet]. 2013;3(7):54–61. Available from: [<URL>](#).
- Salman JM. Preparation of mesoporous-activated carbon from branches of pomegranate trees: optimization on removal of methylene blue using response surface methodology. Giuliani A, editor. J Chem [Internet]. 2013 Jan 12;2013(1):489670. Available from: [<URL>](#).
- Njewa JB, Vunain E, Biswick T. Synthesis and characterization of activated carbons prepared from agro-wastes by chemical activation. Guo W, editor. J Chem [Internet]. 2022 Mar 22;2022(1):975444. Available from: [<URL>](#).
- Islam MN, Khatton A, Sarker ahid, Sikder HA, Chowdhury AMS. Preparation and characterization of activated carbon from jute stick by chemical activation: Comparison of different activating agents. Saudi J Eng Technol [Internet]. 2022 Feb 28;7(2):112–7. Available from: [<URL>](#).
- Al-Hyali EAS, Al-Khazraji AAH, Al-Taey SIK. A Thermodynamic and kinetic study for adsorption of a number of dyes from their aqueous solutions on a new kind of activated carbon prepared by pomegranate (*Punica granatum*) peels via chemical treatment. Int J Enhanc Res Sci [Internet]. 2016;5(3):82–116. Available from: [<URL>](#).
- AL-Taey SIK. Preparation of new types of activated carbon and testing their efficiency by the adsorption of some dyes, thermodynamic and kinetic studies. 2017.

24. Ma R, Qin X, Liu Z, Fu Y. Adsorption property, kinetic and equilibrium studies of activated carbon fiber prepared from liquefied wood by ZnCl₂ activation. Materials (Basel) [Internet]. 2019 Apr 28;12(9):1377. Available from: [<URL>](#).

25. ASTM D2854-70. Standard test method for apparent density activated carbon. 2000.

26. Test method for activated carbon. Roster bau int. Engineering GMBH. W. Germany Devtschos Arzneibuch 6th Edition. 1999.

27. Sunanda, Tiwari DP, Sharma DN, Thakur S, Kumar RTS. Sapindus based activated carbon by chemical activation. Res J Mater Sci [Internet]. 2013;1(7):9–15. Available from: [<URL>](#).



Chemical Analysis of Pomegranate Flower Essential Oil in Türkiye

Damla Kırcı^{1*}, Safa Gümüşok², Ceyda Sibel Kılıç², Betül Demirci³

¹Selçuk University, Department of Pharmacognosy, Faculty of Pharmacy, Konya, Türkiye.

²Ankara University, Department of Pharmaceutical Botany, Faculty of Pharmacy, Ankara, Türkiye.

³Anadolu University, Department of Pharmacognosy, Faculty of Pharmacy, Eskişehir, Türkiye.

Abstract: *Punica granatum* L. (Pomegranate) grows naturally in a wide area from northwest Türkiye to western and northern Pakistan and is also cultivated throughout subtropical and tropical regions of the world. Pomegranate is in the form of a spiny shrub or a small tree. The barks, fruit peels, flowers, and seeds of the plant are used in traditional medicine due to their ellagitannin and polyphenol content and are used to treat circulatory system disorders. In this study, essential oil (EO) of *P. granatum* flowers was obtained by hydrodistillation and analyzed by GC-FID and GC-MS. As a result, the chemical composition of the essential oil obtained was elucidated. As a result, nine compounds representing 99.9% of the essential oil of *P. granatum* flowers were characterized, with hexadecanoic acid (52.4%), linoleic acid (15.2%), heptacosane (10.1%), and pentacosane (10.1%) as the major components. Notably, this research marks the first comprehensive examination of the essential oil of pomegranate flowers in Türkiye.

Keywords: *Punica granatum*, Punicaceae, Essential oil, Hydrodistillation, GC-FID, GC-MS.

Submitted: February 10, 2024. **Accepted:** August 6, 2024.

Cite this: Kırcı D, Gümüşok S, Kılıç CS, Demirci B. Chemical Analysis of Pomegranate Flower Essential Oil in Türkiye. JOTCSA. 2024;11(4): 1417-20.

DOI: <https://doi.org/10.18596/jotcsa.1434861>

***Corresponding author's E-mail:** damla.kirci@ikc.edu.tr

1. INTRODUCTION

The Punicaceae family is represented by a single genus, *Punica* L., is characterized by deciduous shrubs or trees, sometimes with spiny branches. Leaves of the family are simple without stipules. The flowers are located at the tips of the branches. The large fruit has a leathery exocarp and bears many seeds (1). *Punica granatum* L. (pomegranate) is a cosmopolite plant that is distributed widely from northwest Türkiye to western and northern Pakistan and is cultivated in subtropical and tropical regions of the world (1-3).

For centuries, people have used fragrant plants and their processed forms as flavorings. More recently, these plants have become a focus for finding natural antioxidants and antibacterial agents. Pomegranate flowers have a long history of use in traditional Indian medicine systems like Ayurveda and Unani. These flowers possess anti-diabetic and astringent properties, and an infusion made by boiling the flower buds is employed to treat chronic diarrhea, especially in children. As there is growing interest in utilizing plant-derived compounds in food and pharmaceuticals, carefully studying plant extracts for

these beneficial properties has become increasingly important. Moreover, the stem bark, fruit peel, flowers, and seeds of pomegranate are used in folk medicine for their anthelmintic and antimicrobial properties. Despite the low aromatic intensity of fresh pomegranates, only a handful of studies have looked at the volatile aroma compounds in pomegranates, and these mainly focused on pomegranate juices. For example, one study could only identify nine compounds in pomegranate juices from Iran. Later, a pomegranate and berry juice survey found just ten volatile compounds in the pomegranate. Additionally, there is a lack of research on the fatty acids in pomegranate flowers, except for a study that characterized the fatty acid methyl esters in five different Iranian pomegranate flower cultivars (4,5). Other phytochemical components of the plant consist of tannins, flavonoids, alkaloids, organic acids, triterpenes, steroids, coumarins, and lignans (6-10). Pomegranate plant is known to be used to treat circulatory system disorders, it also has antimicrobial, antioxidant, anticancer, antidiabetic, and immunomodulatory activities (11-15). The research also reported that extracts from *P. granatum* arils possess strong *in vitro* antibacterial activity against many bacterial strains tested. Most

of those investigations suggested that the presence of phytochemicals in the extracts, including phenols, tannins, and flavonoids, as major active constituents may be responsible for these activities. However, research on the antibacterial activity of pomegranate flower extracts is scarce. Moreover, it is not well known whether volatile components could be involved in the antibacterial effect of pomegranate flower extracts and essential oils (5). Moreover, the flowers from Türkiye possess significant phytochemical and antioxidant properties, making them a valuable source of bioactive compounds. The flower extracts, particularly rich in phenolic compounds such as punicalagin, have shown good antioxidant activity (16).

When we review the literature, we find that essential oils (EOs) obtained from the fruit peels have been studied extensively. However, there are only a few studies on the composition of the EO obtained from the flowers (5). As far as we know, this is the first study examining the essential oil obtained from the flowers of the pomegranate plant growing in Türkiye naturally.

2. EXPERIMENTAL SECTION

2.1. Plant Material

Plant material was collected from Kahramankazan, Ankara (Türkiye), specifically from Güvenç Köyü at an altitude of 1000 meters on 30/06/2021. A voucher specimen was deposited in the Ankara University Faculty of Pharmacy Herbarium with the herbarium number AEF 30716. Collected flowers were dried in the shade.

2.2. Isolation and Analysis of Essential Oil

The hydrodistilled essential oil was analyzed by GC-MS and GC-FID (17-19). Table 1 contains the result. The EO was obtained by hydrodistillation using a Clevenger-type apparatus for three hours. A small amount of EO of *P. granatum* was trapped in n-hexane. The EO was stored at 4°C in an amber vial.

The essential oil compounds were identified by comparing their relative retention indices (RRI) to those of authentic samples using computer matching against commercial data (MassFinder 4.0 Library, Wiley GC-MS Library). The identification was carried out using an in-house "Başer Library of Essential Oil Constituents" compiled from genuine compounds of recognized essential oils and the MS reported in the literature (17, 18).

3. RESULTS AND DISCUSSION

9 compounds representing 99.9% of the essential oil of the flowers were characterized with hexadecenoic acid (52.4%), linoleic acid (15.2%), heptacosane (10.1%), and pentacosane (10.1%) as major components. The composition of the EO is shown in Table 1. The EO of pomegranate flowers contains various compounds, including nonadecane, tricosane, tetracosane, pentacosane, hexacosane, heptacosane, nonacosane, hexadecenoic acid, and linoleic acid. Hexadecenoic acid, also known as palmitic acid. Palmitic and linoleic acids are fatty

acids. Palmitic acid (C16:0) is a saturated lipid with a 16-carbon chain. Linoleic acid (C18:2) is a polyunsaturated fatty acid (PUFA) with the molecular name omega-6 or cis-9,12-octadecadienoic acid. It is an essential fatty acid, which means that the human body cannot produce it and must receive it from the diet.

Table 1: Composition of the EO of *Punica granatum* flowers.

RRI	Compound	%
1900	Nonadecane	1.0
2300	Tricosane	2.3
2400	Tetracosane	0.8
2500	Pentacosane	10.1
2600	Hexacosane	1.6
2700	Heptacosane	10.1
2900	Nonacosane	6.4
2931	Hexadecenoic acid	52.4
3290	Linoleic acid	15.2
Total		99.9

When we searched the literature, we saw that many studies were performed on fruit juice, particularly focusing on its preservation. And studies conducted on essential oils were performed mostly on the EOs obtained from fruit peels.

In a study by Hadrach et al. (2014), the essential oil of Tunisian pomegranate peels was analyzed, revealing camphor (60.32%), benzaldehyde (20.98%), and borneol (4.75%) as the main components of the EO (20).

In a study, essential oil of the peel was obtained both with hydro-distillation and super fluid extraction methods, and the obtained results were compared. Hydrodistillation yielded 73 compounds; however, superfluid extraction just yielded 46 components. While major compounds of hydrodistillation procedure were found to be (-)-borneol (12.97%), oleic acid (11.65%), and dibutyl phthalate (10.82%), the superfluid extraction procedure yielded oleic acid (12.49%), palmitic acid (11.65%), and (-)-borneol (9.5%) as major components (21).

In another study performed on fruit peels by Wahba (2020), linoleic acid was found to be the main component of the essential oil (29.33%), along with *D*-limonene (13.79%), caryophyllene (13.9%), *cis*-vaccenic acid (12.66%), and squalene (9.12%) (22). In the study conducted by Gültepe et al. (2019) on fruit peels, methyl stearate (43.21%), metilox (16.82%), and methyl palmitate (7.90%) were dominant in the essential oil (23).

As it can be found from the results of these studies, the main components are usually different than the results of our study, which is not surprising by the way since the plant parts used to isolate essential oils were different.

In a study conducted in Tunisia, essential oils obtained from pomegranate flowers were compared to reveal the influence of different types of cultivation methods with respect to the essential oil

composition. 4 different types of cultivators (Tounsi, Nabli, Gabsi, and Chelfi) were selected for this purpose, and the essential oils of flowers were examined. Esters, alcohols, terpenes, aldehydes, ketones, and hydrocarbons were identified to be present in the chemical composition of the EOs. The results of these studies are listed in Table 2 (5).

When we examine the results of this study, we can recommend that only the composition of the Gabsi cultivator was similar to the findings of our study. *n*-Pentacosane found to be present in this cultivar (13.59%) was also present in the essential oil that we have obtained from the flowers.

Table 2: The major components of the essential oils from the flowers of Tunisian pomegranate cultivars.

Cultivar	Major Compounds	(%)
Tounsi	2,3-Butandiol	18.98
	Eugenol	15.85
	Ethyl hexadecanote	5.96
Nabli	Ethyl hexadecanote Ethyl	35.92
	oleate	18.88
	Nezukol	12.75
Gabsi	Ethyl hexadecanote	19.31
	<i>n</i> -Pentacosane	13.59
	Abietadiene	12.37
Chelfi	2,3-Butanediol	20.65
	Eugenol	18.85
	Abietadiene	10.79

Pomegranate is a fruit of significant commercial importance, and it is cultivated in Southern, Middle East, Asia, and Mediterranean regions. Its seeds are rich in bioactive components, including fatty acids, tocopherols, tocotrienols, phytosterols, and carotenoids. Pomegranate seed fixed oil is a non-traditional oil with health benefits, rich in polyunsaturated fatty acids (PUFAs), namely linoleic acid (omega-6) and linolenic acid (omega-3), as well as an effective conjugated linolenic acid, punicic acid (24).

The other study compared three different methods (microwave-assisted extraction (MAE), ultrasound-assisted extraction (UAE), and cold pressing) for extracting pomegranate seed oil and found that the ultrasound-assisted extraction technique was the most efficient, with a maximum extraction efficiency of 26.31% under optimized conditions. The cold pressing method yielded the lowest oil extraction efficiency at 5%, but the extracted oil had the highest punicic acid content at 88.33%. The other major fatty acids in the cold-pressed oil were oleic acid (3.68%), linoleic acid (3.22%), palmitic acid (2.19%), and stearic acid (1.56%). The MAE technique using dimethyl succinate as the solvent had an extraction efficiency range of 5.94 to 22.01%. The extracted oils were also dominated by punicic acid, which ranged from 87.65 to 88.15%. Other notable fatty acids included oleic acid (1.58-3.70%), linoleic acid (3.32-3.64%), and palmitic acid (2.20-2.69%). When hexane was used as the solvent for MAE, the extraction efficiency increased to 25.3%, and the punicic acid content was 88.39%. The UAE method demonstrated the highest extraction efficiency, ranging from 6.71 to 26.3%. The extracted oils had a wider variation in fatty acid composition, with punicic acid ranging from 74.4 to 88.0%. Other significant fatty acids included linoleic acid (3.4-7.5%), oleic acid (3.6-7.1%), and palmitic acid (2.3-5.0%). Using hexane as the solvent for UAE further increased the extraction efficiency to 31.2%, and the punicic acid content was 75.26% (25).

The second main compound of flower essential oil is linoleic acid. Although it is close to the fixed oil content in this aspect, it has a different chemical composition in other compounds.

4. CONCLUSION

In this research, we have investigated the composition of essential oil obtained from pomegranate flowers collected from Ankara, Türkiye. To the best of our knowledge, this is the first research examining the essential oil of pomegranate flowers from plants growing naturally in Türkiye, with hexadecenoic acid (52.4%) identified as the major component. And thus, this study sheds light on the chemical composition of *P. granatum* flower essential oil, showcasing the major of specific compounds that contribute to its aromatic and potentially therapeutic properties. The findings provide valuable insights into the potential applications of pomegranate essential oil in various fields, including aromatherapy and cosmetics, for its bioactive constituents.

5. CONFLICT OF INTEREST

The authors declare that there is no real, potential, or perceived conflict of interest for this article.

7. REFERENCES

- Davis PH. Flora of Türkiye and the east aegean islands. 4th Edition. Edinburgh: Edinburgh University Press; 1972.
- IPNI. International plant names index [Internet]. [cited 2024 Feb 1]. Available from: [<URL>](#).
- POWO. Plants of the world online kew science [Internet]. [cited 2024 Feb 1]. Available from: [<URL>](#).
- Evans W. Pharmacognosy. 5th Edition. Saunders; 2002. 25–26 p.

5. Mekni M, Flamini G, Garrab M, Hmida RB, Cheraief I, Mastouri M, et al. Aroma volatile components, fatty acids and antibacterial activity of four Tunisian *Punica granatum* L. flower cultivars. *Ind Crops Prod* [Internet]. 2013 Jul 1;48:111–7. Available from: [<URL>](#).
6. Badria FA. Melatonin, serotonin, and tryptamine in some Egyptian food and medicinal plants. *J Med Food* [Internet]. 2002 Sep 7;5(3):153–7. Available from: [<URL>](#).
7. Hernández F, Melgarejo P, Tomás-Barberán FA, Artés F. Evolution of juice anthocyanins during ripening of new selected pomegranate (*Punica granatum*) clones. *Eur Food Res Technol* [Internet]. 1999 Nov 3;210(1):39–42. Available from: [<URL>](#).
8. Nawwar MAM, Hussein SAM, Merfort I. Leaf phenolics of *Punica granatum*. *Phytochemistry* [Internet]. 1994 Nov 7;37(4):1175–7. Available from: [<URL>](#).
9. Tanaka T, Nonaka GI, Nishioka I. Punicafolin, an ellagitannin from the leaves of *Punica granatum*. *Phytochemistry* [Internet]. 1985 Jan 1;24(9):2075–8. Available from: [<URL>](#).
10. Wang R, Ding Y, Liu R, Xiang L, Du L. Pomegranate: Constituents, bioactivities and pharmacokinetics. *Fruit, Veg Cereal Sci Biotechnol* [Internet]. 2010;4(2):77–87. Available from: [<URL>](#).
11. Bagri P, Ali M, Aeri V, Bhowmik M, Sultana S. Antidiabetic effect of *Punica granatum* flowers: Effect on hyperlipidemia, pancreatic cells lipid peroxidation and antioxidant enzymes in experimental diabetes. *Food Chem Toxicol* [Internet]. 2009 Jan 1;47(1):50–4. Available from: [<URL>](#).
12. Gosset-Erard C, Zhao M, Lordel-Madeleine S, Ennahar S. Identification of punicalagin as the bioactive compound behind the antimicrobial activity of pomegranate (*Punica granatum* L.) peels. *Food Chem* [Internet]. 2021 Aug 1;352:129396. Available from: [<URL>](#).
13. Khwairakpam AD, Bordoloi D, Thakur KK, Monisha J, Arfuso F, Sethi G, et al. Possible use of *Punica granatum* (Pomegranate) in cancer therapy. *Pharmacol Res* [Internet]. 2018 Jul 1;133:53–64. Available from: [<URL>](#).
14. Gracious Ross R, Selvasubramanian S, Jayasundar S. Immunomodulatory activity of *Punica granatum* in rabbits—a preliminary study. *J Ethnopharmacol* [Internet]. 2001 Nov 1;78(1):85–7. Available from: [<URL>](#).
15. Zeghad N, Ahmed E, Belkhiri A, Heyden Y Vander, Demeyer K. Antioxidant activity of *Vitis vinifera*, *Punica granatum*, *Citrus aurantium* and *Opuntia ficus indica* fruits cultivated in Algeria. *Heliyon* [Internet]. 2019 Apr 1;5(4):e01575. Available from: [<URL>](#).
16. Tekin Z, Kucukbay FZ. Pomegranate leaves, buds, and flowers: phytochemical, antioxidant, and comparative solvent analyzes. *Foods Raw Mater* [Internet]. 2024 May 23;13(1):155–71. Available from: [<URL>](#).
17. Kılıç CS, Demirci B, Kırcı D, Duman H, Gürbüz İ. Essential oils of *Ferulago glareosa* Kandemir&Hedge roots and aerial parts: PCA and HCA analyses. *Chem Biodivers* [Internet]. 2023 May 18;20(5):e202300364. Available from: [<URL>](#).
18. McLafferty F, Stauffer D. The Wiley/NBS registry of mass spectral data. New York; 1989.
19. Hochmuth D. MassFinder 4.0, Hochmuth scientific consulting. Hamburg, Germany; 2008.
20. Hadrich F, Cher S, Gargouri YT, Adel S. Antioxidant and lipase inhibitory activities and essential oil composition of pomegranate peel extracts. *J Oleo Sci* [Internet]. 2014;63(5):515–25. Available from: [<URL>](#).
21. Ara KM, Raofie F. Application of response surface methodology for the optimization of supercritical fluid extraction of essential oil from pomegranate (*Punica granatum* L.) peel. *J Food Sci Technol* [Internet]. 2016 Jul 22;53(7):3113–21. Available from: [<URL>](#).
22. Wahba TF. Antifeedant activity of three essential oils and their nanoemulsions against the rice weevil *Sitophilus oryzae* (L.). *Egypt Sci J Pestic* [Internet]. 2020;6(2):19–31. Available from: [<URL>](#).
23. Gültepe N, M.I. Bufrag S, Abughadyra IRA, A.O. Mohammed K, Alkhunni SBA. Comparison of some medicinal plants and macrofungi essential oil components for antimicrobial activity against the human and fish pathogens. *Int J Curr Microbiol Appl Sci* [Internet]. 2019 Nov 20;8(11):458–73. Available from: [<URL>](#).
24. Iriti G, Bonacci S, Lopreiato V, Frisina M, Oliverio M, Procopio A. Functional compounds of cold-pressed pomegranate seed oil: Fatty acids and phytosterols profile as quality biomarkers for origin discrimination. *Foods* [Internet]. 2023 Jul 5;12(13):2599. Available from: [<URL>](#).
25. Gök A, Uyar H, Demir Ö. Pomegranate seed oil extraction by cold pressing, microwave and ultrasound treatments. *Biomass Convers Biorefinery* [Internet]. 2024 Apr 15; Article in Press. Available from: [<URL>](#).



Antioxidant Activity of Bio-extract which Obtained from Hazelnut Shells and Green Leafy Covers

Farhad Azizov¹ , Vafa Atayeva^{1*} , Zarbali Khalilov¹ 

¹Azerbaijan National Academy of Sciences, Sheki Regional Scientific Center, Sheki, AZ5500, Azerbaijan.

Abstract: The article presents the findings of an antioxidant activity assay conducted using 70% ethanol and deionized water on extracts from green leafy covering (GLC) and hazelnut hard shells (HS) that are grown in the northwest of Azerbaijan. The kinetics of each extract were examined using a UV-2700 vis spectrophotometer, and the DPPH (2,2-Diphenyl-1-picrylhydrazyl) technique was used to determine the extract's free radical scavenger activity. The results show that the bio-extracts obtained in 70% alcohol have radical scavenging activities of FRSA(hs)=59.24% and FRSA(glc)=35.72%, while the bio-extracts obtained in water have radical scavenging activities of FRSA (hs)=31.15% and FRSA(glc)=22.23%. Waste is significant for treatment, affordable, and an effective preventive measure since it is derived from raw resources.

Keywords: Hazelnut hard shell and green leafy covering, Bio-extract, Free radical scavenger activity.

Submitted: October 12, 2023. **Accepted:** August 2, 2024.

Cite this: Azizov F, Atayeva V, Khalilov Z. Antioxidant Activity of Bio-extract which Obtained from Hazelnut Shells and Green Leafy Covers. JOTCSA. 2024;11(4):1421-4.

DOI: <https://doi.org/10.18596/jotcsa.1374892>

***Corresponding author's E-mail:** vefaatayeva81@gmail.com

1. INTRODUCTION

Recent global pandemic-related issues have underscored the importance of exploring and applying novel herbal natural remedies. This is particularly significant given the development of numerous synthetic pharmaceutical preparations used to treat a variety of infectious diseases in humans. Large-scale trials conducted in the past two years have further supported the necessity for therapeutic medications with antioxidant effects in the treatment of these disorders in the general population. It was found that plant-based antioxidants, in contrast to synthetic antioxidants, are the safest option (1).

The presence of antioxidant-containing microelements and bioactive substances in natural treatment solutions contributes to their effectiveness and benefits. It has a more profound effect on the human body and has better therapeutic quality. Inhibiting the redox process in lipids and triggering the removal of free radicals created in the mitochondria during the metabolic process, antioxidants play a unique function in human life and activity. It has been established that when the concentration of free radicals in the body exceeds 5%, they damage cells at the molecular

level and result in the occurrence of various diseases in humans. Currently, plants containing Mn, Zn, Se, Cr, Si, J elements, and the B, C, D, and F group vitamins are employed extensively as natural antioxidants for both medicinal and preventative purposes, with significant advantages (2-5).

Additionally, among the most crucial bioactive compounds are lignans, polyphenols, tannins, and steroidal saponins. They lower the organism's cholesterol content. They have a direct impact on the gut flora and gene expression. Currently, foods like beans, green leafy covering plants, cereal goods, fruit-vegetable combinations, orchards, and tea have many benefits because they are primary sources of antioxidants. Investigations revealed that the extracts from the green leafy covering and the hard shell of hazelnuts were rich in bioactive polyphenols and mineral components with increased antioxidant activity. Italian researchers found that the bio-extract made from hazelnut shells includes tannins and neolignans, two polyphenolic substances with strong antioxidant activity (6-8). Researchers in Turkey have shown that the chemical paclitaxel, which is found in hazelnut shells, has a strong antioxidant impact, helps the body scavenge free radicals, and boosts immunity

(9). The extract taken from the hazelnut shell included 27 phenolic components, according to studies conducted in Singapore (10). Further research has revealed that hazelnut green leafy covering contains 17 phenolic acids, which have been shown to have strong antibacterial and antioxidant properties. As a result, it is advised that these compounds be taken into consideration as possible sources of antioxidants (11). The bio-extract made from green leafy covering and hazelnut shells has radical scavenging properties that are dependent on the extractive materials, extraction technique, and environmental factors (12-14).

After analyzing the chemical composition and biologically active components of the bio-extracts made from the hard shell and green leafy covering of hazelnut plants that grow in Azerbaijan's northwest, it was found that these plants are rich in mineral elements and other organic compounds that are biologically active. Research has indicated that the hazelnut hard shell bio-extract in 70% ethanol includes Cr-8.0 mg/g, Mn-104 mg/g, Zn-12 mg/g, and Si-698 mg/g. Conversely, the green leafy covering bio-extract contains Cr-13.0 mg/g, Mn-17.0 mg/g, Zn-10.0 mg/g, and Si-631.0 mg/g. Eight organic compounds were found in the hazelnut hard shell bio-extract, while five organic compounds were found in the green leafy covering bio-extract. These compounds were found to have antioxidant activity (15,16). The bio-extracts made from the hard shell and the green leafy covering, as can be observed, contain biologically active substances with antioxidant activity as well as essential microelements that are present in the body's daily required amount and work well as a preventative and therapeutic measure.

The investigation on the antioxidant properties of bio-extracts made from the hard shell and green leafy covering of hazelnuts using 70% ethyl alcohol and deionized water is reported in this article.

2. MATERIALS AND METHODS.

2.1. Plant Materials

The hard shell and green leafy covering of the common hazelnut plant in the Shaki region of Azerbaijan are the research objects. The hard shell and green leafy covering were first cleaned with tap water, then dried, ground, and cleaned again with distilled water. The extracts were obtained using 70% ethyl alcohol and deionized water.

2.2. Preparation of Extracts

At room temperature, the hard shell and green leafy covering of samples of typical hazelnut plants were dried and ground into a powder. Fifty grams of the ground sample were added to a 500 ml flask. After

that, 300 mL of distilled water was added to the ground samples. At a temperature of 100 °C, the combinations were removed for 30 minutes. After extraction, the solution was filtered. After that, 100 milliliters of distilled water were combined with the leftover ground material, and the mixture was extracted for fifteen minutes. It was necessary to filter the obtained extract before combining it with the original extract. Once more, the flask's residual was combined with 100 milliliters of distilled water and extracted for 15 minutes. Before being mixed with the original extract, the obtained extract was filtered. At a temperature between 75 and 80 °C in a water bath, the alcohol extraction process was accurately followed. Using an SPT-200 Vacuum-Drier, both extracts were crushed into a powder (15).

2.3 DPPH Radical Scavenging Activity of Extracts

A widely used method to evaluate a material's ability to scavenge free radicals is the stable DPPH radical scavenging model. Using a 70 µM DPPH solution in methanol and the UV-2700 spectrophotometer technique, the free radical scavenging activity (RTA%) of the bio-extracts was calculated in a typical room atmosphere using the formula $RSA\% = (A_0 - A_s) / A_0$ equal (17). First, the absorption of a 70 µM DPPH solution was ascertained. Following kinetic measurements, the absorption of each bioextracts was assigned.

3. RESULTS AND DISCUSSION

The kinetics of free radical scavenger activity were investigated, activity was calculated, and comparative analysis was carried out for each extract (Fig 1).

Initially, a 70 µM DPPH solution was produced in methanol. The absorption was then measured in a 3 ml cuvette using a UV-2700, and the value of absorption was roughly 0.8211 at 516 nm. After extracting 500 µL of DPPH solution from that cuvette and adding 500 µL of bio-extract to another cuvette, the kinetics were observed after 20 minutes.

The graph shows that from 0 to 60 seconds, all kinetics curves have a sharp decline. Still, there is a small decrease from 60 to 260 seconds. Furthermore, kinetics lines nearly continue in later seconds while remaining stable. At first, the control DPPH's absorbance is 0.8211. At the conclusion of each procedure, the absorbance of the combination solution was measured, and radical scavenging activity RSA (%) was computed. Table 1 displays the absorbance and RSA of the bio-extracts made from the hazelnut's green leafy covering and hard shell.

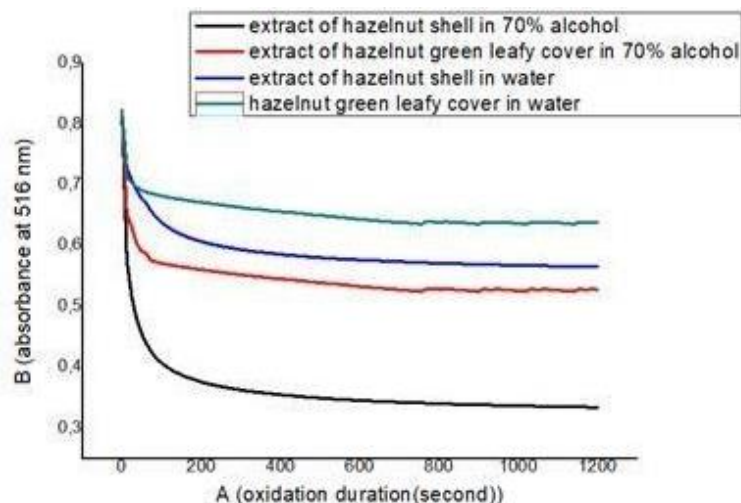


Figure 1: Bio-extracts obtained in 70% ethanol and water: their kinetics.

Table 1: Radical scavenging activities of 70% ethanolic and aqueous bio-extracts from hard shell and green leafy covering of hazelnut.

No	Name of sample	Absorbance		Radical scavenging activity, RSA %	
		In alcohol	In water	In alcohol	In water
1	DPPH	0.8211	0.8210	-	-
2	Bioextract of the hazelnut hard shell	0.3342	0.5653	59.2452	31.1543
3	Bioextract of the hazelnut green leafy covering	0.5278	0.6384	35.7215	22.2366

The results of the analysis of the kinetics of all four bio-extracts indicate that the hard shell bio-extract has a stronger radical scavenging activity than the green leafy covering bio-extract, regardless of the extractants used. The graph shows that while all extracts had 0.8211 absorption features at the beginning, the kinetic lines decreased rapidly between 100 and 150 seconds and then remained stable for the remaining seconds. The bio-extracts derived from the hard shell had a stronger radical scavenging activity than those from the green leafy covering, according to an analysis of the kinetics of each bio-extract. A computation was done regarding the absorption value at the conclusion of the 30 minutes while the kinetics were being recorded. The graph shows that while all extracts had 0.8211 absorption features at the beginning, the kinetic lines decreased rapidly between 100 and 150 seconds and then remained stable for the remaining seconds. The bio-extracts derived from the hard shell had a stronger radical scavenging activity than those from the green leafy covering, according to an analysis of the kinetics of each bio-extract. A computation was done regarding the absorption value at the conclusion of the 30 minutes while the kinetics were being recorded. According to the calculations, the radical scavenging activity of bio-extracts obtained in 70% alcohol is $FRSA(hs)=59.24\%$ and $FRSA(glc)=35.72\%$, but the radical scavenging activity of bio-extracts obtained in water is $FRSA(hs)=31.15\%$ and $FRSA(glc)=22.23\%$.

Studies by Siriwardhana SS. and Shadi F. found that the bio-extract from the hazelnut's green leafy covering had a hydrogen peroxide radical scavenging activity of 66% at 100 ppm concentration and 90% at 200 ppm concentration

and that it cleaned organic free radicals more effectively (18). The presence of polyphenols and other bioactive compounds in hazelnut bio-extracts made from both the hard shell and the green leafy covering are related to their antioxidant activity (19, 20). The hydroxyl groups in polyphenols, the potential for a donor-acceptor pathway, or the metal chelating impact all contribute to their antioxidant potential (21). The fruits, vegetables, and grains that we eat daily have antioxidant activity that is on par alongside and in certain cases even higher than bioextracts derived from hard shells and green leafy covering of hazelnut (22).

4. CONCLUSION

In the northwest of Azerbaijan, where common hazelnut (*Corylus avellana* L.) grows, the radical scavenging activity of bio-extracts obtained in 70% alcohol is $FRSA(hs)=59.24\%$ and $FRSA(glc)=35.72\%$. In contrast, in water, it is $FRSA(hs)=31.15\%$ and $FRSA(glc)=22.23\%$. The high concentration of phenolic compounds and other bioactive components with antioxidant activity accounts for the bio-extract's high relative sound attenuation (RSA) that was extracted from the hard shell. A comparison examination of the data reveals that, in terms of antioxidant indicators, the bio-extracts made from the hard shell and green leafy cover of hazelnuts cultivated in Azerbaijan with 70% ethanol are comparable to those made from hazelnuts grown in other nations. Compared to the antioxidant activity of fruits, vegetables, and cereals that we eat on a regular basis, the RSA activity of bio-extracts made from solid and green bark is comparable and, in certain instances, even higher. Another benefit of bio-extracts from the hard shell and green leafy covering is that, in contrast to fruits

and vegetables, they are year-round and can be produced year-round. Additionally, because they are made from less expensive waste raw materials, they are accessible and economical.

5. REFERENCES

1. Tyug TS, Prasad KN, Ismail A. Antioxidant capacity, phenolics and isoflavones in soybean by-products. *Food Chem* [Internet]. 2010 Dec 1;123(3):583–9. Available from: [<URL>](#).
2. Muraveva DA. *Farmakoqnoziya*. 1981. 656 p.
3. Lovkova My, Rabinovich A, Ponomareva S, Buzuk G, Sokolova S. *Why plants treat*. Moscow: Nauka; 1990. 290 p.
4. Miralieva S, Kubalova L. Биологическая роль хрома. Современная научная технология. 2014;7(2):90–1.
5. Raxmanin O, Egorova N, Krasovskiy Q, Mixaylova R, Алексеева А. Кремний, его биологическое действие при энтеральном поступлении в организм и гигиеническое нормирование в питьевой воде. Обзор литературы. 2017;96(5):492–8. Available from: [<URL>](#).
6. Stévigny C, Rolle L, Valentini N, Zeppa G. Optimization of extraction of phenolic content from hazelnut shell using response surface methodology. *J Sci Food Agric* [Internet]. 2007 Dec 24;87(15):2817–22. Available from: [<URL>](#).
7. Contini M, Baccelloni S, Massantini R, Anelli G. Extraction of natural antioxidants from hazelnut (*Corylus avellana* L.) shell and skin wastes by long maceration at room temperature. *Food Chem* [Internet]. 2008 Oct 1;110(3):659–69. Available from: [<URL>](#).
8. Oğuzkan S, Uğraş S, Can M, Uzun A, Ülger S, Üzmez Ş, et al. Biological activity analysis of hazelnut (*Corylus avellana* L.) green shell and leaf extracts. *Kahramanmaraş Sütçü İmam Üniversitesi Doğa Bilim Derg* [Internet]. 2016;19(4):373–8. Available from: [<URL>](#).
9. Bayil Oguzkan S, Karadeniz S, Karagul B, Uzun A, Aksoy ES, Guler OO, et al. Effects of some adsorbents on the pre-purification of taxol (anticancer drug) from hazelnut nutshells. *Int J Pharmacol* [Internet]. 2018 Aug 1;14(6):835–40. Available from: [<URL>](#).
10. Thi Hanh Phuc D, Popovich Private Bag DG, Popovich DG. Screening for paclitaxel and other taxanes in kernel and shell of *Corylus avellana* (Hazelnut). *J Pharmacogn Phytochem* [Internet]. 2017;6(2):247–54. Available from: [<URL>](#).
11. Shahidi F, Alasalvar C, Liyana-Pathirana CM. Antioxidant phytochemicals in hazelnut kernel (*Corylus avellana* L.) and hazelnut byproducts. *J Agric Food Chem* [Internet]. 2007 Feb 1;55(4):1212–20. Available from: [<URL>](#).
12. Bottone A, Cerulli A, D’Urso G, Masullo M, Montoro P, Napolitano A, et al. Plant specialized metabolites in hazelnut (*Corylus avellana*) kernel and byproducts: An update on chemistry, biological activity, and analytical aspects. *Planta Med* [Internet]. 2019 Aug 27;85(11/12):840–55. Available from: [<URL>](#).
13. Rusu ME, Fizeşan I, Pop A, Gheldiu AM, Mocan A, Crişan G, et al. Enhanced recovery of antioxidant compounds from hazelnut (*Corylus avellana* L.) involucre based on extraction optimization: Phytochemical profile and biological activities. *Antioxidants* [Internet]. 2019 Oct 8;8(10):460. Available from: [<URL>](#).
14. Shahidi F, Ambigaipalan P. Phenolics and polyphenolics in foods, beverages and spices: Antioxidant activity and health effects – A review. *J Funct Foods* [Internet]. 2015 Oct 1;18:820–97. Available from: [<URL>](#).
15. Azizov F, Khalilov Z, Atayeva V, Mustafayev N, Imanlı H. Chemical composition and biological active substances from hazelnut green leafy covers. *J Turkish Chem Soc Sect A Chem* [Internet]. 2022 Nov 30;9(4):999–1006. Available from: [<URL>](#).
16. Ermakov A, Arasimovich V, Iarosh N, Peruanskiy I, Lukovnikova G, Ikonnikova M. *Metody biokhimicheskogo issledovaniia rastenii*. 1987. 430 p.
17. Atayeva V, Aslanov R. EPR-based study to monitor free radicals in treated silk fibroin with anthocyanins. *J Turkish Chem Soc Sect A Chem* [Internet]. 2022 Nov 30;9(4):1055–62. Available from: [<URL>](#).
18. Siriwardhana SSKW, Shahidi F. Antiradical activity of extracts of almond and its by-products. *J Am Oil Chem Soc* [Internet]. 2002 Sep;79(9):903–8. Available from: [<URL>](#).
19. Esposito T, Sansone F, Franceschelli S, Del Gaudio P, Picerno P, Aquino R, et al. Hazelnut (*Corylus avellana* L.) shells extract: Phenolic composition, antioxidant effect and cytotoxic activity on human cancer cell lines. *Int J Mol Sci* [Internet]. 2017 Feb 13;18(2):392. Available from: [<URL>](#).
20. Del Rio D, Calani L, Dall’Asta M, Brighenti F. Polyphenolic composition of hazelnut skin. *J Agric Food Chem* [Internet]. 2011 Sep 28;59(18):9935–41. Available from: [<URL>](#).
21. Fraga CG. Plant polyphenols: How to translate their in vitro antioxidant actions to in vivo conditions. *IUBMB Life* [Internet]. 2007 Jan 3;59(4–5):308–15. Available from: [<URL>](#).
22. Vingrys K, Mathai M, Ashton JF, Stojanovska L, Vasiljevic T, McAinch AJ, et al. The effect of malting on phenolic compounds and radical scavenging activity in grains and breakfast cereals. *J Food Sci* [Internet]. 2022 Sep 23;87(9):4188–202. Available from: [<URL>](#).



Targeting LIMK1 in Alzheimer's Disease: A Multifaceted Computational Investigation Involving ADMET, Virtual Screening, Molecular Docking, and Molecular Dynamics

Defne Eşkin¹ , Harun Nalçakan¹ , Gülbin Kurtay^{2*} , Yiğit Akkan² , Mazlum Türk² ,
Beril Uras² 

¹Ankara University, Department of Chemistry, Ankara, 06100, Turkey.

²Hacettepe University, Department of Chemistry, Ankara, 06800, Turkey.

Abstract: LIM domain kinases (LIMKs), which include LIMK1 and LIMK2, are key proteins in actin dynamics. On this basis, the inhibition of LIMK1 enhances dendritic spine density and size in dementia, reducing Alzheimer's disease (AD) effects. Therefore, several small molecules were discovered as potential therapeutic targets for AD. Herein, a pharmacophore-based virtual screening was employed to identify novel potential LIMK1 inhibitors. The pharmacophore model derived from the co-crystallized receptor structure of PubChem-329823760: LIMK1 (PDB ID: 5NXC) was then used for virtual screening. After applying Lipinski's rules and pharmacophore filters, 29 potential hits were identified. Molecular docking simulations were performed to determine the binding affinities of these candidates against LIMK1, with results ranging from -5.20 to -10.60 kcal/mol. Notably, PubChem-136621040 showed the highest binding affinity against the target protein, with a docking score of -10.60 kcal/mol, slightly surpassing the native ligand, PubChem-329823760, possessing a lower docking score of -9.80 kcal/mol. The drug-likeness and toxicity properties of target compounds were assessed through ADMET evaluations. A series of 75 nanosecond molecular dynamics (MD) simulations were conducted on the complexes generated by the best-docked molecule and the native ligand. RMSD, RMSF, SASA, and Rg calculations of their trajectories were also calculated. PubChem-136621040 possessed an average RMSD value of 0.23 nm, lower than the native ligand's 0.31 nm, indicating a greater binding stability. The RMSF results also revealed that the best-docked compound had a lower value (0.10 nm), while the native ligand possessed a value of 0.12 nm. The SASA values for both the native ligand and the best-docked compound were nearly identical, at 150.20 nm² and 150.80 nm², respectively. The Rg results demonstrated that both complexes maintained their rigidity throughout the simulation, with similar average values of 2.04 nm for the native ligand and 2.06 nm for the best-docked compound.

Keywords: ADMET, LIM kinases, molecular docking, molecular dynamics, virtual screening.

Submitted: April 5, 2024. **Accepted:** September 6, 2024.

Cite this: Eşkin D, Nalçakan H, Kurtay G, Akkan Y, Türk M, Uras B. Targeting LIMK1 in Alzheimer's Disease: A Multifaceted Computational Investigation Involving ADMET, Virtual Screening, Molecular Docking, and Molecular Dynamics. JOTCSA. 2024;11(4): 1425-40.

DOI: <https://doi.org/10.18596/jotcsa.1465547>

***Corresponding author's E-mail:** gulbinkurtay@hacettepe.edu.tr

1. INTRODUCTION

Alzheimer's disease (AD) is a neurodegenerative disorder that progressively decreases cognitive abilities, ultimately resulting in the death of the affected individuals. Recent studies have indicated that AD is the leading cause of dementia among older people (1,2). Remarkably, between 60 and 70% of cases in which the older population has increasing levels of cognitive impairment can be linked to Alzheimer's disease (3).

The emergence of abnormally expanded neuronal processes known as dystrophic neurites is one of the primary features of AD patients (4,5). Tau protein, a key indicator of AD pathology, accumulates in these neurites, and when this protein is hyperphosphorylated, it separates from microtubules and subsequently clumps together to form neurofibrillary tangles (6,7). LIM domain kinase proteins (LIMKs), which are essential regulators of the actin cytoskeleton and cellular motility, contribute to the pathophysiology of AD by causing tau to become hyperphosphorylated, which in turn

causes dystrophic neurites to develop and intensify the neurodegenerative cascade in AD (8–11).

The LIM kinase family is typically composed of two types of proteins, specifically LIM domain kinase 1 (LIMK1) and LIM domain kinase 2 (LIMK2). Despite sharing numerous structural similarities, these two macromolecules exhibit distinct expression and subcellular localization patterns, in addition to functional differences (12,13). LIMK1 protein is composed of 633 amino acids that encompass a

variety of functional domains. These domains include the LIM₁ and LIM₂ domains, the PDZ binding motif, and the serine/proline (Ser/Pro)-rich region (14). In addition, it also includes the kinase domain, which contains the S fragment and the nuclear localization signal (NLS) subdomain. It has also been demonstrated that the regulation of kinase activity is significantly influenced by the LIM and PDZ domains (15). The representation of these domains is depicted in Figure 1.

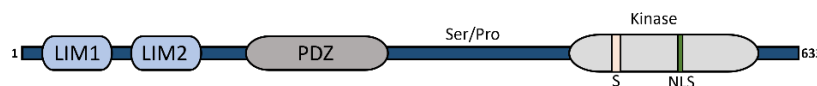


Figure 1: Domain architecture of LIMK1.

These proteins are essential for several physiological functions, including motility, cell cycle control, and brain development. It has been shown that these proteins control the phosphorylation activity of LIMK1 and LIMK2, which influences their capacity to phosphorylate and deactivate cofilin, an essential substrate. It is important to highlight that while LIMK2 is broadly expressed, LIMK1 is primarily present in neural tissues (16). Consequently, among these two proteins, inhibiting LIMK1 could have a more substantial impact on reducing the severity of AD by enhancing the size and density of dendritic spines (17).

In recent years, researchers have focused on the discovery of novel LIMK inhibitors, and various small molecules have been described in the literature. In research, Singh et al. employed similar *in silico* strategies, encompassing pharmacophore-based virtual screening, docking, and ADMET analyses, to identify novel compounds with inhibitory activities against LIMK1 in 2023. They constructed their pharmacophore models and successfully identified three virtual hits based on their compound (18).

In a parallel study, Rangaswamy et al. (2023) pinpointed five potential compounds for LIMK2 inhibition in cancer treatment, which was achieved through pharmacophore-based virtual screening, *in silico* ADMET studies, along with molecular docking and dynamics. Their research highlighted two out of the five compounds as promising candidates that could be further developed for cancer therapy (19).

In 2020, Zhang's group employed an *in silico* virtual screening approach to discover LIMK1 inhibitors for the purpose of inhibiting cell proliferation. Through *in silico* virtual screening, they identified a compound known as luteolin. Subsequent molecular docking assessments and experimental findings of their discovered compound indicated that it has demonstrated significant inhibitory activity against LIMK1 (20).

The literature inquiry offers a comprehensive insight into potential inhibitors of LIMKs and their possible therapeutic applications in various diseases, including neurological disorders and cancer. However, it has been noted that there are only a

limited number of studies specifically investigating the role of LIMK1 activity in Alzheimer's Disease. Therefore, in our study, we initially employed pharmacophore-based virtual screening to detect potential compounds to inhibit LIMK1 for AD treatment. In the subsequent step, the screened candidates were further evaluated with molecular docking simulation along with the determination of ADME (absorption, distribution, metabolism, excretion) profiles using various *in silico* techniques.

The toxicity properties of these screened molecules were also analyzed and calculated to reveal potential risks. Leveraging the findings of these calculations, candidate pharmaceuticals possessing the highest binding affinity and the complex of the native ligand with its macromolecule were further investigated with molecular dynamics simulation {PubChem-329823760: LIMK1 (*native ligand*) and PubChem-136621040: LIMK1 (best-docked ligand) complexes, respectively} to reveal root-mean-square deviation (RMSD), root-mean-square fluctuation (RMSF), solvent-accessible surface area (SASA), and radius of gyration (Rg) graphs to determine the post-dock analysis including binding stability of the system after the docking study, protein rigidity and residue interactions during the MD simulation.

In this scope, our study encompasses the identification and comprehensive analysis of novel LIMK1 inhibitors for the potential treatment of Alzheimer's Disease. Through advanced *in silico* methodologies, including pharmacophore-based virtual screening, molecular docking simulations, and ADME profiling, we aim to evaluate the efficacy, safety, and binding stability of candidate compounds. Furthermore, by employing molecular dynamics simulations, we assess the structural and dynamic behavior of these inhibitors, providing critical insights into their therapeutic potential against LIMK1-mediated neurodegeneration.

In this study, we employed an *in silico* approach to identify candidate molecules with the requisite characteristics for inhibiting the LIMK1 receptor, including the ability to permeate the blood-brain barrier, optimal pharmacokinetic properties, minimal toxicity, and robust binding affinity coupled with binding stability. Our research integrates

methodologies such as pharmacophore-based virtual screening, ADME/T evaluations using various web-based platforms to obtain enhanced pharmacological and pharmacokinetic profiles of the investigated ligands, molecular docking of the compounds to the target receptor, and molecular dynamics (MD) simulations to assess the stability of the docked complexes with LIMK1.

2. COMPUTATIONAL STUDIES

2.1. Pharmacophore-Based Virtual Screening

Pharmacophore-based virtual screening was performed using the Pharmit server (<http://pharmit.csb.pitt.edu>), which allows the use of several databases (PubChem, ZINC, ChEMBL, and Molport, etc.) to identify candidates potentially to inhibit LIMK1. To achieve this, input files of the structure of LIM domain kinase 1 (PDB ID: 5NXC), which is co-crystallized with its native ligand (PubChem-329823) obtained from the RCSB Protein Data Bank (www.rcsb.org), with no mutations in its protein sequence were submitted, and pharmacophore model based on the pharmacophore classes of the native ligand was generated on the server. The initial screening was conducted by applying this pharmacophore model, selecting the PubChem database, which contains a vast collection of 103,302,052 compounds. 419 compounds were discovered through the application of a pharmacophore filter at the initial step. Subsequently, Lipinski's filter was applied to these molecules to identify the desired compounds having the ideal drug-likeness properties. Therefore, parameters to provide the screened ligands to obey this rule were selected. The compounds possessing a molecular weight (MW) lower than 500 Da, hydrogen bond acceptor (HBA) not much than 10, hydrogen bond donor (HBD) less than 5, number of rotatable bonds (nROTb) no more than 10, and $\text{clogP}_{o/w}$ value less than 5 were intentionally configured to eliminate undesired compounds. A total of 78 candidates were successfully obtained following the application of Lipinski's filter. These compounds were further evaluated with the embedded docking application of Pharmit to detect the compounds whose RMSD values are less than 2.0 \AA^2 . As a result, 49 compounds out of 78 hits were also eliminated, and 29 compounds possessing the most desired drug-likeness characteristics were obtained for further analysis.

2.2. Molecular Docking Studies

The docking simulation aimed to generate a comprehensive viewpoint for potential pharmaceuticals that potentially demonstrate their binding ability against LIMK1. For this reason, the OneAngstrom SAMSON platform/2023-R1 software package's AutoDock Vina extension was used to forecast every step of the process, including docking validation, pre-docking preparation, and molecular docking simulations. To verify our chosen docking methodology, docking validation was initially performed, which involved a redocking of the initial conformation of the native ligand with the same structure using our docking parameters. Following this, the native compound was superimposed with

the docked compound, and the RMSD value was computed.

Consequently, pre-docking preparation was concluded for the LIMK1 crystal structure, which was retrieved from the RCSB Protein Data Bank (www.rcsb.org). The macromolecule's co-crystallized native ligand (PubChem-329823) was deleted, along with all ions and water molecules. Subsequently, necessary charges were applied, and hydrogens were included in the system. Since LIMK1 possesses only one chain, no modification, including chain removal, was carried out. Additionally, the target protein and the screened ligands were adjusted to a physiological pH of 7.4. The grid box size was set at $30.00 \times 24.90 \times 24.80 \text{ \AA}^3$ with a grid point spacing of 0.375 \AA , and the center coordinates of the grid box were defined as x: 18.60, y: 16.50, and z: 12.50. The coordinates were also derived using SAMSON, through the identification of the macromolecule's binding site. This operation was performed by selecting an area within a radius of 10.00 \AA around the native ligand.

Furthermore, a library of ligands was constructed from the input file, encompassing 29 potential inhibitors, which was generated in SDF format and downloaded from the Pharmit website. Before the docking procedure, our compounds underwent 5000 steps of energy minimization to determine their most stable conformations. Following the completion of the docking simulation, the top 10 compounds with the highest docking scores were intentionally selected, and their binding affinities, along with the molecular structures, were deeply investigated.

2.3. ADMET Studies

ADME (Absorption, Distribution, Metabolism, and Elimination) evaluations provide valuable insights into a drug's physiological responses and potential interactions. For this reason, evaluating a compound's suitability as a drug candidate requires more than just looking at its docking score; examination of ADME analyses is also necessary. Several web-based platforms, such as SwissADME, PreADMET, OSIRIS, and Molinspiration, were utilized to conduct ADME assessments to evaluate the drug-likeness properties and efficacy of the screened compounds. Furthermore, possible toxicity assessments were assessed using the Syntelly platform, which is based on the application of artificial intelligence to evaluate many toxicity parameters that identify potential negative effects of the pharmaceutical candidates.

2.3.1. SwissADME

SwissADME is a freely available online tool that provides a wide range of information and forecasts about small molecules' physicochemical and pharmacological properties. It also evaluates compounds' ADME, and drug-likeness profiles based on Lipinski's rule of five (RO5), which plays a significant role in drug discovery and development to identify ideal pharmacological properties for candidate small molecules (21). The rule of five outlines essential criteria for assessing the suitability of a compound for drug development. These criteria include a molecular weight (MW) of no more than 500

g/mol, a maximum of 10 hydrogen bond acceptors (HBAs), less than 5 hydrogen bond donors, $\log P_{o/w}$, which indicates the partition coefficient between octanol and water, used to evaluate lipophilicity characteristics not exceeding 5, and topological polar surface area (TPSA) below 140 Å². Moreover, compliance with the rule dictates that the number of rotatable bonds (nROTBs) in a potential pharmaceutical should be less than 9 (22).

2.3.2. PreADMET

ADME properties of our compounds were determined using the PreADMET platform (<http://preadmet.bmdrc.org/>). In this scope, blood-barrier permeability (BBB), passive gastrointestinal absorption (HIA), and protein-plasma binding abilities (PPB) were detected. BBB could be computed as the ratio of steady-state concentrations of radiolabeled compounds in the brain to that in the peripheral blood (23). It is noteworthy that compounds with BBB values less than 0.10 are considered to have low CNS absorption, those with values between 0.10 and 0.20 exhibit moderate absorption, and those with values exceeding 0.2 are characterized by high CNS absorption capacity (24). Furthermore, plasma protein binding (PPB) denotes the extent of interaction between pharmaceutical compounds and various plasma proteins, including human serum albumins (HSAs), present in the bloodstream. This parameter is critical for predicting the pharmacokinetic profile of a drug, particularly in terms of its distribution within the body, and for assessing the proportion of the drug that effectively reaches its target site of action (25).

2.3.3. OSIRIS property explorer

Mutagenicity, tumorigenicity, skin irritability, and reproductive effectiveness assessments of our investigated molecules were completed through the application of the OSIRIS Property Explorer (v.4.5.1), which is a freely downloadable tool (<http://www.organic-chemistry.org/prog/peo/>).

In addition to these assessments, two descriptors, namely drug-likeness (d) and drug score (ds), were also analyzed to support our findings. Therefore, a mathematical approach to the drug-likeness parameter and drug-score evaluation were also implemented, and all results were tabulated in Table 4. Calculation of the drug-likeness (d) of the hit compounds was assessed with Equation 1, where V_i indicates scores of molecular fragments and n denotes the number of molecular fragments.

$$d = \frac{\sum V_i}{\sqrt{n}} \quad (1)$$

Equation 2 is utilized to obtain the drug-score (ds) values of the compounds, where the s_i represents the contributions calculated directly from clogP, logS, molecular weight, and drug-likeness, and t_i represents the contribution taken from the four toxicity risk classes.

$$ds = \pi \left(\frac{1}{2} + \frac{1}{2} s_i \right) \cdot \pi t_i \quad (2)$$

2.3.4. Molinspiration

Along with ADME calculations, potential bioactivities such as G-coupled protein receptor ligand (GPCR), ion-channel modulator (ICM), kinase inhibitor (KI), nuclear receptor ligand (NRL), protease inhibitor (PI), and enzyme inhibitor (KI) were revealed via Molinspiration (<https://www.molinspiration.com>) platform. Notably, G protein-coupled receptors (GPCRs) are an important group of signaling proteins that mediate the responses of cells to a wide range of substances, including hormones, metabolites, cytokines, and neurotransmitters. In addition, ion channels support several cellular functions, including fast cellular rearrangements, heart and skeletal muscle contraction, hormone synthesis, immunological reaction, and tumor cell growth. Furthermore, NRLs are transcription factors that are induced by ligands and, upon translocation to the nucleus, directly influence the transcription of genes, which are essential to several important physiological functions (26). It is essential to note that the assessment of the kinase inhibition (KI) descriptor is of significant importance in determining the bioactivity of the screened candidates against the LIM kinase 1 protein to support the binding scores of our analyzed candidates. The following ranges could be considered in determining the bioactivities: ratings greater than 0.00 indicate substantial bioactivity. Scores that fall within the range of -0.50 to 0.00 represent moderate activity. Bioactivity scores less than -0.50 are considered to indicate inactivity (27).

2.3.5. Syntelly

Syntelly is an online web tool that utilizes artificial intelligence (AI) to accelerate the physicochemical properties, drug-likeness assessments, and toxicity effectiveness of organic compounds. In our study, we have evaluated an alternative perspective on the toxicity profiles of the screened ligands and their drug-likeness properties. For this reason, various toxicity properties, namely Mouse Oral LD₅₀, reproductive toxicity, hepatotoxicity, cardiotoxicity, and carcinogenicity, were predicted to reveal the potential toxicity risks of the investigated candidates.

2.4. Molecular Dynamics

Molecular Dynamics (MD) is a computational simulation commonly employed to evaluate the physical motion of larger molecular systems, with a particular emphasis on protein-ligand complexes. In the most prevalent approach, the trajectories of molecules are ascertained based on Newton's law equations for a system of interacting particles. In this scope, LIMK1: PubChem-136621040, which exhibited the highest docking score, was subjected to MD simulation alongside LIMK1: *native ligand* (PubChem-329823760), serving as the reference protein-ligand complex. The input files of the optimal conformations of these complexes were derived from the docking simulation, and all processes were conducted using the GROningen Machine for Chemical Simulations (GROMACS) 2023.3 software package (28). The preprocessing step was accomplished by selecting the CHARMM36 force field and the TIP3P water model. Subsequently, electrostatic interactions were computed using the

Particle Mesh Ewald (PME) method, with a Fourier spacing of 0.16 nm and a short-range cut-off of 1.2 nm employed for electrostatic treatment. Following the addition of chloride ions to neutralize the system of the complexes, energy minimization was undertaken with 5000 steps of the steepest descent minimization method until the maximum force was less than $10.0 \text{ kJmol}^{-1}\text{nm}^{-1}$. Consequently, system equilibration was performed in two phases, comprising a constant number of particles, volume, and temperature (NVT) ensemble and a continuous number of particles, pressure, and temperature (NPT) ensemble with 5000 steps of steepest descent equilibration. The temperature was escalated within 100 ps in the NVT ensemble and maintained at 300 K with the Berendsen Thermostat to satisfy the room temperature, succeeded by the NPT ensemble at 1 bar for 100 ps. 75 ns MD simulation was completed for both complexes, and corresponding calculations, including root-mean-square deviation (RMSD), root mean square fluctuation (RMSF), solvent-accessible surface area (SASA), and radius of gyration (Rg), were also generated with the GROMACS package to elucidate various dynamic behaviors of our investigated systems.

2.4.1. Root mean square deviation (RMSD) analysis

Root Mean Square Deviation (RMSD) is a metric used to evaluate the average distance between atoms in proteins or ligands that are superimposed after simulation, particularly those that form the backbone. RMSD makes it easier to compare structural differences between different conformational states of proteins or protein-ligand complexes. To calculate the RMSD, the two selected structures must be superimposed. Then, the squared deviation between the coordinates of the respective atoms must be calculated, and the square root of the mean of these squared deviations must be extracted (29). In this context, the conformational stability of complexes during Molecular Dynamics (MD) simulations is often evaluated by the creation of RMSD charts, which may be easily completed with GROMACS.

The following equation (Equation 3) represents the mathematical calculation of RMSD.

$$RMSD = \sqrt{\frac{\sum_{i=1}^N m_i (r_i - r_i')^2}{\sum_{i=1}^N m_i}} \quad (3)$$

2.4.2. Root mean square fluctuation (RMSF) analysis

Root Mean Square Fluctuation (RMSF) is a statistical approach employed to quantify how a particle, including a protein residue, varies from its initial position over a period. It provides important information about areas of a protein that deviate from the typical structure or show the highest degree of flexibility. RMSF is widely used in simulations to identify regions of a protein that exhibit significant flexibility or rigidity (30). RMSF facilitates the evaluation of residue flexibility by helping to identify fluctuating regions during simulations, providing insight into the ways in which ligand binding affects protein flexibility. The formula for computing RMSF is shown in the following equation (Equation 4).

$$RMSF = \sqrt{\frac{1}{N} \sum_j^N (x_{i(j)} - \langle x_i \rangle)^2} \quad (4)$$

2.4.3. Solvent-accessible surface area (SASA) investigation

Surface area of a biological system that is accessible to a solvent is measured by the Solvent-Accessible Surface Area (SASA) method. It is usually computed using a rolling ball algorithm, which examines the molecule's surface using a sphere that represents the solvent of a specific radius (31). The transfer of free energy needed to move a biomolecule from an aqueous solvent to a non-polar solvent, like a lipid environment, is frequently computed using SASA. SASA analysis is especially essential in the context of MD simulations of protein-ligand complexes since it is utilized to estimate the non-polar solvation-free energy, which is a significant part of the protein-ligand complex's binding free energy. The biological activity of the ligand is influenced by the binding free energy, which is a crucial factor in determining the binding affinity between the protein and the ligand. SASA also sheds light on how a ligand interacts with a protein and changes its structure. SASA variations show that the protein is going through significant structural changes in certain areas, which may have an impact on its function. The SASA of the protein-ligand compound is often evaluated during MD simulations at different intervals, providing a real-time view of how the molecule's solvent accessibility changes over time.

2.4.4. Radius of gyration (Rg) assessment

A molecule or a group of atoms can be evaluated for size and structure using the radius of gyration (Rg). It offers a view of the molecule's general shape and spatial extent by revealing the distribution of mass with respect to its center of mass. Rg can be used to monitor conformational changes, such as those that occur during folding or unfolding events, or to characterize the compactness of a molecular structure over time (32). By quantifying this dispersion, Rg helps characterize the compactness, flexibility, and conformational changes of macromolecules during the MD simulation. It offers important details about the size and shape of macromolecules and their dynamics. Mathematically, Rg is defined as the root mean square distance of each particle from the center of mass in Equation 5.

$$Rg = \sqrt{\frac{1}{N} \sum_{i=1}^N m_i \cdot r_i^2} \quad (5)$$

3. RESULTS AND DISCUSSION

3.1. Molecular Docking Studies

3.1.1. Docking validation

Docking validation was initially completed to verify our specified docking methodology. This was achieved by removing the native ligand from the crystal structure and conducting a molecular docking simulation with the same compound, a process known as redocking. The original compound (depicted in green) was then superimposed with the docked compound (shown in blue), and the Root Mean Square Deviation (RMSD) value, measuring the

difference between these two conformations, was determined to be 1.6 Å (Figure 2).

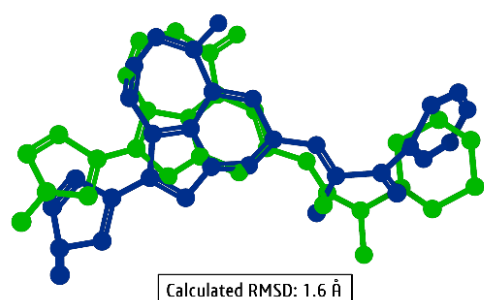
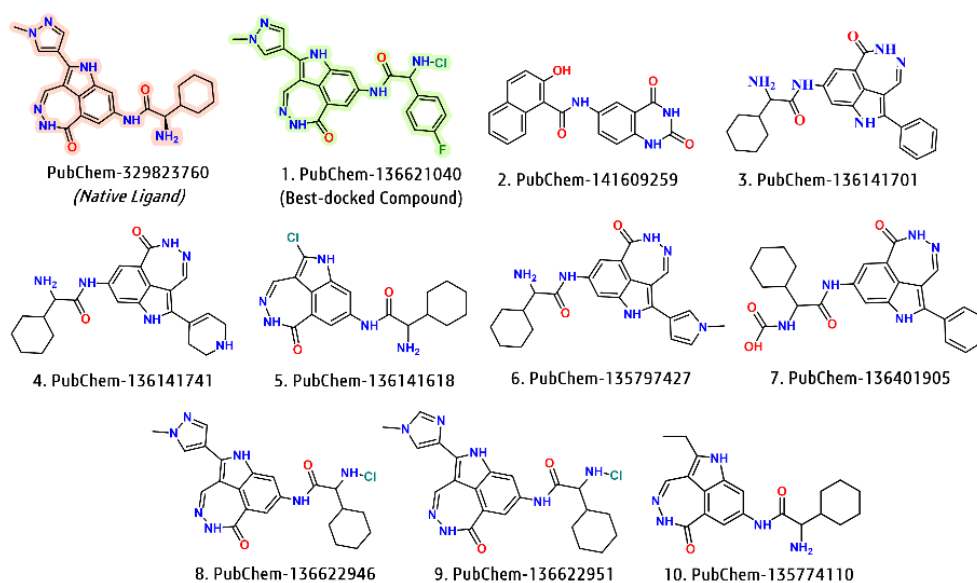


Figure 2: Superimposition of the redocked PubChem-329823760 (*blue*) onto its initial conformation in the active site of LIMK1 (RMSD: 1.6Å).

3.1.2. Docking results

The main purpose of this analysis is to conduct an extensive molecular docking investigation to assess the inhibitory potential of 30 candidate drugs against the LIMK1 receptor (PDB ID: 5NXC). The binding scores of the top 10 ligands, which exhibited the highest binding affinity to the macromolecule, are presented in Table 1, accompanied by the 2D structures of the analyzed ligands. Figure 3, in addition, provides a visual representation of the binding poses and residue interactions between LIMK1 and the best-docked ligand (PubChem-136621040). Moreover, the binding pose and residue interaction of LIMK1 with the native ligand were also depicted. Docking scores, binding poses, and residue interactions of the remaining 20 virtual hits were given in electronic supplementary material in Table S5-S6, and Figure S6, respectively.

Table 1: Docking scores and 2D structure representations of the top 10 ligands.



PubChem ID	Docking Scores (kcal/mol)
329823760 (<i>Native ligand</i>)	-9.80
136621040	-10.60
141609259	-10.10
136141701	-10.00
136141741	-10.00
136141618	-9.80
135797427	-9.60
136401905	-9.50
136622946	-9.50
136622951	-9.50
135774110	-9.30

Our findings have revealed that the binding affinities of the 30 screened molecules ranged from -5.20 to -10.60 kcal/mol. Among these 30 virtual hits, docking scores of the top 10 compounds were specifically selected to evaluate their binding potentials. For the top-ranked four ligands, specifically PubChem-136621040 (-10.60 kcal/mol), PubChem-141609259 (-10.10 kcal/mol), PubChem-136141701 (-10.00 kcal/mol), and PubChem-136141741 (-10.00 kcal/mol), exhibited relatively higher binding affinities in comparison with the native ligand {PubChem-136621040 (-9.80 kcal/mol)}. In

addition, PubChem-136141618 (-9.80 kcal/mol) showed an identical binding potential with the reference ligand. Subsequently, the remaining compounds including, PubChem-135797427 (-9.60 kcal/mol), PubChem-136401905 (-9.50 kcal/mol), PubChem-136622946 (-9.50 kcal/mol), and PubChem-136622951 (-9.50 kcal/mol) demonstrated lower binding potentials, indicating weaker binding interactions with the residues of LIMK1 receptor (Figure 3).

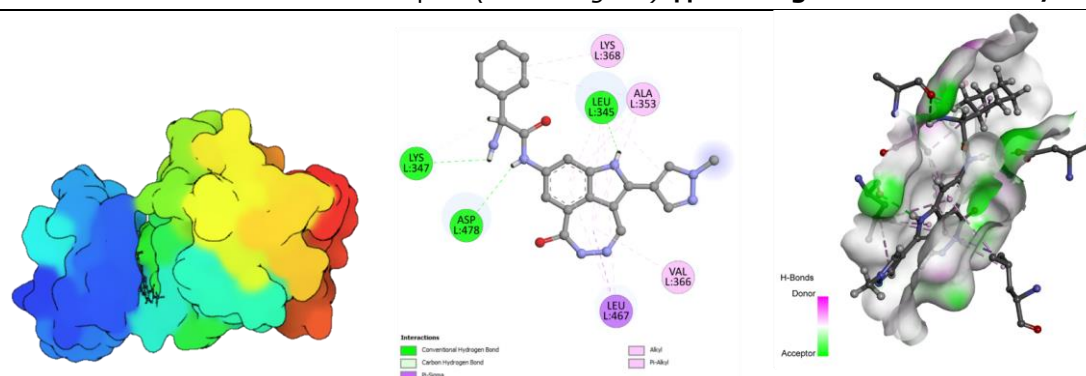
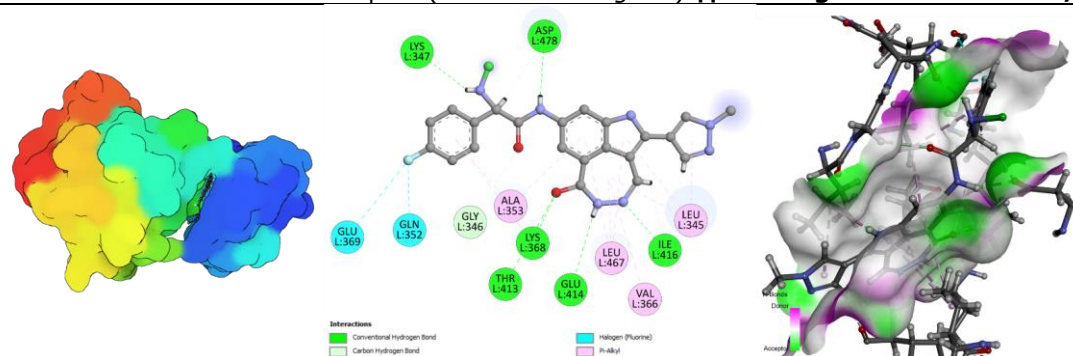
PubChem-329823760: LIMK1 complex (*Native Ligand*) || Binding score: -9.80 kcal/molPubChem-136621040: LIMK1 complex (*Best-docked Ligand*) || Binding score: -10.6 kcal/mol

Figure 3: Binding poses and residue interactions of the native and the screened ligand with LIMK1 (PDB ID: 5NXC).

It is crucial to state that the highest-ranked compound that possessed -10.60 kcal/mol has shown relatively greater binding affinity among these virtual hits in terms of its docking score. Therefore, we have also checked the patent status of the compound. The findings revealed that the molecule had been previously identified in a patent document as an inhibitor of checkpoint kinase 1 (CHK-1 or p56CHK-1), a member of the kinase family. With respect to the binding poses and residue interactions of the native ligand LIMK1 complex (PubChem-329823760), the diazepinoindole subunit of the compound was found to interact with a variety of amino acid residues, including LEU345, LEU467, ALA353, and VAL366. A range of intermolecular interactions were identified between the ligand and the residues, encompassing hydrogen bond interactions, pi-alkyl interactions, and pi-sigma interactions. Various hydrogen bond interactions were also observed with several residues, namely LYS347, LYS368, and ASP478. Our analyzed compound, which exhibited the highest docking score (PubChem-136321040), demonstrated a greater number of residue interactions with the LIMK1 receptor. The diazepinoindole fragment of the ligand showed a higher degree of residue interactions, including various hydrogen bond interactions with residues LYS368, THR413, GLU414, and ILE416, in addition to pi-alkyl interactions with residues ALA353, LEU345, LEU467, and VAL366. Other interactions were observed with residues LYS347 and ASP478. Hydrogen bond interactions were also detected with these two amino acids. Additionally, the substitution of the fluorobenzene unit in our compound with the cyclohexyl fragment

present in the structure of the native ligand enabled the formation of interactions with an increased number of amino acids, including the halogen interactions with GLU352 and GLU369. This could consequently lead to an increase in the docking score of this ligand.

3.2. Prediction of ADMET, Drug-likeness and Pharmacokinetic Properties

3.2.1. SwissADME analysis

SwissADME server was employed to elucidate the pharmacological characteristics of our potential inhibitory agents against the LIMK1 receptor. Within this context, the results for the top 10 compounds were listed in Table 2, whereas the data for the remaining 20 compounds can be found in Table S1 in the electronic supplementary information (ESI[†]). The evaluation process was guided by Lipinski's rule of five. All the compounds demonstrated molecular weights under 500 Da, thereby satisfying the set benchmark. Furthermore, the analysis of hydrogen bond acceptors (HBA) and hydrogen bond donors (HBD) was in accordance with the rule of five, suggesting the compounds possess desirable drug-like characteristics. Analysis of the number of rotatable bonds (nROTB), highly influencing molecular flexibility, revealed that our candidate compounds adhered to the ideal pharmaceutical limit of 9. Importantly, all candidate compounds exhibited topological polar surface area (TPSA) values that were below the threshold of 140 Å², which is indicative of favorable drug absorption potential. Therefore, the majority of our candidate compounds demonstrated a high potential for gastrointestinal absorption. However, four compounds, namely

PubChem-136401905, PubChem-135774106, PubChem-136181657, and PubChem-135794603, were exceptions to this trend. Consensus $\log P_{o/w}$ was

also assessed to evaluate lipophilicity, and all the molecules that ranged from -0.79 to 3.69 showed the desired values that obey Lipinski's rule.

Table 2: ADME Results of the top 10 candidate pharmaceuticals possessing the highest docking scores.

PubChem ID	^a MW (Da)	^b HBA	^c HBD	^d nROTB	^e TPSA (\AA^2)	^f GI abs.	^g BBB	^h clogP _{o/w}	Sol.	Violation
329823760	419.48	5	4	5	134.48	High	No	2.85	PS	0
136621040	465.87	6	4	6	120.49	High	No	2.54	S	0
141609259	347.32	4	4	3	115.05	High	No	2.39	MS	0
146582701	262.29	3	4	3	115.34	High	No	0.57	S	0
136141741	420.51	5	5	5	128.69	High	No	2.22	S	0
136141618	373.84	4	4	4	116.66	High	No	2.54	S	0
135797427	418.49	4	4	5	121.59	High	No	2.56	S	0
136401905	459.50	5	5	7	139.97	Low	No	3.19	MS	0
136622946	453.92	5	4	6	120.49	High	No	2.58	MS	0
136622951	453.92	5	4	6	120.49	High	No	2.45	MS	0
135774110	367.44	4	4	5	116.66	High	No	2.61	S	0

Lipinski's Rule: ^aMW ≤ 500g/mol, ^bHBA ≤ 10, ^cHBD ≤ 5, ^dnROTB ≤ 9, ^eTPSA ≤ 140 \AA^2 , ^fclogP_{o/w} ≤ 5

Abbreviations: ^aMW: Molecular Weight, ^bHBA: Hydrogen Bond Acceptor, ^cHBD: Hydrogen Bond Donor, ^dnROTB: Number of Rotatable Bonds, ^eTPSA: Topological Polar Surface Area, ^fGI abs: Gastrointestinal absorption, ^gBBB: Blood-brain Barrier Permeability, ^hclogP_{o/w}: Consensus ^hclogP_{o/w}, IS: Insoluble, PS: Poorly Soluble, MS: Moderately Soluble, S: Soluble, HS: Highly Soluble.

Among these parameters, the descriptor that assesses blood-brain barrier permeability (BBB) that determines whether the investigated compounds permeate the central nervous system (CNS) plays a critical role in the development of novel drug molecules against Alzheimer's Disease. It was deduced from SwissADME findings that our screened candidates possessed no BBB permeability. Given that these initial calculations did not yield definitive results, particularly in terms of quantifying BBB permeability, we intended to elucidate the CNS permeability of our using additional in silico platforms, which were discussed in the following section.

We have also employed the BOILED-Egg (Brain or Intestinal Estimated Permeation) graphical tool, integrated within the SwissADME platform, to evaluate the passive permeability of the blood-brain barrier, represented by the yellow region, and the passive gastrointestinal absorption (HIA), represented by the white region. These assessments are based on the positioning of the molecules, calculated using the total area of the WLOGP versus TPSA (Wildman & Crippen, 1999). The BOILED-Egg representation of our analyzed pharmaceuticals is given in Figure 4.

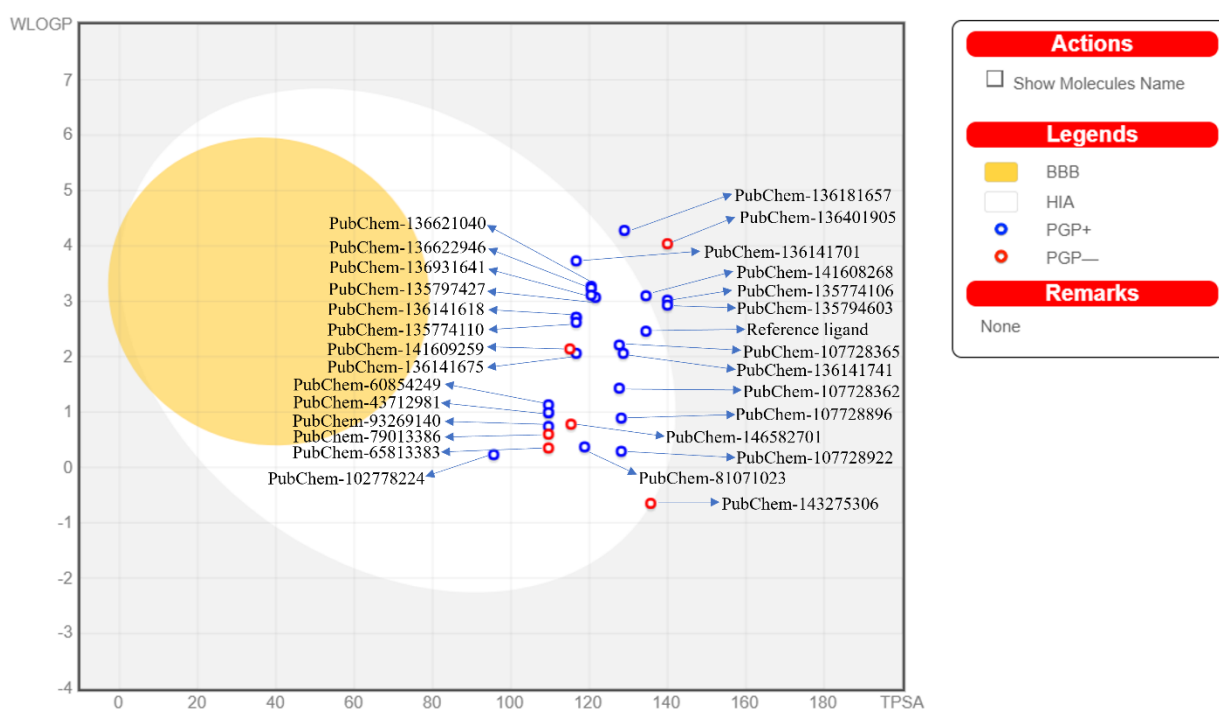


Figure 4: BOILED-EGG representation: Prediction of passive gastrointestinal absorption and passive brain penetration of candidate molecules.

The prediction of P-glycoprotein (P-gp) substrates is crucial, as it is the primary active efflux mechanism implicated in various biological barriers, including the blood-brain barrier. This could be visually represented and evaluated through a color-coded graphical depiction. Passive absorption is indicated by the positioning within or outside the white zone, while passive brain access is denoted by the positioning within or outside the yellow region. The active efflux from the central nervous system or into the gastrointestinal lumen is represented by color-coding: blue dots for P-gp substrates (PGP⁺) and red dots for non-P-gp substrates (PGP⁻). From the graphical representation, it is evident that the majority of our molecules, including PubChem-329823760 (the reference ligand) and PubChem-136621040 (which has the highest docking score against the receptor), are located within the white region of the egg. This suggests that the gastrointestinal system could passively absorb these compounds.

Conversely, several compounds, namely PubChem-136181657, PubChem-136401905, PubChem-141608268, and PubChem-135794603, were unable to traverse the gastrointestinal system passively. As a result, no passive permeation of the BBB was observed with our candidate compounds. Interestingly, compounds denoted as blue dots (PGP⁺) have successfully crossed the central nervous system actively, while those denoted with red dots (PGP⁻) were unable to permeate the CNS actively. Excluding PubChem-136141675, PubChem-79013386, PubChem-65813383, PubChem-146582701, PubChem-143275306, and PubChem-136401905, our compounds have successfully

crossed the CNS, including our best-docked compound (PubChem-136621040) and the native ligand.

Bioavailability radars serve as valuable tools for visually presenting computed physicochemical and pharmacological attributes of potential drug candidates concerning oral drug characteristics, offering insights into their potential oral bioavailability. These radars depict parameters including lipophilicity (LIPO), molecular weight (SIZE), polarity (POLAR), insolubility (INSOLU), unsaturation (INSATU), and flexibility (FLEX). Figure 5 illustrates the bioavailability radars of a reference ligand (PubChem-329823760) and the ligand exhibiting the highest binding affinity (PubChem-136621040) against LIMK1. Parameters crucial for the oral bioavailability of our lead molecule, characterized by the highest docking score, fell within the desired range except for saturation in comparison to the reference ligand. Saturation, delineated by the proportion of carbons in sp³ hybridization within the molecule, ideally falls between 0.25 and 1.

However, a saturation value of 0.09 was observed for our compound, resulting in a deviation from the designated pink hexagonal region. Radar representations of other scrutinized ligands are available in the supplementary material (ESI⁺). These radar plots similarly indicate that the oral availability potential of these candidate molecules conforms to an ideal trend, falling within the pink hexagonal area, except for PubChem-136141701, where the saturation value deviates from the ideal, akin to the highest-docked compound.

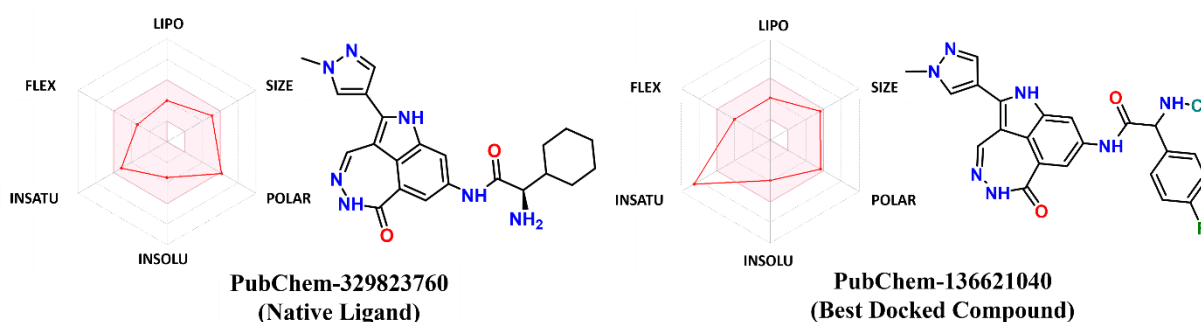


Figure 5: Bioavailability radar representations and structures of the native ligand and best-docked compound.

3.2.2. PreADMET calculations

Our findings showed that most of the candidate pharmaceuticals exhibited substantial absorption capabilities through the central nervous system (CNS) and, consequently, the blood-brain barrier (BBB), with values ranging from 0.01 to 0.35. The native ligand, in comparison, showed a relatively lower absorption with a BBB value of 0.12. Notably, our top-docked compound demonstrated a BBB value of 0.20, indicating its high absorption potential through the BBB. We have also evaluated the passive gastrointestinal absorption, denoted as HIA, and plasma-protein binding (PPB) capacities of our

compounds. The majority of compounds exhibited over 70% passive absorption through the gastrointestinal system except PubChem-143275306 (44.70%), PubChem-107728922 (46.96%), and PubChem-107728896 (49.31%). Specifically, PubChem-136621040 (the best-docked molecule) displayed an impressive HIA value of 89.50%, while the native ligand (PubChem-136621040) had a value of 82.70%. The PPB capacities of our compounds varied from 0.00% to 92.24%. Our compound demonstrated a significantly higher plasma-protein binding capacity (88.00%) compared to the native ligand, which had a value of 50.95% (Table 3).

Table 3: Various ADME profiles of the top 10 compounds with the highest binding affinities.

PubChem ID	BBB ^a ([brain]/[blood])	HIA ^c (%)	PPB ^e (%)
329823760	0.12	82.70	50.95
136621040	0.20	89.50	88.00
141609259	0.04	90.80	78.70
146582701	0.53	87.11	87.29
136141741	0.15	78.64	28.05
136141618	0.22	83.67	46.55
135797427	0.27	85.50	64.53
136401905	0.34	83.45	84.98
136622946	0.35	87.75	86.05
136622951	0.30	87.74	82.83
135774110	0.29	80.76	56.29

Abbreviations: ^aBBB: Blood-brain barrier, ^cHIA: Passive gastrointestinal absorption, ^ePPB: Plasma-protein binding

The rule for BBB permeability: <0.1 low absorption by CNS, between 0.1 and 0.2 moderate absorption, >0.2 high absorption

3.2.3. OSIRIS property explorer analysis

Toxicity risk factors of the compounds, including mutagenicity, tumorigenicity, skin irritability, and reproductive effectiveness, were evaluated using OSIRIS software. Additionally, the studied ligands' drug-likeness characteristics and drug scores were assessed to assess the compounds further, and the results of the top 10 compounds possessing the highest docking scores were illustrated in Table 4. The results of the remaining screened candidates were provided in Table S2 in the electronic supplementary information (ESI⁺).

In the context of mutagenicity assessment, select compounds, namely PubChem-136621040, PubChem-136622946, PubChem-136622951, PubChem-135774106, and PubChem-135794603, demonstrated moderate toxicity, while PubChem-141609259, PubChem-136141701, PubChem-136401905, and PubChem-146582701 exhibited high toxicity. Conversely, the remaining ligands exhibited negligible toxicity. Remarkably, the initial 18 ligands, characterized by the highest binding affinities, displayed significant tumorigenic potential, contrasting with the absence of toxicity indications in

other ligands. Moreover, PubChem-136141701, PubChem-136401905, and PubChem-141608268 exhibited notable irritancy and reproductive toxicity, while others showed minimal to no such effects. Regarding drug-likeness (d), the compound with the best binding score (PubChem-136621040) showcased the highest value at 7.46, surpassing the reference ligands' 1.34, with other ligands ranging from -52.96 to +4.07. Notably, most investigated ligands exhibited superior drug-likeness compared to the reference. Additionally, drug-score values, which is another mathematical approach used to calculate pharmacological features of the studied compounds, ranged from 0.05 to 0.78.

3.2.4. Molinspiration studies

Bioactivity scores and pharmacological aspects of the compounds were also investigated using the Molinspiration Property Calculation tool. Table 5 presents the bioactivity scores of the ligands, and drug-likeness analysis results are listed in Table 6. The remaining results were tabulated in the electronic supplementary information (ESI⁺) in Table S5 and Table S6.

Table 4: Toxicity results of the studied candidates.

PubChem ID	Mut	Tum	Irr.	Rep. E.	d	ds
329823760	●	●	●	●	+1.34	0.33
136621040	●	●	●	●	+7.46	0.27
141609259	●	●	●	●	-2.64	0.12
136141701	●	●	●	●	+0.55	0.05
136141741	●	●	●	●	+0.85	0.32
136141618	●	●	●	●	+0.50	0.31
135797427	●	●	●	●	+1.24	0.33
136401905	●	●	●	●	+3.26	0.05
136622946	●	●	●	●	+3.74	0.25
136622951	●	●	●	●	+4.07	0.28
135774110	●	●	●	●	+0.68	0.32

Abbreviations: Mut: Mutagenic, Tum: Tumorigenic, Irr: Irritation, Rep. E: Reproductive effectiveness, d: Drug-likeness, ds: Drug Score

● No detectable toxicity ● Moderate toxicity ● High toxicity

Table 5: Bioactivity calculations against several receptors of the top 10 molecules with the best docking scores.

PubChem ID	GPCR	ICM	KI	NRL	PI	EI
329823760	0.04	-0.14	0.40	-0.88	-0.04	0.19
136621040	-0.12	-0.30	0.29	-0.72	-0.38	-0.02
141609259	-0.03	-0.25	0.05	-0.20	-0.14	0.04
136141701	0.05	-0.03	0.31	-0.52	0.05	0.23
136141741	0.20	0.09	0.34	-0.51	0.07	0.31
136141618	0.10	0.04	0.31	-0.67	0.07	0.25
135797427	0.14	-0.03	0.51	-0.41	-0.08	0.34
136401905	0.13	0.00	0.19	-0.40	0.15	0.25
136622946	-0.04	-0.17	0.28	-0.81	-0.23	0.07
136622951	0.17	0.04	0.45	-0.44	-0.01	0.35
135774110	-0.02	-0.06	0.22	-0.67	-0.01	0.20

Abbreviations: GPCR: G protein-coupled receptor ligands, ICM: Ion Channel Modulator, KI: Kinase Inhibitor, NRL: Nuclear Receptor Ligand, PI: Protease Inhibitor, EI: Enzyme Inhibitor

Various bioactivity descriptors were effectively computed using the Molinspiration platform, including G protein-coupled receptor ligands (GPCRL), ion-channel modulators (ICM), kinase inhibitors (KI), nuclear receptor ligands (NRL), protease inhibitors (PI), and enzyme inhibitors (EI). As discussed, a bioactivity score exceeding 0.00 denotes significant bioactivity, while values within the range of -0.50 to 0.0 indicate moderate bioactivity, and those below -0.50 indicate a lack of bioactivity. The GPCR inhibitory activity values for these compounds ranged from -0.12 to +0.46, demonstrating bioactivity levels ranging from moderate to significant. Similarly, ICM values varied from -0.30 to +0.24, indicating moderate or

significant bioactivity against ion-channel modulators. NRL capabilities were relatively lower compared to other descriptors, with values ranging from -0.92 to -0.01, suggesting either a lack of bioactivity or moderate bioactivity for certain compounds. Protease and enzyme inhibitory activity also ranged from moderate to high, with values spanning from -0.38 to +0.48 and -0.02 to +0.48, respectively. Notably, kinase inhibition capability emerged as the most crucial descriptor for our investigated candidates, with the top 10 compounds effectively inhibiting kinase proteins, including LIM kinase proteins, with values ranging from -0.66 to +0.51.

Table 6: ADME Assessments of the top 10 ligands having the highest docking score.

PubChem ID	mi-LogP ^a	TPSA ^b	nAtoms ^c	nON ^d	nOHNH ^e	nROTB ^f	Volume	Violation
329823760	1.25	134.49	31	9	5	4	375.50	0
136621040	2.21	120.50	33	9	4	5	376.50	0
141609259	2.60	115.05	26	7	4	2	290.78	0
136141701	2.87	116.67	31	7	5	4	377.73	0
136141741	1.24	128.69	31	8	6	4	385.70	1
136141618	2.00	116.67	26	7	5	3	319.86	0
135797427	1.78	121.60	31	8	5	4	379.66	0
136401905	4.82	139.97	34	9	5	5	405.85	0
136622946	2.74	120.50	32	9	4	5	390.15	0
136622951	2.30	120.50	32	9	4	5	390.15	0
135774110	2.00	116.67	27	7	5	4	339.69	0

Abbreviations: ^amiLogP: Partition coefficient between n-octanol and water (logP_{o/w}), ^bTPSA: Topological polar surface area, ^cnAtoms: Number of atoms, ^dnON: Number of hydrogen bond acceptors (HBA), ^enOHNH: Number of hydrogen bond donors (HBD), ^fnROTB: Number of rotatable bonds

Likewise, ADME analyses were conducted using the Molinspiration platform to corroborate the previous findings obtained from OSIRIS and SwissADME. Thus far, parameters including Hydrogen Bond Acceptors (HBA), Hydrogen Bond Donors (HBD), and the number of Rotatable Bonds (nROTB) have been

determined to adhere to Lipinski's rule, indicating favorable drug-likeness. Furthermore, the lipophilic characteristics of the candidate compounds, assessed through miLogP values, were within the prescribed range, with all compounds falling below the upper limit of miLogP (5), thereby aligning with

Lipinski's rule. This comprehensive evaluation underscores the compatibility of the identified hits with established criteria for drug development, further validating their potential as viable therapeutic candidates.

3.2.5. Syntelly calculations

Several toxicity characteristics of our candidate pharmaceuticals were assessed through the Syntelly platform, an online AI-powered compound characterization tool. In this scope, mouse oral LD₅₀, hepatotoxicity, cardiotoxicity, and carcinogenicity characteristics of our investigated compounds were

calculated. The findings suggest that the LD₅₀ values of our target molecules ranged from 745 to 2320 mg/kg. The compound PubChem-141609259 exhibited the highest LD₅₀ value, indicating relatively lower toxicity in mice. The compound with the highest docking score exhibited an LD₅₀ value of 784 mg/kg, compared to the native ligand's LD₅₀ value of 920 mg/kg. All the investigated compounds showed signs of reproductive toxicity, but none displayed cardiotoxicity. The top-docked conformation was found to be hepatotoxic; however, no signs of carcinogenicity were observed (Table 7).

Table 7: Toxicity assessments of the investigated compounds.

PubChem ID	M.O LD ₅₀ (mg/kg)	Rep. Tox.	Hpt.	Crd.	Crn.	Tox	Phys	Bio	Eco
329823760	920.00	T	NT	NT	NT	●	●	●	●
136621040	784.00	T	T	NT	NT	●	●	●	●
141609259	2320.00	T	T	NT	NT	●	●	●	●
136141701	946.00	T	NT	NT	NT	●	●	●	●
136141741	650.00	T	NT	NT	NT	●	●	●	●
136141618	1280.00	T	NT	NT	NT	●	●	●	●
135797427	1040.00	T	NT	NT	NT	●	●	●	●
136401905	2130.00	T	T	NT	NT	●	●	●	●
136622946	796.00	T	NT	NT	NT	●	●	●	●
136622951	847.00	T	T	NT	NT	●	●	●	●
135774110	745.00	T	NT	NT	T	●	●	●	●

Abbreviations: M.O. LD₅₀: Mouse oral LD₅₀, Rep. Tox: Reproductive toxicity, Hpt: Hepatotoxicity, Crd: Cardiotoxicity, Crn: Carcinogenicity, T: Toxic, NT: Non-toxic, logBB: Logarithmic value of blood-brain barrier permeability

3.3. Molecular Dynamics Simulations

Molecular dynamics simulations were implemented utilizing GROningen Machine for Chemical Simulations (GROMACS) 2023.3 software package to investigate the binding stability of the selected complexes during the simulation. In this scope, MD simulations of PubChem-329823760: LIMK1 (native ligand) and PubChem-136321040: LIMK1 (best-docked compound: LIMK1) complexes were carried out to analyze the binding stabilities during the simulation better. For this reason, root mean square deviation (RMSD), root mean square fluctuation (RMSF), solvent-accessible surface area (SASA), and radius of gyration (Rg) analyses were calculated using the trajectories and corresponding graphs were illustrated in Figure 6-9.

3.3.1. Root mean square deviation (RMSD) analysis

In the evaluation RMSD results, the complex PubChem-329823760: LIMK1 exhibited an average RMSD value of 0.31 nm, while the apo form registered an average of 0.29 nm. Minor fluctuations were observed in both the complex and the apo form in the interval from 10 ns to 25 ns. A notable fluctuation was discerned in the complex around the 40th ns, with an RMSD value approximating 0.50 nm. Concurrently, the apo form was found to be more stable than the complex, with its fluctuation ranging between 0.20 and 0.30 nm. Post the 40 ns mark, both the complex and the apo form were observed to attain relative stability, which was maintained throughout the remaining duration of the simulation (Figure 6).

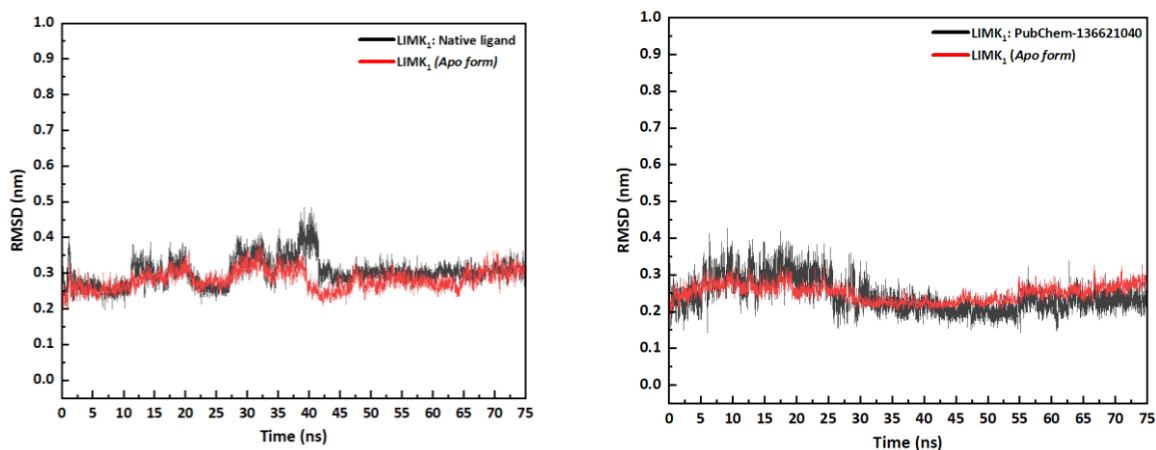


Figure 6: RMSD trajectory plots of PubChem-329823760: LIMK1 (*native ligand*) and PubChem-136621040: LIMK1 (*best-docked*) complexes with their corresponding Apo forms.

Additionally, the complex, including our target compound, exhibited an average RMSD value of 0.23 nm, while the apo form of this complex showed an RMSD of 0.26 nm. This could be interpreted as a sign of the relative stability of our screened candidate during the MD simulation in the binding site of LIMK1. In the initial 25 ns, a slight fluctuation was observed in both the complex and the apo form. During these stages, the complex demonstrated a slightly more substantial fluctuation. However, stability was observed to be achieved subsequent to the 30 ns threshold. The apo form did not present any significant fluctuations, and a state of equilibrium was sustained in the system for the remainder of the simulation period.

3.3.2. Root mean square fluctuation (RMSF) analysis

The computation of RMSF for the trajectories of the complexes PubChem-329823760: LIMK1 (native

ligand) and PubChem-136321040: LIMK1 (best-docked) is depicted in Figure 7. This illustration provides insight into the adaptability of the respective ligands within the receptor network and the mobility of residues within the LIMK1 macromolecule's binding site. A lower RMSF fluctuation is typically indicative of a flexible complex characterized by a rigid protein secondary structure, while a higher RMSF value suggests a relatively weaker bonded structure. The application of C_{α} atoms facilitated a more comprehensive understanding of each residue's average position. The RMSF value for the complex with the native ligand (PubChem-329823760: LIMK1) was determined to be approximately 0.12 nm, while the average RMSF for the highest-ranked complex (PubChem-136321040: LIMK1) was found to be 0.10 nm (Figure 7).

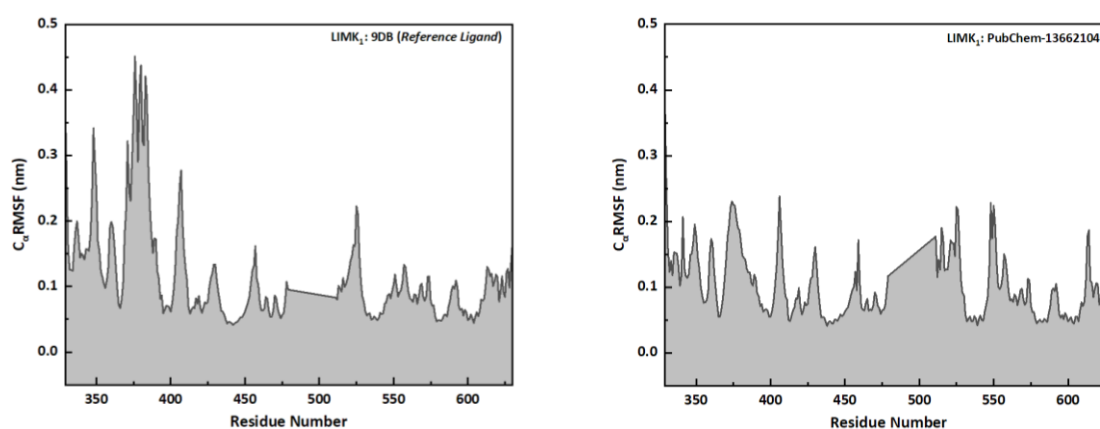


Figure 7: C_{α} RMSF plots of PubChem-329823760: LIMK1 (native ligand) and PubChem-136321040: LIMK1 (best-docked) complexes.

In the residue number range of approximately 350 to 450, substantial fluctuations were observed. Specifically, a significant peak of about 0.45 nm was discerned around residues 375 and 400, suggesting an enhanced interaction between the native ligand and these residues. Minor peaks, each approximately 0.15 nm, were identified between residues 425 and 450. Another peak of note was also identified around residues 520 and 525, with an approximate value of 0.25 nm. Additionally, a series of minor residue fluctuations were detected in the range from 550 to 650 residue numbers, most of which were around 0.10 nm.

A comparatively lower RMSF value with minor peaks was noted for the top-ranked ligand (PubChem-136321040: LIMK1). Specifically, more subtle fluctuations were observed between residue numbers 350 and 450, in contrast to the complex with the native ligand. Two similar peaks were also detected around residues 425 and 450. For these complexes, relatively higher fluctuations were observed in the range of 500 to 650, with various peaks at residues 525, 550, and 610 with an RMSF value of 0.20 nm and a minor fluctuation around residue 580 at approximately 0.10 nm.

3.3.3. Solvent-accessible surface area (SASA) calculation

Solvent Accessible Surface Area is a measure of the surface area of a protein-ligand complex that is directly engaged in interactions with solvent molecules. An increase in SASA values implies a more unfolded or open conformation, signifying a higher degree of exposure to the solvent (33). During 75 ns MD simulation, the average SASA values of the complexes PubChem-329823760: LIMK1 (native ligand) and PubChem-136321040: LIMK1 (best-docked) were observed. The native ligand LIMK1 complex displayed an average SASA value of approximately 150.80 nm², while the best-docked compound, LIMK1, exhibited a nearly identical average value of 150.20 nm². Notably, the complex containing the native compound demonstrated relatively more stability during the first 40 ns.

In contrast, the fluctuation of the complex with the best-docked compound slightly decreased between 30 and 50 ns. Both complexes showed nearly identical fluctuations until the end of the trajectories. Minor fluctuations were noted in the trajectory of the PubChem-136321040: LIMK1 complex between 50 and 75 ns. These comprehensive SASA analyses suggest that both complexes interacted with a similar quantity of solvents throughout the MD simulation (Figure 8).

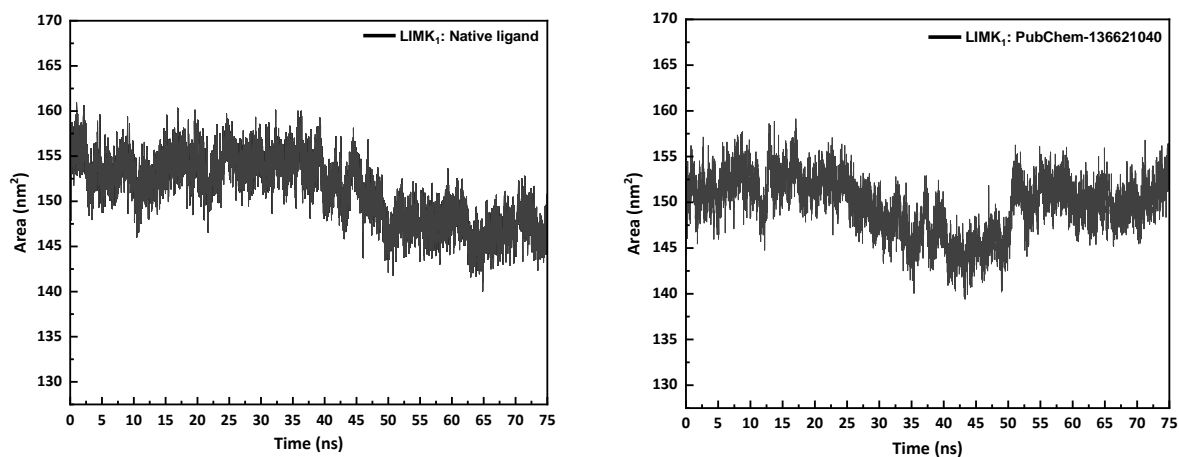


Figure 8: SASA trajectories of PubChem-329823760: LIMK1 (*native ligand*) and PubChem-136321040: LIMK1 (*best-docked*) complexes.

3.3.4. Radius of gyration (*Rg*) analysis

The calculation of the radius of gyration was employed to assess the compactness and rigidity of the macromolecule throughout the MD simulation. The trajectories of *Rg* versus time for our complexes are depicted in Figure 9. The average *Rg* values were determined to be 2.06 nm and 2.04 nm for the PubChem-329823760: LIMK1 and PubChem-

136321040: LIMK1 complexes, respectively. In the initial 20 ns, both complexes exhibited a similar trend, indicative of the molecule's stable compactness at the onset of the simulation. Subsequently, the fluctuation of the native compound complex increased from approximately 2.05 nm to 2.10 nm between 30 and 40 ns.

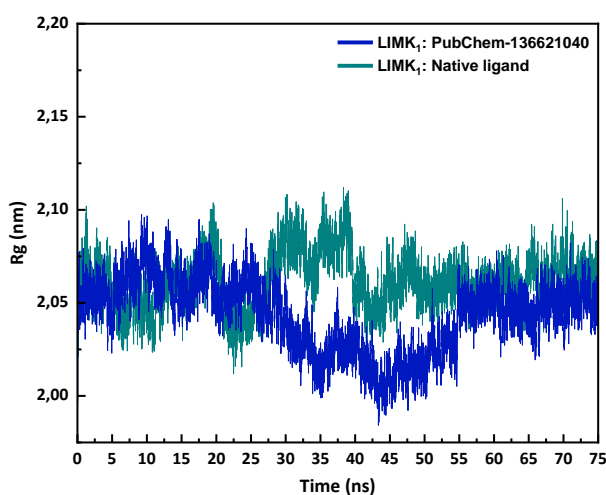


Figure 9: Radius of gyration graphs of PubChem-329823760: LIMK1 (*native ligand*) and PubChem-136321040: LIMK1 (*best-docked*) complexes.

In comparison, the fluctuation of the complex containing our candidate compound slightly decreased from 2.05 nm to around 2.00 nm from 30 ns to 45 ns before this trend slightly increased again and reached equilibrium from 55 ns to 75 ns. The native ligand-LIMK1 complex achieved equilibrium after a significant fluctuation at about 45 ns and maintained its stability for the duration of the simulation. It could be deduced from both complexes that these protein systems maintained their rigidity during the simulation, based on the average results, as discussed above.

4. CONCLUSION

In this study, we successfully identified several candidate compounds possessing the inhibitory potential against LIM domain kinase 1 receptor, playing a pivotal role in Alzheimer's Disease (AD).

PubChem database through Pharmit server was utilized to conduct pharmacophore-based virtual screening to determine similar structures. 419 compounds were discovered at initial, and 29 hit compounds were identified by applying pharmacophore filter and Lipinski's filter.

PubChem-136621040 stood out as particularly promising, exhibiting not only a high binding affinity but also favorable pharmacokinetic and ADMET profiles, as evidenced by comprehensive *in silico* analyses encompassing molecular docking, dynamic simulations, and ADMET predictions.

The docking results corroborated the compound's superior binding affinity for LIMK1 relative to the native ligand, as indicated by a significantly elevated docking score, thereby highlighting its potential as a highly effective inhibitor. The 75 ns MD simulations

offered detailed insights into the interactions between the LIMK1 enzyme and the identified inhibitors. RMSD analysis revealed that PubChem-136621040 maintained a lower average RMSD value of 0.23 nm compared to the native ligand's 0.31 nm, indicating a stable interaction throughout the simulation. RMSF analysis further corroborated these findings, showing that PubChem-136621040 had a lower average RMSF value, suggesting a stable and consistent interaction with key residues within the LIMK1 binding site. The SASA and radius of gyration (Rg) analyses offered further understanding of the dynamic behavior of the ligand-enzyme complexes. The SASA values, approximately 150 nm² for both the native ligand and PubChem-136621040, suggested stable solvation properties during the simulation. Concurrently, the Rg analysis revealed that both complexes preserved their structural integrity and compactness, with PubChem-136621040 exhibiting a modest increase in rigidity relative to the native ligand.

These findings will enhance the expanding research on LIMK1 inhibitors for Alzheimer's disease treatment and set the stage for subsequent *in vitro* and *in vivo* validation studies, structure-activity relationship analyses, and investigations into potential synergistic effects with other AD therapies. This study exemplifies the effectiveness of combining various computational approaches in drug discovery and establishes a robust basis for the development of innovative therapeutic strategies for AD.

5. CONFLICT OF INTEREST

The authors affirm that there are no competing financial interests or personal relationships known to them that might seem to affect the integrity of the work presented in this paper.

6. ACKNOWLEDGMENTS

The computational calculations were executed at TUBITAK-ULAKBIM High Performance and Grid Computing Centre (TRUBA).

7. REFERENCES




- Brejyeh Z, Karaman R. Comprehensive Review on Alzheimer's Disease: Causes and Treatment. *Molecules* [Internet]. 2020 Dec 8;25(24):5789. Available from: [<URL>](#).
- Cummings JL. Alzheimer Disease. *JAMA* [Internet]. 2002 May 8;287(18):2335. Available from: [<URL>](#).
- Brookmeyer R, Evans DA, Hebert L, Langa KM, Heeringa SG, Plassman BL, et al. National estimates of the prevalence of Alzheimer's disease in the United States. *Alzheimer's Dement* [Internet]. 2011 Jan 1;7(1):61–73. Available from: [<URL>](#).
- Gomez-Arboledas A, Davila JC, Sanchez-Mejias E, Navarro V, Nuñez-Díaz C, Sanchez-Varo R, et al. Phagocytic clearance of presynaptic dystrophies by reactive astrocytes in Alzheimer's disease. *Glia*

- [Internet]. 2018 Mar 27;66(3):637–53. Available from: [<URL>](#).
- Sharoar MG, Hu X, Ma XM, Zhu X, Yan R. Sequential formation of different layers of dystrophic neurites in Alzheimer's brains. *Mol Psychiatry* [Internet]. 2019 Sep 21;24(9):1369–82. Available from: [<URL>](#).
- Rajmohan R, Reddy PH. Amyloid-Beta and Phosphorylated Tau Accumulations Cause Abnormalities at Synapses of Alzheimer's disease Neurons. *J Alzheimer's Dis* [Internet]. 2017 Apr 19;57(4):975–99. Available from: [<URL>](#).
- Šimić G, Babić Leko M, Wray S, Harrington C, Delalle I, Jovanov-Milošević N, et al. Tau Protein Hyperphosphorylation and Aggregation in Alzheimer's Disease and Other Tauopathies, and Possible Neuroprotective Strategies. *Biomolecules* [Internet]. 2016 Jan 6;6(1):6. Available from: [<URL>](#).
- Ben Zablah Y, Zhang H, Gugustea R, Jia Z. LIM-Kinases in Synaptic Plasticity, Memory, and Brain Diseases. *Cells* [Internet]. 2021 Aug 13;10(8):2079. Available from: [<URL>](#).
- Manetti F. LIM kinases are attractive targets with many macromolecular partners and only a few small molecule regulators. *Med Res Rev* [Internet]. 2012 Sep 16;32(5):968–98. Available from: [<URL>](#).
- Scott RW, Olson MF. LIM kinases: function, regulation and association with human disease. *J Mol Med* [Internet]. 2007 Jun 10;85(6):555–68. Available from: [<URL>](#).
- Turab Naqvi AA, Hasan GM, Hassan MI. Targeting Tau Hyperphosphorylation via Kinase Inhibition: Strategy to Address Alzheimer's Disease. *Curr Top Med Chem* [Internet]. 2020 Jun 1;20(12):1059–73. Available from: [<URL>](#).
- Hiraoka J, Okano I, Higuchi O, Yang N, Mizuno K. Self-association of LIM-kinase 1 mediated by the interaction between an N-terminal LIM domain and a C-terminal kinase domain. *FEBS Lett* [Internet]. 1996 Dec 9;399(1–2):117–21. Available from: [<URL>](#).
- Park J, Kim SW, Cho MC. The Role of LIM Kinase in the Male Urogenital System. *Cells* [Internet]. 2021 Dec 28;11(1):78. Available from: [<URL>](#).
- Ding Y, Milosavljevic T, Alahari SK. Nischarin Inhibits LIM Kinase To Regulate Cofilin Phosphorylation and Cell Invasion. *Mol Cell Biol* [Internet]. 2008 Jun 1;28(11):3742–56. Available from: [<URL>](#).
- Bernard O. Lim kinases, regulators of actin dynamics. *Int J Biochem Cell Biol* [Internet]. 2007 Jan 1;39(6):1071–6. Available from: [<URL>](#).
- Ohashi K. Roles of cofilin in development and its mechanisms of regulation. *Dev Growth Differ* [Internet]. 2015 May 10;57(4):275–90. Available from: [<URL>](#).

17. Henderson BW, Greathouse KM, Ramdas R, Walker CK, Rao TC, Bach S V., et al. Pharmacologic inhibition of LIMK1 provides dendritic spine resilience against β -amyloid. *Sci Signal* [Internet]. 2019 Jun 25;12(587):eaaw9318. Available from: [<URL>](#).
18. Singh R, Pokle AV, Ghosh P, Ganeshpurkar A, Swetha R, Singh SK, et al. Pharmacophore-based virtual screening, molecular docking and molecular dynamics simulations study for the identification of LIM kinase-1 inhibitors. *J Biomol Struct Dyn* [Internet]. 2023 Sep 2;41(13):6089–103. Available from: [<URL>](#).
19. Rangaswamy R, Hemavathy N, Subramaniyan S, Vetrivel U, Jeyakanthan J. Harnessing allosteric inhibition: prioritizing LIMK2 inhibitors for targeted cancer therapy through pharmacophore-based virtual screening and essential molecular dynamics. *J Biomol Struct Dyn* [Internet]. 2023 Dec 8; Article in Press. Available from: [<URL>](#).
20. Zhang M, Wang R, Tian J, Song M, Zhao R, Liu K, et al. Targeting LIMK1 with luteolin inhibits the growth of lung cancer in vitro and in vivo. *J Cell Mol Med* [Internet]. 2021 Jun 13;25(12):5560–71. Available from: [<URL>](#).
21. Daina A, Michielin O, Zoete V. SwissADME: a free web tool to evaluate pharmacokinetics, drug-likeness and medicinal chemistry friendliness of small molecules. *Sci Rep* [Internet]. 2017 Mar 3;7(1):42717. Available from: [<URL>](#).
22. Chen X, Li H, Tian L, Li Q, Luo J, Zhang Y. Analysis of the Physicochemical Properties of Acaricides Based on Lipinski's Rule of Five. *J Comput Biol* [Internet]. 2020 Sep 1;27(9):1397–406. Available from: [<URL>](#).
23. Meihua Rose Feng BSP. Assessment of Blood-Brain Barrier Penetration: In Silico, In Vitro and In Vivo. *Curr Drug Metab* [Internet]. 2002 Dec 1;3(6):647–57. Available from: [<URL>](#).
24. Ejeh S, Uzairu A, Shallangwa GA, Abechi SE. In Silico Design, Drug-Likeness and ADMET Properties Estimation of Some Substituted Thienopyrimidines as HCV NS3/4A Protease Inhibitors. *Chem Africa* [Internet]. 2021 Sep 17;4(3):563–74. Available from: [<URL>](#).
25. Humphreys SC, Davis JA, Iqbal S, Kamel A, Kulmatycki K, Lao Y, et al. Considerations and recommendations for assessment of plasma protein binding and drug-drug interactions for siRNA therapeutics. *Nucleic Acids Res* [Internet]. 2022 Jun 24;50(11):6020–37. Available from: [<URL>](#).
26. Khan T, Dixit S, Ahmad R, Raza S, Azad I, Joshi S, et al. Molecular docking, PASS analysis, bioactivity score prediction, synthesis, characterization and biological activity evaluation of a functionalized 2-butanone thiosemicarbazone ligand and its complexes. *J Chem Biol* [Internet]. 2017 Jul 4;10(3):91–104. Available from: [<URL>](#).
27. Tariq M, Sirajuddin M, Ali S, Khalid N, Tahir MN, Khan H, et al. Pharmacological investigations and Petra/Osiris/Molinspiration (POM) analyses of newly synthesized potentially bioactive organotin(IV) carboxylates. *J Photochem Photobiol B Biol* [Internet]. 2016 May 1;158:174–83. Available from: [<URL>](#).
28. Abraham MJ, Murtola T, Schulz R, Páll S, Smith JC, Hess B, et al. GROMACS: High performance molecular simulations through multi-level parallelism from laptops to supercomputers. *SoftwareX* [Internet]. 2015 Sep 1;1–2:19–25. Available from: [<URL>](#).
29. Rakhshani H, Dehghanian E, Rahati A. Enhanced GROMACS: toward a better numerical simulation framework. *J Mol Model* [Internet]. 2019 Dec 25;25(12):355. Available from: [<URL>](#).
30. Parra-Cruz R, Jäger CM, Lau PL, Gomes RL, Pordea A. Rational Design of Thermostable Carbonic Anhydrase Mutants Using Molecular Dynamics Simulations. *J Phys Chem B* [Internet]. 2018 Sep 13;122(36):8526–36. Available from: [<URL>](#).
31. Das NC, Labala RK, Patra R, Chattoraj A, Mukherjee S. In Silico Identification of New Anti-SARS-CoV-2 Agents from Bioactive Phytocompounds Targeting the Viral Spike Glycoprotein and Human TLR4. *Lett Drug Des Discov* [Internet]. 2022 Mar 7;19(3):175–91. Available from: [<URL>](#).
32. Liu P, Lu J, Yu H, Ren N, Lockwood FE, Wang QJ. Lubricant shear thinning behavior correlated with variation of radius of gyration via molecular dynamics simulations. *J Chem Phys* [Internet]. 2017 Aug 28;147(8):84904. Available from: [<URL>](#).
33. Singh VK, Chaurasia H, Kumari P, Som A, Mishra R, Srivastava R, et al. Design, synthesis, and molecular dynamics simulation studies of quinoline derivatives as protease inhibitors against SARS-CoV-2. *J Biomol Struct Dyn* [Internet]. 2022 Dec 5;40(21):10519–42. Available from: [<URL>](#).



The Effects of Lipoic Acid on Markers of Oxidative Stress and Inflammation in the Lungs of Valproic Acid-Treated Rats

Burcin Alev-Tuzuner^{1,2*} , Ismet Burcu Turkyilmaz Mutlu³ , Hazal Ipekci⁴ ,
Unsal Veli Ustundag⁵ , Tugba Tunalı-Akbay⁴ , Ebru Emekli-Alturfan⁴ , Refiye Yanardag³ ,
Aysen Yarat⁴ 

¹Istanbul Gelisim University, Faculty of Dentistry, Department of Basic Medical Sciences, Biochemistry, Istanbul, 34315, Türkiye.

²Istanbul Gelisim University, Life Sciences and Biomedical Engineering Application and Research Centre, Istanbul, 34315, Türkiye.

³Istanbul University-Cerrahpaşa, Faculty of Engineering, Department of Chemistry, Istanbul, 34320, Türkiye.

⁴Marmara University, Faculty of Dentistry, Department of Basic Medical Sciences, Biochemistry, Istanbul, 34854, Türkiye.

⁵Istanbul Atlas University, Faculty of Dentistry, Department of Basic Medical Sciences, Medical Biochemistry, Istanbul, 34408, Türkiye.

Abstract: In this experimental study, the effect of lipoic acid (LA) on lung damage caused by valproic acid (VPA) was investigated. The antioxidant, oxidative stress, and inflammation indicators such as glutathione (GSH), lipid peroxidation (LPO), catalase (CAT), superoxide dismutase (SOD), glutathione-S-transferase (GST), nitric oxide (NO), sialic acid (SA), myeloperoxidase (MPO), and tissue factor (TF) were examined. Sprague Dawley rats were used, and they were randomly divided into four groups as follows: Control group, LA group received 50 mg LA/kg/day for 15 days, VPA group received 500 mg VPA/kg/day for 15 days, and VPA+LA group received the same doses of VPA and LA for 15 days. On day 16, lung tissues were taken. VPA caused the decreases in GSH, SA and SOD values and the increases LPO, NO, and TF values. LA reversed the changes in GSH, SOD, and TF values. GST and CAT activities did not change significantly by the effect of VPA or LA. On the other hand, the inhibitory effect of VPA on MPO, which is an inflammatory marker, and the pro-oxidant effects of LA causing the increases in both LPO and MPO values were observed in lung tissue. These regulations may help LA to overcome oxidative stress caused by VPA in the lung. Further studies are needed to confirm the mechanism underlying VPA-induced MPO inhibition in the lung.

Keywords: Lung, Lipoic acid, Valproic acid, Oxidative stress, Antioxidant.

Submitted: July 22, 2024. **Accepted:** August 7, 2024.

Cite this: Alev Tuzuner B, Turkyilmaz Mutlu IB, Ipekci H, Ustundag UV, Tunalı Akbay T, Emekli Alturfan E, Yanardag R, Yarat A. The Effects of Lipoic Acid on Markers of Oxidative Stress and Inflammation in the Lungs of Valproic Acid-Treated Rats. JOTCSA. 2024;11(4): 1441-48.

DOI: <https://doi.org/10.18596/jotcsa.1520611>

***Corresponding author's E-mail:** btuzuner@gelisim.edu.tr

1. INTRODUCTION

Valproic acid (VPA) is a widely used antiepileptic drug for the treatment of various seizure and bipolar disorders. Although generally well tolerated, VPA induces oxidative stress, resulting in an inability to balance the generation of reactive oxygen species (ROS) with the body's capacity to detoxify these harmful compounds. As a result, cellular components such as lipids, proteins, and DNA can be damaged, contributing to deterioration of tissue and organ

function (1). Oztay et al. (2), suggested that VPA-induced oxidative stress may cause structural distortion and fibrotic changes in the rat lung. Lungs are susceptible to many environmental pollutants, toxicants, oxidants, and many infections that can cause oxidative damage. Several studies have demonstrated the role of ROS produced by lung epithelium and inflammatory cells in the pathogenesis of lung diseases, including acute respiratory syndrome, acute lung injury, chronic

obstructive pulmonary disease, pulmonary fibrosis, asthma, and lung cancer (3).

α -lipoic acid (1,2-dithiolane-3-pentanoic acid, LA), a natural organo-sulfur compound, contains a disulfide bond as a part of a dithiolane ring with a five-carbon tail. LA can be found in plant and animal food sources such as tomatoes, spinach, broccoli, kidney, liver, and heart. It is also endogenously produced by the liver. It exists in cells as dihydrolipoic acid (DHLA), LA's reduced form. It is essential for mitochondrial aerobic metabolism. The fact that LA is soluble in both fat and water makes it special compared to other antioxidants. This means that it can act in the plasma membrane as well as in the cytoplasm (4). It is also the redox regulator of several proteins including, thioredoxin, myoglobin, the transcription factor nuclear factor kappa B (NF- κ B), and prolactin, and helps recycle cellular antioxidants involving vitamin C, vitamin E, and glutathione (5,6). High electron density due to the special position of two sulfur atoms in the 1,2-dithiolane ring gives LA a high tendency to reduce other redox-sensitive molecules depending on environmental conditions (6). The antioxidant properties of both LA and DHLA consist of quenching ROS, regeneration of antioxidants, and chelation of redox metals. In recent decades, through its pharmacological effects, such as anti-cancer, anti-oxidant, anti-inflammatory, and anti-viral effects, numerous studies have reported the effects of LA in improving many diseases (4).

This study was designed to investigate the potential protective effect of LA on the lungs of VPA-treated rats by measuring important markers of tissue oxidative stress and inflammation.

2. EXPERIMENTAL SECTION

2.1. Chemicals

VPA was obtained from Merck (Darmstadt, Germany) and LA from Sigma (USA). All other chemicals used in the experiments were of analytical purity and were purchased from Merck (Darmstadt, Germany), Sigma-Aldrich (St. Louis, MO, USA), and Fluka (Buchs, Switzerland).

2.2. Laboratory Animals and Experimental Design

All the experiments in this study were approved by Marmara University Experimental Animals Ethics Committee (Decision No: 34.2015.mar).

Thirty-two Sprague Dawley rats (six-month-old, female) were used in the study. The animals were housed in the standard cage with optimal temperature (20°C \pm 2) and light/dark (12 h light/12 h dark) conditions. All rats were fed orally with standard rat chow and fresh tap water.

The animals were divided into four groups: Control group (n=7), LA given group (50 mg/kg/day, by intraperitoneal, n=8), VPA given group (500 mg/kg/day, by intraperitoneal, n=7), and VPA+LA given group (in same doses and same way, n=10). LA was administered 1 h prior to VPA administration for 15 days. On day 16, the rats were sacrificed, and

lungs were taken. Lung homogenates (10% w/v) were prepared in physiological saline (NaCl, 0.9%).

2.3. Biochemical Analysis

Lung homogenates were analyzed for glutathione (GSH), lipid peroxidation (LPO), superoxide dismutase (SOD), catalase (CAT), glutathione-S-transferase (GST), nitric oxide (NO), sialic acid (SA), myeloperoxidase (MPO), and tissue factor (TF).

2.3.1. Estimation of GSH (μ g GSH per g tissue)

GSH levels were determined by the method using metaphosphoric acid and 5,5'-dithiobis-2-nitrobenzoic acid (DTNB) (7). The extinction coefficient of $1.36 \times 10^4 \text{ M}^{-1}\text{cm}^{-1}$ was used for the calculation. The absorbance was measured spectrophotometrically at 412 nm.

2.3.2. Estimation of LPO (nmol MDA per g tissue)

Malondialdehyde (MDA) is an end product of the peroxidation of lipids. LPO levels were determined using thiobarbituric acid (TBA) assay (8). The pink colour obtained at the end of the reaction was measured with a spectrophotometer at 532 nm.

2.3.3. Estimation of SOD (U SOD per g tissue)

SOD activities were measured as the ability to increase the rate of photooxidation of riboflavin-sensitized o-dianisidine (9). The absorbance was measured spectrophotometrically at 460 nm.

2.3.4. Estimation of CAT (kU CAT per g tissue)

CAT activities were determined based on the reduction of hydrogen peroxide (H₂O₂) to water (H₂O) (10). The decrease in absorbance was measured spectrophotometrically at 240 nm.

2.3.5. Estimation of GST (U GST per g tissue)

GST activities were assayed by measuring the absorbance at 340 nm of the product obtained by conjugation of GSH with 1-chloro-2,4-dinitrobenzene (CDNB) (11).

2.3.6. Estimation of NO (nmol NO per g tissue)

In order to measure NO levels, nitrate was converted to nitrite using vanadium (III) chloride. The complex diazonium compound was obtained by reacting nitrite with sulfanilamide in an acidic medium. This was then coupled with N-(1-naphthyl) ethylenediamine dihydrochloride, and the coloured complex formed was measured spectrophotometrically at 540 nm (12).

2.3.7. Estimation of SA (mg SA per g tissue)

Sodium periodate was used to oxidize SA in concentrated phosphoric acid. Next, TBA was combined with the product of periodate oxidation. A pink chromophore was obtained, which was then extracted into cyclohexanone. The absorbance was measured spectrophotometrically at 549 nm (13).

2.3.8. Estimation of MPO (U MPO per g tissue)

MPO activity was measured by the method using phenol, 4-amino antipyrine (4-AAP), and H₂O₂. The absorbance was measured spectrophotometrically at 510 nm (14).

2.3.9. Estimation of TF (Second)

TF activities were determined by mixing lung homogenate with plasma, then adding calcium chloride and measuring the time for fibrin formation (15). There is an inverse relationship between the clotting time and the activity of the TF.

2.4. Statistics

Statistical analysis (GraphPad Prism 9.0, California, USA) was performed using analysis of variance (ANOVA) followed by Tukey's multiple comparison test. Data are presented as mean \pm standard deviation (SD). P-value below 0.05 is considered significant.

3. RESULTS AND DISCUSSION

VPA is generally well tolerated but has been shown both clinically and experimentally to cause several adverse effects, including lung injury. Symptoms of VPA-induced pleural effusion or interstitial lung disease have been reported to resolve within days of discontinuing the drug (16,17). Oztay et al. proposed that VPA administration at a dose of 500 mg kg⁻¹ day⁻¹

caused pulmonary toxicity via changes in both biochemical and inflammatory markers (2). Therefore, we used a VPA dose of 500 mg kg⁻¹ day⁻¹ in the present study. VPA primarily damages tissue by inducing oxidative stress, which is then followed by inflammation and apoptosis (18). ROS in the lung are generated from both exogenous and endogenous sources, such as environmental gases and the mitochondrial electron transport system (19). VPA induces elevation of mitochondrial ROS (20). Excessive and uncontrolled oxidative stress leads to cell death, but at lower and less harmful levels it can act as a signal to redox signaling that helps restore cellular balance (21).

The present study showed that the administration of VPA was associated with a decrease in the levels of GSH ($p < 0.05$) and SA ($p < 0.0001$), the activities of SOD ($p < 0.01$) and MPO ($p < 0.0001$), and an increase in the levels of MDA, is an end product of the LPO, ($p < 0.0001$), NO ($p < 0.0001$), and activity of TF ($p < 0.0001$) compared to the control group (Figures 1 and 2).

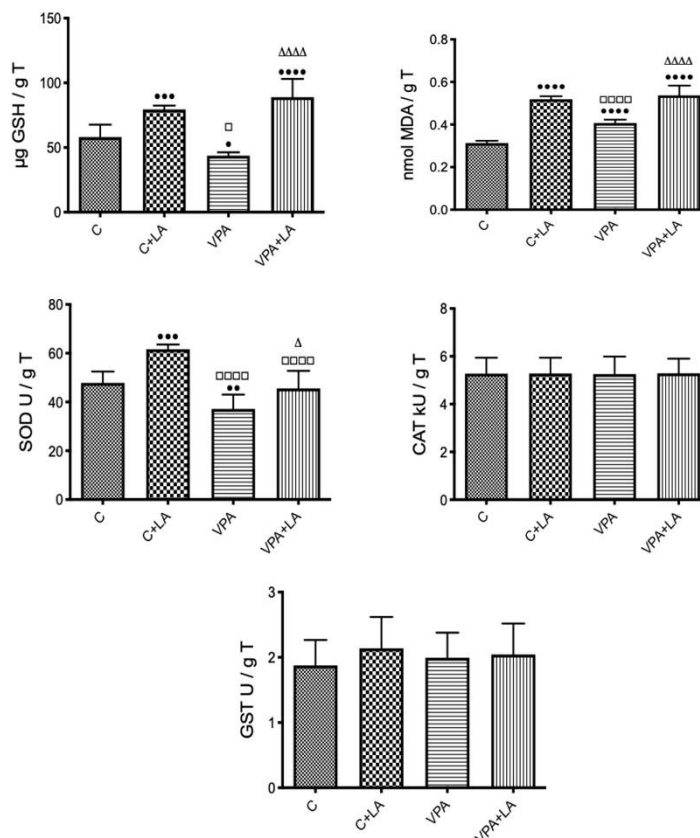


Figure 1: Lung GSH and LPO levels and SOD, CAT, GST activities of the groups. C, control group; C+LA, lipoic acid given control group; VPA, valproic acid given group; VPA+LA, lipoic acid given valproic acid group, T, tissue; GSH, glutathione; MDA, malondialdehyde; LPO, lipid peroxidation; GST, glutathione-S-transferase; SOD, superoxide dismutase; CAT, catalase. Values are represented as mean \pm standard deviation.

* $p < 0.05$, ** $p < 0.01$, *** $p < 0.001$, **** $p < 0.0001$ vs control group; $\square p < 0.05$, $\square\square\square p < 0.0001$ vs C+LA group, $\Delta p < 0.05$, $\Delta\Delta\Delta p < 0.0001$ vs VPA group.

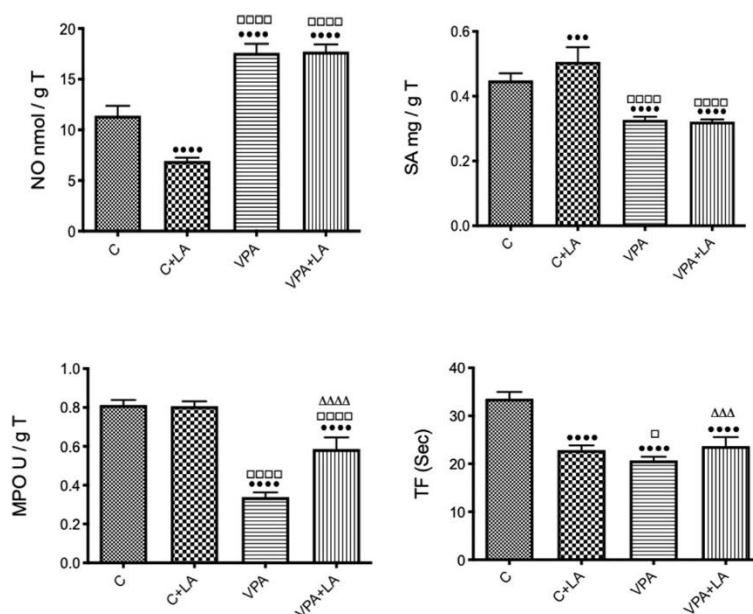


Figure 2: Lung NO, SA levels and MPO, TF activities of the groups

C, control group; C+LA, lipoic acid given control group; VPA, valproic acid given group; VPA+LA, lipoic acid given valproic acid group, T, tissue; NO, nitric oxide; SA, sialic acid; MPO, myeloperoxidase; TF, tissue factor; Sec, second. Values are represented as mean±standard deviation.

p < 0.001, *p < 0.0001 vs control group; □p < 0.05, □□□p < 0.0001 vs C+LA group, △p < 0.05, △△△p < 0.001, △△△△p < 0.0001 vs VPA group.

The two primary antioxidants in the anti-oxidative system are GSH and SOD. These antioxidants reduce the damaging effects of harmful free radicals. LPO is one of the biomarkers of oxidative stress status and indicates oxidative lipid degradation (22). Their levels are closely linked to how cells respond to oxidative stress. Impairment of the lung antioxidant system is linked to a reduction in GSH levels, SOD activities, and an elevation in LPO levels (23). This is supported by our findings. Besides SOD, CAT, and GST are the key antioxidant enzymes that eliminate free radicals from cells. GST is responsible for catalyzing the reaction between GSH and a variety of reactive electrophilic compounds to protect against oxidative stress. CAT prevents the conversion of H₂O₂ to hydroxyl radicals and reduces oxidative stress by catalyzing the conversion of H₂O₂ to water and oxygen. It has been reported that the activities of CAT, SOD, and GST were decreased in the lungs of VPA-treated rats compared to the control group (2). In contrast to these findings, in the present study, VPA did not alter CAT and GST activities.

NO reacts with ROS products to produce peroxynitrite and can alter protein and lipid structure. NO has important neurotransmitter and regulatory roles when released at low levels. However, when combined with superoxide to form harmful peroxynitrite, high levels of NO (produced by the increased activity of inducible NO synthase (iNOS) during inflammation) have a negative effect (24). VPA administration has been reported to increase NO levels in brain tissue (25) and bovine aortic endothelial cells and mouse serum (26) in various VPA toxicity models. In our study, VPA also

caused a significant increase in NO values in lung tissue compared to the control group. SA is a major component of the secreted mucins of the airways and is highly expressed along the epithelial border lining the respiratory tract (27). For lung physiology and respiratory balance, this surface anionic shield may provide a repulsive structure, a hydration barrier and a protective barrier (28). SA has also been suggested to have antioxidant activity against hydroxyl radicals in mucin in the respiratory and gastrointestinal mucus layers (29). Higher levels of SA have also been linked with inflammation (30). So, there are conflicting studies on the effect of VPA on SA levels. While VPA administration increased SA levels in the small intestine (31), they did not change in the gastric tissue (29). In the present study, the damaged respiratory mucosa and the decrease in the activity of defense mechanisms may have caused to a reduction in SA levels.

MPO plays an important role in inflammation and tissue damage (32). One of the major ROS, superoxide anion, is transformed into H₂O₂. Activated MPO converts this to the potent oxidant hypochlorite. As a marker of neutrophil recruitment and lung tissue damage, MPO activity is measured in the lung. MPO activity has been found to be significantly increased in the pancreatic, lung, and liver tissue of VPA-treated rats (2,33,34). However, in contrast to these findings, there have also been studies showing that VPA, as a histone deacetylase inhibitor (HDACI), attenuated lung injury by inhibiting inflammatory cytokine production and NF-κB activation (35). In a model of rat intestinal ischemia-reperfusion study, VPA treatment caused a decrease in MPO activity,

and it has been suggested that VPA decreases neutrophil migration into the lungs (36). The reduction in MPO activity in the present study may be due to the anti-inflammatory effect of VPA through its HDACI action. HDACIs have been shown in the literature to have an anti-inflammatory effect (37, 38). TF is a transmembrane glycoprotein and acts as a cellular initiator of coagulation. The lung is one of the tissues that contain high levels of TF, along with the brain, uterus, heart, and placenta. Alveolar macrophages and airway epithelial cells express TF in the lung. The abnormal expression of TF is associated with thrombotic complications in a variety of diseases, including atherosclerosis, cancer, and inflammation. Alveolar TF production suggests that alveolar epithelium expresses TF when exposed to inflammatory cytokines (39–41). Additionally, it has been suggested that elevated levels of ROS may be an inducer of TF gene expression. The procoagulant activity of TF is strictly regulated to maintain hemostasis and avoid thrombosis (42). VPA is a cause of hematological problems, and coagulation abnormalities are frequently observed during VPA treatment (43). It has been shown that VPA increased TF activity in gingival tissue (44). In parallel with the findings of previous studies, this present study suggests that increased TF activity in the lung in response to inflammation and/or oxidative stress may provide extra hemostatic protection against tissue damage.

LA is a powerful reductant and has the ability to scavenge free radicals. Administration of LA has been shown in several studies to reduce oxidative stress and restore depleted levels of other antioxidants *in vivo*. On the other hand, data show that LA may have pro-oxidant effects (6). The oxidative status of cells and physiological parameters may determine the ability of LA and/or DHLA to act as pro- or antioxidants. According to its chemical structure, LA functions as an oxidative molecule without generating endogenous ROS because of its oxidized dithiolane ring. DHLA may also produce thiol and disulfide radical anion and function as a pro-oxidant. *In vitro* and *in vivo* studies suggest that DHLA causes the production of ROS through the Fenton reaction by reducing ferric iron and the stimulation of the Ca²⁺-induced mitochondrial permeability transition (MPT) by the production of ROS, which depletes mitochondrial antioxidant capacity (45).

In the current study, when the VPA group was treated with LA, the changes in GSH levels ($p < 0.0001$) and SOD ($p < 0.05$), MPO ($p < 0.0001$), TF ($p < 0.001$) activities were reversed by LA compared to VPA, whereas LPO levels were increased more ($p < 0.0001$) (Figure 1 and 2). In addition, LA in combination with VPA had no effect on SOD, CAT activities, or NO, SA levels ($p > 0.05$) (Figures 1 and 2). In the C+LA group, the NO levels were significantly reduced ($p < 0.001$) and SA levels and TF activity were significantly increased ($p < 0.001$) compared to the control group (Figure 2).

The antioxidant effects of LA may act either directly by restoring endogenous antioxidants such as GSH or indirectly by balancing ROS. It has been suggested

that increasing the availability of cysteine is the mechanism by which LA can increase GSH levels (46). Similarly, Cadirci et al. (22) reported that decreased SOD activity and GSH amounts in septic lung tissue were increased by the administration of LA to rats. The both studies (46, 22) support our findings that GSH and SOD values were increased in LA-treated rats. Lung LPO levels were found to be significantly increased in LA+VPA treated rats in our study, which appears to contradict previous findings from a systematic review and meta-analysis suggesting that LA consumption significantly reduces MDA levels (47). It is possible that an induction of SOD activity is involved in the mechanism of LPO induction by LA. The elevated SOD activity and unaltered catalase activity in LA-exposed rats would be expected to result in the deposition of H₂O₂ and hence elevated LPO in the presence of ferrous ions as a consequence of the Fenton reaction. When exogenous LA enters the cell, it is reduced to DHLA with the use of NADPH by the cytosolic enzymes glutathione reductase and thioredoxin reductase. Although DHLA has been demonstrated to have both pro-oxidant and antioxidant effects, both LA and DHLA have been classified as strong antioxidants based on their unique characteristics. Ferric and ferrous iron are both chelated by DHLA *in vitro*, preventing oxidative damage to iron. However, LA also removes iron from ferritin and has the ability to convert Fe³⁺ to Fe²⁺, increasing the risk of oxidative damage. This is because iron is a redox-active metal. Through Fenton chemistry, it can significantly increase oxidative stress by producing hydroxyl radicals. (4,6,45). Briefly, LA may have caused lipid peroxidation by acting as a pro-oxidant and accelerating the formation of iron-dependent hydroxyl radicals in the lungs. Turkyilmaz et al. (25), showed that administration of LA in the VPA group increased CAT activity, decreased GST activity, and the change in SOD activity was insignificant in brain tissue. Differently from Turkyilmaz et al. (25), in the current study, the CAT and GST activities were not modified by LA in the C+LA and VPA+LA groups compared to the respective groups. These results suggested that H₂O₂ degradation processes were unchanged and may have increased the accumulation of superoxide anion and the formation of hydroxyl radicals. In the literature, it has been shown that LA induces apoptosis by increasing mitochondrial superoxide anion production in cancer cells (48). However, more research is needed to explain the mechanism behind these changes.

Preclinical studies have shown that LA can reduce inflammation by inhibiting the iNOS/NO pathway (4). In another study, Oktay & Caliskan (49) found that LA reduced NO levels but had no effect on SA levels compared to the methotrexate group during methotrexate-induced oxidative stress in rat hearts. In the present study, LA reduced NO levels and increased SA levels in LA given control group. This may be due to the antioxidant effect of LA. However, it was not sufficient to reverse the NO and SA levels in the VPA+LA group compared to VPA.

LA (25 mg/kg/day for 21 days) increased colon MPO activity in the mouse model of acute ulcerative colitis

(50), and LA at higher doses (100 mg/kg/day for 45 days) may have a pro-oxidant effect on cardiac tissue in a rat-diabetic model (51). In line with these observations, 15 days of LA (50 mg/kg/day) at proposed doses may be pro-inflammatory based on our available data. Future studies are recommended to clarify the effects of LA in a dose- and time-dependent and oxidative stress-type-dependent manner.

It is known that LA affects iron metabolism. Although findings from clinical studies are conflicting, LA has been shown to reduce serum iron levels. It has been suggested that this may be because DHLA chelates iron, preventing its use (52). Based on this, LA, which increases TF activity in the C+LA group, may be beneficial to keep normal blood clotting to prevent further bleeding when serum iron is low. Iron deficiency causes iron deficiency anemia, which may be associated with decreased thrombogenesis, aberrant platelet function, and elevated inflammatory levels, all of which raise the risk of bleeding (53). Moreover, LA inhibits platelet activation, and co-administration with vitamin E prolongs the clotting time (54). Accordingly, in the current study, LA decreased lung TF activity in VPA group, which may prevent lung tissues from the risk of thrombosis and coagulation problems.

4. CONCLUSION

In conclusion, the present data do not allow the conclusion that LA could prevent VPA-induced lung injury; the data are consistent with LA may contribute to the reduction of TF activity and increase in GSH levels, SOD, and MPO activities in VPA treatment. However, more studies are required to determine the mechanism underlying VPA-induced MPO inhibition in the lung. Also despite its dual modulation of oxidative stress and inflammation, LA may have beneficial effects on lung health.

5. CONFLICT OF INTEREST

There are no conflicts to declare.

6. REFERENCES

1. Safdar A, Ismail F. A comprehensive review on pharmacological applications and drug-induced toxicity of valproic acid. *Saudi Pharm J* [Internet]. 2023 Feb 1;31(2):265–78. Available from: [<URL>](#).
2. Oztay F, Tunali S, Kayalar O, Yanardag R. The protective effect of vitamin U on valproic acid-induced lung toxicity in rats via amelioration of oxidative stress. *J Biochem Mol Toxicol* [Internet]. 2020 Dec 26;34(12):e22602. Available from: [<URL>](#).
3. Hosakote YM, Rayavara K. Respiratory syncytial virus-induced oxidative stress in lung pathogenesis. In: *Oxidative Stress in Lung Diseases* [Internet]. Singapore: Springer Singapore; 2020. p. 297–330. Available from: [<URL>](#).

4. Guo X, Wu S, Shang J, Dong W, Li Y, Peng Q, et al. The effects of lipoic acid on respiratory diseases. *Int Immunopharmacol* [Internet]. 2023 Mar 1;116:109713. Available from: [<URL>](#).
5. Eser Faki H, Tras B, Uney K. Alpha lipoic acid and vitamin E improve atorvastatin-induced mitochondrial dysfunctions in rats. *Mitochondrion* [Internet]. 2020 May 1;52:83–8. Available from: [<URL>](#).
6. Moini H, Packer L, Saris NEL. Antioxidant and prooxidant activities of α -lipoic acid and dihydrolipoic acid. *Toxicol Appl Pharmacol* [Internet]. 2002 Jul 1;182(1):84–90. Available from: [<URL>](#).
7. Beutler E. Glutathione in red blood cell metabolism. In: *A manual of biochemical methods*. New York: Grune & Stratton; 1975. p. 112–4.
8. Ledwoż;yw A, Michalak J, Stępień A, Kądziołka A. The relationship between plasma triglycerides, cholesterol, total lipids and lipid peroxidation products during human atherosclerosis. *Clin Chim Acta* [Internet]. 1986 Mar 28;155(3):275–83. Available from: [<URL>](#).
9. Mylroie AA, Collins H, Umbles C, Kyle J. Erythrocyte superoxide dismutase activity and other parameters of copper status in rats ingesting lead acetate. *Toxicol Appl Pharmacol* [Internet]. 1986 Mar 15;82(3):512–20. Available from: [<URL>](#).
10. Aebi H. Catalase in vitro. In: *Methods in enzymology* [Internet]. *Methods Enzymol*; 1984. p. 121–6. Available from: [<URL>](#).
11. Habig WH, Jakoby WB. Assays for differentiation of glutathione S-Transferases. In: *Methods in Enzymology* [Internet]. Academic Press; 1981. p. 398–405. Available from: [<URL>](#).
12. Miranda KM, Espey MG, Wink DA. A rapid, simple spectrophotometric method for simultaneous detection of nitrate and nitrite. *Nitric Oxide* [Internet]. 2001 Feb 1;5(1):62–71. Available from: [<URL>](#).
13. Warren L. The thiobarbituric acid assay of sialic acids. *J Biol Chem* [Internet]. 1959 Aug 1;234(8):1971–5. Available from: [<URL>](#).
14. Wei H, Frenkel K. In vivo formation of oxidized DNA bases in tumor promoter-treated mouse skin. *Cancer Res* [Internet]. 1991 Aug 15;51(16):4443–9. Available from: [<URL>](#).
15. Ingram GI, Hills M. Reference method for the one-stage prothrombin time test on human blood. International committee for standardization in hematology. *Thromb Haemost* [Internet]. 1976 Aug 31;36(1):237–8. Available from: [<URL>](#).
16. Kim SJ, Jhun BW, Lee JE, Kim K, Choi HY. A case of drug-induced interstitial pneumonitis caused by valproic acid for the treatment of seizure disorders. *Tuberc Respir Dis (Seoul)* [Internet]. 2014 Sep 1;77(3):145. Available from: [<URL>](#).

17. Şimşek F, Kızıldağ N. Eosinophilic pleuropericardial effusion due to valproic acid. *Black Sea J Heal Sci* [Internet]. 2022 Jan 1;5(1):104–6. Available from: [<URL>](#).
18. Akaras N, Kandemir FM, Şimşek H, Gür C, Aygörmez S. Antioxidant, antiinflammatory, and antiapoptotic effects of rutin in spleen toxicity induced by sodium valproate in rats. *Türk Doğa ve Fen Derg* [Internet]. 2023 Jun 22;12(2):138–44. Available from: [<URL>](#).
19. Oztay F, Kayalar O, Yildirim M. Pulmonary oxidative stress and antioxidant defence system in the lung ageing and fibrotic and diabetic lungs. In: *Oxidative Stress in Lung Diseases* [Internet]. Singapore: Springer Singapore; 2019. p. 325–53. Available from: [<URL>](#).
20. Lee M, Ahn C, Kim K, Jeung EB. Mitochondrial toxic effects of antiepileptic drug valproic acid on mouse kidney stem cells. *Toxics* [Internet]. 2023 May 20;11(5):471. Available from: [<URL>](#).
21. Hansen JM, Lucas SM, Ramos CD, Green EJ, Nuttall DJ, Clark DS, et al. Valproic acid promotes SOD2 acetylation: a potential mechanism of valproic acid-induced oxidative stress in developing systems. *Free Radic Res* [Internet]. 2021 Dec 2;55(11–12):1130–44. Available from: [<URL>](#).
22. Cadirci E, Altunkaynak BZ, Halici Z, Odabasoglu F, Uyanik MH, Gundogdu C, et al. Alpha-lipoic acid as a potential target for the treatment of lung injury caused by cecal ligation and puncture-induced sepsis model in rats. *Shock* [Internet]. 2010 May;33(5): 479–84. Available from: [<URL>](#).
23. Thimmulappa RK, Chattopadhyay I, Rajasekaran S. Oxidative stress mechanisms in the pathogenesis of environmental lung diseases. In: *Oxidative Stress in Lung Diseases* [Internet]. Singapore: Springer Singapore; 2020 [cited 2024 Sep 13]. p. 103–37. Available from: [<URL>](#).
24. Mokra D, Mokry J. Oxidative stress in experimental models of acute lung injury. In: *Oxidative Stress in Lung Diseases* [Internet]. Singapore: Springer Singapore; 2020. p. 25–57. Available from: [<URL>](#).
25. Turkeyilmaz IB, Bilgin Sokmen B, Yanardag R. Alpha-lipoic acid prevents brain injury in rats administered with valproic acid. *J Biochem Mol Toxicol* [Internet]. 2020 Nov 14;34(11):e22580. Available from: [<URL>](#).
26. Cho DH, Park JH, Joo Lee E, Jong Won K, Lee SH, Kim YH, et al. Valproic acid increases NO production via the SH-PTP1-CDK5-eNOS-Ser116 signaling cascade in endothelial cells and mice. *Free Radic Biol Med* [Internet]. 2014 Nov 1;76:96–106. Available from: [<URL>](#).
27. Hernández-Jiménez C, Martínez-Cortés J, Olmos-Zuñiga JR, Jasso-Victoria R, López-Pérez MT, Díaz-Martínez NE, et al. Changes in the levels of free sialic acid during ex vivo lung perfusion do not correlate with pulmonary function. *Experimental model. BMC Pulm Med* [Internet]. 2023 Sep 4;23(1):326. Available from: [<URL>](#).
28. Martins M de F, Honório-Ferreira A, Martins P, Gonçalves CA. Presence of sialic acids in bronchioloalveolar cells and identification and quantification of N-acetylneuraminic and N-glycolylneuraminic acids in the lung. *Acta Histochem* [Internet]. 2019 Aug 1;121(6):712–7. Available from: [<URL>](#).
29. Alev B, Tunalı S, Üstündağ ÜV, İpekçi H, Emekli Alturfan E, Tunalı Akbay T, et al. Chard extract increased gastric sialic acid and ameliorated oxidative stress in valproic acid-administered rats. *Food Heal* [Internet]. 2023;9(2):139–47. Available from: [<URL>](#).
30. Berkan Ö, Göl MK, İçağasioğlu S, Çetinkaya Ö, Yıldız E, Doğan K, et al. Sialic acid is a marker of lung injury following lower extremities ischemia/reperfusion. *Eur J Vasc Endovasc Surg* [Internet]. 2004 May 1;27(5):553–8. Available from: [<URL>](#).
31. Oktay S, Alev B, Tunalı S, Emekli-Alturfan E, Tunalı-Akbay T, Koc-Ozturk L, et al. Edaravone ameliorates the adverse effects of valproic acid toxicity in small intestine. *Hum Exp Toxicol* [Internet]. 2015 Jun 10;34(6):654–61. Available from: [<URL>](#).
32. Jomova K, Alomar SY, Alwasel SH, Nepovimova E, Kuca K, Valko M. Several lines of antioxidant defense against oxidative stress: antioxidant enzymes, nanomaterials with multiple enzyme-mimicking activities, and low-molecular-weight antioxidants. *Arch Toxicol* [Internet]. 2024 May 14;98(5):1323–67. Available from: [<URL>](#).
33. Oktay S, Alev-Tüzüner B, Tunalı S, Ak E, Emekli-Alturfan E, Tunalı-Akbay T, et al. Investigation of the effects of edaravone on valproic acid induced tissue damage in pancreas. *Marmara Pharm J* [Internet]. 2017 Jun 20;21(3):570–7. Available from: [<URL>](#).
34. Turkeyilmaz İB, Karatuğ Kaçar A, Bolkent Ş, Yanardağ R. Damage to liver tissue caused by valproic acid used for treating epilepsy: Protective effects of vitamin B6. *Arch Epilepsy* [Internet]. 2023 Mar 1;29(1):9–15. Available from: [<URL>](#).
35. Wu SY, Tang SE, Ko FC, Wu GC, Huang KL, Chu SJ. Valproic acid attenuates acute lung injury induced by ischemia-reperfusion in rats. *Anesthesiology* [Internet]. 2015 Jun 1;122(6):1327–37. Available from: [<URL>](#).
36. Kim K, Li Y, Jin G, Chong W, Liu B, Lu J, et al. Effect of valproic acid on acute lung injury in a rodent model of intestinal ischemia reperfusion. *Resuscitation* [Internet]. 2012 Feb 1;83(2):243–8. Available from: [<URL>](#).
37. Adcock IM. HDAC inhibitors as anti-inflammatory agents. *Br J Pharmacol* [Internet]. 2007 Apr 29;150(7):829–31. Available from: [<URL>](#).

38. Pai P, Vijeev A, Phadke S, Shetty MG, Sundara BK. Epi-revolution in rheumatology: The potential of histone deacetylase inhibitors for targeted rheumatoid arthritis intervention. *Inflammopharmacology* [Internet]. 2024 Aug 7;32(4):2109–23. Available from: [<URL>](#).
39. Alturfan AA, Alturfan EE, Dariyerli N, Zengin E, Aytac E, Yigit G, et al. Investigation of tissue factor and other hemostatic profiles in experimental hypothyroidism. *Endocrine* [Internet]. 2006;30(1): 63–8. Available from: [<URL>](#).
40. van der Poll T. Tissue factor as an initiator of coagulation and inflammation in the lung. *Crit Care* [Internet]. 2008 Nov 26;12(Suppl 6):S3. Available from: [<URL>](#).
41. Grover SP, Mackman N. Tissue Factor. *Arterioscler Thromb Vasc Biol* [Internet]. 2018 Apr 1;38(4):709–25. Available from: [<URL>](#).
42. Mackman N, Antoniak S. Tissue factor and oxidative stress. *Blood* [Internet]. 2018 May 10;131(19):2094–5. Available from: [<URL>](#).
43. Hasanoğlu C, Karalök Z, Kalenderoğlu M, Haspolat Ş. A rare cause of hemorrhage from valproic acid—induced hypofibrinogenemia and review of literature. *Ann Clin Case Reports* [Internet]. 2021;6:1910. Available from: [<URL>](#).
44. Oktay Ş, Alev B, Koç Öztürk L, Tunalı S, Demirel S, Emekli Alturfan E, et al. Edaravone ameliorates valproate-induced gingival toxicity by reducing oxidative-stress, inflammation and tissue damage. *Marmara Pharm J* [Internet]. 2016 May 10;20(3): 232–40. Available from: [<URL>](#).
45. Çakatay U. Pro-oxidant actions of α -lipoic acid and dihydrolipoic acid. *Med Hypotheses* [Internet]. 2006 Jan 1;66(1):110–7. Available from: [<URL>](#).
46. Mohammed MA, Gharib DM, Reyad HR, Mohamed AA, Elroby FA, Mahmoud HS. Antioxidant and anti-inflammatory properties of alpha-lipoic acid protect against valproic acid-induced liver injury. *Can J Physiol Pharmacol* [Internet]. 2021 May;99(5):499–505. Available from: [<URL>](#).
47. Rezaei Zonooz S, Hasani M, Morvaridzadeh M, Beatriz Pizarro A, Heydari H, Yosae S, et al. Effect of alpha-lipoic acid on oxidative stress parameters: A systematic review and meta-analysis. *J Funct Foods* [Internet]. 2021 Dec 1;87:104774. Available from: [<URL>](#).
48. Peng P, Zhang X, Qi T, Cheng H, Kong Q, Liu L, et al. Alpha-lipoic acid inhibits lung cancer growth via mTOR-mediated autophagy inhibition. *FEBS Open Bio* [Internet]. 2020 Apr 18;10(4):607–18. Available from: [<URL>](#).
49. Oktay S, Çalışkan Ş. Potential therapeutic effect of lipoic acid on methotrexate-induced oxidative stress in rat heart. *Eur J Biol* [Internet]. 2023 Sep 27;82(2):306–10. Available from: [<URL>](#).
50. Piechota-Polanczyk A, Zielińska M, Piekielny D, Fichna J. The influence of lipoic acid on caveolin-1-regulated antioxidative enzymes in the mouse model of acute ulcerative colitis. *Biomed Pharmacother* [Internet]. 2016 Dec 1;84:470–5. Available from: [<URL>](#).
51. AL-Rasheed NM, Al-Rasheed NM, Attia HA, Hasan IH, Al-Amin M, Al-Ajmi H, et al. Adverse cardiac responses to alpha-lipoic acid in a rat-diabetic model: Possible mechanisms? *J Physiol Biochem* [Internet]. 2013 Dec 18;69(4):761–78. Available from: [<URL>](#).
52. Ali YF, Desouky OS, Selim NS, Ereiba KM. Assessment of the role of α -lipoic acid against the oxidative stress of induced iron overload. *J Radiat Res Appl Sci* [Internet]. 2015 Jan 1;8(1):26–35. Available from: [<URL>](#).
53. Wang X, Qiu M, Qi J, Li J, Wang H, Li Y, et al. Impact of anemia on long-term ischemic events and bleeding events in patients undergoing percutaneous coronary intervention: a system review and meta-analysis. *J Thorac Dis* [Internet]. 2015;7(11):2041–52. Available from: [<URL>](#).
54. Marsh SA, Coombes JS. Vitamin E and α -Lipoic acid supplementation increase bleeding tendency via an intrinsic coagulation pathway. *Clin Appl Thromb* [Internet]. 2006 Apr 1;12(2):169–73. Available from: [<URL>](#).



Assessment of the Effect of Berberine on Metalloprotease Enzymes Inhibition and Antioxidant Activity: Possible Application in Skin Aging

Shirin Tarbiat^{1*}

¹Department of Molecular Biology and Genetics (English), Faculty of Engineering and Natural Sciences, Uskudar University, Istanbul, Turkey.

Abstract: Skin aging has been defined to enclose both intrinsic and extrinsic aging. Phytochemicals are frequently used for developing skin care formulations and could protect the skin's epidermal and dermal layers, consisting mainly of elastin and collagen, from UV radiation. Berberine is an isoquinoline alkaloid and a biologically active component from plant sources. Our objective was to assess Berberine's anti-aging capabilities by conducting elastase and collagenase enzyme inhibition and kinetic studies and to also evaluating its antioxidant capacity with three different methods. Furthermore, heat stability, pH and sun protection factor (SPF) of the formulated cream containing 1.5% berberine was evaluated. The elastase and collagenase IC₅₀ values of berberine were estimated to be 47.54 and, 22.16 µg/mL respectively. Berberine was determined as an un-competitive inhibitor of elastase and collagenase. It scavenged DPPH and ABTS free radicals with IC₅₀ values of 66.81 and 180.5 µg/mL respectively. 210.387 mg/L of berberine was equivalent in reducing power of 176 mg/L of ascorbic acid. SPF and pH value of cream containing berberine was found to be 12.3 and 5.62 respectively. In conclusion, these findings suggest that Berberine is a promising candidate for use as an active ingredient in cosmeceuticals, offering a natural approach to enhance skin health and reduce the visible signs of aging.

Keywords: Skin aging, Berberine, Collagenase, Elastase.

Submitted: January 23, 2024. **Accepted:** August 2, 2024.

Cite this: Tarbiat S. Assessment of the Effect of Berberine on Metalloprotease Enzymes Inhibition and Antioxidant Activity: Possible Application in Skin Aging. JOTCSA. 2024;11(4): 1449-60.

DOI: <https://doi.org/10.18596/jotcsa.1423131>

***Corresponding author's E-mail:** shirin.tarbiat@uskudar.edu.tr

1. INTRODUCTION

Skin aging has been defined to encompass both intrinsic and extrinsic aging. Intrinsic aging, also called chronologic aging, is influenced by internal physiological factors, while extrinsic aging is influenced by various external factors, including dietary factors, ultraviolet (UV) radiation, and environmental pollution. Exposure to UV radiation is most often referred to as photodamage or photoaging. UV radiation triggers a series of chemical reactions in the skin that ultimately lead to the development of photoaging. Continued exposure to solar radiation results in compromised repair of the skin's underlying structure. The accumulation of unrepaired cells and extracellular materials in the mended skin structure eventually manifests as wrinkles and sagging of the skin over time. Alterations in skin pigmentation are intricately linked to the process of photaging. Furthermore, a range of photo-induced skin cancers have been attributed to

both short-term and prolonged exposure to sunlight (1,2).

Among the UV radiations, specifically UVB (290–320 nm) and UVA (320–400 nm), UVA predominantly exerts its influence on skin structure. Endogenous chromophores, also referred to as photosensitizers, such as retinal, porphyrins, bilirubin, melanin, and hemoglobin, in the presence of UVA and molecular oxygen, initiate destructive effects on skin biomolecules. These reactions lead to DNA damage and the subsequent formation of reactive oxygen species (ROS) such as hydroxyl radicals, hydrogen peroxide, and superoxide (3).

There are specific pathways that contribute to Extracellular matrix remodeling followed by UVA irradiation. They enhance the degradation of structural proteins like collagen and elastin and impair their synthesis, leading to the loss of structural integrity and eventually skin aging. These pathways include Matrix metalloproteases activation

(MMPs) specially MMP1 (Collagenase-1), Mitogen activated protein kinase (MAPKs) particularly ERK (Extracellular signaling regulated kinase) and JNK (c-Jun N-terminal kinase), and Nuclear factor kappa B (NF- κ B) pathways. UVA radiation induces oxidative stress and activates transcription factors like AP-1, which, in turn, leads to the upregulation of matrix metalloproteinases (MMPs) such as collagenase and elastase. The increased production and activity of these enzymes contribute to the degradation of collagen and elastin, resulting in the progressive breakdown of skin structure and elasticity over time (4,5).

Studies demonstrate that lifestyle changes can delay chronologic aging caused by internal factors, which occur naturally (6). It is also possible to delay photoaging by modifying external factors. Photoaging can be prevented and treated by applying cosmeceuticals with antioxidant properties (7). Cosmeceuticals are cosmetic products that contain active compounds, often blurring the line between cosmetics and pharmaceuticals (8). Antioxidants are frequently investigated for their potential to prevent photoaging due to their capacity to quench free radicals and suppress the expression and activity of MMPs (9). In addition to vitamins A, C, and E, natural antioxidants from plant resources such as flavonoids, alkaloids, and terpenes are applied in anti-aging skin products (10). They are continually studied for their beneficial effects on skin aging and their potential to protect the skin from harmful UV radiation. Numerous studies have shown that these plant secondary metabolites have the potential to inhibit the collagenase and elastase metalloproteases in the skin (11). In one of the studies conducted by K. Satyavani, the ethanol extract of *Excoecaria agallocha* L. was identified as a potent, non-competitive inhibitor of elastase and collagenase (12,13). In another study, *Carica papaya* seed water extract was found to be highly protective against oxidative stress induced by hydrogen peroxide (H_2O_2) in human skin Detroit 550 fibroblasts (13). Seo A. Seo also investigated the skin anti-aging effects of *Carica papaya* leaf in UVB-irradiated normal human dermal fibroblast cells and found that *Carica papaya* leaf, through its radical scavenging ability, can suppress AP1 signaling pathway, resulting in a decrease in the expression of collagenase and elastase enzymes (14). Maity et al. (15) reported *Tagetes erecta* Linn flower as an anti-wrinkle agent since it has been shown to effectively inhibit hyaluronidase, elastase, and MMP-1 in-vitro. The flavonoids and phenolic acids present in Pomegranate (*Punica granatum* L.), green tea (*Camelliasinensis* (L) Kuntze) and Rosemary Extract (*Rosmarinus officinalis*) have proven to exhibit powerful antioxidant properties and showed powerful protective effects against UV damage in human skin fibroblast cells (16-18). Many in-vivo studies also suggest that herbal compounds have the ability to protect the skin from the adverse effects of ultraviolet radiation (19).

The human skin is equipped with a complex system of safeguarding antioxidants. These include protective enzyme-based antioxidants such as

catalase and superoxide dismutase, alongside non-enzymatic antioxidants like glutathione, bilirubin, ferritin, and coenzyme Q10. Exposure to UV radiation triggers the oxidation of biomolecules within the human skin, leading to a depletion of endogenous antioxidants (20). Therefore, the application of antioxidants and enzyme inhibitors in cosmeceuticals may be highly effective candidates for the protection and treatment of skin photoaging. Commonly used antioxidants in topical formulations are vitamins E, and C, lipoic acid, and ubiquinone (CoQ10). Antioxidants can mitigate photoaging by suppressing the generation of reactive oxygen species caused by photooxidative stress and enhancing the epidermal defense mechanism against UV damage (21).

Berberine is an isoquinoline alkaloid with a tetracyclic skeleton. It is the ammonium salt of benzylisoquinoline and is present in the barks, rhizomes, stems, and roots of plants such as *Berberis vulgaris*, *Berberis thunbergii*, *Berberis aristata*, *Hydrastis canadensis*, *Xanthorhiza simplicissima*, *Mahonia aquifolium*, and *Phellodendron amurense*. Berberine is considered an active ingredient in these plants and serves both edible and medicinal functions (22). Several methods have been applied for the extraction of berberine from different plants, including maceration, percolation or Soxhlet extraction, solvent extraction, and green extraction approach. In another study, scientists synthesized special magnetic nanoparticles for the extraction of berberine (23-27).

Berberine exhibits various pharmacological properties, including anticancer, antiarrhythmic, ischemic, cardioprotective, antidepressant, antidiabetic, and anti-asthmatic effects. It also serves as a potential new therapy for neurodegenerative disorders such as Parkinson's disease (28-33).

In a comprehensive study conducted by Shekarabi, SPH et al. (34), the antioxidant and antibacterial properties of berberine fruit were investigated, along with its potential to enhance immune function. The study involved the examination of dietary Berberine fruit extract in the serum of one hundred and fifty fish specimens. Their findings strongly support the notion that dietary berberine fruit extract, particularly at a dosage of 750 mg/kg, represents a promising candidate for the regulation of immune responses and bolstering antioxidant defense systems (34).

El-Zahar, KM et al. (35) demonstrated the high antioxidant activities of phenolic and flavonoid components derived from the ethanolic extract of barberry leaf and roots in-vitro. In a subsequent in-vivo study by Gholampour, et al. (36), evidence emerged supporting the administration of barberry hydro-alcoholic extract at 160 mg/kg/day for ten days as an effective measure against cisplatin-induced nephro- and hepato-toxicity. This treatment exhibited an increase in exogenous enzyme activation and a concomitant decrease in malodialdehyde levels compared to cisplatin-induced toxicity. They concluded that Barberry extract,

notably its active component berberine, exhibits significant potential in mitigating cisplatin-induced oxidative stress within hepatic and kidney tissues (36).

Ashraf, H and Zare, S. (37) have reported on the antidiabetic potential of the aqueous extract derived from *Berberis integerrima* Bge root. Their research findings underscore the preventive capabilities of berberine extract against hepatic impairment and oxidative stress instigated by streptozotocin-induced diabetes mellitus in rats. These results substantiate the utility of *Berberis integerrima* Bge root extracts as a promising agent for managing diabetes and its associated complications (37).

Yadawa, et al. (38) explored the biological effectiveness of Berberine in rat models induced with aging through D-galactose treatment. Their investigation revealed that D-galactose administration elevated pro-oxidants, including malondialdehyde, plasma membrane redox system, and advanced oxidation protein products in the plasma. This led to a decrease in antioxidant levels such as reduced glutathione (GSH), plasma thiols and sialic acid. However, when berberine was administered alongside D-galactose in rat models, it successfully reinstated both pro-oxidants and antioxidant levels in erythrocytes (38).

Recent studies have identified moisturizing properties of berberine hydrochloride when incorporated into cellulose-derived and biodegradable hydrogel films. These films were analyzed for their water uptake profile and skin permeation properties (39). Kim, SM et al. (40) provided evidence that berberine reduces the expression of MMP-1 genes and increases type I procollagen expression in human dermal fibroblasts. The cells were treated with berberine for 72 hours prior to a one-hour period of exposure to fluorescent sun lamps with an emission spectrum of 275–380 nm and 310–315 nm. Their findings suggest that the reduction of MMP-1 and induction of type I procollagen may be mediated by the antioxidant activity of berberine in human dermal fibroblasts (40). While the mentioned study investigated the impact of Berberine on MMP-1 expression levels, there has been limited scientific inquiry into the inhibitory action of berberine chloride on MMPs. MMPs constitute a family of enzymes critical in remodeling the extracellular matrix (ECM) within tissues, including skin. The ECM is a complex network of proteins and carbohydrates that provides structural support to cells and influences various cellular processes. In the context of skin health,

MMPs are involved in maintaining skin structure, wound healing, tissue repair, and turnover. They function by breaking down ECM components, such as collagen and elastin, responsible for skin's elasticity and strength. This breakdown facilitates the removal of damaged tissue and supports tissue regeneration during healing. In skin health, MMPs contribute to balancing ECM synthesis and degradation, which is crucial for maintaining skin elasticity, texture, and overall function. However, their dysregulation can lead to skin disorders such as premature aging and inflammatory conditions. Exposure to UV light also activates the MMPs (41).

Consequently, we aimed to evaluate berberine's potential as an active ingredient in cosmeceuticals. We conducted primary tests on enzyme inhibition and the kinetics of elastase and collagenase, which are relevant in skin health and rejuvenation. We assessed Berberine antioxidant capacity using three methods: 2,2'-azinobis-(3-ethylbenzothiazoline-6-sulfonate) (ABTS), 2,2-Diphenyl-1-picrylhydrazyl (DPPH) and ferric reducing antioxidant power (FRAP) assays, and we also formulated a cream containing 1.5% berberine. We then evaluated the cream's SPF, pH, and heat stability to determine its relevance in the skin anti-aging segment of the cosmetic industry. However, further in vitro and in vivo investigations are necessary to fully substantiate this potential.

2. EXPERIMENTAL SECTION

2.1. Materials

The Berberine chloride (purity >95%), ABTS [2,2'-azinobis-(3-ethylbenzothiazoline-6-sulfonate)], DPPH [2,2-Diphenyl-1-picrylhydrazyl], and all other reagents were purchased from sigma-Adrich.

2.2. Elastase (Type IV, EC 3.4.21.36) Inhibitory Activity

The inhibitory potential of berberine was measured using a modified spectrophotometric method based on Kraunsoe et al. (42) and Deniz et al. (43). A mixture of 10 μ L of berberine at various concentrations (50, 100, and 200 μ g/mL), 10 μ L of elastase (from porcine pancreas) at a concentration of 0.5 mU/mL, and 180 μ L of 0.1 M tris buffer (pH 8.0) was pre-incubated for 20 minutes at 25°C. To the reaction mixture, 10 μ L of N-Sucanyl-Ala-Ala-Ala-p-Nitroanilide substrate (1 mM) was added, followed by a 10-minute incubation at 25 °C. The amount of product (p-nitroaniline) produced from the substrate was recorded at 410 nm using an ELISA microplate reader. Each experiment was performed in triplicate and enzyme inhibitory activity was calculated using the equation below:

$$\text{Enzyme inhibitory activity (\%)} = \frac{(\Delta A/\text{min}) \text{ control} - (\Delta A/\text{min}) \text{ sample}}{(\Delta A/\text{min}) \text{ control}} \times 100 \text{ (Eq. 1)}$$

The IC₅₀ value was obtained by plotting a graph between concentration and percentage inhibition at a substrate concentration of 1 μ mol/mL using GraphPad Prism software version 9.5.1.

2.3. Collagenase (Type I, EC 3.4.24.3) Inhibitory Activity

The collagenase inhibitory activity of berberine was measured by spectrophotometer according to the modified method of Kozachok et al. (44). A reaction mixture was prepared by dissolving different concentrations of berberine (25, 50, and 100 μ g/mL) in 700 μ L of 50 mM tricine buffer (pH 7.5) and

incubated with 100 μL of collagenase enzyme solution for 20 min at 37 $^{\circ}\text{C}$. Subsequently, 200 μL of N-(3-[2-furyl]-acryloyl)-Leu-Gly-Pro-Ala (FALGPA) was added as the substrate. Optical

densities were measured in 5-minute intervals for 20 minutes at 345 nm. Each experiment was performed in triplicate and enzyme inhibitory activity was calculated according to the equation below:

$$\text{Enzyme inhibitory activity (\%)} = (\Delta A/\text{min}) \text{ control} - (\Delta A/\text{min}) \text{ sample} / (\Delta A/\text{min}) \text{ control} \times 100 \text{ (Eq. 2)}$$

The IC_{50} value was obtained by plotting a graph between concentration and percentage inhibition at a substrate concentration of 1 $\mu\text{mol/mL}$ using GraphPad Prism software version 9.5.1.

The inhibitory effectiveness of berberine chloride against collagenase and elastase was studied by observing its action against different substrate concentrations. The enzymatic reaction took place at a temperature of 25 $^{\circ}\text{C}$ for a duration of 20 minutes. The most effective doses of berberine were determined based on the results of the inhibitory activity test. The data obtained from the Lineweaver-Burk plot analysis, calculated using Michaelis-Menten kinetics, were fitted to a sigmoidal dose-response equation with a variable slope through linear regression.

2.4. Antioxidant Assays

The antioxidant activity of berberine hydrochloride was quantified using three methods; DPPH, ABTS,

and FRAP assays. A detailed description of the antioxidant assays can be reviewed in our previous study. IC_{50} values were calculated using GraphPad Prism software version 9.5.1. (45).

2.5. Cream Formulation

The oil-in-water (O/W) creams used in this study were prepared based on the solubility of the different components of the formulation:

Water 67%, Glycerin 2.3%, Tetrasodium EDTA 0.2%, Xanthan Gum 0.5%, Mineral Oil 15%, Polysorbate 60+Cetearyl Alcohol (1:1) 4%, Cetyl Alcohol 2%, Stearic Acid 1%, Triglyceride 7%, Phenoxyethanol 1%.

The prepared cream was divided into three batches. The first batch served as the negative control and did not contain berberine, while the second batch contained 1.5% berberine and the third batch contained 1.5% vitamin C as the positive control.

Table 1: Cream constituents with percentage content.

Aqueous Phase (70%) Constituents	
Water	67%
Glycerin	2.3%
Tetrasodium EDTA	0.2%
Xanthan Gum	0.5%
Oily Phase (30%)	
Mineral Oil	15%
Polysorbate 60 + Cetearyl Alcohol (1:1)	4%
Cetyl Alcohol	2%
Stearic Acid	1%
Triglyceride	7%
Phenoxyethanol	1%

Table 2: Antiaging lotions' oil-in-water cream formulas.

Formulations	Contents
F1	Base cream without active compound (negative control)
F2	Base cream + 1.5% Berberine
F3	Base cream + 1.5% Vitamin C (positive control)

2.6. In-vitro SPF Determination

The cream's SPF was assessed using the UV absorbance technique. A 0.1% hydro-alcoholic solution of berberine was prepared, and its absorbance was measured within the 290–320 nm range. The in-vitro photoprotection level was calculated using the Mansur equation, which was employed to establish the SPF values of the formulations. The equation is as follows:

$$\text{SPF} = \text{CF} \sum_{290}^{320} \frac{\text{EE}(\lambda) \cdot \text{I}(\lambda)}{\text{Abs}(\lambda)} \text{ (Eq. 3)}$$

Where $\text{CF}=10$ (Correction Factor), $\text{EE}(\lambda)=$ Erythemogenic Effect of radiation at wavelength λ , $\text{I}(\lambda) =$ Intensity of solar light at wavelength λ , and $\text{Abs}(\lambda) =$ Absorbance of wavelength λ by a solution of the preparation (46).

2.7. pH Determination

The pH of the lotions was measured using a pH meter (EDGE pH meter) at 25 $^{\circ}\text{C}$.

2.8. Stability Studies

To assess the formulation's stability, heat stability study were carried out as per ICH guidelines. Cream-

filled bottles were placed in a humidity chamber maintained at temperatures of $8^{\circ}\text{C} \pm 0.1^{\circ}\text{C}$, $25^{\circ}\text{C} \pm 1^{\circ}\text{C}$, $40^{\circ}\text{C} \pm 1$, and $65 \pm 5^{\circ}\text{C}$ in 20-30% humidity for 3 months. At the end of the studies, the samples were analyzed for their physical properties.

2.9. Statistical Analysis

The results were expressed as mean value \pm standard error mean (SEM) of triplicate experiments. The analysis of the data was performed using GraphPad Prism software version 9.5.1.

3. RESULTS AND DISCUSSION

3.1. Inhibitory Effect of Berberine on Elastase and Collagenase

The IC_{50} values of berberine for elastase and collagenase were estimated to be 47.54 and 22.16 $\mu\text{g}/\text{mL}$ respectively, indicating that berberine exhibited stronger inhibition of collagenase compared to elastase. Several natural compounds were identified with MMP inhibitory activities. For instance, Curcuma mangga Val. Contains bioactive compounds such as curcumin, known for its anti-aging properties. The IC_{50} values for elastase inhibitory activities by *C. mangga* extracts from different solvent types were reported to range from 26.34 to 532.38 $\mu\text{g}/\text{mL}$ (47). The inhibition of elastase by phytochemicals, such as phenolic compounds, is known to enhance capillary wall integrity, protect components of the extracellular matrix, and initiate the process of tissue reconstruction (48).

In our study to identify the inhibitory kinetics of elastase by berberine, Lineweaver–Burk plots were employed. Different substrate concentrations (1-8 mM) were incubated with elastase along with berberine (at concentrations of 50, 100, and 200 mM). An uninhibited enzyme reaction (control) was carried out in the absence of berberine. The results are illustrated in Figure 1a. As depicted in Figure 1a, the reciprocal graph reveals that the slope corresponds to K_m/V_{max} , while the intercept on the $1/v$ -axis is augmented by a factor of $(1+c_i/k_i)$. Consequently, increasing the concentration of the inhibitor results in a set of parallel lines, wherein the intercept on the y-axis progressively rises in response to the increasing inhibitor concentration, suggesting that berberine functions as an uncompetitive inhibitor of elastase. Both V_{max} and K_m values were reduced from 1.821 to 0.744 mU/min and 0.351 to 0.191 mM, respectively.

Figure 1b illustrates the kinetics of collagenase enzyme inhibition by berberine. Lineweaver-Burk plots of the enzymatic reaction catalyzed by collagenase were generated in the absence or presence of berberine at different concentrations (25, 50, and 100 $\mu\text{g}/\text{mL}$). The reverse of substrate concentrations plotted on the X-axis versus $1/V$ (mU/min)-1 values (obtained from the Lineweaver-Burk analysis) plotted on the Y-axis. Results indicated that berberine acts as an uncompetitive inhibitor of collagenase, as evidenced by the reduction in both V_{max} and K_m values, from 1.222

to 0.516 mU/min for V_{max} and 0.33 to 0.125 mM for K_m , with increasing berberine concentrations.

Elastase and collagenase were both found to be uncompetitively inhibited by berberine against their respective substrates. In uncompetitive inhibition, the inhibitor binds to the enzyme that is already associated with the substrate, making substrate concentration an important factor for inhibition. In the current study, both V_{max} and K_m decreased with increasing inhibitor concentration. K_m is considered as the substrate concentration at which the rate of enzymatic reaction reaches half of V_{max} . The lower K_m values were observed in the presence of different concentrations of berberine, which suggested that the presence of berberine as an uncompetitive inhibitor causes the pretense affinity of the enzyme for the substrate to increase, meaning that K_m decreases (49).

Uncompetitive inhibitors bind to the enzyme–substrate complex, but they do so at a site other than the enzyme's active site. Since the substrate is already bound to the enzyme, this binding by the inhibitor decreases both the K_m and V_{max} . Berberine exhibited significant inhibitory activity against the studied MMPs, which might be attributed to the formation of hydrogen bonds between berberine and the site of the enzyme-substrate complex or other critical sites, disrupting the essential catalytic configuration (50).

Table 3 presents the data on the inhibitory effect of berberine on enzymatic activity and the kinetics of enzyme inhibition. IC_{50} is the concentration of an inhibitor that produces half-maximum inhibitory effect against the enzyme. The inhibition constant K_i , referred to as the inhibitor concentration required to produce half of maximum inhibition, indicates the potency of the inhibitor; the lower the value of K_i , the more potent the inhibitor. K_i is a constant value for an inhibitor and enzyme pairing, whereas IC_{50} is a relative value that varies based on the substrate concentration employed in the assay. As listed in Table 3, berberine exhibited lower K_i values, demonstrating its stronger affinity for binding to elastase and collagenase (50).

Inhibiting MMPs presents a promising strategy for combating and preventing skin photoaging. Notably, numerous studies have identified plant secondary metabolites, such as polyphenols, as effective inhibitors of MMPs (51). For instance, Madhan et al. (52) demonstrated that polyphenols, namely catechin and epigallocatechin gallate (EGCG) from green tea, possess potential inhibitory activity against collagenase, with rates of inhibition reaching 70 and 88 % respectively. Their kinetic study on the inhibition of collagenase by catechin and EGCG, using the hydrolysis of 2-furanacryloyl-L-leucyl-glycyl-L-prolyl-L-alanine as a substrate, revealed that both catechin and EGCG exhibited competitive type of inhibition against collagenase. They concluded that EGCG's heightened inhibitory effect, in contrast to catechin, is a result of EGCG's superior ability to form hydrogen bonds and engage in hydrophobic interactions with collagenase (52). As a result,

phytochemicals hold potential applications in both pharmaceuticals and cosmeceuticals for skin care. MMP inhibitors can be formulated within cosmeceutically compatible formulations or pharmaceutically approved carriers such as creams, lotions, or ointments. When used in cosmeceuticals,

this innovative MMP inhibitor composition can be applied to the skin to proactively diminish wrinkles, pigmentation irregularities, loss of skin elasticity, and other manifestations linked to aging or sun-induced damage (53).

Table 3: Inhibitory Effect of Berberine on Elastase and Collagenase; IC₅₀ values and values of inhibition constant from kinetic studies.

	Berberine IC ₅₀ value (µg/mL)	Berberine K _i value
Elastase ¹	47.54	0.003733
Collagenase ¹	22.16	0.003557

¹ IC₅₀ values for both enzyme inhibitions were calculated at substrate concentration of 1 µg/mL.

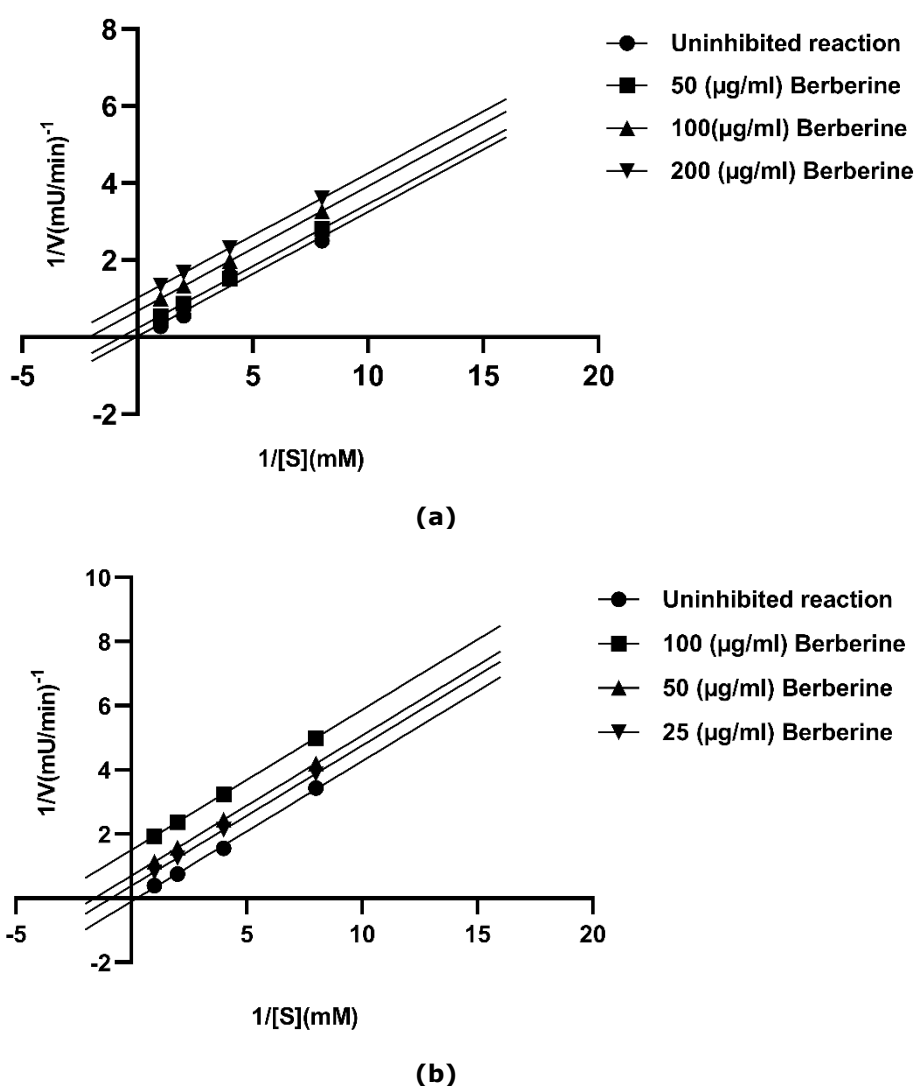


Figure 1: Effect of berberine on (a) elastase and (b) collagenase enzyme kinetics.

One of the primary limitations is the limited solubility of berberine in aqueous solutions, which can affect its bioavailability and make it challenging to achieve desired concentrations in formulations. To address this, we dissolved berberine in ethanol, given its solubility in ethanol, DMSO, and DMF, and used this solution for various experiments in the study.

Additionally, using high concentrations of berberine for inhibition studies may interfere with assay components and skew results. To minimize this potential interference, we selected a concentration range of 50-200 µg/mL. Despite these challenges, the study provides valuable insights, but the findings should be interpreted with these limitations in mind.

3.2. Antioxidant Capacity

Prolonged and repeated exposure to UV can lead to the accumulation of a substantial number of active oxygen products within skin tissues. The mechanisms underlying photoaging induced by UV radiation primarily involve the generation of ROS and DNA damage, ultimately resulting in cellular damage. A key factor in this process is the imbalance between ROS production and their neutralization by the body's natural antioxidant systems, leading to oxidative stress. ROS can promote the peroxidation of the lipid components in cell membranes and alter the structure and function of various enzymatic systems (54).

The results from the current study indicate that berberine possesses significant potential in

neutralizing free radicals and demonstrates remarkable reduction capabilities when compared to the control substance, ascorbic acid. Our findings, as determined by the FRAP assay, indicate that 210.387 mg of berberine is equivalent to 1 mM of ascorbic acid in reducing power. A comprehensive investigation into berberine's antioxidant capacity was conducted by Aoxue Luo and Yijun Fan (55) employing six distinct methods. Their research revealed that berberine displayed scavenging abilities against radicals, particularly with regards to ABTS, hydroxyl, and DPPH radicals. Overall, berberine's impressive antioxidant prowess can be attributed to the existence of electron-donating groups within the molecular structure of this alkaloid compound (56).

Table 4: Antioxidant activity of berberine using FRAP, DPPH and ABTS radical scavenging assays.

Antioxidant Assays	Berberine	Ascorbic acid (AA)
DPPH Radical Scavenging Activity IC ₅₀ Values (µg/mL)	66.81	55.1
ABTS Radical Scavenging Activity IC ₅₀ Values (µg/mL)	180.5	125.7
FRAP	210.387 mg/L Berberine/176 mg/L AA	

3.3. Determination of SPF, pH and Stability of Berberine in Formulated Cream

In daily life, the skin's exposure to sunlight stands out as the primary factor that accelerates photoaging. This condition can activate the extrinsic mechanism responsible for ROS synthesis throughout skin cells. Excessive ROS production, in turn, leads to the appearance of wrinkles and a reduction in skin elasticity. Sunscreens were developed with the aim of averting these effects by either dispersing or absorbing the UV light (57).

In this study, the SPF value of the berberine in formulated creams was evaluated using UV spectrophotometry and the Mansur mathematical equation. Figure 2 shows the SPFs of the formulated creams. It was demonstrated that the SPF of the

berberine-containing cream (F2) was significantly higher than that of the base cream, comparable to the cream containing 1.5% ascorbic acid (F1). These results indicate that berberine can effectively function as a highly efficient anti-solar agent against harmful UV radiation.

Brinda, S et al. (58) evidenced the effectiveness of aqueous extract of three types of naturally occurring herbs separately and in combinations, in the formulation of sunscreen creams aiming to avoid the addition of synthetic active ingredients due to their adverse effects. They estimated the SPF value of creams using the spectrophotometric method and Mansur equation. They found the highest SPF value for the creams containing integrated herbal ingredients (58).

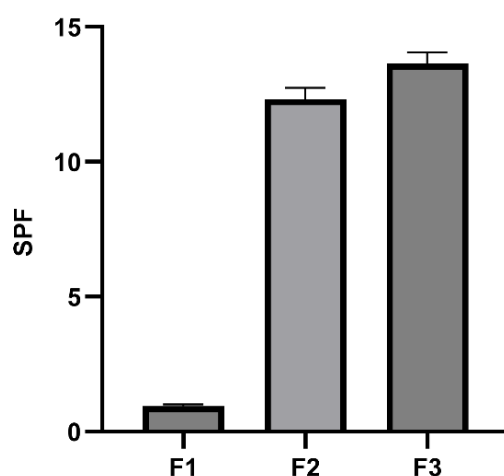


Figure 2: Determination of the Sun Protection Factor (SPF) of Oil-in-Water Creams containing berberine (F2) and Ascorbic Acid (F3) and negative control without active ingredient (F1). Values are the mean ± standard deviation (n=3).

The pH values of formulated creams are presented in Table 2. The pH of F3, compared to F2, was lower; however, the changes in the pH values during three-time intervals were not significantly different at $P < 0.01$. All samples exhibited a pH level close to skin's natural pH.

The stability of formulations was determined at three different temperatures: $8^{\circ}\text{C} \pm 0.1^{\circ}\text{C}$, $25^{\circ}\text{C} \pm 1^{\circ}\text{C}$, $40^{\circ}\text{C} \pm 1$, and $65 \pm 5^{\circ}\text{C}$ relative humidity for a duration of 3 months. All of the formulations

demonstrated strong stability when exposed to different temperatures for three months.

The pH level of sunscreen is a critical factor that affects both its effectiveness in providing sun protection and heat stability of the cream. It should be compatible with the skin's natural pH, which is typically around 5.5 (59). The pH of our formulations was found to be 5.6 and remained stable for a duration of 24 days.

Table 5: pH values of formulated creams.

Formulations	0 Day	14 days	28 days
F1 ^{1a}	6.72 ± 0.1	6.75 ± 0.08	6.77 ± 0.05
F2 ^{1b}	5.62 ± 0.08	5.62 ± 0.2	5.6 ± 0.3
F3 ^{1c}	5.39 ± 0.1	5.4 ± 0.1	5.4 ± 0.15

¹The change in the pH values during three time intervals was not significantly different at $p < 0.01$. ^a Negative control without active ingredient (F1), ^b berberine (F2) and ^c Ascorbic Acid (F3).

4. CONCLUSION

Collagen and elastin are crucial structural proteins that maintain skin integrity and elasticity. A decrease in their levels is closely associated with the appearance of aging signs, such as wrinkles and sagging skin.

In recent years, Cosmeceuticals-cosmetic products with bioactive compounds- have gained significant attention for their potential to combat skin aging. These products often contain active antioxidant and anti-aging compounds derived from various plant sources, offering natural and effective solutions for skincare.

Our research highlights Berberine, as a potent antioxidant and an effective agent in inhibiting collagenase and elastase activity. In our studies, a formulated cream containing Berberine demonstrated promising results, showing reasonable sun protection factor (SPF), skin-suitable pH values, and excellent heat stability. These findings suggest that Berberine is a promising candidate for use as an active ingredient in cosmeceuticals, offering a natural approach to enhance skin health and reduce the visible signs of aging.

5. CONFLICT OF INTEREST

The authors declare no competing financial interest.

6. ACKNOWLEDGMENTS

I would like express my sincere gratitude to Uskudar University for providing the necessary facilities and study environment that enabled us to conduct this study. I would like to extend my sincere appreciation to Ali Reza Mohseni for his assistance in preparing and reviewing this manuscript. No financial grant was received for this research.

7. REFERENCES

1. Svobodová A, Vostálová J. Solar radiation induced skin damage: Review of protective and preventive options. Int J Radiat Biol [Internet]. 2010 Dec;86(12):999–1030. Available from: [<URL>](#).
2. Polefka TG, Meyer TA, Agin PP, Bianchini RJ. Effects of solar radiation on the skin. J Cosmet Dermatol [Internet]. 2012 Jun 4;11(2):134–43. Available from: [<URL>](#).
3. Shin DW. Various biological effects of solar radiation on skin and their mechanisms: implications for phototherapy. Animal Cells Syst (Seoul) [Internet]. 2020 Jul 3;24(4):181–8. Available from: [<URL>](#).
4. Masaki H. Role of antioxidants in the skin: Anti-aging effects. J Dermatol Sci [Internet]. 2010 May 1;58(2):85–90. Available from: [<URL>](#).
5. Garg C, Sharma H, Garg M. Skin photo-protection with phytochemicals against photo-oxidative stress, photo-carcinogenesis, signal transduction pathways and extracellular matrix remodeling—An overview. Ageing Res Rev [Internet]. 2020 Sep 1;62:101127. Available from: [<URL>](#).
6. Malik A, Hoenig LJ. Can aging be slowed down? Clin Dermatol [Internet]. 2019 Jul 1;37(4):306–11. Available from: [<URL>](#).
7. Lee C. Fifty years of research and development of cosmeceuticals: A contemporary review. J Cosmet Dermatol [Internet]. 2016 Dec 6;15(4):527–39. Available from: [<URL>](#).
8. Kerscher M, Buntrock H. Update on cosmeceuticals. JDDG J der Dtsch Dermatologischen Gesellschaft [Internet]. 2011 Apr 3;9(4):314–28. Available from: [<URL>](#).
9. Nam EJ, Yoo G, Lee JY, Kim M, Jhin C, Son YJ, et al. Glycosyl flavones from *Humulus japonicus* suppress MMP-1 production via decreasing oxidative

stress in UVB irradiated human dermal fibroblasts. BMB Rep [Internet]. 2020 Jul 31;53(7):379–84. Available from: [<URL>](#).

10. Varma S, Mishra A, Vijayakumar M, Paramesh R. Anti-skin ageing phytochemicals in cosmetics: An appraisal. Agro Food Ind Hi-Tech [Internet]. 2017;28(2):15–8. Available from: [<URL>](#).

11. Shoko T, Maharaj VJ, Naidoo D, Tselanyane M, Nthambeleni R, Khorombi E, et al. Anti-aging potential of extracts from *Sclerocarya birrea* (A. Rich.) Hochst and its chemical profiling by UPLC-Q-TOF-MS. BMC Complement Altern Med [Internet]. 2018 Dec 7;18(1):54. Available from: [<URL>](#).

12. Satyavani K, Gurudeeban S, Ramanathan T. Inhibitory effect of *Excoecaria Agallocha* L. extracts on elastase and collagenase and identification of metabolites using HPLC-UV-MS techniques. Pharm Chem J [Internet]. 2018 Feb 14;51(11):960–4. Available from: [<URL>](#).

13. Panzarini E, Dwikat M, Mariano S, Vergallo C, Dini L. Administration dependent antioxidant effect of *Carica papaya* seeds water extract. Eddouks M, editor. Evidence-Based Complement Altern Med [Internet]. 2014 Jan 25;2014(1):281508. Available from: [<URL>](#).

14. Seo SA, Ngo HTT, Hwang E, Park B, Yi TH. Protective effects of *Carica papaya* leaf against skin photodamage by blocking production of matrix metalloproteinases and collagen degradation in UVB-irradiated normal human dermal fibroblasts. South African J Bot [Internet]. 2020 Jul 1;131:398–405. Available from: [<URL>](#).

15. Maity N, Nema NK, Abedy MK, Sarkar BK, Mukherjee PK. Exploring *Tagetes erecta* Linn flower for the elastase, hyaluronidase and MMP-1 inhibitory activity. J Ethnopharmacol [Internet]. 2011 Oct 11;137(3):1300–5. Available from: [<URL>](#).

16. Pacheco-Palencia LA, Noratto G, Hingorani L, Talcott ST, Mertens-Talcott SU. Protective effects of standardized pomegranate (*Punica granatum* L.) polyphenolic extract in ultraviolet-irradiated human skin fibroblasts. J Agric Food Chem [Internet]. 2008 Sep 24;56(18):8434–41. Available from: [<URL>](#).

17. Chaikul P, Sripisut T, Chanpirom S, Dittawutthikul N. Anti-skin aging activities of green tea (*Camelliasinensis* (L) Kuntze) in B16F10 melanoma cells and human skin fibroblasts. Eur J Integr Med [Internet]. 2020 Dec 1;40:101212. Available from: [<URL>](#).

18. Mao F, Wu Z, Shen Y, Ren Y, Yang M, Li X, et al. Regulatory mechanism of rosemary extract (*Rosmarinus officinalis*) on human skin fibroblasts during ultraviolet a photoaging. Iran J Sci Technol Trans A Sci [Internet]. 2021 Apr 23;45(2):427–36. Available from: [<URL>](#).

19. Lohakul J, Chairprasongsuk A, Jeayeng S, Saelim M, Muanjumpon P, Thanachaiphawat S, et al. The protective effect of polyherbal formulation, harak formula, on UVA-induced photoaging of human

dermal fibroblasts and mouse skin via promoting Nrf2-regulated antioxidant defense. Front Pharmacol [Internet]. 2021 Apr 12;12:649820. Available from: [<URL>](#).

20. Md Jaffri J. Reactive oxygen species and antioxidant system in selected skin disorders. Malaysian J Med Sci [Internet]. 2023 Feb 28;30(1):7–20. Available from: [<URL>](#).

21. Ascenso A, Margarida Ribeiro H, Cabral Marques H, Simoes S. Topical delivery of antioxidants. Curr Drug Deliv [Internet]. 2011 Nov 1;8(6):640–60. Available from: [<URL>](#).

22. Yang F, Gao R, Luo X, Liu R, Xiong D. Berberine influences multiple diseases by modifying gut microbiota. Front Nutr [Internet]. 2023 Aug 3;10:1187718. Available from: [<URL>](#).

23. Rojsanga P, Gritsanapan W, Suntornsuk L. Determination of berberine content in the stem extracts of *Coscinium fenestratum* by TLC densitometry. Med Princ Pract [Internet]. 2006 Aug 1;15(5):373–8. Available from: [<URL>](#).

24. Sakai T. Solvent extraction–spectrophotometric determination of berberine and benzethonium in drugs with tetrabromophenolphthalein ethyl ester by batchwise and flow injection methods. Analyst [Internet]. 1991 Jan 1;116(2):187–90. Available from: [<URL>](#).

25. Wang Y, Yin S, Zhao C, Chen G, Yang F. Preparation of a zirconium terephthalate metal-organic framework coated magnetic nanoparticle for the extraction of berberine prior to high-performance liquid chromatography analysis. J Sep Sci [Internet]. 2021 Mar 18;44(6):1220–30. Available from: [<URL>](#).

26. Liu S, Chen Y, Gu L, Li Y, Wang B, Hao J, et al. Effects of ultrahigh pressure extraction conditions on yields of berberine and palmatine from cortex *Phellodendri amurensis*. Anal Methods [Internet]. 2013 Aug 8;5(17):4506–12. Available from: [<URL>](#).

27. Naz I, Masoud MS, Chauhdary Z, Shah MA, Panichayupakaranant P. Anti-inflammatory potential of berberine-rich extract via modulation of inflammation biomarkers. J Food Biochem [Internet]. 2022 Dec 19;46(12):e14389. Available from: [<URL>](#).

28. Aly S, El-Kamel AH, Sheta E, El-Habashy SE. Chondroitin/Lactoferrin-dual functionalized pterostilbene-solid lipid nanoparticles as targeted breast cancer therapy. Int J Pharm [Internet]. 2023 Jul 25;642:123163. Available from: [<URL>](#).

29. Hu H, Zhou S, Sun X, Xue Y, Yan L, Sun X, et al. A potent antiarrhythmic drug N-methyl berbamine extends the action potential through inhibiting both calcium and potassium currents. J Pharmacol Sci [Internet]. 2020 Apr 1;142(4):131–9. Available from: [<URL>](#).

30. Huang M, He Y, Tian L, Yu L, Cheng Q, Li Z, et al. Gut microbiota-SCFAs-brain axis associated with the

- antidepressant activity of berberine in CUMS rats. J Affect Disord [Internet]. 2023 Mar 15;325:141–50. Available from: [<URL>](#).
31. Yang L, Cheng CF, Li ZF, Huang XJ, Cai SQ, Ye SY, et al. Berberine blocks inflammasome activation and alleviates diabetic cardiomyopathy via the miR-18a-3p/Gsdmd pathway. Int J Mol Med [Internet]. 2023 Apr 24;51(6):49. Available from: [<URL>](#).
32. Tehrani SO, Rahbardar MG, Shoorgashti K, Nayeri MJD, Mohammadpour AH, Hosseinzadeh H. Evaluation of berberine pellet effect on clinical recovery time in COVID-19 outpatients: A pilot clinical trial. Avicenna J Phytomedicine [Internet]. 2023 May 1;13(3):265–79. Available from: [<URL>](#).
33. Dadgostar E, Moghanlou M, Parvaresh M, Mohammadi S, Khandan M, Aschner M, et al. Can berberine serve as a new therapy for parkinson's disease? Neurotox Res [Internet]. 2022 Aug 6;40(4):1096–102. Available from: [<URL>](#).
34. Shekarabi SPH, Mehrgan MS, Ramezani F, Dawood MAO, Van Doan H, Moonmanee T, et al. Effect of dietary barberry fruit (*Berberis vulgaris*) extract on immune function, antioxidant capacity, antibacterial activity, and stress-related gene expression of Siberian sturgeon (*Acipenser baerii*). Aquac Reports [Internet]. 2022 Apr 1;23:101041. Available from: [<URL>](#).
35. El-Zahar KM, Al-Jamaan ME, Al-Mutairi FR, Al-Hudiab AM, Al-Einzi MS, Mohamed AAZ. Antioxidant, antibacterial, and antifungal activities of the ethanolic extract obtained from *Berberis vulgaris* roots and leaves. Molecules [Internet]. 2022 Sep 19;27(18):6114. Available from: [<URL>](#).
36. Gholampour F, Masoudi R, Khaledi M, Rooyeh MM, Farzad SH, Ataellahi F, et al. *Berberis integerrima* hydro-alcoholic root extract and its constituent berberine protect against cisplatin-induced nephro- and hepato-toxicity. Am J Med Sci [Internet]. 2022 Jul 1;364(1):76–87. Available from: [<URL>](#).
37. Ashraf H, Zare S. Preventive effects of aqueous extract of *Berberis integerrima* Bge. Root on liver injury induced by diabetes mellitus (Type 1) in rats. Iran J Pharm Res IJPR [Internet]. 2015 Dec 1;14(1):335–43. Available from: [<URL>](#).
38. Yadawa AK, Srivastava P, Singh A, Kesharwani R, Bhoumik S, Kumar R, et al. Berberine may provide redox homeostasis during aging in rats. Zeitschrift für Naturforsch C [Internet]. 2023 Jul 26;78(7–8):307–15. Available from: [<URL>](#).
39. Cometa S, Bonifacio MA, Licini C, Bellissimo A, Pinto L, Baruzzi F, et al. Innovative eco-friendly hydrogel film for berberine delivery in skin applications. Molecules [Internet]. 2021 Aug 13;26(16):4901. Available from: [<URL>](#).
40. Kim S, Chung JH. Berberine prevents UV-induced MMP-1 and reduction of type I procollagen expression in human dermal fibroblasts. Phytomedicine [Internet]. 2008 Sep 3;15(9):749–53. Available from: [<URL>](#).
41. Dzobo K, Dandara C. The extracellular matrix: Its composition, function, remodeling, and role in tumorigenesis. Biomimetics [Internet]. 2023 Apr 5;8(2):146. Available from: [<URL>](#).
42. Kraunsoe JAE, Claridge TDW, Lowe G. Inhibition of human leukocyte and porcine pancreatic elastase by homologues of bovine pancreatic trypsin inhibitor. Biochemistry [Internet]. 1996 Jan 1;35(28):9090–6. Available from: [<URL>](#).
43. Senol Deniz FS, Orhan IE, Duman H. Profiling cosmeceutical effects of various herbal extracts through elastase, collagenase, tyrosinase inhibitory and antioxidant assays. Phytochem Lett [Internet]. 2021 Oct 1;45:171–83. Available from: [<URL>](#).
44. Kozachok S, Pecio Ł, Orhan IE, Deniz FSS, Marchyshyn S, Oleszek W. Reinvestigation of *Herniaria glabra* L. saponins and their biological activity. Phytochemistry [Internet]. 2020 Jan 1;169:112162. Available from: [<URL>](#).
45. Tarbiat S, Unver D, Tuncay S, Isik S, Yeman KB, Mohseni AR. Neuroprotective effects of Cubebin and Hinokinin lignan fractions of *Piper cubeba* fruit in Alzheimer's disease *in vitro* model. Turkish J Biochem [Internet]. 2023 Jul 19;48(3):303–10. Available from: [<URL>](#).
46. Sharma T, Tyagi V, Bansal M. Determination of sun protection factor of vegetable and fruit extracts using UV-Visible spectroscopy: A green approach. Sustain Chem Pharm [Internet]. 2020 Dec 1;18:100347. Available from: [<URL>](#).
47. Pujimulyani D, Suryani L, Setyawati A, Amalia A, Qodaniah RL, Kusuma HSW, et al. Elastase, Hyaluronidase and Tyrosinase inhibitor activities antiaging of *Curcuma mangga* Val. extract and its fractions. IOP Conf Ser Earth Environ Sci [Internet]. 2019 Nov 1;379(1):012004. Available from: [<URL>](#).
48. Bourgeois C, Leclerc ÉA, Corbin C, Doussot J, Serrano V, Vanier JR, et al. Nettle (*Urtica dioica* L.) as a source of antioxidant and anti-aging phytochemicals for cosmetic applications. Comptes Rendus Chim [Internet]. 2016 May 19;19(9):1090–100. Available from: [<URL>](#).
49. Masson P, Mukhametgalieva AR. Partial reversible inhibition of enzymes and its metabolic and pharmacotoxicological implications. Int J Mol Sci [Internet]. 2023 Aug 19;24(16):12973. Available from: [<URL>](#).
50. Copeland RA. Reversible modes of inhibitor interactions with enzymes. In: Evaluation of enzyme inhibitors in drug discovery: A guide for medicinal chemists and pharmacologists. John Wiley & Sons, Inc. Hoboken, New Jersey; 2005. p. 57–121.
51. Bosch R, Philips N, Suárez-Pérez J, Juarranz A, Devmurari A, Chalensouk-Khaosaat J, et al. Mechanisms of photoaging and cutaneous photocarcinogenesis, and photoprotective strategies

with phytochemicals. *Antioxidants* [Internet]. 2015 Mar 26;4(2):248–68. Available from: [<URL>](#).

52. Madhan B, Krishnamoorthy G, Rao JR, Nair BU. Role of green tea polyphenols in the inhibition of collagenolytic activity by collagenase. *Int J Biol Macromol* [Internet]. 2007 Jun 1;41(1):16–22. Available from: [<URL>](#).

53. Thomas N, Kim SK. Beneficial effects of marine algal compounds in cosmeceuticals. *Mar Drugs* [Internet]. 2013 Jan 14;11(1):146–64. Available from: [<URL>](#).

54. Chen X, Yang C, Jiang G. Research progress on skin photoaging and oxidative stress. *Adv Dermatology Allergol* [Internet]. 2021;38(6):931–6. Available from: [<URL>](#).

55. Luo A, Fan Y. Antioxidant activities of berberine hydrochloride. 2011;5(16):3702–7. Available from: [<URL>](#).

56. Lee CY, Sharma A, Semenya J, Anamoah C, Chapman KN, Barone V. Computational study of ortho-substituent effects on antioxidant activities of phenolic dendritic antioxidants. *Antioxidants* [Internet]. 2020 Feb 25;9(3):189. Available from: [<URL>](#).

57. Kockler J, Oelgemöller M, Robertson S, Glass BD. Photostability of sunscreens. *J Photochem Photobiol C Photochem Rev* [Internet]. 2012 Mar 1;13(1):91–110. Available from: [<URL>](#).

58. Brinda S, Gitika D, Varsha V. Formulation and in-vitro evaluation of sun protection factor in a polyherbal cream. *International J Pharm Sciences Res* [Internet]. 2017;8(1):197–200. Available from: [<URL>](#).

59. Frasheri L, Schielein MC, Tizek L, Mikschl P, Biedermann T, Zink A. Great green tea ingredient? A narrative literature review on epigallocatechin gallate and its biophysical properties for topical use in dermatology. *Phyther Res* [Internet]. 2020 Sep 18;34(9):2170–9. Available from: [<URL>](#).



Spectrophotometric Determination of Meloxicam in Pure Form and its Pharmaceutical Formulation following Azo Dye Formation with 4-nitroaniline

Ali M. Atiyah^{1*} , Kameran S. Hussein¹ , Abdul Majeed K. Ahmed² 

¹Department of Chemistry, College of Science, University of Kirkuk, Kirkuk, Iraq.

²Department of Chemistry, College of Education For pure sciences, University of Kirkuk, Kirkuk, Iraq.

Abstract: A fast, cheap, and straightforward spectrophotometric method has been proposed to determine meloxicam (MEL) in its pure form and pharmaceutical formulation. The technique involves diazotizing the (NH₂) group in 4-nitroaniline with NaNO₂ followed by a reaction with meloxicam to produce a stable and colored complex in a basic medium. This complex demonstrates maximum absorbance at 514 nm. The developed method's linearity ranges from 2.0 - 25 µg mL⁻¹, and the molar absorptivity is 1.5989 × 10⁴ L mol⁻¹ cm⁻¹. The RSD% is lower than 1.55%. Additionally, the limit of detection (LOD) is 0.2019 µg mL⁻¹. The method successfully determines the pharmaceutical preparation containing meloxicam (Loxim tablets) with a recovery rate of no less than 97.9%.

Keywords: Spectrophotometric, Diazotization coupling reaction, Meloxicam, 4-nitroaniline.

Submitted: March 12, 2024. **Accepted:** August 22, 2024.

Cite this: Atiyah AM, Hussein KS, Ahmed AMK. Spectrophotometric Determination of Meloxicam in Pure Form and its Pharmaceutical Formulation following Azo Dye Formation with 4-nitroaniline. JOTCSA. 2024;11(4): 1461-72.

DOI: <https://doi.org/10.18596/jotcsa.1451322>

***Corresponding author's E-mail:** alimohammed@uokirkuk.edu.iq

1. INTRODUCTION

Meloxicam is 4-Hydroxy-2-methyl-N-(5-methyl-2-thiazolyl)-2H-1,2-benzothiazine-3-carboxamide 1,1-dioxide (Figure 1), with the chemical formula C₁₄H₁₃N₃O₄S₂ a molecular weight of 351.4g mol⁻¹. Meloxicam is a pale-yellow crystalline powder. It is practically insoluble in water but shows higher solubility in strong acids and bases. It is also very slightly soluble in 96% aqueous ethanol (1).

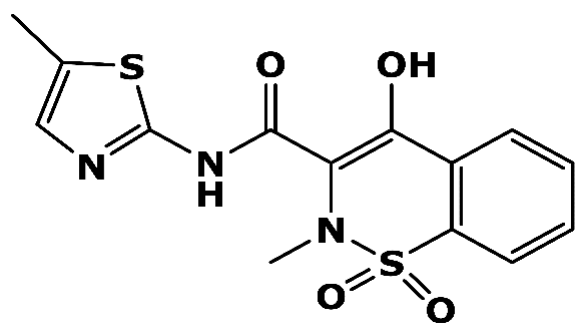


Figure 1: The structure of meloxicam.

An oxycam derivative called meloxicam is a nonsteroidal anti-inflammatory medication (NSAID) that selectively inhibits cyclooxygenase-2 (COX-2). MEL treats symptoms of ankylosing spondylitis, acute exacerbations of osteoarthritis, and rheumatoid arthritis. It is also used as a short-term symptomatic treatment. Moreover, juvenile idiopathic arthritis may be treated with it (2). MEL easily permeates the synovial fluid, suggesting that the active ingredient plays a role in eradicating the infectious process within the joint tissues. With a 20-fold selectivity towards COX-2 over COX-1, MEL exerts a beneficial influence on cartilage tissue metabolism and exhibits chondroprotective characteristics (3). Several methods have been applied for the estimation of meloxicam, such as spectrophotometric methods(4-12), high performance liquid chromatographic methods (HPLC) (13-19), ultra-high performance liquid chromatography (20), High-performance thin layer Chromatography (HPTLC) (21), polarography (22,23), voltammetry (24-26), and flow injection analysis (FIA) methods (27,28).

Azo dyes are synthetic compounds containing an azo bond (-N=N-) (29). Most azo dyes are produced by diazotization of an aromatic primary amine, followed by coupling with one or more electron-rich nucleophiles such as NH₂ or OH group (30). The spectrophotometric measurement of Meloxicam in this work is based on the drug's azo dye coupling with diazotized 4-nitroaniline in a basic medium.

2. EXPERIMENTAL

2.1. Apparatus

All spectrophotometric measurements were made using a T92+ spectrophotometer double beam, China, with a 1.0 mm quartz cell. Solution pH was measured using a Jenway 3310 pH meter, and all weight measurements were made using a Sartorius Balance BL210 SAG, Germany.

2.2. Reagents and Chemical Materials

The pharmaceutical and medical supplies company (SDI), Samarra, Iraq, provided the meloxicam (pure standard powder). Fluka and BDH provided all other analytical chemical reagents, including 4-nitroaniline, hydrochloric acid, sodium hydroxide, and sodium nitrite. The pharmaceutical formulation (tablets) was provided by the company of Ajanta Pharma Limited, Mumbai, India. All materials were of the highest possible quality. Each solution was made from scratch using distilled water.

2.3. Preparation of Solutions

2.3.1. Meloxicam solution (1000 µg mL⁻¹)

It was prepared by dissolving 0.1g of meloxicam in 5.0 mL of sodium hydroxide at a concentration of 0.1N (31) and then completing the volume to 100 mL with distilled water using a volumetric flask. Then, 25 mL of this solution is diluted to 100 mL with distilled water to obtain a solution with a concentration of 250 µg mL⁻¹ (7.1×10^{-4} mol L⁻¹).

2.3.2. Hydrochloric acid solution, approximate concentration 1.0 mol L⁻¹

This solution was prepared by diluting 8.5 mL of the concentrated acid (11.8 mol L⁻¹) with distilled water and then completing the volume to 100 mL in a volumetric flask.

2.3.3. Sodium Hydroxide solution, approximate concentration 0.1 mol L⁻¹

In a 100 mL volumetric flask, 0.4 g of sodium hydroxide was dissolved in the appropriate volume of distilled water, and the flask was then filled to the mark.

2.3.4. Diazotized 4-nitroaniline solution (D-4NA) 5×10^{-3} mol L⁻¹

These steps are carried out in a dark flask: in the beginning, defrost 0.0345g of 4-nitroaniline in 2.0 mL of hydrochloric acid, and in another beaker, dissolve 0.0172g of NaNO₂ in 5.0 mL of distilled water. Both beakers were placed in an ice bath for 10 minutes at a temperature of 0-5°C, then the sodium nitrite solution (NaNO₂) was added drop by drop to the reagent solution, then stirred for 5 minutes and completing the volume to 50 mL with water. The color dye product must be kept in the ice

bath; the concentration of NaNO₂ (1×10^{-3} mol L⁻¹) in equimolar solution 1×10^{-3} mol L⁻¹ of 4-nitroaniline, so we do not need to add sulfamic acid in this method to get rid of excess NaNO₂.

2.3.5. Sample solution of meloxicam from tablets formulation 250 µg mL⁻¹

In the pharmaceutical formulation tablet (Loxim), every tablet contains 15 mg of MEL; this solution was prepared as follows: Ten tablets were weighed accurately. After grinding and mixing well, the weight of ten tablets was equal to 2.477 g. Then, a weight of 0.413 g of this powder, which is equivalent to 0.025 g of the drug, was dissolved in 5.0 mL of NaOH with distilled water. The solution was filtered to remove any insoluble material, and then the volume was completed with water at 100 mL.

3. RESULTS AND DISCUSSION

3.1. The Fundamental Idea for the Method

The reaction involved the formation of the D-4NA, followed by reacting with MEL in the presence of NaOH to yield a reddish-orange colored azo dye that has the highest absorbance at 514 nm.

3.2. Study of the Typical Circumstances for Reaction

The effect of various variables on the absorbance intensity of the azo dye formed from the reaction of MEL with diazotized 4-nitroaniline was investigated, and the optimum conditions have been selected as follows:

3.2.1. The impact of acid-type

The impact of different types of acids used in the formation of diazonium salt (D-4NA) was investigated. First, 4-nitroaniline was diazotized as previously described (4-NA & NaNO₂) in the presence of 2 mL of various types of acids at a concentration of 1.0 mol L⁻¹. Then, 1.0 mL of the formed diazotized solution was added to volumetric flasks containing 1.0 mL of MEL. Finally, 1.5 mL of NaOH was added. The outcomes are indicated in Table 1.

Table 1: Impact of acid-type.

Acid type	Absorbance
HCl	0.564
H ₂ SO ₄	0.505
HNO ₃	0.509
CH ₃ COOH	0.415

To clarify: The optimal amount of NaOH was used when analyzing each acid in the study. The reason for this is that we will be measuring the absorption of the azo dye product formed in the last step, not the diazonium salt formed by the reaction of the amino group in the reagent in the presence of sodium nitrite and acid.

3.2.2. The impact of the quantity of acid

The congruent quantities and sequences of sodium nitrite were added to a diverse amount of hydrochloric acid (1.0 mol L⁻¹) used in the formation of D-4NA solution, and the diazotized was utilized as earlier indicated in the preparation of azo dye. At 514

nm, the absorbance of the colored azo dye was measured in comparison to the blank solution. According to Figure 2, 2.0 mL of HCl (1.0 mol L^{-1})

gives the maximum absorbance intensity for the azo dye. Therefore, this volume was adopted in the later experiments.

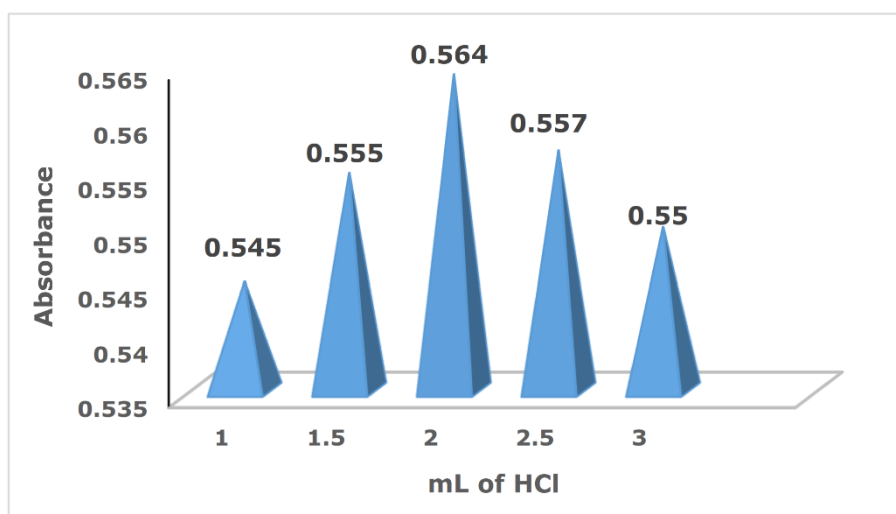


Figure 2: The impact of the quantity of acid.

3.2.3. Effect of amount of diazotized agent

The effect of different amounts of diazotized 4-nitroaniline(D-4NA) was studied by adding it to a series of 25 mL volumetric flasks containing 1.0 mL of MEL, followed by adding about 1.5 mL of sodium hydroxide. Then, the solution was completed with water. The results shown in Table 2 indicated that 1.0 mL of the diazotized agent solution produced the highest azo dye absorbance intensity.

From the results in Figure 3, it was clear that sodium hydroxide gives the highest absorbance. Therefore, it was used in subsequent experiments.

Table 2: Effect of amount of diazotized agent.

Amount of diazotized agent	Absorbance
0.5	0.552
1.0	0.563
1.5	0.556
2.0	0.544
2.5	0.532

3.2.4. The impact of the base type solutions

The coupling reaction between D-4NA and MEL occurs in an alkaline medium, so the impact of various bases and alkaline salts was probed to determine which produced the highest absorbance.

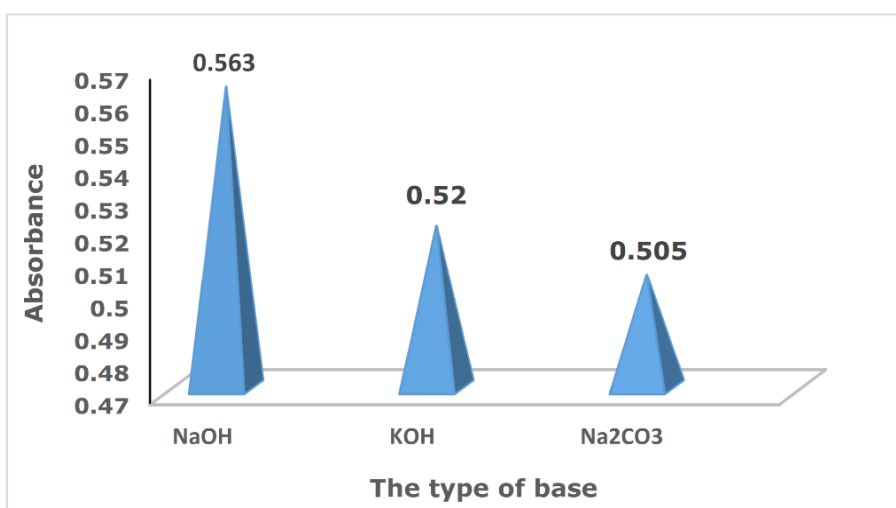


Figure 3: The impact of the base type solutions.

3.2.5. The impact of the amount of base

A study was carried out to establish the typical amount of base solution by adding diverse volumes (0.5-2.5 mL) of sodium hydroxide. It was found that 1.5 mL of NaOH gives the highest absorbance at pH=10.9. From the results listed in Table 3, it is clear to us that the relationship is a positive one at the

beginning. Then, after the added quantity reaches 1.5 mL (pH 10.9), we will obtain the highest absorption of the dye formed, and then it may plateau or decrease. The reason for an increase, in the beginning, is that the sodium ion originating from the sodium hydroxide displaces the chloride ion in the diazonium salt. Consequently, a positively

charged diazonium ion is formed, which functions as an electrophile and undergoes a reaction with the MEL, resulting in the formation of an azo dye. The reason for the decrease in absorbance after that is due to the ionization of MEL.

3.2.6. The impact of time on the stability of the dye formed

The stability of the produced dye was investigated by examining how time affected the absorbance of three different concentrations (5.0, 10, and 15 $\mu\text{g}\cdot\text{mL}^{-1}$) of MEL, following the suggested method procedure. The outcomes in Table 4 show that the reddish-orange dye remains stable for 50 minutes.

3.3. The Eventual Absorption Spectrum

After selecting the optimum conditions shown in Table 5, the eventual absorption spectrum was measured using 1.0 ml of MEL, 1.0 mL of D-4NA, and 1.5 mL of NaOH. The reaction was carried out in an ice bath (0-5°C), and then the solution was left for 5.0 minutes to complete the reaction. The volume was then finished with water to 25 mL. The absorption was measured against the blank solution. It was found to give a higher absorbance at 514 nm, while its blank gave a little absorption at the same wavelength. The results are shown in Figure 4.

Table 3: The impact of the amount of base.

Amount of NaOH (0.1 M)	Absorbance	pH
0.5	0.482	5.9
1.0	0.541	8.2
1.5	0.563	10.9
2.0	0.554	11.1
2.5	0.513	11.6

Table 4: The impact of time on the stability of the dye formed.

Time (min)	Absorbance		
	5.0 $\mu\text{g mL}^{-1}$	10 $\mu\text{g mL}^{-1}$	15 $\mu\text{g mL}^{-1}$
5	0.261	0.563	0.734
10	0.261	0.563	0.734
15	0.261	0.563	0.733
20	0.261	0.562	0.733
25	0.260	0.562	0.733
30	0.260	0.562	0.732
35	0.260	0.561	0.732
40	0.260	0.561	0.731
45	0.258	0.560	0.731
50	0.258	0.559	0.730
55	0.251	0.552	0.725
60	0.242	0.522	0.686

Table 5: Summary of optimum conditions.

Parameter	Optimum conditions
λ_{max}	514 mL
Amount of 7.1×10^{-4} mol L ⁻¹ (MEL)	1.0 mL
Amount of 5×10^{-3} mol L ⁻¹ (D-4NA)	1.0 mL
Amount of HCl (1.0 mol L ⁻¹)	2.0 mL
Amount of NaOH (0.1 mol L ⁻¹)	1.5 mL
Solvent	Water

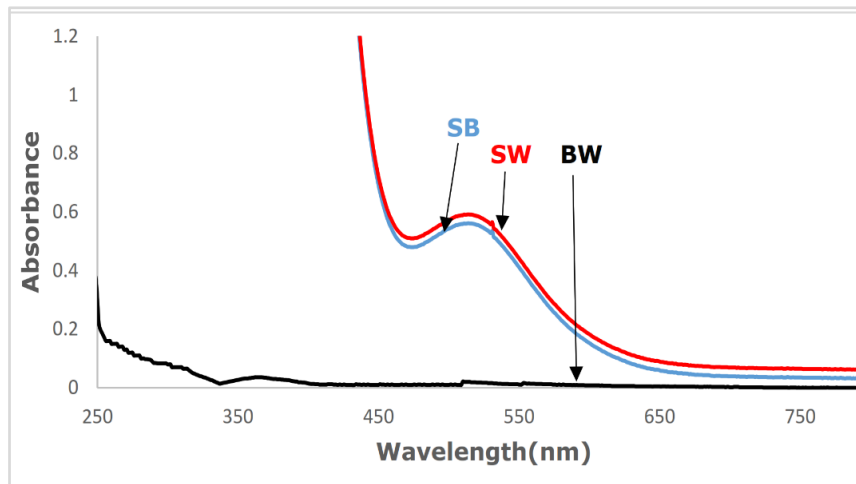


Figure 4: The eventual absorption spectrum for the determination of MEL ($10\mu\text{g mL}^{-1}$) versus water (SW), MEL vs. blank solution (SB), and blank solution vs. water (BW).

3.4. The Calibration Graph

After selecting the optimized experimental conditions, ranging from 0.2 to 2.5 mL of MEL drug solutions were transferred to a series of volumetric flasks (25 mL). These volumes corresponded to concentrations ranging from $2.0\mu\text{g mL}^{-1}$ to $25\mu\text{g mL}^{-1}$. Subsequently, 1.0 mL of diazotized 4-nitroaniline solution was added, followed by the addition of 1.5 mL of NaOH. The volumes were then

completed with water, and the absorbance was measured against the blank solution at 514 nm. Figures 5 and 6 demonstrate that the calibration graph adheres to Beer's law in the range of 2.0 to $25\mu\text{g mL}^{-1}$, while higher concentrations appear to show a negative deviation from Beer's law. The molar absorptivity was determined to be $1.5989 \times 10^4\text{ L mol}^{-1}\text{ cm}^{-1}$, and Sandall's index value was $0.02198\mu\text{g cm}^{-2}$.

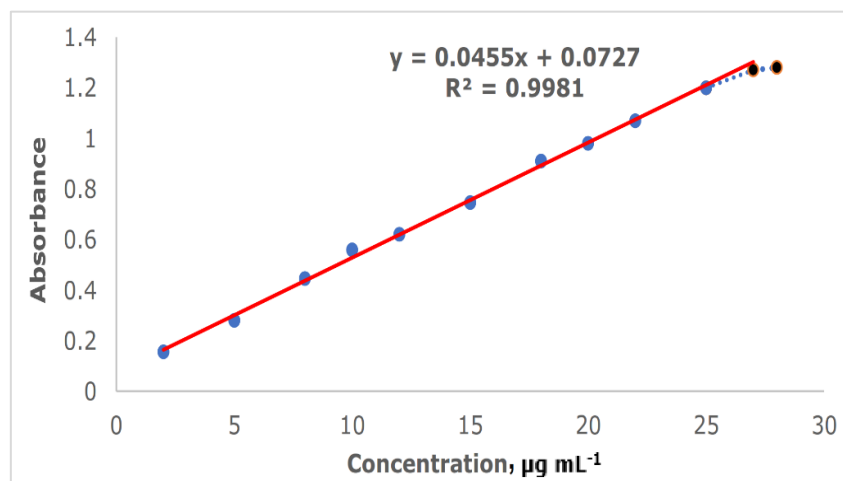


Figure 5: The calibration graph for the estimation of MEL using the suggested method.

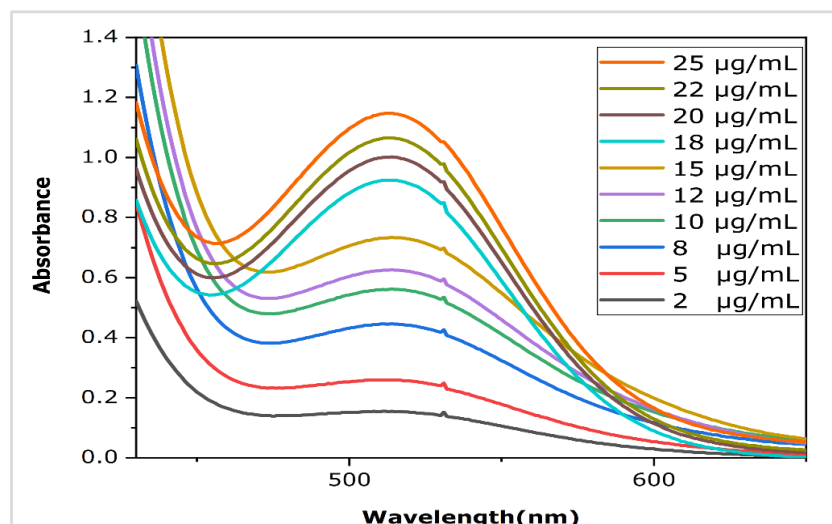


Figure 6: The calibration graph spectra for the estimation of MEL using the suggested method.

3.5. The Precision & Accuracy

The precision and accuracy of the method were examined by measuring the recovery percentage, as well as the relative standard deviation (RSD%) and the relative error (RE%). This was done for three different concentrations (5.0, 10, and 15) $\mu\text{g mL}^{-1}$,

with the absorbance being measured six times at a wavelength of 514 nm for each concentration. The average was then taken. The findings in Table 6 showed that the method for determining MEL had acceptable precision and accuracy.

Table 6: The results of precision and accuracy.

Amount of MEL ($\mu\text{g mL}^{-1}$) Taken	Amount of MEL ($\mu\text{g mL}^{-1}$) Measured	*RE%	*Recovery%	*RSD%
5	5.05	1.0	101	1.42
10	10.12	1.2	101.20	1.55
15	14.83	-1.13	98.86	0.96

*Average of six times

3.6. The Limit of Detection

The limit of detection was calculated by measuring the absorption of the blank solution (32) under optimized conditions (six times) at a wavelength of 514 nm using Equation: $\text{LOD} = 3.3 \text{ SD}/b$ (33,34), where (SD) is the standard deviation and (b) is the slope of the calibration curve. The limit of detection of the method was found to be $0.2109 \mu\text{g mL}^{-1}$.

3.7. Studying the Ratio of MEL and Diazotized 4-Nitroaniline in Forming Azo Dye

The stoichiometry of the product was investigated through the employment of the continuous variation method, also known as Job's method. This method was utilized to determine the characteristics of the resulting product and the proportion of the drug's ability to bind with the diazotized agent (35). The outcomes in Figure 7 indicate that the ratio of azo dye formed between diazotized 4-NA and MEL is 1:1.

Scheme 1 shows the suggested mechanisms for the reddish-orange dye formed by the reaction of MEL with the diazotized 4-NA in the basic medium.

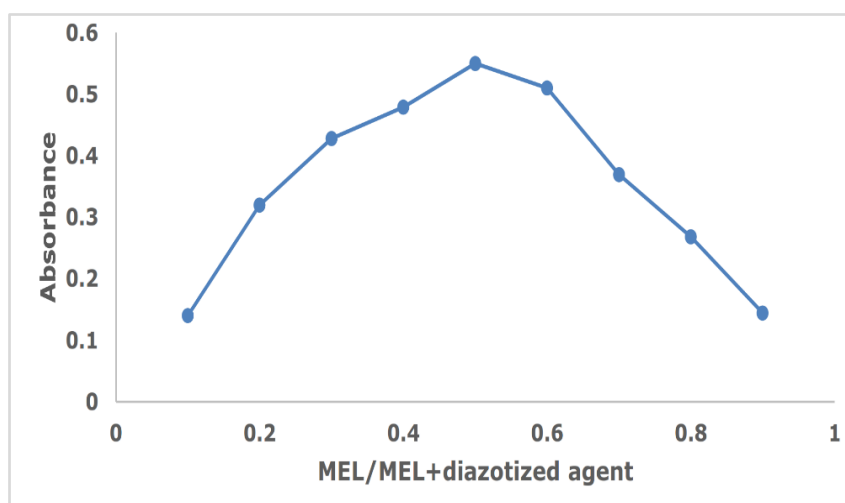
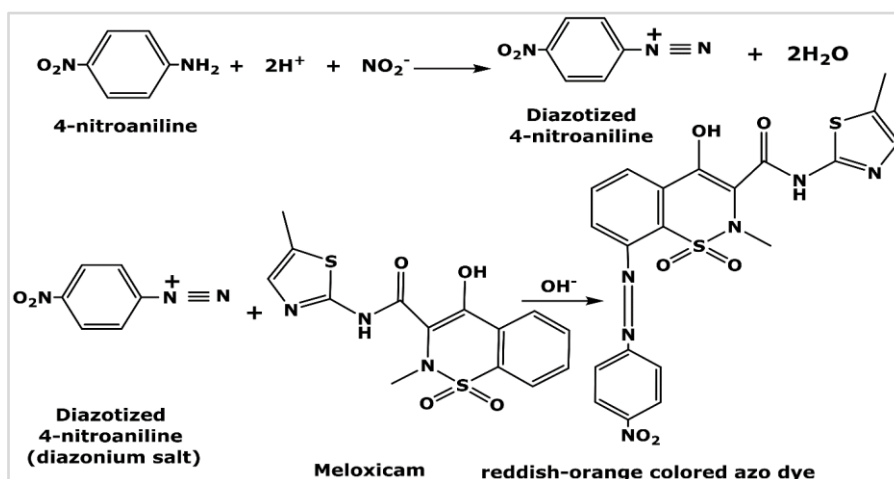


Figure 7: Continuous variation method of azo compound.



Scheme 1: The suggested mechanisms for the reaction.

3.8. Stability Constant of the Dye Formed (K_s)

To determine the stability constant for the 1:1 formed product (MEL and diazotized 4-NA), we utilized the outcomes of the Job's method as detailed in Section (3.7). Solutions were prepared containing equimolar quantities of MEL and diazotized 4-NA, each having a concentration of 7.1×10^{-4} mol L⁻¹. The absorbance of each solution was measured in comparison to its respective blank and denoted as (A_s). Furthermore, solutions were also prepared with the same quantity of MEL but with an excess amount (2 mL) of the diazotized agent, and their absorbance

was denoted as (A_m). The degree of dissociation (α) was determined using Equation 1. Subsequently, the stability constant of the reddish-orange dye produced in the aqueous solution was calculated using Equation 2. The results shown in Table 7 indicate that the product is highly stable.

$$\alpha = \frac{A_m - A_s}{A_m} \quad (1)$$

$$K_s = \frac{1 - \alpha}{\alpha^2 C} \quad (2)$$

Table 7: Stability constant.

*Concentration (C) mol L ⁻¹	Absorbance		α	K_s , L.mol ⁻¹
	A_s	A_m		
7.1×10^{-4}	0.568	0.580	0.02069	3.2×10^6

*(C) The concentration of the colored product.

3.9. The Applications Part

The methods were applied to a pharmaceutical formulation containing MEL drug, which is the pharmaceutical formulation (Loxim) produced by Ajanta Pharma Limited, Mumbai, India, in the form of tablets, and each tablet contained 15 mg of MEL.

3.9.1. Direct method

In order to demonstrate the validity of the suggested method in the estimation of MEL in the form of tablets with three different concentrations, the results are summarized in Table 8. The assay results indicated that the proposed method is applicable.

3.9.2. The standard addition method

To demonstrate that the method was free from interferences, the standard additions method was used to determine the concentration of MEL in its pharmaceutical preparation. Two series of six 25 mL volumetric flasks were prepared, with constant volumes (0.5 and 1.0 mL) of the pharmaceutical preparation added, equivalent to a concentration of (5.0 and 10 $\mu\text{g.mL}^{-1}$). Increasing volumes of MEL solutions were added, and then the absorption was measured against the blank solution at the wavelength of 514 nm. Table 9 and Figure 8 show the accordance of the standard addition method with the suggested method.

Table 8: The results of the direct method for the determination of MEL in pharmaceutical preparations.

Amount of MEL ($\mu\text{g mL}^{-1}$)		*RE%	*Recovery%	*RSD%
Taken	Measured			
5	5.10	2.0	102	1.91
10	9.92	-0.8	99.2	1.13
15	15.02	0.13	100.13	1.61

*Average of six times

Table 9: The results of standard-addition method for the identification of MEL in tablets

Amount of MEL ($\mu\text{g mL}^{-1}$)		*RE%	*Recovery%	*RSD%
Taken	Measured			
5	5.10	2.0	102	1.86
10	9.79	-2.1	97.9	1.12

*Average of six determinations

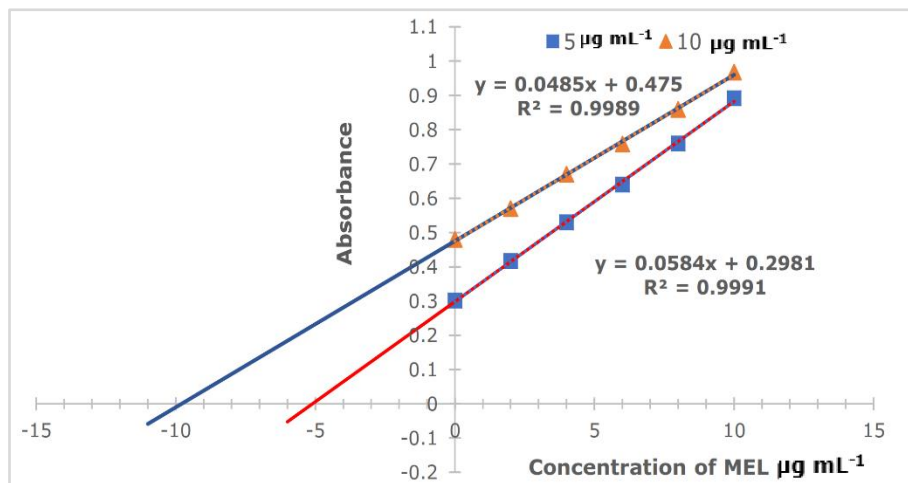


Figure 8: The standard addition curve for the identification of MEL in tablets.

3.10. Advantages of Our Spectrophotometric Method Compared to Other Analytical Technique

In this section, a comprehensive analysis is provided to elucidate the advantage of our spectrophotometric approach in contrast to other frequently employed analytical methodologies, including high-performance liquid chromatography (HPLC), polarography, and flow injection analysis. Emphasizing crucial factors such as precision, expenditure, temporal efficacy, usability, and instrumental prerequisites.

Accuracy: The current method offers high accuracy and consistent results. HPLC also provides very high accuracy, precise analysis, and separation but demands intricate preparation. Electrochemical conditions and impurities in the sample influence accuracy in polarography. Flow injection analysis delivers good accuracy but is susceptible to changes in flow rate and environmental factors.

The cost: The current method is cost-effective because it requires minimal equipment and no expensive reagents. In contrast, HPLC is expensive due to its complex instruments and costly chemicals. Polarography has moderate costs involving specialized electrochemical equipment. Flow injection analysis has medium to high costs due to precise flow control and fluid handling systems.

Time Efficiency: The current method provides fast results within minutes. HPLC is slow, taking hours for preparation and analysis. Polarography is moderately time-consuming, contingent on electrochemical response time. Flow injection analysis is quick but needs a pre-analysis setup.

The simplicity of utilization: Our method is user-friendly and does not necessitate sophisticated technical competencies, rendering it appropriate for regular laboratory assessments conducted by skilled technicians. Conversely, HPLC demands advanced

technical proficiency and practical know-how to manage and uphold the intricate machinery. Polarography necessitates a grasp of electrochemical examination but is comparatively less intricate than HPLC, whereas flow injection analysis mandates technical expertise to supervise flow systems and calibrate the equipment.

Equipment Requirements: The utilization of the spectrophotometric approach necessitates solely a basic spectrophotometer and an illuminating source, rendering it feasible for the majority of laboratory settings. Conversely, the application of HPLC mandates sophisticated chromatographic apparatus and equipment for sample preparation. Polarography, on the other hand, calls for a polarograph and supplementary electrochemical devices, whereas flow injection analysis necessitates a precise continuous flow mechanism and linked control instruments.

This comparison clearly illustrates the superiority of our spectrophotometric method in terms of simplicity, cost-effectiveness, and rapid analysis, making it an ideal choice for routine laboratory analysis compared to the more complex and expensive alternatives.

3.11. Comparison of the Method

Table 10 displays a comparison of various analytical variables between the current method and alternative methods found in the literature.

3.12. Statistical Agreement t-Test

Both the current method and the method described in the literature (36) were simultaneously utilized in the calculation of the t-test, with the obtained value then compared against statistical tables for eight degrees of freedom at a 95% confidence level. The findings presented in Table 11 demonstrate that there is no significant discrepancy between the two methodologies.

Table 10: The comparison study between the suggested method and other techniques reported in the literature.

Method	λ_{max} nm	Linear range $\mu\text{g mL}^{-1}$	RSD%	Recovery%	LOD $\mu\text{g mL}^{-1}$	Literature method Ref.	
Current method	514	2	0.96-1.42	98.86-101.2	0.2109	-	
Literature method	Spectroscopy	708	0.1-11	0.25-0.73	98.7-99.5	0.0092	7
	HPLC	290	1.0-50	< 3.9	100.4	0.25	13
	Polarography	-	0.38-15.0	0.27	99.20	0.02	23
	Voltammetry	-	10-90 in both *SWV & **DPV	2.72 for SWV & 3.06 for DPV	98.5 for SWV 98.7 for DPV	1.50 in both SWV & DPV	26
	FIA	530	10-160	1.2	97.0-104	6.0	28

*(SWV) Square wave voltammetric method, **(DPV) Differential pulse voltammetry.

Table 11: The results of t-test analysis.

Drug	Pharmaceutical preparation	*Recovery%		t. exp
		Current method	Literature method (36)	
Loxim	Tablet	99.95	98.4	0.77

*Average of five determinations

4. CONCLUSION

A robust spectrophotometric method was developed and validated for determining meloxicam in pure form and its pharmaceutical formulation through azo dye formation. Key performance metrics highlighted method efficacy. The linear range was 2.0-25 $\mu\text{g mL}^{-1}$ with a high correlation coefficient, showing excellent linearity for quantitative analysis. Molar absorptivity was $1.5989 \times 10^4 \text{ L mol}^{-1} \text{ cm}^{-1}$, and Sandell's sensitivity was $0.02198 \mu\text{g cm}^{-2}$, indicating high sensitivity to detect small meloxicam quantities. LOD was $0.2109 \mu\text{g mL}^{-1}$, demonstrating the method's capability to identify low concentrations accurately. The recovery rate was 98.86% - 101.20%, ensuring accuracy and reliability with common excipients. Relative standard deviation values were 0.96% to 1.55%, highlighting method precision and reproducibility. The stability constant of the azo dye complex was 3.2×10^6 , which indicates that it is a highly stable complex suitable for routine analysis. The method's applicability to the pharmaceutical formulation Loxim was confirmed, showing that common excipients did not interfere with the determination of meloxicam. This validation suggests that the proposed method is robust and versatile for quality control purposes in the pharmaceutical industry.

5. CONFLICT OF INTEREST

The authors declare that there is no conflict of competing financial interests.

6. ACKNOWLEDGMENTS

The authors are grateful for the facilities by the chemistry department, College of Science, Kirkuk University and for the state company for drug

industries and medical appliance (Samarra-Iraq) for conducting this study.

7. REFERENCES

- Chaudhary M, Bhardwaj K, Verma G, Kumar P. Validated analytical method development for the determination of Meloxicam by UV spectroscopy in API and pharmaceutical dosage form. Asian J Pharm Educ Res [Internet]. 7(2):60-9. Available from: [<URL>](#).
- Hasan SH, Othman NS, Surchi KM. Spectrophotometric method for determination of meloxicam in pharmaceutical formulations using N-bromosuccinimide as an oxidant. Int J Pharma Sci Res [Internet]. 2014;5(12):963-9. Available from: [<URL>](#).
- Ganna Olegivna S, Tetyana Stanislavivna T, Olga Leonidivna L, Olena Valeryivna S. Biochemical confirmation of anti-inflammatory activity of oxicam-based pharmaceutical compositions. J Turkish Chem Soc Sect A Chem [Internet]. 2018 Sep 1;5(3):1407-12. Available from: [<URL>](#).
- Donchenko A, Vasyuk S, Nahorna N. Extraction-free spectrophotometric determination of meloxicam using bromothymol blue. Ankara Univ Eczac Fak Derg [Internet]. 2023 Jul 17;47(3):752-60. Available from: [<URL>](#).
- Abbas RF, Mahdi NI, Waheb AA, Aliwi AG, Fali MS. Fourth derivative and compensated area under the curve spectrophotometric methods used for analysis meloxicam in the local market tablet. Al-Mustansiriyah J Sci [Internet]. 2018;29(3):70-6. Available from: [<URL>](#).

6. Gurupadayya BM, Trinath MN, Shilpa & K. Spectrophotometric determination of meloxicam by sodium nitroprusside and 1,10-phenanthroline reagents in bulk and its pharmaceutical formulation. *Indian J Chem Technol* [Internet]. 2013;20:111-5. Available from: [<URL>](#).
7. Mahood AM, Najm NH. Spectrophotometric estimation of meloxicam using charge transfer complex. *IOP Conf Ser Mater Sci Eng* [Internet]. 2019 Jul 1;571(1):012081. Available from: [<URL>](#).
8. Chaplenko AA, Monogarova O V., Oskolok K V. Spectroscopic and colorimetric determination of meloxicam, lornoxicam, tenoxicam in drugs. *Int J Pharm Biol Arch* [Internet]. 2018 Apr 26;9(1):31-5. Available from: [<URL>](#).
9. Aydoğmuş Z, Alim F. Determination of meloxicam in tablets by third derivative uv spectrophotometric method. *J Adv Res Heal Sci* [Internet]. 2024 Jan 19;7(1):61-7. Available from: [<URL>](#).
10. Antonio M, Carneiro RL, Maggio RM. A comparative approach of MIR, NIR and raman based chemometric strategies for quantification of form I of meloxicam in commercial bulk drug. *Microchem J* [Internet]. 2022 Sep 1;180:107575. Available from: [<URL>](#).
11. El-Malla SF, Hamza AA, Elagamy SH. Simultaneous determination of meloxicam and bupivacaine via a novel modified dual wavelength method and an advanced chemometric approach. *Sci Rep* [Internet]. 2024 Jan 22;14(1):1893. Available from: [<URL>](#).
12. Ndueche CA, Ogbeide UM, Okeri HA. Colorimetric determination of meloxicam in bulk and tablet dosage forms. *J Sci Pract Pharm* [Internet]. 2022 Dec 31;9(1):465-73. Available from: [<URL>](#).
13. Çelik RS, Bayrak B, Kadioğlu Y. Development and validation of HPLC-UV method for determination of meloxicam in tablet dosage formulation. *Pharmata* [Internet]. 2023 Jul 28;3(3):59-63. Available from: [<URL>](#).
14. Karpicarov D, Apostolova P, Arev M, Arsova-Sarafinovska Z, Gjorgjeska B. Development and validation of HPLC method for content determination of Meloxicam in injections. *Knowl - Int J* [Internet]. 2023;57(4):517-22. Available from: [<URL>](#).
15. Seles KS, Padmavath S, Abdul Rahaman S, Azmi S, Grace S, Sahana MA. Development and validation of stability indicating assay for simultaneous determination of bupivacaine and meloxicam in bulk and pharmaceutical formulations by using RP-HPLC method. *Int J Life Sci Pharma Res* [Internet]. 2022 Oct 21;12(6):117-31. Available from: [<URL>](#).
16. Zaman M, Hanif M, Khan NUH, Mahmood A, Qaisar MN, Ali H. Development and validation of stability-indicating RP-HPLC method for the simultaneous determination of tizanidine HCL and meloxicam in rabbit's plasma. *Acta Chromatogr* [Internet]. 2019 Sep 1;31(3):173-8. Available from: [<URL>](#).
17. Chikanbanjar N, Semwal N, Jyakhwa U. Analytical method validation of Meloxicam and Paracetamol tablet in combination by HPLC method. *Int J Pharm Sci Innov* [Internet]. 2020;1(1):84-94. Available from: [<URL>](#).
18. Bahgat EA, Hashem H, Saleh H, Kamel EB, Eissa MS. Stability-indicating HPLC-DAD and TLC-densitometry methods for the quantification of bupivacaine and meloxicam in their co-formulated mixture. *Microchem J* [Internet]. 2023 Jul 1;190:108683. Available from: [<URL>](#).
19. Ahmad R, Hailat M, Zakaraya Z, Al Meanazel O, Abu Dayyih W. Development and validation of an HPLC method for the determination of meloxicam and pantoprazole in a combined formulation. *Analytica* [Internet]. 2022 Apr 1;3(2):161-77. Available from: [<URL>](#).
20. Rani JDB, Deepti CA. Stability indicating method development of RP-UPLC, validation of simultaneous quantitation of bupivacaine and meloxicam in pure and formulation. *RASAYAN J Chem* [Internet]. 2023;16(03):1359-68. Available from: [<URL>](#).
21. Ivanova S, Todorova V, Dyankov S, Ivanov K. High-performance thin-layer chromatography (HPTLC) method for identification of meloxicam and piroxicam. *Processes* [Internet]. 2022 Feb 18;10(2):394. Available from: [<URL>](#).
22. Altiokka G, Atkosar Z, Tuncel M. Pulse polarographic determination of meloxicam. *Pharmazie* [Internet]. 2001 Feb;56(2):184-5. Available from: [<URL>](#).
23. Altınöz S, Nemutlu E, Kir S. Polarographic behaviour of meloxicam and its determination in tablet preparations and spiked plasma. *Farm* [Internet]. 2002 May 22;57(6):463-8. Available from: [<URL>](#).
24. Šelešovská R, Hlobeňová F, Skopalová J, Cankař P, Janíková L, Chýlková J. Electrochemical oxidation of anti-inflammatory drug meloxicam and its determination using boron doped diamond electrode. *J Electroanal Chem* [Internet]. 2020 Feb 1;858:113758. Available from: [<URL>](#).
25. Cerón-Pérez A, Juárez-Moreno MG, Martínez-Sánchez MM, González-Leal M, Sosa-Domínguez A. Developing a voltammetric method for meloxicam determination using a glassy carbon electrode modified with multi-walled carbon nanotubes (GC/MWCNT). *ECS Trans* [Internet]. 2021 Jan 11;101(1):57-67. Available from: [<URL>](#).
26. Miloglu FD, Saruhan T. Square wave and differential pulse voltammetric determination of meloxicam in pharmaceutical formulations. *Int J PharmATA* [Internet]. 2022 Jan 25;2(1):1-10. Available from: [<URL>](#).
27. Abed RI, Hadi H. Determination of meloxicam using direct and indirect flowinjection spectrophotometry. *Curr Pharm Anal* [Internet]. 2021 Jan 25;17(2):254-64. Available from: [<URL>](#).

28. Al-Momani IF. Indirect flow-injection spectrophotometric determination of meloxicam, tenoxicam and piroxicam in pharmaceutical formulations. *Anal Sci* [Internet]. 2006 Dec 10;22(12):1611–4. Available from: [<URL>](#).
29. Al-Rubaie LAAR, Mhessn RJ. Synthesis and characterization of azo dye para red and new derivatives. *J Chem* [Internet]. 2012 Jan 5;9(1):465–70. Available from: [<URL>](#).
30. Benkhaya S, M'rabet S, El Harfi A. Classifications, properties, recent synthesis and applications of azo dyes. *Heliyon* [Internet]. 2020 Jan 1;6(1):e03271. Available from: [<URL>](#).
31. Sawant R, Joshi R, Kawade D, Sarode V. Development and validation of spectrophotometric methods for simultaneous estimation of paracetamol and meloxicam in pure and tablet dosage form. *Der Pharm Lett* [Internet]. 2010;2(2):471–8. Available from: [<URL>](#).
32. Valcárcel Cases M, López-Lorente ÁI, López-Jiménez MÁ. Foundations of analytical chemistry [Internet]. Foundations of Analytical Chemistry. Cham: Springer International Publishing; 2018. Available from: [<URL>](#).
33. Shakkor SJ, Mohammed N, Shakor SR. Spectrophotometric method for determination of methyl dopa in pure and pharmaceutical formulation based on oxidative coupling reaction. *Chem Methodol* [Internet]. 2022 Nov 1;6(11):851–60. Available from: [<URL>](#).
34. Abdul Majeed Khorsheed Ahmed, Zahraa Turhan Wehbe Ahmed2. Estimation of furosemide spectrophotometrically in pharmaceutical preparations by oxidative coupling reaction. *Tikrit J Pure Sci* [Internet]. 2022 Nov 28;27(4):39–46. Available from: [<URL>](#).
35. Hussein KS, Ahmed AMK, Mohammed FY. Spectrophotometric determination of salbutamol by oxidative coupling reaction with 1-Naphthylamine-4-sulfonic acid in the presence of potassium per sulfate. *Med J Babylon* [Internet]. 2021 Jul 1;18(3):249–56. Available from: [<URL>](#).
36. O. Baban S, F. Jallal A. Determination of meloxicam in pharmaceutical formulation by azo-coupling reaction with sulphanilic acid using both batch and flow-injection technique. *Rafidain J Sci* [Internet]. 2011 Oct 1;22(7):121–32. Available from: [<URL>](#).



Exploring Promising Multi-targeted Drug Candidate for Alzheimer's Disease from Compounds Based on Benzalaniline with 1,3,4-Oxadiazole Skeleton: An *In Silico* Modeling and Docking Study

Rahul Kizhakeveedu¹ , Devi Thamizhamban^{1*} , Hariraj Narayanan² 

¹Chettinad School of Pharmaceutical Sciences, Chettinad Hospital and Research Institute, CARE, Kelambakkam-603103, Tamil Nadu, India.

²Department of Pharmaceutical Sciences, Government Medical College Kannur, 670503, Kerala, India.

Abstract: In general, oxadiazole and benzalaniline derivatives have shown promising activity against a variety of diseases. Combining these two scaffolds into a single drug candidate is a strategy that has garnered increasing interest in multi-targeted drug discovery. This study aims to identify potential ligands from benzalaniline derivatives containing 1,3,4-oxadiazole, targeting various proteins associated with Alzheimer's disease through molecular modeling and docking studies. *In silico* ADME screening was also performed to predict drug-likeness and blood-brain barrier (BBB) permeability, using the QikProp tool from the Schrodinger suit 2023-1 (Maestro 13.5.128). The crystallographic structure of the molecular targets was obtained from the PDB database, specifically Acetylcholinesterase (PDB ID: 4EY7), Butyrylcholinesterase (PDB ID: 4BDS), Monoamine Oxidase (PDB ID: 2V60), and BACE-1 (PDB ID: 7B1P). The designed ligands demonstrated strong affinity with key amino acid residues and their drug-likeness. Along with BBB permeability, it highlights their potential as inhibitors for these targets. In particular, chloro substitution on benzalaniline, combined with hydroxyl aromatic substitution on oxadiazole, exhibited favorable binding affinity with the four receptors selected for this study. A ligand with 3-Chloro and 3'-hydroxy substitution (R139) displayed a strong binding affinity for acetylcholinesterase, with a docking score of -10.247. When the chloro group was positioned at the second site (R114), it was more effective against butyrylcholinesterase, yielding a docking score of -7.723. Furthermore, a ligand with 3-chloro and 4'-hydroxy substitution showed a superior binding score (-10.545) with MAO-B. All proposed compounds fell within the acceptable ADME range (BBB permeability: QPPMCK value >500; QPlog BB 3 to 1.2). Based on the data presented in this study, the suggested ligands should be considered as potential inhibitors.

Keywords: 1,3,4-Oxadiazole, Benzalaniline, Multi-targeted drug discovery, Alzheimer's disease.

Submitted: March 18, 2024. **Accepted:** August 29, 2024.

Cite this: Kizhakeveedu R, Thamizhamban D, Narayanan H. Exploring Promising Multi-targeted Drug Candidate for Alzheimer's Disease from Compounds Based on Benzalaniline with 1,3,4-Oxadiazole Skeleton: An *In Silico* Modeling and Docking Study. JOTCSA. 2024;11(4): 1473-82.

DOI: <https://doi.org/10.18596/jotcsa.1454468>

***Corresponding author's E-mail:** devrajmphd@gmail.com

1. INTRODUCTION

Oxadiazole is a compound containing two nitrogen atoms and oxygen atoms in a five-membered ring (1). It exists in several isomeric forms, with 1,2,4-Oxadiazole being the most common. Oxadiazoles have a variety of applications in medicinal chemistry and agrochemicals due to their electronic and physicochemical properties (2). In medicinal chemistry, these compounds exhibit promising activity against cancer, microbial infections, and neurodegenerative disorders. Additionally, they possess anti-inflammatory and antioxidant properties (3).

Bioisosteric replacement is a technique used in drug design to enhance the activity of the original compound. This method is commonly applied in drug discovery to optimize biological activity, selectivity, and safety. Aza-resveratrol is an analog of resveratrol, in which one of the carbon atoms in the structure is replaced by a nitrogen atom (4).

Due to its improved bioavailability and pharmacological properties, this bioisostere-containing molecule may be a promising therapeutic candidate. These aza compounds demonstrate anti-inflammatory and antioxidant properties, as well as the pot-

essential to treat neurological diseases. Resveratrol, a polyphenol found in berries, grapes, and peanuts, is produced by plants in response to fungal infections and injury. As a result, it functions as a phytoalexin, contributing to plant defense. Because of this, resveratrol is believed to offer similar protective benefits in humans (5). Researchers have discovered various benefits of resveratrol in human health, including its anti-aging properties, which keep it under continued scientific investigation.

The nitrogen atom in aza-resveratrol forms a hydrogen bond, which enhances its solubility in aqueous media, thereby improving its bioavailability and therapeutic potential (6). Aza derivatives also exhibit greater stability and a longer shelf life than

resveratrol. However, further research is needed to fully understand their pharmacological Properties and to demonstrate their efficacy in humans. Aza-resveratrol primarily consists of benzalaniline (6).

The neurodegenerative process in Alzheimer's disease is both complicated and multifaceted (7), with cognitive decline being the primary symptom. Several pathological mechanisms contribute to the disease. The major factors include oxidative stress, inflammation of the brain, and the accumulation of beta-amyloid and tau protein (Figure 1) (8). Since no single clinical issue can be effectively targeted to treat Alzheimer's disease, a multifaceted approach is necessary.

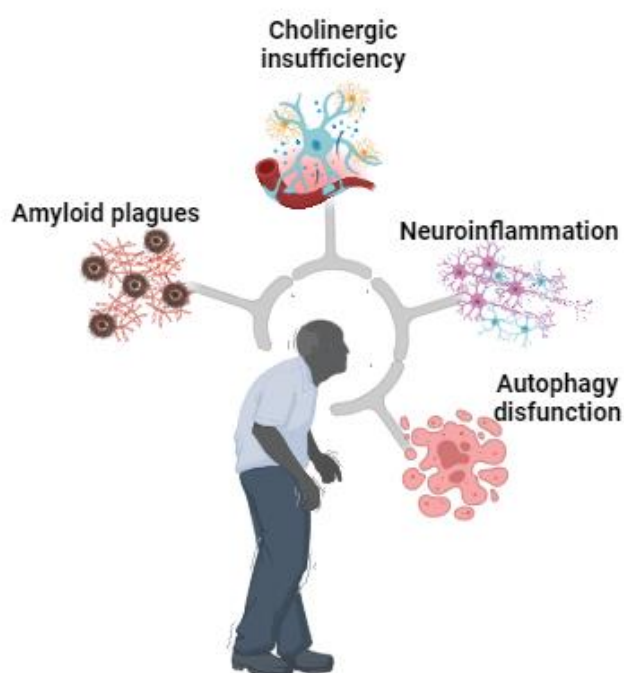


Figure 1: Multiple disease mechanisms of Alzheimer's Disease.

Multi-targeted drug candidates, i.e., compounds that target various pathways in disease-related processes, are crucial in the development of Alzheimer's Disease treatments (9,10). Such drugs offer more therapeutic benefits than single-target approaches (11). To prevent the accumulation of tau and amyloid-beta proteins, reduce neuronal inflammation, and promote neuronal survival in Alzheimer's Disease, the creation of a multi-targeted drug is essential (12). Given that Alzheimer's disease is influenced by multiple clinical factors, this strategy may prove effective. Additionally, by applying these realistic strategies, it may be possible to reduce dosage, toxicity risk, and drug-drug interactions.

Multi-targeted drugs represent an important and effective strategy in the development of new treatments due to their ability to address different pathological processes simultaneously (13). Combining different scaffolds into a single drug framework, known as scaffold hybridization or

scaffold merging, is another approach to developing potent and effective drugs (9). This strategy aims to create compounds that incorporate the beneficial properties of both scaffolds, leading to increased potency and efficacy. Scaffold merging can be achieved by covalently linking the two scaffolds (11).

The challenges of bioavailability, toxicity, and selectivity associated with individual scaffolds can be addressed through the fusion of two or more compounds (14). This approach optimizes the pharmacokinetic and pharmacodynamic profiles of the drug and may improve therapeutic outcomes (15). Additionally, scaffold hybridization creates compounds that not only target multiple pathways but are also less likely to lead to drug-resistant (16). A promising strategy for developing new drug candidates for Alzheimer's disease involves the hybridization of oxadiazole with benzalaniline (Figure 2).

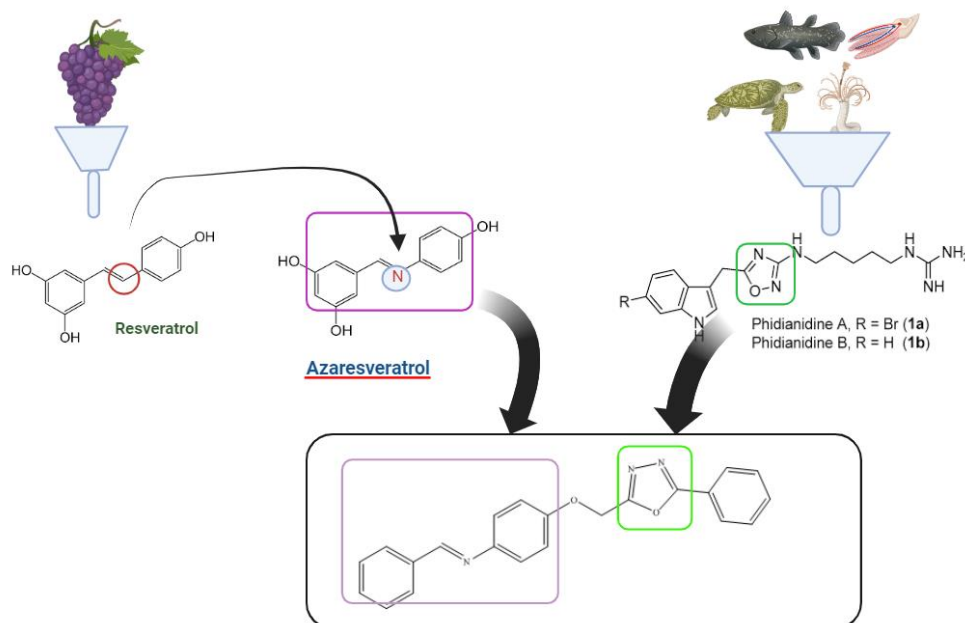


Figure 2: Hybridization of two scaffolds-new strategies for drug discovery.

2. MATERIALS AND METHODS

2.1. Materials

For our study, we utilized the Schrodinger Maestro software suite (2023-1, Maestro 13.5.128) and various biological databases, including the Protein Data Bank (PDB). The tools employed include the 2D sketcher for ligand preparation, Glide for molecular docking, LigPrep for generating flexible and accurate 3D molecular models, SiteMap for predicting binding sites, and QikProp for rapid ADME predictions of compounds. The Protein Data Bank, the only global repository of structural data on biological macromolecules, contains structural information obtained through techniques such as NMR and X-ray crystallography.

2.2. Protein Preparation

The crystal structure of recombinant human acetylcholinesterase in complex with donepezil (PDB ID: 4EY7) at 2.35 Å, human butyrylcholinesterase in complex with tacrine (PDB ID: 4BDS) at 2.1 Å, human beta-secretase (BACE1) (PDB ID: 7B1P) at 1.77 Å, and human MAO B (PDB ID: 2V60) at 2 Å were downloaded from the Protein Data Bank (PDB) and used to model the protein structure in this study. The protein structures were preprocessed and refined using the protein preparation wizard tool from Schrodinger software, version 13.5.128. This process included assigning bond orders, adding missing hydrogen atoms, setting zero-order for metals, creating disulfide bonds, and deleting water molecules beyond 5 Å. The possible ionization states were generated, and the most stable state was selected. Protein structure minimization was performed using the OPLS3e force field (17).

2.3. Preparation of Ligands

The structures of the chemical compounds were designed using the 2D sketch tool in Schrodinger Maestro, version 13.5.128. These ligands were then processed through the LigPrep module in the Schrodinger suite 2023-1. This process involved

converting the 2D ligand structures to 3D, optimizing stereochemistry and ionization states, generating tautomeric variations, and performing energy minimization and geometric optimization. Chirality was corrected, missing hydrogens were added, bond orders were adjusted, and charged groups were neutralized. Ionization and tautomeric states were generated using the Epik module. The compounds were then minimized using the OPLS3e force field (18).

2.4. Receptor Grid Generation

Grid generation involves creating a 3D grid of points within the receptor protein (19), representing potential binding sites for a ligand. This helps in calculating interaction energies. The co-crystallized ligands of acetylcholinesterase, butyrylcholinesterase, and beta-secretase enzymes were retained and used for grid preparation (20). This was done using the receptor grid generation tool in Schrodinger. However, in the case of MAO, the sitemap tool was used to identify the largest binding pocket.

2.5. Glide Ligand Docking and ADME Prediction

The *in-silico* ADME properties, including BBB permeability and drug-likeness, of the proposed compounds were determined using the Qikprop module in Schrodinger Maestro, Version 13.1.141. Glide docking of the proposed compounds was performed using the previously created receptor grid and the ligand molecules. Positive interactions between the ligand molecules and the receptor were recorded using the Glide ligand docking program. All these calculations were carried out in extra precision (XP) mode, which provides more accuracy compared to other modes (21). QikProp is a module in Schrodinger software that predicts various physicochemical and pharmacokinetic properties of ligand molecules. These predictions include:

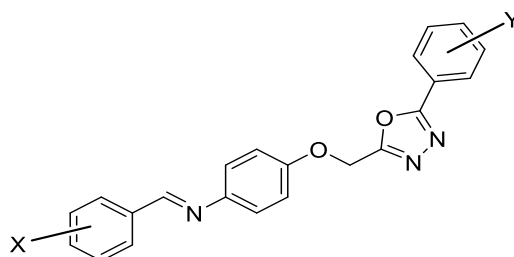
1. Property prediction: Molecular weight, log P, polar surface area, hydrogen bond donors, and

acceptors, in line with lead-likeness property prediction (Lipinski's Rule of Five).

- Pharmacokinetic properties: Oral bioavailability, blood-brain barrier penetration, and CYP450 metabolism. These predictions are useful for prioritizing compounds based on their pharmacokinetic profiles.
- Lipophilic Efficiency: This module calculates the balance between a compound's lipophilic properties and its potency, helping to identify compounds with optimal hydrophobicity.

3. RESULTS AND DISCUSSION

Based on the availability of chemicals and information gathered from the literature, 150 ligands (R1-R150) were designed using the 2D sketch tool in Schrodinger software (Figure 3). These ligands were then subjected to ligand preparation. ADME properties are crucial in the development of anti-Alzheimer's drugs, as they influence the drug's efficacy, safety, and pharmacokinetic profile. The ADME properties of the synthesized compounds can be predicted *in-silico* using the Qikprop module in the Schrödinger suite 2023-1.



**X = Ortho, Meta, Para-Cl,
Ortho, Meta, Para-CH₃**

**Y = o-Cl; m-Cl; p-Cl;
o-CH₃; m-CH₃; p-CH₃
o-Br; m-Br; p-Br
o-F; m-F; p-F
o-OH; m-OH; p-OH
2,3-dihydroxy; 2,4-dihydroxy; 3,4-dihydroxy;
3,5-dihydroxy; 3,4,5-trihydroxy; 2,3,4-trihydroxy
2-methoxy; 3-methoxy; 4-methoxy; 2-CHO**

Figure 3: Ligands R1 to R150.

The computed dipole moment of the molecules ranges from 2.535 to 8.006. The total solvent-accessible surface area (SASA) is between 485.52 and 767.341. The hydrophobic components (FOSA) of SASA, i.e., saturated carbon and attached hydrogen, are in the range of 34.228 and 405.756, while the hydrophilic component (FISA) of SASA is in the range of 32 and 216.885. The π component (PISA) of SASA is in the range of 115.719 to 513.439. The number of hydrogen bonds donated by the solute to water molecules in aqueous solution ranges from 0 to 3, while the number of hydrogen bonds formed by the solute from water molecules is between 4.25 and 6.5. The predicted octanol/water partition coefficient values for the compounds are in the range of 1.717 to 6.216. Prediction for binding to human serum albumin (QPlogKhsa) range from -0.372 to 0.98. Some

violations of Lipinski's rule of five were observed, with the number of violations ranging from 0 to 1. Out of the 150 compounds, only 57 obey Lipinski's rule. Many of the compounds show human oral absorption percentage between 50 % and 100%. Two parameters were used to predict the blood-brain permeability of the ligands: QplogBB and QPPMDCK. The QPlogBB values for all the compounds fall within the accepted range of -3.00 to 1.2, and the QPPMDCK values are greater than 25 (values below 25 indicate poor permeability, while values above 500 are considered excellent). These results suggest that all the compounds exhibit BBB permeability. Based on the drug-likeness properties and strong BBB permeability, 12 compounds were selected for docking studies (Figure 4). The detailed ADME properties of these 12 compounds are presented in Table 1.

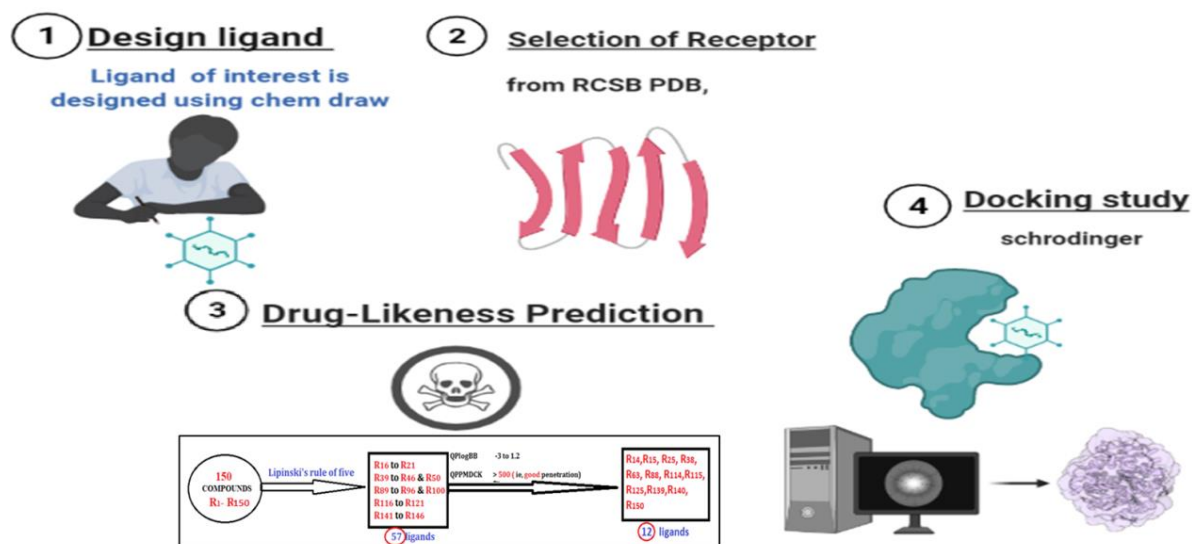


Figure 4: Workflow of the computational study.

Advanced molecular docking using Schrodinger Maestro, version 13.5.128, was conducted to determine the binding affinities of the compounds towards four key receptors involved in Alzheimer's disease. The docking protocol for ligand docking included the following steps: (1) protein preparation with Protein Preparation Wizard, (2) ligand preparation with LigPrep, (3) site prediction with SiteMap, (4) grid generation with the receptor grid generation tool, and (5) ligand docking with Glide.

Predicting the protein binding sites is represented as a group of points called site points (22). Based on the ligand-binding sites, grids were created, with details provided in Table 2 and Figure 5. Ligand docking searches for the best fit and potential interactions between a ligand and the receptor grid. The grid serves as the search area, containing information about the force field surrounding the receptor protein (23).

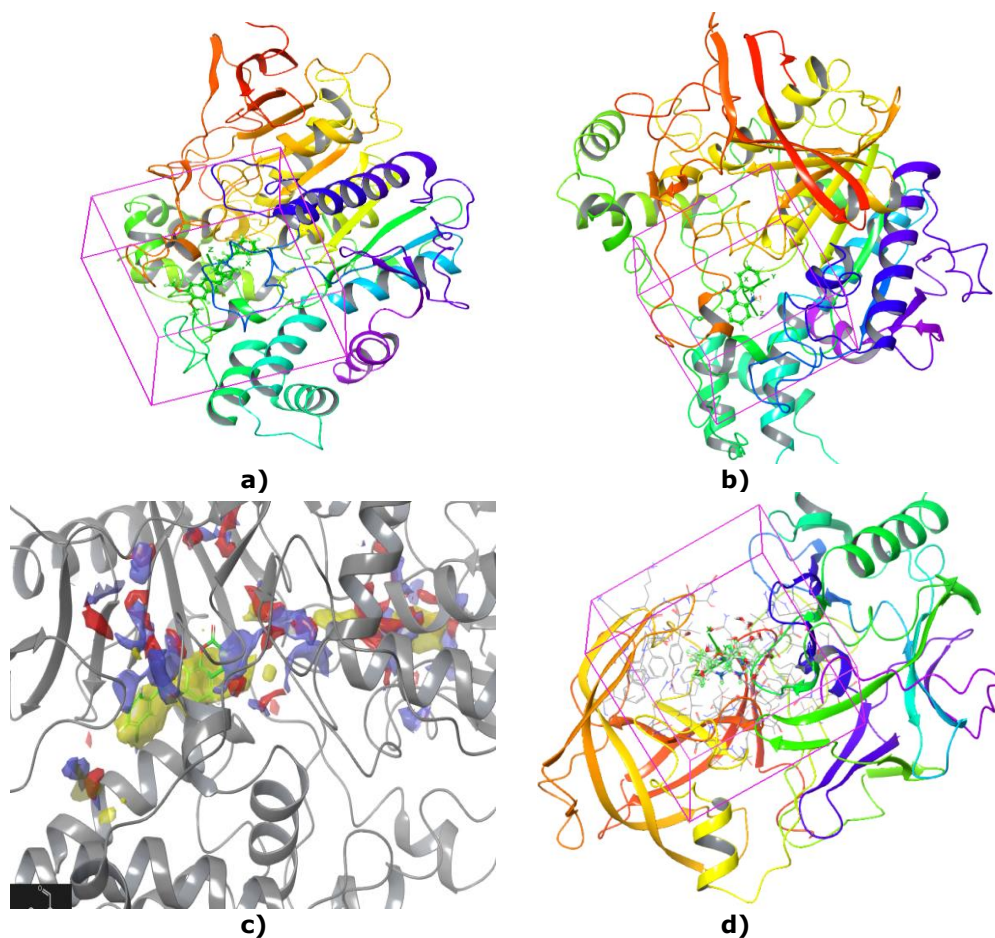


Figure 5: a) 4EY7 with grid box; b) 4BDS with grid box; c) 2V60 with site map; d) 7B1P with grid box.

Table 1: ADME properties of compounds.

Ligands	Dipole	SASA	HB Donor	HB Acceptor	QPlogPo/w	QPlogBB	QPPMDCK	Rule of five (violations)
R14	3.411	734.296	1	5	4.983	-1.095	802.237	0
R15	3.605	734.296	1	5	4.983	-1.095	802.237	0
R25	7.22	742.301	0	6.25	4.651	-0.955	1037.661	0
R38	5.124	721.235	1	5	4.843	-0.999	526.02	0
R63	5.024	727.676	1	5	4.877	-1.011	526.02	0
R88	5.357	736.187	1	5	4.907	-1.036	523.193	0
R114	5.194	730.92	1	5	4.922	-1.12	685.391	0
R115	3.457	730.92	1	5	4.922	-1.12	685.39	0
R125	7.928	737.078	0	6.25	4.587	-0.963	908.692	0
R139	4.013	734.836	1	5	4.986	-1.097	802.234	0
R140	4.078	734.836	1	5	4.986	-1.097	802.234	0
R150	7.649	740.673	0	6.25	4.651	-0.939	1063.453	0
Recommended range	1 - 12.5	300-1000	0.0-6.0	2 - 20	-2 -6.5	-3 - 1.2	<25 poor >500 good	Max 4

Table 2: Grid box dimensions.

Receptors	Xcent	Ycent	Zcent	Xrange	Yrange	Zrange
4EY7	-14.029	-43.997	27.959	27.782	27.782	27.782
4BDS	133.238	116.200	41.060	21.641	21.641	21.641
2V60	53.794	148.823	21.943	50.345	50.345	50.345
7B1P	29.174	74.215	19.706	24.284	24.284	24.284

The ligands were docked to the receptors, and the results indicated that compound R139 exhibited a strong affinity for acetylcholinesterase compared to other derivatives. In contrast, compounds R114, R88, and R140 demonstrated higher Glide scores with butyrylcholinesterase, BACE-1, and MAO-B, respectively. These variations can be attributed to the different positions of similar functional groups. The findings are detailed in Table 3 and are illustrated by 2D and 3D representations (Figures 6, 7, 8, and 9) of the docked ligands. A hydrogen bond (bond length 2.69 Å) was formed between R139 and a water molecule within the binding site of acetylcholinesterase, highlighting the significance of water molecules within the 3A° region and their influence on ligand binding in the active site. Additionally, R139 interacts with the amino acid residues TYR 337, PHE 338, and TRP 286 through pi-pi interactions. For butyrylcholinesterase, the

ligand R114 exhibited strong affinity, forming a pi-pi bond with PHE 329 and TRP 82 and a hydrogen bond with TYR 332 (bond length 2.06). R88 showed a greater affinity for BACE-1 compared to other ligands, displaying a pi-pi interaction with TYR 71, a hydrogen bond (bond length 2.68) with a water molecule in the binding pocket, and an additional hydrogen bond (bond length 2.09) with ASP 32, involving the oxygen of oxadiazole ring and the benzal aniline nucleus. Moreover, R140 exhibited improved interaction with MAO-B. Chlorine and hydroxyl substitutions vary in position across these four ligands, suggesting that these substitutions are necessary; receptor affinities are affected by their positions. The results are summarized in Table 4. The bioavailability of all four ligands, as predicted using SwissADME, is similar, with each ligand showing a bioavailability score of 0.55.

Table 3: Docking studies for compounds.

Ligands	Acetylcholinesterase (PDB ID: 4EY7)		Butyrylcholinesterase (PDB ID: 4BDS)		β Secretase (PDB ID: 7B1P)		MAO-B (PDB ID: 2V60)	
	Docking Score	Glide Score	Docking Score	Glide Score	Docking Score	Glide Score	Docking Score	Glide Score
R14	-7.484	-7.485	-7.314	-7.315	-4.181	-4.182	-7.230	-7.231
R15	-7.600	-7.609	-6.817	-6.826	-2.972	-5.451	-6.906	-6.915
R25	-9.199	-9.199	-6.645	-6.645	-2.702	-2.702	-8.750	-8.750
R38	-9.956	-9.985	-6.808	-6.837	-3.144	-3.173	-6.538	-6.567
R63	-9.994	-10.023	-5.652	-5.681	-2.620	-2.649	-8.135	-8.164
R88	-9.283	-9.311	-4.762	-6.571	-5.185	-5.213	-9.575	-9.604
R114	-9.240	-9.242	-7.723	-7.724	-2.860	-2.861	-7.248	-7.249
R115	-9.176	-9.185	-6.642	-6.651	-2.456	-2.465	-9.158	-11.637
R125	-9.351	-9.351	-6.829	-6.829	-2.901	-2.901	-5.868	-5.868
R139	-10.247	-10.248	-6.828	-6.829	-3.862	-3.863	-8.014	-8.015
R140	-9.398	-9.407	-4.555	-4.564	-3.049	-3.058	-10.545	-10.555
R150	-9.190	-9.190	-7.300	-7.300	-2.192	-2.192	-9.728	-9.728
Ligands having High affinity	R139		R114		R88		R140	

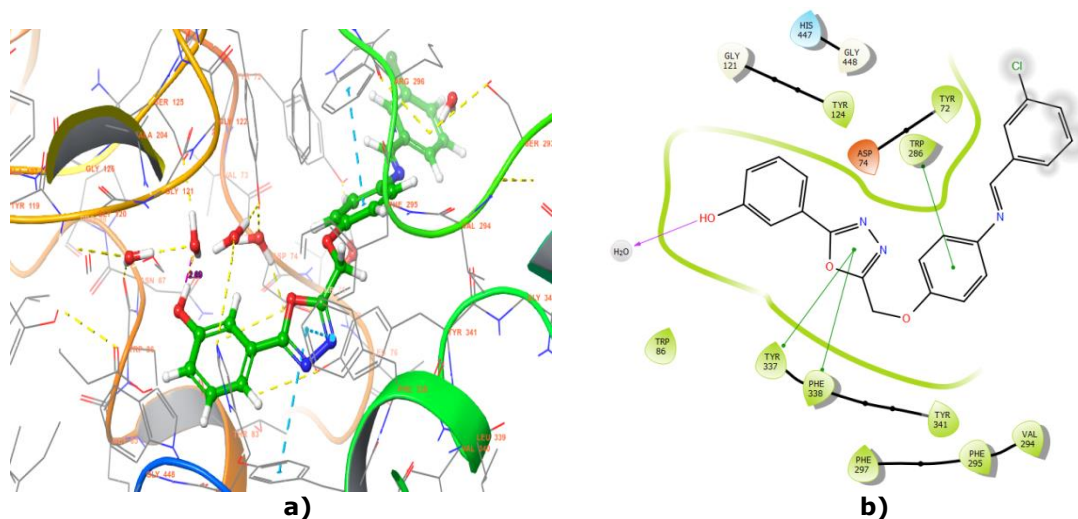


Figure 6: Docked pose of R139 in 4EY7; a)3D representation; b) 2D representation.

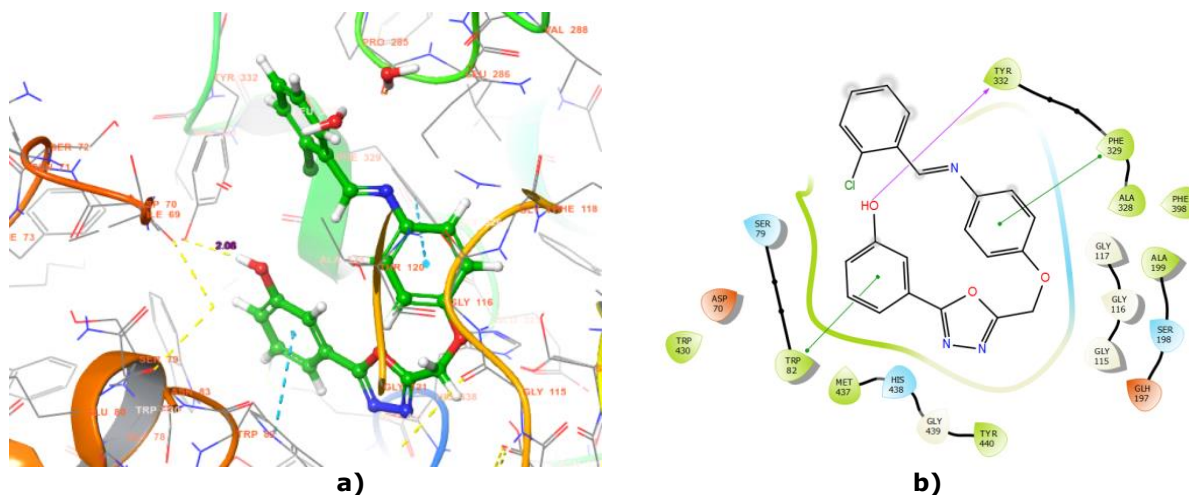


Figure 7: Docked pose of R114 in 4BDS; a) 3D representation; b) 2D representation.

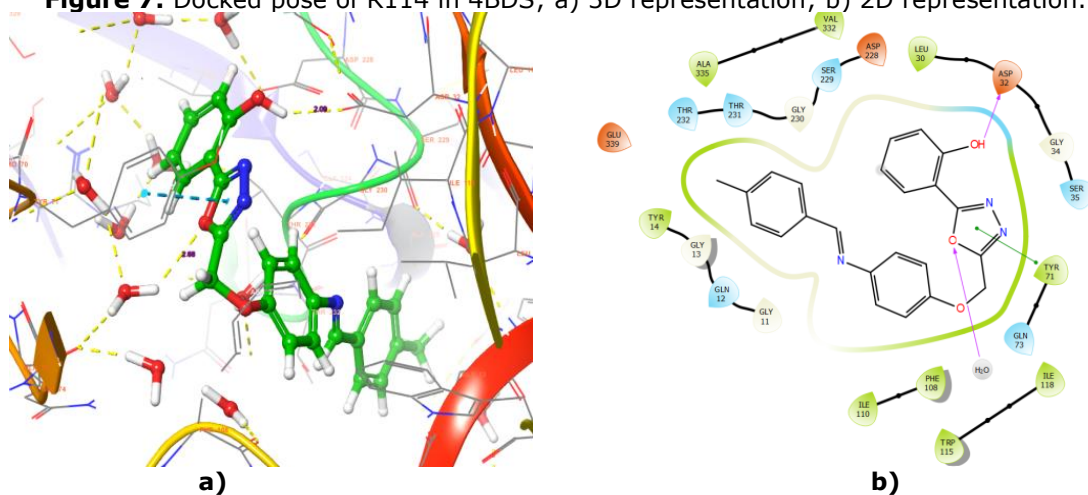


Figure 8: Docked pose of R88 in 7B1P; a) 3D representation; b) 2D representation.

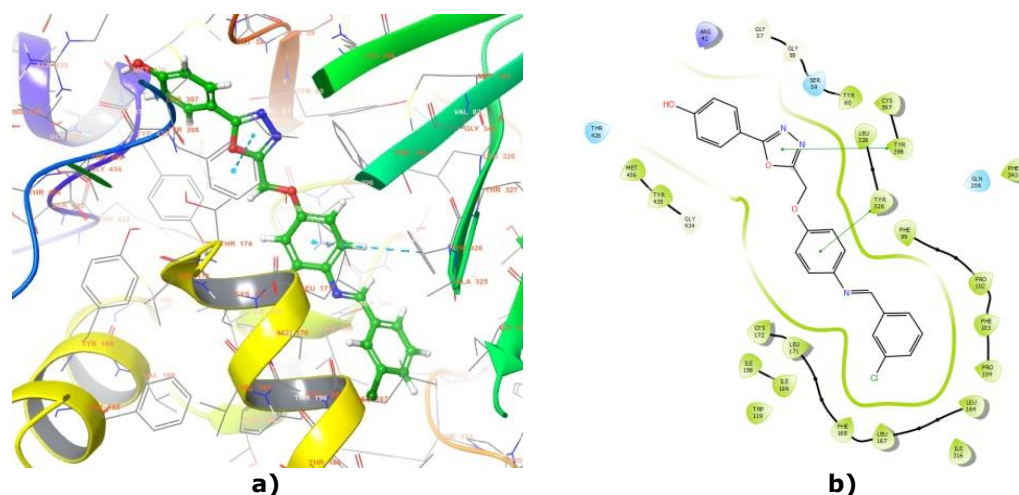
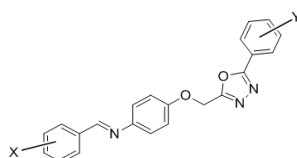


Figure 9: Docked pose of R140 in 2V60; a- 2d representation; b- 2D representation.

Table 4: Summary of result.

Basic structure



Ligand	X	Y'	Affinity with
R 139	3-Cl	3'-OH	Acetylcholinesterase (4EY7)
R114	2-Cl	3'-OH	Butyrylcholinesterase (4BDS)
R140	3-Cl	4'-OH	MAO β (2V60)
R88	4-CH ₃	1'-OH	BASE (7B1P)

4. CONCLUSION

A computer-based approach was used to identify potential drug candidates for treating Alzheimer's disease, focusing specifically on a group of chemical compounds known as 1,3,4-oxadiazole derivatives with benzal aniline. These compounds were validated through docking simulations, which demonstrated their ability to effectively bind to the active sites of four different receptors in the brain that are known to play a role in Alzheimer's disease. This *in-silico* approach helped to identify promising lead compounds for further investigation. In this study, we conclude that a series of chloro-substituted benzal aniline compounds combined with hydroxyl aromatic-substituted 1,3,4-oxadiazole showed inhibitory activity against the four key receptors. Specifically, R139, R114, R88, and R140 demonstrated significant anti-Alzheimer activity. The ADME analysis also confirmed that all these ligands possess the necessary ADME properties required for anti-Alzheimer's activity. With further testing and refinement, these candidates may serve as promising drug treatments for Alzheimer's disease in the future.

5. CONFLICT OF INTEREST

The authors declare that there are no conflicts of interest regarding this publication.

6. ACKNOWLEDGMENT

The authors express their gratitude to Shahin Muhammed, Assistant Professor at the College of Pharmaceutical Sciences, Government Medical College Kannur, for providing the necessary facilities to conduct this study.

7. REFERENCES

- Bajaj S, Asati V, Singh J, Roy PP. 1,3,4-Oxadiazoles: An emerging scaffold to target growth factors, enzymes and kinases as anticancer agents. *Eur J Med Chem* [Internet]. 2015 Jun 5;97:124-41. Available from: [<URL>](#).
- Vaidya A, Pathak D, Shah K. 1,3,4-oxadiazole and its derivatives: A review on recent progress in anticancer activities. *Chem Biol Drug Des* [Internet]. 2021 Mar 27;97(3):572-91. Available from: [<URL>](#).
- Qadir T, Amin A, Sharma PK, Jeelani I, Abe H. A review on medicinally important heterocyclic compounds. *Open Med Chem J* [Internet]. 2022 Apr 28;16(1):e187410452202280. Available from: [<URL>](#).
- Deacon RMJ. A novel approach to discovering treatments for Alzheimer's disease. *J Alzheimers Dis Park*. 2014;4(2):142-5.
- Lizard G, Latruffe N, Vervandier-Fasseur D. Aza-

- and Azo-stilbenes: Bio-isosteric analogs of resveratrol. *Molecules* [Internet]. 2020 Jan 30;25(3):605. Available from: [<URL>](#).
6. Siddiqui A, Dandawate P, Rub R, Padhye S, Aphale S, Moghe A, et al. Novel aza-resveratrol analogs: Synthesis, characterization and anticancer activity against breast cancer cell lines. *Bioorg Med Chem Lett* [Internet]. 2013 Feb 1;23(3):635–40. Available from: [<URL>](#).
7. Alanazi FK, Radwan AA, Aou-Auda H. Molecular scaffold and biological activities of anti-alzheimer agents. *Trop J Pharm Res* [Internet]. 2022 Apr 28;21(2):439–51. Available from: [<URL>](#).
8. Melchiorri D, Merlo S, Micallef B, Borg JJ, Dráfi F. Alzheimer's disease and neuroinflammation: will new drugs in clinical trials pave the way to a multi-target therapy? *Front Pharmacol* [Internet]. 2023 Jun 2;14:1196413. Available from: [<URL>](#).
9. Kumar N, Kumar V, Anand P, Kumar V, Ranjan Dwivedi A, Kumar V. Advancements in the development of multi-target directed ligands for the treatment of Alzheimer's disease. *Bioorg Med Chem* [Internet]. 2022 May 1;61:116742. Available from: [<URL>](#).
10. Hasan AH, Abdulrahman FA, Obaidullah AJ, Alotaibi HF, Alanazi MM, Noamaan MA, et al. Discovery of novel coumarin-schiff base hybrids as potential acetylcholinesterase inhibitors: Design, synthesis, enzyme inhibition, and computational studies. *Pharmaceuticals* [Internet]. 2023 Jul 6;16(7):971. Available from: [<URL>](#).
11. Alcaro S, Bolognesi ML, García-Sosa AT, Rapposelli S. Editorial: Multi-Target-Directed Ligands (MTDL) as challenging research tools in drug discovery: from design to pharmacological evaluation. *Front Chem* [Internet]. 2019 Feb 18;7:448718. Available from: [<URL>](#).
12. Alarcón-Espósito J, Mallea M, Rodríguez-Lavado J. From hybrids to new scaffolds: the latest medicinal chemistry goals in multi-target directed ligands for alzheimer's disease. *Curr Neuropharmacol* [Internet]. 2021 May 27;19(6):832–67. Available from: [<URL>](#).
13. Ibrahim M, Gabr M. Multitarget therapeutic strategies for Alzheimer's disease. *Neural Regen Res* [Internet]. 2019 Mar 1;14(3):437–40. Available from: [<URL>](#).
14. Cummings J, Zhou Y, Lee G, Zhong K, Fonseca J, Cheng F. Alzheimer's disease drug development pipeline: 2023. *Alzheimer's Dement Transl Res Clin Interv* [Internet]. 2023 Apr 25;9(2):e12179. Available from: [<URL>](#).
15. Choubey PK, Tripathi A, Tripathi MK, Seth A, Shrivastava SK. Design, synthesis, and evaluation of N-benzylpyrrolidine and 1,3,4-oxadiazole as multitargeted hybrids for the treatment of Alzheimer's disease. *Bioorg Chem* [Internet]. 2021 Jun 1;111:104922. Available from: [<URL>](#).
16. Wang Y, Sun Y, Guo Y, Wang Z, Huang L, Li X. Dual functional cholinesterase and MAO inhibitors for the treatment of Alzheimer's disease: synthesis, pharmacological analysis and molecular modeling of homoisoflavonoid derivatives. *J Enzyme Inhib Med Chem* [Internet]. 2015 Mar 23;31(3):389–97. Available from: [<URL>](#).
17. Remya C, Dileep KV, Koti Reddy E, Mantosh K, Lakshmi K, Sarah Jacob R, et al. Neuroprotective derivatives of tacrine that target NMDA receptor and acetyl cholinesterase – Design, synthesis and biological evaluation. *Comput Struct Biotechnol J* [Internet]. 2021 Jan 1;19:4517–37. Available from: [<URL>](#).
18. Mehta S, Pathak SR. In silico drug design and molecular docking studies of novel coumarin derivatives as anticancer agents. *Asian J Pharm Clin Res* [Internet]. 2017 Apr 1;10(4):335–40. Available from: [<URL>](#).
19. Tantoso E, Wahab HA, Chan HY. Molecular docking: An example of grid enabled applications. *New Gener Comput* [Internet]. 2004 Jun;22(2): 189–90. Available from: [<URL>](#).
20. Ali SK, Hamed AR, Soltan MM, El-Halawany AM, Hegazy UM, Hussein AA. Kinetics and molecular docking of vasicine from *Adhatoda vasica*: An acetylcholinesterase inhibitor for Alzheimer's disease. *South African J Bot* [Internet]. 2016 May 1;104:118–24. Available from: [<URL>](#).
21. Friesner RA, Murphy RB, Repasky MP, Frye LL, Greenwood JR, Halgren TA, et al. Extra precision glide: Docking and scoring incorporating a model of hydrophobic enclosure for protein–ligand complexes. *J Med Chem* [Internet]. 2006 Oct 1;49(21):6177–96. Available from: [<URL>](#).
22. Ban T, Ohue M, Akiyama Y. Multiple grid arrangement improves ligand docking with unknown binding sites: Application to the inverse docking problem. *Comput Biol Chem* [Internet]. 2018 Apr 1;73:139–46. Available from: [<URL>](#).
23. Pissurlenkar R, Shaikh M, Iyer R, Coutinho E. Molecular mechanics force fields and their applications in drug design. *Antiinfect Agents Med Chem* [Internet]. 2009 Apr 1;8(2):128–50. Available from: [<URL>](#).



Characterization and Lidocaine Release Behavior of Chitosan/ Sodium Alginate/ Clinoptiolite Nanocomposite Hydrogel

Sarkis SÖZKES^{1*} , Betül TAŞDELEN¹ , Sevil ERDOĞAN² , Nadide Gülşah GÜLENÇ¹ ,
Aslıhan KORUYUCU³ 

¹Biomedical Engineering Department, Çorlu Engineering Faculty, Namık Kemal University, Çorlu, Tekirdağ, Turkey

²Department of Laborant and Veterinary Health, Vocational School of Keşan, Trakya University, Keşan, Edirne, Turkey

³Textile Engineering Department, Çorlu Engineering Faculty, Namık Kemal University, Çorlu, Tekirdağ, Turkey

Abstract: In this study, the novel nanocomposites were prepared from the natural biopolymers, chitosan (CS), sodium alginate (SA) and clinoptiolite (CL) particles, and also having glutaraldehyde as a crosslinker by cryogelation technique. CS biopolymer was produced from crayfish *Astacus leptodactylus* Eschscholtz, 1823. Characterization of the prepared CS, CS-co-SA (CS/SA) and drug loaded CS/SA/ CL nanocomposite were performed by Fourier Transform Infrared Spectroscopy (FTIR) and Scanning Electron Microscopy (SEM) analyses. The anesthetic drug release behavior of the prepared nanocomposite was investigated for the model drug lidocaine (LD) using UV-Vis spectrophotometry and High Performance Liquid Chromatography (HPLC) techniques. The effect of different LD and CL content on the drug release behavior of the prepared nanocomposite were studied. LD release data was fitted to various kinetic models to study the drug release behavior. The LD release from all the prepared nanocomposite hydrogels fitted zero-order, first-order, Higuchi, and Korsmeyer-Peppas models. The swelling and drug release properties of the new CS-based nanocomposite hydrogels were improved with the inclusion of SA and CL in the gel structure.

Keywords: Chitosan, Clinoptiolite, Drug Release, Lidocaine, Sodium alginate.

Submitted: February 20, 2024. **Accepted:** August 28, 2024.

Cite this: Sözkes S, Taşdelen B, Erdoğan S, Gülenç NG, Koruyucu A. Characterization and Lidocaine Release Behavior of Chitosan/ Sodium Alginate/ Clinoptiolite Nanocomposite Hydrogel. JOTCSA. 2024;11(4):1483–94.

DOI: <https://doi.org/10.18596/jotcsa.1440521>.

***Corresponding author. E-mail:** ssozkes@nku.edu.tr.

1. INTRODUCTION

In recent years, interest in controlled drug release systems in which polymers are used as a means of controlling drug delivery has increased greatly all over the world (1-5). This technology enables the drug to remove the harmful toxic side effects that will be caused by the systemic route by giving the drug in large doses continuously and in small amounts with controlled drug release systems instead of giving many drugs in the conventional way. Controlled drug release technology, which is developing rapidly day by day, offers many advantages such as transporting the drug to the desired target area only, keeping it in the desired time and therapeutic value, and preventing the breakdown of drugs with a short in

vivo half-life. Some limitations on the usage of hydrogels in terms of providing homogeneity and stability have led researchers to search for new materials, namely polymeric nanocomposite hydrogels (6,7). In numerous studies conducted today, zeolite minerals in polymeric composite nanohydrogels are used in the formulations of polymer composites and drugs for many reasons such as increasing the stability of the drug, extraordinary swelling, improving mechanical and drug release properties, and being economical (8,9). In this study, a natural polysaccharide such as chitosan (CS) was used to synthesize the hydrogel. CS is a bio-polysaccharide of interest in the pharmaceutical industry as a polymeric drugs carrier thanks to its non-toxicity, low allergenicity,

biocompatibility, biodegradability, bioactivity, and mucoadhesiveness (2,4-9). Chitosan exhibits a remarkable water retention ability due to its hydrophilic nature, which renders it a superb choice for drug release applications (4-10). It also forms micelles, forming a hydrophobic center for hydrophobic drugs (2,4). Recent research has brought focus to the CS nanoparticles in the development of a drug delivery system aimed at enhancing the therapeutic effectiveness of anesthetic agents while minimizing the required dosage (9). Sodium alginate (SA) is one of the most promising natural polymers and has also excellent properties like its non-toxicity, biodegradability, good biocompatibility, hydrophilicity properties and low price (3,4).

Since zeolite materials are abundant in nature and are economical, the use of them in gel formulation to improve material properties is increasing today (9-11). The reasons for the interest in zeolite are the swelling capacity of zeolites in water, their effect on stable gel structure, adsorption capacity, and large ion exchange capacity. Clinoptilolite (CL), one of the most common zeolite minerals in nature, is used in many fields such as dentistry, medicine, treatment of burn wounds and cancer treatment. In the field of dentistry of this material, there are studies in the fields of prosthesis, canal filling material, periodontology and oral surgery (9-12).

The aim of the study is to develop a CA/SA/CL nanocomposite containing lidocaine (LD) as a model drug. Although there are many examples in the literature where SA and CS are used as drug carrier systems, the fact that CL and LD used in this study is not included in the literature and that chitosan was obtained by isolating it from a freshwater crayfish species adds some novelty to the study.

2. EXPERIMENTAL SECTION

2.1. Materials

Chitosan, derived from the crayfish species *Astacus leptodactylus* Eschscholtz, 1823 was obtained from specimens captured by local fishermen in July 2020 at Kocahıdır Dam Lake located in Edirne, Turkey. Glutaraldehyde (Pcode: 1003100323, Sigma-Aldrich, İstanbul, Turkey), phosphate-buffered saline (Pcode: 1003090549, Sigma-Aldrich, İstanbul, Turkey), alginic acid sodium salt (Pcode:180947, Sigma-Aldrich, İstanbul, Turkey) and lidocaine hydrochloride monohydrate (Pcode: L5647, Sigma-Aldrich Company, İstanbul, Turkey) clinoptilolite (Etibank Company, İstanbul, Turkey) are all chemicals and reagents were of analytical grade and used without further purification. Drug release was calculated using UV-VIS spectrophotometer (Shimadzu UV-VIS

2401, Shimadzu, İstanbul, Turkey) and High Performance Liquid Chromatography (Shimadzu HPLC Prominence Modular LC20A, Shimadzu, İstanbul, Turkey). SEM (FEI-QUANTA FEG 250 SEM, Madrid, Spain) and FTIR (Bruker FTIR VERTEX 70 ATR, Bruker, Switzerland) instruments were used to characterize the prepared hydrogels.

2.2. Preparation of chitosan

Crayfish shells, previously washed and dried, were crushed in a mortar. In order to obtain chitin, approximately 40 g of ground crayfish shell, was first demineralized by refluxing with 450 mL of 2.2 M HCl at 80 °C, and 800 rpm for 6.5 hours. After demineralization, it was filtered through a filter paper and washed with distilled water. Then, the filtrate was treated with 450 mL of 2.2 M NaOH for 23 hours at 80 °C for deproteinization. Then it was washed again with distilled water until the pH was neutral and filtered. The resulting chitin was dried in an oven at 45 °C for a few days. In order to produce chitosan, 13.3 g of dry chitin was deacetylated with 199.5 mL of 70% NaOH solution at 150 °C for 4 hours. Then the obtained chitosan was washed with pure water until the pH was neutral, filtered, and dried in the oven at 45 °C.

2.3. Preparation of hydrogels

CS, CS/SA, CS/SA/CL, and drug loaded CS/SA/CL composite hydrogels were prepared from chitosan and sodium alginate (SA) using glutaraldehyde as a crosslinker by hydrogelation technique (5). Initially, 0.1 g of crayfish CS was dissolved in a 1% acetic acid solution consisting of 10 mL. This dissolution process took place through stirring on a magnetic stirrer set at 25 °C and 500 rpm for a duration of 10 minutes. Then, a 2% (wt/v) aqueous solution of SA was added to 10 mL of CS solution. Different amounts of CL were added into beakers containing CS/SA solution. Different amounts of a model drug (LD) were added to CS/SA/CL solutions and stirred for one hour. A crosslinker, consisting of a 0.4% glutaraldehyde solution measuring 2.5 mL, was introduced into the resulting solution. The mixture was then agitated for a duration of 10 minutes. Subsequently, the thick gel blend was introduced into compact glass tubes measuring 5 mm in inner diameter and 10 cm in length. These tubes were then placed in a deep freezer set at -20 °C for a duration of 48 hours. Following this, the resultant hydrogels were acquired as cylindrical rods by fracturing the glass tube, and subsequently defrosted in distilled water (5). Since LD was loaded in polymer/CL dispersions, all the amount of drug was entrapped into the hydrogel with maximum drug loading efficiency. The preparation of the hydrogels is shown in Figure 1.

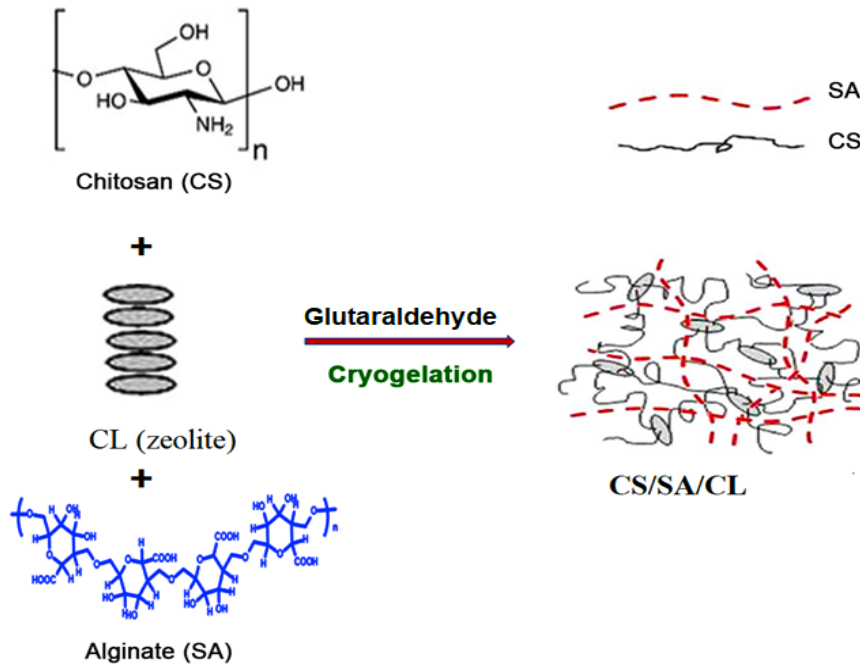


Figure 1: The preparation of CS/SA/CL hydrogels.

2.4. Drug release

The drug was loaded on the CS/SA/CL gels during gel synthesis. The gel containing the drug was immersed in a phosphate buffer (PBS) solution at a temperature of 37 °C and pH 7.4 to facilitate drug release, and their release behavior was examined using a UV-Vis spectrophotometer at a wavelength of 262 nm depending on time. After selected intervals, 3 mL of the released drug solution was drawn from the solution to conduct spectroscopic measurements at a wavelength of 262 nm using a UV-VIS spectrophotometer and placed again into the same vial so that the liquid volume was kept constant. The amounts of the drug released were calculated using a calibration curve (Figure S1).

How much drug the gels released at equilibrium was calculated using HPLC. HPLC device was worked in the isocratic mobile phase. The mobile phase used 80% ammonium acetate (0.2 mol/L), 20% acetonitrile, and 0.2% (w/v) trifluoroacetic acid. 5 μ m C18 (150 \times 4.6 mm) column (Kinetex C18 HPLC column, Germany) was used, and the UV-Vis detection wavelength was 262 nm. The injection volume was 20 μ L and the flow rate was 1.5 mL/min. In HPLC analysis, as can be seen in Figure S2, the characteristic peak of retention (retention time (RT) LD) appears at 1.819 minutes. Based on the areas in the chromatograms given by standard LD solutions prepared at different concentrations in 1.819 minutes, an HPLC calibration line was created (Figure S2). The amount of time to reach equilibrium was determined as 1 week. The release amount of the synthesized gels at the time of equilibrium was calculated as a result of HPLC analysis.

2.5. Theory and calculation for hydrogels

Equations (1) and (2) were used to calculate mass swelling and equilibrium mass swelling (%):

$$\text{Mass Swelling (\%)} = \frac{(m_t - m_0)}{m_0} * 100 \quad (1)$$

$$\text{Equilibrium Mass Swelling (S}_{eq}\text{ \%)} = \frac{(m_\infty - m_0)}{m_0} * 100 \quad (2)$$

where m_0 is mass of the dry gel, m_t and m_∞ are mass of the swollen gel at time t and at equilibrium, respectively (13-15).

Equations 3-5 are applied to analyze the drug release kinetics of the various hydrogels that were assessed using zero-order, first-order, Higuchi, and Korsmeyer-Peppas models.

For zero-order kinetics (16):

$$M_t/M_\infty = K_0 t \quad (3)$$

where K_0 is the zero-order release constant.

For first-order kinetics (17):

$$\ln(1 - M_t/M_\infty) = -K_1 t \quad (4)$$

where K_1 is the zero-order release constant.

For Higuchi model (18):

$$F = K_2 t^{1/2} \quad (5)$$

where K_2 is the Higuchi constant.

For Korsmeyer-Peppas model (19)

$$F = \frac{M_t}{M_\infty} = k t^n \quad (6)$$

where M_t/M_∞ , where M_t is the amount of absorbed at time t , M_∞ is the maximum amount absorbed, k is a constant, n is the diffusional exponent.

3. RESULTS AND DISCUSSION

3.1. FTIR and SEM analysis

FT-IR spectra of CS, CS/SA, CL, Lidocaine, and drug loaded CS/SA/CL are shown in Figure 2. The characteristic absorption peaks of CS are 3281 cm^{-1} ($-\text{OH}$ stretching band), 2919 cm^{-1} (aliphatic $-\text{CH}_2$ groups) and 2897 cm^{-1} (aliphatic $-\text{CH}_3$ groups), 1643 cm^{-1} (amide I peak, $\text{N}-\text{H}$ bending), 1377 cm^{-1} ($\text{C}-\text{O}-\text{C}$) and 1027 cm^{-1} ($\text{C}-\text{O}$ stretching) (20,21). The characteristic absorption peaks of SA were shown at 1550 and 1407 cm^{-1} (COO^- carboxylic groups) (22). Characteristic peaks of CL are seen at $1627,62\text{ cm}^{-1}$ (the presence of water in the natural zeolite) and $1019,72\text{ cm}^{-1}$ ($\text{Al}-\text{O}$ or $\text{Si}-\text{O}$ bonds), and 791 cm^{-1} ($(\text{T}-\text{O}-\text{T})$ symmetrical stretching vibrations, $\text{T} = \text{Al}$ or Si) and $448,77\text{ cm}^{-1}$ ($\text{O}-\text{Al}-\text{O}$ or $\text{Al}-\text{O}$ group ; $\text{O}-\text{Si}-\text{O}$ or $\text{Si}-\text{O}$ group) (23). Characteristic peaks of LD, as seen in the FT-IR spectrum of the model drug Lidocaine: 3451 cm^{-1} ($\text{N}-\text{H}$ stretch), 3383 cm^{-1} ($\text{N}-\text{H}$ stretch), 1686 cm^{-1} (carbonyl group of amide group), 1474 cm^{-1} (hydrochloride), 1271 cm^{-1} (tertiary amine), 1152 , 714 and 597 cm^{-1} (aromatic ring) (1,3).

In the FT-IR spectrum of CS/SA/CL hydrogel seen in Figure 2, chitosan's 2821 cm^{-1} (aliphatic $-\text{CH}_3$ groups) and 1026 cm^{-1} ($\text{C}-\text{O}$ stretching) are seen. The characteristic peaks of SA in the FT-IR spectrum of CS/SA/CL are observed at 1550 and 1410 cm^{-1} (COO^- -carboxyl groups), 2923 cm^{-1} ($\text{C}-\text{H}$ stretching) and 807 cm^{-1} ($\text{Na}-\text{O}$). Characteristic peaks of CL in the FT-IR spectrum of CS/SA/CL are seen at $1627,62\text{ cm}^{-1}$ (the presence of water in the natural zeolite) and 791 cm^{-1} ($(\text{T}-\text{O}-\text{T})$ symmetrical stretching vibrations, $\text{T} = \text{Al}$ or Si) The characteristics peaks of LD are illustrated at 1471 cm^{-1} (hydrochloride), 1284 cm^{-1} (tertiary amine), 1152 , 714 and 597 cm^{-1} (aromatic ring) in the FT-IR spectrum of CS/SA/CL hydrogel.

Figure 3 shows SEM micrographs of CS, CS/SA, CS/CL, CS/SA/CL and drug loaded CS/CL and CS/SA/CL composite hydrogels. As can be seen in Figure 3, pure CS and CS/SA have a porous structure and a smooth surface morphology. In contrast, it is seen that when zeolite CL particles are added in CS/SA gel formulation, the structure of the hydrogel composites becomes inhomogeneous. This was expected that CS was intercalated in CL because of the strong interaction between the CS/SA matrix and silicate layers (11,20). Finally, when drug LD particles are added to the structure, they filled the porous structure of the hydrogel composites and coated them (Figure 3e and 3f).

3.2. Swelling properties of the hydrogels

The swelling properties of the prepared hydrogels in water are shown in Figure 4. As can be seen in Figure 4, the mass of the synthesized gels in distilled water increased with time. The value of $\text{Seq}\%$ of CS is 1003 but $\text{Seq}\%$ of CS/SA is 1545 due to the incorporation of SA (ionizable groups) groups into CS chains. SA contains many ionic units ($-\text{COOH}$). The amount of SA included in the CS gel leads to a noticeable increase in swelling since their addition to the reaction medium increases the hydrophilicity of the prepared hydrogel because of their high hydrophilic character (23). So, the CS/SA gel structure has many hydrophilic functional groups including $-\text{OH}$, $-\text{COOH}$, and NH_2 groups (4,20,21).

Mass swelling percentages of the synthesized CS/SA/CL and CS/CL hydrogels are less than those without zeolite content (pure CS, CS/SA). This indicates that the CL particles fill the pores and reducing the volume required for swelling in the composite hydrogel (24). When the SEM analyses seen in Figures 5 are examined, it is seen that the CL particles fill the porous structure and empty spaces of the chitosan polymer, and swelling supports the SEM results (9).

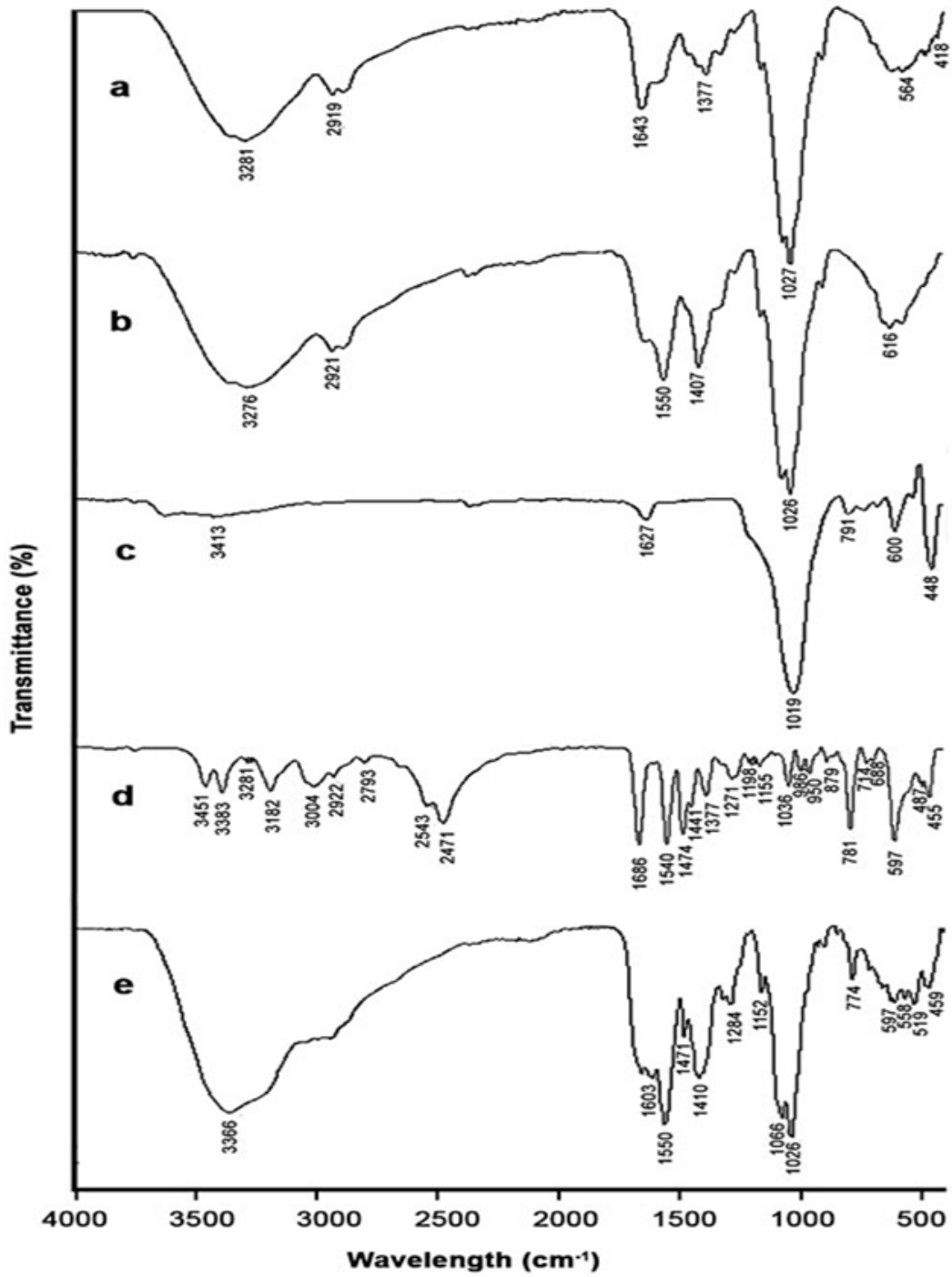


Figure 2: Fourier transform infrared spectra of (a) CS, (b) CS/SA, (c)CL, (d) LD drug (e)drug loaded CS/SA/CL.

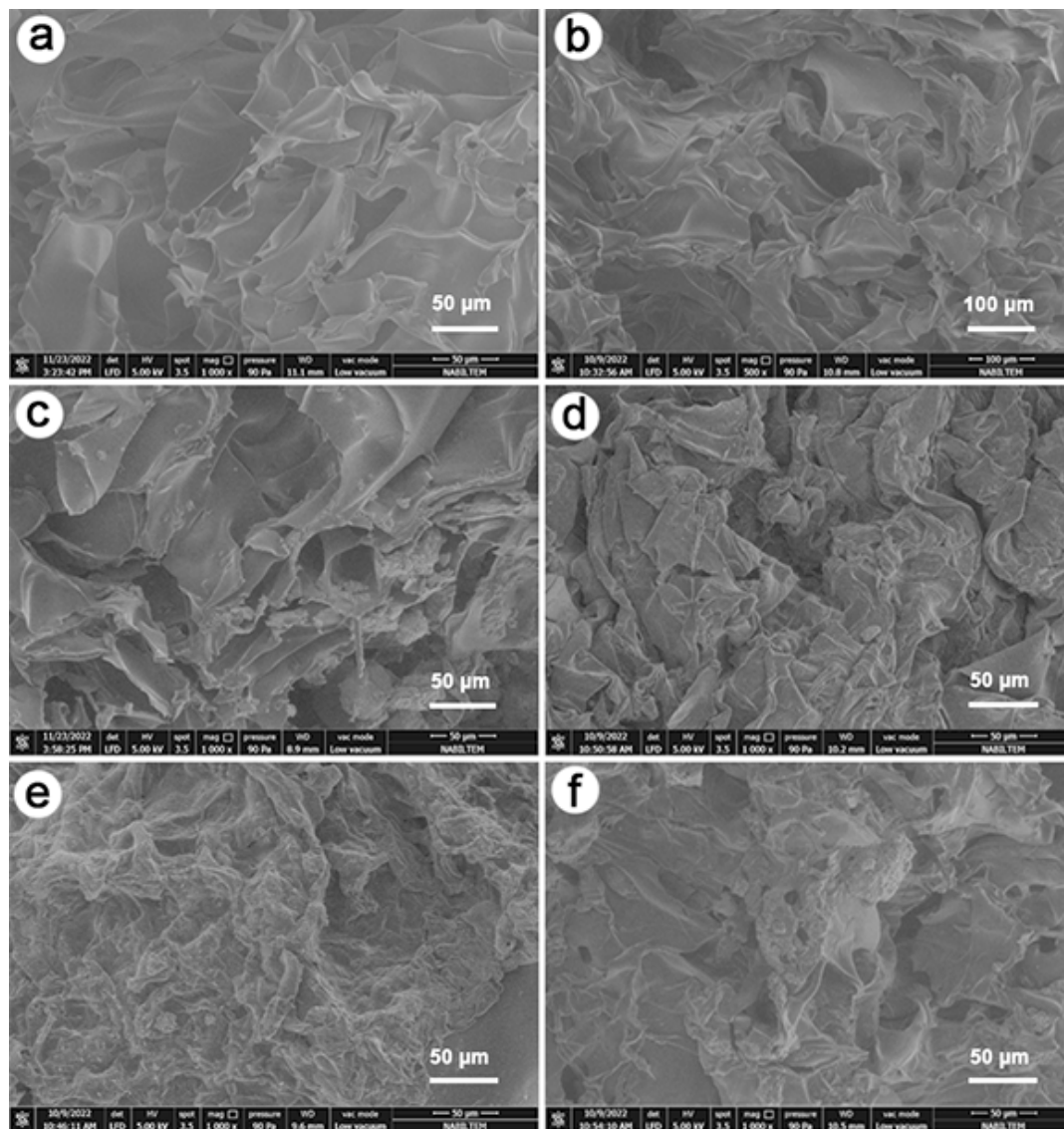


Figure 3: The SEM images of the hydrogels: a) CS, b)CS/SA, c) CS/SA/CL, d)CS/CL, e)drug loaded CS/SA/CL, f)drug loaded CS/CL.

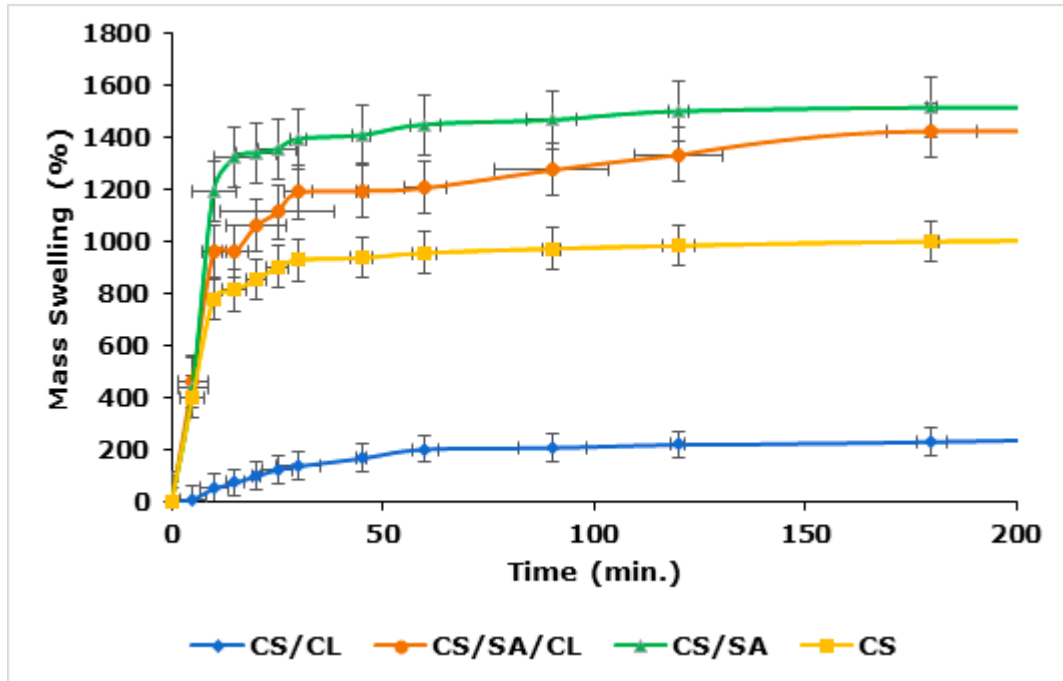


Figure 4: The swelling properties of CS, CS/SA, CS/CL, CS/SA/CL.

3.3. Effect of CL on drug release amount

As can be seen in Figures 5a and 5b, the time-dependent drug release amounts and release percentages of the CL-free chitosan (CS) hydrogels are higher than that of the CL-containing hydrogels. As seen in the SEM analysis, the structure becomes denser with the increase of the CL content in the structure. Thus, the CL layers act as a barrier and slow the release of drug molecules (9, 22). The absence of burst in drug release from CS/SA/CL samples may be due to surface characteristics of the nanocomposite hydrogels, intrinsic dissolution rate of drug, heterogeneity of matrices (26).

It is seen from Table 1 that an increase in the amount of drug loading leads to an increase in the cationic LD drug adsorption capacity of CS/SA/CL composite hydrogels. At pH 7.4, CL and sodium alginate have negative charge potential on the composite surface and this leads to an increase in the anionic character of CS/SA/CL hydrogel. These gels have many anionic carboxyl groups which can increase the interactions between cationic groups of cationic LD and carboxyl groups of gel (24,25). As shown in Figure 5, these interactions cause the release of the drug to be delayed from the composite having higher drug content, and LD release (%) decreases when the drug loading amount in the composite increases (25,27).

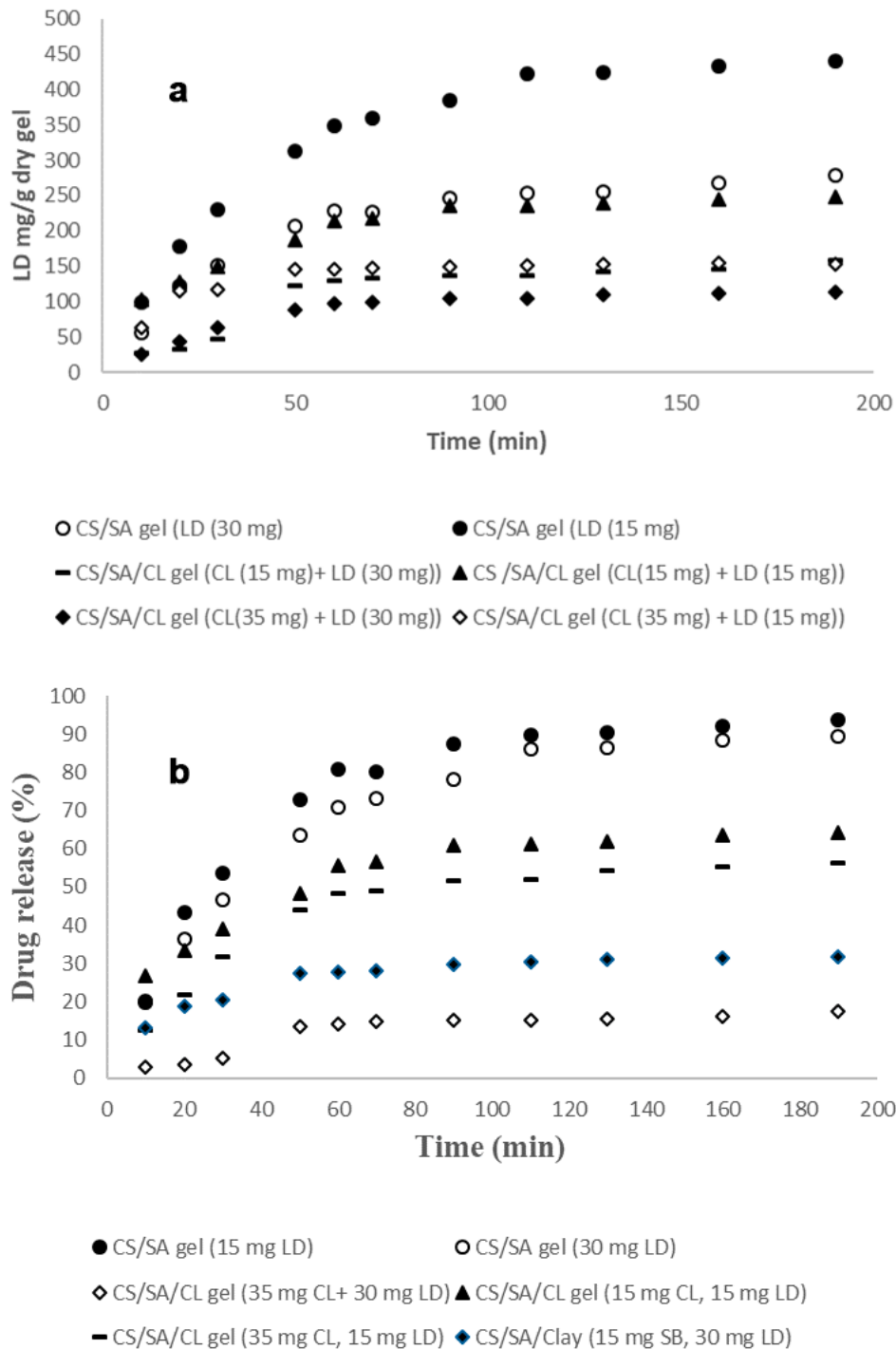


Figure 5: Drug release properties of CS, CS/SA, CS/CL, CS/SA/CL hydrogels.

Table 1: Equilibrium drug uptake capacity and equilibrium drug release (%).

LD loaded hydrogels	Equilibrium LD uptake (mg LD/g gel) and eq. LD release	(%)
CS/SA	1500291.50 mg/g (LD:15 mg)	98.97%
	490.30 mg/g (LD:30 mg)	89.50%
CS/SA/CL	141.25 mg/g (LD:15 mg, CL:15 mg)	70.30%
	166.63 mg/g (LD:15 mg, CL:35 mg)	61.70%
	151.22 (LD:30 mg, CL:35 mg)	44.10%

3.4. Drug release kinetics

In Figure 6, LD release kinetics of all the prepared hydrogels were used by zero-order, first-order, Higuchi, and Korsmeyer-Peppas models. The best-

fitted model with the release data was evaluated by the values of the regression coefficient. All the model constants are presented in Table 2 together with the r values. It is evident that all the kinetic models fitted

well to the release data ($r^2 > 0.99$). The $n < 0.5$ value indicates that the release mechanism is diffusion controlled (27,28). For samples CS/SA and CS/SA/CL, the value of n is between 0.5–1, indicating that the LD released follows a non-Fickian diffusion

mechanism, and the LD released by diffusion and relaxation of the polymer chains occurs simultaneously (29).

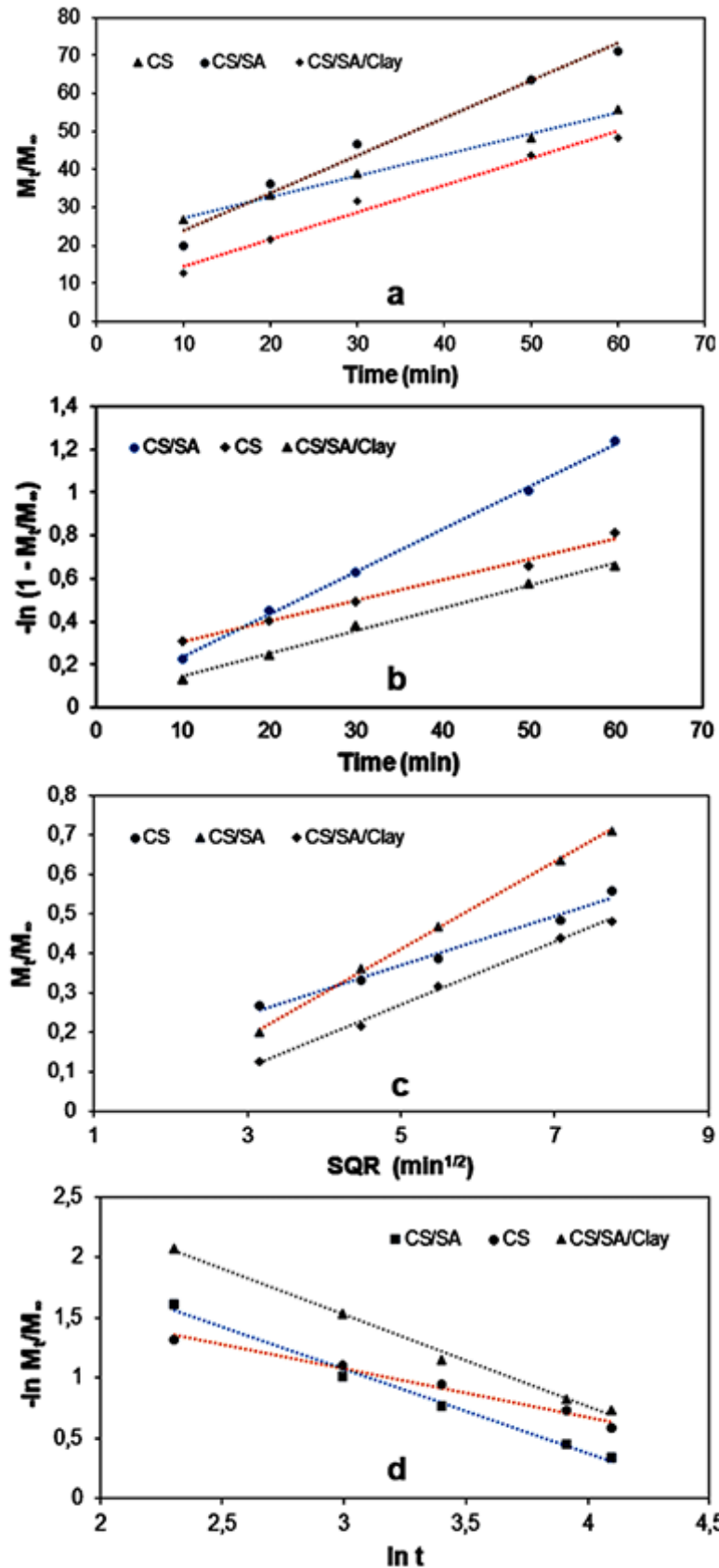


Figure 6: LD release kinetics of all the prepared hydrogels were used by (a) zero-order, (b) first-order, (c) Higuchi and (d) Korsmeyer-Peppas models.

Table 2: LD release kinetics of all the prepared nanocomposite hydrogels were used by (a) zero-order, (b) first-order, (c) Higuchi and (d) Korsmeyer-Peppas models.

Kinetic Models	CS	CS/SA	CS/SA/CL
Zero order Kinetics			
K_0 (min ⁻¹)	0.56	0.98	0.71
R^2	0.9983	0.9789	0.9855
First-order Kinetics			
K_1 (min ⁻¹)	0.0097	0.0199	0.0106
R^2	0.9893	0.9988	0.9944
Higuchi Model			
K_2 (min ⁻¹)	0.062	0.110	0.0795
R^2	0.9855	0.9989	0.9970
Korsmeyer- Peppas model			
N	0.40	0.76	0.69
K	0.10	0.04	0.02
R^2	0.9833	0.9918	0.9947

4. CONCLUSION

In this work, a new type of drug loaded CS/SA/CL nanocomposite hydrogels was prepared by cryogelation technique from the natural biopolymers, chitosan and sodium alginate using glutaraldehyde as a crosslinker. FTIR spectroscopy and SEM analysis confirmed the successful preparation of the nanocomposite hydrogels. The improvements in swelling, diffusion, and drug adsorption and release properties of the new CS composite hydrogels with the addition of sodium alginate and clinoptilolite in the gel structure were achieved. Thus, the experimental results suggest that the prepared nanocomposite hydrogels can be suitable for potential use in biomedical applications.

5. CONFLICT OF INTEREST

Authors declare no conflict of interest.

6. ACKNOWLEDGMENTS

The authors would thank the Scientific Research Office of Tekirdağ Namik Kemal University (NKUBAP.06.GA.21.330) for funding this work.






7. REFERENCES

1. Kevadiya BD, Joshi GV, Mody HM, Bajaj HC. Biopolymer-cl hydrogel composites as drug carrier: host-guest intercalation and in vitro release study of lidocaine hydrochloride. *Applied Clay Science*, 2011; 52: 364-367. Available from: <DOI>.
2. Fonseca JM, Medeiros SF, Alves GM, Santos DM, Campana-Filho SP, Santos AM. Chitosan microparticles embedded with multi-responsive poly (N-vinylcaprolactam-co-itaconic acid-co-ethylene-glycol dimethacrylate)-based hydrogel nanoparticles as a new carrier for delivery of hydrophobic drugs. *Colloids Surfaces B: Biointerfaces*, 2019; 175: 73-83. Available from: <DOI>.
3. Wu M, Lin M, Li P, Huang X, Tian K, Li C. Local anesthetic effects of lidocaine loaded carboxymethyl chitosan cross-linked with sodium alginate hydrogels for drug delivery system, cell adhesion, and pain management. *Journal of Drug Delivery and Science*, 2023; 79: 104007. Available from: <DOI>.
4. Phan VH, Mathiyalagan R, Nguyen MT, Tran TT, Murugesan M, Ho TN, Huong H, Li Y, Thambi T. Ionically cross-linked alginate-chitosan core-shell hydrogel beads for oral delivery of insulin. *International Journal of Biological Macromolecules*, 2022; 222: 262-272. Available from: <DOI>.
5. Kutlusoy T, Oktay B, Apohan NK, Süleymanoğlu M, Kuruca SE. Chitosan-co-hyaluronic acid porous hydrogels and their application in tissue engineering. *International Journal of Biological Macromolecules*, 2017; 103: 366-378. Available from: <DOI>.
6. Zhao F, Yao D, Guo R, Deng L, Dong A, Zhang J. Composites for polymer hydrogels and nanoparticulate systems for biomedical and pharmaceutical applications. *Nanomaterials (Basel)*, 2015; 5: 2054-2130. Available from: <DOI>.
7. Zhang J, Lin X, Liu J, Zhao J, Dong H, Deng L, Liu J, Dong A. Sequential thermo-induced self-gelation and acid-triggered self-release process of drug-conjugated nanoparticles: A strategy for sustained and controlled drug delivery to tumor. *Journal of Materials Chemistry B*, 2013; 1: 4667-4677. Available from: <DOI>.
8. Serati-Nouri H, Jafari A, Roshangar L, Dadashpour M, Pilehvar-Soltanahmadi Y, Vlierberghe SV, Sarghami N. Biomedical applications of zeolite-based materials: a review, *Materials Science and Engineering: C Materials for Biological Applications*, 116, 111225, (2020). Available from: <DOI>.
9. Moradi S, Barati A, Tonelli AE, Hamed H. Effect of clinoptilolite on structure and drug release behavior of chitosan/thyme oil γ -Cyclodextrin inclusion compound hydrogels. *Journal of Applied Polymer Science*, 2021; 138: e49822. Available from: <DOI>.
10. Dragan ES, Dinu MV. Advances in porous chitosan-based composite hydrogels: Synthesis and applications. *Reactive and Functional Monomers*, 2020; 146: 104372. Available from: <DOI>.
11. Tondar M, Parsa MJ, Yousefpour Y, Sharifi AM, Shetaboushehri SV. Feasibility of clinoptilolite application as a microporous carrier for pH-controlled

- oral delivery of aspirin. *Acta Chimica Slovenica*, 2014; 61: 688-693. Available from: [<DOI>](#).
12. Barbosa GP, Debone HS, Severino P, Souto EB, Silva CF. Design and characterization of chitosan/zeolite composite films – Effect of zeolite type and zeolite dose on the film properties. *Materials Science and Engineering C*, 2016; 60: 246-254. Available from: [<DOI>](#).
 13. Taşdelen B, Kayaman-Apohan N, Güven O, Baysal BM. Swelling and diffusion studies of poly (N-isopropylacrylamide/itaconic acid) copolymeric hydrogels in water and aqueous solutions of drugs. *Journal of Applied Polymer Science*, 2004; 91: 911-915. Available from: [<DOI>](#).
 14. Lee SB, Seo SM, Lim YM, Cho SK, Lee YM. Preparation of alginate/poly (N-isopropylacrylamide) hydrogels using gamma-ray irradiation grafting. *Macromolecular Research*, 2004; 12: 269-275. Available from: [<DOI>](#).
 15. Taşdelen B, Kayaman-Apohan N, Güven O, Baysal BM. Preparation of poly (N-isopropylacrylamide/itaconic acid) copolymeric hydrogels and their drug release behavior. *International Journal of Pharmaceutics*, 2004; 278: 343-351. Available from: [<DOI>](#).
 16. Akkaya R, Ulusoy U. Preparation and characterization of polyacrylamide/maleic acid - based hydrogels Composites. *Hacettepe Journal of Biology and Chemistry*, 2011; 39: 359-370. Available from: [<DOI>](#).
 17. Francis NL, Hunger PM, Donius AE, Riblett BW, Zavaliangos A, Wegst UG, Wheatley MA. An ice-templated, linearly aligned chitosan-alginate scaffold for neural tissue engineering. *Journal of Biomedical Materials Research Part A*, 2013; 101: 3493-3503. Available from: [<DOI>](#).
 18. Higuchi T. Mechanism of sustained-action medication. theoretical analysis of rate of release of solid drugs dispersed in solid matrices. *Journal of Pharmaceutical Sciences*, 1963; 52: 1145-1149. Available from: [<DOI>](#).
 19. Ullah K, Sohail M, Mannan A, Rashid H, Shah A. Murtaza G, Khan SA. Facile synthesis of chitosan based-(AMPS-co-AA) semi-IPNs as a potential drug carrier: enzymatic degradation, cyto-toxicity, and preliminary safety evaluation. *Current Drug Delivery*, 2019; 16: 242-253. Available from: [<DOI>](#).
 20. Taşdelen B, Çiftçi Dİ, Meriç Pagano S. Preparation and characterization of chitosan/AMPS/kaolinite composite hydrogels for adsorption of methylene blue. *Polymer Bulletin*, 2022; 79: 9643-9662. Available from: [<DOI>](#).
 21. Taşdelen B, Çiftçi Dİ, Meriç Pagano S. Preparation and characterization of chitosan/hyaluronic acid/itaconic acid hydrogel composite to remove manganese in aqueous solution. *Desalination and Water Treatment*, 2021; 209: 204-211. Available from: [<DOI>](#).
 22. Taşdelen B. Synthesis, swelling, diffusion and cationic dye adsorption studies of semi-IPN sodium alginate/poly (HEMA-co-MA) hydrogels. *ChemistrySelect*, 2023; 8, e202300707. Available from: [<DOI>](#).
 23. Abukhadra MR, Adlii A, Khim JS, Ajarem JS, Allam AA. Insight into the Technical Qualification of the Sonocogreen CaO/ Clinoptilolite Nanocomposite (CaO(NP)/Clino) as an Advanced Delivery System for 5-Fluorouracil: Equilibrium and Cytotoxicity. *ACS Omega*, 2021; 6: 31982-31992. Available from: [<DOI>](#).
 24. Taşdelen B, Çiftçi Dİ, Meriç Pagano S. Preparation of N-isopropylacrylamide/itaconic acid/pumice highly swollen composite hydrogels to explore their removal capacity of methylene blue. *Colloids and Surfaces A: Physicochemical and Engineering Aspects*, 2017; 519: 245-253. Available from: [<DOI>](#).
 25. Thakur G, Singh A, Singh I. Chitosan-montmorillonite polymer composites: formulation and evaluation of sustained release tablets of aceclofenac. *Scientia Pharmaceutica*, 2016; 84: 603-618. Available from: [<DOI>](#).
 26. Basak SC, Kumar KS, Ramlingam M. Design and release characteristics of sustained release tablet containing metformin HCl. *Revista Brasileira de Ciências Farmacêuticas*, 2008; 44: 477-483. Available from: [<DOI>](#).
 27. Ful Y, Kao WJ. Drug release kinetics and transport mechanisms of nondegradable and degradable polymeric delivery systems. *Expert Opinion on Drug Delivery*, 2010; 7: 429-444. Available from: [<DOI>](#).
 28. Ruocco CD, Acocella MR, Guerra G. Release of cationic drugs from charcoal. *Materials*, 2019; 12: 683-687. Available from: [<DOI>](#).
 29. García-Couce J, Vernhes M, Bada N, Agüero L, Valdés O, Alvarez-Barreto J, Fuentes G, Almirall A, Cruz L J. Synthesis and evaluation of AlgNa-g-Poly (QCL-co-HEMA) hydrogels as platform for chondrocyte proliferation and controlled release of betamethasone. *International Journal of Molecular Sciences*, 2021; 22: 5730. Available from: [<DOI>](#).



Nano-Catalytic Synthesis of 5 Substituted 1H Tetrazole Derivatives and Biological Applications

Jwankar Abdalla Shekh Khdir^{1*} , Dara Muhammed Aziz¹ , Ibrahim Nazem Qader^{2,3} ,
Bashdar Ismael Meena^{1,4} , Bnar Mahmoud Ibrahim¹ 

¹Chemistry Department, Collage of Science, University of Raparin, Rania, 46012, Sulaimanyah, Iraq.

²Physic Department, Collage of Science, University of Raparin, Rania,46012, Sulaimanyah, Iraq.

³Department of Pharmacy, College of Pharmacy, Knowledge University, Erbil 44001, Iraq.

⁴Department of Chemistry, Faculty of Science & Health, Koya University, Koya KOY45, Iraq.

Abstract: This review explores the innovative use of nano-catalysts in the synthesis of 5-substituted 1H-tetrazole derivatives, highlighting their significant biological applications. The novel methodologies discussed demonstrate enhanced efficiency and selectivity in the production of these compounds. Key findings include the optimization of reaction conditions and the discovery of new catalytic pathways that improve yield and reduce reaction time. The synthesized tetrazole derivatives exhibit strong potential as therapeutic agents due to their biological activity. This work provides a comprehensive overview of the state-of-the-art techniques in nano-catalytic synthesis, emphasizing their practical applications in medicinal chemistry and materials science.

Keywords: Nano-Catalyst, Tetrazole derivatives, 5-substituted.

Submitted: February 16, 2024. **Accepted:** September 8, 2024.

Cite this: Khdir JAS, Aziz DM, Qader, IN, Meena BI, Ibrahim BM. Nano-Catalytic Synthesis of 5 Substituted 1H Tetrazole Derivatives and Biological Applications. JOTCSA. 2024;11(4): 1495-514.

DOI: <https://doi.org/10.18596/jotcsa.1436801>

***Corresponding author's E-mail:** jwankarr.abdulla@gmail.com

1. INTRODUCTION

Tetrazoles are artificial heterocyclic organic compounds that have one carbon atom and four nitrogen atoms arranged in a five-membered ring. They are among the stable heterocycles with the highest nitrogen concentration. Tetrazoles are classified into two more common categories according to the number of substituents (Figure 1): (i) the simplest parent tetrazoles, (ii) Tetrazoles that have been mono-, 2-, or 5-substituted, (iii) Tetrazoles that are di-substituted (1,5- or 2,5-disubstituted).

"J. A. Bladin created and described tetrazole for the first time in 1885 (1,2), marking a significant milestone in organic chemistry. His pioneering work, conducted on the campus of Uppsala University, laid the foundation for subsequent studies exploring tetrazole derivatives' diverse applications in pharmaceuticals, materials science, and other fields, as evidenced by numerous scholarly articles available on Google Scholar. Tetrazoles exhibit stability throughout an extensive pH range and demonstrate

resistance to a variety of oxidizing and reducing agents (1). They function as ligands in coordination chemistry and are essential (2) as explosives within the field of material science (3) and serve as substitutes for carboxylic acids in medicinal chemistry (4). Because of the many nitrogen atoms in their structure, they function as flexible pharmacophores in medicinal chemistry. Among the drugs are those with tetrazole rings. Antimicrobial (5), antifungal (6), antiviral (7), analgesic (8), and anti-inflammatory (9).

In recent years, advancements in nanoscience and nanotechnology have brought about revolutionary changes in many sectors, such as biology, medicine, wellness, environmental protection, and catalysis (10,11). Utilizing nanotechnology to capitalize on catalytic processes is one of the most important research fields among them, considering its direct influence on human society and evolution (12,13). The name "Nano" comes from the Greek word "dwarf". Anything that is at least one magnitude smaller than 100 nm in nanotechnology and has a clear view of its limit is called a nanoparticle (NP)

(14). Applications for nanoscale materials are growing in frequency, including fuel conversion, pollution control, and chemical synthesis. Transition metal NPs are of particular interest in nearly every branch of research and industry (15,16). Depending on their size, shape, composition, aggregation, material origin, and similarity, nanocatalysts can be distinguished from one another. Among other factors, the structure and form of NPs have a significant influence in determining how dangerous they are to people and their surroundings (17,18). Because of their enormous catalytic activity, NPs are useful for chemical procedures in both industry and research (19,20). There are several different kinds of NPs, including metal/metal oxide, ceramic, semiconductor, carbon-based, and polymeric NPs (21-26), among the first uses of NPs in catalysis. Several substances and elements, including titanium dioxide, steel, aluminum, and silica, have been employed as nanoscale catalysts over the past decades (27,28). It has been successful in using nanocrystalline metal oxides as poisons and gasses of hazardous substances (29). The literature claims that changing a nanomaterial's size, texture, and composition can change its properties (30-33). The ability of the activity catalyst to be retrieved from the reaction media after the reaction is a critical component in determining its utility in practical applications. On a large scale, this problem poses serious environmental and financial challenges. Because of this, heterogeneous catalysts are much

more varied and often used in industry than homogeneous catalysts (34,35). However, heterogeneous catalysts' lack of efficiency is their worst flaw, which is why developing catalysts with extremely high efficiencies is a top priority. In addition to organic modification, nanocatalysts have many other uses (36,37). Thermal decomposition, organic vapor synthesis, microwave irradiation, sol-gel process, non-sono and sonoelectrooxidation, chemical precipitation, the hydrothermal approach, the photochemical method, shine discharge plasma electrolysis, the antisolvent the process of the precipitation microwave radiation exposure, wet-chemical approach, and sonochemical strategy are among the many techniques utilized for producing these nanocatalysts (36-40). To grasp the significance of nanocatalysts, one can examine the information available on the (Web of Science) platform, covering the period from 2000 to 2022. The volume of publications has shown a consistent annual rise, with notable advancements emerging, particularly after 2010. This observation leads us to posit that the realm of nanotechnology exerts influence across various scientific domains, see (Figure 2). 5-replaced 1H-tetrazoles are among the most significant and fascinating of all the tetrazole classes due to their many applications in the field of medicinal chemistry. Thus, the most recent developments in the synthesis of 5-replaced 1H-tetrazoles will be the main subject of this study.

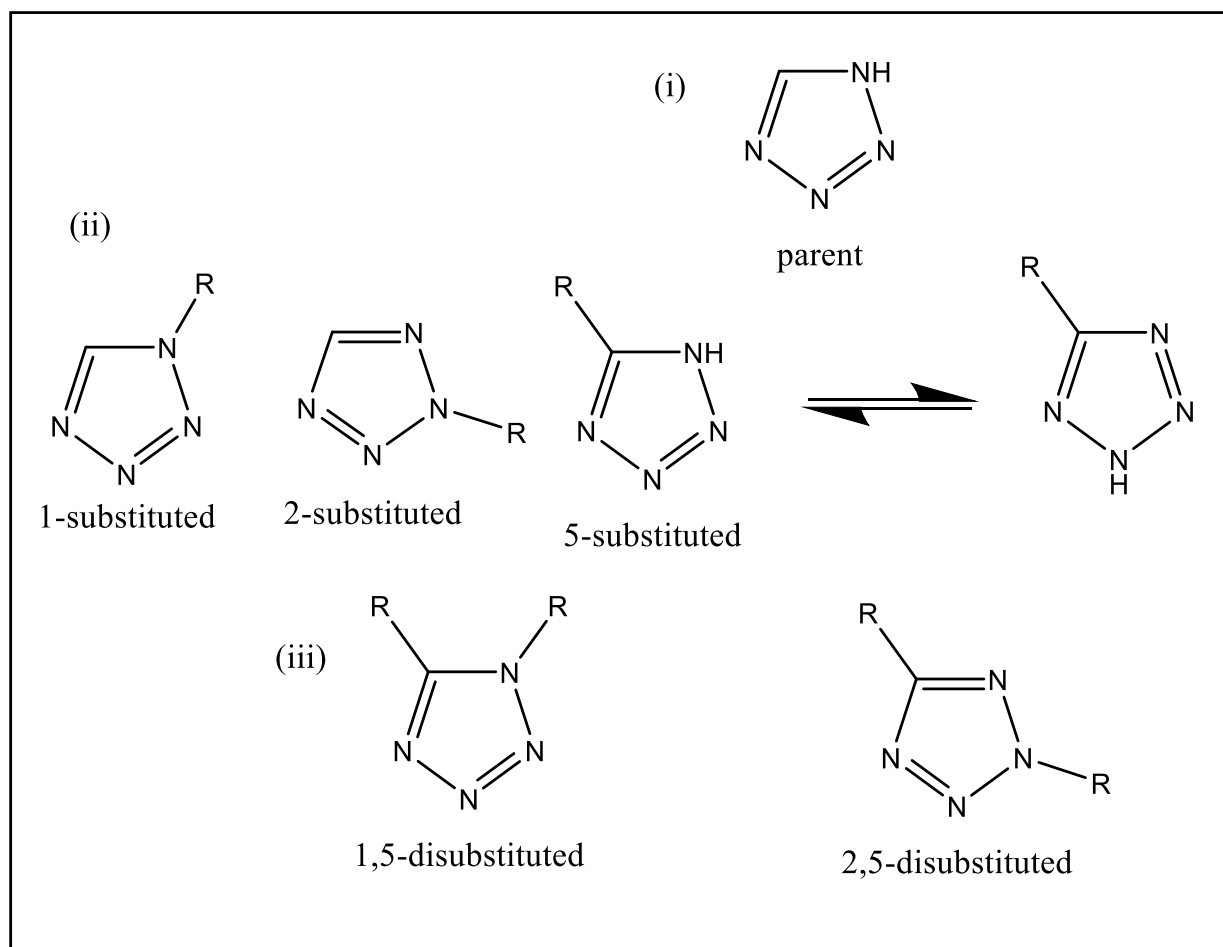


Figure 1: The classification of tetrazoles (37).

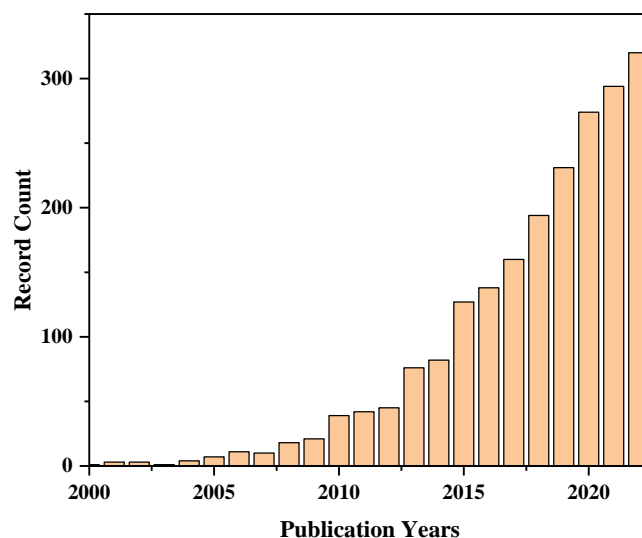
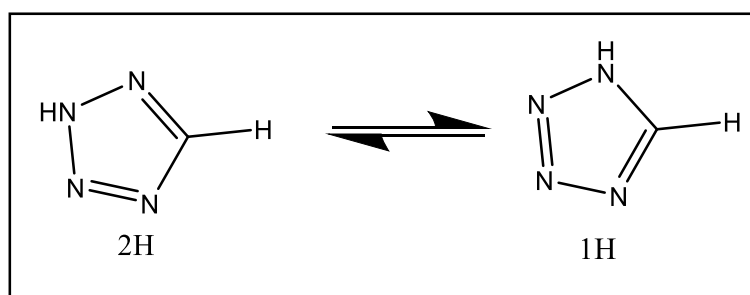


Figure 2: Publication vs. year record of published nanocatalysts.

2. THE FUNCTION OF 1H-TETRAZOLES WITH 5-SUBSTITUTES IN MEDICINAL CHEMISTRY

In medicinal chemistry, 1H-tetrazoles with five substitutes are frequently used as carboxylic acid bioisosteric substitutes or, more precisely, as carboxylic acid surrogates (41). Despite structural differences, neither of these functional groups exhibits comparable biological activity because of substantially related physiochemical characteristics (42). It is known that there are two tautomeric forms of 1H-tetrazoles with five substitutes with a free N-H bond: 1H- and 2H-tautomers in an approximately 1:1 ratio (Scheme 1) (43). Larsen, Liljebris, and coworkers (44) found that, as compared to utilizing the comparable carboxylate counterparts, adding a

lipophilic tetrazole moiety to a range of PTB1B inhibitors dramatically enhanced Caco-2 cell permeability. The impact of substituting a 1H-tetrazole with five substitutes for a carboxylic acid in terms of pharmacodynamics is complex. It is impossible to forecast with any degree of accuracy whether the pharmacodynamics will rise, fall, or even vanish (45). A negative charge resonance in the tetrazole ring may raise or lower the interaction with a certain receptor, according to the electron configuration within a receptor site (46). The primary benefit of 1H-tetrazoles with five substitutes is that one of its nitrogen atoms can be glucuronidated, allowing both of its tautomers to act as platforms (47).



Scheme 1: The two tautomeric forms of 1H-tetrazoles with five substitutes (43).

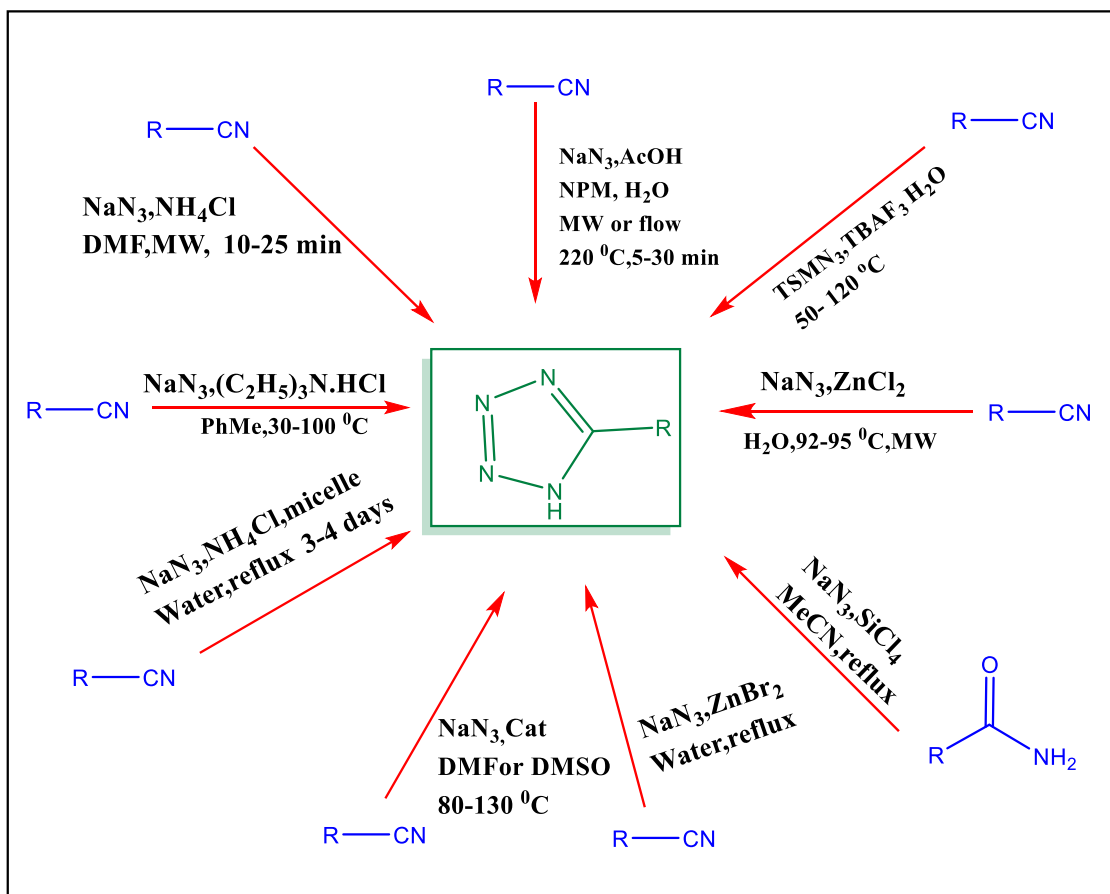
3. DIFFERENT METHODS TO SYNTHESIZE TETRAZOLES WITH FIVE SUBSTITUTES

Tetrazoles with five substitutes have been used in photography, organic chemistry, medicine, and weaponry (45). It is an important intermediate in the synthesis of organic compounds that is derived from tetrazole in organic chemistry. (Scheme 2) and (Table 1) show some indicated methods for producing these specific tetrazole derivatives. The majority of these methods are based on the condensation of a CN group plus an azide moiety. Tetrazoles with five substitutes can be synthesized by (I) Nitrile reaction with NaN_3 and NH_4Cl or $(\text{C}_2\text{H}_5)_3\text{N}\cdot\text{HCl}$ in N, N-dimethylformamide (DMF) with microwave assistance (48), (II) Nitrile, and NaN_3 reacting using

$(\text{C}_2\text{H}_5)_3\text{N}\cdot\text{HCl}$ in toluene (49), (III) ammonium chloride, dodecyl trimethylammonium or hexadecyl trimethylammonium bromides, and nitrile condensation using water with NaN_3 (2), (IV) acetic acid and NaN_3 used to treat nitrile in N-methyl pyrrolidine-2-one (NMP) solution (50), (V) Trimethylsilyl azide (TMSN_3) and nitrile are reacted by tetrabutylammonium fluoride (TBAF) trihydrate (51), Microwave procedure for treating (NaN_3) in H_2O with nitrile and ZnCl_2 (52), (VII) amide, NaN_3 , and HCl_3Si undergo MeCN condensation (53), (VIII) Under a reflux condition, zinc bromide is used to condensate NaN_3 and nitrile in water (54), (IX) using heterogeneous catalysts, such as Pt NPs, to condense nitrile and sodium azide in dimethylformamide (55).

Table 1: Different methods to synthesize Tetrazoles with five substitutes (55-60).

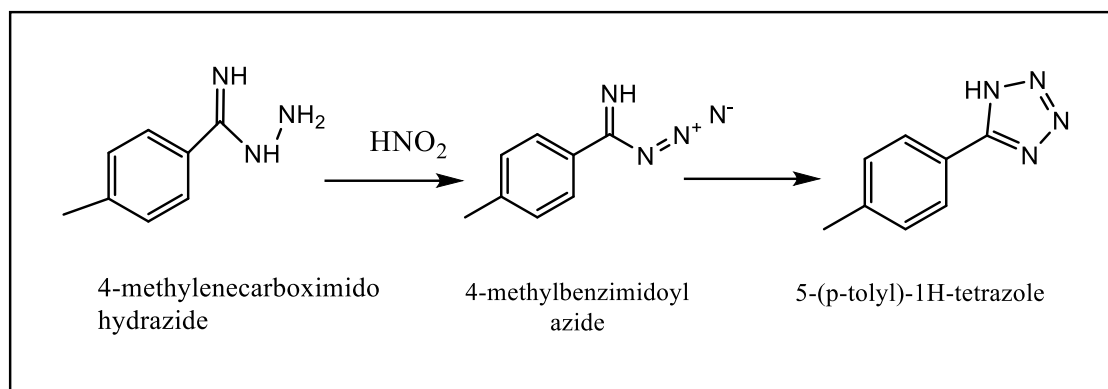
Number	Temperatures, and duration	The solvent and material used	Ref.
I	(--), 10-25 min	NaN ₃ , NH ₄ Cl, (C ₂ H ₅) ₃ N.HCl (DMF)	(48)
II	30-100 °C, (--)	NaN ₃ , (C ₂ H ₅) ₃ N.HCl, toluene	(49)
III	(--), 3-4 days	Nitriles, NaN ₃ , NH ₄ Cl, Dodecyl trimethylammonium	(2)
IV	220 °C, 5-30 min	Nitrile, NaN ₃ , acetic acid, (NMP)	(50)
V	50-120 °C, (--)	TBAF, TSMN ₃ , nitrile	(51)
VI	92-95 °C, (--)	NaN ₃ , ZnCl ₂ , H ₂ O	(52)
VII	Reflux	Amide, NaN ₃ , SiCl ₄ in MeCN	(53)
VIII	Reflux	ZnBr ₂ , NaN ₃ , nitrile	(54)
IX	80-130 °C, (--)	NaN ₃ , nitrile, DMF, cat Pt NPs	(55)

**Scheme 2:** Different routes to synthesize 5-substituted tetrazoles.

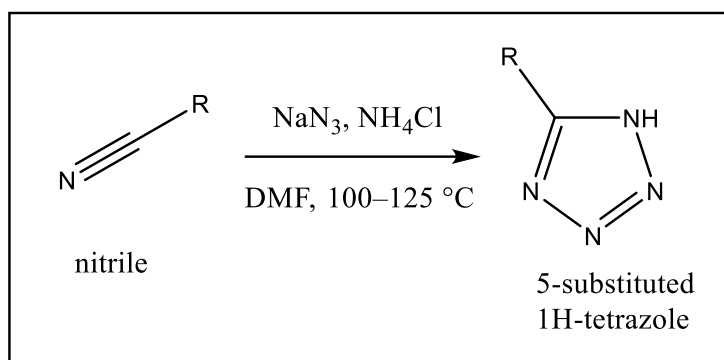
4. SYNTHETIC METHODS OF 1H-TETRAZOLES WITH FIVE SUBSTITUTES

The diazotization of amidrazones was one of the first widely utilized processes for the production of 1H-tetrazoles that are 5-substituted before the [3+2]-cycloaddition process. Hydrazine and imitators were used to create these amidrazones. Using this technique, an imidoyl azide is produced before the 1H-tetrazoles with five substitutes (Scheme 3) (61). Hantzsch and colleagues revealed how to create 5-amino-1H-tetrazole in 1901 by employing azoimide, a hydrazoic acid, and cyanamide (62). Up to the 1950s, the main reactants used to prepare tetrazoles

were hydrogen cyanide and hydrazoic acid. Some of these reactants are dangerous; hydrazoic acid, for instance, is extremely volatile, poisonous, and explosive (63). This method also has a number of other problems, including the use of strong Lewis acids and moisture-sensitive reaction conditions (64). This led to further efforts to modify the protocols for the synthesis of 1H-tetrazoles with five substitutes. 1958 saw Finnegan with associates (65), present their fundamental study as well as an improved procedure for producing 1H-tetrazoles with five substitutes from nitriles in DMF by using inorganic NaN₃ and ammonium chloride (Scheme 4).



Scheme 3: 1H-tetrazoles with five substitutes synthesis from amidrazones.



Scheme 4: 1H-tetrazoles with five substitutes are synthesized from nitriles by employing sodium azide and ammonium chloride.

Consequently, safer, faster reaction times and higher product yields have been achieved through the development of novel synthesis techniques. Utilizing microwave (MW) irradiation, reaction times were shortened (43). Over time, research has been done on the use of various catalysts in various reaction settings. The most common catalyst is the Lewis acid (such as $\text{BF}_3 \cdot \text{OEt}_2$ (66), ZnBr_2 (67), etc.). These catalysts do, however, have drawbacks, such as laborious separation processes and inadequate recovery and recyclable properties. Consequently, to get around these shortcomings, heterogeneous catalysts such as ZnO nanocrystals (68), CuFe_2O_4 NPs (69), CoY zeolite (70) $\text{Fe}_3\text{O}_4 @ \text{SiO}_2$ (71), Ag NPs

(72), SnCl_2 -nano- SiO_2 , Au NPs, graphene, graphene oxide/ ZnO nanocomposites, Pt NPs@rGO (57) etc., used to make 5-substituted 1H tetrazoles. Currently, efforts are being made to improve safer and more efficient synthesis techniques.

This section will give a quick rundown of the four methods for making 1H-tetrazoles with five substitutes: microwave-assisted synthesis, heterogeneous catalysts, miscellaneous methods, and NPs as heterogeneous catalysts. However, we will concentrate on using NPs as heterogeneous catalysts in the synthesis of 1H-tetrazoles with five substitutes (Figure 3).

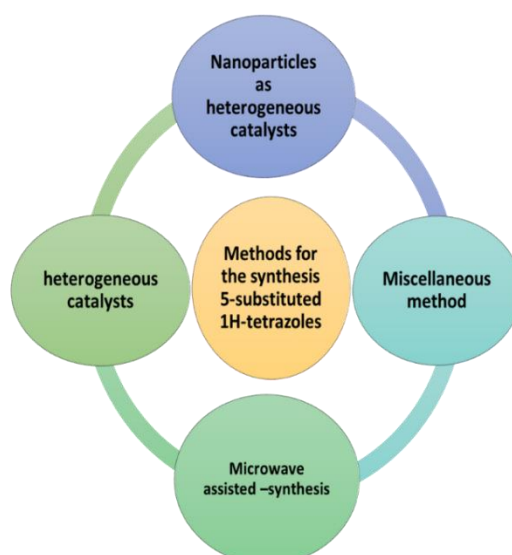
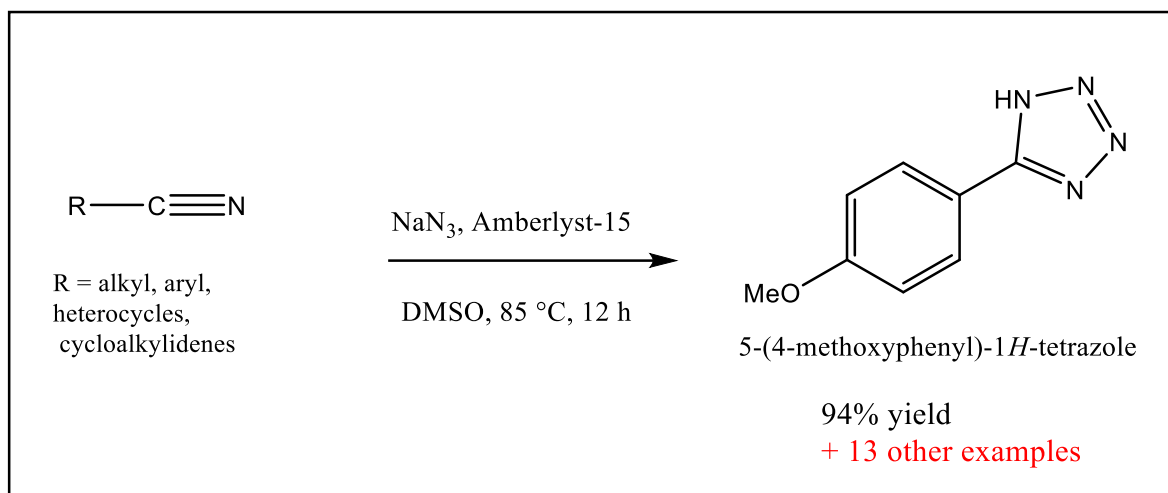


Figure 3: Various methods for producing 1H-tetrazoles with five substitutes Microwave-assisted synthesis.

Another process used to prepare tetrazole derivatives is microwave-assisted synthesis, which we briefly describe as only one method for this preparation. The production of 1H-tetrazoles with five substitutes has difficulties due to extended reaction durations. This disadvantage has been addressed by the use of microwave (MW) irradiation. In 1986, an initial published work involving organic reactions aided by microwaves was released. Despite the expensive

expense of specialized microwave equipment, it is nevertheless widely used. It is thought that microwave irradiation produces reactions with higher yields, less time for reaction, and more purity than traditional heating (73-75). Using MW irradiation, Harusawa, and colleagues (76) for the conversion of 1H-tetrazoles with five substitutes in DMF from inert nitriles (Scheme 5).



Scheme 5: Microwave-assisted synthesis of 1H-tetrazoles with five substitutes.

4.1. Heterogeneous Catalysts Synthesis

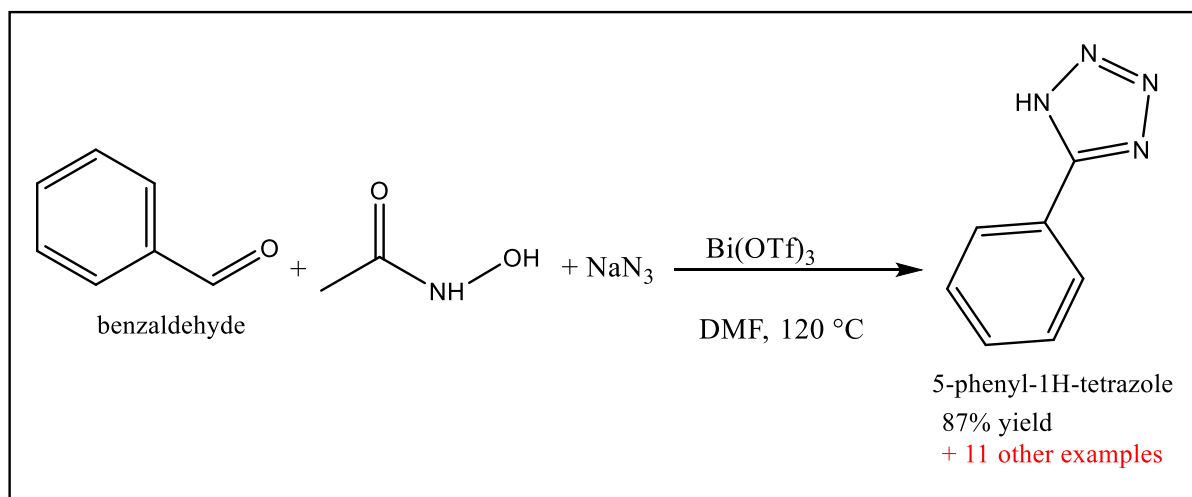
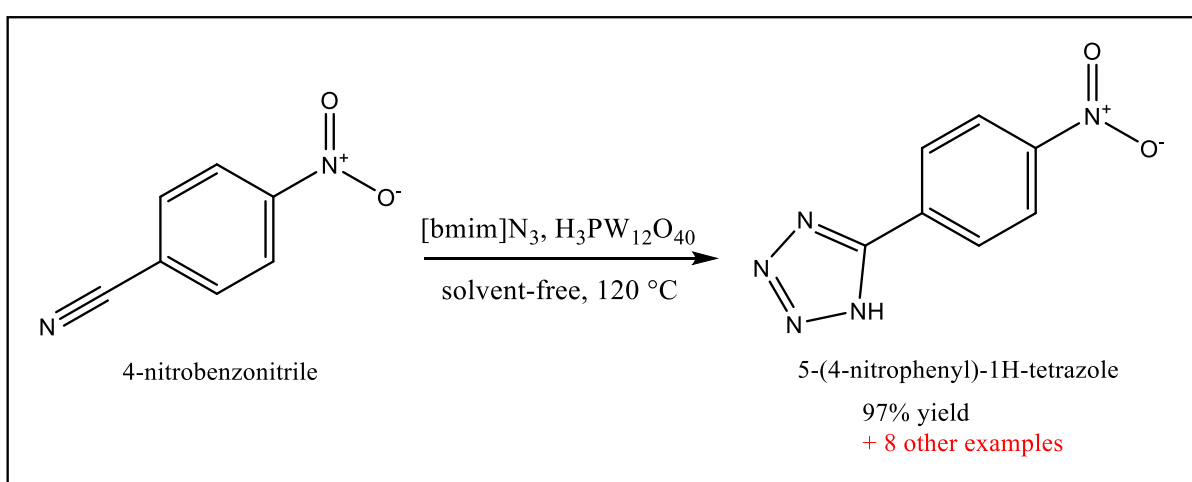
When the phases of the reactants and catalyst are different, this is known as heterogeneous catalysis. Initial homogeneous catalysts for the synthesis of 1H-tetrazoles with five substitutes have low recovery, recyclability, and time-consuming separation processes. Heterogeneous catalysts were created as a solution to these problems, and they are now a common option for the production of 1H-tetrazoles with five substitutes (43). Nagarkar et al. developed a successful process for the synthesis of 1H-tetrazoles with five substitutes using the heterogeneous solid acid resin Amberlyst-15 as a catalyst (77) and employed DMSO as a solvent for 12 hours at 85 °C, yielding a 36-47% product. The highest yield, 94%, was obtained from 5-(4-methoxyphenyl)-1H-tetrazole using 4-methoxybenzotrile. They employed the catalyst subsequently after recovering it eventually by simple filtration. The Akhlaghinia group employed Cu(II) immobilized on aminated epichlorohydrin-activated silica (CAES) in DMSO as a catalyst for the production of 5-substituted 1H-tetrazoles (59). According to the mechanism, Cu(II) first activates the nitrile's nitrogen atom, accelerating the [3+2] cycloaddition. An acidic workup is then performed to produce 5-substituted 1H-tetrazoles. Up to five reuses of the recovered catalyst were possible. Overall, yields ranged from 75 to 96%, with terephthalonitrile (benzene-1,4-dicarbonitrile) yielding the largest amount of 5-(4-cyanophenyl)-1H-tetrazole (96%).

The preparation of tetrazole derivatives by this method has been tried by many others, each using their methods, and some using the same technique as before, but with some changes in solvent or temperature or so on, some of the heterogeneous catalysts used in these preparations with good and satisfactory yields were (Ln(OTf)₃-SiO₂, TBAHS, CAES, and [bmim]N₃ ionic liquid (azide source), etc.).

4.2. Miscellaneous Methods Synthesis

This technique is another good technique that gets reliable results including Metal Azide Precursors, Cyclization of Nitriles, Cyclization of Amidines, Cu(I)-Azide-Alkyne Cycloaddition (CuAAC) and additional processes, such as those described by Sridhar and colleagues (78) can synthesize 1H-tetrazoles with five substitutes in a single step, employing bismuth(III) triflate to catalyze the reaction of aldehydes in DMF at 120 °C with sodium azide and acetohydroxamic acid. With moderate to good (60–87%) production, 5-Aryl, 5-Heteroaryl, 5-Alkyl, and 5-Vinyl-1H tetrazoles were synthesized in 15–28 hours. When benzaldehyde was utilized, the highest output was noted (Scheme 6).

Heravi and colleagues reported a solvent-free, green synthesis of 5-alkyl- and 5-aryl-1H-tetrazoles in high yields (89–97%) utilizing nitriles and [bmim]N₃ at 120 °C for 5–12 hours. The reaction was catalyzed by heteropolyacid (H₃PW₁₂O₄₀) (79). With 4-nitrobenzotrile, the maximum yield was obtained (Scheme 7).

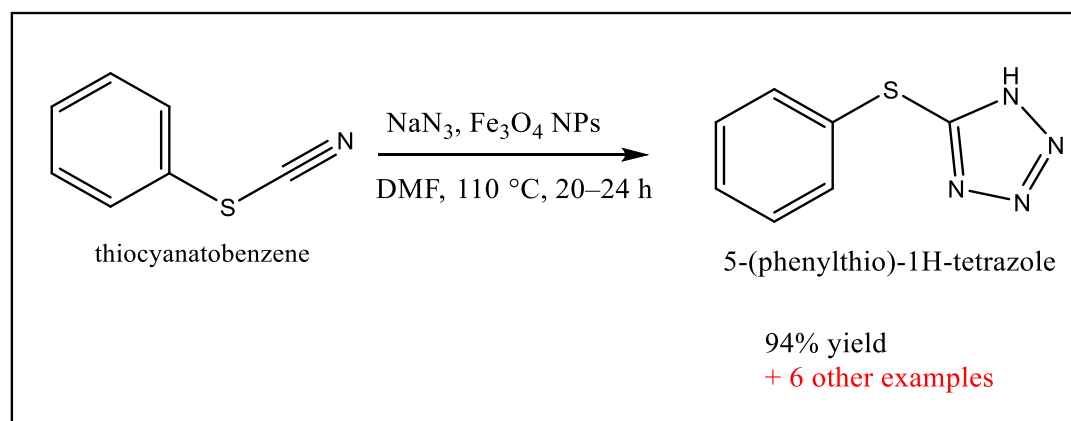
Scheme 6: $\text{Bi}(\text{OTf})_3$ -catalyzed synthesis.Scheme 7: $\text{H}_3\text{PW}_{12}\text{O}_{40}$ -catalyzed synthesis.

4.3. NPs as Heterogeneous Catalysts

In green synthesis, nanomaterials and nanocatalysts are crucial. Benefits like giving the reactant access to a greater surface area and using a minuscule quantity of catalyst to produce meaningful results are attained by shrinking the catalyst. Additionally, it is possible to attain higher selectivity, which will prevent the formation of undesirable products (80). In this section, we will examine some common ways to create the product we want and discuss the importance of each method.

4.3.1. Fe_3O_4 NPs

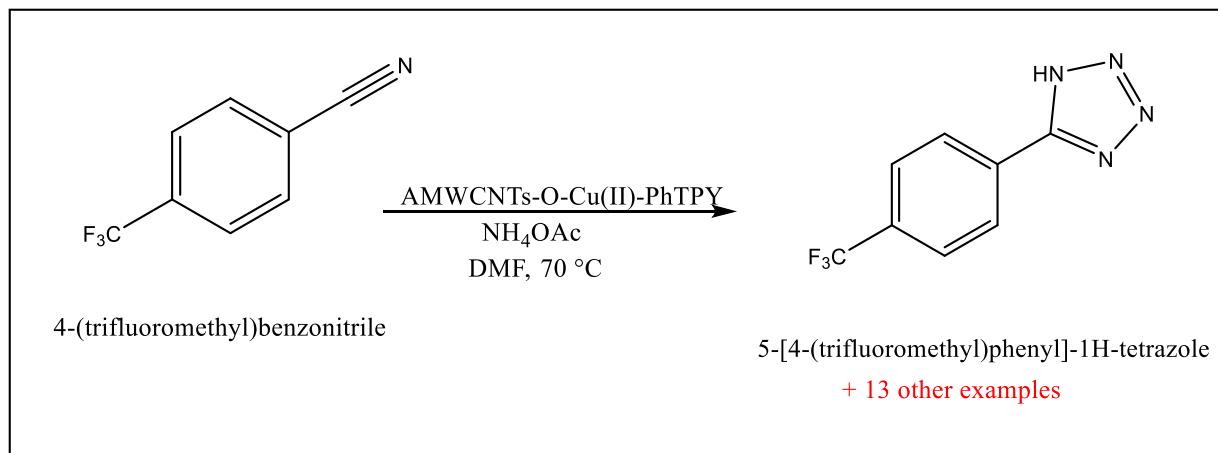
Kolo and Sajad produced 5-(arylthio)-1H and 5-(alkylthio)-1H tetrazoles with yields of up to 94% (81). It employs Fe_3O_4 NPs, which are reused and magnetized recoverable, by using thiocyanates (Scheme 8). The nitrile group of the thiocyanate formed a compound with the catalyst, imparting its electrophilic property, which activated the nitrile group on the catalyst's surface. This is followed by a sodium azide nucleophilic assault. The catalyst's catalytic activity did not significantly decrease throughout its easy recovery and reuse.

Scheme 8: Fe_3O_4 NPs catalyzed synthesis (81).

4.3.2. Cu(II)-O-AMWCNTs-PhTPY NPs

Sharghi et al. produced 1H-tetrazoles with five substitutes with acceptable to good products (75–98%) by immobilizing the 4'-phenyl-2,2':6',2''-terpyridine complex onto multiwalled nanotubes of

carbon with activation [AMWCNTs-O-Cu(II)-PhTPY] in DMF at a temperature of 70 °C (82) (Scheme 9). Up to five cycles of good reusable were shown by the catalyst (43).

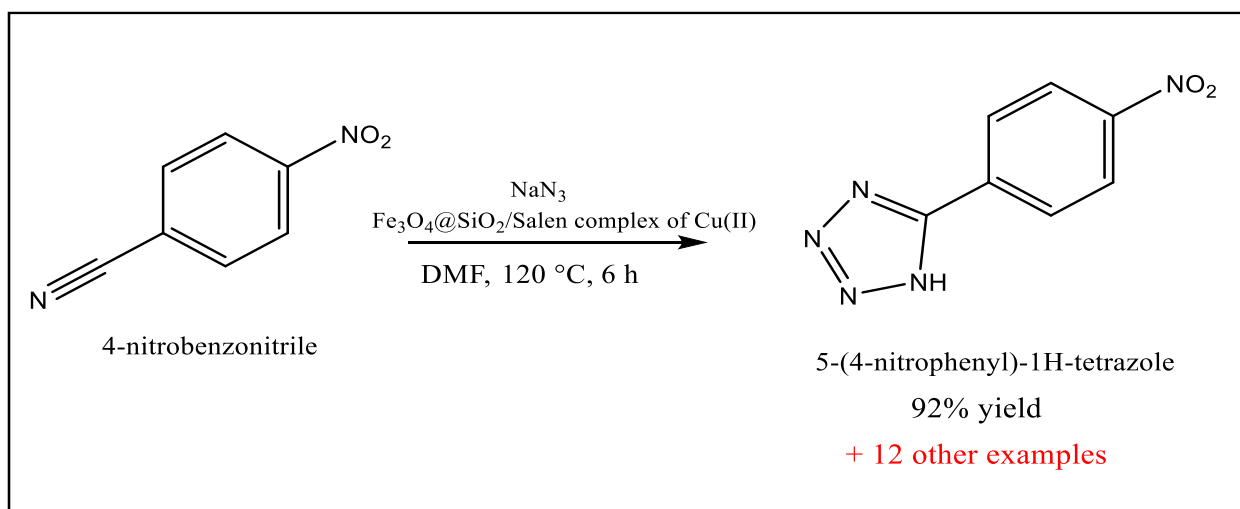


Scheme 9: PhTPY-Cu(II)-O-AMWCNTs catalyzed synthesis (82).

4.3.3. Fe₃O₄@SiO₂/Salen complex of Cu(II) NPs

Superparamagnetic Fe₃O₄@SiO₂ NPs [Fe₃O₄@SiO₂/Salen complex of Cu(II)] are the foundation of the Cu(II) Salen complex. was determined by Sardarian and associates to be the catalyst responsible for the generation of 1H-tetrazoles with five substitutes in DMF at 120 °C (83) seven times without experiencing

a discernible decline in activity. It was possible to get a maximum yield of up to 92% by utilizing terephthalonitrile or 4-nitrobenzonitrile (83). In addition to this product, 12 other products can be obtained from this reaction within 6 hours (Scheme 10).

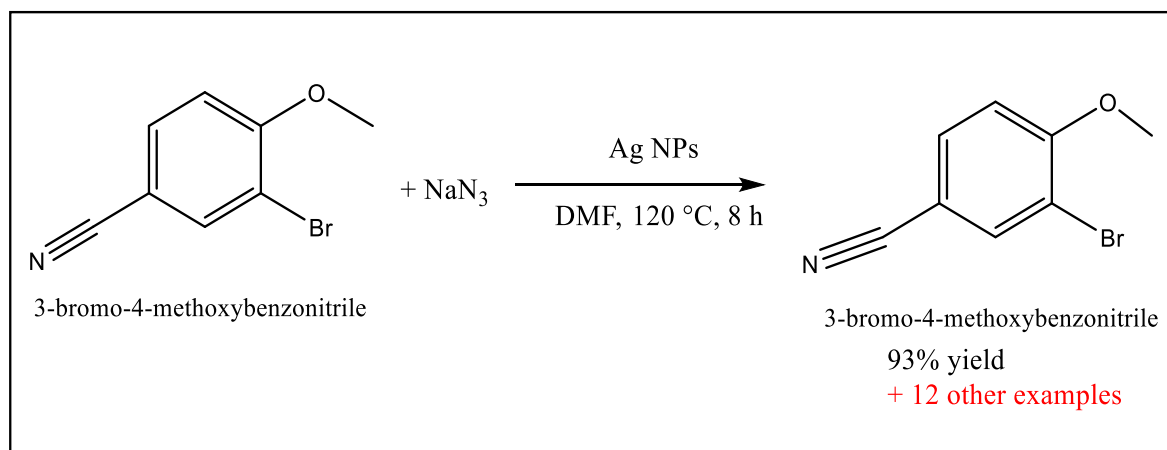


Scheme 10: Cu(II) catalyzed salen compound of Fe₃O₄@SiO₂ synthesis.

4.3.4. Silver NPs (Ag NPs)

Awasthi and coworkers used silver NPs (Ag NPs) in DMF at 120 °C. (72), for the production of (1H-tetrazoles with five substitutes) that produced 93% yields. Chemically, Ag NPs activate the nitrile group's

nitrogen atom, giving the group's carbon atom an electrophilic characteristic. Tetrazoles are also formed as a result of sodium azide's nucleophilic assault. This method does not yield as pleasantly (Scheme 11).

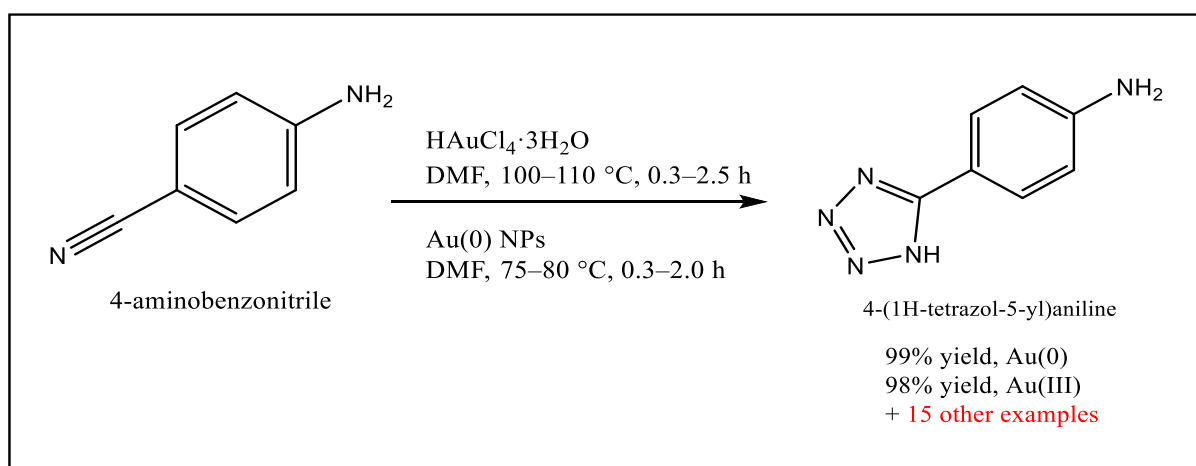


Scheme 11: Using Ag NPs as Catalyzed Synthesis.

4.3.5. Gold (Au) NPs

Gold(III) chloride [$\text{HAuCl}_4 \cdot 3\text{H}_2\text{O}$, Au(III)] and gold nanoparticles [Au NPs, Au(0)] were used as catalysts for the synthesis of 1H-tetrazoles with five substituents in DMF, as reported by Awasthi, Agarwal, and colleagues (84). Chemically, the $\text{C}\equiv\text{N}$ functionality is first activated by the nucleophilic addition of NaN_3 , and it is subsequently activated by protonolysis to produce 1H-tetrazoles with five

substituents through a [3+2]-cycloaddition reaction. For Au(0) NPs, a similar mechanism is expected. Greater reactivity in Au(0) resulted in larger yields in less time. This could be because Au(0) NPs have a higher surface area, which makes it easier for $\text{C}\equiv\text{N}$ and Au(0) to coordinate. Five-substituted 1H-tetrazoles were produced in 83–99% yields (16 instances) by using Au(0) NPs, whereas 82–98% yields were obtained by using Au(III) (Scheme 12).

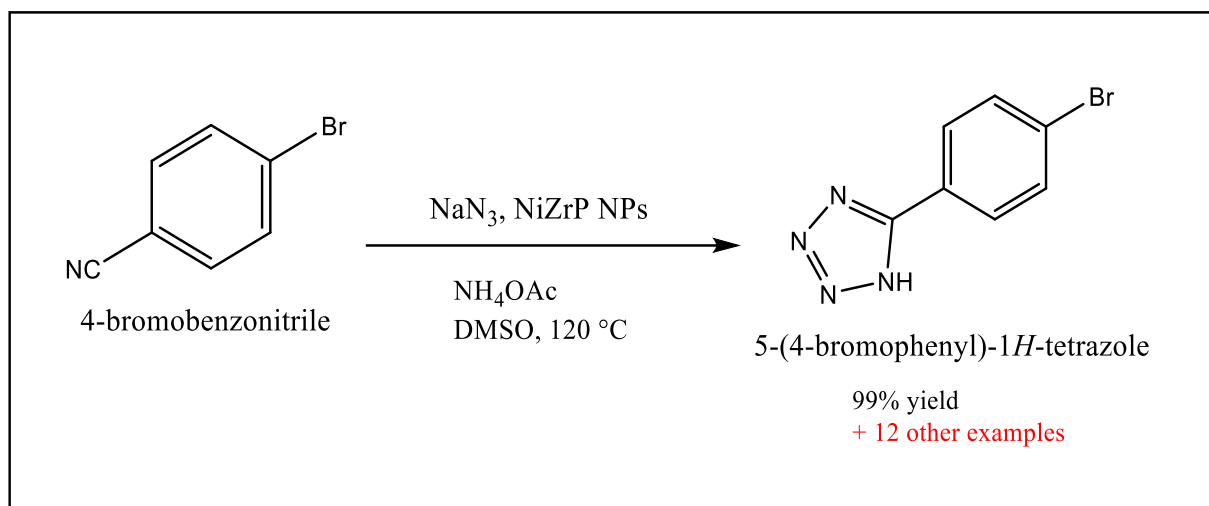


Scheme 12: Au NPs catalyzed synthesis (84).

4.3.6. Nickel zirconium phosphate (NiZrP) NPs

Abrishami and associates used a single nickel zirconium phosphate (NiZrP) nanocatalyst in DMSO at 120 °C to create 1H-tetrazoles with five substituents (85). Up to five cycles of reuse of the

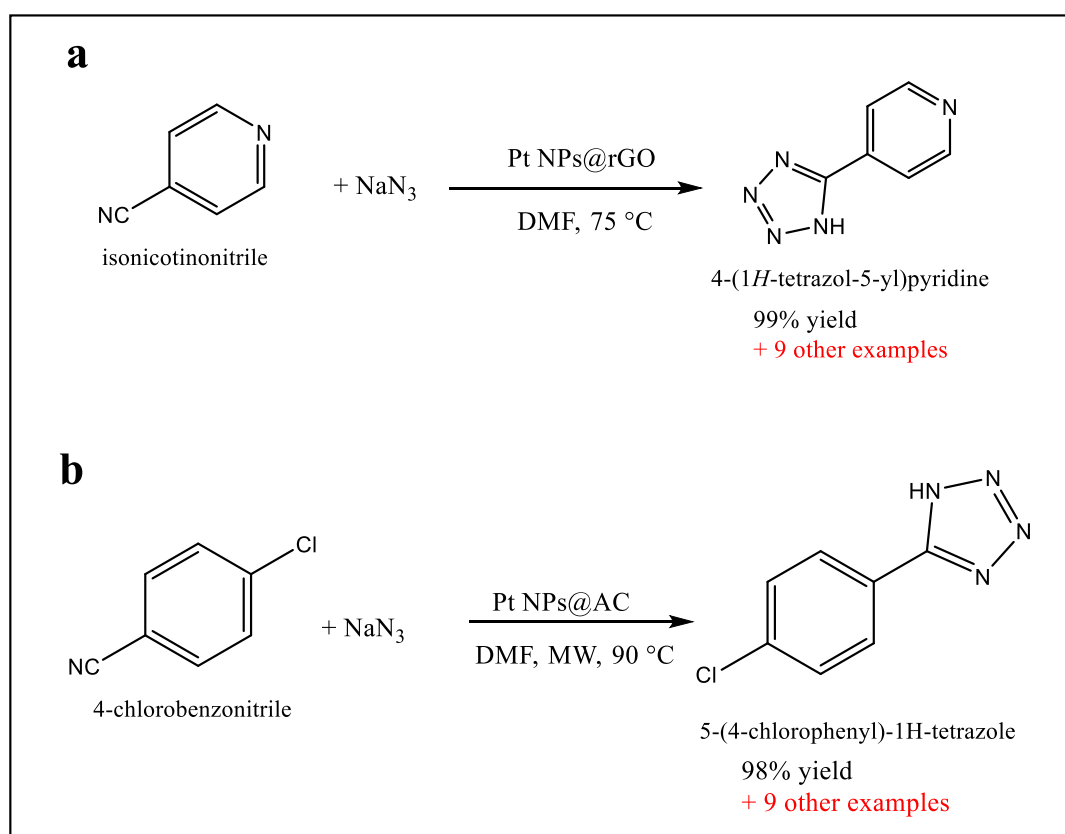
catalyst would not result in a discernible decrease in its capacity to catalyze (Scheme 13). Excellent yields (60–99%) of the 1H-tetrazoles with five substituents were achieved; the greatest yield was produced by 4-bromobenzonitrile.



Scheme 13: NiZrP NPs catalyzed synthesis (85).

4.3.7. Monodisperse platinum (Pt NPs@rGO) NPs
 Tetrazole derivatives were produced in a different method by Kaya, Sen, and associates (55). Applying two techniques, the first Using sodium azide, a heterogeneous catalyst known as monodisperse platinum NPs supported by reduced graphene oxide (Pt NPs@rGO) was employed to perform [3+2] cycloaddition on a variety of benzonitriles (55). 5-aryl- and 5-heteroaryl-1H-tetrazoles were generated in good yields (87–99%) in a short reaction time

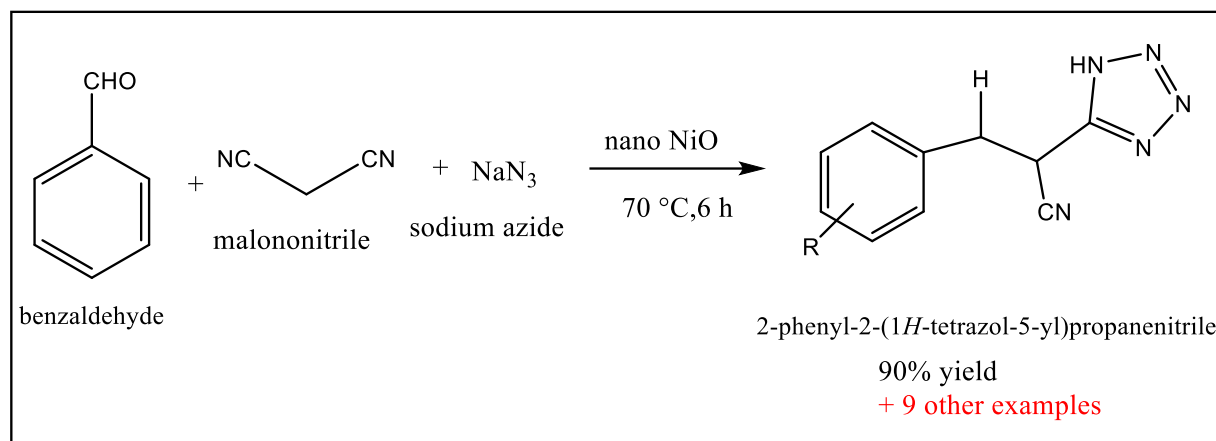
(0.4–5 hours) (Scheme 14a). Up to six times could be retrieved and utilized again without significantly reducing the catalyst's catalytic activity. Second, they prepared another product The subsequent Tetrazoles (5-aryl and 5-heteroaryl-1H) were synthesized with excellent yields (89–99%). Using a brief reaction time (90 °C, 140 W, constant mode, 10–30 minutes) and microwave irradiation in DMF to monodisperse platinum NPs coated on activated carbon (Pt NPs@AC) (Scheme 14.b) (86).



Scheme 14: (a) Synthesis catalyzed by Pt NPs@rGO (55). (b) Pt NPs@AC catalyzed synthesis (86).

4.3.8. Nickel oxide (NiO) NPs
 Nickel oxide is one of the latest NP catalysts with unique properties that are widely used in many fields, Safaei-Ghomi J. and Paymard-Samani S. (87) by

using a Domino Knoevenagel condensation method to react aldehyde, sodium azide, and malononitrile in DMF for six hours at 70 °C while a nano nickel oxide catalyst was present (Scheme 15).



This table details the conditions, kinds, and quantities of NPs utilized, together with the number of items developed by multiple researchers.

While some have just replicated the work of their forebears with variations in solvent, temperature, NP type, and methodology, others have performed exceptionally well and generated compelling results (Table 2).

Table 2: The conditions and types of NPs used and the amount of products worked on by several researchers.

Entry	Reaction Condition: (T) °C, Time, and reflux	Solvent and yield	Type nanocatalysts	Ref
	110 °C, -, -	DMF, (83-97%)	Fe ₃ O ₄ @SiO ₂ /Schiff base/Cu(II)	(88)
	120 °C, 12 h, -	DMF, (92%)	CuFe ₂ O ₄ NPs	(89)
	140 °C, -, -	DMF, (94%)	Cu-MCM-41 NPs	(56)
	-, reflux, 2 h	DMF, (78-95%)	nano-TiCl ₄ ·SiO ₂	(90)
	110 °C, 15-120 min, -	([bmim]N ₃), (70-98%)	Fe ₃ O ₄ @chitin	(91)
	120 °C, various, -	(PEG), (60-98%)	Immobilization of Cu(II) on Fe ₃ O ₄ @SiO ₂ @L-arginine	(92)
	-, -, reflux	H ₂ O/i-PrOH (1:1), (75-94%)	Cu/AC/r-GO nanohybrid	(93)
	130 °C, -, -	PEG-400, (up to 95%)	Cu(II)-Adenine-MCM-41	(94)
	-, -, reflux	H ₂ O, (96%)	Fe ₃ O ₄ @SiO ₂ -TCT-PVA-Cu(II)	(95)
	120 °C, -, -	PEG-400, (up to 95%)	Pd-SMTU@boehmite	(96)

The following nanocatalysts are employed in the manufacture of tetrazole: (Fe₃O₄ NPs (81), AMWCNTs-O-Cu(II)-PhTPY (82), Fe₃O₄@SiO₂ (83), Ag NPs (72), Au NPs (84), NiZrP (85), Pt NPs@rGO (55), nano-NiO (87), etc). Nitriles and sodium azide undergo [3+2] cycloaddition to complete these syntheses. The utilization of green nanocatalysts in the manufacturing of heterocycles with a specific reaction time, low chemical consumption, high yield, and ease of operation are all advantageous. In most processes, the utilized catalyst may be readily extracted from the reaction mixture and recovered without losing its catalytic activity. Nitriles and sodium azide undergo [3+2] cycloaddition to complete these syntheses. The use of green nanocatalysts in the manufacturing of heterocycles with a specific reaction time, low chemical consumption, high yield, and ease of operation are all advantageous. In most processes, the utilized catalyst may be readily extracted and retrieved without losing its catalytic function from the reaction mixture.

To summarize, the utilization of nanocatalysts in synthesis offers a means of attaining more effective, focused, and environmentally friendly chemical reactions, which has implications for both lab-based studies and commercial uses. Scholars persistently investigate and create novel nanocatalysts to tackle certain synthetic chemistry problems.

5. BIOLOGICAL APPLICATIONS OF TETRAZOLE DERIVATIVES

Tetrazoles are a family of synthetic heterocyclic compounds made up of 2 hydrogen atoms, a single atom of carbon, and 4 nitrogen atoms arranged in a five-member ring (Figure 4). Tetrazole's chemical formula is CN₄H₂. Tetrazole is a crystalline solid that is white to pale yellow in color, soluble in alcohol or water, and has a faint, distinctive smell. It has an acidic nature since it contains four nitrogen atoms (97).

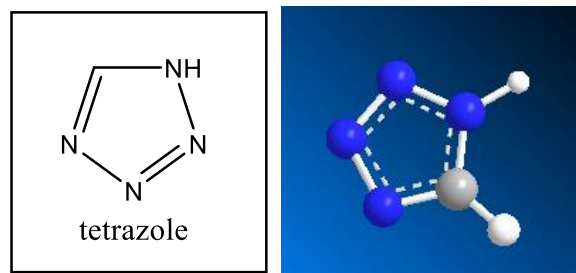


Figure 4: Tetrazole structure.

Numerous uses for tetrazole chemistry are emerging in the domains of biochemistry, medicine, and agriculture (98). The literature has discussed the chemistry of tetrazole derivatives and their medical uses (61). Tetrazole's distinct structure has piqued the curiosity of many in the field of medical chemistry, as have its derivatives. The main reason the tetrazole moiety is important is that it can act as a bioisostere of the carboxylic acid group in supramolecular and pharmaceutical chemistry. Above all, tetrazoles are highly versatile ligands that readily conform to various binding modes.

Derivatives of tetrazole demonstrated antibacterial (99), antifungal (100), anticancer (101), analgesic (102), anti-inflammatory (103), antidiabetic, antihyperlipidemic (104), and antitubercular activities (105). The US FDA has approved a large number of compounds with a tetrazole moiety that are significant for medicine (106). Many studies have been done on the use of tetrazole derivatives in biology, several of which are presented in (Table 3).

Table 3: Some works using Tetrazole derivatives.

Entry	Biological applications	Ref
1.	Antibacterial	(99)
2.	Antifungal	(100)
3.	Anticancer	(101)
4.	Analgesic	(102)
5.	Anti-inflammatory	(103)
6.	Antidiabetic, Antihyperlipidemic	(104)
7.	antitubercular activities	(105)
8.	Anticancer Activity	(120)
9.	Anticonvulsant Activity	(121)

5.1. Anticancer Activity

Numerous research institutions have investigated low-toxicity broad-spectrum medicinal methods (107). They make it rather evident that it can be advantageous if one chemical simultaneously blocks several important pathways and processes (multitherapy). Since patient tumors need to be analyzed for certain mutations to assign patients to the appropriate therapy, many of these treatments can only be loosely referred to as individualized. When considering individual biological variation as a whole, certain mutations only account for the slightest amount of personalization. A far more thorough evaluation of genetic and even lifestyle factors, such as dietary choices, exercise routines, and biobehavioral (stress management) techniques, can be seen in truly customized therapy approaches, along with additional host characteristics including immunological condition and inflammation. The methodical practice of integrative medicine, which was crucial in the creation of this broad-spectrum cancer therapy concept, embodies this kind of

personalized treatment (108,109). Two of the actions taken: A variety of steroidal tetrazole derivatives were synthesized by Shamsuzzaman et al. (2014) using a simple technique in two steps. The MTT assay method was used to examine the synthesized compounds' antiproliferative ability in vitro against cervical cancer (HeLa), myeloid leukemia (KCL-22), breast cancer (MDA-MBA-231), and normal cell lines. It was discovered that the class one molecule exhibited significant action ($IC_{50} > 60$ M) against the three human cancer cell lines while being innocuous to the normal cell lines (110). The MCF-7, MDA-MB-231, and ZR-75 cell lines were employed to test a range of novel substituted tetrazole derivatives that were synthesized by Arshad et al. (2014) (111).

Bhaskar et al. produced a novel class of tetrazole derivatives (2010). With a growth percent of 34–94, compound in (Figure 5) was discovered to be the most effective and potent anticancer drug against ovarian cancer cell lines, SK-OV-3 (112).

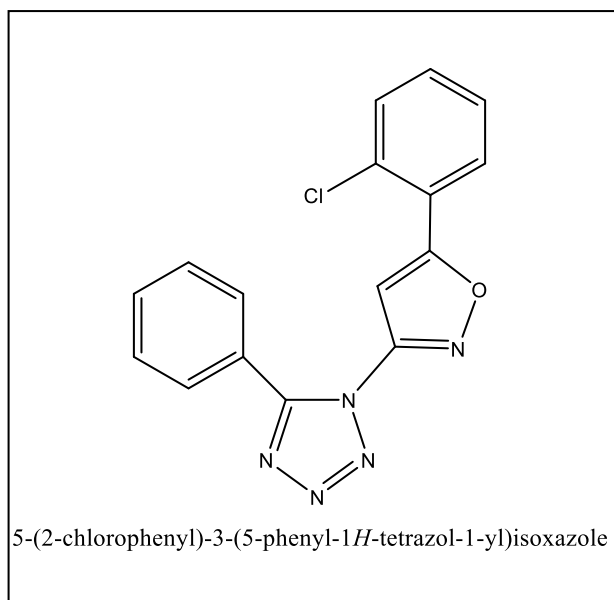


Figure 5: Tetrazole derivative.

5.2. Antimicrobial Activity

Arora et al. (2004) synthesized numerous triazole derivatives using a 5-substituted tetrazole and evaluated their antifungal activity against *Candida* spp. in vitro, *Cryptococcus neoformans*, and *Aspergillus* spp. It has been determined that compound (1) (Figure 6) is a crucial structural

element of antifungal efficacy (113). A novel class of substituted-3-mercapto-1, 2, 4-triazoles was synthesized and assessed as an antifungal agent by Collin et al. (2003). Compound (2) (Figure 6) shows significant efficacy in inhibiting *Candida tropicalis* and *Candida albicans* (114). Many others have worked, but we have mentioned only these two.

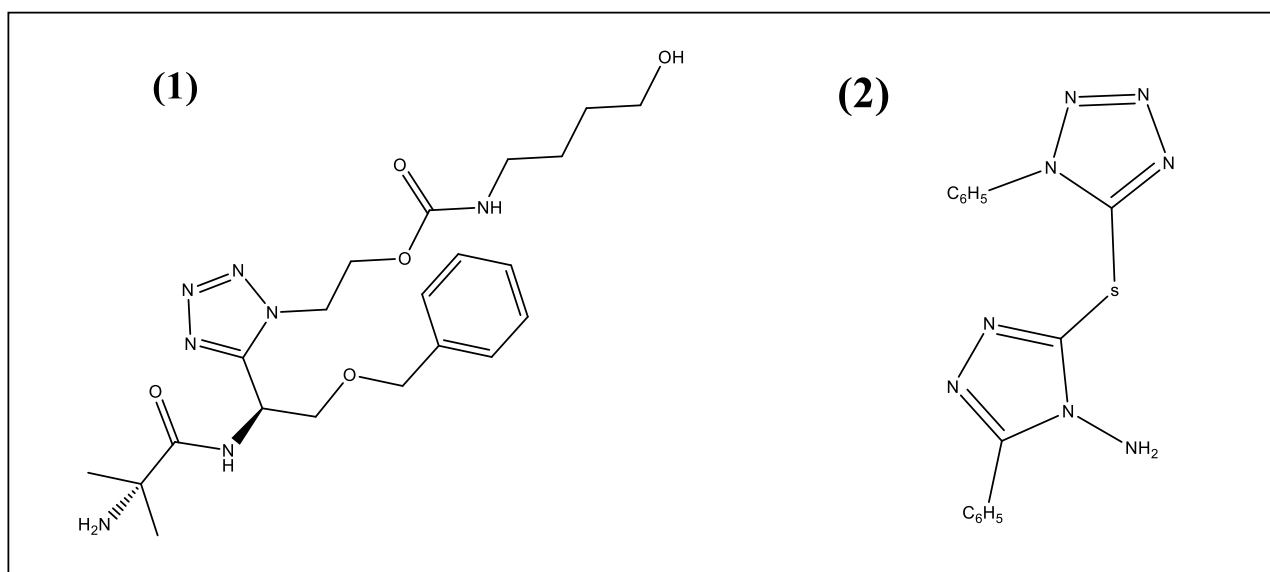


Figure 6: Compounds (1) and (2).

5.3. Antioxidant Activity

Elmegeed et al. (2011) produced a novel family of derivatives of indolyl tetrazolopropanoic acid. (Figure 7.a) had been discovered to possess antioxidant qualities that could be effective against oxidative stress brought on by ACR treatment (115).

A unique series of 3-substituted-5-(1-phenyl-1H-tetrazole-5-yl) methyl)benzene-1,2-diol was synthesized by Adibi et al. (2011). Using the 1,1-diphenyl-2-picrylhydrazyl (DPPH) radical scavenging and reducing power test method, the antioxidant activity was carried out. Of the molecules that were produced, (Figure 7.b) demonstrated a higher level of antioxidant activity (116).

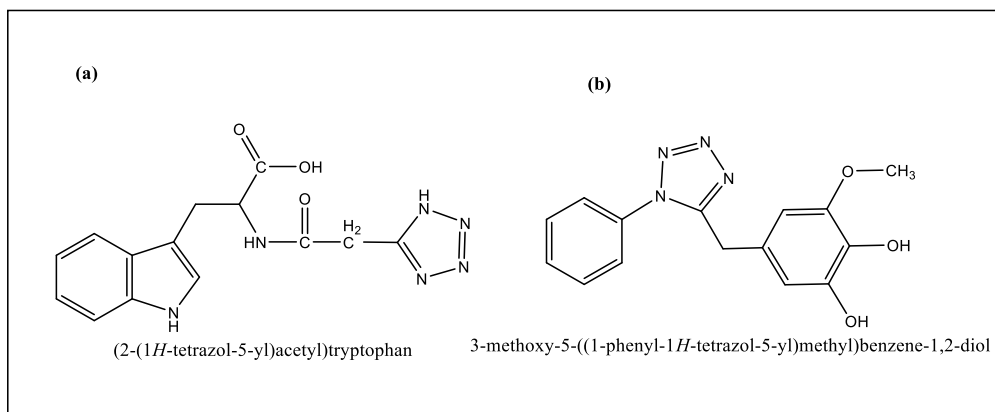


Figure 7: (a) 2-(1H-tetrazol-5-yl)acetyltryptophan, (b) 3-methoxy-5-((1-phenyl-1H-tetrazol-5-yl)methyl)benzene-1,2-diol.

5.4. Anti-diabetic Activity

Gao et al. (2010) synthesized tetrazole (117) using N-glycosides as SGLT2 inhibitors and tested the drug's hypoglycemic effects in vivo on mice using the oral glucose tolerance test (OGTT). The most potent molecule against the common drug dapagliflozin was found to be one particular one. Nicolaou and colleagues employed pyrrolyl-tetrazole derivative as

a nonclassical bioisostere of a carboxylic acid moiety. (2010) created a novel series of compounds and assessed their ability to inhibit aldose reductase in vitro. The observations suggest that a compound exhibited strong antioxidant action, and the isomers of pyrrolyl-tetrazole were putative starting points for the synthesis of drugs of selective aldose reductase. See the (Figure 8).

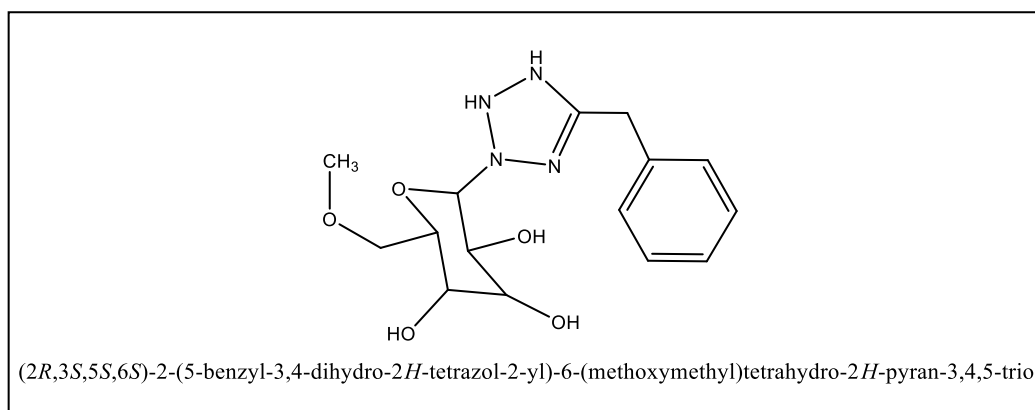


Figure 8: Tetrazole derivative.

5.5. Anti-HIV Activity

Uraglian et al. (2006) developed a novel family of aryltetrazolylacetanilides and assessed them as HIV-1 non-nucleoside reverse transcriptase inhibitors using the therapeutically relevant K103N mutant strain (118). 5-(phosphonomethyl)-1H-tetrazole was

created by Hutchinson et al. (1985), who then assessed its effectiveness against the Herpes Simplex Viruses-1 replication, DNA polymerase inhibitor action, and virus of influenza type A RNA transcriptase activity (119). See the compounds in (Figure 9).

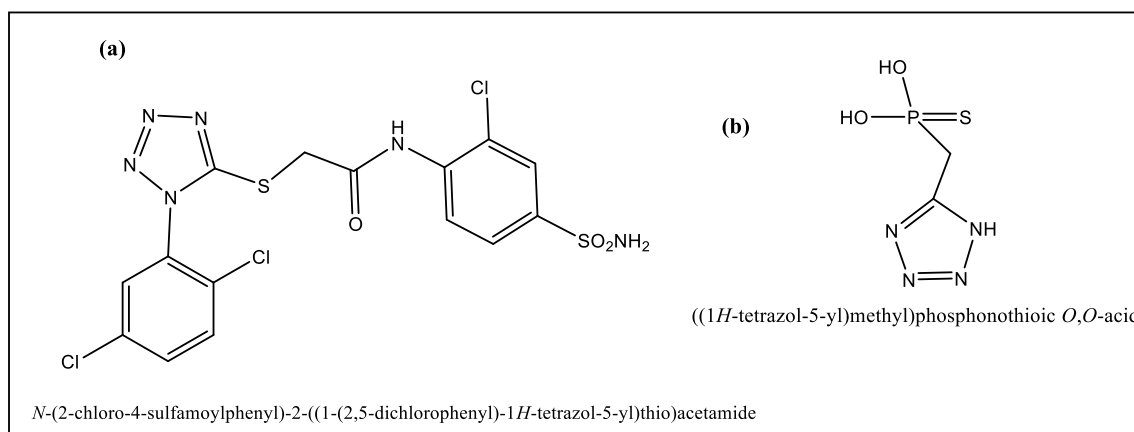


Figure 9: Anti-HIV tetrazole derivatives compounds.

6. CONCLUSION

Tetrazoles are important heterocyclic analogs found in many different chemical and pharmaceutical substances. Following the synthesis and analysis of each of these studies on the tetrazole derivative preparation. Although there are many ways to synthesize these tetrazoles, a green synthetic method is quite effective. Particles with a distinct view of the boundary of something at the nanoscale are known as NPs, and they are less than 100 nm by at least one magnitude. Using nanocatalysts is one of the most popular green synthesis methods for producing tetrazole derivatives. Nitrides and sodium azide undergo [3+2] cycloaddition to complete these syntheses. The utilization of green nanocatalysts in the manufacturing of heterocycles with a specific reaction type, high yield, quick reaction time, little chemical consumption, and ease of operation are all benefits. In the majority of operations, the utilized catalyst may be readily removed and repurposed without losing its catalytic activity from the reaction mixture.

Tetrazole and its derivatives, belonging to the nitrogen-containing heterocycle family, have a wide range of biological actions, including antibacterial, antifungal, anticancer, analgesic, anti-inflammatory, antidiabetic, anti-hyperlipidemic, and antitubercular effects. This review discusses the biological relevance, uses, and distinctive qualities of tetrazole. The many synthesis methods and varied biological activities of substituted tetrazole derivatives are reviewed in this inquiry. This study aimed to gather the literature work offered by researchers on tetrazole for their diverse biological actions, in addition to reporting on current efforts done in this area.

7. REFERENCES

- Butler RN, Fox A, Collier S, Burke LA. Pentazole chemistry: The mechanism of the reaction of aryldiazonium chlorides with azide ion at $-80\text{ }^{\circ}\text{C}$: Concerted versus stepwise formation of arylpentazoles, detection of a pentazene intermediate, a combined 1H and 15N NMR experimental and ab initio theoretical study. *J Chem Soc Perkin Trans 2* [Internet]. 1998 Jan 1;1998(10):2243–8. Available from: [<URL>](#).
- Jursic BS, Leblanc BW. Preparation of tetrazoles from organic nitriles and sodium azide in micellar media. *J Heterocycl Chem* [Internet]. 1998 Mar 11;35(2):405–8. Available from: [<URL>](#).
- Izsák D, Klapötke TM, Lutter FH, Pflüger C. Tailoring the energetic properties of 5-(5-Amino-1,2,3-triazol-4-yl)tetrazole and its derivatives by salt formation: from sensitive primary to insensitive secondary explosives. *Eur J Inorg Chem* [Internet]. 2016 Apr 18;2016(11):1720–9. Available from: [<URL>](#).
- Singh H, Singh Chawla A, Kapoor VK, Paul D, Malhotra RK. Medicinal chemistry of tetrazoles. In:

- Progress in Medicinal Chemistry* [Internet]. Elsevier; 1980. p. 151–83. Available from: [<URL>](#).
- Okabayashi T, Kano H, Makisumi Y. Action of substituted azaindolizines on microorganisms. I. action on lactic acid bacteria. *Chem Pharm Bull* [Internet]. 1960 Feb 25;8(2):157–62. Available from: [<URL>](#).
- Sangal SK, Kumar A. Synthesis of some new antifungal tetrazolyl sulfides. *J. Ind. Chem. Soc.* 1986; 63; 351–3.
- Witkowski JT, Robins RK, Sidwell RW, Simon LN. Design, synthesis, and broad spectrum antiviral activity of 1- β -D-ribofuranosyl-1,2,4-triazole-3-carboxamide and related nucleosides. *J Med Chem* [Internet]. 1972 Nov 1;15(11):1150–4. Available from: [<URL>](#).
- Stewart KD, Loren S, Frey L, Otis E, Klinghofer V, Hulkower KI. Discovery of a new cyclooxygenase-2 lead compound through 3-D database searching and combinatorial chemistry. *Bioorg Med Chem Lett* [Internet]. 1998 Mar 3;8(5):529–34. Available from: [<URL>](#).
- Ray SM, Lahiri SC. Studies on 5-(Indan-1'-yl) tetrazoles as potential non-steroidal antiinflammatory agents. *ChemInform.* 1990;21(46).
- Goodman RP, Schaap IAT, Tardin CF, Erben CM, Berry RM, Schmidt CF, et al. Rapid chiral assembly of rigid DNA building blocks for molecular nanofabrication. *Science* [Internet]. 2005 Dec 9;310(5754):1661–5. Available from: [<URL>](#).
- Regan BC, Aloni S, Jensen K, Ritchie RO, Zettl A. Nanocrystal-powered nanomotor. *Nano Lett* [Internet]. 2005 Sep 1;5(9):1730–3. Available from: [<URL>](#).
- Grunes J, Zhu J, Somorjai GA. Catalysis and nanoscience. *Chem Commun* [Internet]. 2003 Sep 2;3(18):2257–60. Available from: [<URL>](#).
- Somorjai GA, McCreary K. Roadmap for catalysis science in the 21st century: A personal view of building the future on past and present accomplishments. *Appl Catal A Gen* [Internet]. 2001 Dec 20;222(1–2):3–18. Available from: [<URL>](#).
- Roy A, Bharadvaja N. Silver nanoparticle synthesis from *Plumbago zeylanica* and its dye degradation activity. *Bioinspired, Biomim Nanobiomaterials* [Internet]. 2019 Jun 1;8(2):130–40. Available from: [<URL>](#).
- Nacci A, Cioffi N. Nano-catalysts and nanotechnologies for green organic synthesis. *Molecules* [Internet]. 2011 Feb 9;16(2):1452–3. Available from: [<URL>](#).
- Patil A, Mishra V, Thakur S, Riyaz B, Kaur A, Khursheed R, et al. Nanotechnology derived nanotools in biomedical perspectives: An update. *Curr Nanosci* [Internet]. 2019 Apr 26;15(2):137–46. Available from: [<URL>](#).

17. Jeevanandam J, Barhoum A, Chan YS, Dufresne A, Danquah MK. Review on nanoparticles and nanostructured materials: History, sources, toxicity and regulations. *Beilstein J Nanotechnol* [Internet]. 2018 Apr 3;9(1):1050–74. Available from: [<URL>](#).
18. Tan YY, Yap PK, Xin Lim GL, Mehta M, Chan Y, Ng SW, et al. Perspectives and advancements in the design of nanomaterials for targeted cancer theranostics. *Chem Biol Interact* [Internet]. 2020 Sep 25;329:109221. Available from: [<URL>](#).
19. Senanayake SD, Stacchiola D, Rodriguez JA. Unique properties of ceria nanoparticles supported on metals: Novel inverse ceria/copper catalysts for CO oxidation and the water-gas shift reaction. *Acc Chem Res* [Internet]. 2013 Aug 20;46(8):1702–11. Available from: [<URL>](#).
20. Zahin N, Anwar R, Tewari D, Kabir MT, Sajid A, Mathew B, et al. Nanoparticles and its biomedical applications in health and diseases: Special focus on drug delivery. *Environ Sci Pollut Res* [Internet]. 2020 Jun 11;27(16):19151–68. Available from: [<URL>](#).
21. C. Thomas S, Harshita, Kumar Mishra P, Talegaonkar S. Ceramic nanoparticles: Fabrication methods and applications in drug delivery. *Curr Pharm Desig* [Internet]. 2015;21(42):6165–88. Available from: [<URL>](#).
22. Chaudhary RG, Bhusari GS, Tiple AD, Rai AR, Somkuvar SR, Potbhare AK, et al. Metal/metal oxide nanoparticles: Toxicity, applications, and future prospects. *Curr Pharm Des* [Internet]. 2019 Dec 17;25(37):4013–29. Available from: [<URL>](#).
23. Loomba L, Scarabelli T. Metallic nanoparticles and their medicinal potential. Part II: Aluminosilicates, nanobiomagnets, quantum dots and cochleates. *Ther Deliv* [Internet]. 2013 Sep 11;4(9):1179–96. Available from: [<URL>](#).
24. Mishra V, Bansal KK, Verma A, Yadav N, Thakur S, Sudhakar K, et al. Solid lipid nanoparticles: Emerging colloidal nano drug delivery systems. *Pharmaceutics* [Internet]. 2018 Oct 18;10(4):191. Available from: [<URL>](#).
25. Puente Santiago AR, Fernandez-Delgado O, Gomez A, Ahsan MA, Echegoyen L. Fullerenes as key components for low-dimensional (photo)electrocatalytic nanohybrid materials. *Angew Chem Int Ed* [Internet]. 2021 Jan 4;60(1):122–41. Available from: [<URL>](#).
26. Tajzad I, Ghasali E. Production methods of CNT-reinforced al matrix composites: A review. *J Compos Compd* [Internet]. 2020 Feb 1;2(1):1–9. Available from: [<URL>](#).
27. Candelaria SL, Shao Y, Zhou W, Li X, Xiao J, Zhang JG, et al. Nanostructured carbon for energy storage and conversion. *Nano Energy* [Internet]. 2012 Mar 1;1(2):195–220. Available from: [<URL>](#).
28. Yan K, Chen A. Efficient hydrogenation of biomass-derived furfural and levulinic acid on the facilely synthesized noble-metal-free Cu–Cr catalyst. *Energy* [Internet]. 2013 Sep 1;58:357–63. Available from: [<URL>](#).
29. Choudary BM, Mulukutla RS, Klabunde KJ. Benzylolation of aromatic compounds with different crystallites of MgO. *J Am Chem Soc* [Internet]. 2003 Feb 1;125(8):2020–1. Available from: [<URL>](#).
30. Kreibig U, Vollmer M. Optical properties of metal clusters [Internet]. Berlin, Heidelberg: Springer Berlin Heidelberg; 1995. (Springer Series in Materials Science; vol. 25). Available from: [<URL>](#).
31. Liz-Marzán LM. Tailoring surface plasmons through the morphology and assembly of metal nanoparticles. *Langmuir* [Internet]. 2006 Jan 1;22(1):32–41. Available from: [<URL>](#).
32. Tao AR, Habas S, Yang P. Shape control of colloidal metal nanocrystals. *Small* [Internet]. 2008 Mar 3;4(3):310–25. Available from: [<URL>](#).
33. Toshima N, Yonezawa T. Bimetallic nanoparticles—novel materials for chemical and physical applications. *New J Chem* [Internet]. 1998 Jan 1;22(11):1179–201. Available from: [<URL>](#).
34. Gladysz JA. Recoverable catalysts. Ultimate goals, criteria of evaluation, and the green chemistry interface. *Pure Appl Chem* [Internet]. 2001 Aug 1;73(8):1319–24. Available from: [<URL>](#).
35. Sharma N, Ojha H, Bharadwaj A, Pathak DP, Sharma RK. Preparation and catalytic applications of nanomaterials: A review. *RSC Adv* [Internet]. 2015 Jun 15;5(66):53381–403. Available from: [<URL>](#).
36. Kajbafvala A, Ghorbani H, Paravar A, Samberg JP, Kajbafvala E, Sadrnezhaad SK. Effects of morphology on photocatalytic performance of Zinc oxide nanostructures synthesized by rapid microwave irradiation methods. *Superlattices Microstruct* [Internet]. 2012 Apr 1;51(4):512–22. Available from: [<URL>](#).
37. Mazloumi M, Shahcheraghi N, Kajbafvala A, Zanganeh S, Lak A, Mohajerani MS, et al. 3D bundles of self-assembled lanthanum hydroxide nanorods via a rapid microwave-assisted route. *J Alloys Compd* [Internet]. 2009 Apr 3;473(1–2):283–7. Available from: [<URL>](#).
38. Bayati MR, Molaei R, Kajbafvala A, Zanganeh S, Zargar HR, Janghorban K. Investigation on hydrophilicity of micro-arc oxidized TiO₂ nano/microporous layers. *Electrochim Acta* [Internet]. 2010 Aug 1;55(20):5786–92. Available from: [<URL>](#).
39. Kajbafvala A, Samberg JP, Ghorbani H, Kajbafvala E, Sadrnezhaad SK. Effects of initial precursor and microwave irradiation on step-by-step synthesis of zinc oxide nano-architectures. *Mater Lett* [Internet]. 2012 Jan 15;67(1):342–5. Available from: [<URL>](#).
40. Zanganeh S, Kajbafvala A, Zanganeh N, Molaei R, Bayati MR, Zargar HR, et al. Hydrothermal synthesis and characterization of TiO₂ nanostructures using LiOH as a solvent. *Adv Powder Technol*

- [Internet]. 2011 May 1;22(3):336–9. Available from: [<URL>](#).
41. Wittenberger SJ. Recent developments in tetrazole chemistry. A review. *Org Prep Proced Int* [Internet]. 1994 Oct;26(5):499–531. Available from: [<URL>](#).
42. Patani GA, LaVoie EJ. Bioisosterism: A rational approach in drug design. *Chem Rev* [Internet]. 1996 Jan 1;96(8):3147–76. Available from: [<URL>](#).
43. Mittal R, Awasthi SK. Recent advances in the synthesis of 5-substituted 1H-tetrazoles: A complete survey (2013–2018). *Synthesis* [Internet]. 2019 Oct 1;51(20):3765–83. Available from: [<URL>](#).
44. Liljebriis C, Larsen SD, Ogg D, Palazuk BJ, Bleasdale JE. Investigation of potential bioisosteric replacements for the carboxyl groups of peptidomimetic inhibitors of protein tyrosine phosphatase 1B: Identification of a tetrazole-containing inhibitor with cellular activity. *J Med Chem* [Internet]. 2002 Apr 1;45(9):1785–98. Available from: [<URL>](#).
45. Herr RJ. 5-Substituted-1H-tetrazoles as carboxylic acid isosteres: Medicinal chemistry and synthetic methods. *Bioorg Med Chem* [Internet]. 2002 Nov 1;10(11):3379–93. Available from: [<URL>](#).
46. Kraus JL. Isosterism and molecular modification in drug design: Tetrazole analogue of GABA: Effects on enzymes of the γ -aminobutyrate system. *Pharmacol Res Commun* [Internet]. 1983 Feb 1;15(2):183–9. Available from: [<URL>](#).
47. Roh J, Vávrová K, Hrabálek A. Synthesis and functionalization of 5-substituted tetrazoles. *European J Org Chem* [Internet]. 2012 Nov 8;2012(31):6101–18. Available from: [<URL>](#).
48. Alterman M, Hallberg A. Fast microwave-assisted preparation of aryl and vinyl nitriles and the corresponding tetrazoles from organo-halides. *J Org Chem* [Internet]. 2000 Nov 1;65(23):7984–9. Available from: [<URL>](#).
49. Fürmeier S, Metzger JO. Synthesis of new heterocyclic fatty compounds. *European J Org Chem* [Internet]. 2003 Mar 11;2003(5):885–93. Available from: [<URL>](#).
50. Gutmann B, Roduit J, Roberge D, Kappe CO. Synthesis of 5-substituted 1H-tetrazoles from nitriles and hydrazoic acid by using a safe and scalable high-temperature microreactor approach. *Angew Chemie Int Ed* [Internet]. 2010 Sep 17;49(39):7101–5. Available from: [<URL>](#).
51. Amantini D, Beleggia R, Fringuelli F, Pizzo F, Vaccaro L. TBAF-catalyzed synthesis of 5-substituted 1H-tetrazoles under solventless conditions. *J Org Chem* [Internet]. 2004 Apr 1;69(8):2896–8. Available from: [<URL>](#).
52. Myznikov L V., Roh J, Artamonova T V., Hrabalek A, Koldobskii GI. Tetrazoles: LI. Synthesis of 5-substituted tetrazoles under microwave activation. *Russ J Org Chem* [Internet]. 2007 May;43(5):765–7. Available from: [<URL>](#).
53. Sajjadi M, Nasrollahzadeh M, Ghafuri H, Baran T, Orooji Y, Baran NY, et al. Modified chitosan-zeolite supported Pd nanoparticles: A reusable catalyst for the synthesis of 5-substituted-1H-tetrazoles from aryl halides. *Int J Biol Macromol* [Internet]. 2022 Jun 1;209:1573–85. Available from: [<URL>](#).
54. Himo F, Demko ZP, Noodleman L, Sharpless KB. Mechanisms of tetrazole formation by addition of azide to nitriles. *J Am Chem Soc* [Internet]. 2002 Oct 1;124(41):12210–6. Available from: [<URL>](#).
55. Esirden İ, Erken E, Kaya M, Sen F. Monodisperse Pt NPs@rGO as highly efficient and reusable heterogeneous catalysts for the synthesis of 5-substituted 1H-tetrazole derivatives. *Catal Sci Technol* [Internet]. 2015 Aug 17;5(9):4452–7. Available from: [<URL>](#).
56. Abdollahi-Alibeik M, Moaddeli A. Multi-component one-pot reaction of aldehyde, hydroxylamine and sodium azide catalyzed by Cu-MCM-41 nanoparticles: A novel method for the synthesis of 5-substituted 1H-tetrazole derivatives. *New J Chem* [Internet]. 2015 Mar 5;39(3):2116–22. Available from: [<URL>](#).
57. Kumar A, Kumar S, Khajuria Y, Awasthi SK. A comparative study between heterogeneous stannous chloride loaded silica nanoparticles and a homogeneous stannous chloride catalyst in the synthesis of 5-substituted 1H-tetrazole. *RSC Adv* [Internet]. 2016 Aug 8;6(79):75227–33. Available from: [<URL>](#).
58. Nasrollahzadeh M, Nezafat Z, Bidgoli NSS, Shafiei N. Use of tetrazoles in catalysis and energetic applications: Recent developments. *Mol Catal* [Internet]. 2021 Aug 1;513:111788. Available from: [<URL>](#).
59. Razavi N, Akhlaghinia B. Cu(ii) immobilized on aminated epichlorohydrin activated silica (CAES): as a new, green and efficient nanocatalyst for preparation of 5-substituted-1H-tetrazoles. *RSC Adv* [Internet]. 2015 Jan 20;5(16):12372–81. Available from: [<URL>](#).
60. Yıldız Y, Esirden İ, Erken E, Demir E, Kaya M, Şen F. Microwave (Mw)-assisted synthesis of 5-substituted 1H-tetrazoles via [3+2] cycloaddition catalyzed by Mw-Pd/Co nanoparticles decorated on multi-walled carbon nanotubes. *ChemistrySelect* [Internet]. 2016 Jun 9;1(8):1695–701. Available from: [<URL>](#).
61. Benson FR. The chemistry of the tetrazoles. *Chem Rev* [Internet]. 1947 Aug 1;41(1):1–61. Available from: [<URL>](#).
62. Hantzsch A, Vagt A. Ueber das sogenannte diazoguanidin. *Justus Liebigs Ann Chem* [Internet]. 1901 Jan 24;314(3):339–69. Available from: [<URL>](#).

63. Mihina JS, Herbst RM. The reaction of nitriles with hydrazoic acid: Synthesis of monosubstituted tetrazoles. *J Org Chem* [Internet]. 1950 Sep 1;15(5):1082–92. Available from: [<URL>](#).
64. Herbst RM, Wilson KR. Apparent acidic dissociation of some 5-aryltetrazoles 1. *J Org Chem* [Internet]. 1957 Oct 1;22(10):1142–5. Available from: [<URL>](#).
65. Finnegan WG, Henry RA, Lofquist R. An improved synthesis of 5-substituted tetrazoles. *J Am Chem Soc* [Internet]. 1958 Aug 1;80(15):3908–11. Available from: [<URL>](#).
66. Kumar A, Narayanan R, Shechter H. Rearrangement reactions of (hydroxyphenyl) carbenes. *J Org Chem* [Internet]. 1996 Jan 1;61(13):4462–5. Available from: [<URL>](#).
67. Demko ZP, Sharpless KB. Preparation of 5-substituted 1*H*-tetrazoles from nitriles in water. *J Org Chem* [Internet]. 2001 Nov 1;66(24):7945–50. Available from: [<URL>](#).
68. Lakshmi Kantam M, Kumar KBS, Sridhar C. Nanocrystalline ZnO as an efficient heterogeneous catalyst for the synthesis of 5-substituted 1*H*-tetrazoles. *Adv Synth Catal* [Internet]. 2005 Jul 19;347(9):1212–4. Available from: [<URL>](#).
69. Kumar A, Ramani T, Sreedhar B. Magnetically separable CuFe₂O₄ nanoparticles in PEG: A recyclable catalytic system for the amination of aryl iodides. *Synlett*. 2013;24(8):938–42.
70. Rama V, Kanagaraj K, Pitchumani K. Syntheses of 5-substituted 1*H*-tetrazoles catalyzed by reusable CoY zeolite. *J Org Chem* [Internet]. 2011 Nov 4;76(21):9090–5. Available from: [<URL>](#).
71. Dehghani F, Sardarian AR, Esmailpour M. Salen complex of Cu(II) supported on superparamagnetic Fe₃O₄@SiO₂ nanoparticles: An efficient and recyclable catalyst for synthesis of 1- and 5-substituted 1*H*-tetrazoles. *J Organomet Chem* [Internet]. 2013 Oct 15;743:87–96. Available from: [<URL>](#).
72. Mani P, Sharma C, Kumar S, Awasthi SK. Efficient heterogeneous silver nanoparticles catalyzed one-pot synthesis of 5-substituted 1*H*-tetrazoles. *J Mol Catal A Chem* [Internet]. 2014 Oct 1;392:150–6. Available from: [<URL>](#).
73. Dallinger D, Kappe CO. Microwave-assisted synthesis in water as solvent. *Chem Rev* [Internet]. 2007 Jun 1;107(6):2563–91. Available from: [<URL>](#).
74. de la Hoz A, Loupy A. *Microwaves in organic synthesis* [Internet]. John Wiley & Sons; 2013. Available from: [<URL>](#).
75. Roberts BA, Strauss CR. Toward rapid, “green”, predictable microwave-assisted synthesis. *Acc Chem Res* [Internet]. 2005 Aug 1;38(8):653–61. Available from: [<URL>](#).
76. Yoneyama H, Usami Y, Komeda S, Harusawa S. Efficient transformation of inactive nitriles into 5-substituted 1*H*-tetrazoles using microwave irradiation and their applications. *Synthesis* [Internet]. 2013;45(8):1051–9. Available from: [<URL>](#).
77. Shelkar R, Singh A, Nagarkar J. Amberlyst-15 catalyzed synthesis of 5-substituted 1-*H*-tetrazole via [3+2] cycloaddition of nitriles and sodium azide. *Tetrahedron Lett* [Internet]. 2013 Jan 2;54(1):106–9. Available from: [<URL>](#).
78. Sridhar M, Mallu KKR, Jillella R, Godala KR, Beeram CR, Chinthala N. One-step synthesis of 5-substituted 1*H*-tetrazoles from an aldehyde by reaction with acetohydroxamic acid and sodium azide under Bi (OTf)₃ catalysis. *Synthesis* [Internet]. 2013;45(4):507–10. Available from: [<URL>](#).
79. Fazeli A, Oskooie HA, Beheshtiha YS, Heravi MM, Valizadeh H, Bamoharram FF. Heteropolyacid catalyzed click synthesis of 5-substituted 1*H*-tetrazoles from [bmim]N₃ and nitriles under solvent-free conditions. *Monatshefte für Chemie - Chem Mon* [Internet]. 2013 Sep 12;144(9):1407–10. Available from: [<URL>](#).
80. Rekunge DS, Indalkar KS, Chaturbhuj GU. Activated Fuller’s earth as an inexpensive, eco-friendly, efficient catalyst for the synthesis of 5-aryl 1-*H*-tetrazole via [3+2] cycloaddition of nitriles and sodium azide. *Tetrahedron Lett* [Internet]. 2016 Dec 21;57(51):5815–9. Available from: [<URL>](#).
81. Kolo K, Sajadi SM. An efficient synthesis of 5-alkylthio and 5-arylthiotetrazoles using Fe₃O₄ nanoparticles as a magnetically recoverable and reusable catalyst. *Lett Org Chem* [Internet]. 2013;10:688–92. Available from: [<URL>](#).
82. Sharghi H, Ebrahimpourmoghaddam S, Doroodmand MM. Facile synthesis of 5-substituted-1*H*-tetrazoles and 1-substituted-1*H*-tetrazoles catalyzed by recyclable 4'-phenyl-2,2':6',2''-terpyridine copper(II) complex immobilized onto activated multi-walled carbon nanotubes. *J Organomet Chem* [Internet]. 2013 Aug 15;738:41–8. Available from: [<URL>](#).
83. Esmailpour M, Sardarian AR, Firouzabadi H. N-heterocyclic carbene-Pd(II) complex based on theophylline supported on Fe₃O₄@SiO₂ nanoparticles: Highly active, durable and magnetically separable catalyst for green Suzuki-Miyaura and Sonogashira-Hagihara coupling reactions. *J Organomet Chem* [Internet]. 2018 Oct 15;873:22–34. Available from: [<URL>](#).
84. Kumar S, Kumar A, Agarwal A, Awasthi SK. Synthetic application of gold nanoparticles and auric chloride for the synthesis of 5-substituted 1*H*-tetrazoles. *RSC Adv* [Internet]. 2015 Feb 24;5(28):21651–8. Available from: [<URL>](#).
85. Abrishami F, Ebrahimikia M, Rafiee F. Facile synthesis of 5-substituted-1*H*-tetrazoles catalyzed by reusable nickel zirconium phosphate

- nanocatalyst. Iran J Catal [Internet]. 2024 Feb 3;6(3):245–51. Available from: [<URL>](#).
86. Erken E, Esirden İ, Kaya M, Sen F. A rapid and novel method for the synthesis of 5-substituted 1*H*-tetrazole catalyzed by exceptional reusable monodisperse Pt NPs@AC under the microwave irradiation. RSC Adv [Internet]. 2015 Aug 11;5(84):68558–64. Available from: [<URL>](#).
87. Safaei-Ghomi J, Paymard-Samani S. Facile and rapid synthesis of 5-substituted 1*H*-tetrazoles VIA a multicomponent domino reaction using nickel(II) oxide nanoparticles as catalyst. Chem Heterocycl Compd [Internet]. 2015 Feb 6;50(11):1567–74. Available from: [<URL>](#).
88. Esmailpour M, Javidi J, Nowroozi Dodeji F, Mokhtari Abarghoui M. Facile synthesis of 1- and 5-substituted 1*H*-tetrazoles catalyzed by recyclable ligand complex of copper(II) supported on superparamagnetic Fe₃O₄@SiO₂ nanoparticles. J Mol Catal A Chem [Internet]. 2014 Nov 1;393:18–29. Available from: [<URL>](#).
89. Kumar Akula R, S. Adimulam C, Gangaram S, Kengiri R, Banda N, R. Pamulaparthi S. CuFe₂O₄ Nanoparticle mediated method for the synthesis of 5-substituted 1*H*-tetrazoles from (E)-aldoximes. Lett Org Chem [Internet]. 2014 Apr;11(6):440–5. Available from: [<URL>](#).
90. Zamani L, Mirjalili BBF, Zomorodian K, Zomorodian S. Synthesis and characterization of 5-substituted 1*H*-tetrazoles in the presence of nano-TiCl₄.SiO₂. South African J Chem [Internet]. 2015;68:133–7. Available from: [<URL>](#).
91. Zarghani M, Akhlaghinia B. Magnetically separable Fe₃O₄@chitin as an eco-friendly nanocatalyst with high efficiency for green synthesis of 5-substituted-1*H*-tetrazoles under solvent-free conditions. RSC Adv [Internet]. 2016 Mar 29;6(38):31850–60. Available from: [<URL>](#).
92. Ghorbani-Choghamarani A, Shiri L, Azadi G. The first report on the eco-friendly synthesis of 5-substituted 1*H*-tetrazoles in PEG catalyzed by Cu(ii) immobilized on Fe₃O₄@SiO₂@ L-arginine as a novel, recyclable and non-corrosive catalyst. RSC Adv [Internet]. 2016 Apr 4;6(39):32653–60. Available from: [<URL>](#).
93. Soltani Rad MN, Behrouz S, Sadeghi Dehchenari V, Hoseini SJ. Cu/Graphene/Clay nanohybrid: A highly efficient heterogeneous nanocatalyst for synthesis of new 5-substituted-1*H*-tetrazole derivatives tethered to bioactive N -heterocyclic cores. J Heterocycl Chem [Internet]. 2017 Jan 18;54(1):355–65. Available from: [<URL>](#).
94. Nikoorazm M, Ghorbani-Choghamaranai A, Khanmoradi M, Moradi P. Synthesis and characterization of Cu(II)-Adenine-MCM-41 as stable and efficient mesoporous catalyst for the synthesis of 5-substituted 1*H*-tetrazoles and 1*H*-indazolo [1,2-*b*]phthalazine-triones. J Porous Mater [Internet]. 2018 Dec 1;25(6):1831–42. Available from: [<URL>](#).
95. Sardarian AR, Eslahi H, Esmailpour M. Copper(II) Complex supported on Fe₃O₄@SiO₂ coated by polyvinyl alcohol as reusable nanocatalyst in N -arylation of amines and N(H) - heterocycles and green synthesis of 1*H*-tetrazoles. ChemistrySelect [Internet]. 2018 Feb 7;3(5):1499–511. Available from: [<URL>](#).
96. Moradi P, Ghorbani-Choghamarani A. Efficient synthesis of 5-substituted tetrazoles catalysed by palladium– S -methylisothiourea complex supported on boehmite nanoparticles. Appl Organomet Chem [Internet]. 2017 May 4;31(5):e3602. Available from: [<URL>](#).
97. Ram VJ, Sethi A, Nath M, Pratap R. The chemistry of heterocycles: Nomenclature and chemistry of three-to-five membered heterocycles [Internet]. The Chemistry of Heterocycles: Nomenclature and Chemistry of Three to Five Membered Heterocycles. Elsevier; 2019. 1–489 p. Available from: [<URL>](#).
98. Schocken MJ, Creekmore RW, Theodoridis G, Nystrom GJ, Robinson RA. Microbial transformation of the tetrazolinone herbicide F5231. Appl Environ Microbiol [Internet]. 1989 May;55(5):1220–2. Available from: [<URL>](#).
99. Ariza-Roldán A, López-Cardoso M, Tlahuext H, Vargas-Pineda G, Román-Bravo P, Acevedo-Quiroz M, et al. Synthesis, characterization, and biological evaluation of eight new organotin(IV) complexes derived from (1*R*, 2*S*) ephedrinedithiocarbamate ligand. Inorganica Chim Acta [Internet]. 2022 May 1;534:120810. Available from: [<URL>](#).
100. Malik MA, Al-Thabaiti SA, Malik MA. Synthesis, structure optimization and antifungal screening of novel tetrazole ring bearing acyl-hydrazones. Int J Mol Sci [Internet]. 2012 Aug 30;13(9):10880–98. Available from: [<URL>](#).
101. Muralikrishna S, Raveendrareddy P, Ravindranath L, Harikrishna S, Jagadeeswara P. Synthesis characterization and antitumor activity of thiazole derivatives containing indole moiety bearing-tetrazole. Der Pharma Chem [Internet]. 2013;5(6):87–93. Available from: [<URL>](#).
102. Bachar SC, Lahiri SC. Synthesis of chloro and bromo substituted 5-(indan-1'-yl)tetrazoles and 5-(indan-1'-yl)methyltetrazoles as possible analgesic agents. Die Pharm - An Int J Pharm Sci [Internet]. 2004;59(6):435–8. Available from: [<URL>](#).
103. Ostrovskii VA, Koren AO. Alkylation and related electrophilic reactions at endocyclic nitrogen atoms in the chemistry of tetrazoles. Heterocycles [Internet]. 2000 Jun 1;53(6):1421–48. Available from: [<URL>](#).
104. Mohite P B, Bhaskar VH. Potential pharmacological activities of tetrazoles in the new millennium. Int J PharmTech Res CODEN [Internet]. 3(3):1557–66. Available from: [<URL>](#).
105. Adamec J, Waissner K, Kuneš J, Kaustová J. A note on the antitubercular activities of 1-Aryl-5-benzylsulfanyltetrazoles. Arch Pharm (Weinheim)

- [Internet]. 2005 Aug 1;338(8):385–9. Available from: [<URL>](#).
106. Katritzky AR, Jaina R, Petrukhin R, Denisenko S, Schelenz T. QSAR correlations of the algistatic Activity of 5-Amino-1-Aryl-1*H*-Tetrazoles. SAR QSAR Environ Res [Internet]. 2001 Jun 1;12(3):259–66. Available from: [<URL>](#).
107. Li Y, Li PK, Roberts MJ, Arend RC, Samant RS, Buchsbaum DJ. Multi-targeted therapy of cancer by niclosamide: A new application for an old drug. Cancer Lett [Internet]. 2014 Jul 10;349(1):8–14. Available from: [<URL>](#).
108. Berquin IM, Edwards IJ, Chen YQ. Multi-targeted therapy of cancer by omega-3 fatty acids. Cancer Lett [Internet]. 2008 Oct 8;269(2):363–77. Available from: [<URL>](#).
109. Block KI, Gyllenhaal C, Lowe L, Amedei A, Amin ARMR, Amin A, et al. Designing a broad-spectrum integrative approach for cancer prevention and treatment. Semin Cancer Biol [Internet]. 2015 Dec 1;35:S276–304. Available from: [<URL>](#).
110. Shamsuzzaman, Asif M, Ali A, Mashrai A, Khanam H, Sherwani A, et al. Synthesis and biological evaluation of steroidal tetrazoles as antiproliferative and antioxidant agents. Chem Bull [Internet]. 2014;3(11):1075–80. Available from: [<URL>](#).
111. Arshad M, Bhat AR, Pokharel S, Kim JE, Lee EJ, Athar F, et al. Synthesis, characterization and anticancer screening of some novel piperonyl-tetrazole derivatives. Eur J Med Chem [Internet]. 2014 Jan 7;71:229–36. Available from: [<URL>](#).
112. Bhaskar VH, Mohite PB. Synthesis, characterization and evaluation of anticancer activity of some tetrazole derivatives. J Optoelectron Biomed Mater [Internet]. 2(4):249–59. Available from: [<URL>](#).
113. Upadhayaya RS, Sinha N, Jain S, Kishore N, Chandra R, Arora SK. Optically active antifungal azoles: Synthesis and antifungal activity of (2*R*,3*S*)-2-(2,4-difluorophenyl)-3-(5-{2-[4-aryl-piperazin-1-yl]-ethyl}-tetrazol-2-yl/1-yl)-1-[1,2,4]-triazol-1-yl-butan-2-ol. Bioorg Med Chem [Internet]. 2004 May 1;12(9):2225–38. Available from: [<URL>](#).
114. Collin X, Sauleau A, Coulon J. 1,2,4-Triazolo mercapto and aminonitriles as potent antifungal agents. Bioorg Med Chem Lett [Internet]. 2003 Aug 4;13(15):2601–5. Available from: [<URL>](#).
115. Mohareb RM, Ahmed HH, Elmegeed GA, Abd-Elhalim MM, Shafic RW. Development of new indole-derived neuroprotective agents. Bioorg Med Chem [Internet]. 2011 May 1;19(9):2966–74. Available from: [<URL>](#).
116. Adibi H, Rashidi A, Khodaei MM, Alizadeh A, Majnooni MB, Pakravan N, et al. Catecholthioether derivatives: preliminary study of in-vitro antimicrobial and antioxidant activities. Chem Pharm Bull [Internet]. 2011 Sep 1;59(9):1149–52. Available from: [<URL>](#).
117. Gao YL, Zhao GL, Liu W, Shao H, Wang YL, Xu WR, et al. Design, synthesis and in vivo hypoglycemic activity of tetrazole-bearing N-glycosides as SGLT2 inhibitors. Ind J Chem 2010; 49B;1499-1508.
118. Muraglia E, Kinzel OD, Laufer R, Miller MD, Moyer G, Munshi V, et al. Tetrazole thioacetanilides: Potent non-nucleoside inhibitors of WT HIV reverse transcriptase and its K103N mutant. Bioorg Med Chem Lett [Internet]. 2006 May 15;16(10):2748–52. Available from: [<URL>](#).
119. Hutchinson DW, Naylor M. The antiviral activity of tetrazole phosphonic acids and their analogues. Nucleic Acids Res [Internet]. 1985 Dec 9;13(23):8519–30. Available from: [<URL>](#).
120. Alam M, Nami SAA, Husain A, Lee DU, Park S. Synthesis, characterization, X-ray diffraction, antimicrobial and in vitro cytotoxicity studies of 7*a*-Aza-B-homostigmast-5-eno [7*a*,7-*d*] tetrazole. Comptes Rendus Chim [Internet]. 2013 Jan 18;16(3):201–6. Available from: [<URL>](#).
121. Sun XY, Wei CX, Deng XQ, Sun ZG, Quan ZS. Synthesis and primary anticonvulsant activity evaluation of 6-alkoxy-tetrazolo[5,1-*a*]phthalazine derivatives. Arzneimittelforschung [Internet]. 2011 Dec 2;60(06):289–92. Available from: [<URL>](#).



Integrating of *In Silico* and *In Vitro* Approaches to Determine Biological Activities of *Abelmoschus esculentus*'s Seeds

Turgut Taşkın^{1*}, Sultan Mente¹, Ceyda Ekentok Atıcı², Mizgin Ermanoğlu¹,
Mücahit Özdemir³, Bahattin Yalçın³, Gülden Zehra Omurtag⁴

¹Department of Pharmacognosy, Faculty of Pharmacy, Marmara University, Istanbul, Turkey.

²Department of Pharmaceutical Biotechnology, Faculty of Pharmacy, Marmara University, Istanbul, Turkey.

³Department of Chemistry, Faculty of Arts and Sciences, Marmara University, Istanbul, Turkey.

⁴Department of Pharmaceutical Toxicology, School of Pharmacy, Istanbul Medipol University, Istanbul, Turkey.

Abstract: The purpose of this study was to examine the antioxidant, anti-urease, and anticholinesterase properties of extracts from plant seeds, as well as their toxicity on normal cells. In addition, the goal of this work was to use an *in silico* and *in vitro* method to evaluate the biological activity and mechanism of action of *A. esculentus*. DPPH (2,2-diphenyl-1-picrylhydrazyl), CUPRAC (Cupric ion reducing antioxidant capacity), and FRAP (Ferric reducing antioxidant power) techniques were used to examine the antioxidant properties of plant extracts. The extracts' anticholinesterase, anti-urease, and cytotoxic activity were determined using the Ellman, Indophenol, and MTT techniques, respectively. Computer algorithms were used to estimate ADMET and molecular docking techniques for compounds in plant. When the antioxidant activity results were examined, it was determined that water (IC₅₀:0.313 mg/mL) and ethanol (IC₅₀:0.314 mg/mL) extract showed DPPH activities close to each other. It was determined that the water (7.780mM FeSO₄/mg extract, 1.106 mM trolox/mg extract) extract showed higher activity than the ethanol (3.420 mM FeSO₄/mg extract, 0.343 mM trolox/mg extract) extract in FRAP and CUPRAC experiments. Considering the enzyme inhibition results, it was determined that the water extract showed the highest anti-urease activity, while the ethanol extract showed the highest anticholinesterase activity. It was also determined that both extracts had no toxic effect on normal cell lines (L-929). Based on pkCSM values, procyanidin B1 and procyanidin B2 compounds have a low volume of distribution, whereas rutin and quercetin compounds have a high volume of distribution (VDss). Not all compounds were predicted to have mutagenic and hepatotoxicity effects. In terms of score and ligand efficiency, procyanidin B1, procyanidin B2, quercetin, and rutin compounds appear to be superior to the reference. The chemicals quercetin and procyanidin B2 are thought to be key players in the pathophysiology of oxidative stress. In this study, the fact that the seeds' extracts have biological activity and have no toxic effects on normal cell lines suggests that the seeds can be used medicinally and nutritionally in the future.

Keywords: *Abelmoschus esculentus*, Antioxidant, Cytotoxic, Anticholinesterase, Anti-urease, In silico.

Submitted: June 11, 2024. **Accepted:** September 2, 2024.

Cite this: Taşkın T, Mente S, Ekentok Atıcı C, Ermanoğlu M, Özdemir M, Yalçın B, Omurtag GZ. Integrating of *In Silico* and *In Vitro* Approaches to Determine Biological Activities of *Abelmoschus esculentus*'s Seeds. JOTCSA. 2024;11(4): 1515-26.

DOI: <https://doi.org/10.18596/jotcsa.1499076>

***Corresponding author's E-mail:** turguttaskin@marmara.edu.tr

1. INTRODUCTION

Dietary antioxidants are food molecules that diminish the detrimental effects of ROS, RNS, or both on humans' normal physiological functioning. The oxidative damage of these oxidants in cells has been linked to the etiology of non-communicable human illnesses such as diabetes mellitus, rheumatoid arthritis, Parkinson's disease, Alzheimer's disease, and cancer (1,2). Furthermore, it is widely

established that oxidative stress activation is a complex system (including several proteins / pathologies and varies depending on illness etiology), therefore pinpointing the putative antioxidant mechanism is challenging. However, these problems may be solved by combining computer models and laboratory experimentation (3). Alzheimer's disease (AD) is the world's most prevalent neurological ailment. There is currently no

effective treatment that permits the condition to heal; instead, treatment focuses on delaying the disease's development and relieving symptoms. The majority of anti-Alzheimer's are acetylcholinesterase (AChEI) inhibitors (donepezil, rivastigmine, tacrine, and galantamine). However, most of these medicines cause hepatotoxicity, sleeplessness, diarrhea, or illness as a side effect. Many investigations on the usefulness of natural products in the treatment of Alzheimer's disease have been undertaken in recent years. Antioxidant capabilities are found in most therapeutic herbs, which help to remove reactive species. By targeting amyloidogenesis and apoptotic pathways, several chemicals identified in medicinal plants have favorable effects on cell survival and cognition (4-7). Natural treatments that are used to treat human problems and have few side effects have gained popularity in recent years, both in developed and developing nations (8). The Malvaceae family's *Abelmoschus esculentus* L. (or *Hibiscus esculentus* or okra) has long been utilized as a culinary vegetable in many nations. Okra has been shown to come from a variety of species in Southeast Asia, India, West Africa, and Ethiopia, according to genetic analyses. It was first grown by the Egyptians in the 12th century B.C., and it quickly spread throughout the Middle East and North Africa (9). Okra may be eaten raw or cooked, and it can be added to soups, salads, and stews. Okra is a high-moisture vegetable that is also abundant in nutrients and a good source of vitamins and minerals (10). Okra is a valuable crop because its leaves, buds, flowers, pods, stems, and seeds have various uses in traditional and contemporary medicine. Okra fruits have been utilized as aphrodisiac, cooling, appetizer, and astringent agents for centuries. Chronic dysentery, gonorrhea, urinary discharges, bladder obstruction, and diarrhea are among the various ailments for which this herb is used. Okra seeds have been utilized as a fungicide and anticarcinogen (11). Because of its rich fiber, vitamin C, calcium, potassium, and folate content, okra is a popular health food. The roots are high in mucilage and have a significant demulcent effect. Syphilis is treated using an infusion made from the roots. In Nepal, the roots' juice is applied topically to cure cuts, wounds, and boils. The leaves make a soothing poultice. Seeds have antispasmodic and stimulating properties (12). Chemoinformatic computer algorithms now give critical information on whether or not a chemical may be used as a therapeutic without the use of animals. Because certain laboratory bioactivity studies are too expensive, the most essential choice on the journey from plant to drug will be to theoretically show the ADMET properties of the chemicals in the medicinal plant and examine their potential as medications or drug raw materials (13). In an examination of the literature, just a few investigations of the plant's biological activities were uncovered. As a result, the purpose of this study is to look at the antioxidant, anti-urease, and anticholinesterase properties of different extracts from the plant's seeds, as well as their toxicity on normal cells. Polyphenolic compounds are also thought to be responsible for medicinal plants' biological action. As a consequence, the ADMET (absorption, distribution, metabolism, excretion, and

toxicity) properties of procyanidin B1, procyanidin B2, quercetin, and rutin compounds, which were explored in this species in the previous work, were determined *in silico* (14). In addition, using an *in silico* and *in vitro* method, this work intended to evaluate the antioxidant, anti-urease, and anticholinesterase mechanisms of *A. esculentus*, a dietary and traditional medicine.

2. EXPERIMENTAL SECTION

2.1. Preparation of Extracts

Seeds of *Abelmoschus esculentus* were purchased at the market. After weighing 200 g of seeds and grinding them into powder, ethanol and water extracts were prepared using the maceration method. The liquid fractions were filtered through filter paper after the extraction processes, and the solvents were evaporated in a rotary evaporator to obtain crude extracts. The extracts were kept refrigerated at 4 °C until the day of the experiment.

2.2. Antioxidant Activity Assays

2.2.1. 2,2-diphenyl-1-picrylhydrazyl (DPPH) assay

To the 0.1 mL extracts prepared at various concentrations (5, 3, 2, 1, and 0.5 mg/mL), 240 µL DPPH solution (0.1 mM) was added. The prepared mixtures were mixed for 1 minute before being incubated for 30 minutes at 25 °C. The absorbances of the mixtures were determined daily at 517 nm. Determining the absorbance of the control sample was carried out under the same conditions using 10 µL of methanol instead of the extract. DPPH radical scavenging experiments were also performed using ascorbic acid solutions prepared at different concentrations (0.5, 0.4, 0.2, 0.1, 0.05 mg/mL) and were used as a standard. The % DPPH radical scavenging activity was calculated by the formula: DPPH radical inhibition = $((A_0 - A_1)/A_0) \times 100$, where A_0 is the absorbance of the control solution and A_1 is the absorbance of plant extract or standard solutions. The IC_{50} is defined as the extract/standard concentration that causes a 50 percent reduction in DPPH radical concentration. The IC_{50} value was calculated using the equation obtained by calculating the % radical scavenging activity against the concentrations studied. The data obtained from the investigation are given as $IC_{50} = \text{mg/mL}$. The assays were performed three times, and the averages and standard deviations of the results were calculated (15).

2.2.2. Cupric ion reducing/antioxidant power (CUPRAC) assay

In brief, 60 µL of $\text{Cu(II)} \cdot 2\text{H}_2\text{O}$, 60 µL of neocuproine, and 60 µL of 1 M NH_4Ac were mixed, followed by the addition of 60 µL of the extracts at different concentrations (0.5, 1, 2, 3, and 5 mg/mL) and 10 µL of ethanol to the mixture. After 60 min, the absorbances of the mixtures were spectrophotometrically measured at 450 nm against the reference solution, which was prepared using adding ethanol instead of the plant extracts. To obtain the Trolox standard curve, a 1 mM stock Trolox solution was prepared which was diluted to working solutions of 1, 0.8, 0.6, 0.4, 0.2, and 0.1 mM using ethanol. Trolox solutions prepared at different concentrations were

evaluated using the CUPRAC method. The CUPRAC method was also applied to butylated hydroxyanisole (BHA) solutions prepared at different concentrations (0.5, 1, 2, 3, and 5 mg/mL) and used as a standard. For the further procedures, (1) absorbance versus concentration plots were constructed, (2) calibration curves were prepared, and (3) the corresponding linear regression equations were obtained. The calibration equation for Trolox was $A = 3.0550x + 0.2344$ ($R^2 = 0.9933$). The CUPRAC values of the extracts were given as mg Trolox/mg extract (16).

2.2.3. Ferric reducing antioxidant power (FRAP) assay

The FRAP reagent (25 mL 300 mM acetate buffer (pH 3.6), 2.5 mL of 2,4,6-tri(2-pyridyl)-1,3,5-triazine solution, and 2.5 mL of 20 mM $\text{FeCl}_3 \cdot 6\text{H}_2\text{O}$) was kept at 37 °C for 30 min. The absorbance was measured at 593 nm in the 4th minute after dissolution of 190 μL of the FRAP reagent with 10 μL of the plant extracts prepared at concentrations of 0.5, 1, 2, 3, and 5 mg/mL, against the reference prepared by adding distilled water instead of the extract. A 1 mM stock solution of $\text{FeSO}_4 \cdot 7\text{H}_2\text{O}$ was prepared to obtain the FeSO_4 standard curve equation. Subsequently, working solutions of 0.5, 0.4, 0.2, 0.1, and 0.05 mM concentrations were prepared by diluting the stock solution with water. The $\text{FeSO}_4 \cdot 7\text{H}_2\text{O}$ solutions prepared at different concentrations were also evaluated using the FRAP method. The FRAP method was applied to butylated hydroxyanisole (BHA) solutions prepared at different concentrations (0.5, 1, 2, 3, and 5 mg/mL) and were used as a standard. For the further procedures, (1) absorbance versus concentration plots were constructed, (2) calibration curves were prepared, and (3) the corresponding linear regression equations were obtained. The calibration equation for Fe^{2+} was $A = 12.8603x - 0.0066$ ($R^2 = 0.9986$). The FRAP values of the extracts are presented as mg Fe^{2+} /mg extract (17).

2.3. Enzyme Inhibitory Activity

In a phosphate buffer solution (pH 8, 0.1 M, 40 L), AChE (20 μL) and various quantities of extracts (20 μL) were added. This mixture was incubated for 10 minutes at 25°C. After incubation, the mixture was mixed with DTNB (100 μL) and AcI (20 μL) as a substrate. At 412 nm, 5-thio-2-nitrobenzoic acid was spectrophotometrically determined (18). The indophenol technique was used to examine the plants' anti-urease activity (19).

2.4. Determination of the Cytotoxicity of the Extracts

The cytotoxic effect of the extracts was determined using the MTT technique. The extracts were diluted in methanol at a concentration of 1 mg/mL, and their effects on cell viability were investigated using the Cell Proliferation Kit I (MTT kit) (Roche) in the L-929 (ATCC CCI-1) cell line, according to the manufacturer's instructions.

2.5. In silico Molecular Docking

In molecular docking research, Autodock Vina was used to predict binding affinity for procyanidin B1, procyanidin B2, quercetin, and rutin. Galantamine was chosen as a reference for the acetylcho-

linesterase enzyme, thiourea for the urease enzyme, and ascorbic acid and butylated hydroxyanisole-BHA for the oxidoreductase enzymes. PubChem (<https://pubchem.ncbi.nlm.nih.gov>) was used to find 3D structures of compounds. The PubChem IDs are 11250133 for procyanidin B1, 122738 for procyanidin B2, 5280343 for quercetin. Human acetylcholinesterase-AChE (PDB code: 4MOE) (<https://doi.org/10.1021/ml400304w>), urease (PDB code: 4UBP) (<https://doi.org/10.1007/s007750050014>), human cytochrome P450-CYPs (PDB code: 1OG5) (<https://doi.org/10.1038/nature01862>), lipoxygenase (PDB code: 1N8Q) (<https://doi.org/10.1002/prot.10579>), and myeloperoxidase from humans (PDB code: 1DNU) (<https://doi.org/10.1021/bi0111808>). The RCSB Protein Data Bank (<https://www.rcsb.org>) was used to find nicotinamide adenine dinucleotide phosphate oxidase-NAD(P)H oxidase (PDB code: 1DNU) (20) and xanthine oxidase-XO (PDB code: 3NRZ) (21). The protein structures were stripped of water molecules, as well as polar hydrogens and Kollman charges have been added (22). Discovery Studio Visualizer 2021 v21.1.0.20298 (23) was used to determine the amino acids in the catalytic domain of enzymes. Morris *et al.* (1998) (24) used the Lamarckian Genetic Algorithm as the docking engine, with all docking settings set to default. The inhibitors with the lowest energy docking score were selected from 10 conformations provided from Vina docking calculations. For the depiction of 2D and 3D figures, Discovery Studio Visualizer 2021 and UCSF Chimera 1.13.1 (25) were used.

2.6. ADMET Properties

Anticipating the pharmacokinetic features of pharmacological compounds improves the chances of reaching the target faster and more precisely. Absorption, distribution, metabolism, excretion, and toxicity are all abbreviated as ADMET. The properties of investigated chemicals from *A. esculentus* were predicted using pkCSM, a free online web server (<https://biosig.lab.uq.edu.au/pkcsm/>). Molinspiration cheminformatics (<https://molinspiration.com/>) was used to compute the molecular polar surface area and molecular lipophilicity potential.

2.7. Statistical Analysis

The mean standard deviations (SD) of three independent and parallel measurements were used to calculate the results. ANOVA procedures were used to perform a one-way analysis of variance, and a Tukey Multiple Comparison test was used to determine significant differences between means, with $p < 0.05$ considered statistically significant.

3. RESULTS AND DISCUSSION

3.1. Antioxidant Activity

The DPPH method is a quick, easy, low-cost, and commonly used method for determining a compound's potential to act as a free radical scavenger or hydrogen donor, as well as determining the antioxidant activity of foods. This approach for determining the overall antioxidant capacity and free radical scavenging activity of fruit and vegetable

juices is simple and effective (26). The ferric reducing ability of extract (FRAP) assay works on the premise of ferric-tripyridyltriazine (Fe^{3+} -TPTZ) complexes being reduced to ferrous tripyridyltriazine (Fe^{2+} -TPTZ) complexes by antioxidants in a sample at a low pH level. The final product (Fe^{2+} -TPTZ) is blue in color with a maximum absorption at 593 nm, and the decrease in absorbance is proportional to the extract's antioxidant capacity. The CUPRAC method relies on antioxidants in a sample reducing Cu(II) to Cu(I) (27). DPPH, FRAP, and CUPRAC techniques were used to assess the antioxidant activity of the extracts produced from the samples. The results are shown in Table 1. The extracts' and ascorbic acid's free radical scavenging abilities were assessed by comparing their IC_{50} values. According to the findings, the water (IC_{50} : 0.313 mg/mL) and ethanol (IC_{50} : 0.314 mg/mL) extracts had extremely similar

free radical scavenging activity when compared to one another. All extracts demonstrated weaker radical scavenging activity than ascorbic acid (IC_{50} : 0.004 mg/mL). When the FRAP values obtained as a consequence of this investigation were compared, it was discovered that the plant's water extract (7.78 mM FeSO_4 /mg extract) had a higher iron (III) ion reduction potential than the ethanol (3.42 mM FeSO_4 /mg extract). Furthermore, all extracts were shown to have lower FRAP values than the BHA compound (16.91 mM FeSO_4 /mg extract). The water extract (1.106 mM troloxE/mg extract) was shown to have a better capability to reduce Cu(II) to Cu(I) than the ethanol (0.343 mM troloxE/mg extract) extract in this investigation. All extracts were also shown to have lower activity than the reference compound (1.81 mM troloxE/mg).

Table 1: The antioxidant activity of *Abelmoschus esculentus* seeds' extracts.

Extracts	DPPH (IC_{50} : mg/mL)	FRAP (mM FeSO_4 /mg extract)	CUPRAC (mM troloxE/mg extract)
Water	0.313±0.0496*	7.780±1.164*	1.106±0.0263*
Ethanol	0.314±0.0052*	3.420±1.317*	0.343±0.0507*
Ascorbic acid	0.004± 0.007		
BHA		16.91±0.02	1.81±0.001

BHA (Butylated hydroxyanisole): positive control for CUPRAC and FRAP assays; Ascorbic acid: positive control for DPPH assay; TE: Trolox equivalent; Values are mean of triplicate determination (n =3) ±standard deviation; * $P < 0.05$ compared with the positive control.

3.2. Enzyme Inhibitory Activity

The indophenol method was used to assess the percentage inhibition of the urease enzyme in the obtained extracts, and the findings are reported in Table 2. In comparison to the ethanol extract (4.52%), the water extract (12.80%) had the

stronger anti-urease action, according to the data. Furthermore, when all of the data were analyzed, it was discovered that all of the extracts had lesser activity than the standard chemical (78.84%). The indophenol method was used to compare the acetylcholinesterase enzyme inhibition percentages of different extracts derived from the plant. According to the findings, the ethanol extract (41.80%) of the plant had more activity than the water extract (17.38%). The extracts were found to have lower activity than galantamine (88.14%), which was employed as a control.

Table 2: The enzyme inhibition potential of different extracts from the plant.

Extracts	Urease enzyme inhibition (%) (12.5 µg/mL)	AChE inhibition (%) (200 µg/mL)
Water	12.80±0.3510	17.38±2.754
Ethanol	4.52±1.568	41.80±3.322
Thiourea	78.84± 0.09	
Galantamine		88.14±0.14

3.3. Cytotoxicity of *Abelmoschus esculentus* Extracts

The MTT test was used to study the influence of extracts derived from *A. esculentus* seeds on cell viability. Ethanol and water extracts at given

quantities (100 g/mL) have no cytotoxic effect on L929 cells, as demonstrated in Figure 1. Cell viability was determined at 94.62% for ethanol extract and 88.79% for water extract after 24 hours of incubation (Table 3).

Table 3: Cell viability values after 24 h incubation.

Groups	Cell viability (%)
Control (untreated)	100.00
Positive control (15% DMSO)	52.84
Negative control (ultrapure water)	112.24
Ethanol extract (100 µg/mL)	94.62
Water extract (100 µg/mL)	88.79

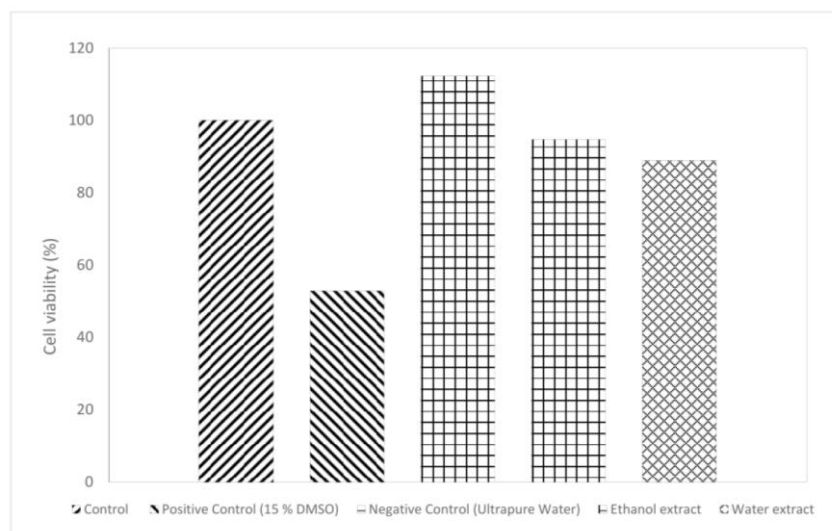


Figure 1: Cytotoxic activity of different extracts from the plant.

3.4. The Results of Molecular Docking *In Silico*

The molecular docking method provides a wide perspective on describing *in vitro* mechanisms and anticipating potential enzyme-substrate interactions (<https://doi.org/10.1016/j.jscs.2021.101418>). Based on the predicted binding scores, possible ligand-amino acid interactions and inhibitory effects of procyanidin B1, pro-cyanidin B2, quercetin, and

rutin compounds in the *A. esculentus* in anticholinesterase, urease and antioxidant tests were assessed. When molecular docking experiments were compared to reference compounds, significant differences in enzyme binding affinity and ligand-enzyme interactions were discovered. Table 4 lists all of the molecular docking results.

Table 4: Molecular docking scores (kcal/mol) of procyanidin B1, procyanidin B2, quercetin, and rutin compounds on anticholinesterase, urease, cytochrome P450, lipoxygenase, myeloperoxidase, xanthine oxidase, and NADPH enzymes.

Enzymes	Procyanidin B1	Procyanidin B2	Quercetin	Rutin
Anticholinesterase	-10.5	-9.1	-7.2	-9.1
Urease	-11.1	-8.1	-7.7	-8.3
Cytochrome P450	-12.8	-10.7	-8.8	-9.0
Lipoxygenase	-10.5	-10.6	-8.4	-9.6
Myeloperoxidase	-11.3	-10.4	-9.7	-10.0
NADPH	-13.0	-9.9	-8.5	-8.7
Xanthine oxidase	-7.9	-6.3	-8.5	-5.7

Docking scores of reference molecules, galantamine for acetylcholinesterase is -7.7 kcal/mol and thiourea for urease is -3.2 kcal/mol. Butylated hydroxyanisole (BHA) docking scores for cytochrome P450, lipoxygenase, myeloperoxidase, NADPH, and xanthine oxidase enzymes are the lowest -5.4 kcal/mol (for lipoxygenase) and the highest (xanthine oxidase) -6.3 kcal/mol. Ascorbic acid docking scores for cytochrome P450, lipoxygenase, myeloperoxidase, NADPH, and xanthine oxidase are the lowest -5.5 kcal/mol (for cytochrome P450) and the highest (xanthine oxidase) -6.2 kcal/mol.

Taking into account the interactions of a few key chemicals and enzymes, Figure 2a shows that the rutin molecule has docked to the active site of the anticholinesterase enzyme with a binding affinity of -9.1 kcal/mol and has formed typical hydrogen bonds, carbon-hydrogen bonds, hydrophobic pi-alkyl, and pi-sigma interactions. Conventional hydrogen bonds between the functional groups of the rutin molecule and the anticholinesterase amino acids have

interaction lengths in the range of 1.86-2.93 Å. Thomas Steiner established a criterion for hydrogen bond strength. In the range of 1.2-1.5 Å, hydrogen bonding is very strong. It is moderate if it is between 1.5 and 2.2 Å, and it is weak if it is larger than 2.2 Å (28). Rutin binds to the anticholinesterase active site with moderate interactions, according to these values. With a binding score of -11.1 kcal/mol, the Procyanidin B1 compound with the highest binding scores is docked in the catalytic region of the urease enzyme (Figure 2b). At the active site of the urease protein, the procyanidin B1 molecule has three conventional hydrogen bonds, five pi-alkyl, and one pi-anion interaction. Procyanidin B1's hydrogen bond lengths are typically in the range of 2.17-3.10 Å. Procyanidin B1 has weaker hydrogen bond contacts than rutin, but both compounds are macrocyclic; therefore it still has six pi-aromatic ring connections. Rutin, on the other hand, has three pi-alkyl and one pi-sigma ring interactions. High ring contacts prevent the ligand from being withdrawn, allowing it to attach more securely to the receptor. On xanthine oxidase

and cytochrome P450 enzymes, quercetin and procyanidin B2 exhibit similar actions (Figures 3a and b). With a binding score of -8.5 kcal/mol, quercetin is attached to the catalytic site of the xanthine oxidase enzyme and has two weak hydrogen bonds (2.73-2.96 Å). Procyanidin B2, on the other hand, is located in the catalytic region of the cytochrome

P450 enzyme with a binding affinity of -10.7 kcal/mol and has three conventional hydrogen bond interactions in the 2.29-2.45 Å range, like the quercetin molecule. The chemicals quercetin and procyanidin B2 are thought to be key players in the pathophysiology of oxidative stress.

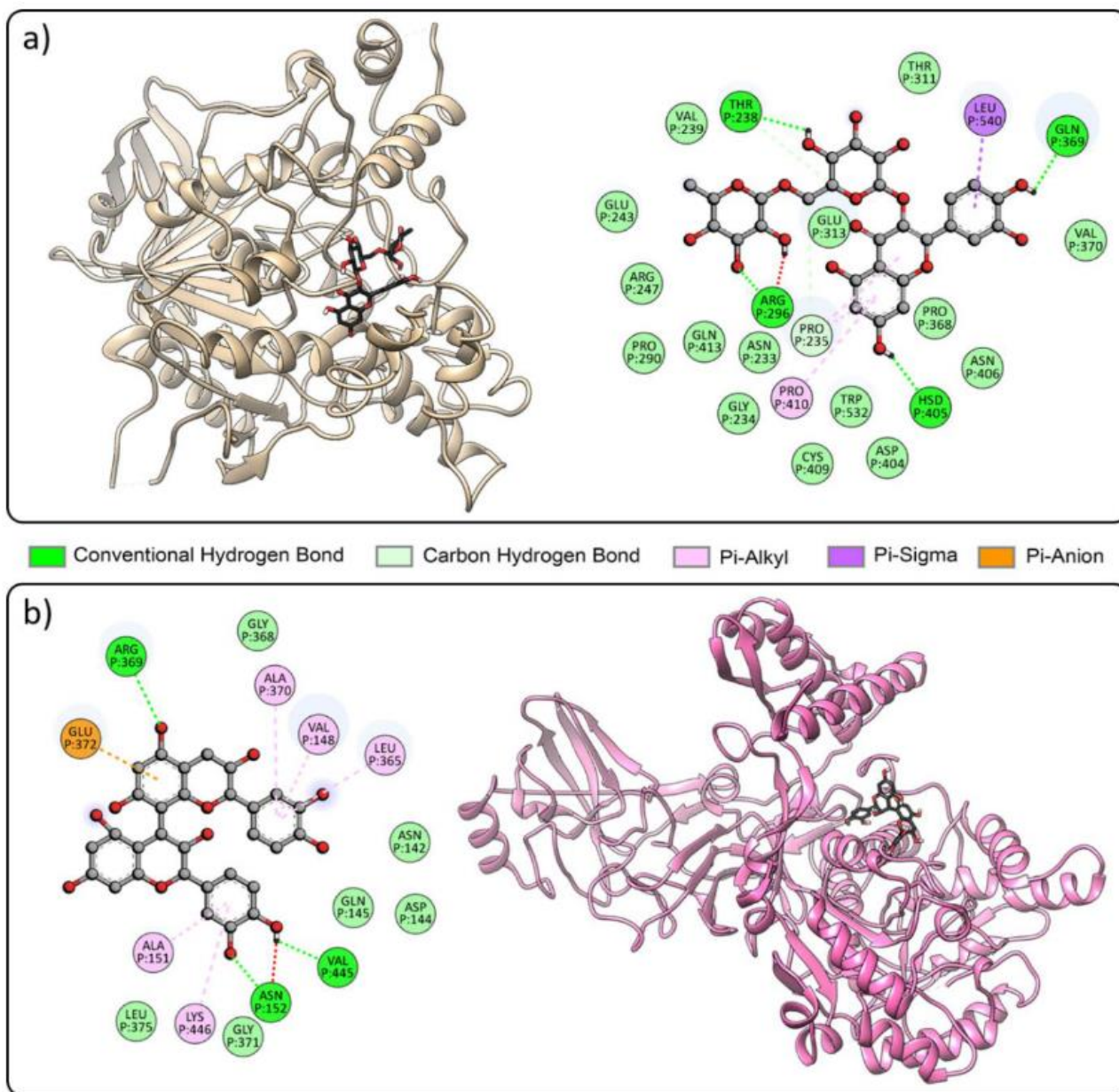


Figure 2: (A) The 2D map of amino acid-ligand interactions and the position of the rutin on the acetylcholinesterase enzyme. (B) The 2D map of amino acid-ligand interactions and the position of the procyanidin B1 on the urease enzyme.

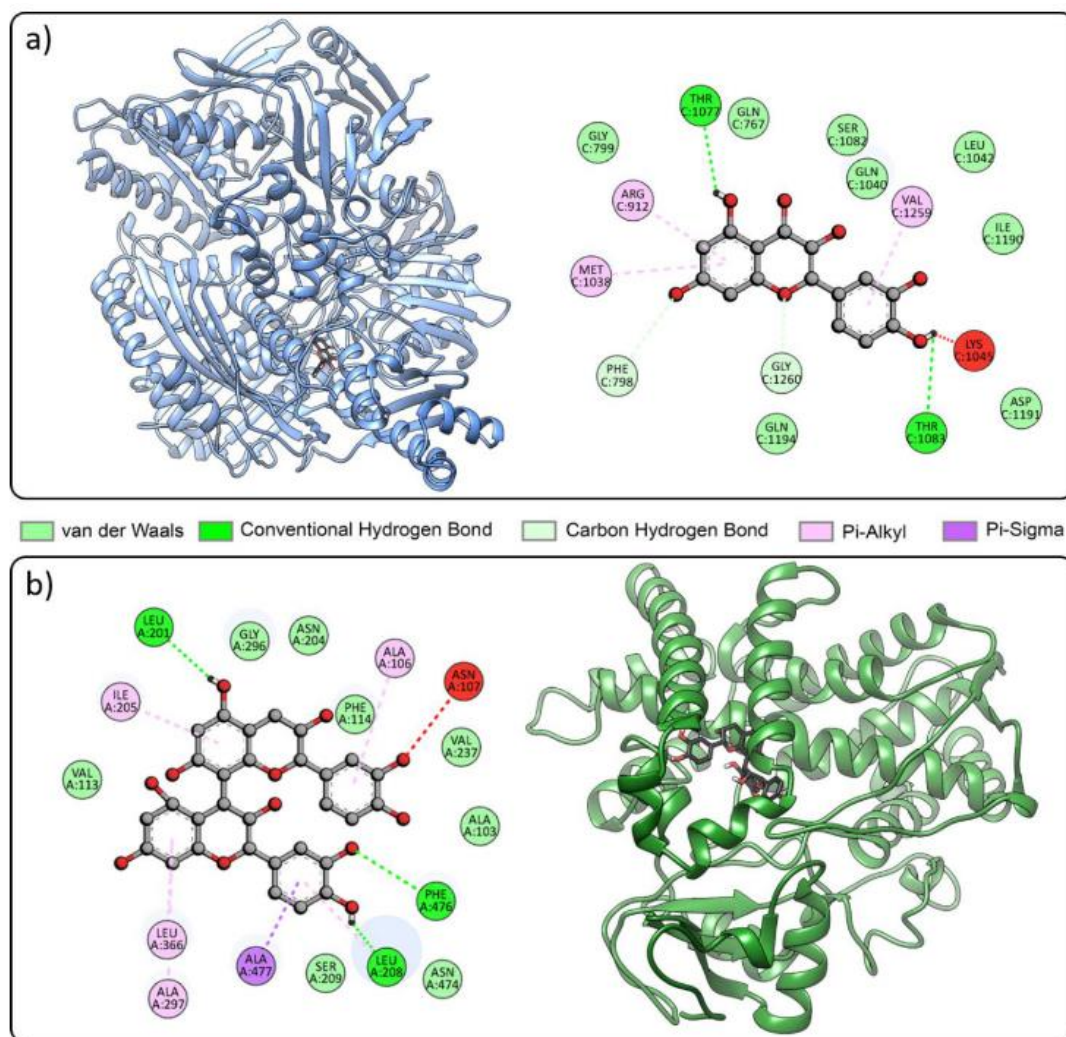


Figure 3: (A) The 2D map of amino acid-ligand interactions and the position of the quercetin on the xanthine oxidase enzyme. (B) The 2D map of amino acid-ligand interactions and the position of the procyanidin B2 on the cytochrome P450 enzyme.

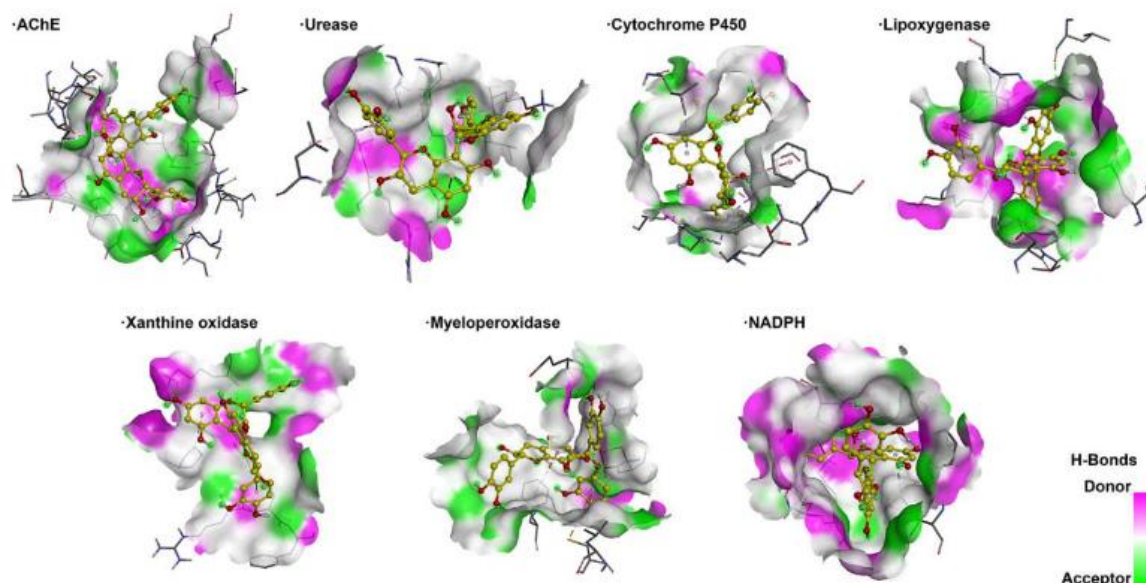


Figure 4: The H-bond interactions between Procyanidin B1 ligand and anticholinesterase, urease, cytochrome P450, lipoxigenase, myeloperoxidase, xanthine oxidase and NADPH enzymes.

The hydrogen bond is the most important of all the directed intermolecular interactions. The procyanidin B1 molecule serves as a hydrogen bond giver and

acceptor, and it is deeply buried in the catalytic sites despite its huge size (Figure 4). This increases the likelihood that the ligand will remain on the enzyme

at high pressure and temperature, functioning as an inhibitor and inhibiting the enzyme. In terms of score and ligand efficiency, procyanidin B1, procyanidin B2, quercetin, and rutin compounds appear to be superior than reference molecules (galantamine for anticholinesterase and thiourea for urease). Because of their naturalness, these compounds might be used as model inhibitors for the treatment of disorders connected to them.

3.5. *In silico* ADMET Properties

Table 4 shows the results of the compounds' ADMET investigations. The percentages of chemicals absorbed from the intestine range from 23.446 to 77.207 percent. In comparison to other chemicals, rutin was determined to have poor intestine absorption based on pkCSM values. All of the studied

compounds' Caco-2 permeability values were assessed to be low. All of the chemicals are thought to pass through the skin. Rutin and quercetin compounds have a large volume of distribution, whereas procyanidin B1 and B2 compounds have a low volume of distribution (VDss). All of the compounds were projected to have a poor blood-brain barrier distribution and be unable to reach the central nervous system. The examined compounds are not thought to be metabolized by p450 enzymes, which are typically located in the liver. Not all of the compounds studied are expected to produce mutagenic or hepatotoxic effects. All phenolic chemicals are absorbed at a low level, according to ADMET calculations, and have no hazardous consequences (Table 5).

Table 5: ADMET profile screening of compounds in the plant.

Compounds	Absorption			
	Caco2 permeability (log Papp in 10 ⁻⁶ cm/s)	Intestinal absorption (human) (% Absorbed)	Skin Permeability (log Kp)	
Procyanidin B1	-1.225	66.749	-2.735	
Procyanidin B2	-1.225	66.749	-2.735	
Quercetin	-0.229	77.207	-2.735	
Rutin	-0.949	23.446	-2.735	
	Distribution			
	VDss (human) log L/kg	BBB permeability (log BB)	CNS permeability (log PS)	
Procyanidin B1	-0.158	-1.94	-3.983	
Procyanidin B2	-0.158	-1.94	-3.983	
Quercetin	1.559	-1.098	-3.065	
Rutin	1.663	-1.899	-5.178	
	Metabolism		Excretion	
	CYP 450 substrate	CYP 450 inhibitor	Total Clearance (log ml/min/kg)	Renal OCT2 substrate
Procyanidin B1	No	No	-0.085	Yes
Procyanidin B2	No	No	-0.085	Yes
Quercetin	No	No	0.407	No
Rutin	No	No	-0.369	No
	Toxicity			
	AMES toxicity	Hepatotoxicity	Oral Rat Acute Toxicity (LD50) (mol/kg)	Skin Sensitisation
Procyanidin B1	No	No	2.482	No
Procyanidin B2	No	No	2.482	No
Quercetin	No	No	2.471	No
Rutin	No	No	2.491	No

When the ROS system and transition metal ions are engaged for a lengthy period of time in the body, it disrupts the work of homeostatic proteins. It is one of the most common causes of sickness and its consequences. Polyphenols and flavonoids have a high hydrogen-donating capacity, allowing them to stabilize and delocalize unpaired electrons by forming hydrogen bonds with free radicals and preventing the Fenton reaction (29). Our present research has also demonstrated the antioxidant performance of several plant extracts in neutralizing free radicals and transition metal ions. Furthermore, *in silico* models are used in current experimental pharmacology to screen phytoconstituents in

therapeutic plants that are being studied. An *in silico* docking analysis was also performed in this work to investigate the binding affinity of proposed antioxidants with a number of proteins implicated in oxidative stress induction. The identification of the lead hit molecule, which may be recognized in three ways, is aided by docking. Binding energy is defined as the sum of binding affinity, hydrogen bond interactions, and hydrogen bond residues. The compounds with the highest abundance in the plant were chosen and docked against five free radical producers, including lipoxygenase, myeloperoxidase, xanthine oxidase, cytochrome P450, and NAD(P)H oxidase, to discover the primary antioxidant. By

changing the active site iron atom from Fe²⁺ to Fe³⁺ state, lipoxygenase oxygenates polyunsaturated free fatty acids (such as linoleic and arachidonic acid) to create lipid metabolites that contribute to pathogenic situations. Myeloperoxidase is mostly generated by circulating neutrophils, which play a crucial role in inflammation and oxidative stress processing. Although this enzyme kills microorganisms within cells, it also damages host tissue on the outside (30). Xanthine oxidase, a convertible form of xanthine dehydrogenase, is produced by a single gene. In epithelial, endothelial, and connective tissue cells, xanthine oxidase has been identified as the principal generator of oxygen radicals. This enzyme may be involved in oxidative stress, aldehyde detoxification, neutrophil mediation, and oxidative stress-mediated ischemia reperfusion (31). Drug metabolism in the liver is aided by CYP450 enzymes. The pathophysiology of inflammation, apoptosis, diabetes, hypertension, hypertrophy, and angiogenesis is linked to NADPH oxidase (32). The current study reflects the anti-binding oxidant's expected affinity for oxidative stress sites.

Abelmoschus esculentus has long been used as a vegetable, and earlier research has revealed that the plant contains antibacterial, antioxidant, antidiabetic, anti-fatigue, anticancer, antihyperlipidemic, and neuroprotective effects. The biological activities of the plant are known to be glycosides, terpenoids, tannins, carotenoids, flavonoids, alkaloids, steroids, and phenolic compounds (33). All portions of the plant were extracted with crude methanol, aqueous soluble fraction, and n-hexane soluble fraction extracts, and their antioxidant properties were compared. According to the findings, aqueous soluble fraction extract (IC₅₀:26.87 µg/mL) had stronger DPPH free radical scavenging activity than crude methanol (IC₅₀:46.99 µg/mL) and n-hexane soluble fraction (IC₅₀:29.37 µg/mL) extracts (34). Quercetin-3-O-gentiobiopyranoside, quercetin-4"-O-methyl-3-O-β-D-glucopyranoside, quercetin-3-O-[β-D-xyl-(1--2)]-β-D-glucopyranoside, quercetin, L-tryptophan, isopropyl (9Z,12Z)-octadeca-9,12-dienoate, stigmasterol, stigmasterol-3-O-β-D-glucopyranoside and uracil compounds were isolated from a 70% methanol extract of the plant's fruit (35). The DPPH radical scavenging activity of a methanol extract from the plant's seeds was examined, and it was shown to be lower than the standard compound. In addition, HPLC-DAD was used to examine procyanidin B1, procyanidin B2, quercetin, and rutin components in this investigation (14). In another investigation, the Soxhlet technique was used to extract 80% methanol and water extracts from the plant's seeds, and it was discovered that the methanol extract had higher ferric reducing power activity than the water extract (36).

In vitro antidiabetic and antioxidant activities of methanol extract prepared from immature fruit of *A. esculentus* by the soxhlet method were investigated. In addition, in this study, the binding interaction of α-amylase and α-glucosidase with the extract was determined by molecular docking method. It was determined that the DPPH radical scavenging

percentage of the extract at concentrations of 31–1000 µg/mL varied between 1.618% and 13.487%. The enzymatic antioxidant activities of methanol extract such as catalase (CAT), peroxidase (POD) and superoxide dismutase (SOD) were found to have significant potentials with the values of 3.99±1.05, 1.27±2.6 and 23.80± 0.03 U/mg protein, respectively. At a concentration of 50–200 µg/mL, the percentage of α-glucosidase and α-amylase inhibition was found to vary between 14.36±0.099% and 19.23± 0.172% and 15.89±1.877% and 37.19 ± 7.430%, respectively. The maximum glucose uptake percentage of the extract was found to be 68.420±1.752% at 3 mg/mL extract and 5 mM glucose concentration. In silico analysis in this study also revealed that the ligand molecule can bind to α-glucosidase and α-amylase molecules (37).

Unlike the previous studies, we used the maceration process to prepare ethanol and water extracts from the plant seeds, and we tested their antioxidant activity using the DPPH, FRAP, and CUPRAC methodologies. The water extract was shown to have higher DPPH and FRAP antioxidant activity than the ethanol extract, according to the findings. This disparity shows that the explanation is due to the extraction procedure and the diversity of solvents utilized. This study also looked at the antiurease, anticholinesterase, and cytotoxic properties of both extracts.

4. CONCLUSION

In this study, the antioxidant, antiurease, anticholinesterase, and cytotoxic activities of various extracts of okra seed used by the public were investigated. It was determined that the water extract obtained from the seed of the plant had stronger antioxidant and antiurease activity than the ethanol extract. The antiacetylcholinesterase activity of the ethanol extract from the plant's semen was the greatest. Furthermore, the cytotoxic activity of the plant on the normal cell line (L-929) was investigated in this study owing to the plant's use as food, and no hazardous effects were discovered. Furthermore, the substances it contains have no mutagenic, hepatotoxic, or minnow toxicity effects, suggesting that the plant's seeds can be employed medicinally and nutritionally in the future. In terms of score and ligand efficiency, procyanidin B1, procyanidin B2, quercetin, and rutin compounds appear to be superior than reference molecules (galantamine for anticholinesterase and thiourea for urease). Furthermore, quercetin and procyanidin B2 chemicals are thought to be key players in the pathogenesis of oxidative stress.

5. CONFLICT OF INTEREST

The authors declare that there are no conflicts of interest related to this article.

6. ACKNOWLEDGMENTS

Acknowledgements: This work is financially supported by TÜBİTAK-2209A program (1919B012000209).

7. REFERENCES

1. Pisoschi AM, Negulescu GP. Methods for total antioxidant activity determination: A review. *Biochem Anal Biochem* [Internet]. 2012;1(1):106. Available from: [<URL>](#).
2. Jaganath IB, Jaganath IB, Mullen W, Edwards CA, Crozier A. The relative contribution of the small and large intestine to the absorption and metabolism of rutin in man. *Free Radic Res* [Internet]. 2006 Jan 7;40(10):1035–46. Available from: [<URL>](#).
3. Khanal P, Patil BM. *In vitro* and *in silico* antioxidant, cytotoxicity and biological activities of *Ficus benghalensis* and *Duranta repens*. *Chinese Herb Med* [Internet]. 2020 Oct 1;12(4):406–13. Available from: [<URL>](#).
4. Uddin MS, Kabir MT, Tewari D, Mathew B, Aleya L. Emerging signal regulating potential of small molecule biflavonoids to combat neuropathological insults of Alzheimer's disease. *Sci Total Environ* [Internet]. 2020 Jan 15;700:134836. Available from: [<URL>](#).
5. Gaudreault R, Mousseau N. Mitigating alzheimer's disease with natural polyphenols: A review. *Curr Alzheimer Res* [Internet]. 2019 Jul 23;16(6):529–43. Available from: [<URL>](#).
6. Gauthier S, Feldman HH, Schneider LS, Wilcock GK, Frisoni GB, Hardlund JH, et al. Efficacy and safety of tau-aggregation inhibitor therapy in patients with mild or moderate Alzheimer's disease: a randomised, controlled, double-blind, parallel-arm, phase 3 trial. *Lancet* [Internet]. 2016 Dec 10;388(10062):2873–84. Available from: [<URL>](#).
7. Noori T, Dehpour AR, Sureda A, Sobarzo-Sanchez E, Shirooie S. Role of natural products for the treatment of Alzheimer's disease. *Eur J Pharmacol* [Internet]. 2021 May 5;898:173974. Available from: [<URL>](#).
8. Jideani AIO, Silungwe H, Takalani T, Omolola AO, Udeh HO, Anyasi TA. Antioxidant-rich natural fruit and vegetable products and human health. *Int J Food Prop* [Internet]. 2021 Jan 1;24(1):41–67. Available from: [<URL>](#).
9. Elkhalfi AEO, Alshammari E, Adnan M, Alcantara JC, Awadelkareem AM, Eltoum NE, et al. Okra (*Abelmoschus esculentus*) as a potential dietary medicine with nutraceutical importance for sustainable health applications. *Molecules* [Internet]. 2021 Jan 28;26(3):696. Available from: [<URL>](#).
10. Dantas TL, Alonso Buriti FC, Florentino ER. Okra (*Abelmoschus esculentus* L.) as a potential functional food source of mucilage and bioactive compounds with technological applications and health benefits. *Plants* [Internet]. 2021 Aug 16;10(8):1683. Available from: [<URL>](#).
11. Esmailzadeh D, Razavi BM, Hosseinzadeh H. Effect of *Abelmoschus esculentus* (okra) on metabolic syndrome: A review. *Phyther Res* [Internet]. 2020 Sep 27;34(9):2192–202. Available from: [<URL>](#).
12. Kumar DS, Tony DE, Praveen Kumar A, Kumar K, Srinivasa Rao DB, Nadendla R. A Review on: *Abelmoschus esculentus* (okra). *Int Res J Pharm Appl Sci* [Internet]. 2013;3(4):129–32. Available from: [<URL>](#).
13. Gasteiger J. Chemoinformatics: Achievements and challenges, a personal view. *Molecules* [Internet]. 2016 Jan 27;21(2):151. Available from: [<URL>](#).
14. Khomsug P, Thongjaroe W, Pakdeenaro N, Suttajit M, Chantirati P. Antioxidative Activities and Phenolic Content of Extracts from Okra (*Abelmoschus esculentus* L.). *Res J Biol Sci* [Internet]. 2010 Apr 1;5(4):310–3. Available from: [<URL>](#).
15. Fu W, Chen J, Cai Y, Lei Y, Chen L, Pei L, et al. Antioxidant, free radical scavenging, anti-inflammatory and hepatoprotective potential of the extract from *Parathelypteris nipponica* (Franch. et Sav.) Ching. *J Ethnopharmacol* [Internet]. 2010 Aug 9;130(3):521–8. Available from: [<URL>](#).
16. Apak R, Güçlü K, Özyürek M, Karademir SE. Novel total antioxidant capacity index for dietary polyphenols and vitamins C and E, using their cupric ion reducing capability in the presence of neocuproine: CUPRAC method. *J Agric Food Chem* [Internet]. 2004 Dec 1;52(26):7970–81. Available from: [<URL>](#).
17. Benzie IFF, Strain JJ. The ferric reducing ability of plasma (FRAP) as a measure of "antioxidant power": The FRAP Assay. *Anal Biochem* [Internet]. 1996 Jul 15;239(1):70–6. Available from: [<URL>](#).
18. Taşkın T, Taşkın D, Çam ME, Bulut G. Phenolic compounds, biological activities and trace elements of *Capparis ovata* var. *canescens*. *Rev Biol Trop* [Internet]. 2020 Mar 19;68(2):590–600. Available from: [<URL>](#).
19. Ahmed D, Younas S, Mumtaz Anwer Mughal Q. Study of alpha-amylase and urease inhibitory activities of *Melilotus indicus* (Linn.) All. *Pak J Pharm Sci* [Internet]. 2014;27(1):57–61. Available from: [<URL>](#).
20. Lountos GT, Jiang R, Wellborn WB, Thaler TL, Bommarius AS, Orville AM. The crystal structure of NAD(P)H oxidase from *Lactobacillus sanfranciscensis*: Insights into the conversion of O₂ into two water molecules by the flavoenzym. *Biochemistry* [Internet]. 2006 Aug 1;45(32):9648–59. Available from: [<URL>](#).
21. Cao H, Pauff JM, Hille R. Substrate orientation and catalytic specificity in the action of xanthine oxidase. *J Biol Chem* [Internet]. 2010 Sep 3;285(36):28044–53. Available from: [<URL>](#).
22. Singh UC, Kollman PA. An approach to computing electrostatic charges for molecules. *J Comput Chem* [Internet]. 1984 Apr 7;5(2):129–45. Available from: [<URL>](#).

23. Dassault Systèmes B. Discovery studio visualizer. San Diego, CA, USA; 2017.
24. Morris GM, Goodsell DS, Halliday RS, Huey R, Hart WE, Bewley RK, et al. Automated docking using a Lamarckian genetic algorithm and an empirical binding free energy function. *J Comput Chem* [Internet]. 1639;19(14):1639–62. Available from: [<URL>](#).
25. Pettersen EF, Goddard TD, Huang CC, Couch GS, Greenblatt DM, Meng EC, et al. UCSF chimera—A visualization system for exploratory research and analysis. *J Comput Chem* [Internet]. 2004 Oct 1;25(13):1605–12. Available from: [<URL>](#).
26. Kedare SB, Singh RP. Genesis and development of DPPH method of antioxidant assay. *J Food Sci Technol* [Internet]. 2011 Aug 25;48(4):412–22. Available from: [<URL>](#).
27. Büyüktuncel E. Main spectrophotometric methods for the determination of total phenolic content and antioxidant capacity. *Marmara Pharm J* [Internet]. 2013 Jan 1;2(17):93–103. Available from: [<URL>](#).
28. Steiner T. The hydrogen bond in the solid state. *Angew Chemie Int Ed* [Internet]. 2002 Jan 4;41(1):48–76. Available from: [<URL>](#).
29. Pham-Huy LA, He H, Pham-Huy C. Free radicals, antioxidants in disease and health. *Int J Biomed Sci* [Internet]. 2008 Jun 15;4(2):89–96. Available from: [<URL>](#).
30. Chung HY, Baek BS, Song SH, Kim MS, Huh JI, Shim KH, et al. Xanthine dehydrogenase/xanthine oxidase and oxidative stress. *Age (Omaha)* [Internet]. 1997 Jul;20(3):127–40. Available from: [<URL>](#).
31. Hrycay EG, Bandiera SM. Involvement of cytochrome P450 in reactive oxygen species formation and cancer. In: *Advances in Pharmacology* [Internet]. Academic Press; 2015. p. 35–84. Available from: [<URL>](#).
32. Paravicini TM, Touyz RM. NADPH oxidases, reactive oxygen species, and hypertension. *Diabetes Care* [Internet]. 2008 Feb 1;31:S170–80. Available from: [<URL>](#).
33. Hafeez M, Mona Hassan S, Sharif Mughal S, Raza Ayub A, Yasin M, Nasir Mehmood Khan M, et al. Evaluation of biological characteristics of *Abelmoschus esculentus*. *Int J Biochem Biophys Mol Biol* [Internet]. 2020;5(2):44–51. Available from: [<URL>](#).
34. Hamiduzzaman M, Sarkar M. Evaluation of biological activities of *Abelmoschus esculentus* (Malvaceae). *Int J Curr Microbiol Appl Sci* [Internet]. 2014;10:43–9. Available from: [<URL>](#).
35. Li YX, Deng DY, Liao HB, Zhou H, Liu H liang, Yuan K. Chemical constituents of *Abelmoschus esculentus* fruit and biological activity. In: *Medicine and Biopharmaceutical* [Internet]. World Scientific; 2016. p. 1040–8. Available from: [<URL>](#).
36. Doreddula SK, Bonam SR, Gaddam DP, Desu BSR, Ramarao N, Pandey V. Phytochemical analysis, antioxidant, antistress, and nootropic activities of aqueous and methanolic seed extracts of ladies finger (*Abelmoschus esculentus* L.) in mice. *Sci World J* [Internet]. 2014 Jan 1;2014(1):519848. Available from: [<URL>](#).
37. Siddique MH, Ashraf A, Hayat S, Aslam B, Fakhar-e-Alam M, Muzammil S, et al. Antidiabetic and antioxidant potentials of *Abelmoschus esculentus*: *In vitro* combined with molecular docking approach. *J Saudi Chem Soc* [Internet]. 2022 Mar 1;26(2):101418. Available from: [<URL>](#).



Synthesis and Characterization of Binary Azides (e.g. RbN_3) via Ion-Exchange Method

Semih Afyon^{1*} 

¹Gebze Technical University, Energy Technologies Institute, Gebze, Kocaeli, 41400 Turkey.

Abstract: Azides have garnered significant interest in chemical research for their diverse properties and applications, ranging from their use in airbags and detonators to their roles in photochemistry. Despite this attention, there remains a dearth of detailed studies focusing on the synthesis and characterization of binary azides. In this study, a robust and safe method for the synthesis of RbN_3 via ion exchange is presented, addressing the inherent challenges associated with handling highly explosive alkali metal azides. The experimental procedure, conducted under stringent safety measures, resulted in the successful production of high-purity RbN_3 , as confirmed by X-ray powder diffraction (XRPD), Fourier-transform infrared spectroscopy (FTIR), and Raman spectroscopy analyses. XRPD data with the reference intensity ratio method (RIR) confirmed phase purity above 99 %, which is in good agreement with the elemental ratio found by SEM-EDX analysis. The synthesized RbN_3 exhibited crystalline white powder morphology, free from impurities, thus demonstrating the efficacy of the ion exchange approach. X-ray powder diffraction (XRPD) and Vibrational spectroscopy analyses provided additional insights into the structure and purity of RbN_3 in accordance with theoretical expectations; the characteristic vibrational modes for N_3^- could be well found at the expected theoretical and experimental ranges. These findings show an easy, safe, and reliable method for synthesizing binary azides and contribute to a deeper understanding of azide chemistry, with implications for various scientific disciplines.

Keywords: Azides, Ion-Exchange, Vibrational Spectroscopy.

Submitted: May 12, 2024. **Accepted:** September 16, 2024.

Cite this: Afyon S. Synthesis and Characterization of Binary Azides (e.g. RbN_3) via Ion-Exchange Method. JOTCSA. 2024;11(4): 1527-34.

DOI: <https://doi.org/10.18596/jotcsa.1482884>

***Corresponding author's E-mail:** safyon@gtu.edu.tr

1. INTRODUCTION

Azides were first discovered 100 years ago, and since then, they have received great attention due to their interesting chemistry and properties, such as shock and friction sensitivity and explosive and energetic nature. With such properties, the applications of azide compounds are rich from the binary azides (e.g., NaN_3) in the fields of nitrogen sources, airbags, detonators, and biocides to the Heteroleptic complex (C_6H_5)₃PAu^I[N_3] in the field of photochemistry (1). The research on azide chemistry is also vast and contains many examples of Homoleptic Azido Complexes (1-6) and Heteroleptic Azido Complexes (7-9). The azide ion (N_3^-) acts as a terminal and a bridging ligand in these complexes, as shown in the literature (10,11).

The azide chemistry was thoroughly investigated by Beck et al. starting in the 1960s (5). More recently,

Haiges discussed the syntheses, properties, and crystal structures of various metal oxopolyazides (12). The coordination properties of the first binary titanium azides, including $[\text{Ti}(\text{N}_3)_4]$, $[\text{Ti}(\text{N}_3)_5]^-$, and $[\text{TiN}_3)_6]^{2-}$ were investigated (13). Christie et al. also studied the crystal structure and vibrational spectroscopy of the binary zirconium and hafnium polyazides $[\text{PPh}_4]_2[\text{M}(\text{N}_3)_6]$ ($\text{M}=\text{Zr}, \text{Hf}$) (14). Polyazido adducts $[(\text{bpy})\text{Ti}(\text{N}_3)_4]$, $[(\text{phen})\text{Ti}(\text{N}_3)_4]$, $[(\text{bipy})_2\text{Zr}(\text{N}_3)_4]_2 \bullet \text{bpy}$, and $[(\text{bipy})_2\text{Hf}(\text{N}_3)_4]_2 \bullet \text{bpy}$ were recently reported by Saal and coworkers (15). Many other successful examples of the synthesis and characterization of rich azide chemistry can be found in a recent review article by Beck et al. (5). In most of these investigations, the binary azides of alkali metals such as LiN_3 , NaN_3 , KN_3 , RbN_3 , and CsN_3 that contain symmetric azide anions are used to synthesize the more complex compounds. These binary azides can be described as hard to handle, unstable, and decomposing when exposed to heat and light. Thus, it is important to obtain binary

azides using a safe and sound method. Most of the investigations use NaN_3 directly in acidic or solvent mediums to directly synthesize other binary azides or complex azides that can lead to impurities and safety hazards, and there is a lack of research in the detailed synthesis and characterization of binary azides (16-18). These methods specifically consist of reacting a soluble inorganic azide (usually NaN_3) with a soluble target compound salt, usually nitrate or acetate salts, in an aqueous solution, forming the target azide compound as a precipitate (19,20). However, in these methods, the precipitate could usually be contaminated with the cation originating from the educt azide (e.g., NaN_3) and the anion coming from the target azide educt (e.g., nitrate or acetate). In addition, there is a lack of research on alternative synthesis methods for binary azides in literature (5,16). Therefore, herein, the high-purity synthesis and characterization of RbN_3 via an ion exchange method are presented. As the soluble inorganic azide cation (e.g., Na^+) is trapped in the ion-exchange column, and carbonates would react to form $\text{CO}_{2(g)}$, leaving the reaction vessel, high purity can be obtained at the end by this method. Binary azide, RbN_3 , is first synthesized through a column ion exchange method, and the compound is later crystallized through the evaporation of a solvent medium. The synthesis and physical characterization, through X-ray powder diffraction, FTIR, and Raman spectroscopy, are reported in detail.

2. EXPERIMENTAL SECTION

2.1. Synthesis

Alkali metal azides have highly explosive natures, so all material handlings must be carried out with utmost care and under extreme safety cautions (e.g. protective shields, goggles, shock-resistant gloves etc.). Also, the minute amount of samples should be used in order to prevent damage in case of an explosion hazard. For the synthesis of alkali metal binary azides, first, the resin column ($l = 800$ mm, $\varnothing_i = 14$ mm) was filled with acidic cation-exchange resin (Merck). Then, the resin column was exchanged for an H^+ cycle using a 1M solution of H_2SO_4 . Distilled water was passed through the ion exchange column afterward to wash away the excess amount of H_2SO_4 . Afterward, NaN_3 (Merck 99.9 %) was dissolved in water to obtain a 2M solution; 2M solution of NaN_3 was then passed through the H^+ loaded ion exchange column, resulting in HN_3 (the drop rate of HN_3 solution is adjusted to 5 mL/min.) at the end of the column reacting with Rb_2CO_3 as shown in Figure 1.

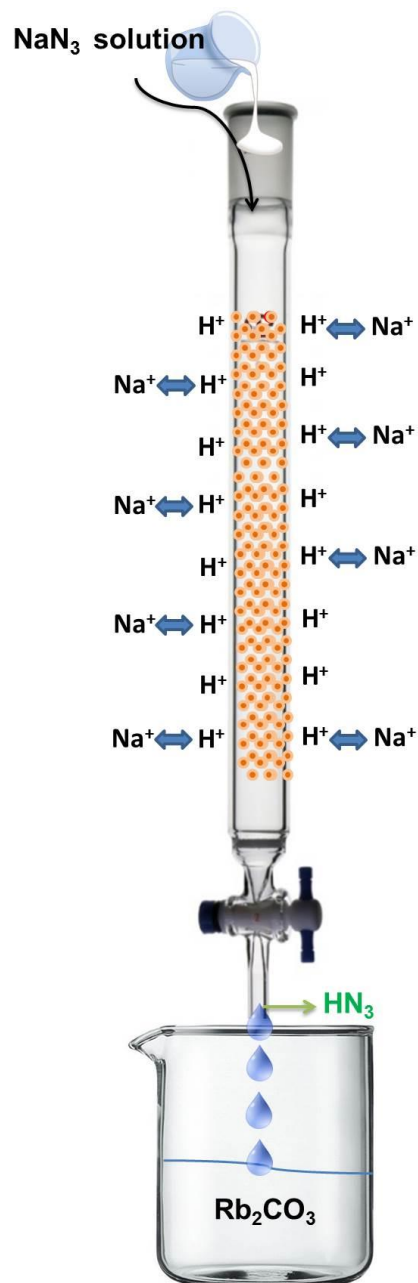


Figure 1: Synthesis scheme of RbN_3 via ion-exchange method.

In order to pass the newly formed HN_3 through the ion column to the end of the column, distilled water was added continuously on top of the column to keep the ion-exchange resin wet during the exchange. The formation of HN_3 at the end of the column was confirmed by checking the pH in different time intervals Table 1.

Table 1: pH control for HN_3 formation.

Time (minutes)	pH
0	6.8
5	6.5
15	5.7
20	4.9
25	4.1

The other binary azides chosen from alkali and earth alkali metals can also be synthesized similarly with the change of carbonate source. The completion of the reaction ($\text{Rb}_2\text{CO}_3 + 2\text{HN}_3 \rightarrow 2\text{RbN}_3 + \text{H}_2\text{CO}_3$) was controlled with the disappearance of any solid residue in the reaction and the pH control of the medium that should be in the range of $\sim \text{pH} = 4$. The white powder, RbN_3 was obtained at the end by the evaporation of the remaining solvent at 40-50 °C overnight. The evaporation temperatures above 50 °C should be prevented due to the explosive nature of azides.

2.2. Characterization

Fourier-transform infrared spectroscopy (FTIR) was measured with a Thermo Scientific Nicolet iS10 spectrometer (a single reflection diamond attenuated total reflectance (ATR) module). Renishaw Raman microscope equipped with a 532 nm laser as the excitation source was used to perform Raman spectroscopy. The phase and purity of RbN_3 were determined by X-ray powder

diffraction (XRPD) using a Rigaku MiniFlex X-ray diffractometer and $\text{Cu K}\alpha_1$ radiation (operated at 15 mA, 40 kV). Scanning electron microscope measurements were performed SEM, Thermo Fisher Quattro ESEM FE-SEM.

3. RESULTS AND DISCUSSION

At the end of the synthesis via the ion exchange method, a crystalline white powder was acquired. This powder was carefully ground in an agate mortar for the X-ray powder diffraction (XRPD) analysis, and excessive force was avoided during grinding to prevent the explosion of azides. The XRD powder pattern (XRPD) of the synthesized RbN_3 is shown in Figure 2. The XRPD pattern of RbN_3 synthesized via ion exchange method directly matches the theoretical pattern, and no impurity phases can be detected. The phase purity was found to be above $\sim 99\%$, which was calculated through the reference intensity ratio (RIR) method (21).

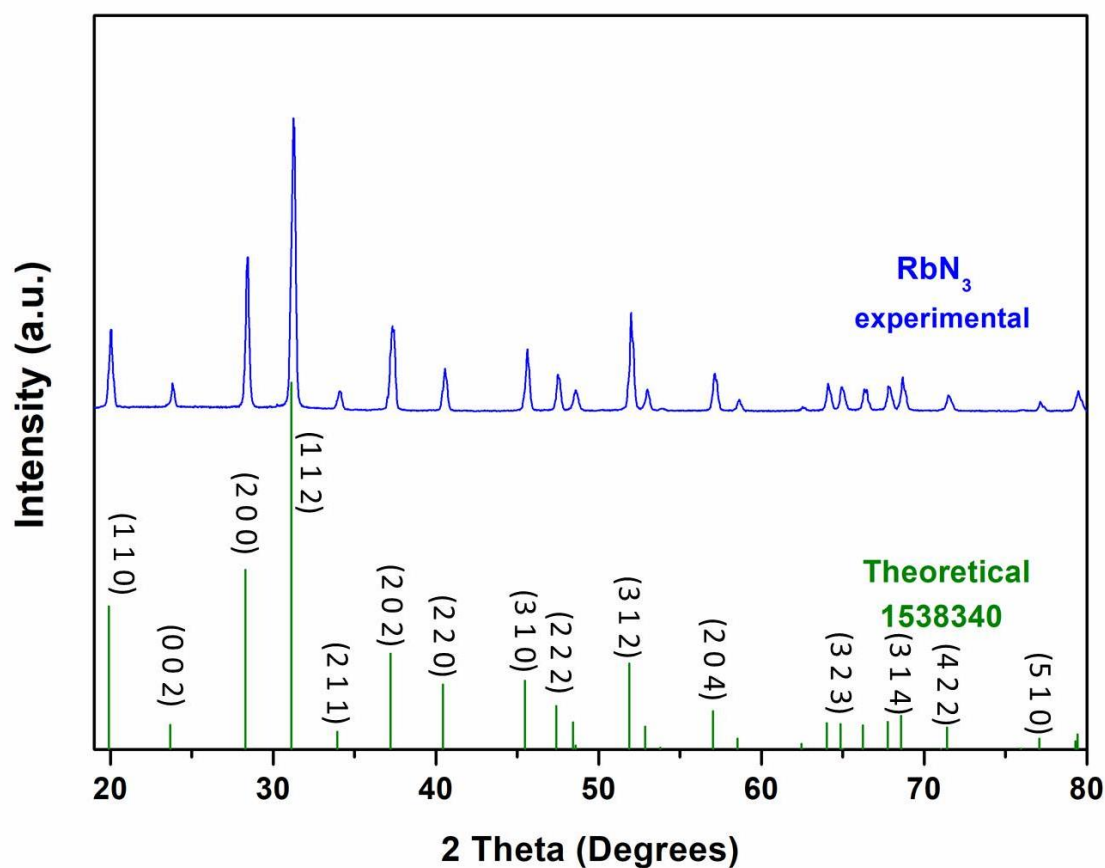


Figure 2: XRPD pattern of the ion-exchange synthesized RbN_3 vs the theoretical pattern (Crystallography Open Database no 1538340).

The vibrational spectroscopy analysis is in good agreement with XRPD analyses in terms of confirming the high purity of the RbN_3 phase after the synthesis and is also comparable to the NaN_3 phase. The common spectroscopic relevant unit in RbN_3 can be assigned as the discrete $(\text{N}_3)^-$ moiety with the symmetry $D_{\infty h}$. In line with this assignment, the vibrational spectra can be investigated in general within four well-separated wave regions (1,5,6,22). The vibrations' most common (N-N-N) stretching modes can be

distinguished into two separate sets of frequencies between $1200\text{--}1500\text{ cm}^{-1}$ and $1700\text{--}2100\text{ cm}^{-1}$. The range $500\text{--}800\text{ cm}^{-1}$ is dominated by in and out of plane (o.o.p.) deformations $\delta(\text{N-N-N})$ and $\gamma(\text{N-N-N})$ of the azido group. The valence and bending vibrations of the metal nitrogen bonds, as well as lattice vibrations, appear below 400 cm^{-1} , which cannot be clearly assigned due to their overlap in Raman spectra and device limitation in FTIR spectra.

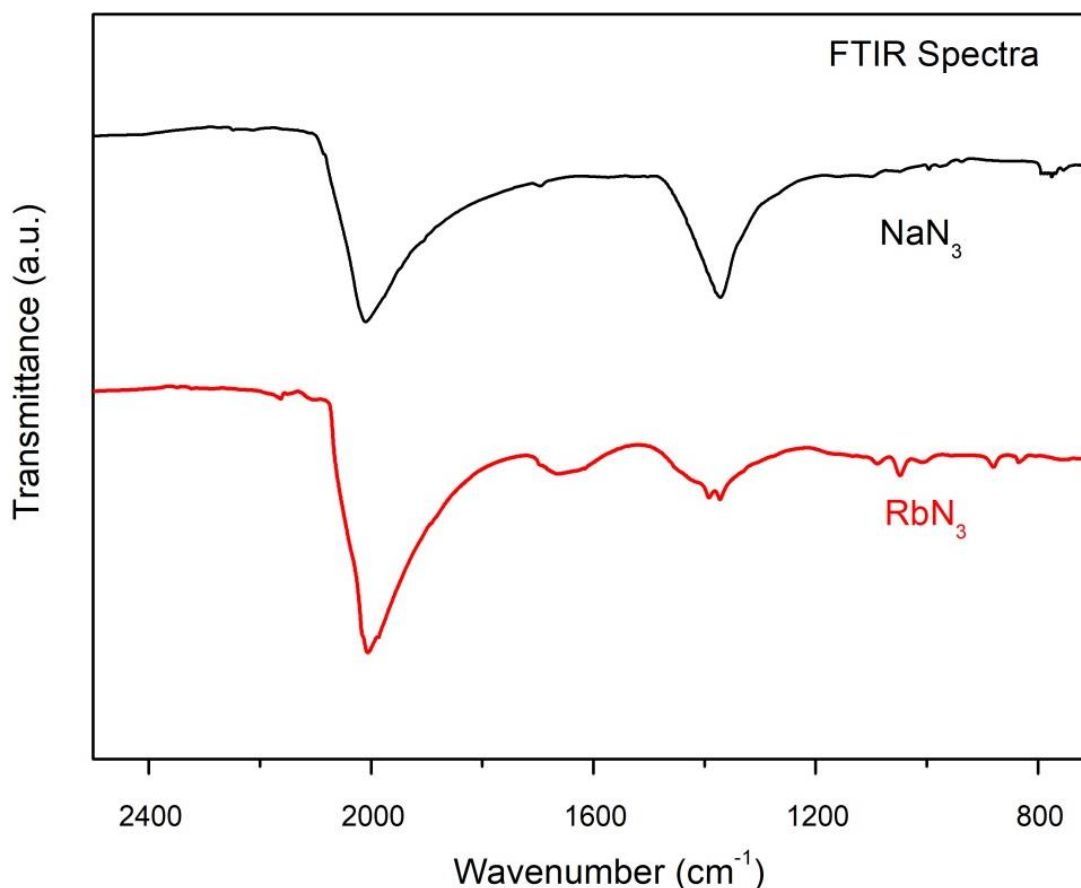


Figure 3: FTIR spectrum of the ion-exchange synthesized RbN₃ vs NaN₃ educt.

Specifically, the FTIR spectra of the synthesized RbN₃ and the comparison to the NaN₃ educt used for the synthesis are depicted in Figure 3. The valence modes for the azido group can be assigned to the peaks at ~ 2010 cm⁻¹ and 1370 cm⁻¹. The peaks below 1000 cm⁻¹ stem from the bending modes of the azide moiety, as well as from combination modes, and the findings are in alignment with literature findings (1,5,6). The valence and bending vibrations of the metal nitrogen bonds are expected to appear below 400-500 cm⁻¹, but they are not recorded due to the device measurement limitation.

The Raman spectra of the synthesized RbN₃ and the comparison to the NaN₃ educt used for the synthesis are depicted in Figure 4. Again, Raman spectroscopy analysis is in good agreement with XRPD and FTIR analyses in terms of confirming the high purity of RbN₃ phase after the synthesis, and also directly comparable to the NaN₃ phase confirming the reaction of Rb₂CO₃ with HN₃ producing RbN₃. The peaks appearing at 1335 cm⁻¹ and 1265 cm⁻¹ in the Raman spectrum of RbN₃ can be assigned as the stretching modes of the azide group in RbN₃ (17). The valence and bending

vibrations of the metal nitrogen bonds are observed below 400 cm⁻¹ in Raman spectra but are hard to distinguish due to the overlap in this region. Nevertheless, all analyses (XRPD, FTIR, and Raman) performed confirmed the successful synthesis via ion exchange method and revealed similar results in terms of the purity of the synthesized compound.

Scanning electron microscopy (SEM)-EDX analysis of the ion-exchange synthesized RbN₃ is depicted in Figure 5. The shape of the particles is not very well-defined, and the crystallite size of RbN₃ particles approximately ranges from 2 μ m to 5 μ m. These crystallites seemingly form larger agglomerates in the range of 20 to 50 microns. The EDX analysis confirms the phase pure synthesis that is in good agreement with XRPD, FTIR, and Raman analyses shown and discussed in detail. The elemental weight ratio for Rb and N were found to be 68.52 wt-% and 31.48 wt-%, respectively, from the analysis, which is very close to theoretical values of 67.03 wt-% and 32.97 wt-% expected for RbN₃, and corroborating the high purity phase obtained by the ion-exchange synthesis.

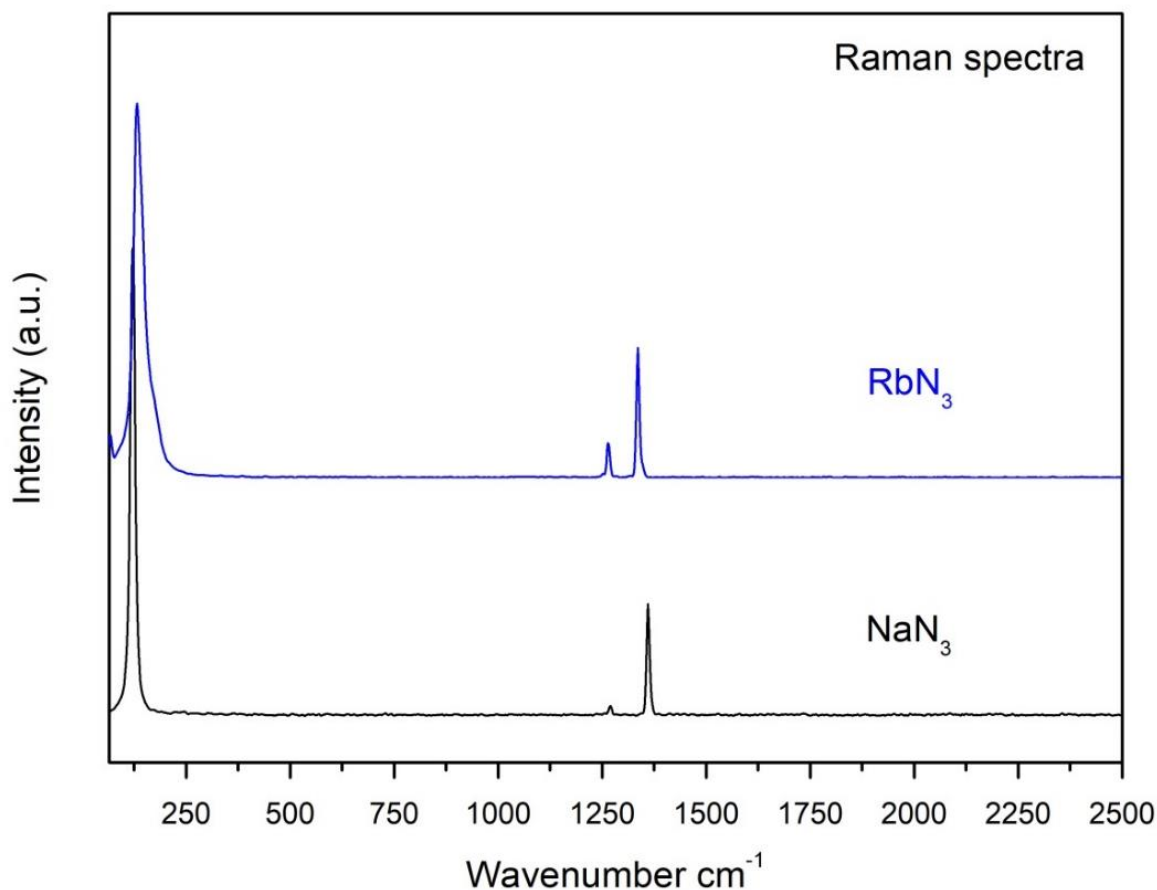


Figure 4: Raman spectrum of the ion-exchange synthesized RbN_3 vs NaN_3 educt.

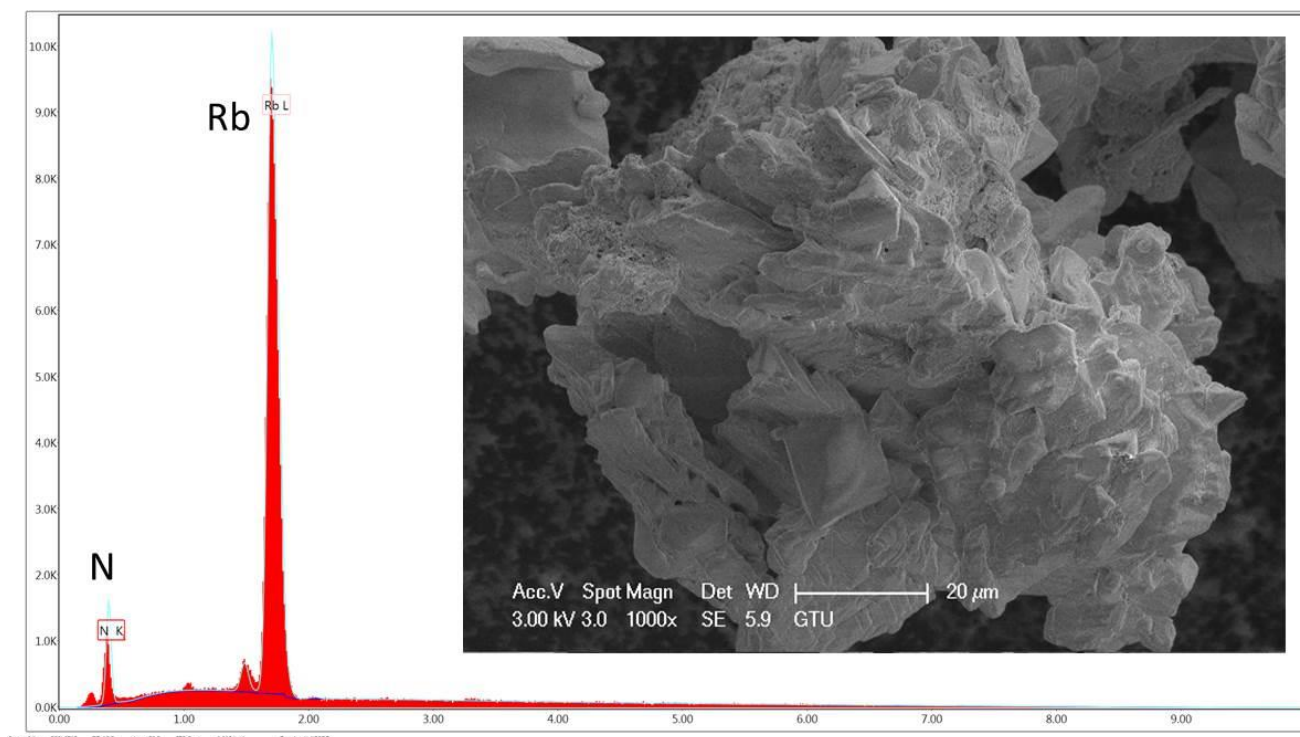


Figure 5: SEM-EDX analysis of the ion-exchange synthesized RbN_3 .

4. CONCLUSION

In conclusion, azides have captivated the interest of researchers for over a century due to their intriguing chemistry and diverse applications, ranging from their use in airbags and detonators to various other fields. Even with the extensive

exploration of azide chemistry in literature, there remains a gap in detailed research on the synthesis and characterization of binary azides. In this study, a robust and safe method for the synthesis of RbN_3 via ion exchange was presented. The meticulous experimental procedure, outlined with utmost safety precautions, yielded high-purity RbN_3 , as confirmed

by X-ray powder diffraction (XRPD), Fourier-transform infrared spectroscopy (FTIR), and Raman spectroscopy analyses. X-ray powder diffraction (XRPD) coupled with the reference intensity ratio (RIR) analysis confirmed a phase purity above $\sim 99\%$. The synthesized RbN_3 exhibited a crystalline white powder morphology confirmed by optical observations and SEM-EDX analysis, devoid of impurities, thus affirming the efficacy of the ion exchange method. Further characterization analyses by vibrational spectroscopy (FTIR and Raman) provided additional insights into the structure and purity of RbN_3 , aligning well with theoretical expectations and confirming the successful synthesis. These findings underscore the importance of developing safe and reliable methods for the synthesis of binary azides and pave the way for future research exploring their potential applications across various fields. Moreover, this study contributes to the broader understanding of azide chemistry, offering valuable insights into the synthesis and characterization of complex azide compounds.

5. CONFLICT OF INTEREST

There is no conflict of interest.

6. ACKNOWLEDGMENTS

The author thanks Koç University and Gebze Technical University for the use of characterization facilities.

7. REFERENCES

1. Guven G, Topcu A, Somer M, Afyon S, Yilmaz A, Bolukbasi O. Vibrational spectra, force constants and quantum chemical calculations of μ -1,3-azide bridged triphenylphosphine complexes of copper(I) and silver(I). *Vib Spectrosc* [Internet]. 2022 Mar;119:103354. Available from: [<URL>](#).
2. Wiberg E, Michaud H. Notizen: Zur kenntnis eines aluminiumtriazids $\text{Al}(\text{N}_3)_3$. *Zeitschrift für Naturforsch B* [Internet]. 1954 Jul 1;9(7):495–6. Available from: [<URL>](#).
3. Wiberg E, Michaud H. Notizen: Zur kenntnis eines bortriazids $\text{B}(\text{N}_3)_3$. *Zeitschrift für Naturforsch B* [Internet]. 1954 Jul 1;9(7):497–9. Available from: [<URL>](#).
4. Wiberg E, Michaud H. Notizen: Zur kenntnis eines magnesiumazids $\text{Mg}(\text{N}_3)_2$. *Zeitschrift für Naturforsch B* [Internet]. 1954 Jul 1;9(7):501–2. Available from: [<URL>](#).
5. Fehlhammer WP, Beck W. Azide chemistry – An inorganic perspective, part I metal -azides: Overview, general trends and recent developments. *Zeitschrift für Anorg und Allg Chemie* [Internet]. 2013 Jun 4;639(7):1053–82. Available from: [<URL>](#).
6. Subaşı Y, Tekin ES, Prots Y, Jach F, Somer M, Afyon S, et al. The first alkaline-earth azidoaurate(III), $\text{Ba}[\text{Au}(\text{N}_3)_4]_2 \cdot 4\text{H}_2\text{O}$. *Chem – A Eur*

J [Internet]. 2023 Feb 21;29(11). Available from: [<URL>](#).

7. Pettinari C. Copper(I) and silver(I) azide complexes containing N-donor ligands. *Polyhedron* [Internet]. 2001 Sep;20(21):2755–63. Available from: [<URL>](#).
8. Beck W, Fehlhammer WP, Pöllmann P, Schuierer E, Feldl K. Darstellung, IR- und elektronenspektren von azido-metall-komplexen. *Chem Ber* [Internet]. 1967 Jul 21;100(7):2335–61. Available from: [<URL>](#).
9. Kreuzer PH, Schorpp KT, Beck W. Darstellung und spektroskopische eigenschaften von planaren dipseudohalogeno-bis(phosphin)-platin(II)-komplexen/preparation and spectroscopic properties of planar dipseudohalogeno-bis(phosphine)-platinum(II) complexes. *Zeitschrift für Naturforsch B* [Internet]. 1975 Aug 1;30(7-8):544–9. Available from: [<URL>](#).
10. Khalaji AD, Amirnasr M, Falvello LR, Soler T. Crystal structure of bis(.MU.2-azido)-tetrakis(triphenylphosphine)-di-silver(I). *Anal Sci X-ray Struct Anal Online* [Internet]. 2006;22:X47–8. Available from: [<URL>](#).
11. Ziolo RF, Dori Z. Photochemical synthesis of thiocyanatobis(triphenylphosphine)copper(I). *J Am Chem Soc* [Internet]. 1968 Nov 1;90(23):6560–1. Available from: [<URL>](#).
12. Haiges R. Recent developments in the chemistry of metal oxopolyazides. *Dalt Trans* [Internet]. 2019;48(3):806–13. Available from: [<URL>](#).
13. Haiges R, Boatz JA, Schneider S, Schroer T, Yousufuddin M, Christe KO. The binary group 4 azides $[\text{Ti}(\text{N}_3)_4]$, $[\text{P}(\text{C}_6\text{H}_5)_4][\text{Ti}(\text{N}_3)_5]$, and $[\text{P}(\text{C}_6\text{H}_5)_4]_2[\text{Ti}(\text{N}_3)_6]$ and on Linear Ti-N-NN Coordination. *Angew Chemie Int Ed* [Internet]. 2004 Jun 14;43(24):3148–52. Available from: [<URL>](#).
14. Deokar P, Vasiliu M, Dixon DA, Christe KO, Haiges R. The binary group 4 azides $[\text{PPh}_4]_2[\text{Zr}(\text{N}_3)_6]$ and $[\text{PPh}_4]_2[\text{Hf}(\text{N}_3)_6]$. *Angew Chemie Int Ed* [Internet]. 2016 Nov 7;55(46):14350–4. Available from: [<URL>](#).
15. Saal T, Deokar P, Christe KO, Haiges R. The binary group 4 azide adducts $[(\text{bpy})\text{Ti}(\text{N}_3)_4]$, $[(\text{phen})\text{Ti}(\text{N}_3)_4]$, $[(\text{bpy})_2\text{Zr}(\text{N}_3)_4]_2\text{bpy}$, and $[(\text{bpy})_2\text{Hf}(\text{N}_3)_4]_2\text{bpy}$. *Eur J Inorg Chem* [Internet]. 2019 May 15;2019(18):2388–91. Available from: [<URL>](#).
16. Reckeweg O, Simon A. Azide und cyanamide – ähnlich und doch anders/azides and cyanamides – Similar and yet different. *Zeitschrift für Naturforsch B* [Internet]. 2003 Nov 1;58(11):1097–104. Available from: [<URL>](#).
17. Klapötke TM, Krumm B, Scherr M. The binary silver nitrogen anion $[\text{Ag}(\text{N}_3)_2]^-$. *J Am Chem Soc* [Internet]. 2009 Jan 14;131(1):72–4. Available from: [<URL>](#).

18. Hakimi M. Binuclear copper(I) complex constructed by two end-to-end, μ -1,3-azide bridges, $[\text{Cu}_2(\text{PPh}_3)_4(\mu\text{-N}_3)_2]$. Orient J Chem [Internet]. 2013;29(1):103–8. Available from: [<URL>](#).
19. Reitzner B, Manno RP. A new synthesis of lead azide. Nature [Internet]. 1963 Jun;198(4884):991–991. Available from: [<URL>](#).
20. Hagenbuch JP. Opportunities and limits of the use of azides in industrial production. Implementation of safety measures. Chimia (Aarau) [Internet]. 2003 Dec 1;57(12):773. Available from: [<URL>](#).
21. Hubbard CR, Evans EH, Smith DK. The reference intensity ratio, I/I_c , for computer simulated powder patterns. J Appl Crystallogr [Internet]. 1976 Apr 1;9(2):169–74. Available from: [<URL>](#).
22. Hathaway CE, Temple PA. Raman spectra of the alkali azides: KN_3 , RbN_3 , CsN_3 . Phys Rev B [Internet]. 1971 May 15;3(10):3497–503. Available from: [<URL>](#).



Adsorption of Ethylene and 1-methylcyclopropene (1-MCP) on Al-doped Graphene Structure: A DFT Study for Gas Sensing Application

Fatma Aydin^{1*} , Kivanc Sel^{2*} 

¹Department of Chemistry, Faculty of Sciences, Çanakkale Onsekiz Mart University, 17100 Çanakkale, Turkey.

²Department of Physics, Faculty of Sciences, Çanakkale Onsekiz Mart University, 17100 Çanakkale, Turkey.

Abstract: Ethylene is the ripening hormone of fruits and vegetables. 1-Methylcyclopropene (1-MCP) is used as the inhibitor of the ethylene actions for extending the postharvest shelf life of the plants. To control the ripening and extending the shelf life of the plants, the adsorption characteristics of ethylene and 1-MCP on Al-doped graphene structure (AIG) were investigated as a gas sensing application by density functional theory (DFT) calculations. The geometric structures were optimized, HOMO and LUMO, energy gap, adsorption energies, the density of states (DOS), electrostatic potential (ESP) and the global reactivities were calculated for different distances between the adsorbed ethylene or 1-MCP and the adsorbent AIG. Chemisorption and physisorption interactions were analyzed. For the chemisorption process of ethylene and 1-MCP on AIG, the adsorption energies were 19.34 kJ/mol and 56.53 kJ/mol, respectively. Whereas for the physisorption process, the adsorption energies of ethylene and 1-MCP were -60.16 kJ/mol and -7.32 kJ/mol, respectively. As a result, it was presented that the AIG structure has sufficient characteristics to be a good adsorbent and a gas sensor of ethylene and 1-MCP.

Keywords: Ethylene, 1-methylcyclopropene (1-MCP), Al-doped graphene, Density functional theory, Gas sensor.

Submitted: May 31, 2024. **Accepted:** September 25, 2024.

Cite this: Aydin F, Kivanc S. Adsorption of Ethylene and 1-methylcyclopropene (1-MCP) on Al-doped Graphene Structure: A DFT Study for Gas Sensing Application. JOTCSA. 2024;11(4): 1535-44.

DOI: <https://doi.org/10.18596/jotcsa.1492945>

***Corresponding author's E-mail:** faydin@comu.edu.tr, kivanc@comu.edu.tr

1. INTRODUCTION

Ethylene is widely known as the phytohormone responsible for the ripening of fruits and vegetables and its involvement in plant growth and development processes. It is naturally produced in plants via biochemical reactions defined as the Yang cycle (1). Additionally, ethylene gas added to the environment is also used in ripening rooms under modified atmosphere conditions. On the other hand, to prevent unwanted ripening the ethylene level better be continuously monitored inside the conservation chambers to maintain the appropriate storage conditions and to extend the shelf life of fruits and vegetables (2). Fruit suppliers will need information to reduce economic losses by control ripening time during fruit storage. For this purpose, the use of practical and sensitive sensors to be developed will be more efficient in completing the processes (3).

1-Methylcyclopropene (1-MCP) (C_4H_6) has been developed commercially and is used as a synthetic

plant regulator. It is a cycloalkene compound and exists as a gas at room temperature (4). Since it inhibits the ethylene receptor, it is used to delay the ripening and softening process of the plants by reducing the respiration rate. Due to the use of 1-MCP for some fruits, color development slows down compared to those that are not used (5,6). It not only significantly reduces the respiration of the plants but also keeps the product hardness, brittleness, color, flavor, aroma and nutrients. As a result of this, the use of 1-MCP in the post-harvest preservation of fruits and vegetables has become widespread. On the other hand, no toxic properties and no detectable odor of its use have been reported (7-10).

There are many studies in the qualitative determination of 1-MCP and various chemical reagents are needed for this (11). Due to the physical and chemical properties of the 1-MCP molecule, such as vapor pressure of 570 mm Hg at 25 °C and molecular weight of 54 g/mol, GC-MS or LC-MS/MS analysis methods are widely used for the analysis of

1-MCP, but effective and accurate quantitative analysis presents difficulties.

However, since the molecular weight of 1-methylcyclopropene is small, the traditional detection method cannot accurately quantify it due to the possibility of interference with trace volatile compounds in fruits and vegetables, and therefore the research needs of sensitive and accurate analysis techniques cannot be met (12). For this reason, since 1-MCP is a gas molecule, the gas sensor to be developed will facilitate the detection process.

Graphene, which is a flat mesh of regular hexagonal rings, is a two-dimensional monolayer structure containing only carbon atoms. Although graphene contains many carbon atoms in two dimensions, it contains only one layer of carbon in the third dimension, making it one of the thinnest materials with the best surface-to-weight ratio. Since its discovery in 2004 (13,14), many theoretical and experimental researches have been carried out on physical or chemical interactions of graphene and various metal-doped graphene structures with various chemicals. Recently, experimental and theoretical gas sensor studies have been reported for the detection of various gases such as NO₂, N₂O, H₂O, HF, CO₂ etc. on graphene (15-17).

The Van der Waals interaction between the carbon atoms of graphene and the atoms of the adsorbed gas molecule is relatively weaker than the other bonding types. In this respect, this interaction with the atoms of various adsorbed gas molecules could occur within the limit of a relatively close band of energies and/or bonding coordination. On the other hand, metal-doped graphene can interact with various gas molecules by the Van der Waals, covalent and especially coordinate covalent bonding types due to their Lewis acid-base properties. In this respect, metal doping to graphene could improve the sensitivity and selectivity of graphene as a gas sensor. Recent studies have shown that various metal-doped graphene systems have much higher adsorption energy and higher net charge transfer value than pure graphene due to Lewis acid-base interaction (18). After graphene is doped with N which has Lewis base properties, carbon atoms lose electrons while nitrogen atoms gain electrons. On the other hand, when graphene is doped with Al, which has Lewis acid properties, carbon gains electrons while aluminum atoms lose electrons. The low frequency absorption peak of Al-doped graphene shifts to lower energy compared to pure graphene, making the transitions between n and n^* easier. This situation shows that it can lead to an opened gap and reveals the feature of being used as a sensor (19).

Many researches have been focused on metal-doped graphene such as Lewis acid Al, Si, P, B, Ge, Ga, etc. (20-23). Most recently, Al-doped graphene (AlG) was suggested to be a promising structure as a novel molecular sensor to NH₃ (24), NO₂ and N₂O (25), CO and CO₂ (26), some halo-methane (27), CH₄ (28), etc. molecules. The B and N doped graphene have also been investigated for the toxic gaseous such as cyanide, formaldehyde and phosgene (29-31).

Moreover, the interactions of various molecules such as acrolein (32), guanine (33), cyanuric fluoride (CF) and s-triazine (ST) (34) onto Al-doped graphene have also been examined theoretically.

In this study, due to its importance for post-harvest preservation of some agricultural products, it was considered to design high-performance gas sensor study for the determination of ethylene and 1-MCP molecules. For this purpose, the adsorption of ethylene and 1-MCP molecules on Al-doped graphene structure (C₂H₄/AlG and 1-MCP/AlG, respectively) was investigated, using the density functional theory (DFT) calculations. The characterization of ethylene, 1-MCP and AlG and also the adsorption of these molecules on the Al-doped graphene were investigated and compared in detail.

2. EXPERIMENTAL SECTION

2.1. Computational Details

In this study, the first principles based on DFT calculations were performed (35,36) by using the Quantum ESPRESSO (QE) computational package (QE) (37-39). The ultrasoft pseudopotential (USPP) (40) approach for the core-valence interactions and Perdew-Burke-Ernzerhof (PBE) (41) approximation for the exchange-correlation functional have been applied as implemented in the QE package. A cubic unit cell and the structures were built by using XCRYSDEN (42) and VESTA (43) packages. In order to prevent the interactions between the adjacent structures, the dimensions of the cubic unit cell were set to 20 Å. In the DFT calculations, all atoms and all the bonds are relaxed. The AlG structure includes 36 carbon atoms and 1 Al atom that was located at the center of the cluster structure. All dangling carbon atom bonds of the AlG were saturated with 15 Hydrogen (H) atoms to neutralize the charge on the structure. The kinetic energy cutoff for the description of Kohn-Sham orbitals and for the charge density and potential were set at 50 Ry and 400 Ry, respectively. The convergence threshold for each consecutive self-consistency step was set at 10⁻⁸ Ry and 7x7x1 Monkhorst-Pack grid were used for k-point sampling (44). The geometry of the structures was optimized and bond lengths were determined. Highest occupied molecular orbital (HOMO) and lowest unoccupied molecular orbital (LUMO) energies were calculated and the energy gap (E_g) was obtained by using the HOMO (E_{HOMO}) and LUMO (E_{LUMO}) energies.

$$E_g = E_{LUMO} - E_{HOMO} \quad (1)$$

The adsorption energies (E_{ads}) were calculated by the following equation.

$$E_{ads} = E_{system} - E_{adsorptive} - E_{adsorbed} \quad (2)$$

where E_{system} refers to the energy of C₂H₄/AlG or 1-MCP/AlG, the adsorptive energy ($E_{adsorptive}$) is the energy of AlG and $E_{adsorbed}$ is the energy of ethylene or 1-MCP. Density of states (DOS) and electrostatic potential (ESP) were calculated. The global indices of reactivity of the structures were investigated by

calculating the chemical hardness (η), chemical potential (μ) and electrophilicity (ω) (45-47).

$$\eta = \frac{(E_{\text{LUMO}} - E_{\text{HOMO}})}{2} \quad (3)$$

$$\mu = -\frac{(E_{\text{LUMO}} + E_{\text{HOMO}})}{2} \quad (4)$$

$$\omega = \frac{\mu^2}{2\eta} \quad (5)$$

3. RESULTS AND DISCUSSION

3.1. The structure of ethylene, 1-MCP and AIG

The structure of ethylene, 1-MCP molecules and AIG, which was optimized by DFT calculations, was presented in Fig. 1 and the optimized bond lengths were listed in Table 1, respectively. From Table 1, 1-MCP, being a cyclopropene, has a shorter π -bond of 1.2994 Å ($\text{C1}_M\text{-C3}_M$) than that of the ethylene, 1.3317 Å. A similar difference was also observed between the C-H bonds of 1-MCP (1.0828 Å) and ethylene (1.0907 Å).

The optimized structure of AIG was presented from the top and the side views in Fig. 1(c) and Fig. 1(d). The $2\text{ sp}^2 - 3\text{ sp}^2$ hybridization of the three carbon atoms in the graphene with the aluminum atom disrupts the planarity at an angle of 120 degrees and turned the planar structure of graphene into an umbrella-like structure. Moreover, the empty p_z hybrid orbital of octet-deficient aluminum gave the AIG extraordinary properties such as Lewis acidity (48). The calculated bond lengths of the Al atom with the neighboring C atoms (1.846 Å) were slightly greater than the C-C bond length in the pristine graphene structure (Table 1). At the same time, the C-C bond lengths of the other neighboring C atoms were different from those of the graphene. In other words, since the remarkable negative potential distributes on the location of the Al atom, in the aluminum-centered-doped graphene (AIG) the aromatic homogeneity of the pure graphene was changed, relatively.

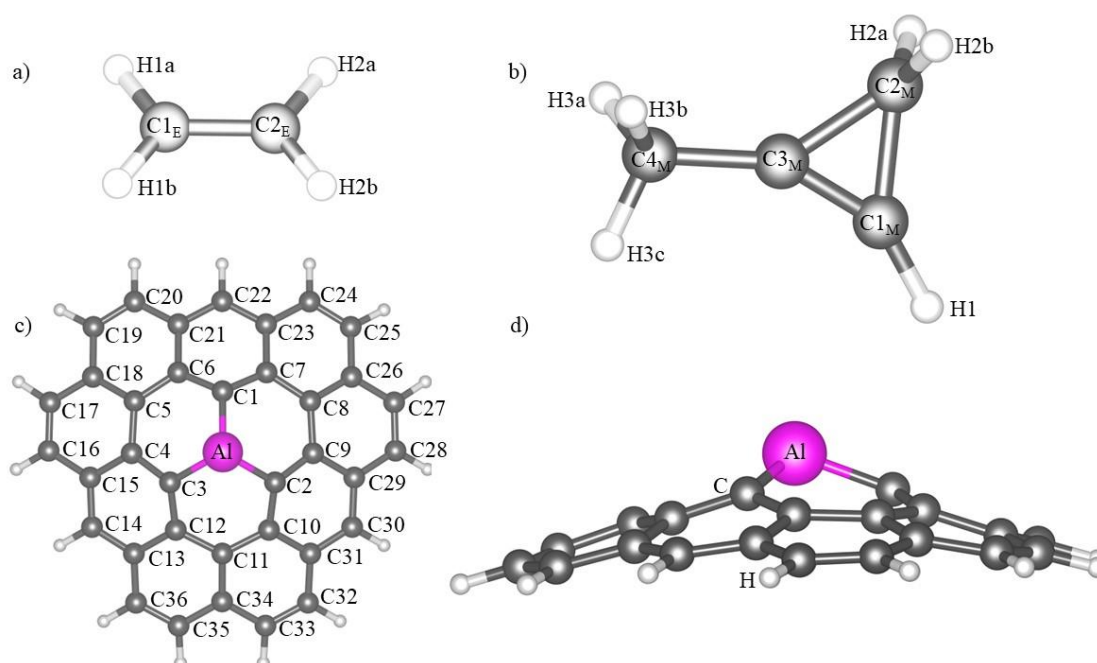


Figure 1: The optimized geometric structure of ethylene (a), 1-MCP (b) and top (c) and side (d) views of AIG.

Table 1: The optimized bond lengths of ethylene, 1-MCP and AIG.

C_2H_4 (Å)		1-MCP (Å)		AIG (Å)			
$\text{C1}_E\text{-C2}_E$	1.3317	$\text{C1}_M\text{-C2}_M$	1.5109	C1-Al	1.8466	C4-C5	1.4781
$\text{C1}_E\text{-H1a}$	1.0907	$\text{C2}_M\text{-C3}_M$	1.5117	C2-Al	1.8466	C5-C6	1.4780
		$\text{C1}_M\text{-C3}_M$	1.2994	C3-Al	1.8466	C6-C21	1.4397
		$\text{C3}_M\text{-C4}_M$	1.4716	C3-C4	1.4114	C19-C20	1.3652

3.2. Orbital Analysis of Ethylene, 1-MCP and AIG

Frontier molecular orbitals (HOMO and LUMO) and the HOMO and LUMO energies and the DOS of ethylene, 1-MCP and AIG were calculated and presented in Fig. 2, Fig. 3, Fig. 4 and Table 2, respectively. As can be seen in Fig. 2, the HOMO of ethylene was symmetrically localized on the $\text{C1}_E\text{-C2}_E$ bond and the LUMO was on the opposite side. The HOMO of 1-MCP was relatively located more on the

carbon atom C1_M due to the inductive effect of the methyl group (Fig. 3). The energy gap (E_g) of 1-MCP, that was calculated by using Eq. (1), ($E_g = 5.01\text{ eV}$) was smaller than that of ethylene ($E_g = 5.68\text{ eV}$).

In Fig. 4, the HOMO of AIG was partially localized over the aromatic π -clouds in the carbon rings, while the LUMO was mainly centered over the Al atom of the AIG. Depending on that the greatest extension of

LUMO shape was on the Al atom, the electrophilic reactions between ethylene or 1-MCP and AIG were expected to be observed on the Al atom. The HOMO and LUMO energies of AIG were -4.47 and -3.01 eV, respectively and the energy gap was 1.48 eV (Table

3). In addition to these, due to the relatively lower LUMO energy with respect to that of ethylene and 1-MCP, AIG can be considered to be a good electron acceptor to adsorb the ethylene or 1-MCP molecules.

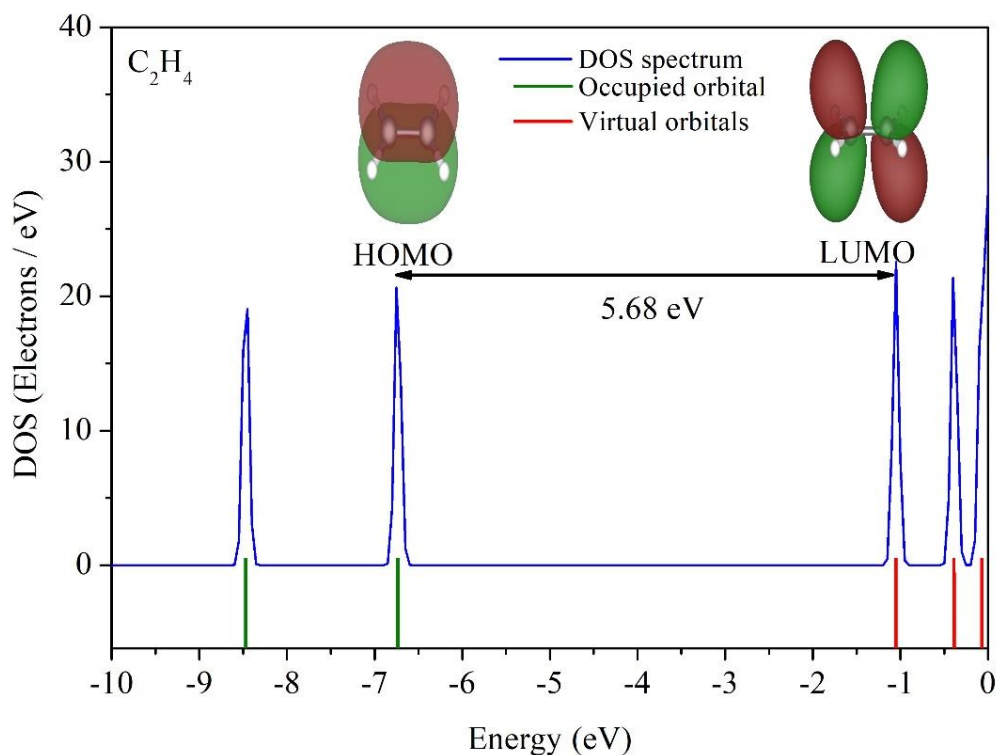


Figure 2: The graph of DOS as a function of energy and the HOMO and LUMO and energy gap of ethylene.

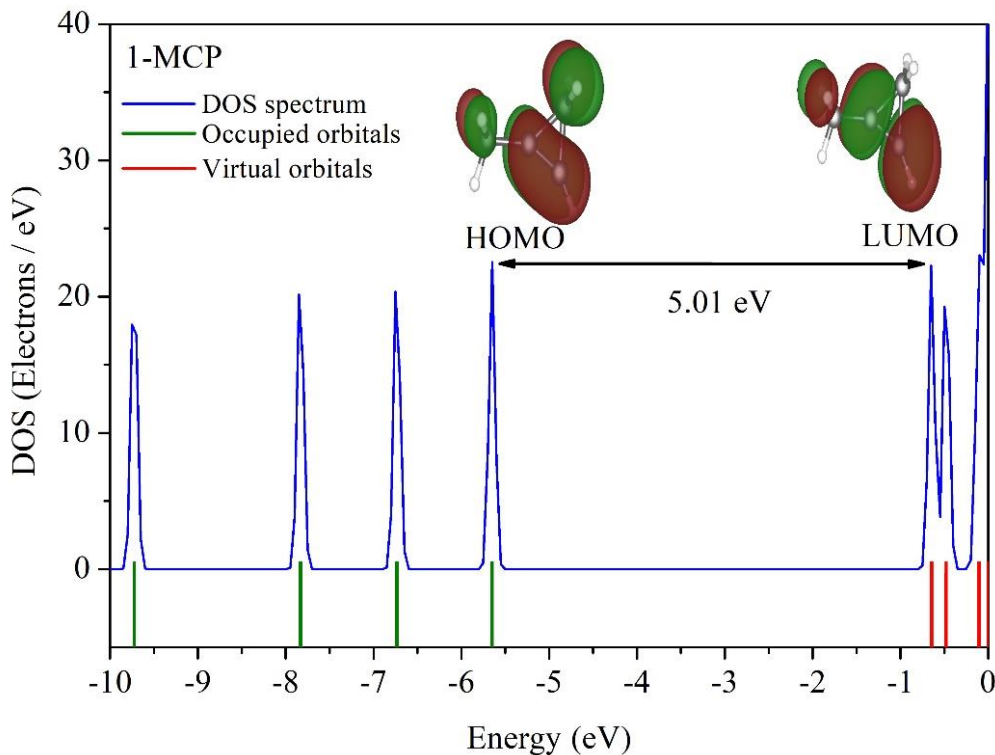


Figure 3: The graph of DOS as a function of energy and the HOMO and LUMO and energy gap of 1-MCP.

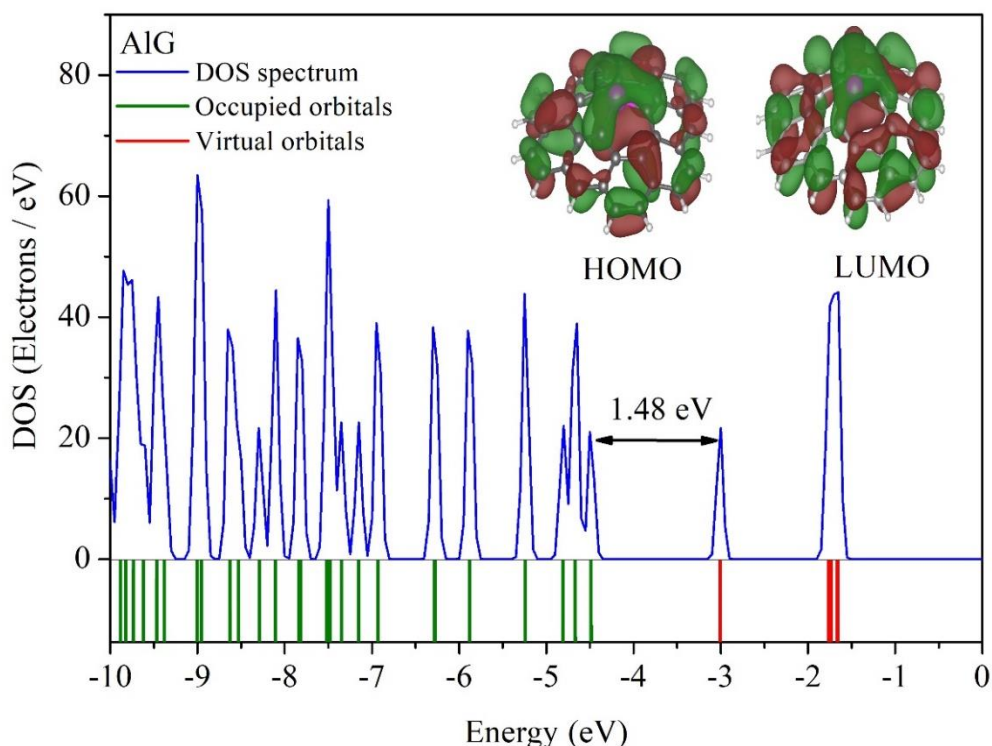


Figure 4: The graph of DOS as a function of energy and the HOMO and LUMO and energy gap of the AlG.

3.3. Adsorption of Ethylene and 1-MCP Molecules on AlG and Global Reactivity Analysis

Ethylene and 1-MCP can be physically and chemically adsorbed on AlG structure. In order to investigate both of these adsorption mechanisms of ethylene and 1-MCP on AlG, the adsorption was analyzed by considering the two structurally optimized systems, that in the first one the adsorbed molecule was relatively nearer to AlG than that in the second one, for each of the adsorbed molecules. In this respect, to determine the corresponding chemical and physical adsorption distances between the adsorbed molecules and the adsorbent structure in the first step of the analysis, a series of structural geometry optimizations and energy convergence analyses were performed for each of the molecules. As a result, for the physical adsorption mechanism of ethylene and 1-MCP at position 1 (P1) (2.38 and 2.45 Å, respectively) and for the chemical adsorption mechanism of them at position 2 (P2) (2.12 and 2.09 Å, respectively) were determined and presented in Fig. 5-8.

Ethylene molecule is π -ligand and it bonded to AlG as η^2 bridging ligand. 1-MCP molecule was bonded to AlG by a coordinate covalent bond, due to both the inductive effect of the methyl group and the steric factor. These differences in the bonding were also confirmed by the difference in the bond lengths in the optimized structure (Table 2). According to Fig. 5, the ethylene molecule was physically adsorbed at a distance of 2.38 Å, while it was chemically adsorbed as a η^2 bridging ligand at a bond length of 2.12 Å (Fig. 6). On the other hand, in Fig. 7, 1-MCP was physically adsorbed at a distance of 2.45 Å, while it was chemically adsorbed with a coordinated covalent bond with a bond length of 2.09 Å (Fig. 8). The difference in bond lengths highlights that 1-MCP was better adsorbed than ethylene on AlG.

The HOMO and LUMO energies of ethylene and 1-MCP on AlG (C_2H_4/AlG and $1-MCP/AlG$, respectively) for P1 were -4.15, -2.61 eV and -4.18, -2.69 eV, and for P2 were -4.19, -2.63 eV and -4.09, -2.57 eV, respectively (Table 3). Since aluminum atom has one valence electron less than that of carbon atom, AlG is an electron-deficient system. During the adsorption, there occurs an electron transfer from ethylene and 1-MCP molecules onto AlG. It was observed that ethylene forms a π -complex (a trigonal ring), and on the other hand, the bonding structure of 1-MCP over $C1_M$ carbon was relatively more stable, due to the steric and inductive effects of the methyl group.

Comparing the DOS of AlG (Fig. 4) to that of the C_2H_4/AlG and $1-MCP/AlG$ (Fig. 5, 6, 7, 8), a change in the confirmation of hybridization was determined. The E_g values of C_2H_4/AlG and $1-MCP/AlG$ structures were slightly greater than that of AlG for both positions (P1 and P2) (Table 3).

The global indices of reactivity of ethylene, 1-MCP, AlG, C_2H_4/AlG and $1-MCP/AlG$ were presented in Table 3, where chemical hardness (η), chemical potential (μ), electrophilicity (ω) were calculated using Eq. 3-5, respectively. The hardness of AlG decreases by the adsorption of ethylene or 1-MCP. The electrophilicity of AlG was higher than that of ethylene and 1-MCP. The adsorption energy (E_{ads}) of ethylene and 1-MCP, that was defined in Eq.2, was -60.16 kJ/mol and -7.32 kJ/mol for P1 and 19.34 kJ/mol and 56.53 kJ/mol for P2, respectively. The larger the adsorption energy and the shorter the distance between the adsorbed molecule and AlG suggest that 1-MCP has a better chemical bonding than ethylene.

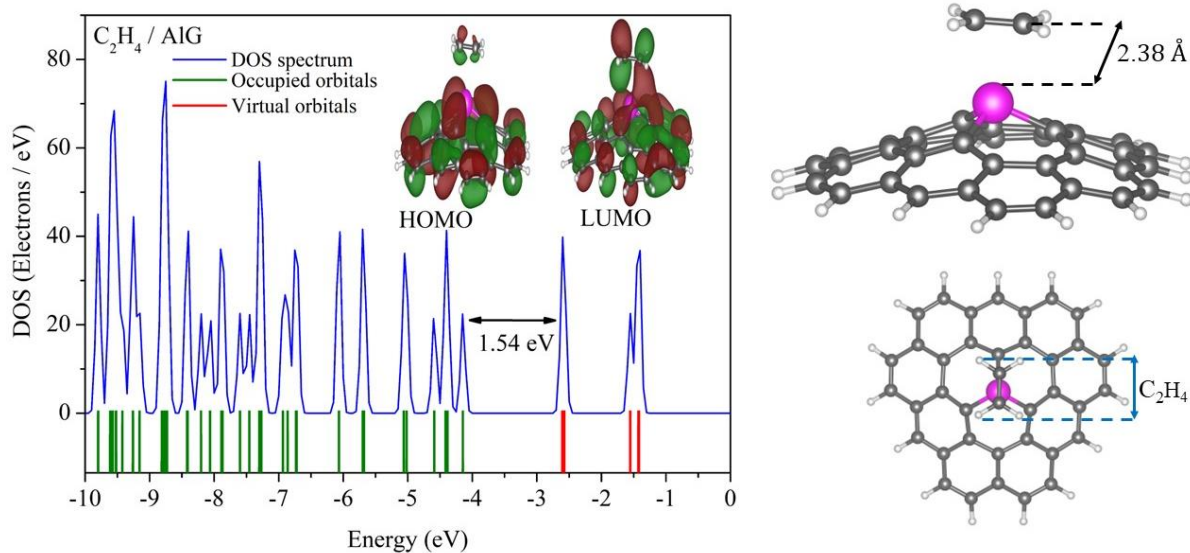


Figure 5: The graph of DOS as a function of energy and the HOMO and LUMO and energy gap of the C_2H_4/AIG for position 1.

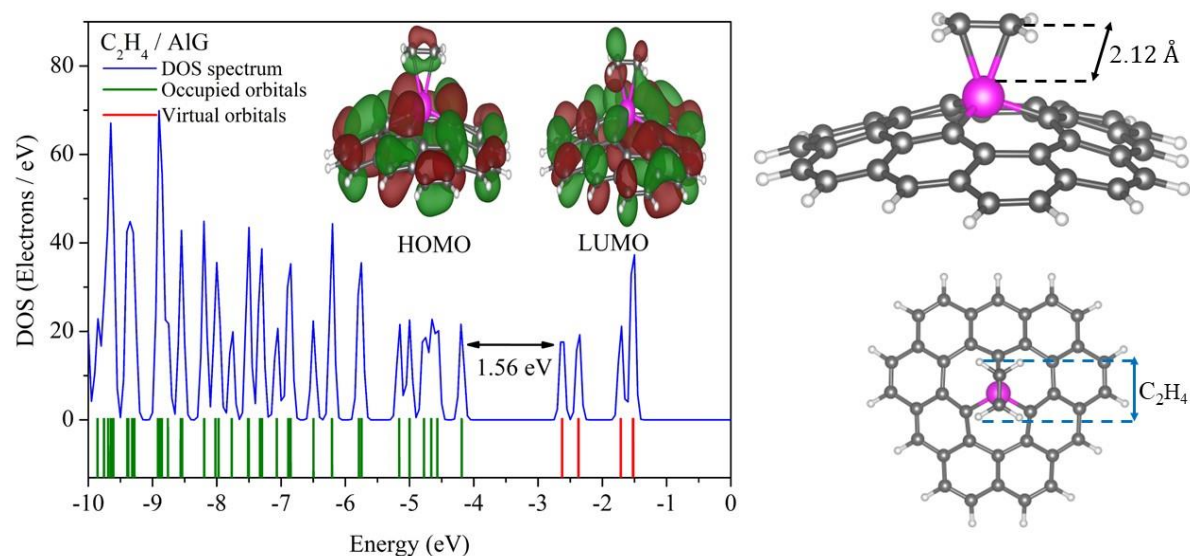


Figure 6: The graph of DOS as a function of energy and the HOMO and LUMO and energy gap of the C_2H_4/AIG for position 2.

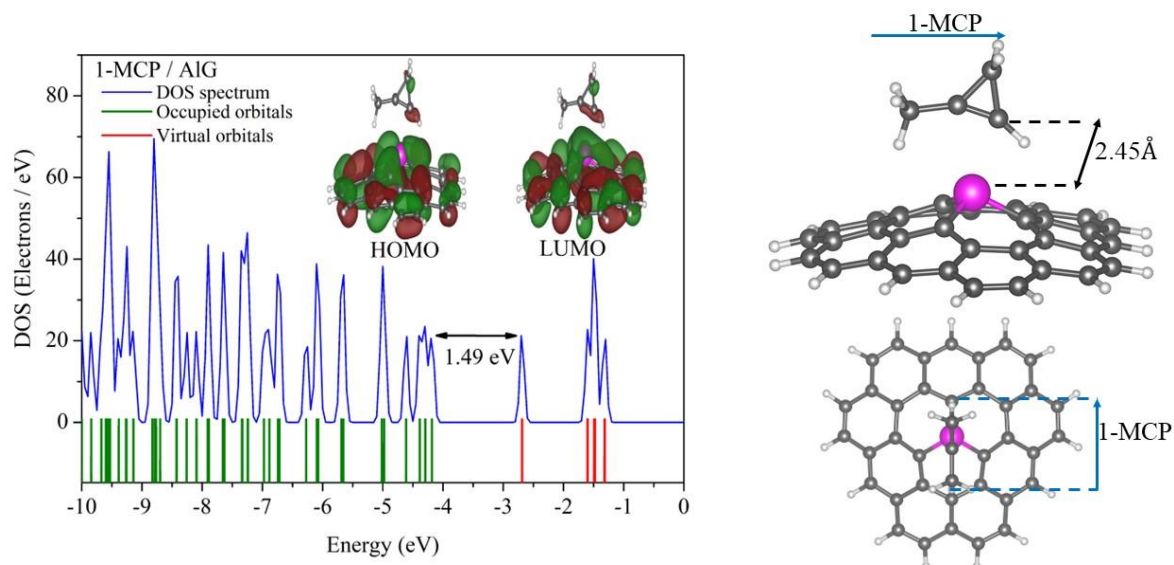


Figure 7: The graph of DOS as a function of energy and the HOMO and LUMO and energy gap of the 1-MCP/AIG for position 1.

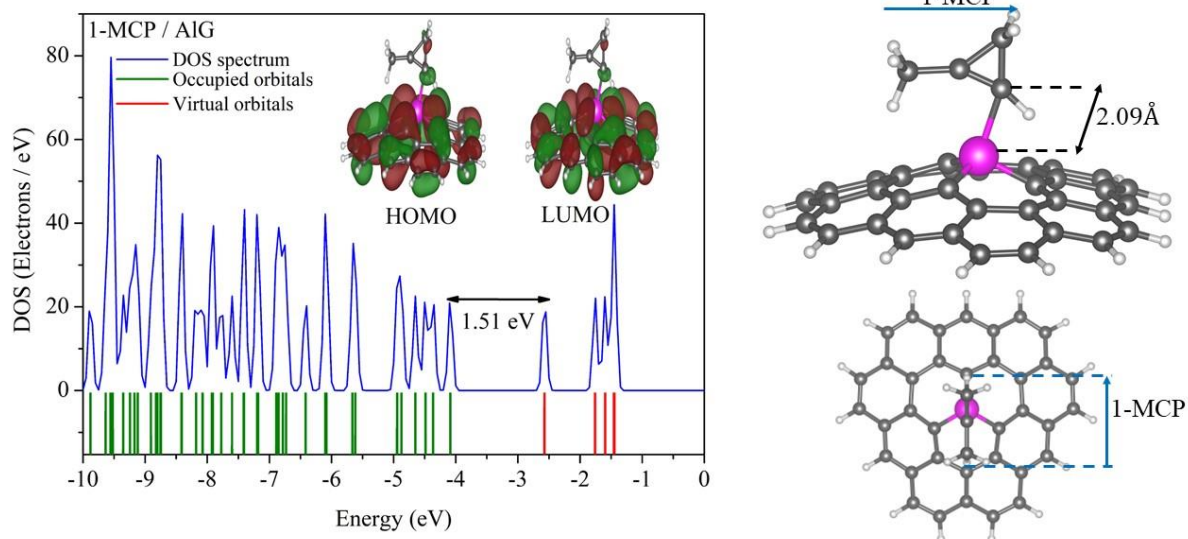


Figure 8: The graph of DOS as a function of energy and the HOMO and LUMO and energy gap of the 1-MCP/AIG for position 2.

Table 2: The optimized bond lengths of C₂H₄/AIG and 1-MCP/AIG for position 1 (P1) and position 2 (P2).

	C ₂ H ₄ / AIG (P1) (Å)	C ₂ H ₄ / AIG (P2) (Å)	1-MCP / AIG (P1) (Å)	1-MCP / AIG (P2) (Å)
C1-Al	1.8873	1.8489	1.8537	1.8354
C2-Al	1.8745	1.8350	1.8550	1.8288
C3-Al	1.8752	1.8365	1.8556	1.8288
C3-C4	1.4082	1.3998	1.4063	1.4055
C4-C5	1.4762	1.4880	1.4758	1.4874
C5-C6	1.4766	1.4873	1.4752	1.4838
C6-C21	1.4416	1.4332	1.4380	1.4386
C19-C20	1.3641	1.3605	1.3700	1.3645

Table 3: The adsorption energy (E_{ads}), HOMO and LUMO energies (E_{HOMO} , E_{LUMO}), energy gap (E_g), chemical hardness (η), chemical potential (μ) and electrophilicity (ω) of ethylene, 1-MCP, AIG, C₂H₄/AIG and 1-MCP/AIG position 1 (P1) and position 2 (P2).

	C ₂ H ₄	1-MCP	AIG	C ₂ H ₄ /AIG (P1)	C ₂ H ₄ /AIG (P2)	1-MCP/AIG (P1)	1-MCP/AIG (P2)
E_{ads} (kJ mol ⁻¹)				-60.16	19.34	-7.32	56.53
E_{HOMO} (eV)	-6.73	-5.65	-4.47	-4.15	-4.19	-4.18	-4.09
E_{LUMO} (eV)	-1.05	-0.64	-3.01	-2.61	-2.63	-2.69	-2.57
E_g (eV)	5.68	5.01	1.48	1.54	1.56	1.49	1.51
η (eV)	2.84	2.50	0.74	0.77	0.78	0.75	0.76
μ (eV)	3.89	3.15	3.75	3.38	3.41	3.43	3.33
ω (eV)	2.67	1.98	9.51	7.40	7.42	7.89	7.31

3.4. The ESP Analysis

The ESP map conveys information about possible reaction sites of electrophilic or nucleophilic attacks. The three-dimensional ESP of ethylene and 1-MCP on AIG were calculated and the ESP maps were presented in Fig. 9 by a blue-green-yellow colored spectrum of the cross-sectional plane, that is passing through the carbon atoms of ethylene or 1-MCP and the Al atom of AIG. The yellow color, that indicates a

negative ESP, is the lower potential region that the charge is depleted most and the blue color, that indicates a positive ESP, is the higher potential. Additionally, the graded black curves on the cross-sectional view of the ESP (Fig. 9) represent the equal ESP curves. Accordingly, the ESP maps shows that the Al atom is on a level of lower potential, which indicates a higher nucleophilic reactive site. In Fig. 9, the ESP changes color around the C, H and Al atoms.

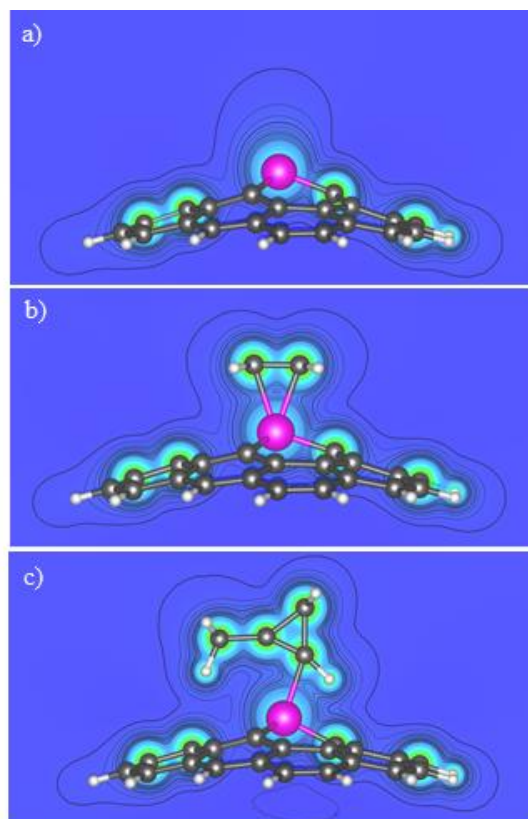


Figure 9: The electrostatic potential (ESP) map of (a) AlG, (b) C₂H₄/AlG and (c) 1-MCP/AlG. The graded black curves represent the equal ESP curves.

4. CONCLUSION

In the present study, the adsorption and activity of ethylene and 1-MCP molecules on Al-doped graphene (AlG) as a theoretical point of view were characterized through structural geometry optimization, HOMO and LUMO, adsorption energy, global reactivity and ESP calculations by using the DFT calculations.

The HOMO was located on the alkene carbon atoms of the ethylene and 1-MCP molecules while LUMO was located on the aluminum atom in AlG. From the HOMO/LUMO graphs corresponding to the interactions of the studied molecules, it is seen that the carbons of the interacting ethylene contribute largely to the HOMO, while in 1-MCP, the interaction center is different due to the steric and inductive effects of the methyl group. Global reactivity analyses confirmed that Al-doped graphene treats as electron acceptor and so ethylene and 1-MCP molecules treat as electron donor. So, the chemical hardness of the Al-doped graphene (0.74 eV) is lower than that of ethylene and 1-MCP (2.84 and 2.50 eV, respectively) and also the values of electrophilicity index (9.91 eV) is higher than of the ethylene and 1-MCP (2.67 and 1.98 eV, respectively) molecules. The adsorption energies of the ethylene and 1-MCP molecules in interaction with Al-doped graphene were calculated as -60.16, 19.34, -7.32 and 56.53 eV for P1 and P2 adsorption mechanism, respectively. The chemical and physical adsorptions of these gas molecules by AlG were effectively confirmed by different analyses such as ESP and DOS. According to these results, AlG is capable to be a new gas sensor for the adsorption of both ethylene

and 1-MCP molecules. Moreover, these analyses implied that AlG is a better adsorbent/gas sensor for 1-MCP molecule than ethylene molecule.

5. CONFLICT OF INTEREST

The authors declare no competing interests.

6. ACKNOWLEDGMENTS

The numerical calculations reported in this paper were fully performed at TUBITAK ULAKBIM, High Performance and Grid Computing Center (TRUBA resources).

7. REFERENCES

1. Yang SF, Hoffman NE. Ethylene biosynthesis and its regulation in higher plants. *Annu Rev Plant Physiol* [Internet]. 1984 Jun;35(1):155–89. Available from: [<URL>](#).
2. Zimmermann H, Walz R. Ethylene. In: *Ullmann's Encyclopedia of Industrial Chemistry* [Internet]. Weinheim, Germany: Wiley-VCH Verlag GmbH & Co. KGaA; 2000. Available from: [<URL>](#).
3. Dias C, Ribeiro T, Rodrigues AC, Ferrante A, Vasconcelos MW, Pintado M. Improving the ripening process after 1-MCP application: Implications and strategies. *Trends Food Sci Technol* [Internet]. 2021 Jul;113:382–96. Available from: [<URL>](#).
4. Magid RM, Clarke TC, Duncan CD. Efficient and convenient synthesis of 1-methylcyclopropene. *J Org Chem* [Internet]. 1971 May 1;36(9):1320–1.

Available from: [<URL>](#).

5. Blankenship SM, Dole JM. 1-Methylcyclopropene: A review. *Postharvest Biol Technol* [Internet]. 2003 Apr 1;28(1):1–25. Available from: [<URL>](#).

6. Sisler EC, Serek M. Inhibitors of ethylene responses in plants at the receptor level: Recent developments. *Physiol Plant* [Internet]. 1997 Jul 28;100(3):577–82. Available from: [<URL>](#).

7. Watkins CB. The use of 1-methylcyclopropene (1-MCP) on fruits and vegetables. *Biotechnol Adv* [Internet]. 2006 Jul;24(4):389–409. Available from: [<URL>](#).

8. Ekinci N, Şeker M, Aydın F, Gündoğdu MA. Possible chemical mechanism and determination of inhibitory effects of 1-MCP on superficial scald of the Granny Smith apple variety. *Turkish J Agric For* [Internet]. 2016;40:38–44. Available from: [<URL>](#).

9. Liu R, Lai T, Xu Y, Tian S. Changes in physiology and quality of Laiyang pear in long time storage. *Sci Hortic* [Internet]. 2013 Feb;150:31–6. Available from: [<URL>](#).

10. Serek M, Sisler EC, Reid MS. Effects of 1-MCP on the vase life and ethylene response of cut flowers. *Plant Growth Regul* [Internet]. 1995 Jan;16(1):93–7. Available from: [<URL>](#).

11. Dong M, Wen G, Li J, Wang T, Huang J, Li Y, et al. Determination of 1-methylcyclopropene residues in vegetables and fruits based on iodine derivatives. *Food Chem* [Internet]. 2021 Oct;358:129854. Available from: [<URL>](#).

12. Lee YS, Beaudry R, Kim JN, Harte BR. Development of a 1-Methylcyclopropene (1-MCP) sachet release system. *J Food Sci* [Internet]. 2006 Jan 31;71(1). Available from: [<URL>](#).

13. Novoselov KS, Geim AK, Morozov S V., Jiang D, Zhang Y, Dubonos S V., et al. Electric field effect in atomically thin carbon films. *Science* (80-) [Internet]. 2004 Oct 22;306(5696):666–9. Available from: [<URL>](#).

14. Geim AK, Novoselov KS. The rise of graphene. *Nat Mater* [Internet]. 2007 Mar;6(3):183–91. Available from: [<URL>](#).

15. Rad AS. First principles study of Al-doped graphene as nanostructure adsorbent for NO₂ and N₂O: DFT calculations. *Appl Surf Sci* [Internet]. 2015 Dec;357:1217–24. Available from: [<URL>](#).

16. Sun Y, Chen L, Zhang F, Li D, Pan H, Ye J. First-principles studies of HF molecule adsorption on intrinsic graphene and Al-doped graphene. *Solid State Commun* [Internet]. 2010 Oct;150(39–40):1906–10. Available from: [<URL>](#).

17. Rouhani M. DFT study on adsorbing and detecting possibility of cyanogen chloride by pristine, B, Al, Ga, Si and Ge doped graphene. *J Mol Struct* [Internet]. 2019 Apr;1181:518–35. Available from: [<URL>](#).

18. Rad AS, Shadravan A, Soleymani AA, Motaghedi N. Lewis acid-base surface interaction of some boron compounds with N-doped graphene; first principles study. *Curr Appl Phys* [Internet]. 2015 Oct;15(10):1271–7. Available from: [<URL>](#).

19. Zhou X, Zhao C, Wu G, Chen J, Li Y. DFT study on the electronic structure and optical properties of N, Al, and N-Al doped graphene. *Appl Surf Sci* [Internet]. 2018 Nov;459:354–62. Available from: [<URL>](#).

20. Esrafil MD, Saeidi N, Nematollahi P. A DFT study on SO₃ capture and activation over Si- or Al-doped graphene. *Chem Phys Lett* [Internet]. 2016 Aug;658:146–51. Available from: [<URL>](#).

21. Singh D, Kumar A, Kumar D. Adsorption of small gas molecules on pure and Al-doped graphene sheet: A quantum mechanical study. *Bull Mater Sci* [Internet]. 2017 Oct 3;40(6):1263–71. Available from: [<URL>](#).

22. Gecim G, Ozekmekci M, Fella MF. Ga and Ge-doped graphene structures: A DFT study of sensor applications for methanol. *Comput Theor Chem* [Internet]. 2020 Jun;1180:112828. Available from: [<URL>](#).

23. Tian YH, Hu S, Sheng X, Duan Y, Jakowski J, Sumpter BG, et al. Non-transition-metal catalytic system for N₂ reduction to NH₃: A density functional theory study of Al-doped graphene. *J Phys Chem Lett* [Internet]. 2018 Feb 1;9(3):570–6. Available from: [<URL>](#).

24. Jappor HR, Khudair SAM. Al-doped graphene as a sensor for harmful gases (CO, CO₂, NH₃, NO, NO₂ and SO₂). *Sens Lett* [Internet]. 2017 Dec 1;15(12):1023–30. Available from: [<URL>](#).

25. Rad AS, Puralijan Foukolaei V. Density functional study of Al-doped graphene nanostructure towards adsorption of CO, CO₂ and H₂O. *Synth Met* [Internet]. 2015 Dec;210:171–8. Available from: [<URL>](#).

26. Ao ZM, Yang J, Li S, Jiang Q. Enhancement of CO detection in Al doped graphene. *Chem Phys Lett* [Internet]. 2008 Aug;461(4–6):276–9. Available from: [<URL>](#).

27. Rad AS. Al-doped graphene as a new nanostructure adsorbent for some halomethane compounds: DFT calculations. *Surf Sci* [Internet]. 2016 Mar;645:6–12. Available from: [<URL>](#).



28. Zhao W, Meng QY. Adsorption of methane on pristine and Al-doped graphene: A comparative study via first-principles calculation. *Adv Mater Res* [Internet]. 2012 Dec;602–604:870–3. Available from: [<URL>](#).

29. Rastegar SF, Peyghan AA, Hadipour NL. Response of Si- and Al-doped graphenes toward HCN: A computational study. *Appl Surf Sci* [Internet]. 2013 Jan;265:412–7. Available from: [<URL>](#).

30. Chi M, Zhao YP. Adsorption of formaldehyde molecule on the intrinsic and Al-doped graphene: A first principle study. *Comput Mater Sci* [Internet]. 2009 Oct;46(4):1085–90. Available from: [<URL>](#).
31. Zhang T, Sun H, Wang F, Zhang W, Ma J, Tang S, et al. Electric-field controlled capture or release of phosgene molecule on graphene-based materials: First principles calculations. *Appl Surf Sci* [Internet]. 2018 Jan;427:1019–26. Available from: [<URL>](#).
32. Rastegar SF, Hadipour NL, Tabar MB, Soleymanabadi H. DFT studies of acrolein molecule adsorption on pristine and Al- doped graphenes. *J Mol Model* [Internet]. 2013 Sep 22;19(9):3733–40. Available from: [<URL>](#).
33. Rad AS, Jouibary YM, Foukolaei VP, Binaeian E. Study on the structure and electronic property of adsorbed guanine on aluminum doped graphene: First principles calculations. *Curr Appl Phys* [Internet]. 2016 May;16(5):527–33. Available from: [<URL>](#).
34. Rad AS, Alijantabar Aghouzi S, Motaghedi N, Maleki S, Peyravi M. Theoretical study of chemisorption of cyanuric fluoride and S-triazine on the surface of Al-doped graphene. *Mol Simul* [Internet]. 2016 Dec 11;42(18):1519–27. Available from: [<URL>](#).
35. Hohenberg P, Kohn W. Inhomogeneous electron gas. *Phys Rev* [Internet]. 1964 Nov 9;136(3B):B864–71. Available from: [<URL>](#).
36. Kohn W, Sham LJ. Self-consistent equations including exchange and correlation effects. *Phys Rev* [Internet]. 1965 Nov 15;140(4A):A1133–8. Available from: [<URL>](#).
37. Giannozzi P, Baroni S, Bonini N, Calandra M, Car R, Cavazzoni C, et al. Quantum espresso: A modular and open-source software project for quantum simulations of materials. *J Phys Condens Matter* [Internet]. 2009 Sep 30;21(39):395502. Available from: [<URL>](#).
38. Giannozzi P, Andreussi O, Brumme T, Bunau O, Buongiorno Nardelli M, Calandra M, et al. Advanced capabilities for materials modelling with quantum espresso. *J Phys Condens Matter* [Internet]. 2017 Nov 22;29(46):465901. Available from: [<URL>](#).
39. Giannozzi P, Barone A, Bonfà P, Bruneau D, Car R, Carnimeo I, et al. Quantum espresso toward the exascale. *J Chem Phys* [Internet]. 2020 Apr 21;152(15). Available from: [<URL>](#).
40. Vanderbilt D. Soft self-consistent pseudopotentials in a generalized eigenvalue formalism. *Phys Rev B* [Internet]. 1990 Apr 15;41(11):7892–5. Available from: [<URL>](#).
41. Perdew JP, Burke K, Ernzerhof M. Generalized Gradient Approximation Made Simple. *Phys Rev Lett* [Internet]. 1996 Oct 28;77(18):3865–8. Available from: [<URL>](#).
42. Kokalj A. Computer graphics and graphical user interfaces as tools in simulations of matter at the atomic scale. *Comput Mater Sci* [Internet]. 2003 Oct;28(2):155–68. Available from: [<URL>](#).
43. Momma K, Izumi F. VESTA 3 for three-dimensional visualization of crystal, volumetric and morphology data. *J Appl Crystallogr* [Internet]. 2011 Dec 1;44(6):1272–6. Available from: [<URL>](#).
44. Monkhorst HJ, Pack JD. Special points for Brillouin-zone integrations. *Phys Rev B* [Internet]. 1976 Jun 15;13(12):5188–92. Available from: [<URL>](#).
45. Makov G. Chemical hardness in density functional theory. *J Phys Chem* [Internet]. 1995 Jun 1;99(23):9337–9. Available from: [<URL>](#).
46. Pearson RG. The electronic chemical potential and chemical hardness. *J Mol Struct THEOCHEM* [Internet]. 1992 Mar;255:261–70. Available from: [<URL>](#).
47. Chattaraj PK, Parr RG. Density functional theory of chemical hardness. In: *Chemical Hardness* [Internet]. Berlin/Heidelberg: Springer-Verlag; p. 11–25. Available from: [<URL>](#).
48. Coster D, Blumenfeld AL, Fripiat JJ. Lewis acid sites and surface aluminum in aluminas and zeolites: A high-resolution NMR study. *J Phys Chem* [Internet]. 1994 Jun 1;98(24):6201–11. Available from: [<URL>](#).



Study of Sulfur Purification from Bituminous Material in The Mishraq Sulfur Mine Using Acidic Sulfur Waste (Foam)

Hala Saad Jasim^{1*} , Deena Mazin Abd Al-Jawad¹ , Thaeer Abed Hellow¹ ,
Mote`a O. Abdulla² 

¹Department of Chemistry, Collage of Education for Girl, University of Mosul, Mosul, Iraq.

²Mishraq Sulfur State Company, Ministry of Industry and Minerals-Iraq, 41001, Mosul, Iraq.

Abstract: In conclusion, the sulfur wastes obtained from chemical and thermal methods for sulfur purification in the Mashreq field has been present for decades in significant quantities, approaching two million tons, with its harmful impact on the environment. Our research focused on using a different approach by utilizing the acidic sulfur wastes (foam) as a source of sulfuric acid and elemental sulfur containing bituminous materials. The goal was to make use of the sulfuric acid present in the sulfur wastes to oxidize bituminous materials. This was achieved by mixing various proportions of elemental sulfur at a temperature of 150-160 °C to achieve the best viscosity while monitoring chemical and spectroscopic changes using SEM, XRD, and FTIR devices. The aim was to eliminate the negative effects of bituminous and acidic materials and repurpose sulfur wastes, converting it into economically and scientifically valuable materials. The filtration of molten elemental sulfur from foam was conducted using a specially designed metal filter for the filtration process, along with the use of a filtration aid. This process successfully recovered 81% of the elemental sulfur, and the results met the Iraqi Standard Specification 2199.

Keywords: Wastes, Carsul, Mining sulfur, Carbosulfur.

Submitted: December 14, 2023. **Accepted:** September 16, 2024.

Cite this: Jasim HS, Al-Jawad DMA, Hellow TA, Abdulla MO. Study of Sulfur Purification from Bituminous Material in The Mishraq Sulfur Mine Using Acidic Sulfur Waste (Foam). JOTCSA. 2024;11(4): 1545-52.

DOI: <https://doi.org/10.18596/jotcsa.1400248>

***Corresponding author's E-mail:** hala.saad@uomosul.edu.iq

1. INTRODUCTION

Various methods are employed in the extraction of elemental sulfur, ranging from chemical methods using chemical substances to thermal methods using heat, or using physical methods through using clayd or suitable hydrocarbon solvents Al-jubori MO (1). Jasim HS et al. (2) extracted elemental sulfur from sulfur deposits in the Mashraq mine by adding concentrated sulfuric acid within a temperature range of (130-190) °C and in the presence of air. The effect of air on the carbon particles formed due to the carbonization of organic materials by the air and sulfuric acid became evident through an increase in their size and agglomeration as a result of the increased polarity of the system. Ibrahim (3) successfully recovered sulfur from the sulfuric wastes residues left behind by the chemical method using a solvent, kerosene, with a 91% Treating molten sulfur with concentrated sulfuric acid to oxidize organic matter and then adding a type of silica earth (celite) to adsorb organic matter and

facilitate separation of heavy molten sulfur from the foam layer. Alkhafaji et al. (4) employed an undisclosed hydrocarbon solvent for extracting elemental sulfur from solid sulfuric wastes residues resulting from the thermal method. Shareef et al. (5) was able to recover 75% of the elemental sulfur present in the sulfuric wastes residues, known as "foam," using air-based thermal treatment within a temperature range of 130-180 °C, under industrial filtration conditions.

Patwardhan (6) were able to recover sulfur from industrial wastes rich in sulfur by raising the temperature to its boiling point and then condensing the resulting sulfur, which is characterized by high purity and direct usability for industrial and agricultural purposes. Masotta et al. (7) and others used a rotary kiln to burn the sulfur filtration residues in a concentrated sulfuric acid reactor known as "cake", which is rich in sulfur. Sulfur is burned in the range of 1100-1400 °C to obtain sulfur dioxide gas, which is used in the

production of sulfuric acid. Golub et al. (8) and others recovered elemental sulfur by heating sulfur-rich residues between 120-160 °C to separate solid materials. Then, they heated the remaining substances between 450-500 °C to produce sulfur vapor, which was passed into condensers operating in the range of 120-140 °C to obtain molten sulfur. The residue left in the furnace consists of wastes materials. In our research, we used both foam-containing bituminous impurities and sulfur with organic materials in the production of sulfuric acid.

2. THE EXPERIMENTAL METHOD

1. The Air blowing instrument of the Dawson Mc Dawson type.
2. The air blowing device of the Dawson Mc Dawson variety.
3. A German (delta) style electrical furnace that can reach temperatures of up to 1100 °C.
4. The Hamburhao Shaker Germany electric motor gadget.
5. Mantel Heater.
6. The Fifth Ae ADAM Sensitive Balance.
7. The Expert Phillips Holland X-Ray Diffraction Device 9.
8. Energy Dispersive Spectroscopy Eds Tescan Mira3 France.
9. French SEM Tescan Mira3 10. Using electron microscopy.
10. Raw materials: sulfur residues, mattress sulfur, ethanol, phenolphthalein

2.1. The Raw Materials' Preparation

Preparation of models of sulphur and sulphur residues by mixing vomit and sulfur bed ratios according to the following table.

No	%Mining Sulfur	%Foam
1	5	95
2	10	90
3	15	85
4	20	80
5	25	75
6	30	70

2.2. Oxidation Using Sulfur Residues and Air

Weigh 5 grams of powdered sulfur and 95 grams of foam. Place this mixture into a three-necked round-bottom flask. In the first neck, insert a thermometer, the second neck is connected to a condenser, and the third neck is connected to an air supply at a rate of 120 cm³/min. Melt the sulfur at a temperature between 150 °C and 160 °C, and maintain this temperature for one hour. Monitor the temperature within the specified range. After completion, pour the resulting sample into a special mold. Repeat this process for the other proportions as specified in the table until obtaining the desired samples. After the oxidation process, perform chemical analyses on the samples, including measuring acidity, extracting organic material, and determining the carbon content. Additionally, conduct XRD (X-Ray Diffraction), SEM (Scanning Electron Microscopy), EDS (Energy-Dispersive X-

Ray Spectroscopy), FTIR (Fourier Transform Infrared Spectroscopy), and mapping histogram measurements for each sample

2.3. Estimation of Acidity in Sulfur Residues and Oxidized Samples

Place 10 grams of sulfur residues, 2 mL of ethanol, and 200 mL of distilled water in a beaker. Mix the components thoroughly. Cover the beaker with a watch glass and heat it on an electric hot plate until it boils. Boil for 15 minutes. Allow it to cool to room temperature, then filter it into a 250 mL volumetric flask. Wash the residue with distilled water and complete the volume to the mark. Transfer 100 mL of the filtrate to an Erlenmeyer flask and titrate with 0.01 N sodium hydroxide using phenolphthalein as an indicator. Prepare a standard solution by dissolving 10 mL of ethanol and 90 mL of distilled water. Heat until boiling for 15 minutes, cool, and titrate with sodium hydroxide using the same indicator. Repeat the experiment for the remaining oxidized samples. Calculate the acidity based on the sulfur residues using the following equation:

$$\% \text{H}_2\text{SO}_4 = \frac{F(V-V_1)}{W}$$

V = Volume of sodium hydroxide used for titrating the sample. V1 = Volume of sodium hydroxide used for the standard solution. W = Weight of the sample. F = A constant that can be determined after finding the standardized NaOH through titration with a 0.01 N HCl solution with known concentration (1).

$$F = N. \text{ exact} \times 4.9 \times 2.5$$

2.4. To Measure The Carbon Content (Carsul) in Sulfur, Sulfur Residues, and Oxidized Samples: For Carbon Extraction from Sulfur Residues and Oxidized Samples

Place 10 grams of the sample (sulfur, sulfur residues, or oxidized samples) into a 250 mL glass flask. Add 2 mL of 96% ethanol and 25 mL of a 10% sodium hydroxide solution. Heat the mixture using a Bunsen burner to a temperature of 80-90 °C for two hours while stirring continuously. Filter the mixture through a G4-grade filter funnel. Rinse the residue several times with hot water and dry it in an oven at 80 °C for one hour. Treat the residue several times with 5 mL of carbon tetrachloride until it becomes colorless. Drip dry the organic material and dry it at 105 °C for 24 hours. Weigh the dried organic material and calculate its percentage, representing the organic material content in the oxidized samples. The remaining residue on the filter paper is dried again at 80-90 °C, collected, weighed, and its percentage calculated (9).

2.5. To Estimate the Free Sulfur Content in Mined Sulfur

Weigh 0.5 grams of finely ground sulfur and place it in a 250 mL glass flask. Add 50 mL of a 20% sodium thiosulfate solution. Attach a reflux condenser and heat for five hours while stirring. Transfer the solution to a separation funnel, allowing two layers to form (organic and water).

Separate the water layer, filter it, and transfer it to a 250 mL volumetric flask. Complete the volume with distilled water to the mark. Transfer 25 mL of the solution to an Erlenmeyer flask, add 20-30 mL of water, 1-2 drops of phenolphthalein indicator, and 5 mL of a 20% formaldehyde solution. The solution should turn gray. Leave the sample for five minutes, add acetic acid drop by drop until the gray color disappears, and titrate with 0.1N iodine solution, using starch solution as an indicator. Record the volume of iodine used in the titration and calculate the free sulfur percentage according to the given equation. Repeat the same experiment to calculate the free sulfur percentage in sulfur residues (1).

$$\text{Free sulfur \%} = \text{V.of I}_2 * \text{N.of I}_2 \frac{\text{Eq. wt of sulfur } \frac{250}{1000} * 100}{\text{Wt of sample } 25}$$

3. RESULTS AND DISCUSSION

Considering the undesirable properties added by the bituminous materials impregnated in sulfur extracted by the Frasch method (10), such as the change in its color from yellow sulfur to dark brown

sulfur, as well as their economic effects in reducing the market value of sulfur and their negative impact on reactions, various methods have been developed to eliminate these materials to obtain pure sulfur. These methods have ranged from chemical methods using oxidizing agents such as concentrated sulfuric acid and nitric acid to thermal methods, thermal oxidation methods This method is known as submerged combustion distillation The filtration unit consists of three main units: the bath burning unit, the sulfur recovery unit, and the filtration unit, and physical methods using solvents or adsorption on special carriers. In this research, sulfuric acid present in sulfur wastes (foam) was used for the purpose of oxidizing bituminous materials. The research included the following:

3.1. Study of The Composition of The Raw Materials

To monitor the changes that occur in the composition of the raw materials, represented by elemental sulfur and sulfur wastes (foam), the results recorded in Table (1).

Table 1: Main components of mining sulfur and sulfur wastes (foam).

Hem	Parometer %wt	Mine Sulfur	Sulfur Wastes (Foam)
1	Bitumenous materials	1.011	0.00
2	Carbonous materials	0.134	1.2432
3	Acidity as H ₂ SO ₄	0.00	0.833

were obtained. From Table (1), it can be observed that elemental sulfur is characterized by a high content of bituminous materials known for their negative effects. The sulfur wastes (foam) were also characterized by its acidity as a result of the use of concentrated sulfuric acid in carbonizing and oxidizing bituminous materials (10). The above indicates the availability of suitable conditions for purifying elemental sulfur on one hand and eliminating the negative effects of both bituminous and acidic materials, as well as utilizing sulfur wastes (foam) on the other hand.

3.2. Study of Purification of Elemental Sulfur

The study of purifying elemental sulfur involved several stages as follows

Reaction of Raw Materials at a Thermal Range of 150-160 °C To reach the minimum viscosity: Different proportions (5%, 10%, 15%, 20%, 25%, 30%) of elemental sulfur were mixed with foam and thermally treated at a temperature of 150-160 °C to maintain the viscosity within the specified limits. Changes in the carbosulfur, bituminous, and acidic materials were monitored. The results obtained are illustrated in Table (2).

Table 2: The main components of the mined sulfur mixture are foam in different proportions and heat treated with a temperature range of 150-160 °C.

No	Ratio of Mine Sulfur %	Carbon-sulfur Materials %	Acidity as H ₂ SO ₄ %	Bitumenous Materials %
1	5	2.618	0.800	0.00
2	10	3.873	0.379	0.00
3	15	4.002	0.376	0.041
4	20	4.652	0.3675	0.024
5	25	4.996	0.316	0.025
6	30	5.249	0.235	0.012

Basic components of foam-mixed elemental sulfur at different ratios and thermally treated at a thermal range of 150-160 °C. To align the results with the required standard specifications, it is necessary for the decrease in both bituminous and acidic materials to be parallel. Therefore, different quantities of elemental sulfur were used to achieve the best conditions and results. From the table

above, it can be observed that even though the percentage of bituminous materials decreased in experiments (1,2), the acidity remains high, causes a black mass that covers the equipment, and the presence of these materials causes blockage of valves and sewers and slows down the transfer of heat, which leads to corrosion of the equipment (12) which affects the quality of sulfur by impacting

equipment, whether during loading or use. With an increase in the quantity of elemental sulfur, there is a presence of bituminous materials, albeit in low amounts, which can still influence the color of industrial sulfur. Despite the decrease in acidity, it did not approach the required standard specifications (Iraqi Standard Specification).

3.3. Study of Carbosulfur Materials Extracted by Sodium Hydroxide Solution

To comprehensively address the topic and propose appropriate treatments, the nature of the

carbosulfur materials present in foam and the resulting reaction between sulfuric acid and bituminous materials or sulfur and bituminous materials were studied. Nature of Carbosulfur Materials of Raw Materials:

The nature of carbosulfur materials was studied using scanning electron microscopy Scanning electron Microscopy (SEM), and the images captured in sulfur wastes (foam) and elemental sulfur showed that they have nanoscale fine nature with spherical and semi-spherical shapes.

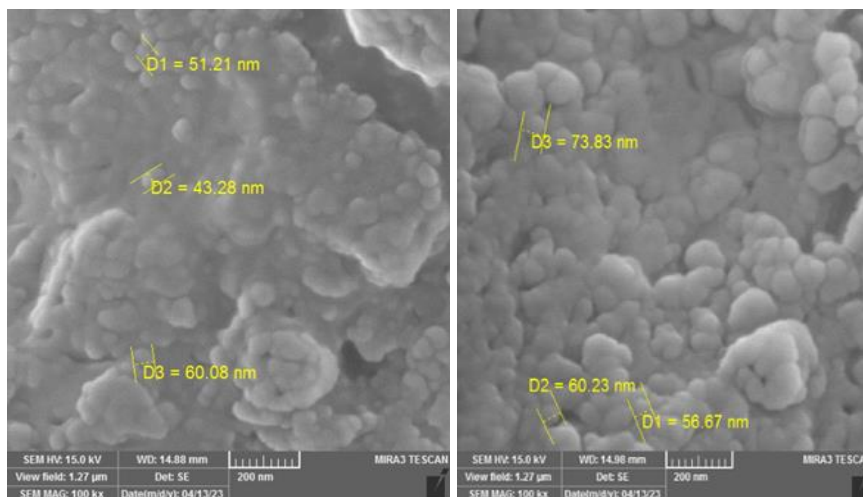


Figure 1: Scanning electron microscope (SEM) analysis of the reaction of raw materials with a temperature range of 150-160 °C in the presence of air.

The figure also indicates that the granular size of carbosulfur materials in sulfur wastes ranged from (60.08-43.28) and in elemental sulfur from (73.83-56.67). The presence of carbosulfur materials of these sizes requires special conditions for industrial sulfur filtration. X-ray Energy Dispersive Spectroscopy (EDS) study associated with SEM

technology revealed the elemental arrangement of these materials. Elemental arrangement determined by (EDS) Reaction of Raw Materials at a Thermal Range of 150-160 °C in the Presence of Air: To obtain optimal conditions, the same experiments (1-2-3) were conducted in the presence of air, and the same changes were monitored.

Table 3: The main components of the mixture of mined sulfur and foam in different proportions, which are heat treated with a temperature range of 150-160 °C.

No	Ratio of Mine Sulfur%	Carbon Sulfur Materials%	Acidity %	Bitumen
1	5	3.942	0.5145	0.033
2	10	4.303	0.3185	0.028
3	15	4.948	0.3082	0.023
4	20	5.050	0.252	0.017
5	25	6.173	0.119	0.016
6	30	8.694	0.005	0.005

Illustrates the most important results obtained: Table (3): Basic components of a mixture of elemental sulfur and foam at different ratios, thermally treated at a thermal range of 150-160 °C. From the table, it can be observed that there is a parallel decrease between bituminous and acidic materials, accompanied by an increase in carbosulfur materials. The mine sulfur ratio yielded the best results, achieving two goals simultaneously: getting rid of bituminous materials in elemental sulfur and the acidity present in the foam. After obtaining positive results, before starting the filtration processes, it is essential to

study the nature of the carbosulfur materials resulting from both treatments.

Table 4: Studying the nature of carboxy sulfur materials resulting from thermal and pneumatic treatment.

No	Element %wt	Mine Sulfur	Foam
1	Carbon	26.98	22.36
2	Sulfur	69.68	77.47
3	Oxygen	3.34	0.17

From the table above, it is noticeable that carbosulfur compounds primarily consist of sulfur and carbon chemically bonded (11), along with a small percentage of oxygen. One of the main

objectives of purifying elemental sulfur is to separate these materials from the elemental sulfur in a suitable manner, as shown in the figure.

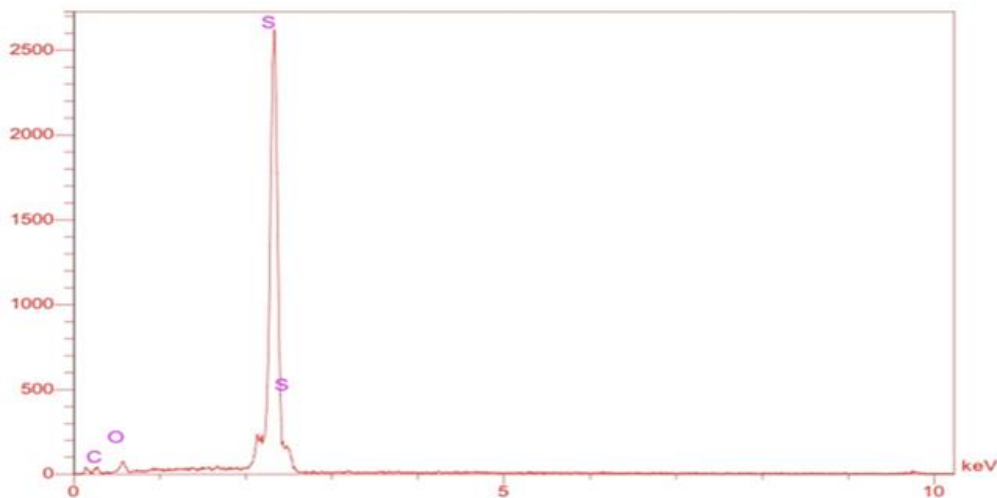


Figure 2: The X-ray power spectrum EDS for the basic components of carbs.

3.4. Study of The Nature of Carbosulfur Materials in The Thermally and Thermally-Air Treated Reaction Mixture

The percentage of the major elements in the carbosulfur materials of the mixture of elemental sulfur and foam was theoretically calculated to understand the changes resulting from the reaction conditions, We note from the table the percentages (C%. S%O%.) are not parallel due to the elements present in the device’s detector and materials added to the model to increase its electrical conductivity. as shown in Table (5).

Table 5: The main components of sulfur materials for the mixture of mine sulfur and foam calculated theoretically.

% Mine Sulfur	C%	S%	O%
5	22.59	77.08	0.33
10	22.82	76.69	0.49
15	23.05	76.33	0.62
20	23.38	75.92	0.70
25	23.52	75.52	0.96
30	23.75	75.13	1.12

Major components of carbosulfur materials in the mixture of elemental sulfur and foam theoretically calculated. The carbosulfur materials resulting from the reaction between elemental sulfur and foam were separated and studied using scanning electron microscopy (SEM), as depicted in the Figure (3).

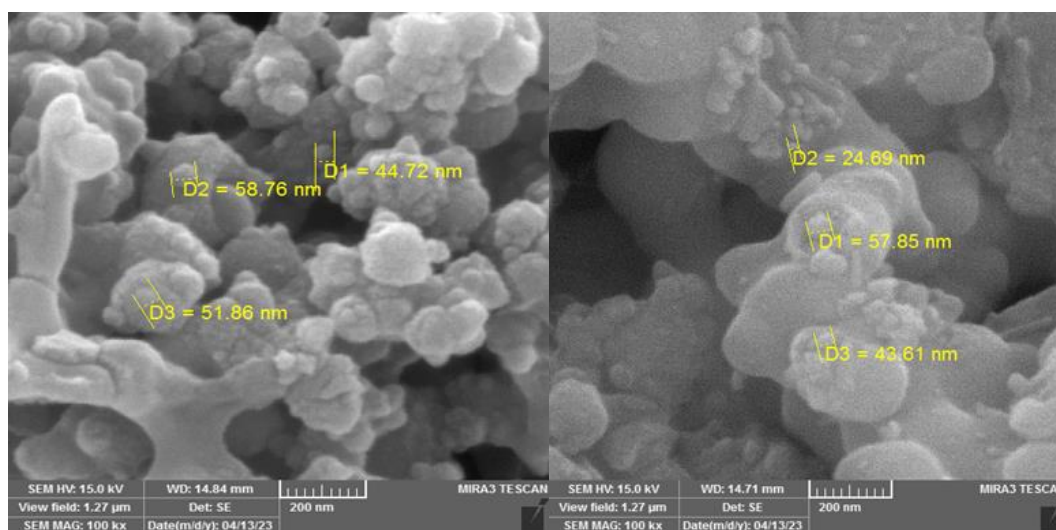


Figure 3: Scanning electron microscopy (SEM) analysis of carboxylate materials after heat treatment.

The figure shows an increase in the percentage of elemental sulfur and a decrease in granular size to (24.69 nm). The carbonaceous materials from the

reaction of the bituminous material present in elemental sulfur with both sulfur and sulfuric acid did not undergo significant changes in granular size

so far. In the case of thermal-air treatment, an increase in granular size was observed. This is due to an increase in the polarity of carbosulfur materials, resulting from the entry of oxygen into

the structure, leading to the aggregation of molecules with each other, as shown in the Figure (4).

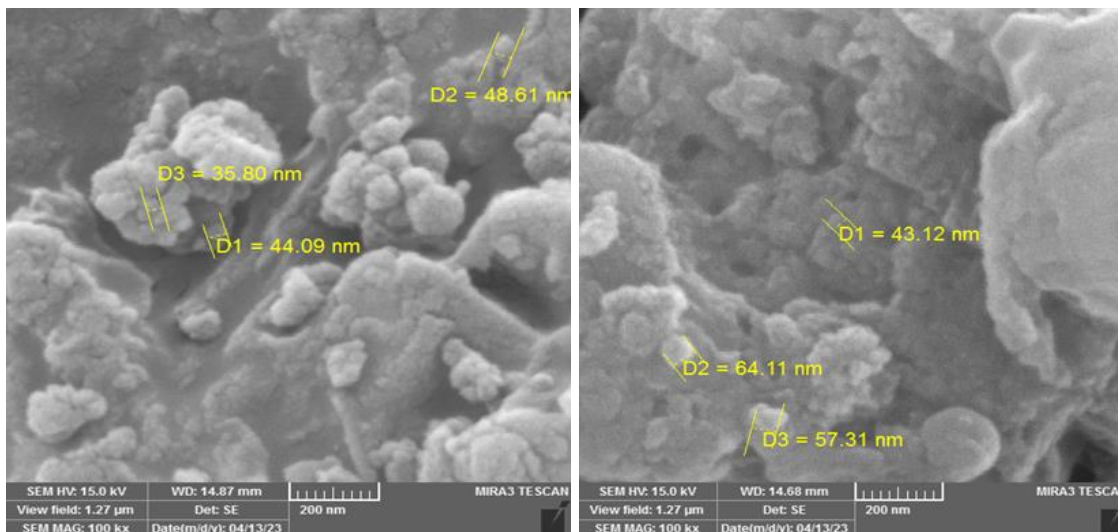


Figure 4: Scanning electron microscope (SEM) analysis of carboxylate materials after heat and air treatment.

3.5. Filtration of Molten Elemental Sulfur from Foam

The process of filtering molten sulfur differs from regular liquid filtration, requiring special conditions and equipment. To achieve this, a metal filter was used, consisting of an outer part that forms an oil bath made of carbon steel with a diameter of 3 cm and a length of 50 cm. It is externally heated and equipped with a thermostat to provide and adjust the appropriate temperature, which should be between 130-140 °C. The inner tube represents the actual filter, made of stainless steel with a diameter of 4 cm and a length of 53 cm, ending with a wire mesh made of stainless steel grade (110*24) with a diameter of 85 microns. It is connected from above to a tube for the passage of compressed air, exerting a pressure of 4 cm³/kg on the surface of the sulfur to accelerate the filtration process. The 24/110 Stainless Steel Grade 304 Hollander Mesh offers numerous benefits for filtration applications. Its precise weave and dual wire thicknesses

(0.35mm and 0.25mm) provide an excellent balance between strength and functionality, allowing for effective filtration with absolute micron retention of 110-112. Before starting the filtration process of the molten sulfur, a filtration aid, which is salt, was used to pass through the pure molten sulfur containing the filtration aid. Without this process, solid particles would quickly accumulate on the surface of the metal mesh, leading to its clogging, and the filtered sulfur would not achieve the required purity. The filtration aid is an inert material capable of forming a filtration layer, transferring the filtration process from the metal mesh to the entire mass of the filtration aid. After that, the molten sulfur was passed through for the purpose of filtration to obtain pure sulfur. Douglas managed to recover 81% of the elemental sulfur present in the fusion mixture. Table (6) shows the results obtained in comparison with the Iraqi Standard Specification 2199.

Table 6: Specifications of pure sulfur resulting from the treatment of 30% sulfur mine smelt into foam, treated pneumatically and thermally with a range of 150-160 °C.

No	Element%wt	Pure sulfur	Iraqi stardaid 2199
1	Sulfur	99.78	99.6%
2	Carbon	0.073	0.08%
3	Ash	0.006	0.08%

Table (6): Specifications of pure sulfur resulting from the treatment of a 30% mixture of elemental sulfur with foam, thermally and thermally-air treated at a range of 150-160 °C. From the table, it is evident that the filtered sulfur complies with the Iraqi Standard Specification 2199 for the year 2002. The purity of industrial sulfur is one of the most important factors determined by industries that consume it. This highlights the focus on getting rid of bituminous impurities, which are among the most

significant impurities affecting sulfur purity. Bituminous materials resulting from the combustion of bituminous impurities would cover equipment surfaces, reducing their efficiency and requiring continuous cleaning. As for the sulfuric acid present, its corrosive effect on equipment is well-known.

4. CONCLUSION

Industrial sulfur has been purified, and a solution was found to eliminate critical impurities that negatively affect the quality of pure sulfur, specifically bituminous and acidic materials. These impurities were found in two different sources of elemental sulfur and elemental sulfur foam wastes. The process involved the reaction of elemental sulfur with sulfur foam wastes and a filtration procedure similar to industrial sulfur filtration, resulting in the production of pure sulfur that meets standard specifications. High-quality sulfur is produced using the Claus method and submerged combustion distillation.

5. CONFLICT OF INTEREST

There are no conflict of interest.

6. REFERENCES

- Al-jubori M. Study of the purification of sulfur raw materials and its refining products and their use in the chemical industries. Doctoral dissertation, Ph. D. thesis, University of Mosul-College of Education; 2011.
- Jasim H, halo thaer, Al jbouri M. A Study of the chemical nature of sulfur-containing rocks and Frasch sulfur in the Al-Mishraq Sulfur field. *J Educ Sci* [Internet]. 2021 Mar 1;30(1):1–9. Available from: [<URL>](#).
- Ibrahim JA. Pollution of mining industry sulfur purification plant at al mishraq. *J Eng* [Internet]. 2011;5(17):1159–73. Available from: [<URL>](#).
- Alkhafaji MW, Connan J, Engel MH, AL-Jubouri SW. Origin, biodegradation, and water washing of bitumen from the Mishraq Sulfur Mine, northern Iraq. *Mar Pet Geol* [Internet]. 2021 Feb;124:104786. Available from: [<URL>](#).
- Shareef SS, H TA, A and Motèa O. Concentration and study of the carbon-sulfur residues resulting from the thermal purification of Frasch sulfur in the Al-Mishraq sulfur mine. *J Surv Fish Sci* [Internet]. 2023 May 4;10(1S):5355–67. Available from: [<URL>](#).
- Patwardhan A. Industrial solid waste [Internet]. New Delhi: The Energy and Resources Institute (TERI); 2013. Available from: [<URL>](#).
- Masotta M, Rocchi I, Pazzagli G, D'Ambrosio R, Seggiani M. Recovery of sulfur from sulfur-rich filter cakes in a rotary kiln: Process optimization. *Waste Manag* [Internet]. 2021 May;126:567–77. Available from: [<URL>](#).
- Golub G, Subovich J, Garden O, Garden I. Recovery of sulfur from sulfur-containing waste [Internet]. United States patent US 9,216,904 B2, 2012. Available from: [<URL>](#).
- Mohammud B. The use of sulfur residues from mishraq sulfur as a raw material in the preparation of nanoparticle sulfur. Master's thesis, University of Mosul-College of Education for Girls; 2021.
- Shareef SS, Halo TA, Abdulla MO. Recovery of sulfur from the residues of the chemical method for the purification of sulfur from the farsch mine in the Al-Mishraq Mine. *Iraqi J Ind Res* [Internet]. 2023 Jun 14;10(1):15–25. Available from: [<URL>](#).
- Louie DK. Handbook of sulphuric acid manufacturing [Internet]. Ontario, Canada: DKL Engineering, Inc.; 2005. Available from: [<URL>](#).
- Lipps D. Process for heat-treating liquid sulfur containing carbonaceous impurities [Internet]. Vol. 316. United States patent US 3,316,063, 1967. p. 63. Available from: [<URL>](#).



***Lannea microcarpa* Leaves Extract as Corrosion Inhibitor for Al Metal in HCl Acid Medium**

Umaru Umar¹ , Abdullahi Muhammad Ayuba^{1*} 

¹Bayero University, Faculty of Physical Sciences, Department of Pure and Industrial Chemistry, Kano, 700241, Nigeria.

Abstract: Techniques for weight loss, electrochemistry, scanning electron microscopy (SEM), and Fourier transform infrared spectroscopy (FTIR) were used to investigate the inhibitory impact of *Lannea microcarpa* leaves extract. The weight loss data showed that the plant extract's ability to suppress corrosion increased with higher concentrations and decreased with higher temperatures and HCl acid concentrations. According to the electrochemical data, the plant extract uses a mixed type mechanism to limit both cathodic and anodic reaction rates. Calculated activation energies were found to be higher in inhibited systems than in uninhibited systems, indicating physisorption, while negative values of ΔG point to a process that is both possible and spontaneous. The inhibitory mechanism was demonstrated by FTIR spectra to be an adsorption process through the functional groups present in the phytochemicals of the plant extract onto the surface of Al metal. SEM surface morphology study demonstrated the protection that the extract provided on the metal surface. Compared to other isotherm models that were examined, the adsorption data were found to be more reliable and suited the Langmuir isotherm well.

Keywords: Aluminium, *Lannea microcarpa*, Weight loss, Inhibition efficiency.

Submitted: October 20, 2022. **Accepted:** September 26, 2024.

Cite this: Umar U, Ayuba AM. *Lannea microcarpa* Leaves Extract as Corrosion Inhibitor for Al Metal in HCl Acid Medium. JOTCSA. 2024;11(4): 1553-64.

DOI: <https://doi.org/10.18596/jotcsa.1192167>

***Corresponding author's E-mail:** ayubaabdullahi@buk.edu.ng

1. INTRODUCTION

Due to their low cost, high strength, ductility, formability, durability, and conductivity, aluminium and its alloys are employed in a variety of industries and in a variety of capacities (1). Despite the fact that aluminium promotes the formation of a compact, adherent passive oxide film to protect it from corrosion in a variety of environments, this film's surface is amphoteric and dissolves significantly when the metal is exposed to strong acid or base solutions, making it susceptible to corrosion (2). Metal corrosion management can be achieved using a variety of approaches, but using inhibitors is the most efficient, secure, and cost-efficient approach (3). Due to the hazardous effects of synthetic chemicals on human and animal life during their manufacturing and usage, synthetic inhibitors are increasingly causing greater environmental problems (4). For their eco-friendliness, accessibility, cost, and effectiveness, phyto-inhibitors are now receiving more attention in the research community than their synthetic equivalents (5).

Lannea microcarpa, an African grape that is dioecious and a member of the Anacardiaceae family, is found in the Sudanian zone (6). It has a 70cm diameter and a maximum height of 15 meters. It has a spherical parasol-like top with a few branches that fall and have dense foliage (7). The species can be found over much of Nigeria and the western Sahel (typically in rocky regions with pockets of sand) (8). We have found that there is a dearth of literature on the use of *Lannea microcarpa* as a corrosion inhibitor for Al metal. This paper focuses on the application of weight loss, electrochemical, FITR and SEM techniques in using *Lannea microcarpa* leaf extract as a corrosion inhibitor for Al metal in acid solution.

2. EXPERIMENTAL SECTION

2.1. Plant Sample Collection

From the Bayero University Kano (Old campus), Gwale local government area, Kano state, Nigeria, fresh leaves of *Lannea microcarpa* were harvested. It was identified by a botanist from the Bayero University Kano's Department of Plant Biology and

given the herbarium registration number BUKHAN 280 for records and references. The leaves were then washed, let to air dry, powdered into a powder, and sieved to pass through a sieve with a mesh size of 250nm.

2.2. Plant Extraction

500 g of the sieved, powdered plant extract sample was soaked in 1.5 L of 95 percent ethanol for two weeks while being constantly stirred. Following that, the mixture was filtered and concentrated using rotavapor (BUCHI Labortechnik AG/9230 Flawil/Switzerland) to remove the extract from the ethanol. After one week of air drying, the concentrated extract was weighed and labelled for future use.

2.3. Aluminium Coupons Preparation

Al (99.36%), Si (0.02%), Fe (0.14%), S (0.04%), Cl (0.03%), K (0.03%), Cu (0.02%), Ti (0.01%), Ga (0.01%), and Mn (0.01%) are the components of the aluminium sheet employed in this investigation. The sheet was mechanically cut into coupons that were each 4 x 3 x 0.11 cm in size. Each voucher was cleaned with ethanol, dipped in acetone, left to dry in the open air to remove any remaining grease, and then preserved in a dessicator (9).

2.4. Preparation of Plant Extract Solutions

Weighing 0.2, 0.4, and 0.6 g of the extract, respectively, and dissolving each in 5 mL of ethanol, then transferring each into 1 litre of 0.2 M HCl separately and making up to the mark, were used to prepare 0.2, 0.4, and 0.6 gL⁻¹ of the extract in 0.2 M HCl. The extract solutions (0.2, 0.4, and 0.6 gL⁻¹) in 0.4 and 0.6 M HCl were made using the same method. In order to balance the solutions, 5ml of ethanol was added to 0.2, 0.4, and 0.6 M HCl to create blank corrodent solutions.

2.5. Phytochemical Analysis of the Plant Extract

The ethanolic extract of *Lannea microcarpa* leaves underwent phytochemical analysis using the procedure described by Prishant *et al.* (10). Alkaloids, saponins, phytosterols, phenols, flavonoids, proteins, amino acids, and triterpenes are a few of the secondary metabolites that were examined.

2.6. Weight Loss Experiments

Aluminium coupons that had already been processed and weighed were immersed separately and completely in 100 mL beakers containing test solutions at various concentrations, both with and without the inhibitor. The beakers were sealed before being placed inside a thermostatic water bath that was kept at a specific temperature. For a total of 4 hours, the coupons were removed from the test solutions at 1-hour intervals, washed with distilled water and a soft brush, dried in acetone, and reweighed. The weight disparities were interpreted as weight reduction (11). The temperature (303, 313 and 323 K), corrodent concentration (0.2, 0.4 and 0.6 M HCl), and extract concentration (0.2, 0.4 and 0.6 g/L) were varied

during the weight loss experiment. The inhibition effectiveness (%I) of the inhibitor, the degree of surface covering (θ), and the corrosion rate of the Al metal coupon (CR) were determined using equations 1-3, respectively, from the weight loss findings (12):

$$\%I = \left(1 - \frac{w_1}{w_2}\right) \times 100 \quad (1)$$

$$\theta = 1 - \frac{w_1}{w_2} \quad (2)$$

$$CR(\text{gh}^{-1}\text{cm}^{-2}) = \frac{\Delta w}{At} \quad (3)$$

Where w_1 and w_2 represent the weight loss (g) of aluminium in the presence and absence of an inhibitor, respectively, in HCl solutions, θ denotes the degree of surface coverage, CR denotes the rate of corrosion, Δw denotes the weight loss (g), A denotes the area of the specimen (cm²), and t denotes the time spent submerged (h).

2.7. Electrochemical Measurements

The electrochemical tests used Al metal samples that were 1 cm x 1 cm in size. Then, these were covered with epoxy resin, leaving only one square surface measuring 1.0 cm² exposed. The exposed surface underwent acetone degreasing, distilled water rinsing, and warm air drying. At a scan rate of 0.333mV per second and a temperature of 298K, linear polarization studies on uninhibited and inhibited (0.2, 0.4, and 0.6 g/L) samples in 0.2 M HCl were performed on potential ranges of -1000 to -2000 mV (13).

2.8. Fourier Transform Infrared Spectrophotometry (FT-IR) Analysis

The main functional groups in the leaves extract of *Lannea microcarpa* and the corrosion by product of inhibited Al metal in HCl solution were identified using an FT-IR instrument type Cary 630 FTIR Spectrophotometer (Agilent Technologies). The material was scanned 32 times at a resolution of 8 cm⁻¹ throughout a wave number range of 650 to 4000 cm⁻¹ for the analysis (14).

2.9. Scanning Electron Microscopy (SEM) Analysis

Using a scanning electron microscope, morphological analyses of the aluminium coupon surfaces exposed to uninhibited and inhibited corrosion systems (0.6 M HCl) for 4 hours at 323 K were taken (Phenom World Eindhoven). A very little amount of the materials to be examined were distributed on the stub during the sample preparation process for SEM analysis, and the stub was then viewed in the instrument to obtain micrographs at an accelerating voltage of 15.00 kV and x500 magnification (13).

3. RESULTS AND DISCUSSION

3.1. Phytochemical Screening

According to the phytochemical analysis of an ethanolic extract of *Lannea microcarpa* leaves, flavonoids, tannins, phenols, proteins, sterols, and saponins were present (Table1). The corrosion

prevention properties of plant extracts on metal surfaces have been attributed to the presence of secondary metabolites (4). The phytoconstituents in the ethanolic extract of *Lannea microcarpa* leaves are thought to have prevented aluminium from corroding because the chemical structures of the majority of these phytoconstituents contained electron-rich bonds or heteroatoms, which facilitate their ability to donate electrons. Researchers have

obtained similar conclusions on the inhibition of metal corrosion by plant extracts (15–16). Additionally, Obi-Egbedi and Obot (17) reported that the presence of π -electrons or appropriate functional groups may facilitate the transfer of charge from the inhibitor's molecule to the charged metal surface (physical adsorption) or the transfer of electrons from the inhibitor's molecule to the vacant orbitals of the metal (chemical adsorption).

Table 1: Phytochemical Screening of the Leaves Extract of *Lannea macrocarpa*.

Bioactive agent	Qualitative analysis
Flavonoids	+
Phenols	+
Proteins/amino acids	+
Alkaloids	-
Saponins	+
Triterpenes	-
Phytosterols	+
Tannins	+

key: + indicates the presence of phytochemical, - indicates the absence of phytochemical.

3.2. Weight Loss Experiment Results

3.2.1. Effect of corrodent concentration

Studying the weight loss of aluminium in 0.2, 0.4, and 0.6 M HCl solutions for 4 hours at 303, 313 and 323 K examined the effect of corrodent concentration. The findings demonstrated that weight loss and the rate of corrosion in unhindered aluminium are both accelerated by an increase in acid concentration (Figure 1). The corrosion rate of aluminium in blanked 0.2 M HCl at 303 K is $0.0875 \text{ mgh}^{-1}\text{cm}^{-2}$, while that in blanked 0.6 M HCl at the same temperature is $1.8229 \text{ mgh}^{-1}\text{cm}^{-2}$, as shown in Table 2. The aforementioned finding might be explained by the fact that chemical reaction rates rise as active species concentrations do (18). In general, the presence of water, air, and H^+ is thought to speed up the corrosion process. As a

result, as the acid concentration rises, the active species, H^+ , rises as well, increasing the corrosion rate. The observation might possibly be the result of an increase in the rate of active species' diffusion and ionization during corrosion reactions (19).

Additionally, the increase in weight loss brought on by an increase in acid concentration on aluminium that has been inhibited may be explained by the fact that acid molecules at higher concentrations can break the bond between extract compounds and aluminium surface to form a hydrogen-aluminium bond (20), which leads to a higher accumulation of the active sites by acid molecules and prevents the penetration of extract molecules to the surface of the aluminium.

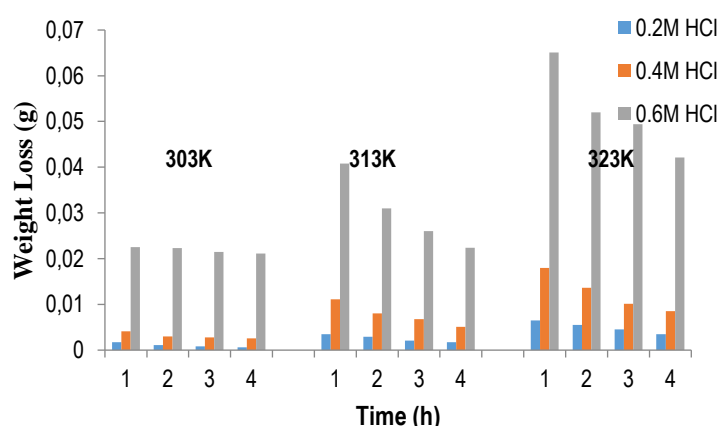


Figure 1: Variation of Weight Loss with Time for the Corrosion of Aluminium in Blank HCl at Varying Temperatures.

3.2.2. Effect of inhibitor on the corrosion process

At 303, 313 and 323 K, the influence of the inhibitor *Lannea microcarpa* at varied concentrations (0.2, 0.4 and 0.6 g/L) on the corrosion process of aluminium has been investigated. The weight loss over time of aluminium immersed in 0.2, 0.4, and 0.6 M HCl with varied extract concentrations at 303, 313 and 323 K is depicted in Figures 2a-c. The

results clearly show that, in all three concentrations of HCl and at all temperatures, the weight loss of aluminium increases with increasing contact time but reduces with increasing inhibitor concentration. The findings also show that all three doses of *Lannea microcarpa* prevented aluminium corrosion in all concentrations of HCl and at all research temperatures. Table 2 showed that while surface

coverage and inhibition effectiveness increased with increasing inhibitor doses, the rate of corrosion of aluminium decreased. The inhibition efficiency rises from 57.14% to 76.19% when the inhibitor concentration is changed from 0.2 g/L to 0.6 g/L in 0.2 M HCl. This demonstrates how *Lansea microcarpa* extract can prevent aluminium from corroding in HCl solutions by acting as an inhibitor. The adsorption of extract molecules onto the Al metal, which reduces the area of contact between Al metal and corrosive media, is responsible for the decrease in weight loss and corrosion rate that is observed with increasing extract concentrations.

According to Thilagavathy and Saratha (21), similar outcomes were obtained.

However, Table 2 shows that the extract's ability to prevent growth declines as temperature rises. For example, the extract's ability to inhibit growth (0.6 g/L) in 0.2 M HCl at 303 K was 76.19 %, but when the temperature was raised to 323 K under the same conditions, the effectiveness dropped to 47 % (Table 2). This shows that the physical adsorption mechanism described by Awe *et al.* (13) is consistent with the adsorption of extract of *Lansea microcarpa* on Al metal.

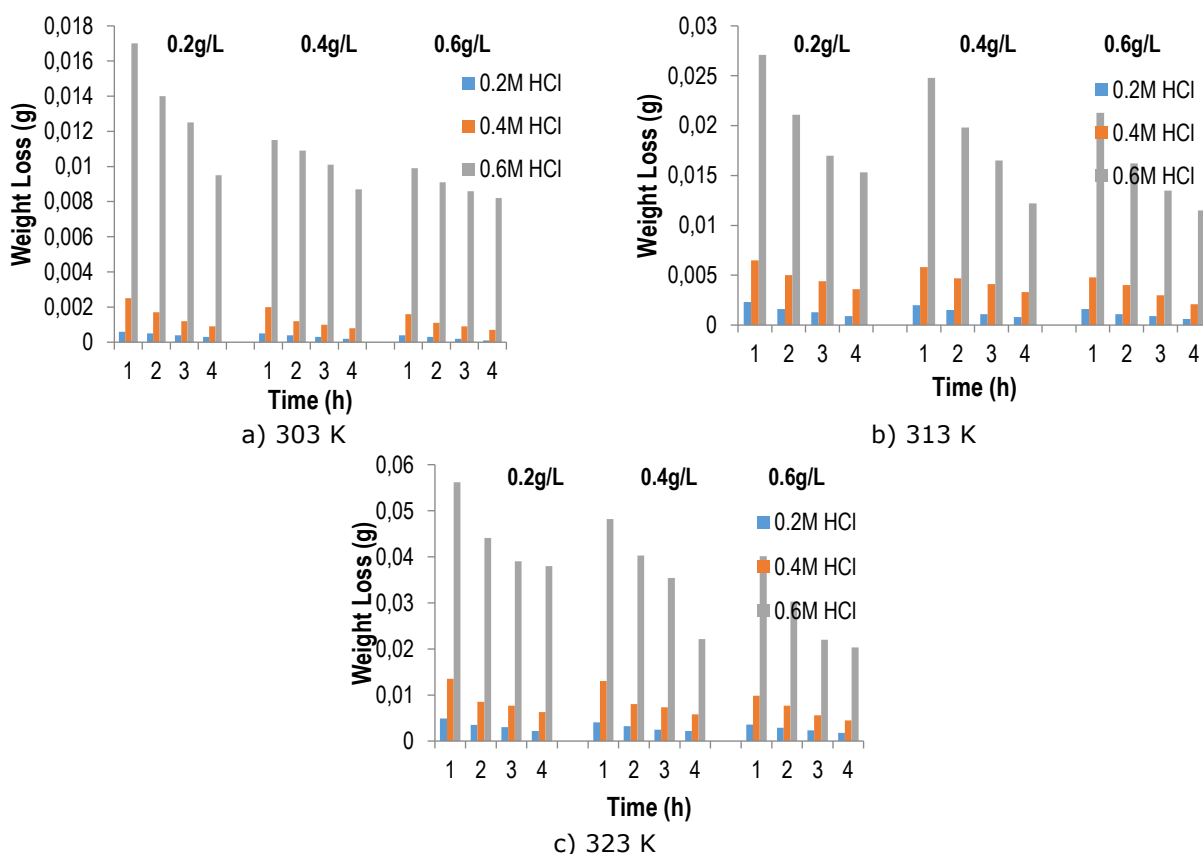


Figure 2: Variation of Weight Loss with Time of Aluminium Immersed in different Concentrations of Extract in 0.2, 0.4 and 0.6M HCl at Varying Temperatures (303, 313 and 323K).

3.2.3. Effect of temperature on the corrosion process

By adjusting the temperature (303, 313 and 323 K), it was possible to determine the impact of temperature on the weight loss and corrosion rate of Al metal immersed in 0.2, 0.4, and 0.6 M HCl for four hours. The results are shown in the Figures (3a-c). The data show that the weight loss of Al metal, both inhibited and uninhibited, increases with temperature in all three acid concentrations. Additionally, Table 2 shows that in all three acid concentrations, the corrosion rate rises with rising temperature. At 303 K, the corrosion rates of the blank and the 0.6 g/L inhibited Al metal were 0.0875 and 0.0208 mg/h.cm² respectively, whereas at 323 K, the rates increase to 0.4167 mg/h.cm² and 0.2208 mg/h.cm², respectively (Table 2). This observation demonstrates that a rise in temperature improves the reactivity of the corrosion medium's active ingredients. A boost in temperature typically

accelerates the cathode's hydrogen evolution reaction, which raises the rate at which metals dissolve. The fact that chemical reactions intensify with rising temperature is another argument in favour of it (general rule guiding the rate of chemical reactions). Additionally, a rise in temperature boosts the kinetic energy of the molecules in the corrosion medium, allowing corrosion to more quickly overcome the energy barrier.

Table 2 also shows that inhibitory effectiveness diminishes as temperature rises. This can be ascribed to the protective coatings on the metal being more soluble, increasing the metal's sensitivity to corrosion (22). Due to the increased molecule desorption at higher temperatures, this data shows poor physical adsorption contact between the inhibitor and Al surface (23).

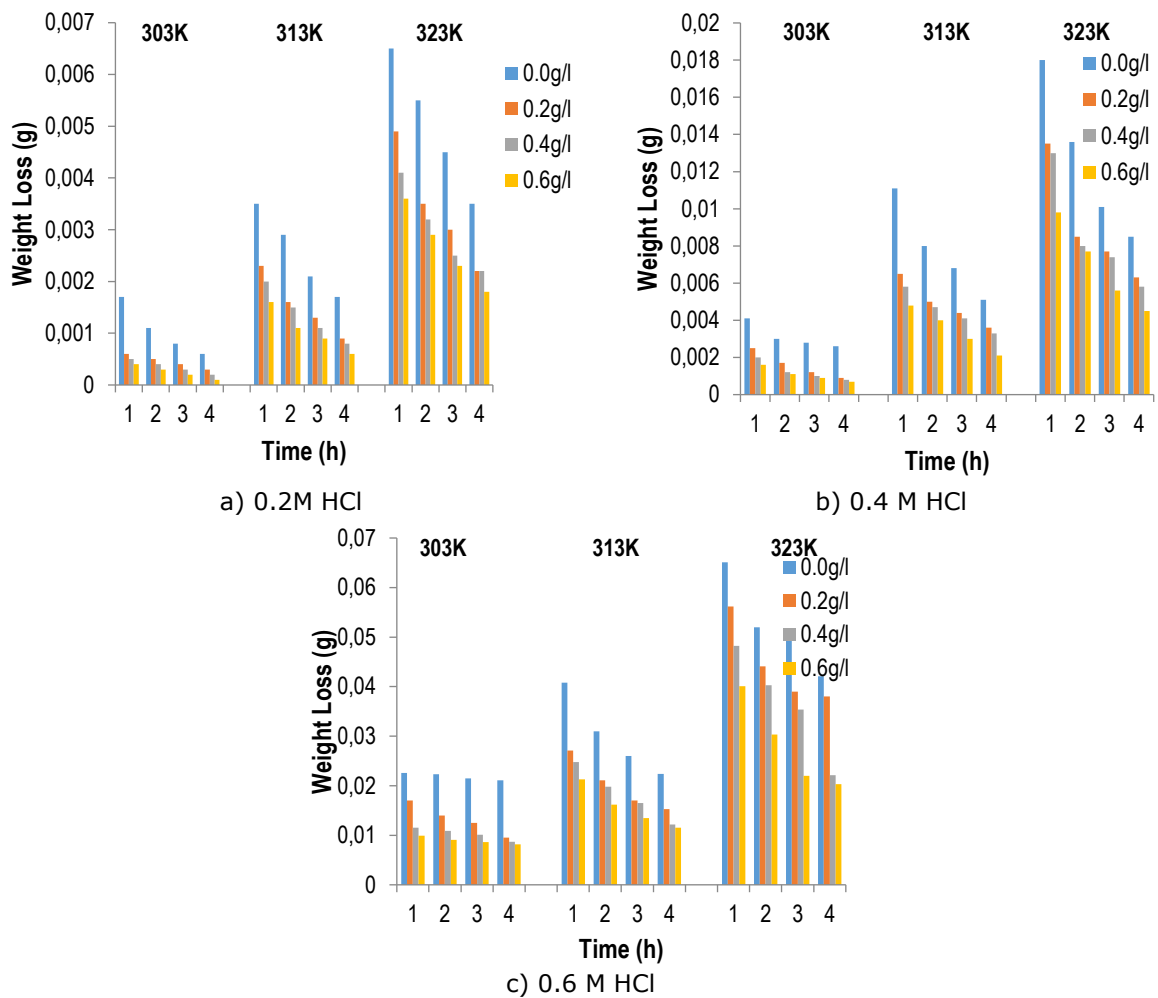


Figure 3: Variation of Weight Loss with Time of Aluminium Immersed in Various Concentrations of Extract at Varying HCl Concentration at 303, 313 and 323 K.

Table 2: Weight Loss Calculated Parameters of Various Concentrations of *Lannea microcarpa* Extract.

Temp. (K)	Conc. of extract (g/L)	0.2 M HCl			0.4 M HCl			0.6 M HCl		
		CR (mg/cm.h) $\times 10^{-2}$	θ	% I (%)	CR (mg/cm.h) $\times 10^{-2}$	θ	% I (%)	CR (mg/cm.h) $\times 10^{-2}$	θ	% I (%)
303	0.0	8.8	-	-	26.0	-	-	182.2	-	-
	0.2	3.8	0.57	57.1	12.9	0.50	50.4	100.0	0.45	45.1
	0.4	2.9	0.67	66.7	10.6	0.59	59.2	85.8	0.53	52.9
	0.6	2.1	0.76	76.2	10.0	0.62	61.6	74.6	0.59	59.1
313	0.0	21.3	-	-	64.6	-	-	250.4	-	-
	0.2	12.7	0.40	40.2	40.6	0.37	37.1	167.7	0.33	33.0
	0.4	11.3	0.47	47.1	37.3	0.42	42.3	152.7	0.39	39.0
	0.6	8.8	0.59	58.8	28.9	0.55	55.2	130.2	0.48	48.0
323	0.0	41.7	-	-	104.6	-	-	434.6	-	-
	0.2	28.3	0.32	32.0	77.1	0.26	26.3	369.4	0.15	15.0
	0.4	25.0	0.40	40.0	70.8	0.32	32.3	317.1	0.27	27.0
	0.6	22.1	0.47	47.0	57.5	0.45	45.0	269.2	0.38	38.1

3.3. Polarization Measurements

Tafel's polarization curves of an aluminium electrode in 0.2 M HCl are shown in Figure 4 in both the presence and absence of various amounts of extract from *Lannea microcarpa*. The plots also show that both cathodic and anodic reactions were suppressed with the addition of various concentrations of *Lannea microcarpa*, indicating that the plant extract served as a mixed-type inhibitor, reducing the rates of both anodic dissolution and cathodic hydrogen

evolution reactions. It can be seen from Figure 4 that the cathodic and anodic reactions in blank HCl follow Tafel's law.

Additionally, it can be seen from Figure 4 that the polarization plots for the inhibited electrodes don't differ significantly from those for the uninhibited electrode, indicating that the presence of *Lannea microcarpa* extract only slows down corrosion rather than changing the electrochemical reactions that

cause corrosion (24).

In Table 3, the electrochemical characteristics obtained by extrapolating Tafel lines are shown, including inhibition efficiency (IE), corrosion rate (CR), corrosion potential (E_{corr}), cathodic and anodic Tafel slopes (β_c and β_a , respectively), and corrosion current density (I_{corr}). The inhibitory efficiencies were determined using equation 4 and it was

discovered that they rose as extract concentration rose (25).

$$IE(\%) = \frac{i_{corr}^0 - i_{corr}}{i_{corr}^0} \times 100 \quad (4)$$

Where i_{corr}^0 and i_{corr} are the corrosion current densities obtained from uninhibited and inhibited solutions respectively.

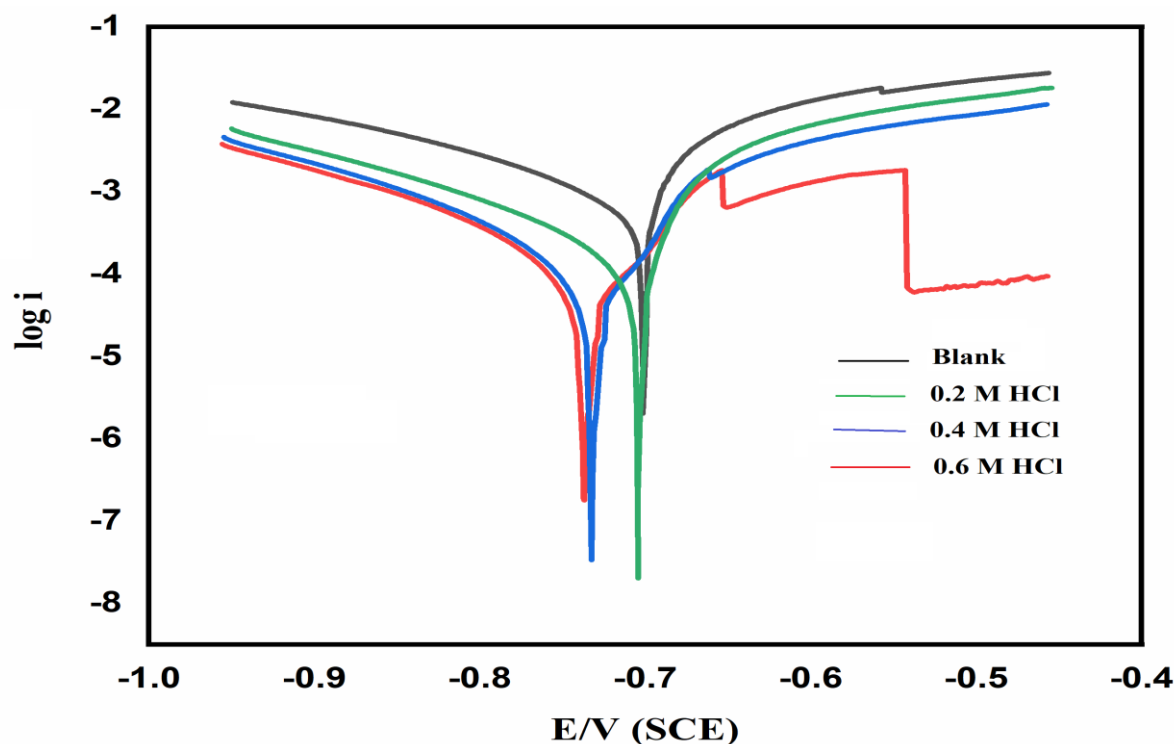


Figure 4: Overlaid Tafel Polarization Curves Recorded for Al in 0.2 M HCl Solution at Varying Concentrations of *Lannea microcarpa*.

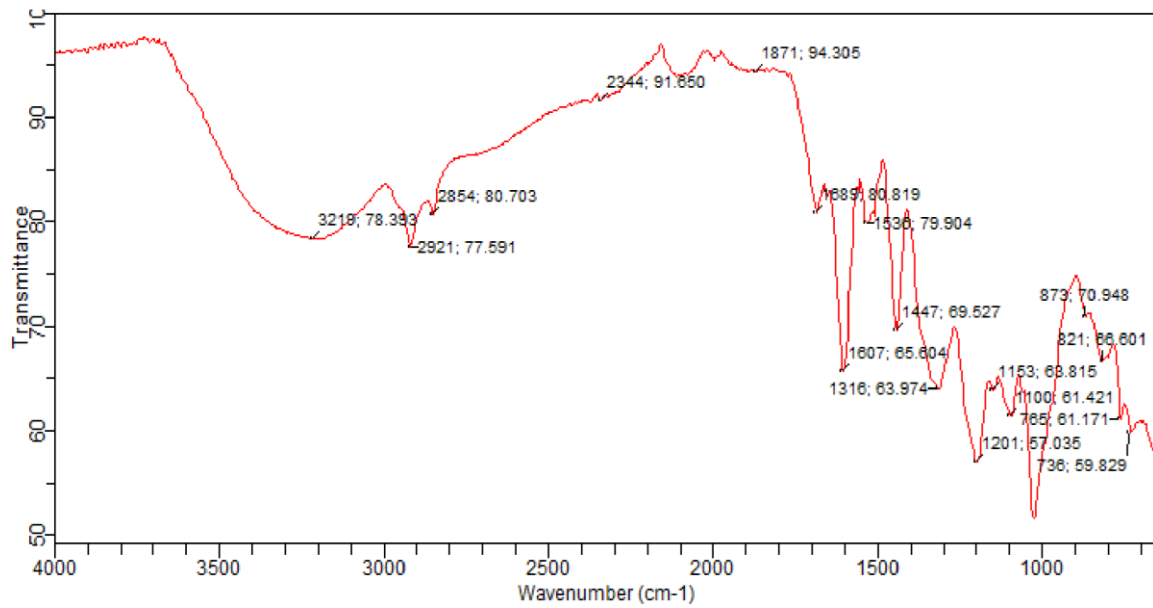
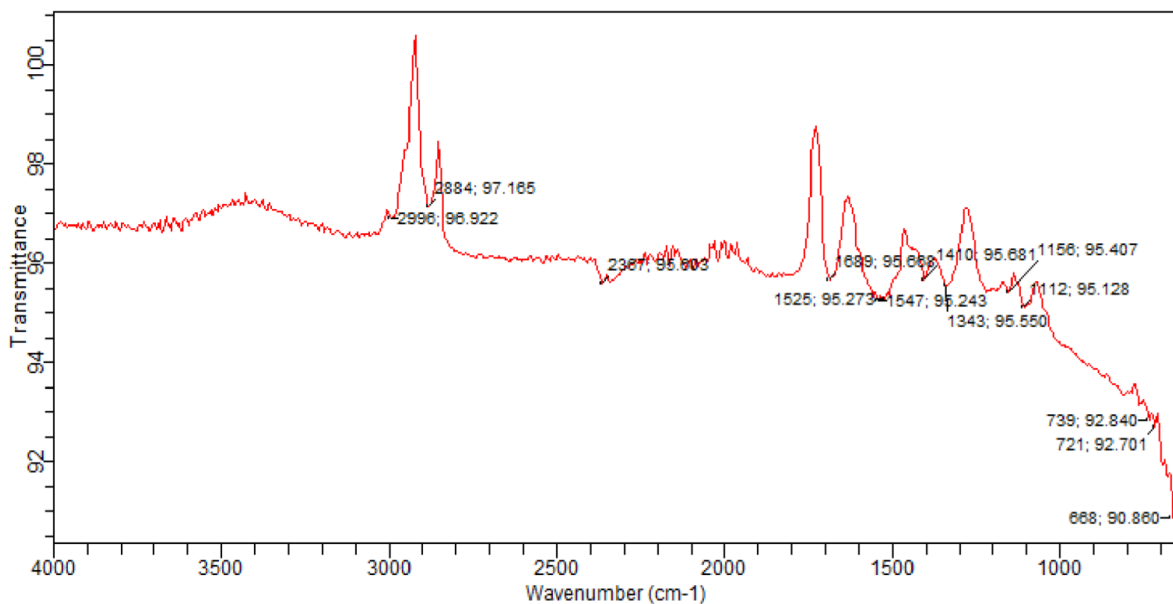
Table 3: Electrochemical Parameters Obtained from Tafel polarization technique for Al in 0.2 M HCl Solution at Varying Concentrations of Extract at 25 °C

Extract concentration (gL ⁻¹)	i_{corr} (μAcm^{-2})	E_{corr} (mV)	β_a (mV dec ⁻¹)	β_c (mV dec ⁻¹)	% I (%)
0.0	-389.197	-701.151	29.996	102.27	-
0.2	-37.571	-737.556	56.091	50.156	90.35
0.4	-28.892	-730.858	37.206	53.955	92.58
0.6	-22.704	-703.843	14.729	36.837	94.17

3.4. Fourier Transform Infrared (FT-IR) Spectroscopic Results

In the images, the IR spectra of a corrosion product with an inhibitor and a powdered extract of *Lannea microcarpa* leaves are displayed (Figures 5 a-b). The C-N stretch at 1100 cm⁻¹ shifts to 1112 cm⁻¹, the C-O stretch at 1153 cm⁻¹ shifts to 1156 cm⁻¹,

the N-O stretch at 1316 cm⁻¹ changes to 1343 cm⁻¹, the C-C stretch in the ring at 1447 cm⁻¹ drops down to 1410 cm⁻¹, and the N-H bend shifts from 1607 cm⁻¹ to 1547 cm⁻¹, according to a comparison of the spectrum of extract and corrosion product with inhibitor. The change in frequency suggests that the metal and plant extract are interacting (26).

(a) FTIR Spectra of the Ethanol Leaves Extract of *Lannea microcarpa*(b) FTIR Spectra of the Corrosion Product of Aluminium in Extract of *Lannea microcarpa***Figure 5:** FTIR Spectra of the studied species.

3.5. Scanning Electron Microscopy

After immersion in the test solutions for 4 hours at 323 K, morphological investigations of the surfaces of uncorroded aluminium and corroded (inhibited and uninhibited acids) specimen were performed using scanning electron microscopy (SEM) (6). The uninhibited system (Fig. 6a) exhibits the most severely corroded surface, which is thoroughly damaged by the presence of cracks, pits, and patches throughout the surface. This is followed by

the metals in the inhibited acid Figures (6b-d), which are clearly less corroded than the uninhibited metal. Uncorroded Al metal doesn't have any surface flaws (Fig.6e). This implies that addition of extract of *Lannea microcarpa* leaves to acid solutions protected the Al metal from undergoing severe corrosion by formation of protective layer on the surface through adsorption of the extract on the aluminium surface.

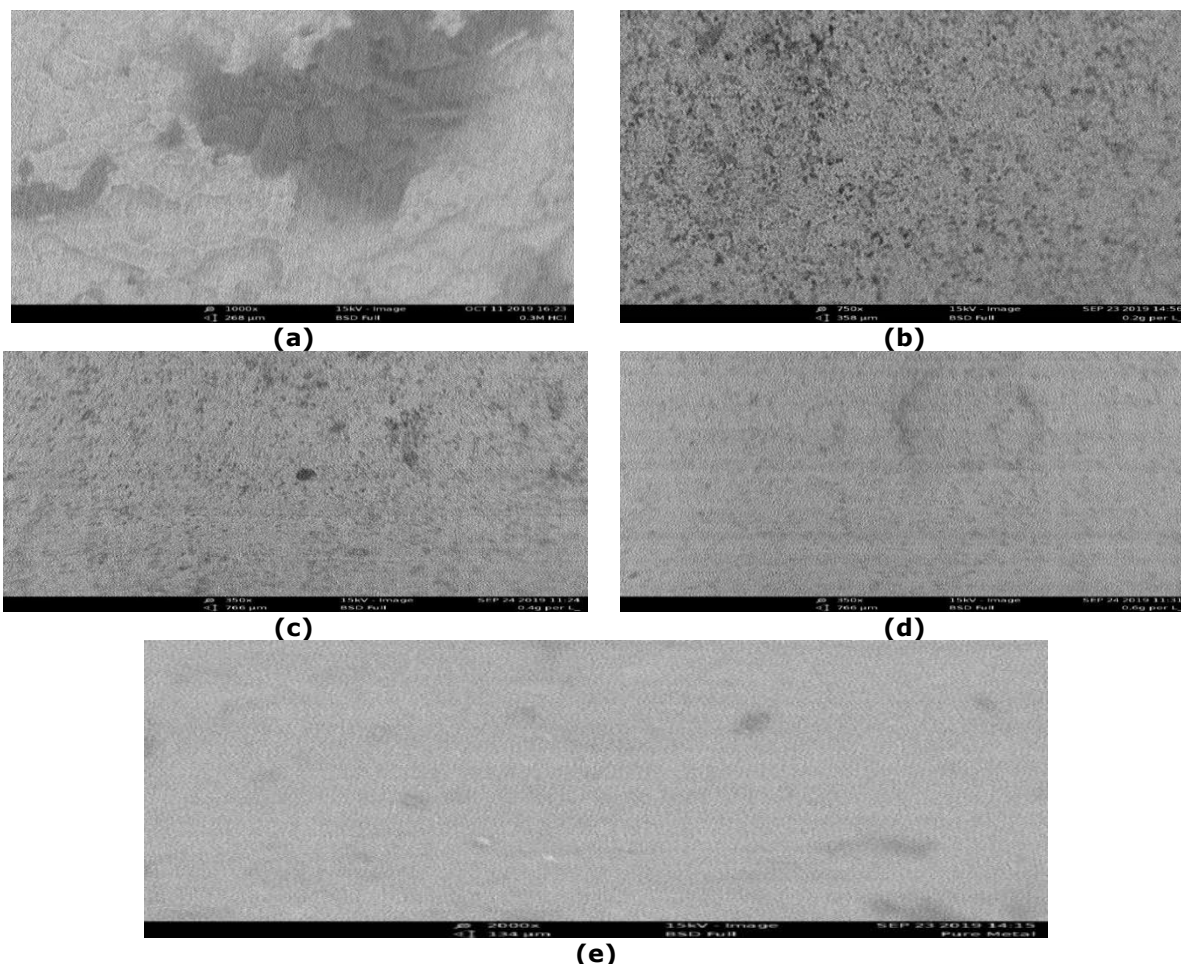


Figure 6: SEM Micrographs of Aluminium Dipped in 0.6 M HCl for (a) 0.0 g/L (Blank) (b) 0.2g/L (c) 0.4 g/L (d) 0.6 g/L of *Lannea microcarpa* Extract, (e) Uncorroded Aluminium.

3.6. Adsorption Isotherms

By creating a thin adsorption layer on the metal surface, inhibitors prevent corrosion on metal surfaces. The degree of inhibitor molecule adsorption on the metal surface has a significant impact on an inhibitor's effectiveness. The adsorption properties of the inhibitors have been used to determine the type of corrosion inhibitors (21). Surface coverage (θ) and inhibitor concentrations can be used to assess the adsorption properties of inhibitors. The interactions between inhibitors and metals are described by a variety of isotherm models. Langmuir, Freundlich, Temkin, Florry-Huggins, and El-Awady isotherm were five of these models that were utilized. The best fit isotherm among them was chosen using the correlation coefficients (R^2) between them. The parameters from the plots of each isotherm at 303, 313 and 323 K are shown in Table 4, and the best fit was determined by taking into account the values of R^2 at all the temperatures. The extract of *Lannea microcarpa* leaves demonstrated strong adherence of the inhibitory process to the Langmuir adsorption

isotherm due to its near to unity when compared to the other isotherms, according to the values of R^2 of the investigated isotherms at all temperatures.

The creation of a monolayer adsorbate layer on the adsorbent's outer surface is quantitatively described by the Langmuir adsorption isotherm. The model assumes homogeneous adsorption energies on the surface and prevents adsorbate transmigration in the surface's plane (27). For both chemical and physical adsorption, the Langmuir equation is the ideal isotherm (28). The equilibrium constants K_{ads} values in Table 4 are all positive, indicating a favorable adsorption (29). Equation 5 presents the Langmuir isotherm.

$$\frac{C}{\theta} = 1/K_{ads} + C \quad (5)$$

Where C is the concentration of inhibitor, θ is the surface coverage and K_{ads} the adsorption equilibrium constant

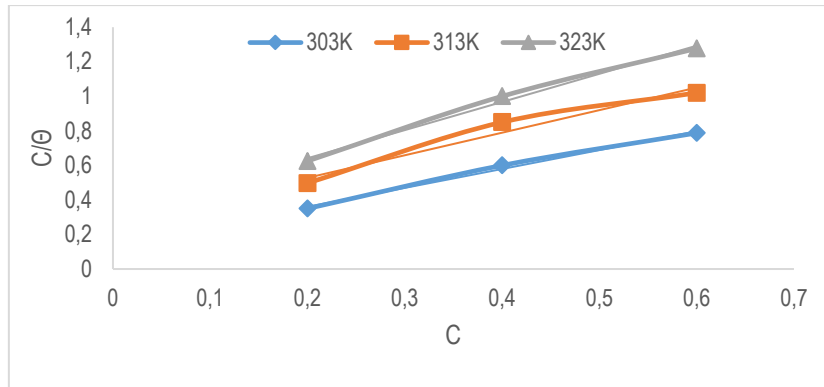


Figure 7: Langmuir Adsorption Isotherm for Al metal in HCl at Different Temperatures.

Table 4: Adsorption Parameters for the Adsorption of *Lannea microcarpa* Extract on Aluminium Surface.

Isotherm	Temperature (K)	Slope	ΔG_{ads} (kJmol ⁻¹)	R ²	K _{ads}
Langmuir	303	1.09	-15.043	0.9932	7.06
	313	1.38	-13.894	0.9690	3.75
	323	1.63	-13.885	0.9925	3.17
Freundlich	303	0.26	-9.738	0.9883	0.86
	313	0.33	-9.428	0.9395	0.67
	323	0.35	-9.214	0.9968	0.56
Temkin	303	0.39	-22.579	0.9777	140.48
	313	0.37	-20.919	0.9122	55.74
	323	0.31	-21.442	0.9876	52.81
Flory-Huggins	303	1.35	-15.460	0.9286	8.33
	313	1.75	-14.268	0.7913	4.33
	323	2.87	-14.921	0.9686	4.66
EL-Awady	303	0.77	-13.894	0.9635	4.47
	313	0.66	-12.043	0.9138	1.84
	323	0.57	-11.187	0.9914	1.16

3.7. Thermodynamic Studies

The free energy of adsorption, ΔG_{ads} was calculated according to the equation (6):

$$\Delta G_{ads} - 2.303RT \log(55.5K_{ads}) \quad (6)$$

ΔG_{ads} is the Gibbs free energy, K_{ads} is the equilibrium constant for adsorption calculated from the intercept of each adsorption isotherm, R is the universal gas constant, T is the system temperature, and 55.5 is the molar concentration of water. For all of the investigated isotherms, the computed values of ΔG_{ads} vary from -2.238 to -22.579 kJmol⁻¹, which is significantly less than the threshold value of -40kJmol⁻¹ needed for the mechanism of chemical adsorption to operate (30). As a result, the adsorption of the *Lannea microcarpa* leaf extract on the surface of aluminium is spontaneous and consistent with physical adsorption (31). Table 4 shows the computed values for ΔG_{ads} and K_{ads} for the tested isotherms at 303, 313 and 323 K. The activation energy for the corrosion process was calculated by using the

Arrhenius equation 7:

$$\log CR = \log A - \frac{E_a}{2.303RT} \quad (7)$$

Where CR is the corrosion rate of metal, A is Arrhenius pre-exponential factor, E_a is activation energy (minimum energy needed before the corrosion reaction of the metal proceed), R is universal gas constant and T is the temperature of the system.

The activation energies were computed and are shown in Table 5 as a straight line with a slope equal to $-E_a/2.303R$ when the logCR plot versus the reciprocal of absolute temperature from equation 7 is performed. While the E_a found for the blank is 36.121 kJmol⁻¹, the computed values of E_a for the extract range from 53.363 to 54.340 kJmol⁻¹. The computed values of E_a were found to be higher in inhibited aluminium than in blank aluminium, pointing to the possibility of an adsorption coating that is physically electrostatic in nature (32-33).

Table 5: Energy Parameters for the Dissolution of Aluminium in HCl in Absence and Presence of Different Concentrations of *Lannea macrocarpa*.

Extract Conc. (gL ⁻¹)	E_a (KJmol ⁻¹)	ΔH_a (kJmol ⁻¹)	ΔS_a (kJmol ⁻¹)
0.0 (blank)	36.121	33.575	-0.1296
0.2	54.330	51.544	-0.0754
0.4	54.340	51.726	-0.0759
0.6	54.363	50.711	-0.0804

The values of enthalpy and entropy changes of the corrosion inhibition processes were calculated according the transition state equation:

$$\log\left(\frac{CR}{T}\right) = \left\{ \log\frac{R}{N_a h} + \frac{\Delta S_a}{2.303R} \right\} - \frac{\Delta H_a}{2.303RT} \quad (8)$$

Where ΔH_a signifies the enthalpy of the corrosion process, ΔS_a denotes the entropy of activation for the corrosion process, N_a is Avogadro's number and h is plank's constant.

The enthalpy and entropy change of activation for the corrosion inhibition process were estimated from the straight line with slope equal to $(-\Delta H_a)/(2.303R)$ and intercept equal to $\log R(N_a h + (\Delta S_a)/(2.303R))$ that results from the plot of CR/T vs reciprocal of absolute temperature, as shown in Table 5. The endothermic nature of the aluminium dissolving process is shown by the positive values of enthalpy change of activation in both the presence and absence of extract (34). While the activated complex in the rate-determining stage represents association rather than dissociation, as shown by the negative values of adsorption entropies, there is a decrease in disorderliness as one moves from reactant to activated complex (35).

4. CONCLUSION

The results of this investigation employing weight loss, electrochemical, SEM, and FTIR demonstrate that the leaves extract of *Lannea microcarpa* efficiently suppresses the corrosion of aluminium under the examined conditions. With a rise in extract concentration but a decrease in corrosion concentration or temperature, the extract's ability to suppress aluminium corrosion increases. Because several phytochemicals were detected in the extract, it was determined that the inhibitory process was of the mixed type by adsorption. Thermodynamic measurements showed that the extract spontaneously and endothermally adhered to the aluminium surface, supporting the physical adsorption process mechanism.

5. CONFLICT OF INTEREST

The authors declare no conflict of interest.

6. ACKNOWLEDGMENTS

The contribution of the staff of Central Laboratory Complex, Bayero University, Kano, Nigeria is highly appreciated in conducting the surface characterization of the aluminium coupon samples.

7. REFERENCES

1. Ayuba AM, Uzairu A, Abba H, Shallangwa GA. Hydroxycarboxylic acids as corrosion inhibitors on aluminium metal: A computational study. J Mater Environ Sci [Internet]. 2018;9(11):3026–34. Available from: [<URL>](#).
2. Umaru U, Ayuba A. Quantum chemical calculations and molecular dynamic simulation studies on the corrosion inhibition of aluminium

metal by myricetin derivatives. J New Technol Mater [Internet]. 2020;10(2):18–28. Available from: [<URL>](#).

3. Umar U, Muhammad AA. Computational study of anticorrosive effects of some thiazole derivatives against the corrosion of aluminium. RHAZES Green Appl Chem [Internet]. 2020 Nov 27;10:113–28. Available from: [<URL>](#).
4. Ayuba AM, Abubakar M. Inhibiting aluminium acid corrosion using leaves extract of *Guiera senegalensis*. J Fundam Appl Sci [Internet]. 2021;13(2):634–56. Available from: [<URL>](#).
5. Al-Otaibi MS, Al-Mayouf AM, Khan M, Mousa AA, Al-Mazroa SA, Alkhathlan HZ. Corrosion inhibitory action of some plant extracts on the corrosion of mild steel in acidic media. Arab J Chem [Internet]. 2014 Jul 1;7(3):340–6. Available from: [<URL>](#).
6. Arbonnier M. Arbres, arbustes et lianes des zones sèches d'Afrique de l'Oues [Internet]. Paris; 2009. Available from: [<URL>](#).
7. Marquet M, Jansen PCM. *Lannea microcarpa* Engl. & K. Krause. Prota 3 Dye Tann Tanins. 2005;
8. Awodoyin RO, Olubode OS, Ogbu JU, Balogun RB, Nwawuisi JU, Orji KO. Indigenous fruit trees of tropical Africa: Status, opportunity for development and biodiversity management. Agric Sci [Internet]. 2015 Jan 8;6(1):31–41. Available from: [<URL>](#).
9. Bereket G, Öğretir C, Yurt A. Quantum mechanical calculations on some 4-methyl-5-substituted imidazole derivatives as acidic corrosion inhibitor for zinc. J Mol Struct THEOCHEM [Internet]. 2001 Aug 27;571(1–3):139–45. Available from: [<URL>](#).
10. Tiwari P, Kumar B, Kaur M, Kaur G, Kaur H. Phytochemical screening and extraction: A review. Int Pharm Sci. 2011;1(1):98–106.
11. Matter HAB, Ayad TM, Alkatly AAI. Grape leaves and ziziphus spina-christi, extracts as a green inhibitors corrosion for the carbon steel and oil pipelines in 1M H₂SO₄. Almanara Sci J [Internet]. 2024 May 4;2024(6):124–45. Available from: [<URL>](#).
12. Matter H, Ayad TM. Study the effect of extract berry and mango leaves as a corrosion inhibitor of Cu, carbon steel and oil pipelines. J Pure Appl Sci [Internet]. 2022 Jun 20;21(1):154–64. Available from: [<URL>](#).
13. Awe FE, Idris SO, Abdulwahab M, Oguzie EE. Theoretical and experimental inhibitive properties of mild steel in HCl by ethanolic extract of *Boscia senegalensis*. Slawin AMZ, editor. Cogent Chem [Internet]. 2015 Dec 31;1(1):1112676. Available from: [<URL>](#).
14. Eddy NO, Odoemelam SA, Odiongenyi AO. Ethanol extract of *Musa acuminata* peel as an eco-friendly inhibitor for the corrosion 24 of mild steel in H₂SO₄. Adv Nat Appl Sci [Internet]. 2008;2(1):35–

42. Available from: [<URL>](#).

15. Ayuba AM, Abdullateef A. Corrosion inhibition potentials of *Strichnos spinosa* L. on Aluminium in 0.9 M HCl medium: Experimental and theoretical investigations. Alger J Eng Technol [Internet]. 2020;3:28. Available from: [<URL>](#).

16. Ebenso EE, Eddy NO, Odiongenyi AO. Corrosion inhibitive properties and adsorption behaviour of ethanol extract of *Piper guinensis* as a green corrosion inhibitor for mild steel in H₂SO₄. African J Pure Appl Chem [Internet]. 2008;2(11):107–15. Available from: [<URL>](#).

17. Obi-Egbedi NO, Obot IB. Xanthione: A new and effective corrosion inhibitor for mild steel in sulphuric acid solution. Arab J Chem [Internet]. 2013 Apr 1;6(2):211–23. Available from: [<URL>](#).

18. Hossain N, Asaduzzaman Chowdhury M, Kchaou M. An overview of green corrosion inhibitors for sustainable and environment friendly industrial development. J Adhes Sci Technol [Internet]. 2021 Apr 3;35(7):673–90. Available from: [<URL>](#).

19. Ayuba AM, Auta MA, Shehu NU. View of comparative study of the inhibitive properties of ethanolic extract of *Gmelina arborea* on corrosion of aluminium in different media. Appl J Environ Eng Sci [Internet]. 2020;6(4):374–86. Available from: [<URL>](#).

20. Krishnaveni K, Ravichandran J. Effect of aqueous extract of leaves of *Morinda tinctoria* on corrosion inhibition of aluminium surface in HCl medium. Trans Nonferrous Met Soc China [Internet]. 2014 Aug 1;24(8):2704–12. Available from: [<URL>](#).

21. Thilagavathy P, Saratha R. Mirabilis Jalapa flowers extract as corrosion inhibitor for the mild steel corrosion in 1M HCL. IOSR J Appl Chem [Internet]. 2015;8(1):30–5. Available from: [<URL>](#).

22. Udom G, Cooney G, Abia A. The effect of *Acanthus montanus* leaves extract on corrosion of aluminium in hydrochloric acid medium. Curr J Appl Sci Technol [Internet]. 2017 Dec 26;25(2):1–11. Available from: [<URL>](#).

23. Zhao Q, Tang T, Dang P, Zhang Z, Wang F. The corrosion inhibition effect of triazinedithiol inhibitors for aluminum alloy in a 1 M HCl solution. Metals [Internet]. 2017 Feb 5;7(2):44. Available from: [<URL>](#).

24. Khaled KF, Amin MA. Electrochemical and molecular dynamics simulation studies on the corrosion inhibition of aluminum in molar hydrochloric acid using some imidazole derivatives. J Appl Electrochem [Internet]. 2009 Dec 23;39(12):2553–68. Available from: [<URL>](#).

25. Tang H, Sun J, Su D, Huang Y, Wu P. Coumarin

as a green inhibitor of chloride-induced aluminum corrosion: theoretical calculation and experimental exploration. RSC Adv [Internet]. 2021 Jul 16;11(40):24926–37. Available from: [<URL>](#).

26. Okafor PC, Osabor VI, Ebenso EE. Eco-friendly corrosion inhibitors: inhibitive action of ethanol extracts of *Garcinia kola* for the corrosion of mild steel in H₂SO₄ solutions. Pigment Resin Technol [Internet]. 2007 Sep 18;36(5):299–305. Available from: [<URL>](#).

27. Fadare OO, Okoronkwo AE, Olasehinde EF. Assessment of anti-corrosion potentials of extract of *Ficus asperifolia*-Miq (Moraceae) on mild steel in acidic medium. African J Pure Appl Chem [Internet]. 2016;10(1):8–22. Available from: [<URL>](#).

28. Eddy NO, Ebenso E. Adsorption and inhibitive properties of ethanol extracts of *Musa sapientum* peels as a green corrosion inhibitor for mild steel in H₂SO₄. African J Pure Appl Chem [Internet]. 2008;2(6):46–54. Available from: [<URL>](#).

29. Nnanna LA, Onwuagba BN, Mejeha IM, Okeoma KB. Inhibition effects of some plant extracts on the acid corrosion of aluminium alloy. African J Pure Appl Chem [Internet]. 2010;4(1):11–6. Available from: [<URL>](#).

30. Prabhu D, Padmalatha R. Corrosion inhibition of 6063 aluminum alloy by *Coriandrum sativum* L seed extract in phosphoric acid medium. J Mater Environ Sci [Internet]. 2013;4(5):732–43. Available from: [<URL>](#).

31. Loto CA. Inhibition effect of tea (*Camellia Sinensis*) extract on the corrosion of mild steel in dilute sulphuric acid. J Mater Environ Sci [Internet]. 2011;2(4):335–44. Available from: [<URL>](#).

32. Awad MI. Eco friendly corrosion inhibitors: Inhibitive action of quinine for corrosion of low carbon steel in 1 M HCl. J Appl Electrochem [Internet]. 2006 Oct 29;36(10):1163–8. Available from: [<URL>](#).

33. Oguzie EE, Adindu CB, Enenebeaku CK, Ogukwe CE, Chidiebere MA, Oguzie KL. Natural products for materials protection: Mechanism of corrosion inhibition of mild steel by acid extracts of *Piper guineense*. J Phys Chem C [Internet]. 2012 Jun 28;116(25):13603–15. Available from: [<URL>](#).

34. Cooney GA, Tambari BL, Iboroma DS. Evaluation of the corrosion inhibition potentials of green-tip forest lily (*Clivia nobilis*) leaves extract on mild steel in acid media. J Appl Sci Environ Manag [Internet]. 2018 Feb 8;22(1):90. Available from: [<URL>](#).

35. Oguzie EE. Corrosion inhibitive effect and adsorption behaviour of *Hibiscus Sabdariffa* extract on mild steel in acidic media. Port Electrochim Acta [Internet]. 2008;26:303–14. Available from: [<URL>](#).



Catalytic Performance of Newly Synthesized Heterocyclic Hydrazone Derivatives for Production of High Yield Neem Biodiesel

Mussarat Jabeen^{1*} , Irum Razzaq², Sajida Noureen², Syed Ubaid Hassan² , Noreen Aslam¹ 
Ansa Madeeha Zafar¹, Karamat Mehmood², Misbah-ul-Ain Khan²

¹Department of Chemistry, Govt. Sadiq College Women University, Bahawalpur 63100, Pakistan.

²Chemistry Department, The Islamia University of Bahawalpur, Bahawalpur 63100, Pakistan.

Abstract: Biodiesel, a sustainable and environmentally friendly substitute for diesel, has attracted growing attention in recent years. The reuse of non-edible neem oil as a feedstock for biodiesel production is affordable and naturally safe. This study aimed to understand the understudied benefits of using heterocyclic organic hydrazone derivatives as catalysts for high yield biodiesel production. The catalysts were characterized using techniques such as EIMS, NMR, CHN and FTIR analysis, which revealed the morphological and functional characteristics of the catalyst. The optimum process conditions were found to be catalyst concentration of 50mg/10mL, methanol-to-oil molar ratio of 3:1, reaction temperature of 60 °C, and reaction duration of 60 min; these conditions yielded 95% biodiesel. The produced biodiesel was analyzed using FTIR, and different parameters like moisture content, saponification value, density, acid value, iodine value, and FFA value. The use of neem oil and organic based catalysts for biodiesel production is an economical and environmentally sustainable process.

Keywords: Biodiesel, Neem oil, Hydrazone, Energy crisis, Catalysis.

Submitted: May 31, 2024. **Accepted:** September 22, 2024.

Cite this: Jabeen M, Razzaq I, Noureen S, Hassan SU, Aslam N, Zafar AM, Mehmood K, Khan MUA. Catalytic Performance of Newly Synthesized Heterocyclic Hydrazone Derivatives for Production of High Yield Neem Biodiesel. JOTCSA. 2024;11(4): 1565-80.

DOI: <https://doi.org/10.18596/jotcsa.1493074>

***Corresponding author's E-mail:** dr.mussaratjabeen@gmail.com

1. INTRODUCTION

In terms of energy security, modern society faces a number of challenges. As a result of overpopulation, energy demand has increased significantly on earth (1,2). Energy needs around the world are largely met by fossil fuels. Increasing population is causing these natural resources to rapidly deplete because of overconsumption of energy (3). In addition, fossil fuels are non-renewable and their combustion causes a number of environmental problems (4). Globally, 89 million barrels of fossil fuel diesel are consumed each year. In 2007, there were 806 million cars and trucks on the road, which will rise to 1.3 billion by 2030 and 2 billion by 2050 (5).

Currently, researchers are exploring alternative energy sources, and biodiesel (fatty acid methyl ester (FAME)) known as neat-fuel (6) or bio-oil (7) is one of the best options due to its cheapness, non-polluting, environmentally friendly, non-toxic nature, and recyclable properties (8-10). Almost 95% of biodiesel is produced from plant oils extracted from

seeds (11). Here is a high demand for edible oils (sunflower, palm, coconut, soya bean, etc.), but non-edible oils (neem, castor, karanja, tobacco, jojoba, rubber seed, etc.) can also be used for biodiesel production (12). Since, neem (*Azadirachta indica*) is natural antiseptic and widely harvested around the globe (13), however, a large amount of neem seeds wasted. It is estimated that neem seeds contain 30-40% oil, with a very high value of free fatty acids (1). Biodiesel production for oils with high FFA (free fatty acid) value have two major steps, 1st step (esterification), to reduce FFA by using an acid catalyst and 2nd step (transesterification), to convert esterified oil into monoester by using alkaline catalyst (14,15).

The production of biodiesel is accelerated by the use of catalysts. In order to accomplish this goal, various catalysts can be used, including homogeneous, heterogeneous, enzyme, and biocatalyst catalysts (16). In homogeneous catalysts, triglycerides are converted into esters when sodium hydroxide or potassium hydroxide react with methanol or ethanol

to form alkoxide ions (17). The product is difficult to separate because of its extremely basic nature (16). Apart from these, sodium carbonate and sodium bicarbonate also show effective results (18). Since heterogeneous catalysts can be used both for esterification and transesterification, researchers prefer heterogeneous catalysts (19,20) due to their hydrothermal stability and acid-base nature (21), which include metal salts, metal oxides (14) like MgO (22,23), CdO₂ (24), CaO (10,25,26), Al₂O₃ (27), ZnO, Mn-doped ZnO (28,29), BaO (30), TiO₂ (31), heteropoly acids (32), zeolites (33), ZrO₂-SBA-15 (34), lipases (35), laccases (36), LOBE (37).

Besides these inorganic catalysts, a limited number of organic compounds can also be used to catalyze biodiesel production, including imidazole (38), sulphonic acid derivatives (39), organic amine derivative (40), cellulose derivatives (41,42), graphene-based heterogeneous catalyst (43,44) and MOFs (45-49). Organic-based catalysts can be easily separated or recycled due to their organic nature and exhibit promising results (50).

In recent years, organic compounds have attracted a great deal of attention for the production of biodiesel due to their ease of use, high thermal stability, easy racialization, less CO & CO₂ emissions and high yield (51). The current work aims to synthesize some heterocyclic-organic compounds (hydrazones) and investigate the efficiency of these synthesized catalysts for biodiesel production from neem oil. Hydrazone contain azomethine linkage and gained much importance during the past few decades due to its unique nature, structure and properties (52). The synthesized catalysts were characterized a variety of spectroscopic techniques including EIMS, NMR, FTIR, and CHN, while FTIR was used to confirm and characterize produced biodiesel. Based on the results of this study, more than 75% of the production can be achieved with these synthesized heterocyclic catalysts in a shorter time frame.

2. MATERIAL METHOD

2.1. Feedstock

Neem oil is readily available on the local market, obtained from the neem tree and stored at room temperature for a long time.

2.2. Catalyst Preparation

For the production of neem biodiesel, eight heterocyclic hydrazone derivatives were synthesized. previously, three hydrazone (L2, L21 & L24) were reported (53,54) while five (L12, L19, L20, L22 & L23) were newly synthesized. All furan-2-carbaldehyde derivatives were synthesized by the reaction of substituted anilines and furan-2-carboxyaldehyde via Meerwien Arylation (55). These substituted aldehydes were refluxed with different hydrazides (benzohydrazide, isoniazide, nicotinic acid hydrazide, salicylic acid hydrazide) in ethanol for 3 hours with 2-3 drops of catalyst (HCl). Recrystallization of synthesized yellow colored products was carried out with ethanol and ethyl acetate (3:1). For further use, the desired products were characterized and stored.

2.3. Characterization

Vactor 22 FTIR, Bruker AV 300 & 400 NMR, Thermo Scientific FLASH 2000 CHN analyzer, and MAT 312 mass spectrometer were used to characterize all synthesized hydrazone derivatives. A pre-coated TLC was used to minister the reaction, and spots were visualized in a UVC-11 compact UV lamp at 254nm and 365nm.

2.4. Acid Value & Free Fatty Acid Value

Acid value and free fatty acid values of neem oil, esterified oil and biodiesel were calculated via titration method as reported (56,57), the sample was titrated with 0.1N KOH solution while phenolphthalein was used as indicator until solution become light pink. The acid value and free fatty acid value was calculated by the mentioned formula equation 1&2.

$$\text{FFA (\%)} = \frac{A \times N \times 28.2}{W} \quad (1)$$

$$\text{Acid value (mg/g)} = \frac{A \times N \times 56.1}{W} \quad (2)$$

2.5. Reaction Procedure

Free Fatty acid value of neem oil is very high, so, to reduce this FFA value and increase efficiency of biodiesel, two-step process esterification before transesterification was performed (15). This was accomplished by using organic heterocyclic hydrazone derivatives instead of normal acid as catalysts in 1st step and alkali catalyst in 2nd step.

2.6. Esterification of Neem Oil

50mg catalyst (hydrazone) and 15 mL methanol were added to 10 mL neem oil. In a Pyrex container, the mixture was heated for 60 minutes at 40°C. The resulting mixture was then poured into a funnel and kept undisturbed for 24 hours until two clear layers were formed. Oil layer was separated, washed and stored for further use.

2.7. Transesterification of Esterified Oil

10mg KOH in 8mL methanol was mixed with 10mL of pretreated oil for 60 mint at 60°C. The mixture was poured in separating funnel until two layers formed. During this synthesis, the top layer contains biodiesel, the middle layer contains glycerin, and the bottom layer mostly contains unreacted catalysts.

2.8. Washing & Drying of Biodiesel

Hot distil water was added in biodiesel layer and separated. Process was continued for several times until a clear biodiesel layer separated. After washing biodiesel, it may contain traces of water, that are removed by heating it at 100°C. In order to characterize, it was cooled and stored at room temperature.

Percentage yield was calculated by Equation below;

$$\text{Percentage yield} = \frac{\text{Weight of biodiesel produced}}{\text{Weight of neem oil used}} \times 100 \quad (3)$$

3. RESULTS AND DISCUSSION

3.1. Synthesis of Heterocyclic Hydrazone Catalysts

Substituted aldehydes were prepared according to the reported procedure (Meerwien Arylation). These aldehydes were treated with four different hydrazides to produce hydrazone moieties.

Prior to their use as catalysts for biodiesel production, all yellow colored synthesized heterocyclic compounds were purified, recrystallized and characterized.

3.2. Characterization of Heterocyclic Catalysts

Structure, ketonic nature, purity and bonding of these moieties was confirmed by spectral analysis and elemental analysis. EIMS confirms the structure by molecular ion peak and fragmentation peaks. Important functional groups like N-H, O-H, C=O, N-N, C=N, and C-N show absorption bands at 3200 cm^{-1} , above 3000 cm^{-1} , above 1600 cm^{-1} , $\sim 1030\text{ cm}^{-1}$, ~ 1600 and $\sim 1100\text{ cm}^{-1}$ in FTIR. Two singlet peaks appeared in the 11-12 ppm region, confirming the presence of N-H and O-H. A singlet at 8.4 ppm was also a sign of hydrogen directly attached to C=N.

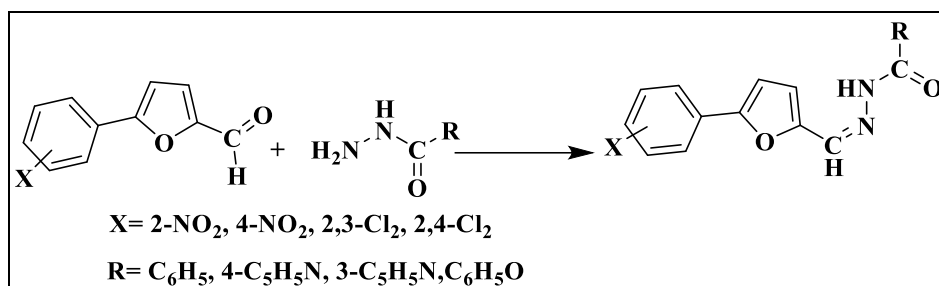


Figure 1: General scheme for synthesis of catalysts.

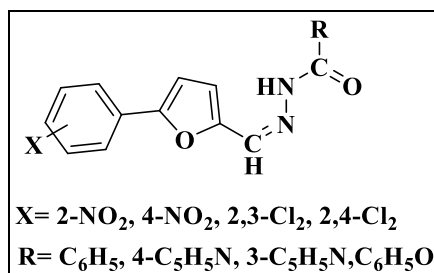


Figure 2: Ketonic structure of synthesized catalysts.

3.3. Production of Biodiesel

These synthesized compounds were used as an efficient acid catalyst for biodiesel formation from neem oil. The N-H group in these compounds enhances their acidic activity. In the same way, the electronic effects of azomethine groups influence the acidic character indirectly. With these hydrazone derivatives, we achieved yields of over 75% within a short period of time.

3.4. Optimization of Reaction Parameters

Several parameters can effect on the yield of biodiesel, including reaction time, reaction temperature, choice of solvent and amount of catalyst.

3.4.1. Reaction Time

Reaction time, an important parameter that effect biodiesel's yield and quality. Daramola reported that an increase in reaction time can lead to an increase in impurities or soap formation (58). The goal is to test the efficiency of the synthesized catalysts during esterification, which produces biodiesel. The yields of all catalysts increase from 20 mints to 60 mints but decrease when time increases to 80 mints, which may be caused by side reactions. As the time increased to 80 mints, a thick waxy layer formed that was difficult to separate.

Table 1: Characterization of synthesized hydrazone catalysts.

Heterocyclic catalyst	EIMS	FTIR	¹ H-NMR	CHN (found)
L2	[M ⁺] 336, [M ⁺ -NO] 306, [M ⁺ -C ₆ H ₄ NO ₂] 214, [M ⁺ -C ₁₁ H ₈ N ₃ O ₃] 106, [M ⁺ -C ₁₂ H ₈ N ₃ O ₄] 78	N-H (3219.0), C=O (1664.9 ^{sh}), C=N (1602.7), C-N (1147.9)	N-H (12.2, s), C-H=N (8.44, s)	60.63 (C) 3.38 (H) 16.37 (N)
L12	[M ⁺] 351, [M ⁺ -NO] 321, [M ⁺ -C ₇ H ₅ O ₂] 231, [M ⁺ -C ₈ H ₇ N ₂ O ₂] 188, [M ⁺ -C ₁₀ H ₆ NO ₃] 163, [M ⁺ -C ₁₁ H ₇ N ₂ O ₃] 137, [M ⁺ -C ₁₁ H ₈ N ₃ O ₃] 121	N-H (3237.7), O-H (3060.3 ^b), C=O (1623.9 ^{sh}), C-N (1148.4), N-N (1034.5)	N-H (11.9, s), O-H (11.8, s), CH=N (8.412, s)	61.55 (C) 3.76 (H) 11.81 (N)
L19	[M ⁺⁺²] 361, [M ⁺] 359, [M ⁺ -CO] 329, [M ²⁺ -C ₂ H ₂ Cl] 302, [M ²⁺ -C ₆ H ₅ N ₂ O] 239, [M ⁺ -C ₆ H ₅ N ₂ O] 237, [M ⁺ -C ₁₁ H ₈ N ₃ O ₂] 145, [M ⁺ -C ₁₁ H ₇ Cl ₂ N ₂ O] 106, [C ₅ H ₄ N] ⁺ 78	N-H (3177.0), C=O (1654.4 ^{sh}), C=N (1564.8), C-N (1153.5), N-N (1026.8), C-Cl (794.3)	N-H (12.1, s), CH=N (8.39, s)	56.73 (C) 3.03 (H) 19.56 (Cl) 11.49 (N)
L20	[M ⁺⁺²] 376, [M ⁺] 374, [M ²⁺ -C ₄ H ₂ Cl ₂] 256, [M ⁺ -C ₄ H ₂ Cl ₂] 254, [M ⁺ -C ₇ H ₆ NO ₂] 237, [M ⁺ -C ₇ H ₅ Cl ₂] 219, [M ⁺ -C ₉ H ₇ N ₂ O ₃] 182, [M ⁺ -C ₁₁ H ₇ Cl ₂ N ₂ O] 121, [C ₆ H ₅ O] ⁺ 93	N-H (3218.3), O-H (3072.2 ^b), C=O (1640.8 ^{sh}), C=N (1559.9), C-N (1169.9), N-N (1028.2), C-Cl (801.2 Sh)	N-H (11.9, s), O-H (11.8, s), CH=N (8.417, s)	57.48 (C) 3.18 (H) 18.84 (Cl) 7.36 (N)
L21	[M ⁺⁺²] 360, [M ⁺] 358, [M ⁺⁻²] 356, [M ⁺ -C ₅ H ₇] 295, [M ²⁺ -C ₇ H ₅ O] 255, [M ²⁺ -C ₇ H ₆ NO] 240, [M ²⁺ -C ₁₀ H ₅ Cl ₂ O] 149, [C ₅ H ₇] ⁺ 69	N-H (3217.7), C=O (1649.5 ^{sh}), C=N (1150.4), C-N (1142.8), N-N (1026.7), C-Cl (796.6)	N-H (12.0, s), CH=N (8.44, s)	59.91 (C) 3.29 (H) 19.79 (Cl) 7.82 (N)
L22	[M ⁺⁺²] 361, [M ⁺] 359, [M ²⁺ -C ₂ H ₂ Cl] 302, [M ⁺ -C ₆ H ₅ N ₂ O] 237, [M ²⁺ -C ₆ H ₅ N ₃ O] 225, [M ⁺ -C ₈ H ₅ Cl ₂ O] 174, [M ²⁺ -C ₁₁ H ₈ N ₃ O ₂] 147, [M ⁺ -C ₁₁ H ₇] 220, [Cl ₂ N ₂ O ₃] ⁺ 106, [C ₅ H ₄ N] ⁺ 78	N-H (3146.2), C=O (1667.2 ^{sh}), C=N (1550.0), N-N (1030.6), C-Cl (790.6)	N-H (12.19, s), C-H=N (8.44, s)	56.39 (C) 3.02 (H) 19.62 (Cl) 11.55 (N)
L23	[M ⁺⁺²] 361, [M ⁺] 359, [M ^{+-Cl}] 324, [M ²⁺ -C ₂ H ₂ Cl] 302, [M ⁺ -C ₂ H ₂ Cl ₂] 266, [M ²⁺ -C ₆ H ₅ N ₂ O] 239, [M ⁺ -C ₆ H ₅ N ₂ O] 237, [M ⁺ -C ₈ H ₅ Cl ₂ O] 174, [M ²⁺ -C ₁₁ H ₈ N ₃ O ₂] 147, [M ⁺ -C ₁₁ H ₇ Cl ₂ N ₂ O] 106, [C ₅ H ₄ N] ⁺ 78	N-H (3192.3), C=O (1611.1 ^{sh}), C=N (1552.3), C-N (1150.0), N-N (1026.6), C-Cl (797.8)	H-N (12.12, s), C-H=N (8.43, s)	56.57 (C) 3.02 (H) 19.69 (Cl) 11.56 (N)
L24	[M ⁺⁺²] 376, [M ⁺] 374 [M ²⁺ -C ₂ H ₃ O] 335, [M ^{+-2Cl}] 305, [M ⁺ -C ₄ H ₂ Cl ₂] 254, [M ⁺ -C ₁₂ H ₉ N ₂ O ₃] 145, [M ⁺ -C ₁₁ H ₆ Cl ₂ NO] 135, [M ⁺ -C ₁₁ H ₇ Cl ₂ N ₂ O] 121, [C ₆ H ₅ O] 93, [M ²⁺ -C ₁₃ H ₉ Cl ₂ N ₂ O ₂] 85, [M ⁺ -C ₁₄ H ₉ Cl ₂ N ₂ O ₂] 69	N-H (3234.4), O-H (3083.4 ^b), C=O (1619.4 ^{sh}), C=N (1538.0), C-N (1140.6), N-N (1024.2), (C-Cl) (790.4)	N-H (11.96, s), O-H (11.74, s), CH=N (8.44, s)	57.81 (C) 3.18 (H) 18.97 (Cl) 7.37 (N)

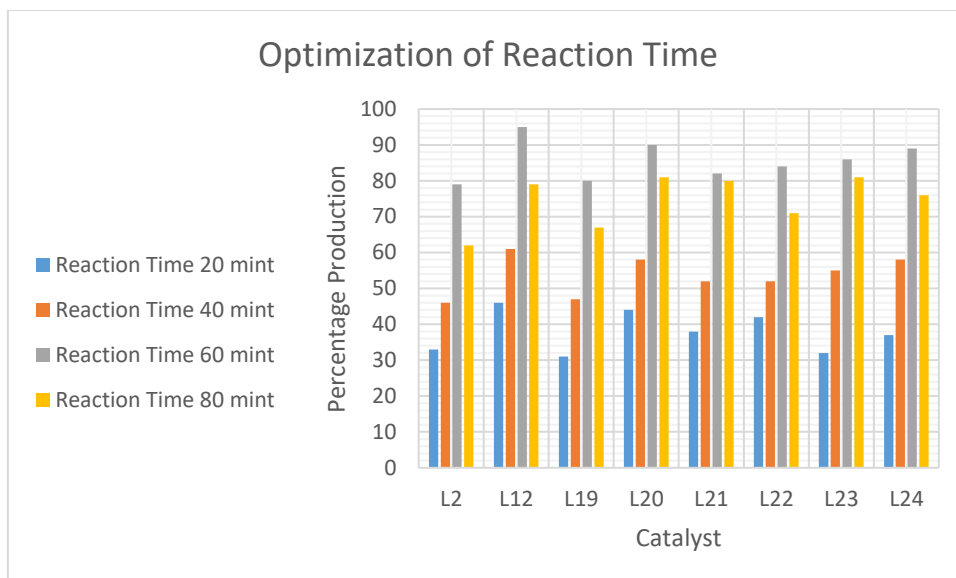


Figure 3: Optimization of reaction time.

3.4.2. Reaction Temperature

No doubt, the reaction temperature is one of the most critical parameters that affects the production and quality of biodiesel. Leung reported, the yield is generally increased as the temperature is increased during the esterification and transesterification process (59), but the quality is usually decreased because of the presence of byproducts during these processes (60). Using the silica-based catalysts, Zuo and coworkers proposed that 60°C is the optimal

temperature for esterification (61). During the esterification process, the highest yield (up to 95%) was obtained at 60°C, but this decreased (up to 80%) as the temperature increased to 80°C. Similarly, the same effect was observed in transesterification. The maximum yield was obtained at 60°C and as the temperature increased, the yield decreased due to the formation of soap and by-products as the temperature increased.

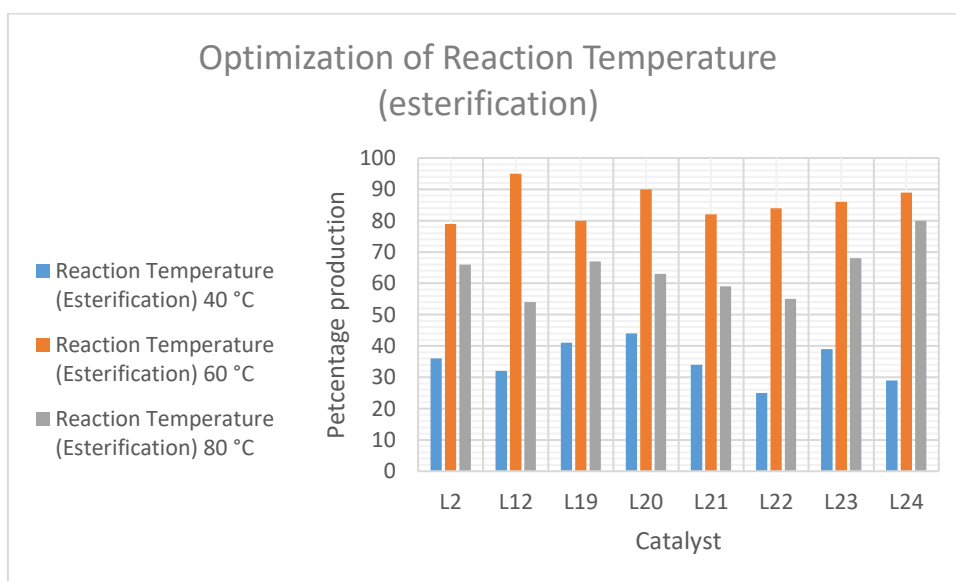


Figure 4: Optimization of reaction temperature during esterification.

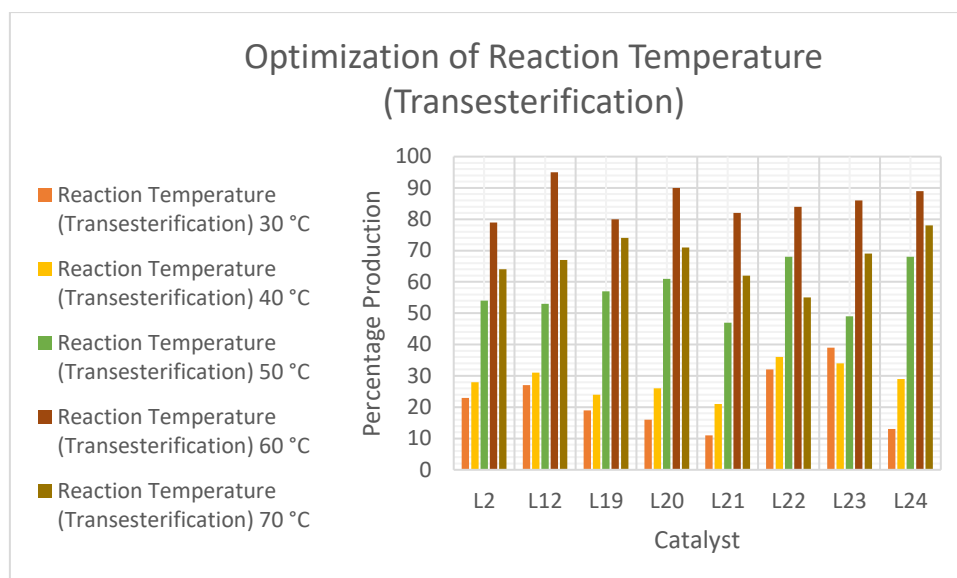


Figure 5: Optimization of reaction temperature for transesterification.

3.4.3. Solvent Type

Additionally, solvent is directly related to biodiesel production. A polar solvent, such as methanol, or an alcohol, can facilitate and solubilize the reactants in order to improve biodiesel yields. It was preferable to use methanol as a solvent instead of ethanol or any other alcohol since it was easy to separate with less soap precipitation (34). There is a larger amount of solvent required for non-edible oils as compared to edible oils, less alcohol amount causes thick material to form, which is more difficult to separate. Ali et.al., reported the molar ratio of oil and methanol should be 1:3 for high production (1). Furthermore, the use of ethanol in non-edible oils can lead to the formation of soap. It has also been reported that heptane, hexane, and toluene have been used as co-solvents to increase the yield of biodiesel. However, this can lead to toxic environmental effects or increase biodiesel toxicity (62).

3.4.4. Catalyst Amount

Biodiesel production is strongly influenced by the amount and type of catalyst used. The basic catalyst can be used for biodiesel production if the free fatty acid content is less than 1-2% (63). However, the free fatty acid content in non-edible oils like neem oil exceeds 20% and the basic catalyst causes soap formation (64). As a result, it is necessary to minimize this FFA value by esterifying with an acid catalyst before transesterification or using a basic catalyst (65). The study used organic derivatives as acid catalysts during esterification, which affected biodiesel production. The optimal amount of acid catalyst for biodiesel production was 50mg, and by increasing or decreasing the amount, the yield also decreased, possibly due to the formation of by-products or side reactions.

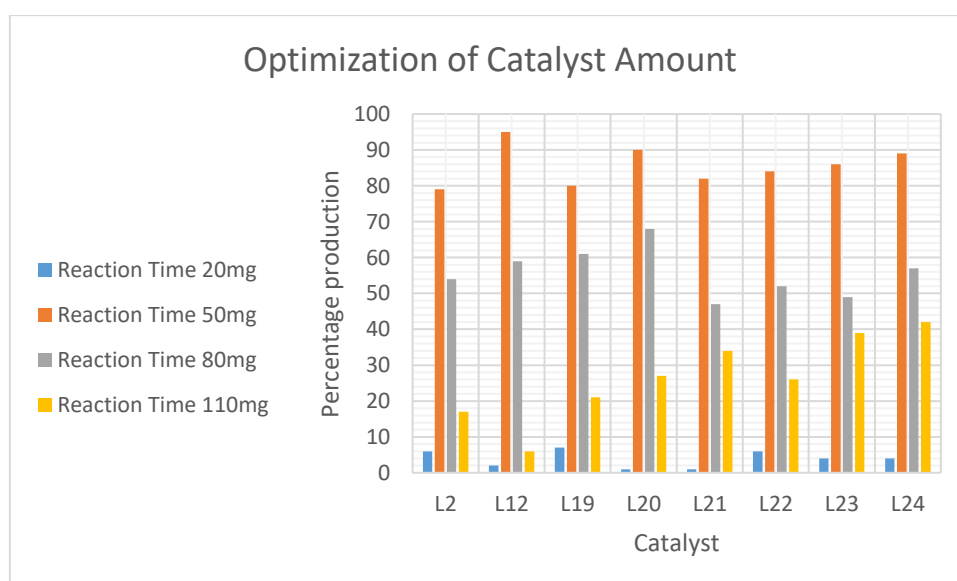


Figure 6: Optimization of catalyst's amount.

Similarly, the biodiesel production is also effected by concentration of basic catalyst (transesterification). The optimum amount calculated experimentally was

10mg of KOH. According to Aboelazayem and co-workers, the optimum KOH ratio should be 1:3-1:7 for high production yields (66). Strong alkali causes

soap formation and decreases the yield of biodiesel (64). To avoid this problem, KOH was preferred as a best activator for transesterification (67) with FAME's yield up-to 99% (68).

3.5. Characterization of Biodiesel

A range of parameters such as moisture content, viscosity, density, pH and color were presented in Table 2.

Table 2: Characterization of biodiesel synthesized from organic heterocyclic catalysts.

Sample	Color	%age Yield	Density g/cm ³	Viscosity mm ² /s	pH	Moisture content (%)
Neem Oil (69,70)	light yellow	-	0.91	31.99	6.10	4.61
Biodiesel (71) (standard)	Yellow-colorless	-	0.83-0.89	1.9-6	5.97-6.76	0.3-6.0
Neem Biodiesel (70,72) (standard)	Golden yellow	-	0.89	4.99-5.21	6.69	>0.5
L2	Bright yellow	79	0.81	5.1	6.52	0.3
L12	Yellow	95	0.86	4.79	6.73	0.13
L19	Light yellow	80	0.87	5.16	6.66	0.27
L20	Yellow	90	0.81	5.41	6.91	0.19
L21	Dull yellow	82	0.86	5.33	6.36	0.14
L22	Light yellow	84	0.86	4.66	6.71	0.22
L23	Light yellow	86	0.83	4.82	6.71	0.19
L24	Golden	89	0.87	4.97	6.55	0.15

As, high moisture content promote microbial growth (9). Moisture content of neem biodiesels was low ranging 0.13-0.3 % that was within the standard limits indicating purity of these biodiesels. The samples ranged in color from yellow to colorless, with little variation in pH between 6.3 and 6.91. According to the results, FFA value of neem oil was very high 24.76(mg/g), therefore, alone transesterification cause soap formation and affect the quality as well as yield of biodiesel (73). To reduce this FFA, esterification with acid catalysts (organic hydrazone derivatives) was successfully performed and FFA value is less than 1 in all cases indicating it as an excellent diesel fuel. Density of biodiesel is 0.83-0.89 g/cm³ while for neem biodiesel 0.91g/cm³. All the synthesized biodiesel exhibit densities ranges 0.81-0.87g/cm³ suggest the good quality of these biodiesels. Viscosity of neem oil is very high 31.99 (mm²/s) and cause smoke while standard biodiesel and neem biodiesel has low viscosity 1.9-6 (mm²/s) and 4.99-5.21 (mm²/s) respectively. All the

synthesized biodiesel has also low viscosity ranges 4.66-5.33 (mm²/s) that is better for good combustion and less smoky. Moisture content is also low in all biodiesels indicate the purity.

Basically, acid value is the mg of KOH to neutralize FFA of 1g oil/fat, higher the acid value less will the quality and quantity of biodiesel (9). Acid value of neem oil is very high due to high FFA (9.163 mg/g) while biodiesels have low acid value (0.161-0.261 mg/g) within the standards. Iodine value indicate the unsaturation of neem oil due to the presence of unsaturated fatty and is very high 73.814 (mg I₂/100g), while neem biodiesel has 49.49 (mg I₂/100g), other biodiesels also have low iodine value 51-58 (mg I₂/100g). Saponification value of neem oil is also very high (199.810 mg/g) indicating its high tendency to form soap when reacted to basic catalyst which reduces to (167-176 mg/g) significantly and presented in Table 3.

Table 1: Acid value, iodine value, FFA and saponification value of biodiesels.

Sample	Acid value (mg/g)	Iodine value (mg I ₂ /100g)	FFA value	Saponification value (mg/g)
Neem Oil (71,74)	9.163	73.814	24.76	199.810
Biodiesel (71,75) (standard)	≤0.80	8.9	≥2	-
Neem Biodiesel (71,76) (standard)	0.13	49.49	0.7	167.36
L2	0.228	56.31	0.87	171.33
L12	0.161	51.55	0.76	167.37
L19	0.182	53.20	0.82	170.29
L20	0.166	52.11	0.71	167.61
L21	0.171	53.04	0.83	167.67
L22	0.299	57.93	0.81	176.31
L23	0.261	55.63	0.83	170.11
L24	0.223	56.79	0.89	172.74

3.6. FTIR Characterization

In addition to the physical parameters mentioned above, the synthesized biodiesels were characterized using FTIR (Figure 7-14). Broad absorption band of -OH near 3000-3400cm⁻¹ is absent indicate these biodiesels are almost free from moisture. Sharp absorption peak near 1743 cm⁻¹ are caused by C=O stretch indicating the presence of esters in all samples, while CH stretching results in peaks near

2922 cm⁻¹ and 2850 cm⁻¹. Asymmetric and symmetric deformation vibrations of CH are approximated at 1458 cm⁻¹ and 1380 cm⁻¹, respectively indicate mono, di or triglyceride glycols in all tested samples. Due to C-O stretching, there are absorption peaks near 1166 cm⁻¹, 1240 cm⁻¹, and 1100 cm⁻¹, while long chain absorption peaks appear at 720 cm⁻¹.

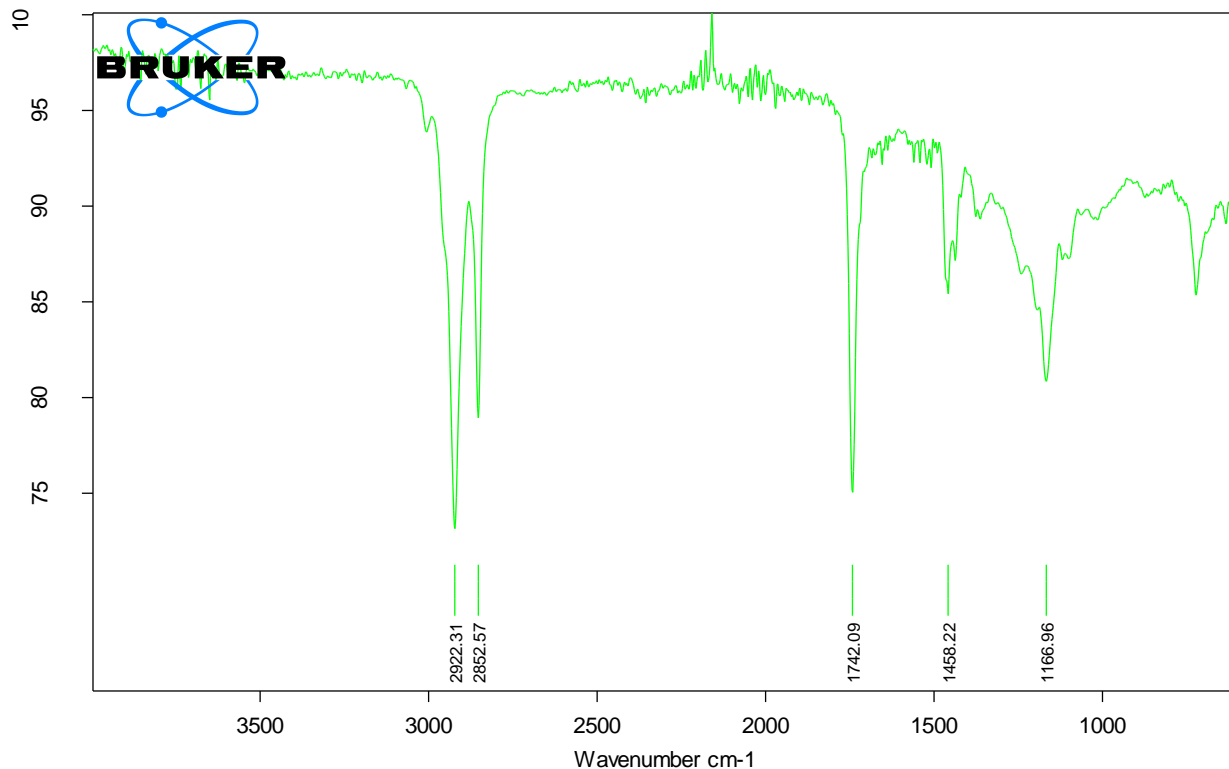


Figure 7: FTIR spectra of biodiesel prepared by L2 as a catalyst.

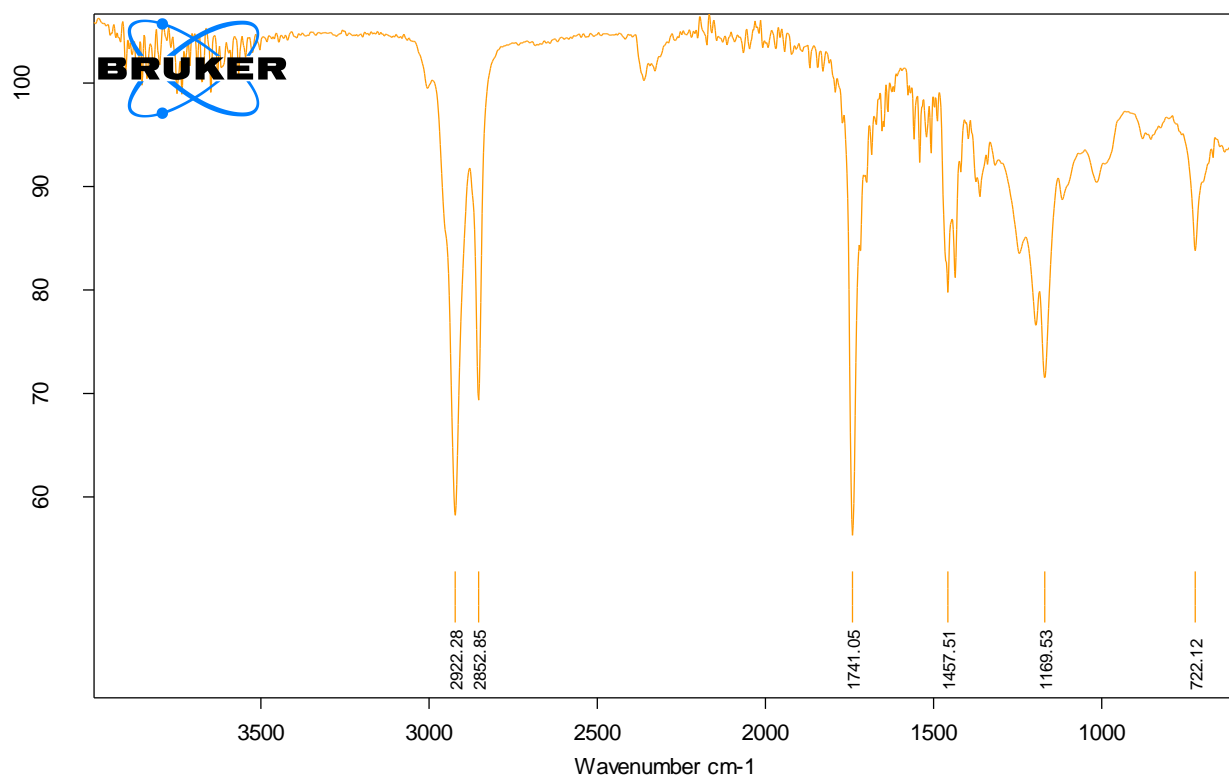


Figure 8: FTIR spectra of biodiesel prepared by L12 as a catalyst.

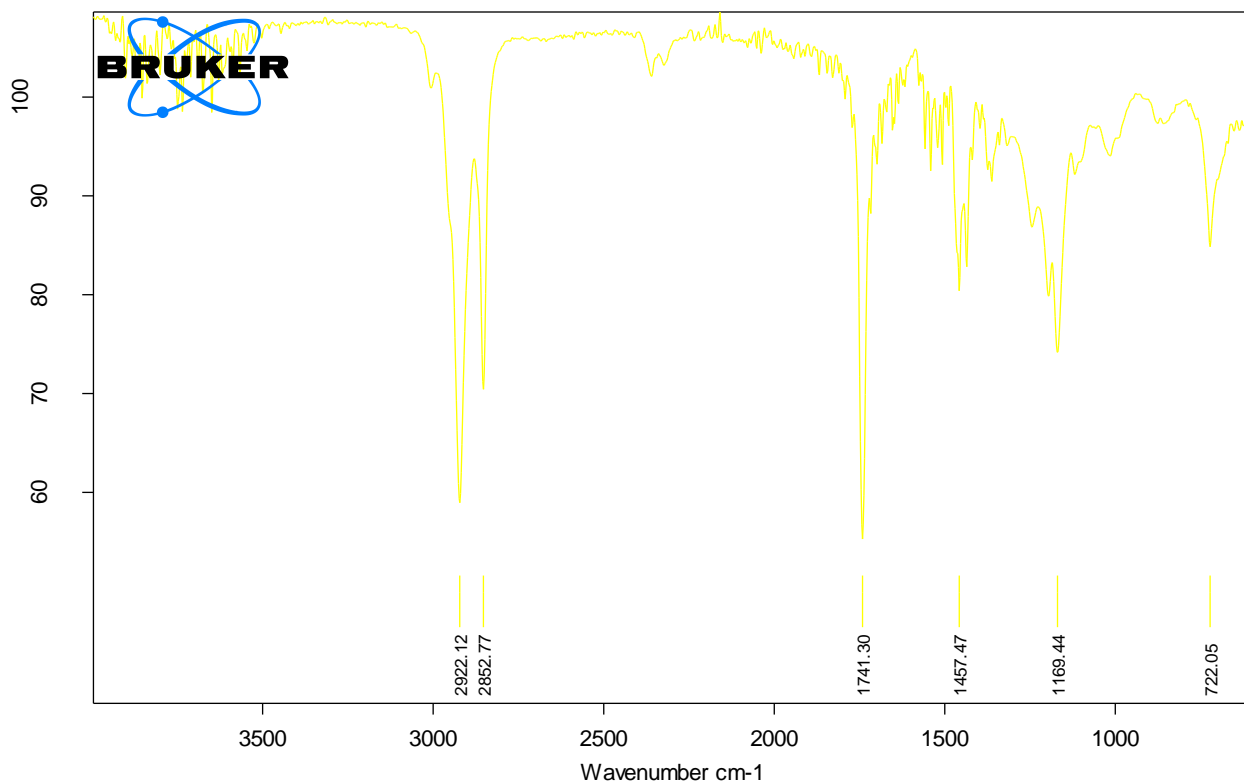


Figure 9: FTIR spectra of biodiesel prepared by L19 as a catalyst.

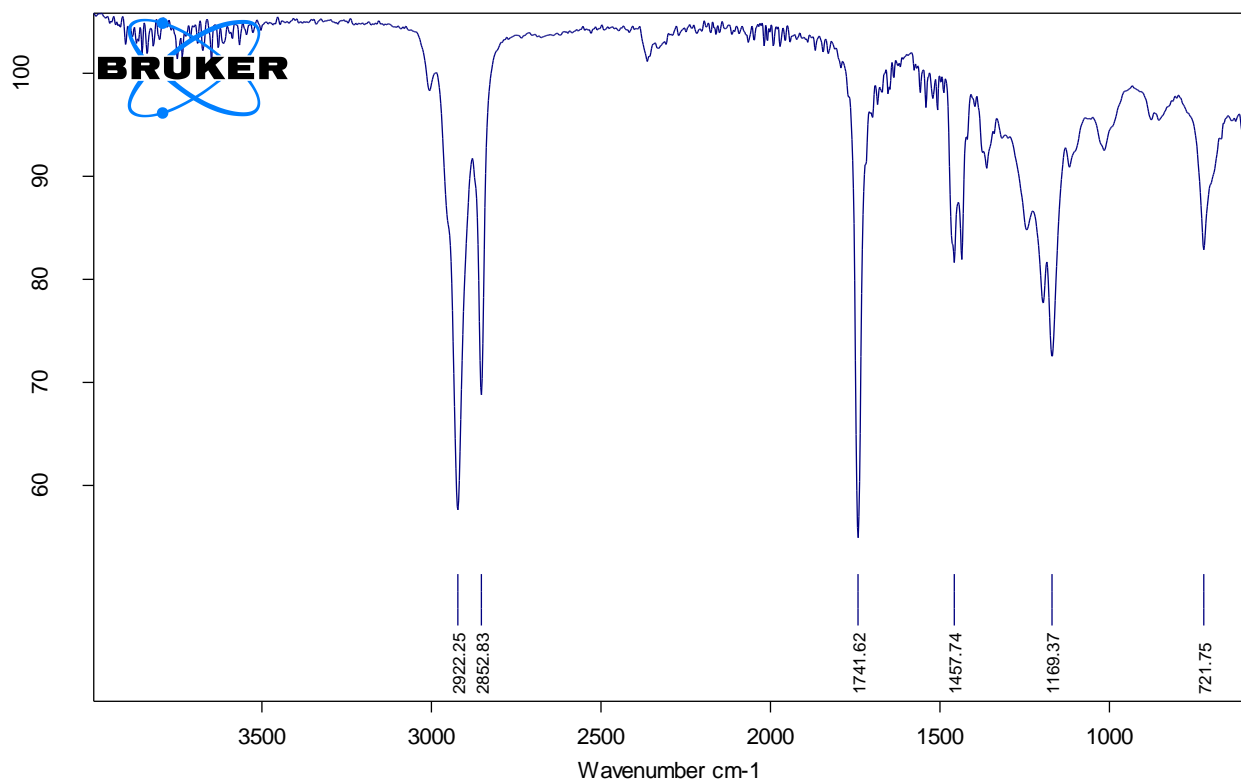


Figure 10: FTIR spectra of biodiesel prepared by L20 as a catalyst.

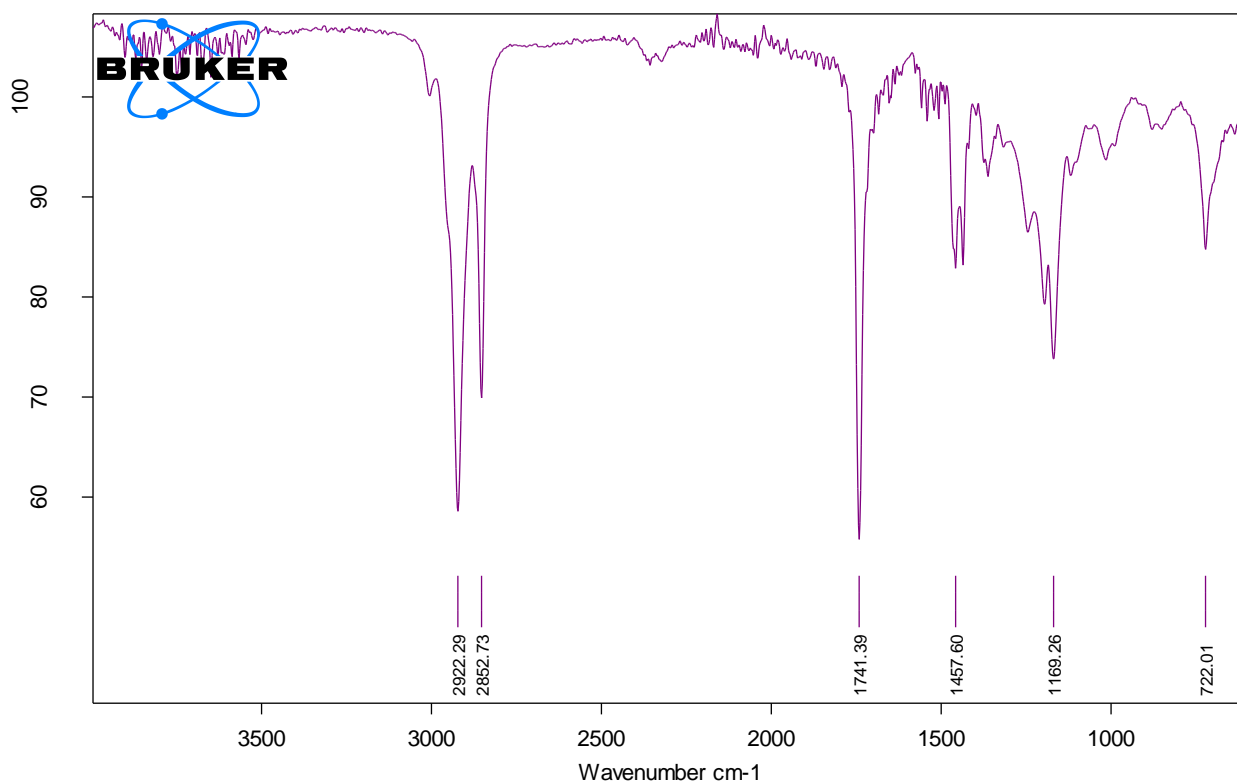


Figure 11: FTIR spectra of biodiesel prepared by L21 as a catalyst.

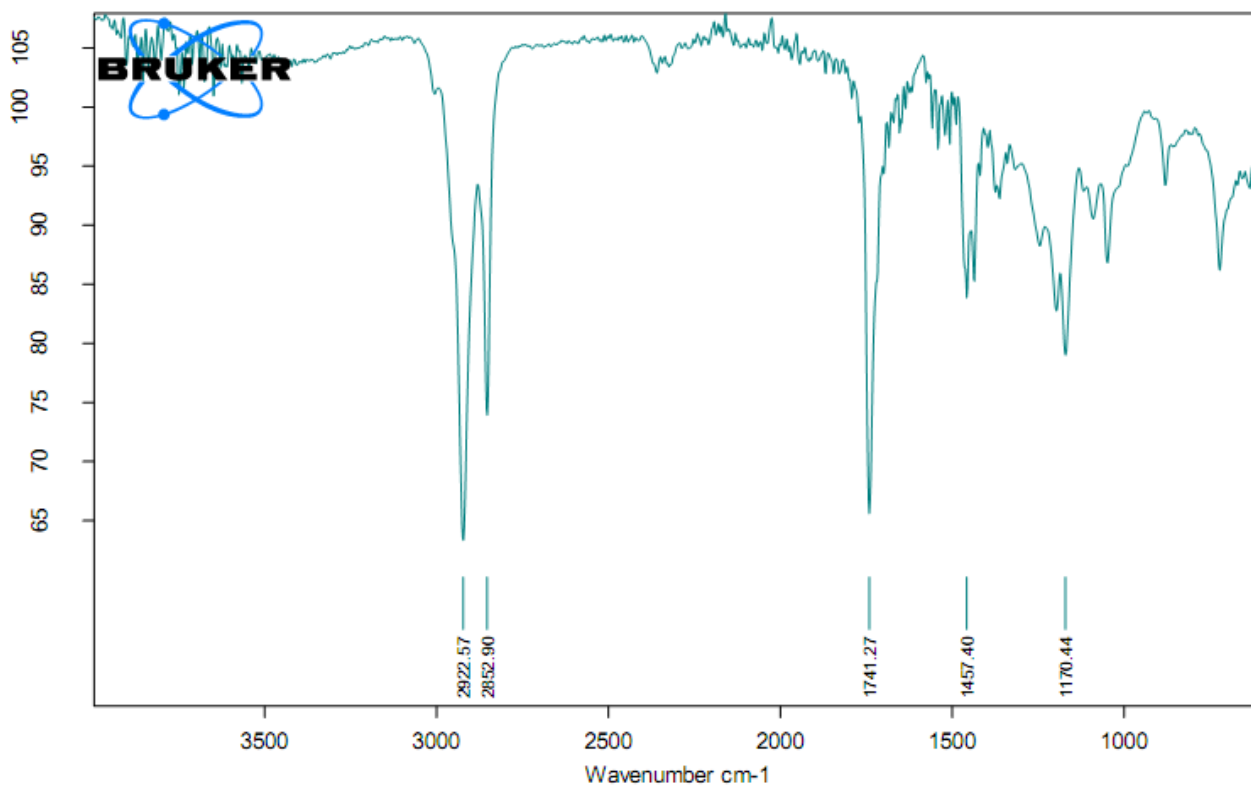


Figure 12: FTIR spectra of biodiesel prepared by L22 as a catalyst.

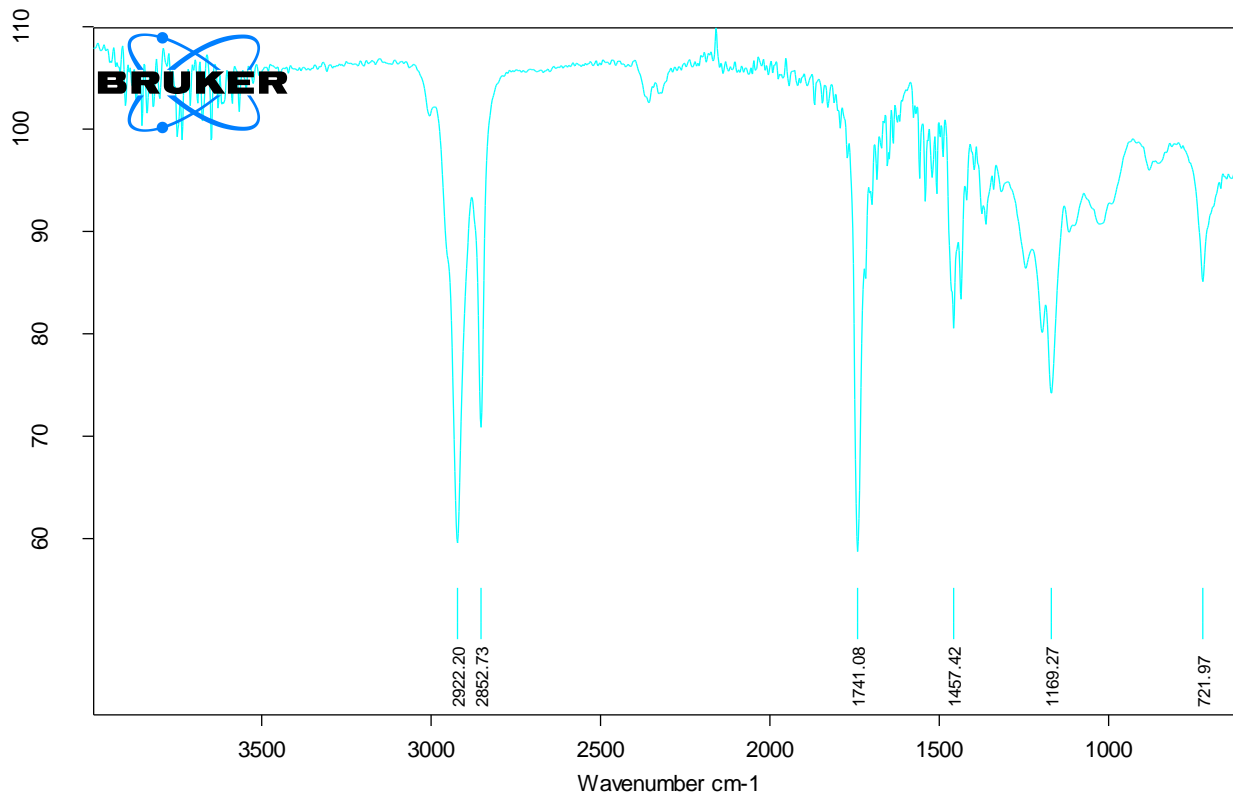


Figure 13: FTIR spectra of biodiesel prepared by L23 as a catalyst.

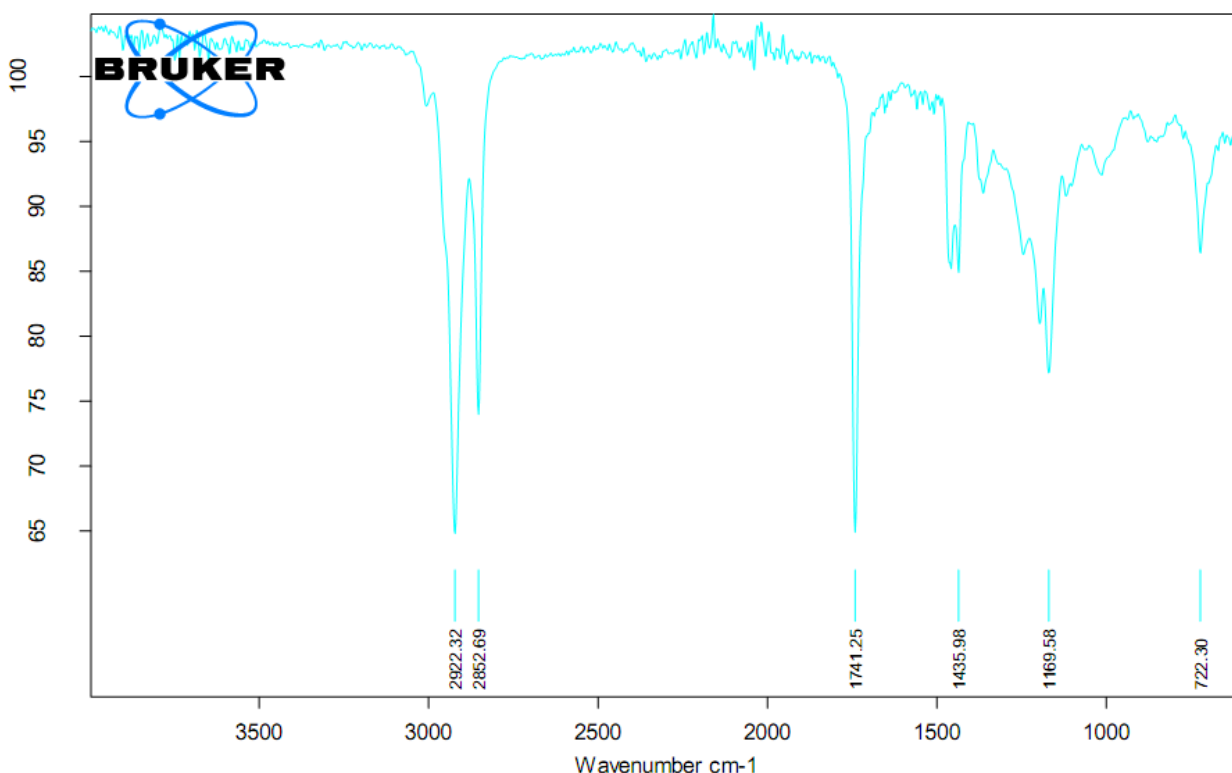


Figure 14: FTIR spectra of biodiesel prepared by L24 as a catalyst.

4. CONFLICTS OF INTEREST

No conflict of interest was declared by the authors.

5. CONCLUSION

Biodiesel is an alternative fuel that contributes to energy stability. A variety of renewable sources can be used to produce biodiesel today, making it an

extremely attractive alternative to fossil fuels that is non-toxic, biodegradable, and can be produced from a variety of renewable energy sources. In recent years, the extraction of neem oil from neem seeds has attracted the attention of many scientists based on the ease of cultivation, the lack of impact on food production, and the ability to grow on non-cultivable lands, compared to other biomass sources.

This paper summarizes the use of some newly synthesized organic heterocyclic hydrazone derivatives as catalysts for the production of neem biodiesel instead of previously reported catalysts due to their high yields and ease of optimization. Using ultrasonic irradiation method, we synthesized hydrazone derivatives in less than three minutes and were able to characterize these compounds using EIMS, NMR, FTIR and CHN spectroscopic methods. It was expected that these compounds exist in ketonic form and were highly pure since they showed a significant N-H peak in the $^1\text{H-NMR}$ range of 11.9-12.2 ppm and in the FTIR range of $3146\text{-}3237\text{ cm}^{-1}$, which confirmed their purity. Accordingly, the O-H absorption peak was found at 11.8 ppm in $^1\text{H-NMR}$, and the broad band was found to be above 3000 cm^{-1} in FTIR. A sharp peak range of $1600\text{-}1700\text{ cm}^{-1}$ was observed by FTIR for the carbonyl group. Elemental analysis and mass spectra confirmed their molecular weights and molecular formula.

As, FFA acid value of neem oil is very high 4.2% and before biodiesel formation it should be reduced and esterification performed before transesterification. For this purpose, we use, these derivatives as acid catalysts instead of simple acids. The reaction parameters like reaction temperature, reaction time, solvent and catalyst amount were optimized for better understandings. The optimized time for esterification was 60mint, optimized temperature for esterification as well as for transesterification was 60°C , methanol used as optimized solvent while optimized amount of catalyst was 50mg. These optimized parameters produced high yield and highly purified biodiesel ranges 79-95%.

These produced biodiesels showed 6-6.91 pH range, density ($0.81\text{-}0.87\text{ g/cm}^3$), viscosity ($5.41\text{-}4.79\text{ mm}^2/\text{s}$) and moisture content less than 0.5. Acid value, FFA, iodine value and saponification value of all these biodiesels were 0.161-0.261(mg/g), 0.71-0.89 (%) 51-58(mgI₂/100g), and 167.37-176.31 (mg/g) very close to the reported standard neem biodiesel. These neem biodiesels were characterized by FTIR spectra, exhibited CH stretching peaks near 2900 cm^{-1} and 2800 cm^{-1} while sharp absorption peak for C=O above 1700 cm^{-1} while -OH absorption band was absent. This conclude that hydrazone derivatives can be used as excellent acid catalysts in esterification for production of highly purified biodiesel from neem oil with a yield up to 95%.

6. REFERENCES

1. Ali MH, Mashud M, Rubel MR, Ahmad RH. Biodiesel from neem oil as an alternative fuel for diesel engine. *Procedia Eng* [Internet]. 2013 Jan 1;56:625-30. Available from: [<URL>](#).
2. Bouzarovski S. Transforming urban energy demand: A timely challenge. *Front Sustain Cities* [Internet]. 2020 May 27;2:29. Available from: [<URL>](#).
3. Asif M, Muneer T. Energy supply, its demand and security issues for developed and emerging economies. *Renew Sustain Energy Rev* [Internet]. 2007 Sep 1;11(7):1388-413. Available from: [<URL>](#).
4. Rastogi A, Shaban M, Saxena S, Singh TP. Neem biodiesel: An alternative fuel. *Innovare J Eng Technol* [Internet]. 2021 Nov 1;9:18-21. Available from: [<URL>](#).
5. Banik SK, Rouf M. A., Rabeya T, Khanam M, Sajal SI, Sabur SB, et al. Production of biodiesel from neem seed oil. *Bangladesh J Sci Ind Res* [Internet]. 2018;53(3):211-8. Available from: [<URL>](#).
6. Demirbas A. Characterization of biodiesel fuels. *Energy Sources, Part A Recover Util Environ Eff* [Internet]. 2009 Jun 12;31(11):889-96. Available from: [<URL>](#).
7. Dueso C, Muñoz M, Moreno F, Arroyo J, Gil-Lalaguna N, Bautista A, et al. Performance and emissions of a diesel engine using sunflower biodiesel with a renewable antioxidant additive from bio-oil. *Fuel* [Internet]. 2018 Dec 15;234:276-85. Available from: [<URL>](#).
8. Sentanuhady J, Hasan WH, Muflikhun MA. Recent progress on the implementation of renewable biodiesel fuel for automotive and power plants: Raw materials perspective. *Riccio A, editor. Adv Mater Sci Eng* [Internet]. 2022 Jan 4;2022(1):5452942. Available from: [<URL>](#).
9. Ubaid Hussain S, Noureen S, Razzaq I, Alkter S, Mehmood F, Razzaq Z, et al. Optimization and characterization of acid catalyzed castor biodiesel and its blends. *J Turkish Chem Soc Sect A Chem* [Internet]. 2022 Nov 30;9(4):1007-22. Available from: [<URL>](#).
10. Hoekman SK, Broch A, Robbins C, Cenicerros E, Natarajan M. Review of biodiesel composition, properties, and specifications. *Renew Sustain Energy Rev* [Internet]. 2012 Jan 1;16(1):143-69. Available from: [<URL>](#).
11. Dhar Dubey KK, Jeyaseelan C, Upadhyaya KC, Chimote V, Veluchamy R, Kumar A. Biodiesel production from *Hiptage benghalensis* seed oil. *Ind Crops Prod* [Internet]. 2020 Feb 1;144:112027. Available from: [<URL>](#).
12. Demirbas A. Potential resources of non-edible oils for biodiesel. *Energy Sources, Part B Econ Planning, Policy* [Internet]. 2009 Oct 30;4(3):310-4. Available from: [<URL>](#).
13. Fadairo A, Adeyemi G, Ogunkunle T, Ling K, Rasouli V, Effiong E, et al. Study the suitability of neem seed oil for formulation of eco-friendly oil based drilling fluid. *Pet Res* [Internet]. 2021 Sep 1;6(3):283-90. Available from: [<URL>](#).
14. Thangaraj B, Solomon PR, Muniyandi B, Ranganathan S, Lin L. Catalysis in biodiesel production—a review. *Clean Energy* [Internet]. 2019 Feb 27;3(1):2-23. Available from: [<URL>](#).
15. Awolu OO, Layokun SK. Optimization of two-step transesterification production of biodiesel from neem

(*Azadirachta indica*) oil. Int J Energy Environ Eng [Internet]. 2013 Nov 14;4(1):39. Available from: [<URL>](#).

16. Rizwanul Fattah IM, Ong HC, Mahlia TMI, Mofijur M, Silitonga AS, Rahman SMA, et al. State of the art of catalysts for biodiesel production. Front Energy Res [Internet]. 2020 Jun 19;8:546060. Available from: [<URL>](#).

17. Pasae Y, Tangdilintin S, Bulu L, Allo EL. The contribution of heterogeneous and homogeneous catalysts towards biodiesel quality. J Phys Conf Ser [Internet]. 2020 Feb 1;1464(1):012054. Available from: [<URL>](#).

18. Rijo B, Fernando E, Ramos M, Dias APS. Biodiesel production over sodium carbonate and bicarbonate catalysts. Fuel [Internet]. 2022 Sep 1;323:124383. Available from: [<URL>](#).

19. Basumatary SF, Patir K, Das B, Saikia P, Brahma S, Basumatary B, et al. Production of renewable biodiesel using metal organic frameworks based materials as efficient heterogeneous catalysts. J Clean Prod [Internet]. 2022 Jul 15;358:131955. Available from: [<URL>](#).

20. Kusmiyati K, Prasetyoko D, Murwani S, Nur Fadhilah M, Oetami TP, Hadiyanto H, et al. Biodiesel production from reutealis trisperma oil using KOH impregnated eggshell as a heterogeneous catalyst. Energies [Internet]. 2019 Sep 28;12(19):3714. Available from: [<URL>](#).

21. Feng W, Tie X, Duan X, Yan S, Fang S, Wang T, et al. Polymer functionalization of biochar-based heterogeneous catalyst with acid-base bifunctional catalytic activity for conversion of the insect lipid into biodiesel. Arab J Chem [Internet]. 2023 Jul 1;16(7):104814. Available from: [<URL>](#).

22. Tahvildari K, Anaraki YN, Fazaeli R, Mirpanji S, Delrish E. The study of CaO and MgO heterogenic nano-catalyst coupling on transesterification reaction efficacy in the production of biodiesel from recycled cooking oil. J Environ Heal Sci Eng [Internet]. 2015 Dec 23;13(1):73. Available from: [<URL>](#).

23. Demirbas A. Biodiesel from vegetable oils with MgO catalytic transesterification in supercritical methanol. Energy Sources, Part A Recover Util Environ Eff [Internet]. 2008 Jul 29;30(17):1645–51. Available from: [<URL>](#).

24. Arshad S, Ahmad M, Munir M, Sultana S, Zafar M, Dawood S, et al. Assessing the potential of green CdO₂ nano-catalyst for the synthesis of biodiesel using non-edible seed oil of Malabar Ebony. Fuel [Internet]. 2023 Feb 1;333:126492. Available from: [<URL>](#).

25. Manurung R, Parinduri SZDM, Hasibuan R, Tarigan BH, Siregar AGA. Synthesis of nano-CaO catalyst with SiO₂ matrix based on palm shell ash as catalyst support for one cycle developed in the palm biodiesel process. Case Stud Chem Environ Eng [Internet]. 2023 Jun 1;7:100345. Available from: [<URL>](#).

26. Nabgan W, Nabgan B, Ikram M, Jadhav AH, Ali MW, Ul-Hamid A, et al. Synthesis and catalytic properties of calcium oxide obtained from organic ash over a titanium nanocatalyst for biodiesel production from dairy scum. Chemosphere [Internet]. 2022 Mar 1;290:133296. Available from: [<URL>](#).

27. Eugen Raducanu C, Ionuta Gavrilă A, Dobre T, Chipurici P. Study on alumina supported heterogeneous catalysts for biodiesel production. Rev Chim [Internet]. 2018;69(8):2138–43. Available from: [<URL>](#).

28. Wang A, Quan W, Zhang H, Li H, Yang S. Heterogeneous ZnO-containing catalysts for efficient biodiesel production. RSC Adv [Internet]. 2021 Jun 8;11(33):20465–78. Available from: [<URL>](#).

29. Dasta P, Pratap Singh A, Pratap Singh A. Zinc oxide nanoparticle as a heterogeneous catalyst in generation of biodiesel. Mater Today Proc [Internet]. 2022 Jan 1;52:751–7. Available from: [<URL>](#).

30. Ghanbari Zadeh Fard R, Jafari D, Palizian M, Esfandyari M. Biodiesel production from beef tallow using the barium oxide catalyst. React Kinet Mech Catal [Internet]. 2019 Dec 14;128(2):723–38. Available from: [<URL>](#).

31. Carlucci C, Degennaro L, Luisi R. Titanium dioxide as a catalyst in biodiesel production. Catalysts [Internet]. 2019 Jan 11;9(1):75. Available from: [<URL>](#).

32. Esmi F, Borugadda VB, Dalai AK. Heteropoly acids as supported solid acid catalysts for sustainable biodiesel production using vegetable oils: A review. Catal Today [Internet]. 2022 Nov 15;404:19–34. Available from: [<URL>](#).

33. Buchori L, Widayat W, Muraza O, Amali MI, Maulida RW, Prameswari J. Effect of temperature and concentration of zeolite catalysts from geothermal solid waste in biodiesel production from used cooking oil by esterification–transesterification process. Processes [Internet]. 2020 Dec 10;8(12):1629. Available from: [<URL>](#).

34. Dhinakaran G, Vijayakumar G, Prashanna Suvaitha S, Harichandran G, Venkatachalam K. Conversion of neem oil (*Azadirachta indica*) to biodiesel over SBA-15 supported sulphated zirconia catalysts. Catal Letters [Internet]. 2024 May 1;154(5):2124–39. Available from: [<URL>](#).

35. Fan X, Niehus X, Sandoval G. Lipases as biocatalyst for biodiesel production. In: Methods in Molecular Biology [Internet]. Humana Press; 2012. p. 471–83. Available from: [<URL>](#).

36. Mate DM, Alcalde M. Laccase: A multi-purpose biocatalyst at the forefront of biotechnology. Microb Biotechnol [Internet]. 2017 Nov 3;10(6):1457–67. Available from: [<URL>](#).

37. Ferrero GO, Faba EMS, Eimer GA. Biodiesel production from alternative raw materials using a heterogeneous low ordered biosilicified enzyme as

biocatalyst. *Biotechnol Biofuels* [Internet]. 2021 Dec 15;14(1):67. Available from: [<URL>](#).

38. Maiti S, Chowdhury AR, Das AK. Benzosenadiazole-based nanoporous Covalent Organic Polymer (COP) as efficient room temperature heterogeneous catalyst for biodiesel production. *Microporous Mesoporous Mater* [Internet]. 2019 Jul 15;283:39–47. Available from: [<URL>](#).

39. Gomes R, Bhanja P, Bhaumik A. Sulfonated porous organic polymer as a highly efficient catalyst for the synthesis of biodiesel at room temperature. *J Mol Catal A Chem* [Internet]. 2016 Jan 1;411:110–6. Available from: [<URL>](#).

40. Yao J, Ji L, Sun P, Zhang L, Xu N. Low boiling point organic amine-catalyzed transesterification of cottonseed oil to biodiesel with trace amount of KOH as co-catalyst. *Fuel* [Internet]. 2010 Dec 1;89(12):3871–5. Available from: [<URL>](#).

41. Saikia K, Ngaosuwan K, Assabumrungrat S, Singh B, Okoye PU, Rashid U, et al. Sulphonated cellulose-based carbon as a green heterogeneous catalyst for biodiesel production: Process optimization and kinetic studies. *Biomass and Bioenergy* [Internet]. 2023 Jun 1;173:106799. Available from: [<URL>](#).

42. Deandra PP, Santoso H, Witono JRB. Carbon based sulfonated catalyst as an environment friendly material: A review. In: *AIP Conference Proceedings* [Internet]. American Institute of Physics Inc.; 2022. p. 040006. Available from: [<URL>](#).

43. Nazloo EK, Moheimani NR, Ennaceri H. Graphene-based catalysts for biodiesel production: Characteristics and performance. *Sci Total Environ* [Internet]. 2023 Feb 10;859:160000. Available from: [<URL>](#).

44. Athar Hussain A, Nazir S, Ullah Khan A, Tahir K, Albalawi K, Ibrahim MM, et al. Preparation of zinc oxide graphed nickel incorporated mesoporous SBA-16 doped graphene oxide: An efficient catalyst for transesterification of waste edible oil to biodiesel and photocatalytic degradation of organic dyes. *Inorg Chem Commun* [Internet]. 2022 May 1;139:109379. Available from: [<URL>](#).

45. Cirujano FG, Corma A, Llabrés i Xamena FX. Zirconium-containing metal organic frameworks as solid acid catalysts for the esterification of free fatty acids: Synthesis of biodiesel and other compounds of interest. *Catal Today* [Internet]. 2015 Nov 15;257(Part 2):213–20. Available from: [<URL>](#).

46. Pangestu T, Kurniawan Y, Soetaredjo FE, Santoso SP, Irawaty W, Yuliana M, et al. The synthesis of biodiesel using copper based metal-organic framework as a catalyst. *J Environ Chem Eng* [Internet]. 2019 Aug 1;7(4):103277. Available from: [<URL>](#).

47. Hassan HMA, Betiha MA, Mohamed SK, El-Sharkawy EA, Ahmed EA. Salen- Zr(IV) complex grafted into amine-tagged MIL-101(Cr) as a robust

multifunctional catalyst for biodiesel production and organic transformation reactions. *Appl Surf Sci* [Internet]. 2017 Aug 1;412:394–404. Available from: [<URL>](#).

48. Jamil U, Husain Khoja A, Liaquat R, Raza Naqvi S, Nor Nadyaini Wan Omar W, Aishah Saidina Amin N. Copper and calcium-based metal organic framework (MOF) catalyst for biodiesel production from waste cooking oil: A process optimization study. *Energy Convers Manag* [Internet]. 2020 Jul 1;215:112934. Available from: [<URL>](#).

49. Cheng J, Qian L, Guo H, Mao Y, Shao Y, Yang W. A new aminobenzoate-substituted s-triazin-based Zr metal organic frameworks as efficient catalyst for biodiesel production from microalgal lipids. *Fuel Process Technol* [Internet]. 2022 Dec 15;238:107487. Available from: [<URL>](#).

50. Ruatpuia JVL, Changmai B, Pathak A, Alghamdi LA, Kress T, Halder G, et al. Green biodiesel production from *Jatropha curcas* oil using a carbon-based solid acid catalyst: A process optimization study. *Renew Energy* [Internet]. 2023 Apr 1;206:597–608. Available from: [<URL>](#).

51. Chhabra M, Saini BS, Dwivedi G, Behura AK, Kumar A, Jain S, et al. Investigation of the shelf life of the optimized Neem biodiesel and its execution and excretion characteristics on automotive diesel engine. *Energy Sources, Part A Recover Util Environ Eff* [Internet]. 2021 Feb 1; Article in Press. Available from: [<URL>](#).

52. Jabeen M. A comprehensive review on analytical applications of hydrazone derivatives. *J Turkish Chem Soc Sect A Chem* [Internet]. 2022 Aug 31;9(3):663–98. Available from: [<URL>](#).

53. Jabeen M, Mehmood K, Khan MUA, Aslam N, Zafar AM, Sajid N, et al. Microwave and conventional synthesis of Co(II), Cu(II) and Ni(II) metal complexes of some acid hydrazones with their spectral characterization and biological evaluation. *Pak J Pharm Sci* [Internet]. 2018 May 13;31(3(Supplementary)):1003–11. Available from: [<URL>](#).

54. Jabeen M, Mehmood K, Khan MA, Nasrullah M, Maqbool T, Jabeen F, et al. Comparative study of microwave assisted and conventional synthesis of furfuraldehyde based hydrazone derivatives and their metal complexes with biological evaluation. *Asian J Chem* [Internet]. 2017;29(2):431–6. Available from: [<URL>](#).

55. Rondstvedt CS. Arylation of unsaturated compounds by diazonium salts (The Meerwein arylation reaction). In: *Organic Reactions* [Internet]. Wiley; 2011. p. 225–59. Available from: [<URL>](#).

56. Suraj CK, Anand K, Sundararajan T. Investigation of biodiesel production methods by altering free fatty acid content in vegetable oils. *Biofuels* [Internet]. 2020 Jul 3;11(5):587–95. Available from: [<URL>](#).

57. Helrich K. Official methods of analysis of the

association of official analytical chemists [Internet]. Vol. 3. Association of Official Analytical Chemists.; 1990. Available from: [<URL>](#).

58. Daramola MO, Mtshali K, Senokoane L, Fayemiwo OM. Influence of operating variables on the transesterification of waste cooking oil to biodiesel over sodium silicate catalyst: A statistical approach. J Taibah Univ Sci [Internet]. 2016 Sep 16;10(5):675–84. Available from: [<URL>](#).

59. Leung DYC, Wu X, Leung MKH. A review on biodiesel production using catalyzed transesterification. Appl Energy [Internet]. 2010 Apr 1;87(4):1083–95. Available from: [<URL>](#).

60. Chozhavendhan S, Vijay Pradhap Singh M, Fransila B, Praveen Kumar R, Karthiga Devi G. A review on influencing parameters of biodiesel production and purification processes. Curr Res Green Sustain Chem [Internet]. 2020 Feb 1;1–2:1–6. Available from: [<URL>](#).

61. Zuo D, Lane J, Culy D, Schultz M, Pullar A, Waxman M. Sulfonic acid functionalized mesoporous SBA-15 catalysts for biodiesel production. Appl Catal B Environ [Internet]. 2013 Jan 17;129:342–50. Available from: [<URL>](#).

62. Simonelli G, Ferreira Júnior JM, Pires CA de M, Santos LCL dos. Biodiesel production using co-solvents: A review. Res Soc Dev [Internet]. 2020 Jan 1;9(1):e99911672. Available from: [<URL>](#).

63. Ban S, Shrestha R, Chaudhary Y, Jeon JK, Joshi R, Uprety B. Process simulation and economic analysis of dolomite catalyst based biodiesel production from Nepalese *Jatropha Curcas*. Clean Chem Eng [Internet]. 2022 Jun 1;2:100029. Available from: [<URL>](#).

64. Gebremariam SN, Marchetti JM. Process simulation and techno-economic performance evaluation of alternative technologies for biodiesel production from low value non-edible oil. Biomass and Bioenergy [Internet]. 2021 Jun 1;149:106102. Available from: [<URL>](#).

65. Thanh LT, Okitsu K, Boi L Van, Maeda Y. Catalytic technologies for biodiesel fuel production and utilization of glycerol: A review. Catalysts [Internet]. 2012 Mar 22;2(1):191–222. Available from: [<URL>](#).

66. Aboelazayem O, El-Gendy NS, Abdel-Rehim AA, Ashour F, Sadek MA. Biodiesel production from castor oil in Egypt: Process optimisation, kinetic study, diesel engine performance and exhaust emissions analysis. Energy [Internet]. 2018 Aug 15;157:843–52. Available from: [<URL>](#).

67. Inayat A, Jamil F, Ghenai C, Kamil M, Bokhari A, Waris A, et al. Biodiesel synthesis from neem oil

using neem seeds residue as sustainable catalyst support. Biomass Convers Biorefinery [Internet]. 2021 Aug 6;Article in Press. Available from: [<URL>](#).

68. Changmai B, Vanlalveni C, Ingle AP, Bhagat R, Rokhum SL. Widely used catalysts in biodiesel production: A review. RSC Adv [Internet]. 2020 Nov 13;10(68):41625–79. Available from: [<URL>](#).

69. Musa H, N. Usman S. Preparation and antimicrobial evaluation of neem oil alkyd resin and its application as binder in oil-based paint. Environ Nat Resour Res [Internet]. 2016 May 7;6(2):92. Available from: [<URL>](#).

70. Taiwo AG, Ijaola TO, Lawal SO, LanreIyanda YA. Characterization of neem seed oil and its biodiesel (B100). NIPES J Sci Technol Res [Internet]. 2020 Jun 1;2(2):178. Available from: [<URL>](#).

71. Hamadou B, Djomdi, Falama RZ, Delattre C, Pierre G, Dubessay P, et al. Influence of physicochemical characteristics of neem seeds (*Azadirachta indica* A. Juss) on biodiesel production. Biomolecules [Internet]. 2020 Apr 17;10(4):616. Available from: [<URL>](#).

72. Hasni K, Ilham Z, Dharma S, Varman M. Optimization of biodiesel production from *Brucea javanica* seeds oil as novel non-edible feedstock using response surface methodology. Energy Convers Manag [Internet]. 2017 Oct 1;149:392–400. Available from: [<URL>](#).

73. Devasan R, Ruatpuia JVL, Gouda SP, Kodgire P, Basumatary S, Halder G, et al. Microwave-assisted biodiesel production using bio-waste catalyst and process optimization using response surface methodology and kinetic study. Sci Rep [Internet]. 2023 Feb 13;13(1):2570. Available from: [<URL>](#).

74. Muthu H, SathyaSelvabala V, Varathachary TK, Kirupha Selvaraj D, Nandagopal J, Subramanian S. Synthesis of biodiesel from Neem oil using sulfated zirconia via transesterification. Brazilian J Chem Eng [Internet]. 2010 Dec;27(4):601–8. Available from: [<URL>](#).

75. Banu HD, Shallangwa TB, Joseph I, Odey Magu T, Hitler L, Ahmed S. Biodiesel production from neem seed (*Azadirachta indica*) oil using calcium oxide as heterogeneous catalyst. J Phys Chem Biophys [Internet]. 2018 Nov 27;8(2):1000266. Available from: [<URL>](#).

76. Gunawardena S, Hewa Walpita D, Ismail M. Method for quantification of methanol and sulfuric acid required for esterification of high free fatty acid oils in biodiesel production. Int J Renew Energy Res [Internet]. 2017;7(4):1639–45. Available from: [<URL>](#).



Nanocarriers for Controlled Drug Delivery A Convergence of Polymer and Nanochemistry

Asia Asos Hama^{1*} , Dara Muhammed Aziz¹ , Ibrahim Nazem Qader^{2,3} , Bnar M. Ibrahim¹ 
 Bashdar Ismael Meena⁴ 

¹Chemistry Department, College of Science, University of Raparin, Rania, 46012, Sulaymaniyah, KRG, Iraq.

²Department of Physics, College of Science, University of Raparin, Rania, 46012, Sulaymaniyah, KRG, Iraq.

³Department of Pharmacy, College of Pharmacy, Knowledge University, Erbil, 44001, Iraq.

⁴Department of Physics, Faculty of Science & Health, Koya University, Koya, KOY45, Iraq.

Abstract: Nanotechnology has emerged as a leading and widely adopted technology, particularly in the improvement of healthcare strategies and other fields. In the near future, the pharmaceutical and biotechnology industries are expected to undergo significant transformations due to the integration of nanoscale technology in drug delivery systems, particularly through the use of polymeric nanoparticles. These nanoparticles have been extensively studied as particulate carriers in the pharmaceutical and medical fields because of their potential as drug delivery systems, owing to their controlled and sustained release properties, subcellular size, and biocompatibility with tissues and cells. Several methods are employed in the preparation of polymeric nanoparticles, which are considered crucial for drug encapsulation. Materials such as PLGA, PLA, and chitosan are frequently used for encapsulating anticancer, antihormonal, and antimalarial drugs to enhance their release rates. Additionally, polymeric nanoparticles have applications in dentistry and oral health systems, particularly in the treatment of infections. The combination of polymeric nanoparticles with antibacterial drugs helps reduce infections. To achieve effective drug delivery, it is essential to understand the interactions of nanomaterials with the biological environment, including targeting cell-surface receptors, drug release, multiple drug administration, stability of therapeutic agents, and the molecular mechanisms of cell signaling involved in the pathobiology of the disease.

Keywords: Nanochemistry, Polymeric nanoparticles, Drug delivery system.

Submitted: February 16, 2024. **Accepted:** October 8, 2024.

Cite this: Hama AA, Aziz DM, Qader IN, Ibrahim BM, Meena BI. Nanocarriers for Controlled Drug Delivery A Convergence of Polymer and Nanochemistry. JOTCSA. 2024;11(4): 1581-1594.

DOI: <https://doi.org/10.18596/jotcsa.1436845>

***Corresponding author's E-mail:** asiaasos28@gmail.com

1. INTRODUCTION

Nanochemistry is a branch of chemistry that studies chemical systems and processes at the nanoscale. The primary focus is on the properties, behavior, and manipulation of materials at the nanometer scale—typically between 1 and 100 nanometers. Due to the enhanced surface-to-volume ratio and quantum mechanical effects, nanoscale systems exhibit unique phenomena and characteristics (1). Polymeric nanoparticles, a type of nanoparticle used in drug delivery systems, are polymers prepared at the nanoscale (1-100 nm). They play a crucial role in various fields, as evidenced by numerous publications on polymeric nanoparticles, as illustrated in Figure 1. Drug delivery systems (DDSs) involve a multi-step process that includes the

administration of a therapeutic product, the controlled release of active ingredients, and the transport of these active ingredients across biological membranes to reach the target site. DDSs can take various forms, such as formulations (e.g., capsules, tablets, or patches) or devices (e.g., pumps or implants) (2).

Nanochemistry is recognized as an important technique with applications across multiple fields, but it also faces limitations. To address these challenges, drug delivery systems can be integrated with nanochemistry to reduce their respective limitations. By combining these two systems, their limitations can be minimized, making them even more significant in various applications (3).

In particular, the drug delivery system has been used to overcome some of the limitations of nanochemistry. The linkage between these two systems can reduce constraints on both sides. As a result, pharmaceuticals and other drugs can be enhanced through nanochemistry to improve their effectiveness. The use of polymeric nanoparticles with drugs enhances their efficiency, and when drugs are encapsulated with polymeric nanoparticles, the result is a highly biocompatible drug. For example, anticancer drugs encapsulated with polymeric

nanoparticles become more effective and are released more rapidly at the target site (3).

This study aims to link two important systems—nanochemistry and drug delivery systems—and explain each system individually before demonstrating their combined significance. By using polymeric nanoparticles for drug encapsulation and applying them in oral and dental applications, more effective therapeutic outcomes can be achieved.

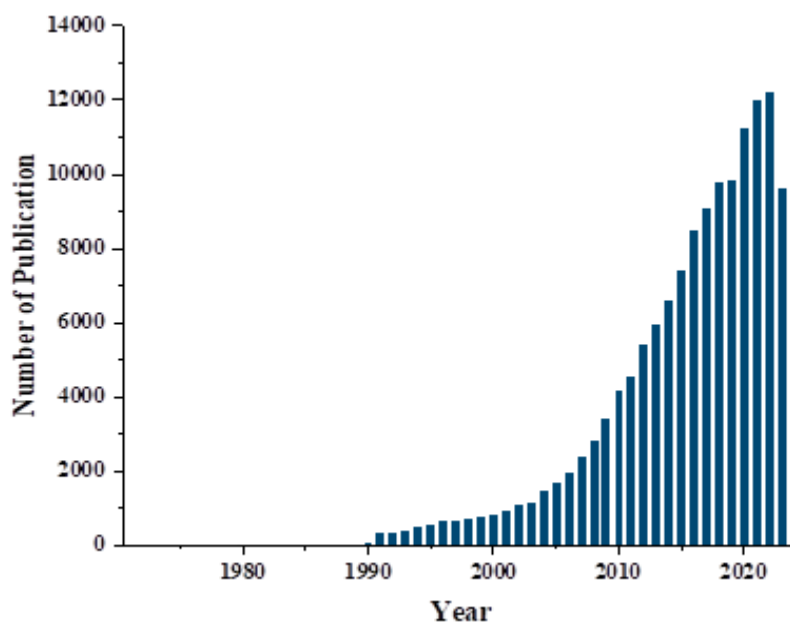


Figure 1: A visual depiction of the number of publications of polymeric particles during the period cited in Web of Science.

2. IMPORTANCE OF CONTROLLED DRUG DELIVERY

A Drug Delivery System (DDS) is defined as a system that facilitates the delivery of therapeutic drugs into the body while enhancing safety and efficiency by regulating the rate, time, and location of drug release and absorption. The DDS also refers to the interaction between the drug and the patient, determining the required dosage and administration. This process includes the use of a medicinal product, the release of active chemicals from the product, and the subsequent transport of these active compounds across biological membranes to their site of action. A substance that stimulates the development of an active therapeutic agent *in vivo*, such as in gene therapy, is also referred to as a therapeutic substance (2).

2.1. Drug Delivery Routes

Drugs are absorbed by the human body through several anatomical pathways. These drugs may be directed toward specific organs or intended for systemic effects. The choice of the route of administration depends on the illness, the desired outcome, and the available materials. Drug delivery routes are classified into several types. One common route is oral administration, which is preferred due to two factors: patient acceptance and ease of use. Another route is nasal drug delivery. For many years,

medications have been inhaled for both topical and systemic effects. Topical treatments include medications for sinusitis, rhinitis, nasal blockages, allergies, and other long-term conditions. Examples of drugs used include corticosteroids, antihistamines, anticholinergics, and vasoconstrictors. The nasal route is appealing because it can bypass the disadvantages of oral administration, such as rapid first-pass metabolism and gastrointestinal drug breakdown.

3. POLYMERIC NANOPARTICLES

Polymeric nanoparticles (PNs) are derived from natural, semi-synthetic, or synthetic polymers. These nanoparticles are tiny, typically in the nanometer size range, often between 1 and 100 nanometers. Polymeric nanoparticles (PNs) are produced through polymerization processes involving monomer units. Under controlled conditions, these nanoparticles self-assemble into nanoscale structures (4).

3.1. Types of Polymeric Nanoparticles

Polymeric nanoparticles (PNs), based on their structural organization, are categorized into two types: nanospheres and nanocapsules. Nanocapsules differ from nanospheres in that they have a reservoir structure, but both are important types of polymeric nanoparticles. Nanospheres, one type of polymeric

nanoparticle, trap the drug within the polymer matrix. On the other hand, nanocapsules consist of a polymeric membrane encasing a liquid core of either

water or oil, where the drug must dissolve within the liquid core to be effective (5). Figure 2 shows the schematics of polymeric nanoparticles.

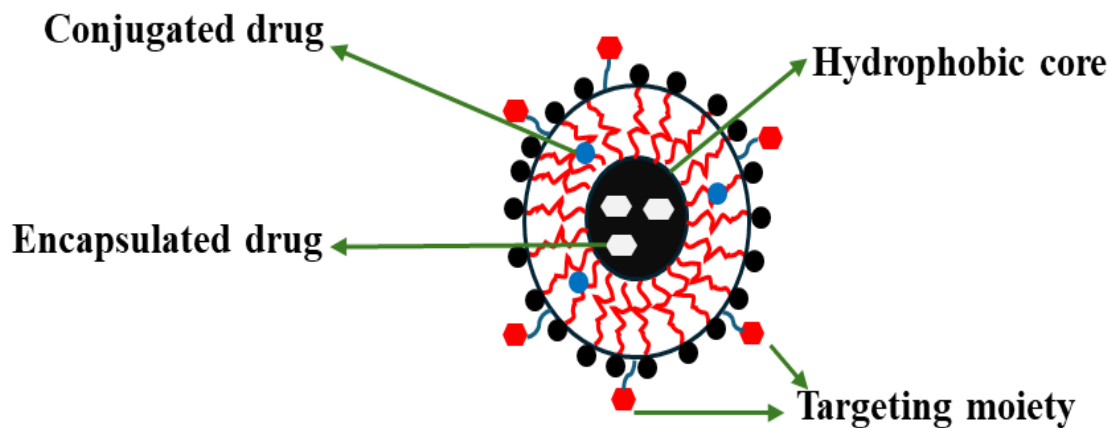


Figure 2: Schematics of polymeric nanoparticles.

3.2. Methods for Synthesizing a Polymer Nanoparticle

Polymeric nanoparticles can be prepared based on their desired application across different fields, making the preparation process crucial to their effectiveness. Two primary techniques are used for the preparation and formulation of PNs: preformed polymer dispersion and direct polymerization of monomers. The first method, preformed polymer dispersion, includes several useful approaches in polymer chemistry, such as solvent evaporation, dialysis, salting out, the use of supercritical fluid technology, and nanoprecipitation, which involves the dispersion of preformed polymers. Some

preparation techniques are explained further, starting with solvent evaporation, which is the first technique under type 1. Solvent evaporation was the original method developed to produce (PNPs). The process begins by creating emulsions after preparing polymer solutions in volatile solvents. In the past, dichloromethane and chloroform were commonly used as solvents for preformed polymers, but ethyl acetate has gained popularity due to its better toxicological profile. As the solvent evaporates and the emulsion disperses into its continuous phase, it forms a suspension of nanoparticles (6). Figure 3 reveals solvent evaporation represented in schematic form.

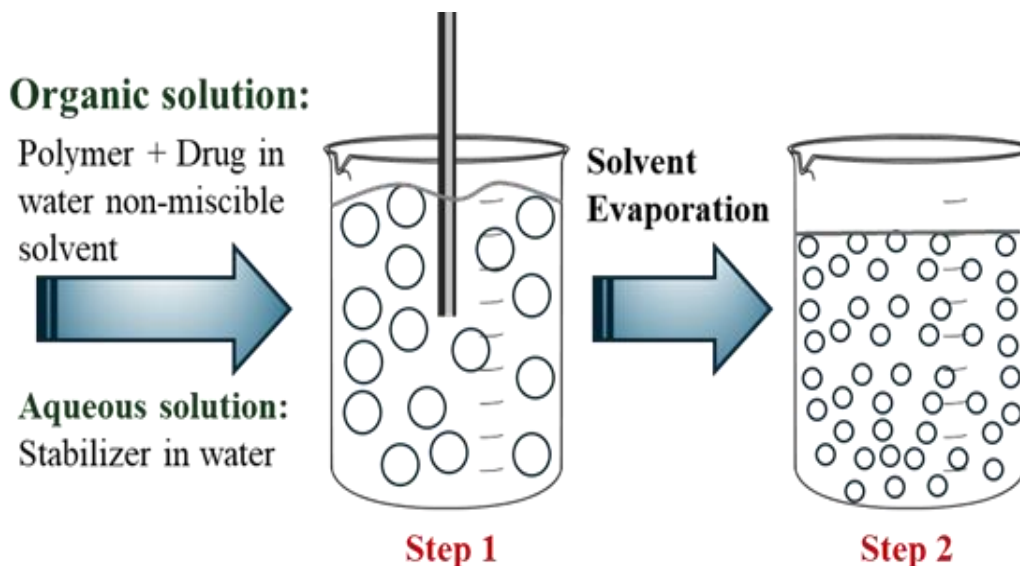


Figure 3: Solvent evaporation represented in schematic form (6).

Another technique is salting out. In this method, instead of using chlorinated solvents, a water-miscible solvent such as acetone, ethanol, or N-methyl-2-pyrrolidone is used. The aqueous phase can be saturated with electrolytes like magnesium acetate, magnesium chloride, or calcium chloride to prevent the mixing of organic and aqueous phases.

To create an O/W emulsion, an organic solution containing the drug and polymer is emulsified into an aqueous phase that includes a colloidal stabilizer and salt. The emulsion is then diluted with enough water to enhance acetone penetration into the aqueous phase, leading to polymer precipitation (7). Figure 4 The schematic representation of salting out.

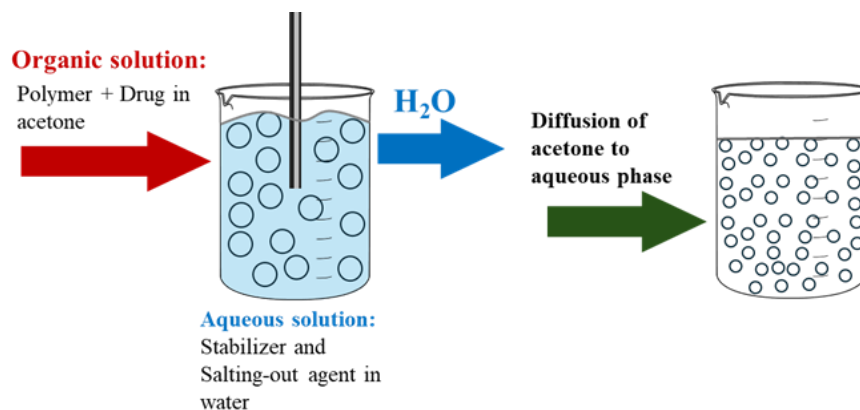


Figure 4: The schematic representation of salting out (6).

Type (2) is monomer direct polymerization, which includes several techniques such as controlled radical polymerization, microemulsion and emulsification-based polymerization, interfacial polymerization, and single-molecule direct polymerization, including mini-emulsion polymer formation (8).

Some preparation techniques are explained further. The first technique in Type 2 is emulsion polymerization, which is a highly scalable and efficient method for creating nanoparticles. This approach is divided into two categories depending on whether an aqueous or organic continuous phase is used. In the continuous organic phase method, a single molecule is distributed in an oily solution, an inverse microemulsion, or a material in which the monomer is insoluble. Several mechanisms can initiate the polymerization process. The process begins when an initiating molecule, which might be an ion or a free radical, comes into contact with a monomer molecule dissolved in the continuous phase. Alternatively, high-energy radiation, such as UV radiation or intense visible light, can convert a single substance into a starting radical. An anionic polymerization mechanism leads to the collision of monomer ions or radicals with other monomer molecules, triggering chain growth. Phase separation and the formation of solid particles can occur either

before or after the polymerization process is completed (6).

Another technique is interfacial polymerization, a well-established method for creating polymer nanoparticles with a proven track record. The process involves step polymerization of two reactive monomers or agents dissolved in two separate phases: the dispersed phase and the continuous phase. The reaction occurs at the interface between these two liquids. The monomer is carried by the organic solvent, which is miscible with water, and polymerization occurs at the interface (6).

Polymers that are commonly prepared include polyprotic acid, polyglutamic acid, polycaprolactone, polylactic acid, and polyglycolic acid. On the other hand, examples of natural polymers include albumin, alginate, chitosan, collagen, and gelatin (5).

3.3. Nanotechnology-based Drug Delivery System Design

The unique properties of nanoparticles have garnered significant attention in the field of drug delivery. They enhance drug delivery in various ways, especially for poorly soluble drugs. In Figure 5, the difference between drugs that can utilize nanotubes (i.e., polymeric nanoparticles) and those that cannot is explained (9).

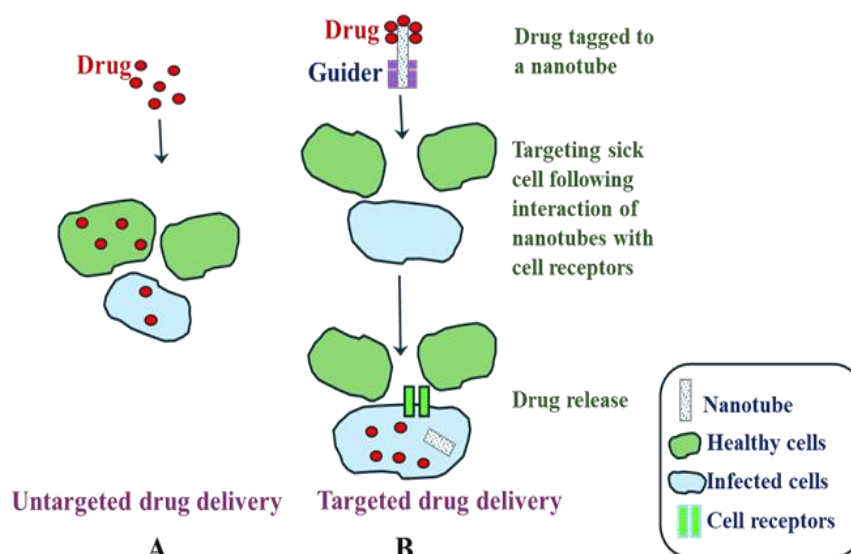


Figure 5: The distinction between targeted and untargeted delivery of drugs (9).

The following describes the role of nanoparticles in targeted drug delivery:

Better Solubility: The low solubility of many medications can limit their absorption and therapeutic effectiveness. Nanoparticles offer large surface areas and can be engineered to encapsulate or solubilize poorly soluble drugs, thereby enhancing their bioavailability. **Targeted Drug Delivery:** Nanoparticles can be functionalized or modified to target specific tissues or cells. This targeted delivery concentrates the drug at the site of action, reducing side effects and minimizing systemic exposure. **Surface modifications,** such as ligand conjugation, allow nanoparticles to recognize and bind to target cell receptors.

The Enhanced Permeability and Retention (EPR) effect is a phenomenon in which abnormal vasculature in tumors tend to accumulate nanoparticles more than in normal tissues. Nanoparticles can exploit this property, enabling passive targeting of drugs to tumor sites and thereby enhancing the effectiveness of cancer therapies.

Controlled Release: A sustained therapeutic effect can be achieved by engineering nanoparticles to release medication in a controlled manner. This is particularly useful for drugs with a narrow therapeutic window or those that need to act gradually.

Protection of Drugs: Polymeric nanoparticles can shield drugs from degradation and metabolic

breakdown, which may prolong the stability and potency of certain medications.

Combination of Diagnostic and Therapeutic: Nanoparticles can be engineered to carry both therapeutic agents and diagnostic imaging agents. This enables simultaneous diagnosis and treatment, a practice known as theragnostic.

Personalized Medicine: The ability to customize nanoparticle-based drug delivery systems makes personalized medicine possible for specific patient populations.

Biocompatibility: The body can easily tolerate many materials that can be used to create biocompatible nanoparticles, reducing the likelihood of adverse reactions and immunological responses.

The use of nanoparticles in drug delivery holds great promise for enhancing the therapeutic effectiveness of medications while minimizing adverse effects. Researchers continue to explore and develop innovative nanoparticle formulations for various medical applications (10).

3.4. Drug Delivery Using Polymeric Nanoparticles

The nanoparticles of polymers known as (poly-d,l-lactide-co-glycolide, polylactic acid, polycaprolactone, poly-alkyl-cyanoacrylates, chitosan, and gelatin) are the most widely used in drug delivery systems. The most popular polymeric nanoparticles in drug delivery systems are explained in Table 1.

Table 1: Polymeric nanoparticles that are most frequently utilized in drug delivery systems

Material	Full name	Abbreviation	Reference
Artificially created polymers	Poly(lactide) Poly(lactide-co-glycolide)	PLA PLGA	(11)
Natural polymers	Chitosan Gelatin Alginate		(11)
Copolymers	Poly(lactide)-poly (ethylene glycol)	PLA-PEG	(11)
Colloid stabilizers	Poly (vinyl alcohol) dextran	PVA	(11)

Characteristics that make nanoparticles an excellent drug delivery system:

1. Non-toxic, Biodegradable, and Biocompatible: Non-toxic: Nanoparticles used for drug delivery should not harm the body. They should not induce toxicity or cause adverse reactions.

Biodegradable: The system should be capable of breaking down into non-toxic components after delivering the drug, allowing for natural elimination from the body.

Biocompatible: The nanoparticles should interact favorably with biological systems without causing harm or triggering immune responses.

2. Improved Formulation Design:

Solubility Enhancement: Use various techniques such as micronization, nanosuspensions, or complexation to improve drug solubility.

Bioavailability Enhancement: Incorporate excipients that enhance drug absorption, such as surfactants, penetration enhancers, and lipid-based formulations.

Stability Enhancement: Develop formulations with stabilizers, antioxidants, and appropriate packaging to protect drugs from degradation.

3. Benefits of therapy:

Controlled Bioavailability: Maintaining therapeutic drug levels in the body is crucial. A drug delivery system that allows precise regulation of bioavailability ensures a predictable release of the medication.

Biodistribution and Tissue Uptake: The distribution of drugs in the body and the tissues' ability to absorb medications can significantly impact treatment outcomes. Targeted drug delivery can increase drug concentration in specific areas while reducing exposure in non-targeted cells.

Enhanced Drug Efficacy: Prolonged and controlled drug release can improve the overall efficacy of treatment, especially for medications with a narrow therapeutic window or those requiring continuous exposure for optimal effectiveness.

Improved Patient Compliance: Controlled drug delivery systems often require less frequent dosing, which can improve patient adherence to the treatment regimen.

Reduction of Side Effects: Controlled drug release can help mitigate side effects by avoiding sharp peaks and troughs in drug concentration. This results in a more stable and tolerable treatment experience for the patient (7).

4. ENCAPSULATION OF DRUGS IN POLYMERIC NANOPARTICLES

As mentioned above, polymeric nanoparticles are prepared using various methods depending on the application and the type of drug encapsulation. To demonstrate the effectiveness of nanomedicine, polymeric nanoparticles are used for the encapsulation of various drugs. The most useful polymers for this purpose are biodegradable polymeric nanoparticles. These nanoparticles offer successful drug release properties, as well as optimal subcellular size and bioactivity when interacting with cells (12). The general linkage between the encapsulation and polymeric nanoparticles is shown below in Figure 6.

5. PLGA (Poly D, L-lactide-co-glycolide)

PLGA (poly-D,L-lactide-co-glycolide) is an important nanoparticle used in nanomedicine and drug delivery systems. It is composed of biodegradable monomers, lactic acid and glycolic acid, which break down naturally in the body (4). Such as explained in Figure 7.

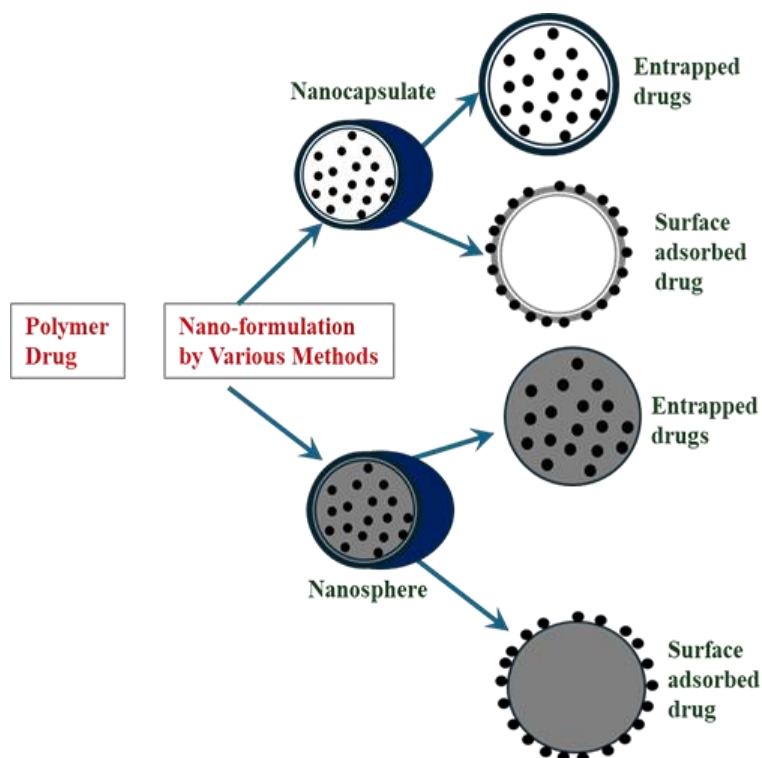


Figure 6: The encapsulation of drug and polymer nanoparticles.

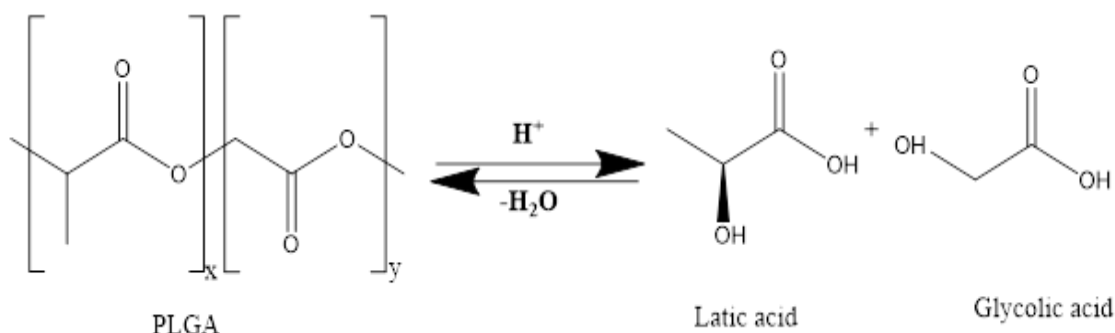


Figure 7: Hydrolysis of PLGA.

Different cancer-fighting drugs encapsulated on PLGA nanoparticles:

The FDA accepts PLGA for therapeutic use in treatment due to its beneficial properties in nanomedicine. Key characteristics of PLGA nanoparticles include:

Particle Size: The particle size of nanoparticles significantly impacts the drug delivery system. With sizes ranging from 1 to 100 nm, their small size enhances tissue penetration, cellular uptake, and provides an increased surface area for interactions.

Surface Morphology: Well-defined surface morphology improves stability, cellular uptake, and overall biocompatibility, making it an important property in nanomedicine.

Surface Charge: The stability of nanoparticles in suspension and their interaction with biological membranes are influenced by their surface charge.

9-Nitrocamptothecin (9-NC) is a potent anticancer agent, but its low water solubility and instability at physiological pH present challenges for effective delivery. Nanoprecipitation techniques can address these issues, and PLGA (poly (lactic-co-glycolic acid)) is often used to encapsulate such lipophilic drugs. By encapsulating 9-NC in PLGA nanoparticles, you can achieve high encapsulation efficiency (over 30%) while preserving the drug's biological activity and preventing degradation of the lactone ring, which is crucial for its anticancer efficacy. This approach improves the drug's stability and bioavailability, making it a promising strategy for enhancing the therapeutic potential of 9-NC (12).

Cisplatin is a widely used anticancer agent with a mechanism of action that involves forming cross-links with DNA, which inhibits DNA replication and transcription, and can affect both genomic DNA (gDNA) and mitochondrial DNA (mtDNA). This action can effectively kill cancer cells, but its clinical use is

limited by side effects and the development of drug resistance (13).

To overcome these challenges, cisplatin has been encapsulated in PLGA-mPEG (poly(lactic-co-glycolic acid)-methoxy poly(ethylene glycol)) nanoparticles using a double-emulsion method. This formulation helps improve the stability and controlled release of cisplatin at the targeted site, which can enhance its therapeutic efficacy and reduce side effects. The quick degradation of these nanoparticles and their prolonged release at the tumor site contribute to better inhibition of cancerous tumor growth, potentially improving the overall effectiveness of cisplatin-based treatments (12).

Paclitaxel is a highly effective anticancer agent used to treat various cancers, including breast, endometrial, and cervical carcinomas. However, its clinical use is often limited by its poor solubility in water, which complicates drug delivery (14). To address this issue, paclitaxel can be encapsulated using PLGA (poly(lactic-co-glycolic acid)) nanoparticles combined with vitamin E and tocopherol. The solvent evaporation/extraction methods used in this approach help trap paclitaxel within the nanoparticles, improving its solubility and stability. This method not only enhances the drug's solubility but also allows for faster and more efficient drug administration. The encapsulation in PLGA-vitamin E-tocopherol nanoparticles can improve the pharmacokinetics of paclitaxel, leading to better therapeutic outcomes and potentially reducing side effects (12).

6. POLYLACTIC ACID (PLA)

Poly(lactic acid) (PLA) is an aliphatic polyester characterized by the presence of ester bonds connecting its monomer units. It is highly valued in the biomedical field for its biocompatibility and biodegradability, with a variety of uses for suture threads that are active, bone-fixing screws, and drug-delivery equipment (15). Figure 8 reveals the formation of poly(lactic acid) (PLA).

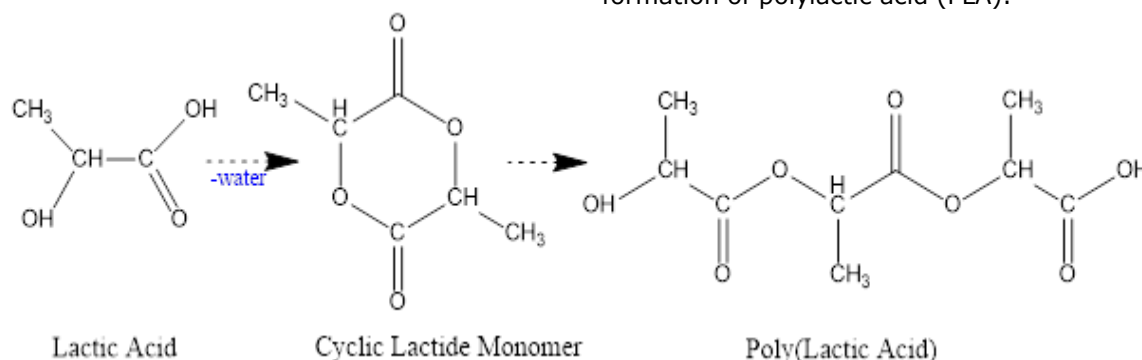


Figure 8: The formation of poly(lactic acid) (PLA)

6.1. Encapsulation of Oridonin on PLA Nanoparticles

Oridonin (C₂₀H₂₈O₆) is a kaurene-type diterpenoid extracted from *Rabdosia rubescens*, known as "Donglingcao" in Chinese. It exhibits a range of biological activities, including anticancer, antibacterial, anti-inflammatory, and anti-fibrotic

effects. However, its clinical use is limited by its low therapeutic index and poor water solubility (16). To address these limitations, oridonin can be encapsulated in poly (lactic acid) (PLA) nanoparticles using an improved spontaneous emulsion technique. This formulation helps overcome the drug's solubility issues and enhances its stability. The PLA

nanoparticles facilitate a prolonged blood circulation time, which can improve the drug's therapeutic efficacy by increasing its bioavailability and allowing for sustained release at the target site (12).

6.2. Hormone (Progesterone) Encapsulation on PLA Nanoparticle

Progesterone, a C-21 steroid hormone, plays crucial roles in the female menstrual cycle, pregnancy, and embryonic development across various species. Its therapeutic applications extend beyond these physiological roles, including potential uses in cancer treatment.

To enhance the delivery and efficacy of progesterone, it can be encapsulated in PLA-PEG-PLA (poly(lactic acid)-poly(ethylene glycol)-poly(lactic acid)) nanoparticles using the solvent evaporation method (12).

7. GELATIN

Gelatin is Naturally occurring, biocompatible, and sustainable, biopolymer and contains an active group for this reason it is used in many applications and it has a low cost. Gelatin contains both anionic and cationic groups which means poly-ampholyte in nature (17).

Didanosine and chloroquine phosphate are both important medications with specific challenges in their clinical use, which can be addressed by encapsulating them in gelatin nanoparticles.

Didanosine Encapsulation

Didanosine (ddI) is an anti-HIV medication with a strong affinity for water, which facilitates its ability to cross the blood-brain barrier (BBB). However, effective delivery to the brain requires precise formulation. By encapsulating didanosine in mannan-coated gelatin nanoparticles using the desolvation method, several benefits are achieved:

Enhanced BBB Penetration: The gelatin nanoparticles, especially with mannan coating, help didanosine effectively traverse the BBB.

Improved Efficiency: Encapsulation enhances the stability and bioavailability of didanosine, ensuring better therapeutic outcomes in the treatment of HIV.

Chloroquine Phosphate Encapsulation

Chloroquine phosphate is an antimalarial drug used to treat malaria by killing the parasite that infects red blood cells. Despite its efficacy, it is associated with side effects such as headache, drowsiness, vomiting, and nausea. Encapsulating chloroquine phosphate in gelatin nanoparticles offers several advantages:

Reduced Side Effects: The gelatin nanoparticles can help mitigate adverse reactions by controlling the release of the drug and reducing its systemic exposure.

Improved Drug Functionality: Encapsulation enhances the stability and effectiveness of

chloroquine phosphate, potentially leading to better therapeutic outcomes with fewer side effects.

Both encapsulation strategies illustrate how gelatin nanoparticles can be utilized to improve the delivery, efficacy, and safety profiles of medications, addressing their inherent limitations and enhancing their therapeutic potential (12).

8. CHITOSAN

Chitosan, a biopolymer derived from chitin, is indeed a valuable material for drug delivery systems due to its unique chemical properties and biological compatibility. Three functional groups make up chitosan: hydroxyl groups both primary and secondary at places C2, C3, and C6, as well as an amino group. The hydroxyl groups in chitosan have a significant impact by chemically supplying side groups to the reactive hydroxyl groups; this process is carried out without altering the physical in natural functions of the material (18).

8.1. Encapsulation of Insulin on Chitosan Nanoparticles

Enterocytes cells lining the small intestine responsible for nutrient absorption. The absorption of insulin is facilitated by cells of intestine lining. For the purpose of enhanced intestinal absorption, The intestinal absorption of insulin was significantly improved by the insulin-loaded chitosan nanoparticles (12).

Antihormonal (glycyrrhizin) medications encapsulated on chitosan tiny particles:

Glycyrrhizin (GL) indeed a major bioactive compound found in licorice root (*Glycyrrhiza glabra*), and it has been recognized for diverse pharmacological and biological activities, like.

Antiviral Activity: Glycyrrhizin has proven to have antiviral properties against several viruses, such as the HIV, the influenza virus, and the herpes simplex virus.

Anti-Inflammatory Activity: According to reports, GL has anti-inflammatory qualities, which it might be helpful for inflammation-related conditions.

Antioxidant Activity: The compound exhibits antioxidant effects, which help combat oxidative stress in the body.

Anticancer Activity: Studies, both in vitro and in vivo, have suggested glycyrrhizin may have anticancer properties, with potential effects on various types of cancer cells (19).

Chitosan have demonstrated a remarkable ability to bind with ammonium glycyrrhizinate. The pattern of release of ammonium glycyrrhizinate exhibits a noticeable peak and a gradually increasing release phase; however, if the nanoparticles are employed, they may enhance the uptake of ammonium glycyrrhizinate orally (12).

9. POLY-CAPROLACTONE (PCL)

One of the rare synthetic biodegradable polymers with great potential for use in drug delivery systems is poly-caprolactone (PCL). This polymer is hydrophobic and has a crystalline structure, with its crystallinity decreasing with increasing molecular weight. This kind of polymeric nanoparticles is made using widely used methods, like the ring-opening polymerization of 2-methylene-1-3-dioxepane by free radicals. It can also be made using a different method that doesn't involve free radicals, which is ring-opening polymerization (20).

PCL nanoparticles are used to encapsulate insulin and other diabetes medications: One of the hormones made by the pancreatic beta cells that regulates our blood sugar levels and is absorbed in the intestines is insulin. Insulin administered orally via poly-caprolactone (PCL) polymeric nanoparticles is one of the most commonly used insulin carrier medications. Since the cells in the small intestine adsorb strongly to FITC-insulin-loaded nanoparticles, the cells in the intestine absorb insulin more readily when the insulin is loaded onto PCL nanoparticles (21).

Encapsulation of clonazepam drugs on PCL nanoparticles:

One medication that calms the brain and nerves is clonazepam. It is a member of the benzodiazepine drug class. The copolymer known as poly (N-isopropyl acrylamide)-b-poly(3-caprolactone) (PNPCL) is highly effective in the encapsulation of clonazepam. Additionally, poly-N-isopropyl acrylamide (PNiPAAm) is formed; the formation of these PNiPAAm hydrogel layers delayed the release of the drug because they can function as a barrier and an additional part. Consequently, the PCL copolymer has a significant impact that facilitates clonazepam's release and absorption more successfully (12).

10. BIOCOMPATIBILITY AND TOXICITY

Biocompatible Materials in Dental and Oral Systems: To boost the effectiveness of dental and oral systems, biocompatible polymeric nanoparticles are

employed. Antibiotics have been added to a range of biomaterials to target specific areas and boost the efficacy of antibiotic therapy because of this. In dentistry, where localized drug delivery can help treat infections and prevent complications, this tactic is particularly crucial. Chitosan, gelatin, and alginate, as well as Poly(lactic-co-glycolic acid), also known as PLGA and Polylactic Acid (PLA), are the two most significant polymeric nanoparticles utilized in dentistry. In addition, PLA is a biodegradable polymer nanoparticle that can be employed in dental applications, acting as a carrier and gradually releasing medication. It A naturally occurring polymeric nanoparticle that serves as an antibiotic increases the delivery of antibiotics locally, encouraging healing and lowering the risk of infections (22).

10.1. PLGA in Dentistry

PLGA is one of the most common polymer-based nanoparticles used in dentistry. They serve a variety of purposes, including screw bone fixation and periodontal pairing (23). In the form of implants, disks, and dental care films, PLGA can be used to treat periodontal disease, improve local antibiotic delivery, and lessen the systemic side effects of general antibiotic delivery (24). Direct pulp capping is used to treat exposed dental pulp, which is typically the result of trauma or caries, in order to maintain pulp vitality and promote the formation of reparative dentin. The use of PLGA composites with bioceramics in direct pulp capping is being studied, with an emphasis on different materials and techniques to increase the procedure's success. PLGA is a well-liked polymer for controlled drug delivery systems because it is biocompatible and biodegradable. On the other hand, bioceramics—a term for materials that are compatible with biological tissues—are widely used in orthopaedic and dental applications (23). The positive results of the PLGA materials indicate that more research is required, especially in the areas of material delivery to dental tissues and pulp capping ability of PLGA composites. To elaborate, the dental field employs PLGA materials for a multitude of purposes. Figure 9 illustrates the most commonly used PLGA substances and their respective applications in dentistry (25).

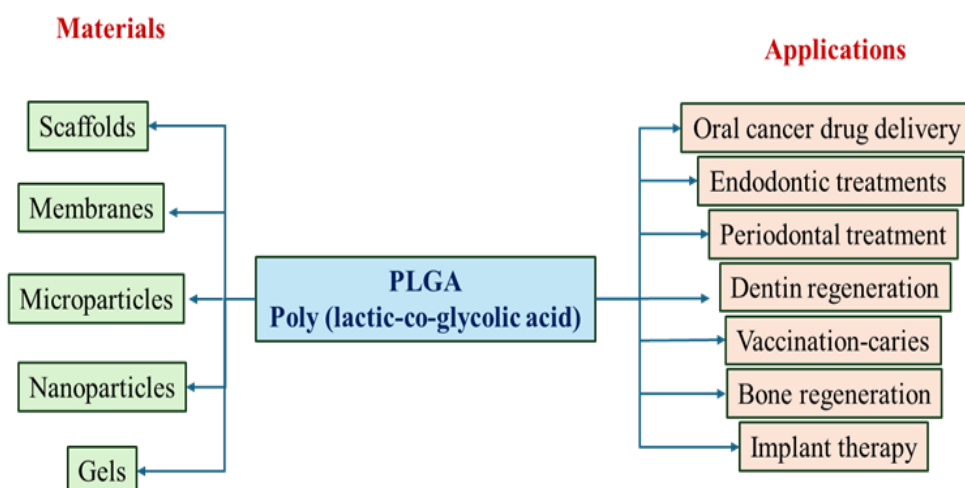


Figure 9: The most popular PLGA substances and how they are used in dentistry (25).

Dental cavity system of administration using chitosan as a natural polymeric carrier for dental disorders:

Chitosan is a natural polymer of significant functional importance, making it one of the most crucial natural polymeric nanoparticles used today due to its high biocompatibility, nontoxicity, and excellent degradability (26). Chitosan-based carriers are employed to deliver nutrients, antimicrobial agents, anti-inflammatory compounds, chemotherapy medications, and vaccines to specific cells through various forms such as films, fibers, sponges, micro/nanoparticles, and gels (26). In dental fields, chitosan-based drug delivery systems are used to treat conditions such as tooth caries and periodontitis, as well as to provide extended local anesthesia and support endodontic treatments for root canals (27).

The disadvantages of systemic antibiotic and anti-inflammatory drug administration have shifted the focus toward targeted drug delivery systems. These systems allow for the continuous release of medications in specific areas, sustaining therapeutic concentrations at the site for extended periods (28). Chitosan exhibits anti-inflammatory properties on human gingival fibroblasts (HGFs) by downregulating chemokines (such as CXCL-8) and cytokines (such as TNF- α and IL-1 β). This suggests that chitosan may play a significant role in modulating the inflammatory response, which is crucial for tissue healing. The impact of chitosan on inflammation can vary depending on the substances and components involved. This underscores the importance of understanding the unique properties of chitosan formulations to maximize their beneficial effects. The potential for chitosan to support the regeneration of injured gingival tissue is supported by observed increases in cell survival and metabolic rates, as well as its anti-inflammatory effects. Thus, chitosan may be a promising option for promoting wound repair and tissue renewal in the oral cavity (29). Since gram-negative rods are the primary cause of gingivitis, metronidazole is considered an essential antibiotic for the management of gum disease. Research suggests using chitosan-based gels and films to deliver metronidazole locally, reducing the number of applications, potential systemic side effects, and the healing time (30). A study led by Pichay Korn et al. examined chitosan nanoparticles filled with metronidazole (MTZ-MPs). The findings indicate that MTZ-MPs loaded into hydrogels exhibit a more favorable release profile compared to MTZ-MPs incorporated into films (31).

Chitosan-based drug transporters are used for the management of root canal diseases. Chitosan/gelatin nanoparticles have been applied in endodontic treatments and root canal infections, with one of the most important applications being the sustained release of calcium hydroxide. Calcium hydroxide is widely used in endodontics due to its antimicrobial properties and its ability to promote tissue repair. Nano-carriers, with their high surface area, can provide controlled release of the encapsulated drug, prolonging its therapeutic effect. This sustained release is particularly advantageous in root canal treatments, as it ensures that the therapeutic agent

remains active within the root canal system for an extended period, increasing the chances of eliminating or controlling infection. Additionally, the biodegradability of chitosan is beneficial in such applications, as the nano-carriers can gradually break down and be eliminated from the body, minimizing potential long-term side effects (32). Consequently, calcium hydroxide combined with chitosan nanoparticles exhibits greater antibacterial activity compared to calcium hydroxide alone (33).

Modifications of oral hygiene products:

Porphyromonas gingivalis and *Streptococcus mutans* are the main pathogens that cause gingivitis and dental cavities, two common conditions in the oral cavity. Mouthwashes, dentifrices, toothpaste, and other dental products come in liquid, paste, gel, or powder form. These products contain active ingredients that work in multiple ways to maintain dental health and enhance oral hygiene. Recent advancements in dental care product development have concentrated on utilizing naturally occurring anti-plaque agents with potent anti-cariogenic efficaciousness (34). Cytotoxicity, consistency, and biofilm-inhibiting properties have all been examined when comparing the broad spectrum prolonged antibacterial activity of chitosan-based toothpaste and mouthwashes to commercial ones evaluated. In the field of oral care, toothpastes containing stannous material and fluoride modified by chitosan have been the focus of much research. Chitosan-modified Fluoride Toothpaste: Fluoride is well-known for its ability to prevent tooth decay by encouraging remineralization and preventing demineralization of enamel. When combined with chitosan, this toothpaste seeks to maximize the protective effects of fluoride on tooth enamel.

The efficacy and adherence of the mixture might be enhanced by the addition of chitosan. Stannous-containing Toothpaste: Another ingredient found in toothpaste formulas is stannous fluoride. Its capacity to offer several advantages, such as antibacterial qualities and sensitivity alleviation, has been acknowledged. It is thought that stannous compounds create a layer of protection on the surface of the teeth, preventing dentin and enamel loss. In contrast to store-bought toothpaste: These altered formulations are frequently compared in studies to toothpaste products that are sold commercially. Fluoride is added to toothpaste formulations for enamel protection, along with other additives for flavor and texture, and standard cleaning ingredients. Assessing factors like bacterial inhibition, abrasion resistance, enamel hardness, and overall tissue loss reduction efficacy may be part of the comparison (34).

10.2. Antifungal Properties Substances

Numerous studies have demonstrated that chitosan coating medical devices lowers the risk of poisoning. Tissue conditioning products and denture adhesives, two of chitosan's derivatives, are expected to be effective in treating denture stomatitis and other common oral fungal infections due to their strong anti-fungal properties (36). The anti-fungal mechanism of chitosan is believed to be fungistatic

as opposed to fungicidal, and it is similar to the antibacterial mechanism that was previously discussed (37). One of chitosan's well-known antimicrobial qualities is antifungal activity. By adding high-molecular-weight chitosan to the denture adhesive, wearers of dentures may benefit from improved oral health by preventing fungal growth. A low-molecular-mass chitosan solution applied for two weeks is a more effective treatment for denture stomatitis than nystatin (38). Additionally, when treating oral inflammatory and candidiasis lesions, chitosan-curcumin mouthwash without alcohol yielded better results than chlorhexidine (39).

10.3. Tissue Engineering

Periodontitis is a very serious inflammation that affects not only the bone but also the soft tissues that support the teeth, as well as dental tendons and ligaments. The phases of periodontitis are as follows: Gingivitis, the early stage of periodontal disease, is characterized by gum inflammation. Gingivitis is often brought on by plaque, a sticky bacterial film that forms on teeth. Gingivitis can lead to periodontitis if it is not properly treated. also, Periodontal Pocket Formation: As gingivitis advances, inflammation cause creation of periodontal pockets. These are openings where bacteria can grow and proliferate between teeth and gums. The pockets offer a conducive environment for growth of more harmful bacteria. bone loss: when Periodontitis is not treated the bone that shields the teeth loss results in defect the bone of the teeth. Tooth Loosening: the continued methods leads to the tooth losing bone, causing in the teeth loosening also it may be in severe cases tooth mobility becomes evident and leads to an increase in the effect of tooth loss (40). Chitosan and its derivatives are naturally occurring biomaterials that meet all of the necessary requirements and characteristics for tissue scaffolding. When the new target tissue forms, chitosan does not break down into hazardous compounds, especially when broken down by lysosomes, nor does it trigger the immune system when it is inserted. In dentistry, bone, gums, and tooth pulp are regenerated using scaffolds made of chitosan (41).

Metallic-Based Concoction for Medicine Administration in Dental Issues:

Because of their unique properties, which include their high surface-to-volume ratio and importance in the study of dental issues, nanoparticles have attracted a great deal of interest in a variety of fields, including the medical sciences and dentistry. Another characteristic of nanoparticles that makes them significant is their shapes. Another type of nanoparticle used in dentistry are metallic ones. Titanium nanoparticles, for example, are used in dental implants due to their remarkable biological compatibility and durability. Gold: Used in imaging and with special optical properties for therapeutics and diagnostics. Silver: Silver nanoparticles are utilized in dental materials to prevent infections because of their well-known antimicrobial qualities (42).

11. CONCLUSION

nanotechnology has become a new revolution It is a cutting-edge method for finding and delivering drugs. Polymeric Nanoparticles that are prepared from polymers are the most types of nanoparticles used in the field of nanotechnology to improve many functions of drugs and sustain the release of the drugs in a shorter time than the drug without the use of polymeric nanoparticles, the most important polymeric nanoparticles that explained are PLGA and poly lactic acid(PLA) and chitosan also alginate, they are the most important polymeric nanoparticles and prepared by polymerization process that discussed, they are used in encapsulation of drugs such as encapsulation of anticancer and antihormonal and antimalarial also insulin most other drugs were discussed that uses polymeric nanoparticles in their encapsulation by encapsulation improve their efficiency also improve their releasing rate also can act most beneficial drugs that reduce side effects of drugs. by means polymeric nanoparticles can be used in the field of dentistry, to boost the effectiveness of dental and oral systems, biocompatible polymeric nanoparticles are employed. Antibiotics have been incorporated into a range of biomaterials to target specific regions and enhance the efficacy of antibiotic therapy due to these reasons. PLGA, PLA, and chitosan are the most important polymeric nanoparticles that are used in dental problems, chitosan used in toothpaste, has more benefits than the toothpaste used without using chitosan as a part of it, also PLGA is the most multi-functional uses in the field of dentistry such as used in endodontic treatments and oral cancer therapy, at the end of the study explained that two systems that work and link together most benefit system.

12. REFERENCES

1. Velammal M. Nano Chemistry-Overview. Front Chem Biol Pharm Sci. 1:79.
2. Jain KK. Drug delivery systems [Internet]. Jain KK, editor. New York, NY: Springer New York; 2020. (Methods in Molecular Biology; vol. 2059). Available from: [<URL>](#).
3. Sahu T, Ratre YK, Chauhan S, Bhaskar LVKS, Nair MP, Verma HK. Nanotechnology based drug delivery system: Current strategies and emerging therapeutic potential for medical science. J Drug Deliv Sci Technol [Internet]. 2021 Jun 1;63:102487. Available from: [<URL>](#).
4. Avramović N, Mandić B, Savić-Radojević A, Simić T. Polymeric nanocarriers of drug delivery systems in cancer therapy. Pharmaceutics [Internet]. 2020 Mar 25;12(4):298. Available from: [<URL>](#).
5. Din F ud, Aman W, Ullah I, Qureshi OS, Mustapha O, Shafique S, et al. Effective use of nanocarriers as drug delivery systems for the treatment of selected tumors. Int J Nanomedicine [Internet]. 2017 Oct 5;Volume 12:7291–309. Available from: [<URL>](#).
6. Nagavarma BVN, Hemant KSY, Ayaz A, Vasudha

LS, Shivakumar HG. Different techniques for preparation of polymeric nanoparticles-a review. *Asian J Pharm Clin Res.* 2012;5(3):16–23.

7. Ahlin Grabnar P, Kristl J. The manufacturing techniques of drug-loaded polymeric nanoparticles from preformed polymers. *J Microencapsul [Internet].* 2011 Jun 17;28(4):323–35. Available from: [<URL>](#).

8. Aundhia CJ. Nanocapsules. In: *Nanocarriers: Drug Delivery System [Internet].* Singapore: Springer Singapore; 2021. p. 125–38. Available from: [<URL>](#).

9. Ould-Ouali L, Noppe M, Langlois X, Willems B, Te Riele P, Timmerman P, et al. Self-assembling PEG-p(CL-co-TMC) copolymers for oral delivery of poorly water-soluble drugs: A case study with risperidone. *J Control Release [Internet].* 2005 Feb 16;102(3):657–68. Available from: [<URL>](#).

10. Kipp J. The role of solid nanoparticle technology in the parenteral delivery of poorly water-soluble drugs. *Int J Pharm [Internet].* 2004 Oct 13;284(1–2):109–22. Available from: [<URL>](#).

11. Vauthier C, Bouchemal K. Methods for the preparation and manufacture of polymeric nanoparticles. *Pharm Res [Internet].* 2009 May 24;26(5):1025–58. Available from: [<URL>](#).

12. Kumari A, Yadav SK, Yadav SC. Biodegradable polymeric nanoparticles based drug delivery systems. *Colloids Surfaces B Biointerfaces [Internet].* 2010 Jan 1;75(1):1–18. Available from: [<URL>](#).

13. Ghosh S. Cisplatin: The first metal based anticancer drug. *Bioorg Chem [Internet].* 2019 Jul 1;88:102925. Available from: [<URL>](#).

14. Wiseman LR, Spencer CM. Paclitaxel. *Drugs Aging [Internet].* 1998 Aug 31;12(4):305–34. Available from: [<URL>](#).

15. Casalini T, Rossi F, Castrovinci A, Perale G. A perspective on polylactic acid-based polymers use for nanoparticles synthesis and applications. *Front Bioeng Biotechnol [Internet].* 2019 Oct 11;7:483145. Available from: [<URL>](#).

16. Liu X, Xu J, Zhou J, Shen Q. Oridonin and its derivatives for cancer treatment and overcoming therapeutic resistance. *Genes Dis [Internet].* 2021 Jul 1;8(4):448–62. Available from: [<URL>](#).

17. Yasmin R, Shah M, Khan SA, Ali R. Gelatin nanoparticles: A potential candidate for medical applications. *Nanotechnol Rev [Internet].* 2017 Apr 1;6(2):191–207. Available from: [<URL>](#).

18. Divya K, Jisha MS. Chitosan nanoparticles preparation and applications. *Environ Chem Lett [Internet].* 2018 Mar 31;16(1):101–12. Available from: [<URL>](#).

19. Bakr AF, Shao P, Farag MA. Recent advances in glycyrrhizin metabolism, health benefits, clinical

effects and drug delivery systems for efficacy improvement; a comprehensive review. *Phytomedicine [Internet].* 2022 May 1;99:153999. Available from: [<URL>](#).

20. Woodruff MA, Huttmacher DW. The return of a forgotten polymer—Polycaprolactone in the 21st century. *Prog Polym Sci [Internet].* 2010 Oct 1;35(10):1217–56. Available from: [<URL>](#).

21. Damgé C, Socha M, Ubrich N, Maincent P. Poly(ϵ -caprolactone)/eudragit nanoparticles for oral delivery of aspart-insulin in the treatment of diabetes. *J Pharm Sci [Internet].* 2010 Feb 1;99(2):879–89. Available from: [<URL>](#).

22. Prakasam M, Locs J, Salma-Ancane K, Loca D, Largeteau A, Berzina-Cimdina L. Biodegradable materials and metallic implants—A review. *J Funct Biomater [Internet].* 2017 Sep 26;8(4):44. Available from: [<URL>](#).

23. Gala-Garcia A, Teixeira KIR, Wykrota FHL, Sinisterra RD, Cortés ME. Bioceramic/Poly (glycolic)-poly (lactic acid) composite induces mineralized barrier after direct capping of rat tooth pulp tissue. *Braz Oral Res [Internet].* 2010 Mar;24(1):08–14. Available from: [<URL>](#).

24. Ahuja A, Ali J, Rahman S. Biodegradable periodontal intrapocket device containing metronidazole and amoxicillin: Formulation and characterisation. *Die Pharm - An Int J Pharm Sci [Internet].* 2006;6(1):25–9. Available from: [<URL>](#).

25. Virlan MJR, Miricescu D, Totan A, Greabu M, Tanase C, Sabliov CM, et al. Current uses of Poly(lactic-co-glycolic acid) in the dental field: A comprehensive review. *J Chem [Internet].* 2015 Jan 1;2015(1):525832. Available from: [<URL>](#).

26. G Dehghan MH, Marzuka M. Lyophilized chitosan/xanthan polyelectrolyte complex based mucoadhesive inserts for nasal delivery of promethazine hydrochloride. *Iran J Pharm Res IJPR [Internet].* 2014;13(3):769–84. Available from: [<URL>](#).

27. Zhang L, Wang J, Chi H, Wang S. Local anesthetic lidocaine delivery system: Chitosan and hyaluronic acid-modified layer-by-layer lipid nanoparticles. *Drug Deliv [Internet].* 2016 Nov 21;23(9):3529–37. Available from: [<URL>](#).

28. Goodson JM, Offenbacher S, Farr DH, Hogan PE. Periodontal disease treatment by local drug delivery. *J Periodontol [Internet].* 1985 May 1;56(5):265–72. Available from: [<URL>](#).

29. Arancibia R, Maturana C, Silva D, Tobar N, Tapia C, Salazar JC, et al. Effects of chitosan particles in periodontal pathogens and gingival fibroblasts. *J Dent Res [Internet].* 2013 Aug 20;92(8):740–5. Available from: [<URL>](#).

30. Zupančič Š, Potrč T, Baumgartner S, Kocbek P, Kristl J. Formulation and evaluation of chitosan/polyethylene oxide nanofibers loaded with metronidazole for local infections. *Eur J Pharm Sci*

[Internet]. 2016 Dec 1;95:152–60. Available from: [<URL>](#).

31. Pichayakorn W, Boonme P. Evaluation of cross-linked chitosan microparticles containing metronidazole for periodontitis treatment. *Mater Sci Eng C* [Internet]. 2013 Apr 1;33(3):1197–202. Available from: [<URL>](#).

32. Farhadian N, Godiny M, Moradi S, Hemati Azandaryani A, Shahlaei M. Chitosan/gelatin as a new nano-carrier system for calcium hydroxide delivery in endodontic applications: Development, characterization and process optimization. *Mater Sci Eng C* [Internet]. 2018 Nov 1;92:540–6. Available from: [<URL>](#).

33. del Carpio-Perochena A, Kishen A, Felitti R, Bhagirath AY, Medapati MR, Lai C, et al. Antibacterial properties of chitosan nanoparticles and propolis associated with calcium hydroxide against single- and multispecies biofilms: An *in vitro* and *in situ* Study. *J Endod* [Internet]. 2017 Aug 1;43(8):1332–6. Available from: [<URL>](#).

34. Belstrøm D, Constancias F, Liu Y, Yang L, Drautz-Moses DI, Schuster SC, et al. Metagenomic and metatranscriptomic analysis of saliva reveals disease-associated microbiota in patients with periodontitis and dental caries. *npj Biofilms Microbiomes* [Internet]. 2017 Oct 2;3(1):23. Available from: [<URL>](#).

35. Ganss C, Lussi A, Grunau O, Klimek J, Schlueter N. Conventional and anti-erosion fluoride toothpastes: Effect on enamel erosion and erosion-abrasion. *Caries Res* [Internet]. 2011 Dec 1;45(6):581–9. Available from: [<URL>](#).

36. Lee HL, Wang RS, Hsu YC, Chuang CC, Chan HR, Chiu HC, et al. Antifungal effect of tissue conditioners containing poly(acryloyloxyethyltrimethyl

ammonium chloride)-grafted chitosan on *Candida albicans* growth *in vitro*. *J Dent Sci* [Internet]. 2018 Jun 1;13(2):160–6. Available from: [<URL>](#).

37. Silva-Dias A, Palmeira-de-Oliveira A, Miranda IM, Branco J, Cobrado L, Monteiro-Soares M, et al. Anti-biofilm activity of low-molecular weight chitosan hydrogel against *Candida* species. *Med Microbiol Immunol* [Internet]. 2014 Feb 8;203(1):25–33. Available from: [<URL>](#).

38. Atai Z, Atai M, Amini J, Salehi N. *In vivo* study of antifungal effects of low-molecular-weight chitosan against *Candida albicans*. *J Oral Sci* [Internet]. 2017;59(3):425–30. Available from: [<URL>](#).

39. Mustafa MW, Ungphaiboon S, Phadoongsombut N, Pangsomboon K, Chelae S, Mahattanadul S. Effectiveness of an alcohol-free chitosan-curcuminoid mouthwash compared with chlorhexidine mouthwash in denture stomatitis treatment: A randomized trial. *J Altern Complement Med* [Internet]. 2019 May 9;25(5):552–8. Available from: [<URL>](#).

40. Fakhri E, Eslami H, Maroufi P, Pakdel F, Taghizadeh S, Ganbarov K, et al. Chitosan biomaterials application in dentistry. *Int J Biol Macromol* [Internet]. 2020 Nov 1;162:956–74. Available from: [<URL>](#).

41. Wang W, Meng Q, Li Q, Liu J, Zhou M, Jin Z, et al. Chitosan derivatives and their application in biomedicine. *Int J Mol Sci* [Internet]. 2020 Jan 12;21(2):487. Available from: [<URL>](#).

42. Bapat RA, Chaubal T V., Dharmadhikari S, Abdulla AM, Bapat P, Alexander A, et al. Recent advances of gold nanoparticles as biomaterial in dentistry. *Int J Pharm* [Internet]. 2020 Aug 30;586:119596. Available from: [<URL>](#).



Preparation of Modified Surfaces Based on Tannic Acid and Carbon Nanotubes and Investigation of Their Electrochemical Properties

Hilal İncebay^{1*} , Rumeysa Saylakçı¹ 

¹Nevşehir Hacı Bektaş Veli University, Department of Molecular Biology and Genetics, Nevşehir, 50300, Turkey.

Abstract: This study focuses on the electrochemical investigation of modifiers and their components that can provide the easiest and most sensitive results for electrochemical sensors. For this purpose, a nanocomposite of tannic acid and carbon nanotubes with extraordinary properties was obtained. The nanocomposite and its components were immobilized on glassy carbon electrode surfaces by the drop-drying technique. The morphological and electrochemical properties of the nanocomposite and its components were examined by scanning electron microscopy and cyclic voltammetry techniques. The surfaces modified with the nanocomposite and its components exhibited different electrochemical behaviors. Tests performed in ferricyanide, ferrocene, ruthenium hexamine (III) chloride, and ferricyanide/ferricyanide probes showed that the nanocomposite-modified surface exhibited the best voltammetric behavior. Scan rate and pH studies showed that the nanocomposite-modified surface catalyzed electron transfer more and increased the active surface area.

Keywords: Carbon nanotube, Modification, Nanocomposite, Tannic acid.

Submitted: August 6, 2024. **Accepted:** September 27, 2024.

Cite this: İncebay H, Saylakçı R. Preparation of Modified Surfaces Based on Tannic Acid and Carbon Nanotubes and Investigation of Their Electrochemical Properties. JOTCSA. 2024;11(4): 1595-604.

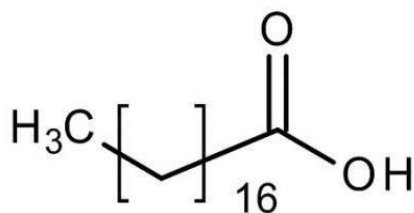
DOI: <https://doi.org/10.18596/jotcsa.1528731>

***Corresponding author's E-mail:** hilalincebay@gmail.com

1. INTRODUCTION

Tannins are also known as tannic acid. Tannins are compounds with polyphenolic structures and are obtained from plants such as tea, rapeseed, broad bean, and sorghum. Tannic acid (TA) is present in numerous vegetables, fruits, and beverages, including wine, beer, coffee, black tea, and white tea. Simultaneously, due to the presence of numerous hydroxyl and functional groups in their structures, they are capable of forming cross-links with proteins and other macromolecules. TA, a water-soluble polyphenol compound, has been actively used to treat many diseases for years (1,2). TA analysis is gaining importance due to its wide range of studies, such as environment, medicine, and food. TA is used as a food additive and sweetener (3) as well as an additive in medicine and veterinary fields due to its antimicrobial, anticarcinogenic, and antimutagenic potential. At the same time, TA protects cells against oxidation properties (4,5). Determining the amount of tannic acid contained in fruit, tea, and beer is very important in evaluating the quality of the products (6). TA, which has a very wide area of use in medicine, is used in the treatment of tonsils, pharyngitis, hemorrhoids, and some diseases due to

its astringent effects on vessels and mucosa. This compound also has antioxidant, antitumor, antimutagenic, and antiviral properties and other types of physiological activities (7-9). An important feature of TA is its strong interaction with metal ions, polymers, and proteins (10). The TA molecule contains a large number of active phenolic groups and is easily converted to polytannic acid (PTA), which can bind to various molecules through covalent or non-covalent bonds. Therefore, PTA has attracted great interest in surface modification due to its good adhesion, excellent biocompatibility, biodegradability, antimicrobial and antioxidant effects (11,12). In addition, thanks to its active phenolic groups, it easily forms composites by integrating with various molecules (13). Therefore, it can be effectively used as a modifier for electrochemical sensors.



Scheme: The molecular formula of tannic acid.

Nowadays, it has been determined that nanocomposites are superior to pure polymers in terms of thermal, optical, mechanical, electronic, and catalytic properties. Studies have shown that the incorporation of nanoparticles in nanocomposites has several beneficial and enhancing effects (14). This is due to the fact that nanoparticles or nanostructured materials increase the adhesion/bonding between the matrix and nanostructured materials thanks to their large surface areas (15). In addition, the easy and homogeneous incorporation of nanostructures into the matrix also takes their positive effects to the next level. Considering these properties of nanostructures, carbon nanotubes (CNTs) are known to be the hardest and most durable man-made nanomaterials known so far (16). In addition to all the advantages they offer, they have also attracted interest in areas related to electrical devices and communication thanks to their high electrical conductivity properties (17,18). Moreover, due to their very small dimensions, these structures can also be used if they are homogeneously embedded in matrices. To increase the chemical affinity of carbon nanotubes (CNTs) to polymer matrices, chemical modification of graphitic sidewalls and ends is required. The properties and applications of CNTs have been very active areas of research in the last decade (19-23). CNTs exhibit high flexibility, low bulk density, and a large aspect ratio (typically greater than 1000). MWCNTs can transport electrons along long lengths without significant interruption, making them more conductive than copper (24). The main advantage of CNTs, which makes them ideal reinforcements for several applications, is that their mechanical and electrical properties can be utilized in combination (25,26).

TA is an oligomeric polymer of carbon-carbon bonded flavonoid units resistant to hydrolysis and can work in harmony with nanostructures during enzymatic/chemical reactions. This allows the integration of TA with carbon-based nanostructures or nanoparticles as a sensor interface to trigger the correct enzymatic reactions and significantly increase the detection capability of the modified electron. Thus, it provides the potential to provide innovative, fast, simple, durable, and accurate high-sensitivity measurements in the development of electrochemical sensor systems. The combination of carbon nanotubes with the advantageous features of tannic acid is anticipated to yield novel composite forms, offering cost-effective and efficient modifiers

and facilitating the development of revolutionary electrochemical sensors (13).

This study aims to prepare a nanocomposite by taking advantage of the superior properties of tannic acid active phenolic groups and multi-walled carbon nanotubes. For this purpose, the nanocomposite suspension prepared by sonication in chloroform was modified on glassy carbon electrode surfaces via the drop-drying technique. Tannic acid and multi-walled carbon nanotubes, which are the components constituting the nanocomposite, were also prepared in the same manner, and modified electrodes were obtained. Then, the electrochemical and morphological characteristics of the obtained surfaces were investigated and compared with both each other and the bare GCE.

2. EXPERIMENTAL SECTION

2.1. Materials

Potassium ferricyanide ($\geq 99\%$), tannic acid (99%), ferrocene (98%), acetonitrile (97%), tetrabutylammonium tetrafluoroborate (99%), potassium ferrocyanide (99.9%), and chloroform ($\geq 99.5\%$) were ensured by Merck, VWR, and Sigma-Aldrich. Carbon nanotubes (110–170 nm) were purchased from Sigma. Ultrapure water was used in aqueous solutions, acetonitrile was used in non-aqueous solutions, and all solutions were kept at $+4^\circ\text{C}$. 99% pure $\text{N}_{2(g)}$ was used to remove dissolved oxygen in the cell before electrochemical experiments.

A Gamry Interface 1000B Potentiostat/Galvanostat/Zra analyzer was used for electrochemical experiments. In this analyzer, which has a three-electrode system, a nanocomposite-modified glassy carbon electrode (BASi Model MF-2012) served as the working electrode. The reference electrodes employed were the BASi model MF-2052 of Ag/AgCl/KCl (3M), the BASi model MF-2062 of Ag(AgNO₃(0.1M)), and the counter electrode was a Pt wire (0.5mm).

2.2. Functionalization of MWCNTs

Before modification, commercial MWCNTs were sonicated in a concentrated HClO₄(98.5-102.0%) + HNO₃(96-98%) (3:7, v:v) solution for 5 h to functionalize their surfaces (27). The functionalized MWCNTs were then filtered, repeatedly washed with ultrapure water to neutralize, and dried at room temperature.

2.3. Preparation of Modifier Suspensions

MWCNTs suspension: prepared by sonicating 1 mg of MWCNTs within 5 mL chloroform for 1 h.

TA suspension: prepared by sonicating 1 mg of TA within 5 mL chloroform for 1 h. TA/MWCNTs suspension: prepared by sonicating 1 mg of MWCNTs within 5 mL chloroform for 5 min, then adding 10 mg TA to the solution and sonicating the solution for another 1 h.

2.4. Modification

After the preparation of MWCNTs, TA, and TA/MWCNTs suspensions, 5.0 μL of each suspension was immobilized on the cleaned glassy carbon electrode surfaces by the drop-drying technique. Three modified electrodes defined as MWCNTs/GCE, TA/GCE and TA/MWCNTs/GCE were obtained.

2.5. Characterization

For the morphological characterization, SEM images were taken of the MWCNTs/GCE, TA/GCE, and TA/MWCNTs/GCE surfaces at 1 μm .

For the electrochemical characterization of bare GCE, TA/GCE, MWCNTs/GCE, and TA/MWCNTs/GCE surfaces with cyclic voltammetry (CV) technique in ferrocene, ferricyanide (HCF(III)), ruthenium hexamine(III) chloride and ferri-ferricyanide (HCF(III)-HCF(II)) redox probes, respectively;

- ✓ In 1.0 mM ferrocene solution, within the -0.2/+0.4 V range, at 100 mV/s scan rate, against Ag/AgNO₃ reference electrode,
- ✓ In 1.0 mM HCF(III) solution, within the +0.6/0.0 V range, at 100 mV/s scan rate, Ag/AgCl reference electrode, In 1.0 mM ruthenium hexamine(III) chloride solution, within the -0.5/0.2 V range, at 100 mV/s scan rate, against Ag/AgCl reference electrode,
- ✓ In 1.0 mM HCF(III)-(II) solution, within the -0.3/0.8 V range, at 100 mV/s scan rate, against Ag/AgCl reference electrode, voltammograms were recorded.

To provide insight into the TA, MWCNTs, and TA/MWCNTs structures to the GCE surface and to obtain information on whether there is an active group or groups that can be protonated on the surfaces after modification, voltammograms of each of the bare GCE, TA/GCE, MWCNTs/GCE and TA/MWCNTs/GCE surfaces were recorded separately on 1.0 mM HCF(III) probes prepared with BR buffer solutions at pH 2.0; 3.0; 5.0; 7.0; 9.0; and 11.0 (within the +0.6/0.0 V range, at 100 mV/s scan rate against an Ag/AgCl/KCl_(sat) reference electrode).

To determine the electron transfer pattern of TA, MWCNTs and TA/MWCNTs structures on the GCE surface, voltammograms of each of the bare GCE, TA/GCE, MWCNTs/GCE, and TA/MWCNTs/GCE surfaces were recorded against the Ag/AgNO₃ reference electrode within the -0.2/0.4 V range in 1.0 mM ferrocene probe prepared in CH₃CN containing 100 mM TBA-TFB at scan rates of 25, 50, 100, 200, 300, 400, 500, 600, 700 mV/s.

3. RESULTS AND DISCUSSION

3.1. Scanning Electron Microscope Examination of MWCNTs/GCE, TA/GCE, and TA/MWCNTs GCE Surfaces

Elucidating the morphology of modified surfaces provides important ideas. For this reason, 1 μm surface images of the prepared MWCNTs/GCE, TA/GCE, and TA/MWCNTs/GCE modified electrodes

were recorded with the SEM technique and presented in Figure 1. When the SEM image of the MWCNTs/GCE surface given in Figure 1A is examined, it is observed that MWCNTs are homogeneously distributed on the GCE surface, and there is no agglomeration. In Figure 1B, it is observed that TA also exhibits a homogeneous distribution without agglomeration. When Figure 1C is examined, it is determined that the TA/MWCNTs/GCE surface exhibits a complex structure by homogeneously dispersing the structure of MWCNTs functionalized with the multi-armed polyphenol structure of TA and flavonoid oligomer polymers. The homogeneous dispersion of MWCNTs, one of the components forming the nanocomposite (TA/MWCNTs), into the TA structure, showed that the adhesion/bonding between the matrix and nanostructured materials increased thanks to the large surface areas of the nanostructured materials (15).

3.2. Electrochemical behaviors of Bare GCE, TA/GCE, MWCNTs/GCE, and TA/MWCNTs/GCE in Redox Probes

Electrochemical tests performed by cyclic voltammetry (CV) in the presence of redox probes are an effective method to reveal whether electron transfer occurs between the surface and the electrolyte. Therefore, the electrochemical behaviors of bare GCE, TA/GCE, MWCNTs/GCE, and TA/MWCNTs/GCE were individually examined using the CV technique in the presence of HCF(III), ferrocene, HCF(III) – HCF(II), and ruthenium hexamine(III) chloride probes. The electrochemical behaviors of the modified GCE surfaces were compared with the electrochemical behavior of the bare GCE surface. Figure 2A presents the voltammograms of bare GCE, MWCNTs/GCE, TA/GCE, and TA/MWCNTs/GCE in the HCF(III) probe within the 0.0/0.6 V range at 100 mV/s scan rate. The voltammograms reveal that the peak current for MWCNTs/GCE is higher than that for TA/GCE, which can be attributed to the large surface area of MWCNTs and their functional groups that enhance catalytic activity and conductivity on the electrode surface (28). TA/MWCNTs/GCE showed the best voltammetric response compared to TA/GCE and MWCNTs/GCE modified surfaces. This is due to the synergistic effect created by combining the functional groups within the structure of MWCNTs and groups in TA with a multi-armed polyphenolic structure (29,30). Therefore, we can say that this effect improves the sensing ability of the surface and increases the electrode surface area and conductivity, improving the electron transfer rate.

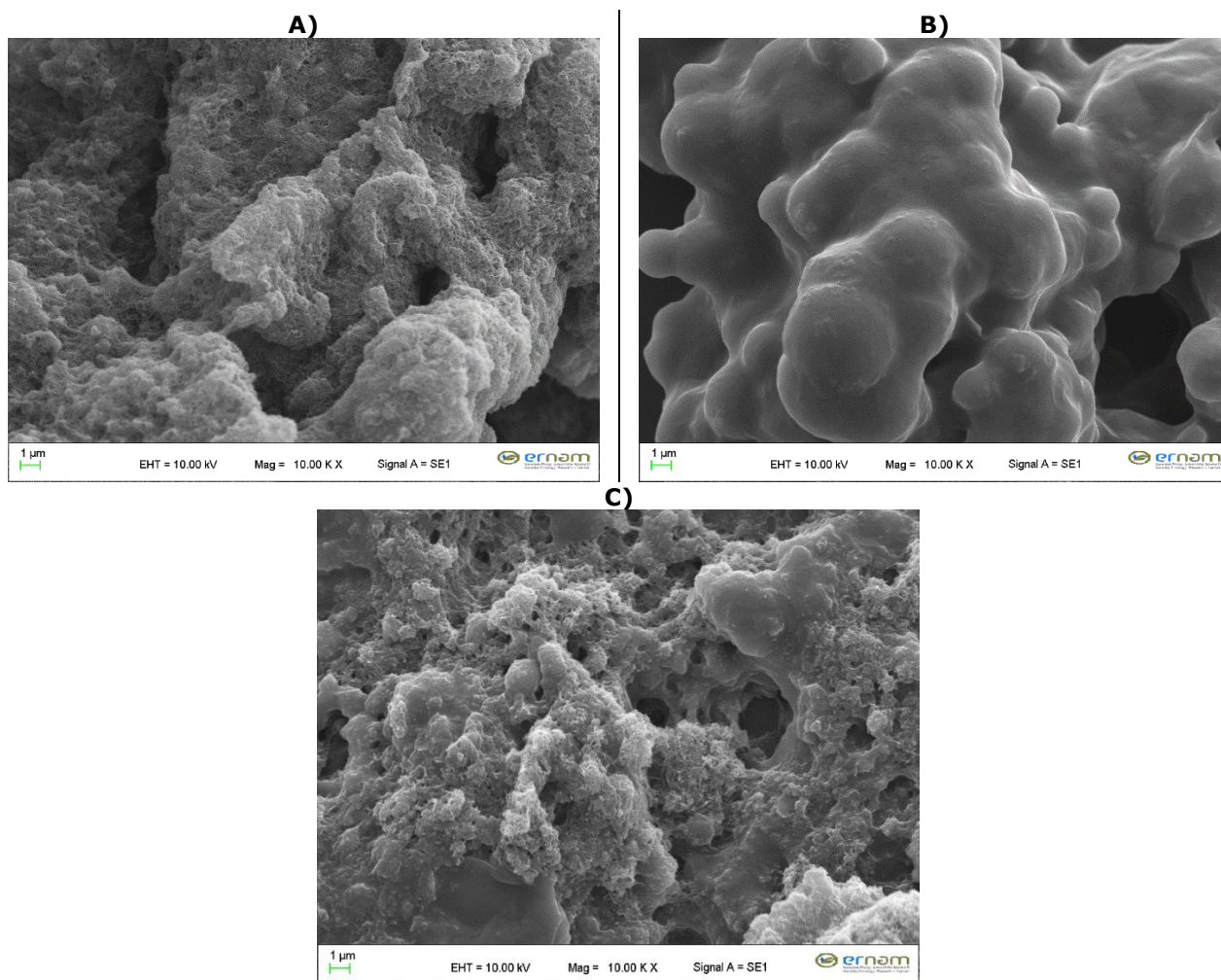


Figure 1: SEM micrograph **A)** MWCNTs/GCE, **B)** TA/GCE and **C)** TA/MWCNTs/GCE.

Figure 2B. represents the voltammograms of the ferrocene probe within the $-0.2/0.4\text{V}$ range at 100 mV/s scan rate for the bare/GCE, TA/GCE, MWCNTs/GCE, TA/MWCNTs/GCE surfaces. The anodic peak currents of the bare GCE, TA/GCE, and MWCNTs/GCE surfaces are found to be similar, while the TA/MWCNTs surface exhibits the highest peak current by showing the best electrocatalytic activity. This can be attributed to the formation of cross-links with electrochemical molecules with a large number of hydroxyl groups and functional groups in the structure of TA. In addition, due to the presence of a large number of active phenolic groups, it is also associated with the successful modification of the surface by transforming into a multiple TA structure that can adhere to various electrode surfaces through covalent or non-covalent bonds. Moreover, it has been observed that the composite structures used as modifier species do not make the electrode surface electro-inactive. Therefore, the voltammetric responses observed with the ferrocene probe indicated that electron transfer occurred on both the bare GCE and the modified GCE surfaces without any obstruction impeding the process (31,32).

Figure 2C shows the surface voltammograms for bare GCE, TA/GCE, MWCNTs/GCE, and TA/MWCNTs/GCE within the -0.3 to 0.8 V range at 100 mV/s scan rate using the HCF(III)-HCF(II) probe. Both reduction and oxidation peaks are visible on the bare GCE and

modified GCE surfaces. This is due to the oxidation of Fe^{2+} ions to Fe^{3+} ions and the subsequent reduction of Fe^{3+} ions back to Fe^{2+} ions. Moreover, the voltammetric responses for the HCF(III)-HCF(II) probe show that while bare GCE and MWCNTs/GCE surfaces have similar peak currents and potential shifts, the TA/MWCNTs/GCE surface provides the most favorable voltammetric response. This improved performance is likely due to the excellent surface compatibility provided by the carbon-carbon bonded flavonoid units of TA, which are resistant to hydrolysis, in combination with functionalized carbon nanotubes on the surfaces (33). Thus, the electron transfer of TA/MWCNTs/GCE in the HCF(III)-HCF(II) probe was more catalyzed.

Figure 2D represents the voltammograms for bare GCE, TA/GCE, MWCNTs/GCE, and TA/MWCNTs/GCE surfaces within the -0.5 to 0.2 V range at 100 mV/s scan rate using the ruthenium hexamine(III) chloride probe. All surfaces exhibit sensitivity to ruthenium for both reduction and oxidation reactions. While the bare GCE, MWCNTs/GCE, and TA/GCE surfaces show similar voltammetric responses to the ruthenium hexamine(III) chloride, the TA/MWCNTs/GCE surface demonstrates a more pronounced peak current. This enhanced sensitivity of the TA/MWCNTs/GCE surface to the ruthenium hexamine(III) chloride probe may be attributed to TA's role as a compatible polymer material, forming

strong π - π interactions through the stacking of hydroxyl groups esterified with phenolic structures when combined with carbon-based nanostructures

(34,35). It can be concluded that TA/MWCNTs/GCE significantly increases the detection capability and sensitivity thanks to this interaction.

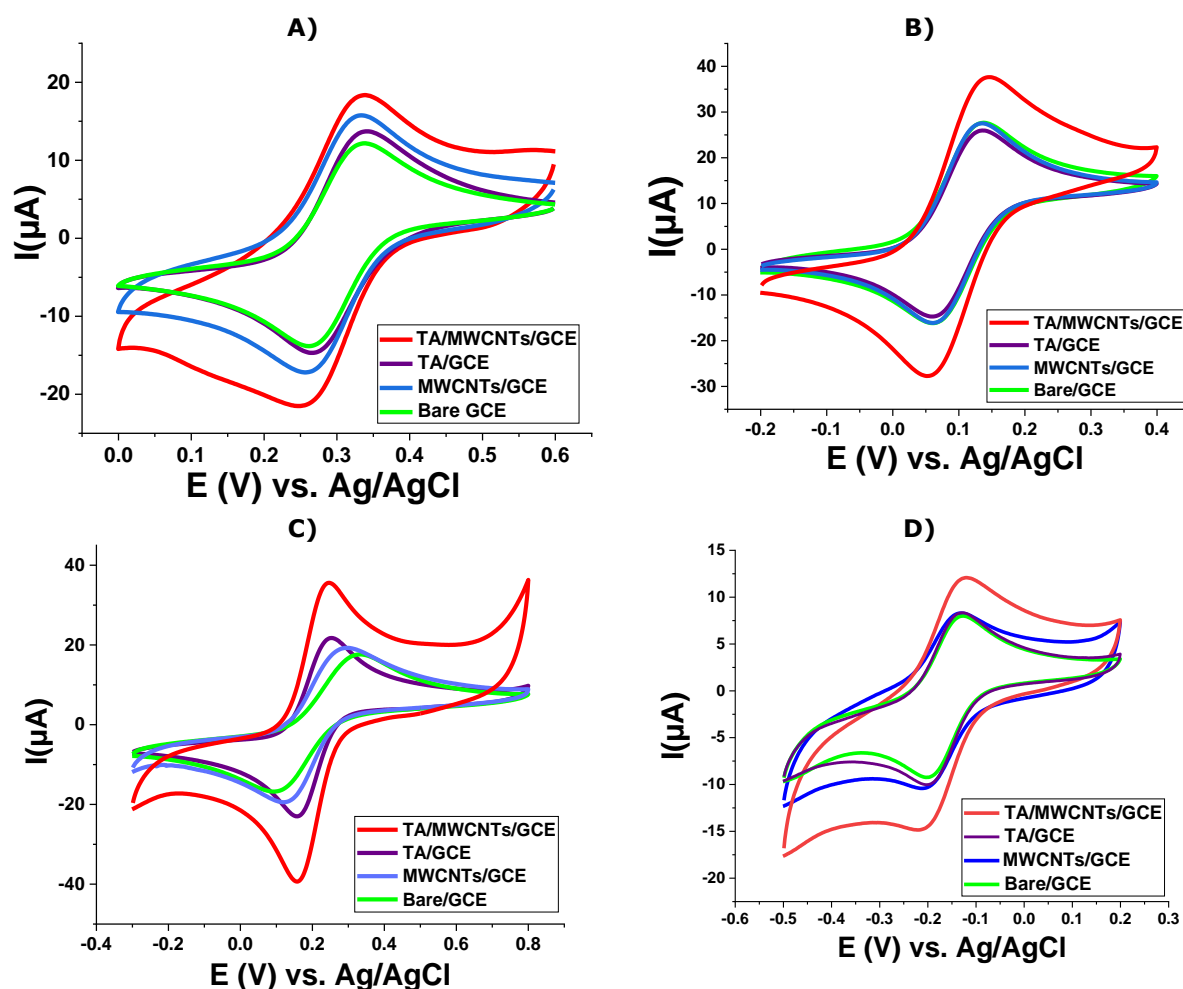


Figure 2: Surface voltammograms of bare/GCE, TA/GCE, MWCNTs/GCE, TA/MWCNT/GCE against at 100 mV/s scan rate **A)** Ag/AgCl/KCl(sat) reference electrode in 0.0/0.6 V potential range in 1.0 mM HCF(III); **B)** Ag/AgNO₃ reference electrode in the potential range of -0.2/0.4 V in 1.0 mM Ferrocene, **C)** Ag/AgCl/KCl(sat) reference electrode in the potential range of -0.3/0.8 V in 1.0 mM HCF(III)-HCF(II) solution **D)** against Ag/AgCl/KCl(sat) reference electrode in the potential range of -0.5/0.2 V in 1.0 mM ruthenium hexaamine(III) chloride solution.

5.3. pH Effect on Bare GCE, MWCNTs/GCE, TA/GCE and TA/MWCNTs/GCE Surfaces

The voltammetric responses of bare GCE, TA/GCE, MWCNTs/GCE and TA/MWCNTs/GCE surfaces in the +0.6–0.0 V potential range in the pH range from 2.0 to 11.0 in 1.0 Mm HCF(III) redox probe were investigated by CV technique and are presented in Figure 3. Peak currents were observed at pH 2.0 and 3.0 on bare GCE surface (Figure 3A). However, there were decreases in peak currents with increasing pH and peak currents were not observed at high pHs. Therefore, it was concluded that the bare GCE surface was sensitive to pH in acidic media. As presented in Figure 3B, the MWCNTs/GCE surface is sensitive to pH, but no peak current is observed on the surface at basic pH values such as pH 7.0, 9.0, 11.0, while a good peak current is obtained at acidic pH values, especially at pH 2.0. The reason for this decrease in peak currents with increasing pH can be associated with the negatively charged OH⁻ ions, which increase as a result of the basicity of the medium, repel the negatively charged HCF(III) ions,

thus reducing electron transfer and thus decreasing the voltammetric peak currents of the MWCNTs/GGCE surface. In Figure 3C, it is observed that the TA/GCE surface gives similar peak currents with small shifts in peak potentials at pH 3.0, 5.0, 7.0 and 9.0, and the best voltammetric peak current occurs at pH 2.0. However, it is seen that it does not form a peak current by being blocked at basic pH values such as pH 11.0. It can be said that this situation is due to the repulsion of negatively charged molecules in TA and the OH⁻ ions that increase in the media at high pHs. It can also be explained by the fact that structures such as gallic acid and polyphenolic acid in the TA structure negatively affect the electron transfer on the surface and prevent the formation of a voltammetric response (36,37). As presented in Figure 3D, the TA/MWCNTs/GCE surface exhibits similar sensitivity at pH 3.0, 5.0, and 7.0. A well-defined peak current was obtained with a shift in the peak potential at pH 2.0. However, it was also determined that the surface was blocked at pH 11.0 and did not produce a peak current response. This

can be associated with the OH⁻ groups attached to the carbohydrate (usually D-glucose) and phenolic groups in the center of the TA structure and the OH⁻ ions abundant in the media at pH 11.0 repelling each other and negatively affecting the electrocatalytic

activity of the modified surface. Experimental findings showed that the reactions of modified GCE surfaces in the HCF(III) redox probe were more reversible at low pH values.

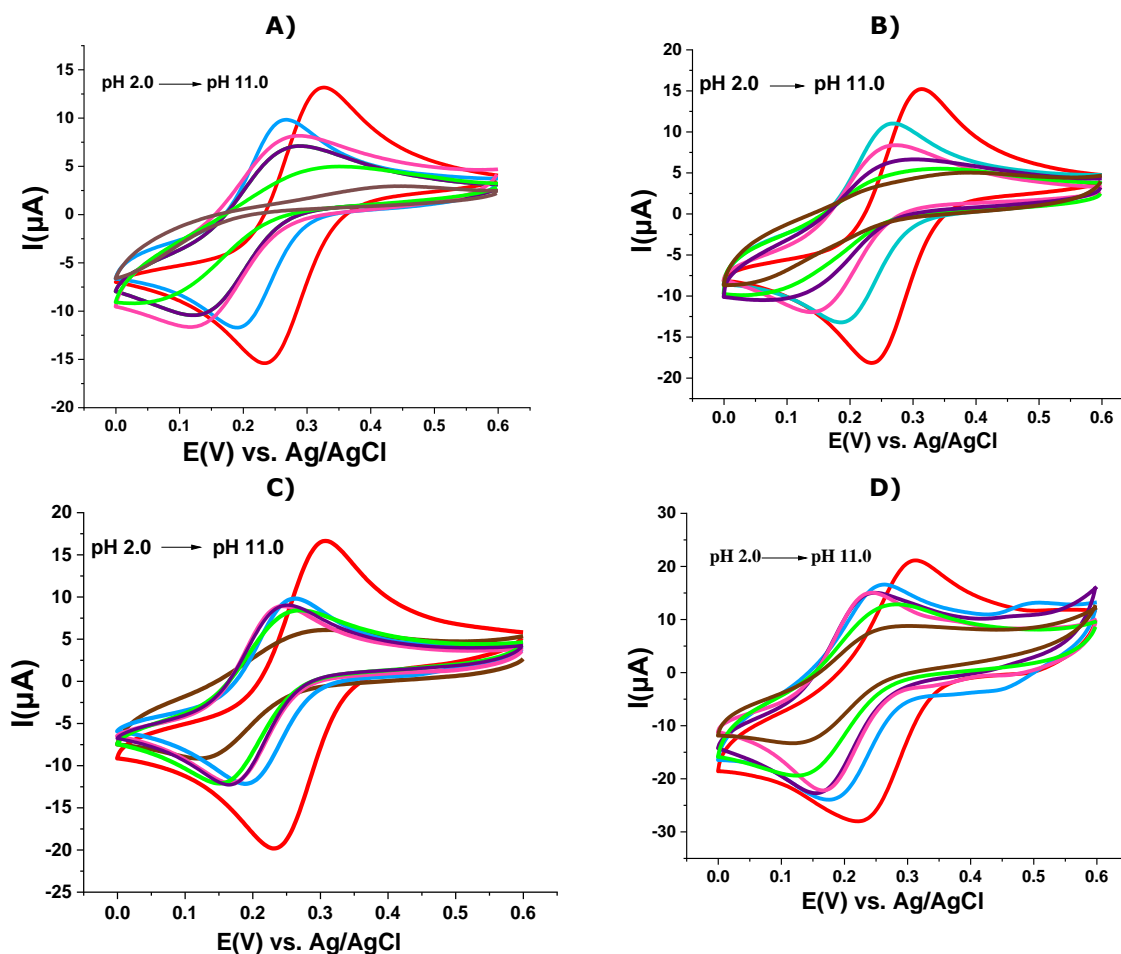


Figure 3: CV voltammograms of **A)** bare GCE, **B)** MWCNTs/GCE, **C)** TA/GCE, **D)** TA/MWCNTs/GCE surface in 1.0 mM HCF(III) probe against Ag/AgCl/KCl_(sat) reference electrode in the potential range +0.6-0.0 V at 100 mV/s scan rate in the potential range +0.6-0.0 V at pH 2; 3; 5; 7; 9; 11.

5.4. Scan Rate Effect on Bare GCE, TA/GCE, MWCNTs/GCE and TA/MWCNTs/GCE Surfaces

To investigate the properties such as reversibility and electron transfer pattern of bare GCE, TA/GCE, MWCNTs/GCE and TA/MWCNTs/GCE surfaces, voltammograms were recorded at 25, 50, 100, 200, 300, 400, 500, 600 and 700 mV/s scan rates against Ag/AgNO₃ reference electrode within the -0.2/0.4 V range using CV technique in 1.0 mM ferrocene probe and are presented in Figure 4A-D. While almost no change was observed in the peak potentials of all surfaces with the increasing scan rates, a linear increase in the peak currents was observed. The same situation occurred in the reverse scan. To better understand the reaction mechanism on the electrode surface, peak currents were plotted against both the scan rate and the square root of the scan rate. A linear relationship was observed between the

peak currents and the square root of the scan rate (Figure 4E-H). For adsorption-controlled reactions on electrode surfaces, the graphs should be linear, and the slopes should be greater than 0.5. However, it is known that the reaction is diffusion-controlled if the slope value is less than 0.5 (38). The peak currents versus the square root of the scan rate were plotted, R² values were calculated, and it was found that R² = 0.9997 for the bare GCE surface, R² = 0.9977 for the MWCNTs surface, R² = 0.9989 for the TA/GCE surface, and R² = 0.9997 for the TA/MWCNTs/GCE surface. Since the obtained R² values were very close to 1.0 and the slope values were greater than 0.5, it was determined that the electrochemical reaction taking place on the bare GCE, MWCNTs/GCE, TA/GCE and TA/MWCNTs/GCE surfaces was an adsorption-controlled reaction.

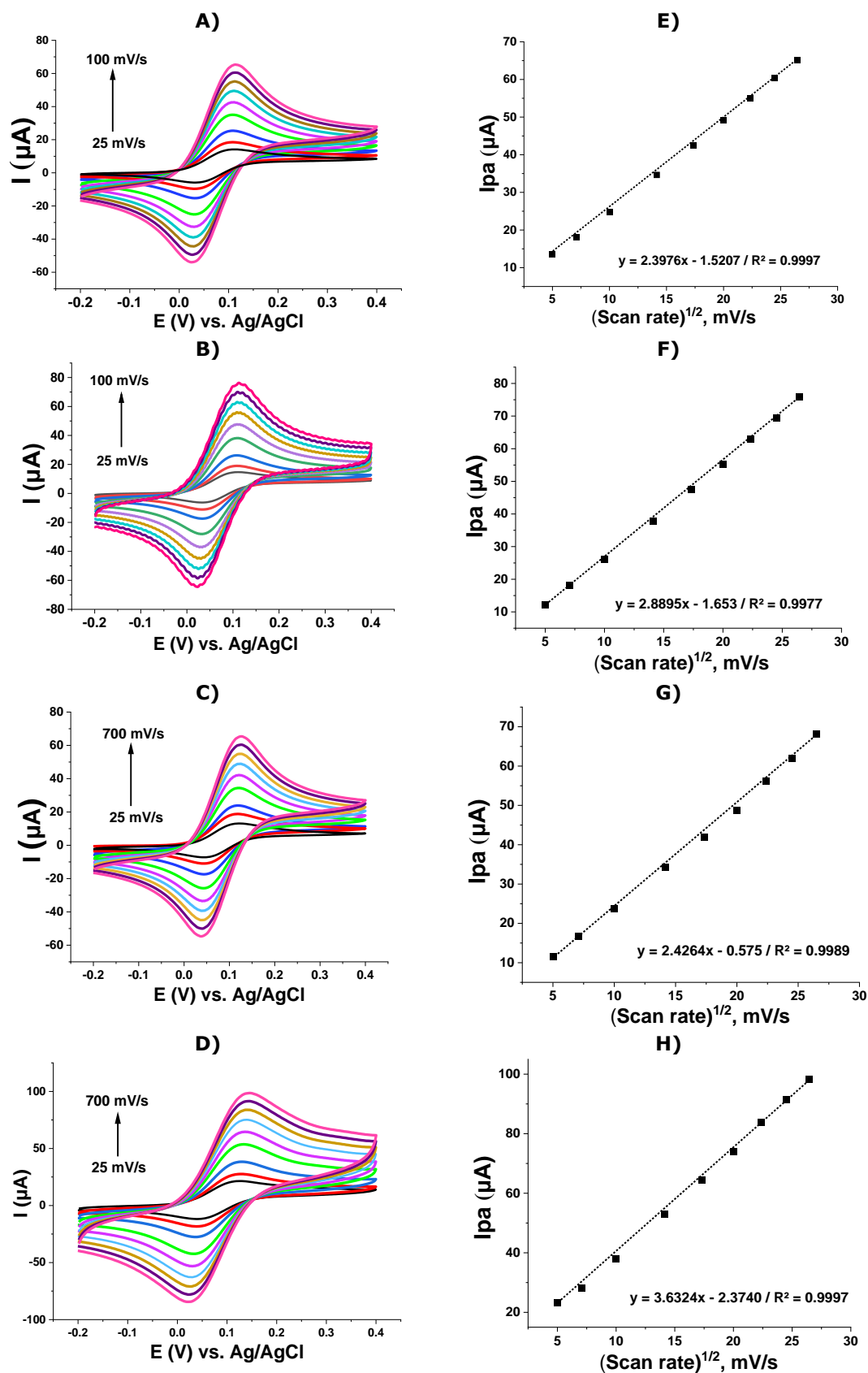


Figure 4: CV voltammograms of **A)** bare/GCE, **B)** MWCNTs/GCE, **C)** TA//GCE, **D)** TA/MWCNTs/GCE surface in 1.0 mM ferrocene solution against Ag/AgNO₃ reference electrode at scan rates of 25; 50; 100; 200; 300; 400; 500; 600; 700 mV/s. Peak currents plot against the square root of scan rate for **E)** bare/GCE, **F)** MWCNTs/GCE, **G)** TA//GCE, **H)** TA/MWCNTs/GCE.

4. CONCLUSION

This study focused on gaining features that are fast, easy, cheap, and environmentally friendly by using fewer chemicals for the preparation of nanocomposites, which are becoming increasingly popular. Superior properties were gained by incorporating carbon nanotubes into its structure using a natural polymer such as tannic acid. Homogeneous distribution of the components of the nanocomposite within each other was confirmed morphologically. As a result of detailed electrochemical examinations of the nanocomposite and its components, when the voltammograms of HCF(III), ruthenium hexamine (III) chloride, and HCF(III) – HCF(II) probes were compared, it was determined that the TA/MWCNTs/GCE surface exhibited the best voltammetric behavior. In pH studies, it was determined that the surfaces were sensitive to pH, and in scan rate studies, the electrochemical reaction taking place on the TA/MWCNTs/GCE surface was an adsorption-controlled reaction. The active surface areas were calculated as 0.124 cm² for GCE and 0.3405 cm² for TA/MWCNTs/GCE. This indicated that nanocomposite-modified electrode TA/MWCNTs/GCE has a large and active surface area and can be successfully used to detect analytes in electrochemical sensor technology (13).

5. CONFLICT OF INTEREST

The authors declare that they have no known competing financial interests or personal relationships that could have appeared to influence the work reported in this paper.

6. ACKNOWLEDGMENTS

We would like to thank Nevşehir Hacı Bektaş Veli University (NEÜ ABAP20F19) for their financial support.

7. REFERENCES

- Orlowski P, Krzyzowska M, Zdanowski R, Winnicka A, Nowakowska J, Stankiewicz W, et al. Assessment of in vitro cellular responses of monocytes and keratinocytes to tannic acid modified silver nanoparticles. *Toxicol Vitr* [Internet]. 2013 Sep 1;27(6):1798–808. Available from: [<URL>](#).
- Ghasemian M, Kazeminava F, Naseri A, Mohebzadeh S, Abbaszadeh M, Kafil HS, et al. Recent progress in tannic acid based approaches as a natural polyphenolic biomaterial for cancer therapy: A review. *Biomed Pharmacother* [Internet]. 2023 Oct 1;166:115328. Available from: [<URL>](#).
- Ahmed GHG, Laíño RB, Calzón JAG, García MED. Fluorescent carbon nanodots for sensitive and selective detection of tannic acid in wines. *Talanta* [Internet]. 2015 Jan 15;132:252–7. Available from: [<URL>](#). <https://linkinghub.elsevier.com/retrieve/pii/S0039914014008030>
- Ren A, Zhang W, Thomas HG, Barish A, Berry S,

Kiel JS, et al. A tannic acid-based medical food, cesinex®, exhibits broad-spectrum antidiarrheal properties: A mechanistic and clinical study. *Dig Dis Sci* [Internet]. 2012 Jan 12;57(1):99–108. Available from:

[<URL>](http://link.springer.com/10.1007/s10620-011-1821-9).http://link.springer.com/10.1007/s10620-011-1821-9

5. Fu X, Yuan S, Yang F, Yu H, Xie Y, Guo Y, et al. Characterization of the interaction between boscalid and tannic acid and its effect on the antioxidant properties of tannic acid. *J Food Sci* [Internet]. 2023 Apr 14;88(4):1325–35. Available from: [<URL>](#).

6. Anderson HE, Santos IC, Hildenbrand ZL, Schug KA. A review of the analytical methods used for beer ingredient and finished product analysis and quality control. *Anal Chim Acta* [Internet]. 2019 Nov 28;1085:1–20. Available from: [<URL>](#).

7. Bigham A, Rahimkhoei V, Abasian P, Delfi M, Naderi J, Ghomi M, et al. Advances in tannic acid-incorporated biomaterials: Infection treatment, regenerative medicine, cancer therapy, and biosensing. *Chem Eng J* [Internet]. 2022 Mar 15;432:134146. Available from: [<URL>](#).

8. Baldwin A, Booth BW. Biomedical applications of tannic acid. *J Biomater Appl* [Internet]. 2022 Mar 7;36(8):1503–23. Available from: [<URL>](#).

9. Lee HY, Hwang CH, Kim HE, Jeong SH. Enhancement of bio-stability and mechanical properties of hyaluronic acid hydrogels by tannic acid treatment. *Carbohydr Polym* [Internet]. 2018 Apr 15;186:290–8. Available from: [<URL>](#).

10. Higazy A, Hashem M, ElShafei A, Shaker N, Hady MA. Development of anti-microbial jute fabrics via *in situ* formation of cellulose–tannic acid–metal ion complex. *Carbohydr Polym* [Internet]. 2010 Mar 17;79(4):890–7. Available from: [<URL>](#).

11. Oulad F, Zinadini S, Zinatizadeh AA, Derakhshan AA. Fabrication and characterization of a novel tannic acid coated boehmite/PES high performance antifouling NF membrane and application for licorice dye removal. *Chem Eng J* [Internet]. 2020 Oct 1;397:125105. Available from: [<URL>](#).

12. Sahiner N, Sagbas S, Aktas N, Silan C. Inherently antioxidant and antimicrobial tannic acid release from poly(tannic acid) nanoparticles with controllable degradability. *Colloids Surfaces B Biointerfaces* [Internet]. 2016 Jun 1;142:334–43. Available from: [<URL>](#).

13. Saylakçı R, Incebay H. An electrochemical platform of tannic acid and carbon nanotubes for the sensitive determination of the antipsychotic medication clozapine in pharmaceutical and biological samples. *J Electroanal Chem* [Internet]. 2021 Oct 1;898:115638. Available from: [<URL>](#).

14. Çiçek Ozkan B, Güner M, Şeker TS. Thermal and morphological properties of HDPE/ZnO and HDPE/HAp nanocomposites. *Firat Univ J Eng Sci* [Internet]. 2020 Mar 3;32(1):259–66. Available from: [<URL>](#).

15. Langat J, Bellayer S, Hudrlik P, Hudrlik A, Maupin PH, Gilman JW, et al. Synthesis of imidazolium salts and their application in epoxy montmorillonite nanocomposites. *Polymer (Guildf)* [Internet]. 2006 Sep 7;47(19):6698–709. Available from: [<URL>](#).
16. Ali A, Rahimian Kolor SS, Alshehri AH, Arockiarajan A. Carbon nanotube characteristics and enhancement effects on the mechanical features of polymer-based materials and structures – A review. *J Mater Res Technol* [Internet]. 2023 May 1;24:6495–521. Available from: [<URL>](#).
17. Ben Messaoud N, Ghica ME, Dridi C, Ben Ali M, Brett CMA. Electrochemical sensor based on multiwalled carbon nanotube and gold nanoparticle modified electrode for the sensitive detection of bisphenol A. *Sensors Actuators B Chem* [Internet]. 2017 Dec 1;253:513–22. Available from: [<URL>](#).
18. Mehmandoust M, Khoshnavaz Y, Tuzen M, Erk N. Voltammetric sensor based on bimetallic nanocomposite for determination of favipiravir as an antiviral drug. *Microchim Acta* [Internet]. 2021 Dec 27;188(12):434. Available from: [<URL>](#).
19. Incebay H, Aktepe L, Leblebici Z. An electrochemical sensor based on green tea extract for detection of Cd(II) ions by differential pulse anodic stripping voltammetry. *Surfaces and Interfaces* [Internet]. 2020 Dec 1;21:100726. Available from: [<URL>](#).
20. Valenzuela-Muñiz AM, Alonso-Nuñez G, Miki-Yoshida M, Botte GG, Verde-Gómez Y. High electroactivity performance in Pt/MWCNT and PtNi/MWCNT electrocatalysts. *Int J Hydrogen Energy* [Internet]. 2013 Sep 19;38(28):12640–7. Available from: [<URL>](#).
21. Power AC, Gorey B, Chandra S, Chapman J. Carbon nanomaterials and their application to electrochemical sensors: A review. *Nanotechnol Rev* [Internet]. 2018 Feb 23;7(1):19–41. Available from: [<URL>](#).
22. Shahrokhian S, Rastgar S, Amini MK, Adeli M. Fabrication of a modified electrode based on Fe₃O₄NPs/MWCNT nanocomposite: Application to simultaneous determination of guanine and adenine in DNA. *Bioelectrochemistry* [Internet]. 2012 Aug 1;86:78–86. Available from: [<URL>](#).
23. Tigari G, Manjunatha JG. A surfactant enhanced novel pencil graphite and carbon nanotube composite paste material as an effective electrochemical sensor for determination of riboflavin. *J Sci Adv Mater Devices* [Internet]. 2020 Mar 1;5(1):56–64. Available from: [<URL>](#).
24. Ali Z, Yaqoob S, Yu J, D'Amore A. Critical review on the characterization, preparation, and enhanced mechanical, thermal, and electrical properties of carbon nanotubes and their hybrid filler polymer composites for various applications. *Compos Part C Open Access* [Internet]. 2024 Mar 1;13:100434. Available from: [<URL>](#).
25. Guldi DM, Rahman GMA, Zerbetto F, Prato M. Carbon nanotubes in electron donor–acceptor nanocomposites. *Acc Chem Res* [Internet]. 2005 Nov 1;38(11):871–8. Available from: [<URL>](#).
26. Rathinavel S, Priyadarshini K, Panda D. A review on carbon nanotube: An overview of synthesis, properties, functionalization, characterization, and the application. *Mater Sci Eng B* [Internet]. 2021 Jun 1;268:115095. Available from: [<URL>](#).
27. Kutluay A, Aslanoglu M. An electrochemical sensor prepared by sonochemical one-pot synthesis of multi-walled carbon nanotube-supported cobalt nanoparticles for the simultaneous determination of paracetamol and dopamine. *Anal Chim Acta* [Internet]. 2014 Aug 11;839:59–66. Available from: [<URL>](#).
28. Niu JJ, Wang JN, Jiang Y, Su LF, Ma J. An approach to carbon nanotubes with high surface area and large pore volume. *Microporous Mesoporous Mater* [Internet]. 2007 Mar 23;100(1–3):1–5. Available from: [<URL>](#).
29. Salinas-Torres D, Huerta F, Montilla F, Morallón E. Study on electroactive and electrocatalytic surfaces of single walled carbon nanotube-modified electrodes. *Electrochim Acta* [Internet]. 2011 Feb 1;56(5):2464–70. Available from: [<URL>](#).
30. Moore KE, Flavel BS, Yu J, Abell AD, Shapter JG. Increased redox-active peptide loading on carbon nanotube electrodes. *Electrochim Acta* [Internet]. 2013 Feb 1;89:206–11. Available from: [<URL>](#).
31. Fagan-Murphy A, Kataria S, Patel BA. Electrochemical performance of multi-walled carbon nanotube composite electrodes is enhanced with larger diameters and reduced specific surface area. *J Solid State Electrochem* [Internet]. 2016 Mar 6;20(3):785–92. Available from: [<URL>](#).
32. Guan JF, Zou J, Liu YP, Jiang XY, Yu JG. Hybrid carbon nanotubes modified glassy carbon electrode for selective, sensitive and simultaneous detection of dopamine and uric acid. *Ecotoxicol Environ Saf* [Internet]. 2020 Sep 15;201:110872. Available from: [<URL>](#).
33. Krywko-Cendrowska A, Marot L, Mathys D, Boulmedais F. Ion-imprinted nanofilms based on tannic acid and silver nanoparticles for sensing of Al(III). *ACS Appl Nano Mater* [Internet]. 2021 May 28;4(5):5372–82. Available from: [<URL>](#).
34. Liao W, Yu C, Peng Z, Xu F, Zhang Y, Zhong W. Ultrasensitive Mg²⁺-modulated carbon nanotube/tannic acid aerogels for high-performance wearable pressure sensors. *ACS Sustain Chem Eng* [Internet]. 2023 Feb 13;11(6):2186–97. Available from: [<URL>](#).
35. Kruusenberg I, Alexeyeva N, Tammeveski K. The pH-dependence of oxygen reduction on multi-walled carbon nanotube modified glassy carbon electrodes. *Carbon N Y* [Internet]. 2009 Mar 1;47(3):651–8. Available from: [<URL>](#).
36. Rai P, Mehrotra S, Sharma SK. Development of a

paper-based chromogenic strip and electrochemical sensor for the detection of tannic acid in beverages. LWT [Internet]. 2022 Nov 1;169:113999. Available from: [<URL>](#).

37. Xu L, He N, Du J, Deng Y, Li Z, Wang T. A detailed investigation for determination of tannic acid by anodic stripping voltammetry using porous

electrochemical sensor. Anal Chim Acta [Internet]. 2009 Feb 16;634(1):49–53. Available from: [<URL>](#).

38. Lin CS, Denton EB, Gaskill HS, Putnam GL. Diffusion-controlled electrode reactions. Ind Eng Chem [Internet]. 1951 Sep 1;43(9):2136–43. Available from: [<URL>](#).



Quantification and Evaluation of Plasma-free Amino Acid Concentrations by LC-MS/MS After Total Gastrectomy

Tugrul Cagri Akman^{1*} , Yucel Kadioglu² , Burak Bayrak² , Mehmet İlhan Yildirgan³ ,
Esra Disci³ 

¹Department of Analytical Chemistry, Faculty of Pharmacy, Erzincan Binali Yildirim University, Erzincan, Turkey.

²Department of Analytical Chemistry, Faculty of Pharmacy, Atatürk University, Erzurum, Turkey.

³Department of General Surgery, Faculty of Medicine, Atatürk University, Erzurum, Turkey.

Abstract: The effect of total gastrectomy (TG) on plasma free amino acid (PFAA) concentrations in patients with stage II gastric cancer was investigated in the study. Nineteen patients' plasma samples were collected before and three months post-gastrectomy, and PFAA levels were quantified using LC-MS/MS. For gradient elution of amino acids, the mobile phases (A: 3% formic acid-5% methanol-30 mM ammonium formate, B: acetonitrile) and a Hypersil C18 column (100 mm x 2.1 m, 1.9 µm) were used. The findings revealed substantial modifications in the profile of PFAA after TG. In particular, the concentrations of twenty amino acids increased significantly, including branched-chain amino acids, L-glutamate, L-alanine, L-methionine, glycine, L-cystine, and L-histidine. Conversely, L-arginine was also reduced statistically. These alterations in the PFAA profile indicate the favorable effects of TG on various physiological processes, such as enhanced immune function, improved tissue healing, and increased energy production. Investigating the effects of various surgical techniques on PFAA profiles is a promising approach for optimizing surgical procedures, improving metabolic function, increasing immunological responses, and improving overall quality of life. These findings highlight the significance of evaluating amino acid metabolism as an important part of treatment, given its potential to improve clinical outcomes and general well-being.

Keywords: Amino acids, Total gastrectomy, Gastric cancer, LC-MS/MS.

Submitted: August 6, 2024. **Accepted:** September 24, 2024.

Cite this: Akman TC, Kadioglu Y, Bayrak B, Yildirgan Mİ, Disci E. Quantification and Evaluation of Plasma-free Amino Acid Concentrations by LC-MS/MS After Total Gastrectomy. JOTCSA. 2024;11(4): 1605-22.

DOI: <https://doi.org/10.18596/jotcsa.1529042>

***Corresponding author's E-mail:** eczcagri87@gmail.com

1. INTRODUCTION

Radiation and chemotherapy are the most popular treatment options for gastric cancer. However, the disease's recurrence and high death rate following these therapies necessitated a variety of surgical resections. As a result, total and subtotal gastrectomy is frequently favored in gastric cancer (1,2).

Total gastrectomy (TG) is a surgical procedure that removes the entire stomach. As a result, the rate and amount of macronutrients such as amino acids, carbs, and lipids entering the systemic circulation vary (3,4). In addition, gastrectomy influences the release of numerous digestive enzymes (pepsin and pepsinogen) from the intestine. As a result, protein digestion and amino acid absorption are impaired.

Insufficient intake of macronutrients disrupts biological reactions and metabolic functioning, causing malabsorption, symptoms, and mortality (5).

Eliminating the negative consequences of TG will both allow long-term survival and increase the quality of life of patients. Biochemical parameters to be used in monitoring the health status of patients after TG are guided in the development of new treatment strategies. In recent studies, parameters such as amino acids, metabolites, and trace elements have been investigated in detail to monitor diseases and treatments. Thanks to these studies, molecular mechanisms and biological processes leading to complications can be clearly revealed (6).

Amino acids contribute to immune function by activating T lymphocytes, B lymphocytes, and macrophages and by producing antibodies, cytokines, and other cytotoxic substances. They also play a key role in energy production, tissue repair, and development by providing protein synthesis (7). Previous clinical studies have shown that amino acid supplements can improve the clinical profile and reduce symptoms of various diseases. It is also known that dietary supplementation of certain amino acids to malnourished people improves immune status and thus reduces mortality. Monitoring amino acid profiles in biological fluids can both predict possible organ damage and symptoms and guide the development of different treatment strategies (6,8-12).

Maintaining the balance of plasma-free amino acids (PFAAs) is critical for the continuation of biological and physiological processes in individuals. Many previous studies have shown that gastrectomy affects the fecal microbiome and metabolome profiles over time (13). As can be seen, these studies reveal the effects of the surgical procedure on biological processes. Therefore, changes in amino acid metabolism and concentrations after TG should be taken into consideration. Because changes in the PFAA profile following TG may have profound effects on the nutritional status, weight gain, and general well-being of patients.

There are only two studies in the literature investigating the effects of TG and fundectomy on plasma amino acid concentrations. These studies were conducted only on male individuals and pigs (14,15). More comprehensive studies are needed to elucidate the relationship between TG and amino acid metabolism. Changes in PFAA concentrations following TG were determined by liquid chromatography-tandem mass spectrometry (LC-MS/MS). Thus, the study aimed to contribute to the understanding of changes in plasma amino acid

profiles, metabolic processes, and their long-term effects after TG in patients with stage II gastric cancer.

2. MATERIALS AND METHODS

2.1. Study Design and Participants

Between May 2018 and May 2019, the study was conducted at the Intensive Care Unit of the Department of General Surgery at Atatürk University Research Hospital, including 19 patients with stage II gastric cancer and decided TG (9 females and 10 males, aged 37-81). The tumor histological type of the patients was moderately differentiated adenocarcinomas, and they were diagnosed with stage II stomach cancer according to the classification of malignant tumors (TNM). The study was conducted in Erzurum, Turkey. The study was approved by the Non-Interventional Clinical Trials Ethics Committee, Ataturk University, with ID: B.30.2.ATA.0.01.00/244. This study was conducted in accordance with the World Medical Association's Helsinki Declaration (2000). Prior to the surgery, patients were informed about the study, and written consent was obtained. Gastroscopy-enhanced computed tomography (CT) of the abdomen and pelvis, plain CT of the chest, and ultrasound scanning of the tumors were used for preoperative evaluation. Patient information and tumor characteristics of gastric cancer are presented in Table 1. Patients with poorly/advanced differentiated adenocarcinomas, gastric surgery, different cancer diseases other than stage II gastric cancer, or urgent surgery due to complications such as bleeding, perforation, or obstruction were excluded from the study. To ensure that diet did not affect the concentrations of amino acid in the plasma, a standard nutritional protocol was followed for 3 days before plasma samples were taken. Daily calorie and protein intakes were ensured to be ≥ 25 Kcal/kg and ≥ 1 g/kg, respectively (16). Postoperative treatment protocols were similar for all patients.

Table 1: Demographic and clinical variables of patients.

Patient No	Gender/ Age (years)	Tumor Size (cm)	Depth of Invasion	Lymph Node Metastasis
1	F/59	<5	T2	N0
2	F/37	3.5×2.5×2	T3	N2
3	M/47	2.5×2.5×1.5	T3	N1
4	M/54	2.5	T3	N2
5	F/62	2.5×2×1	T3	N1
6	M/54	2×1.5	T3	N0
7	M/81	3×2×1.5	T3	N2
8	F/53	3	T3	N2
9	M/52	<3	T3	N2
10	F/65	2.5×2.5×1	T4	N2
11	M/75	6×5×2	T3	N2
12	M/51	6.5×5.5×1.5	T3	N0
13	F/47	4×1.5×0.7	T4	N0
14	F/65	3×2×1.5	T3	N0
15	M/54	2.5×2×1.5	T4	N2
16	M/58	4×2.5	T3	N2
17	F/48	4×1.5×1	T4	N0
18	F/64	<5	T2	N0
19	M/71	<5	T2	N0

2.2. LC-MS/MS Analysis of Plasma Amino Acid Levels

The concentrations of amino acids in plasma were determined by the validated LC-MS/MS method developed using the JASEM Amino Acids LC-MS/MS Analysis Kit (12). Following an overnight fasting period, blood samples were collected from the antecubital vein of all participants into blood collection tubes containing ethylenediaminetetraacetic acid (EDTA) as an anticoagulant, both before the operation and 3 months after the operation. To obtain plasma, the tubes were centrifuged at 3500 rpm for 10 minutes. Plasma samples were stored at -80°C until analysis.

After the samples were thawed at room temperature, they were vortexed for 30 seconds. 50 µL of plasma sample from both the before-surgery (BS) and after-surgery (AS) groups were placed in separate Eppendorf tubes. Subsequently, 50 µL of internal standard was added to each tube, followed by vortexing for 10 seconds.

Then, 700 µL of an amino acid solvent solution consisting of Mobile Phase A and Mobile Phase B in a

1:4 volume ratio was added to each tube. The samples were vortexed for 5 seconds and then centrifuged at 4000 rpm for five minutes at 4°C. The supernatant was filtered with 0.45 µm filters. The clear supernatant was decanted into an HPLC vial prior to injection.

The LC-MS/MS system (Agilent 6460 Triple Quadropol, USA) was utilized to quantify the samples. Amino acids were separated using a Hypersil C18 column (100 mm x 2.1 mm, 1.9 µm). The mobile phase (A: Formic Acid-Methanol-30 mM Ammonium Formate (3:5:92; v:v:v), B: Acetonitrile) was passing through the system in gradient elution mode and at a rate of 0.4 mL/min. The analysis time was 22 minutes. Chromatographic conditions and mass spectrometry settings, which enabled the separation and identification of amino acids, are provided in Tables 2 and 3, respectively.

The regression equations, correlation coefficients, linear ranges, and LOQ of the LC-MS/MS method are given in Table 4.

Table 2: Solvent Composition Schedule during the gradient elution for LC-MS/MS.

Flow: 0.7 mL/min	Change Solvent Composition	
Time	A	B
1.00 min	22.00 %	78.00 %
4.00 min	70.00 %	30.00 %
5.00 min	70.00 %	30.00 %
5.10 min	22.00 %	78.00 %
9.00 min	22.00 %	78.00 %

*A: Formic Acid - Methanol-30 mM Ammonium Formate (3:5:92; v:v:v), B: Acetonitrile

Table 3: Mass conditions.

Parameters	Value (+)	Value(-)
Gas Temp (°C)	150.00	150.00
Gas Flow (L/min)	11.00	11.00
Nebulizer (psi)	40.00	40.00
Sheath Gas Heater	375.00	375.00
Sheath Gas Flow	11.00	11.00
Capillary (V)	2000.00	0.00
VCharging	0.00	0.00
Injection Volume (µL)	1.00	
Ion Source	AJS ESI	
Ion Mode	Positive	

2.3. Metabolic Pathway Analysis

The metabolic pathways affected by the changing amino acid profile after TG were determined with MetaboAnalyst 4.0 Software. The number of amino acids involved in the affected metabolic pathways was also determined.

2.4. Data Analysis

The statistical analyses were performed using SPSS Statistics (IBM v.20, Chicago, IL, USA). Initially, the factor analysis was conducted on the cluster of data for normalization. The Non-paired Student's t-test

was used for normally distributed data, and the non-parametric Mann-Whitney U-test was also used for non-normally distributed data. The statistical significance was set at $p < 0.05$. This statistical test allowed for the comparison of mean values between the two groups to determine if there were significant differences in amino acid levels before and after the surgical procedure.

For visualizing amino acids with significant differences among the groups, boxplot graphs were created using the ggpubr package in RStudio (v.

1.3.1093). The correlation graph was generated between plasma concentrations of amino acids over using the GGally package. The Spearman correlation time following TG (12,17). matrix method was used to reveal the correlation

Table 4: The regression equations, correlation coefficients, linear range, and LOQ of the LC-MS/MS method.

Amino Acids	Internal standard	Regression equations	R ²	Linear range (ng/mL)	LOQ (ng/mL)
1-methyl-L-histidine	-	y= 0.009171x - 0.017750	0.99937	1.0-350.0	1.0
3-amino isobutyric acid	-	y= 0.003340x + 0.001234	0.99732	0.1-110.0	0.1
3-methyl-L-histidine	3-methyl-L-histidine IS	y= 0.078033x - 0.410524	0.99922	5.0-350.0	5.0
Beta-alanine	-	y= 0.003194x - 0.004878	0.99605	1.5-50.0	1.5
Ethanolamine	-	y= 0.812943x - 5.866369	0.99768	5.0-270.0	5.0
Gamma-aminobutyric acid	-	y= 0.015012x + 0.001904	0.99956	0.01-110.0	0.01
Glycine	Glycine IS	y= 0.001123x - 0.040868	0.99847	50.0-1700.0	50.0
L-2-aminobutyric acid	-	y= 0.230656x - 0.502684	0.99567	2.5-80.0	2.5
L-alanine	L-alanine IS	y= 0.002418x - 0.067955	0.99813	25.0-1400.0	25.0
L-anserine	-	y= 0.008411x - 0.005699	0.99605	0.01-25.0	0.01
L-arginine	L-arginine IS	y= 0.010397x - 0.050441	0.99930	1.0-320.0	1.0
L-asparagine	L-asparagine IS	y= 0.013342x - 0.037875	0.99728	1.0-200.0	1.0
L-aspartic acid	L-aspartic acid IS	y= 0.023892x - 0.085002	0.99782	5.0-160.0	5.0
L-citrulline	L-citrulline IS	y= 0.013412x + 0.004663	0.99845	0.1-80.0	0.1
L-cystathionine	-	y= 0.012178x + 0.001751	0.99878	0.01-24.0	0.01
L-cystine	DL-Cystine IS	y= 0.008333x - 0.014697	0.99949	1.0-220.0	1.0
L-glutamic acid	L-Glutamic acid IS	y= 0.014644x + 0.171485	0.99881	20.0-1500.0	20.0
L-glutamine	L-glutamine IS	y= 0.004897x + 0.012509	0.99954	1.0-1400.0	1.0
L-histidine	-	y= 0.266900x - 2.381075	0.99968	1.0-1200.0	1.0
L-isoleucine	-	y= 0.001207x - 0.004704	0.99822	5.0-1000.0	5.0
L-leucine	L-leucine IS	y= 6.330595E-004x - 0.005242	0.99783	10.0-440.0	10.0
L-lysine	L-lysine IS	y= 0.018868x - 0.083803	0.99875	5.0-420.0	5.0
L-methionine	L-methionine IS	y= 0.021931x - 0.041218	0.99855	2.5-90.0	2.5
L-norvaline	-	y= 0.082804x + 0.030635	0.99684	0.05-22.0	0.05
L-ornithine	L-ornithine IS	y= 0.016225x - 0.077035	0.99804	2.5-340.0	2.5
L-phenylalanine	L-phenylalanine IS	y= 0.015304x - 0.148367	0.99808	10.0-480.0	10.0
L-proline	L-proline IS	y= 0.005904x - 0.111633	0.99804	10.0-900.0	10.0
L-serine	L-serine IS	y= 0.013875x - 0.225179	0.99866	10.0-900.0	10.0
L-threonine	L-threonine IS	y= 0.010328x + 0.016741	0.99787	1.0-500.0	1.0
L-tryptophan	L-tryptophan IS	y= 0.024814x - 0.086062	0.99747	2.5-150.0	2.5
L-tyrosine	L-tyrosine IS	y= 0.009429x - 0.053190	0.99464	5.0-260.0	5.0
L-valine	DL-Valine IS	y= 0.003244x - 0.031811	0.99781	5.0-750.0	5.0
Taurine	-	y= 1.04617E-004x - 6.482529E-005	0.99873	1.0-440.0	1.0
Trans-4-hydroxy L-proline	-	y= 0.001151x - 0.006470	0.98052	5.0-140.0	5.0

LR: Linear regression equations, R²: Correlation coefficient

3. RESULTS

After TG, patients were put on a diet according to the postoperative treatment protocols. There was no significant difference between the patients' BMI values before and 3 months after TG (25.72 ± 0.69 vs. 24.87 ± 2.47 , $p = 0.059$). Plasma-free amino acid concentrations of the patients were measured. Amino acids whose concentrations changed significantly were identified. The metabolic pathways in which these amino acids take part were determined.

3.1. LC-MS/MS Analyses Results: Alterations in Plasma Amino Acid Concentrations After Gastrectomy

To evaluate the impact of TG on the amino acid profile, a validated LC-MS/MS method was employed

(12). This method was chosen due to its high precision, certainty, and accuracy, enabling the generation of reliable qualitative and quantitative data. Blood samples were collected from 19 individuals who participated in the study, both prior to the operation and three months after the operation. The LC-MS/MS analysis was conducted to measure the levels of 34 specific PFAAs, allowing for a comprehensive assessment of any potential changes in the amino acid profiles resulting from the surgical procedure. The chromatograms and mass spectrums of the BS and AS groups obtained from LC-MS/MS analysis are given in Figure 1a-d. Table 4 shows the linear regression equations and correlation coefficients for PFAAs. The obtained data were analyzed using linear regression equations. The concentrations of PFAA determined by LC-MS/MS are expressed as mean \pm standard deviation in Table 5.

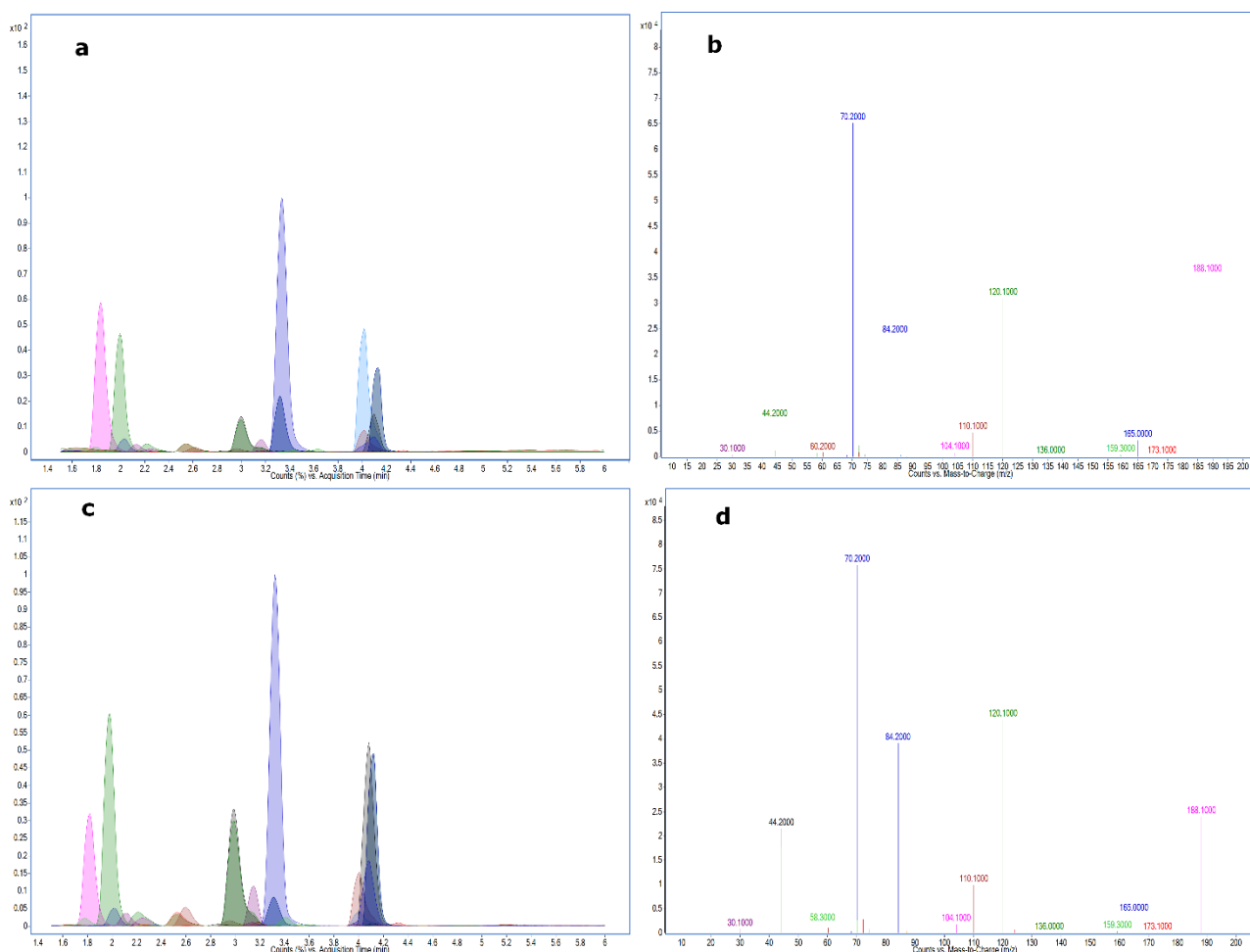


Figure 1: Typical chromatograms and spectrums obtained from LC-MS/MS: a) The chromatogram of the BS group, b) The mass spectrum of the BS group, c) The chromatogram of the AS group, b) The mass spectrum of the AS group.

Table 5: PFAA concentrations (ng/mL) of stage II gastric cancer patients before and after TG (n=19).

Amino acids	Group BS Mean±SD (ng/mL)	Group AS Mean±SD (ng/mL)	p-value*
1-methyl L-histidine	6.67 ±0.94	8.81 ±0.86	0.1502
3-aminoisobutyric acid	2.69±0.81	4.13±0.76	0.0052*
3-methyl L-histidine	9.40±0,24	10.54±0,19	0.0033*
Beta-alanine	3.98±0.40	4.69±0.61	0.0880
Ethanolamine	73.49±6.31	93.00±4.72	0.1685
Gamma-aminobutyric acid	0.14±0.26	0.34±0.19	0.0162*
Glycine	339.01±31.61	512.99±28.73	0.0021*
L-2-aminobutyric acid	32.66±3.76	33.65±1.28	0.8394
L-alanine	547.53±16.76	731.16±21.39	0.0058*
L-anserine	1.03±0,01	0.99±0,03	0.6848
L-arginine	155.11±0,26	93.32±0,58	4.1e-07*
L-asparagine	54.55±2.43	67.65±2.62	0.0063*
L-aspartic acid	39.80±1.93	31.59±2.46	0.1139
L-citrulline	52.98±9.42	41.41±4.76	0.3237
L-cystathionine	0.18±0.03	0.32±0.01	0.0196*
L-cystine	62.76±5.54	76.43±6.31	2.2e-06*
L-glutamic acid	477.70±34.43	1360.88±76.81	0.0037*
L-glutamine	818.56±62.43	683.19±38.16	0.5477
L-histidine	168.65±18.43	210.54±14.36	0.0169*
L-isoleucine	94.82±3.78	136.79±5.14	0.0001*
L-leucine	157.73±9.74	190.88±6.87	0.0302*
L-lysine	231.25±18.29	279.55 ±23.48	0.0135*
L-methionine	20.23±1.93	30.86±1.58	6.21e-07*
L-norvaline	0.56±0.03	0.42±0.02	0.0959
L-ornithine	110.07±19.15	175.97±11.74	0.0009*
L-phenylalanine	126.16±9.26	137.20±10.71	0.3582
L-proline	290.04±35.65	320.32±27.85	0.3512
L-serine	204.06±17.36	211.88±20.3	0.6096
L-threonine	163.58±14.16	199.33±13.11	0.0145*
L-tryptophan	65.28±1.78	66.24±2.41	0.7537
L-tyrosine	75.33±7.43	91.96±8.63	0.0065*
L-valine	202.98±19.59	255.64±24.51	0.0007*
Taurine	332.50±12.37	329.20±17.15	0.9199
Trans-4-hydroxy L-proline	13.30±1.72	16.15±2.09	0.0058*

*: $p < 0.05$; BS: Before surgery, AS: After surgery

3.2. Non-paired Student's t-test Analysis

Through the utilization of the Non-paired Student's *t*-test analysis, significant differences were identified between the BS and AS groups in terms of specific amino acids. The analysis revealed that a total of 20 amino acids exhibited statistically significant changes ($p < 0.05$) in their plasma profiles across the two groups. Table 5 highlights the amino acids that exhibit notable variations in their concentrations subsequent to the surgical procedure. These findings suggest that the operation had a discernible impact on the levels of these specific amino acids, potentially

reflecting underlying metabolic shifts or physiological adaptations associated with the surgery.

After a period of 3 months following TG, no statistically significant differences were observed in the plasma concentrations of L-tryptophan, taurine, L-phenylalanine, L-norvaline, ethanolamine, Beta-alanine, L-2-aminobutyric acid, L-aspartic acid, L-serine, and L-proline. These specific amino acids exhibited no marked alterations in their plasma levels, suggesting that their concentrations remained relatively stable during the postoperative period.

After TG, a notable alteration in the plasma concentrations of L-threonine, L-leucine, L-isoleucine, and L-valine was observed statistically.

Following gastrectomy, the plasma levels of these specific amino acids exhibited a distinct increase (Figure 2a-d).

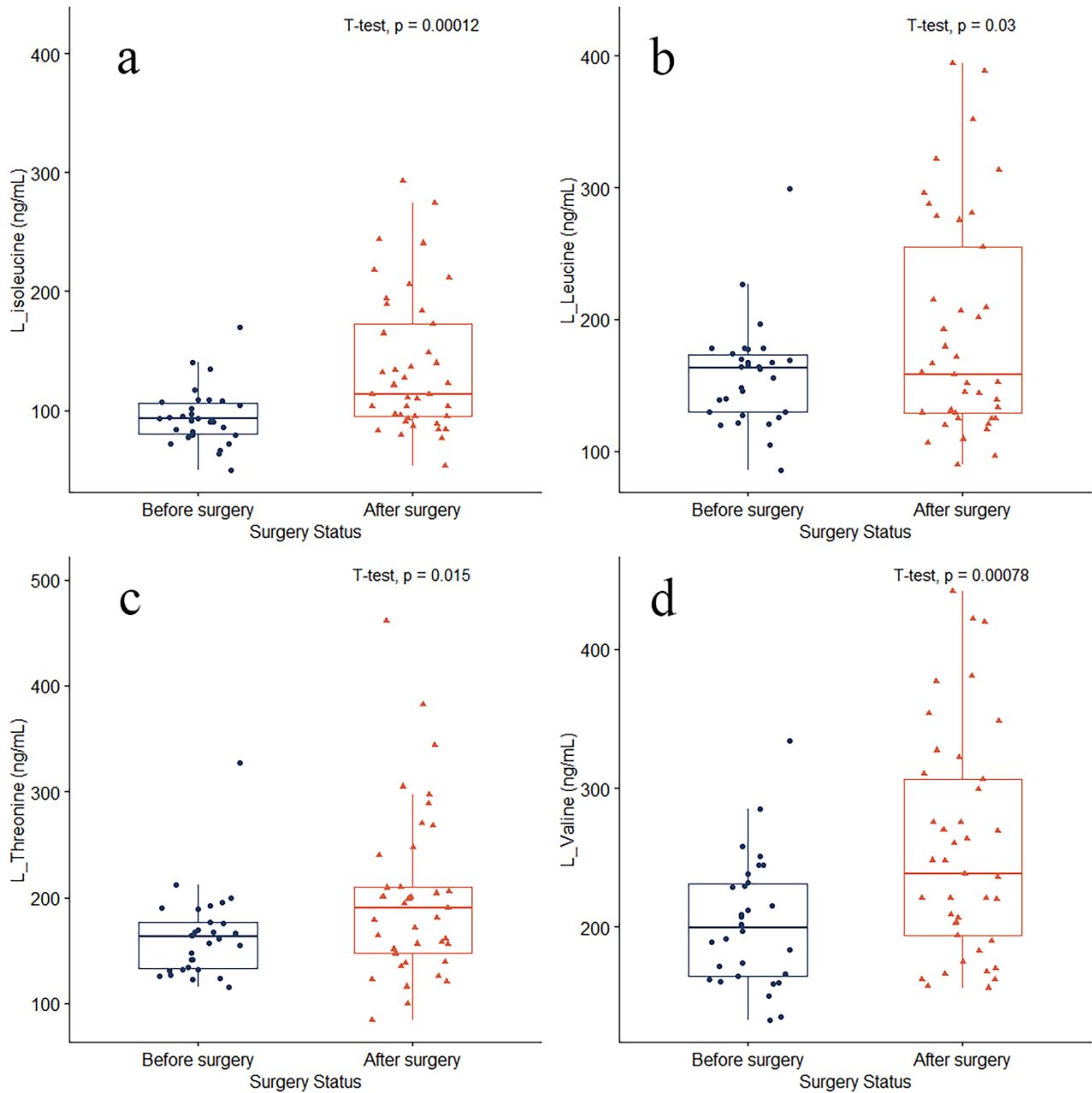


Figure 2: Box plots graphs showing differences in amino acid levels: a) L-isoleucine, b) L-leucine, c) L-threonine, d) L-valine.

After a period of 3 months following surgery, significant changes in plasma levels of L-ornithine, Trans-4-hydroxy L-proline, and L-methionine were observed, with a marked increase in their

concentrations (Figure 3a-d). Conversely, the plasma level of L-arginine exhibited a remarkable decrease during the same timeframe (Figure 3d and Figure 4a-d).

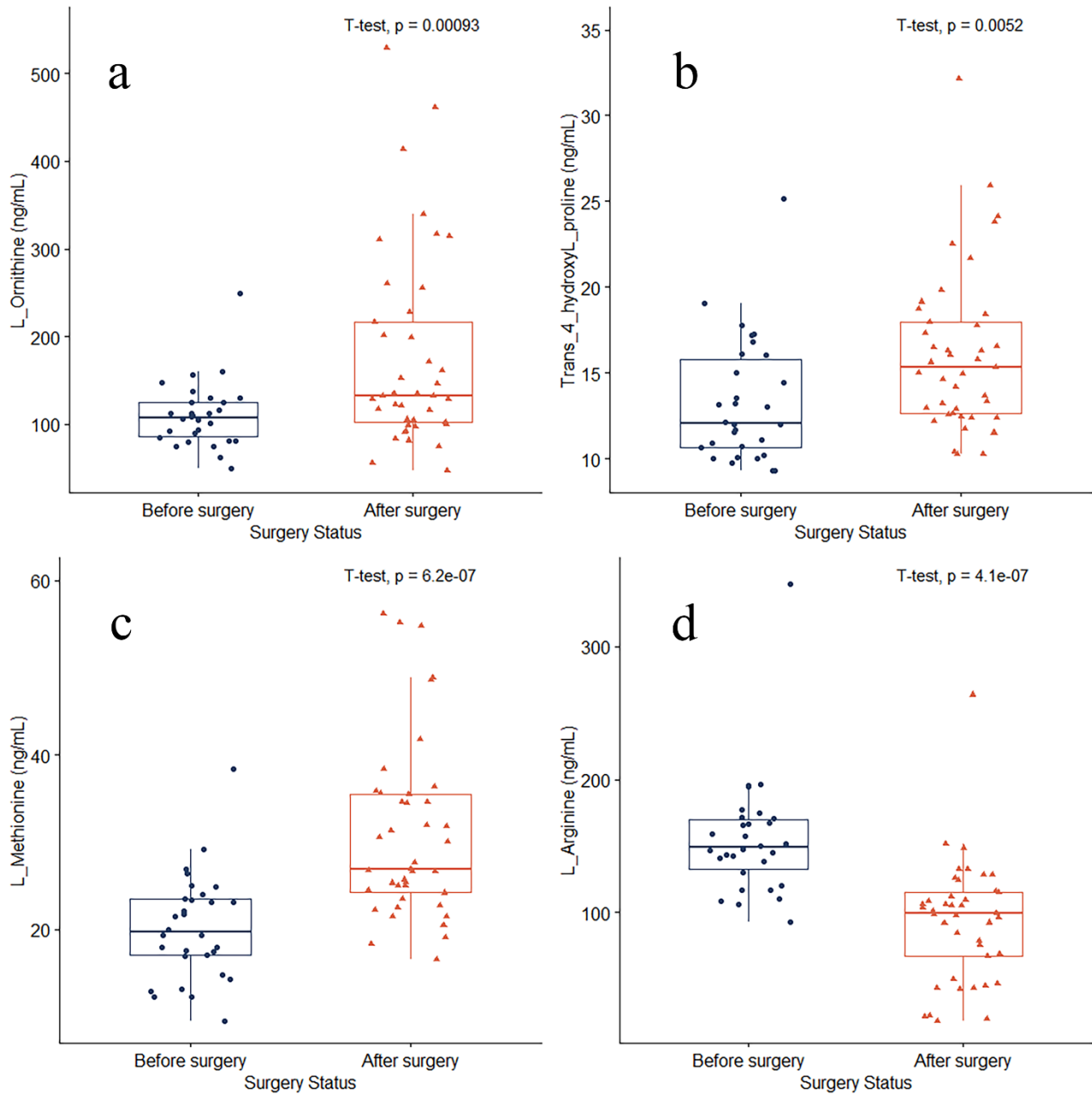


Figure 3: Box plots graphs showing differences in amino acid levels: a) L-ornithine, b) Trans-4-hydroxy L-proline, c) L-methionine, and d) L-arginine.

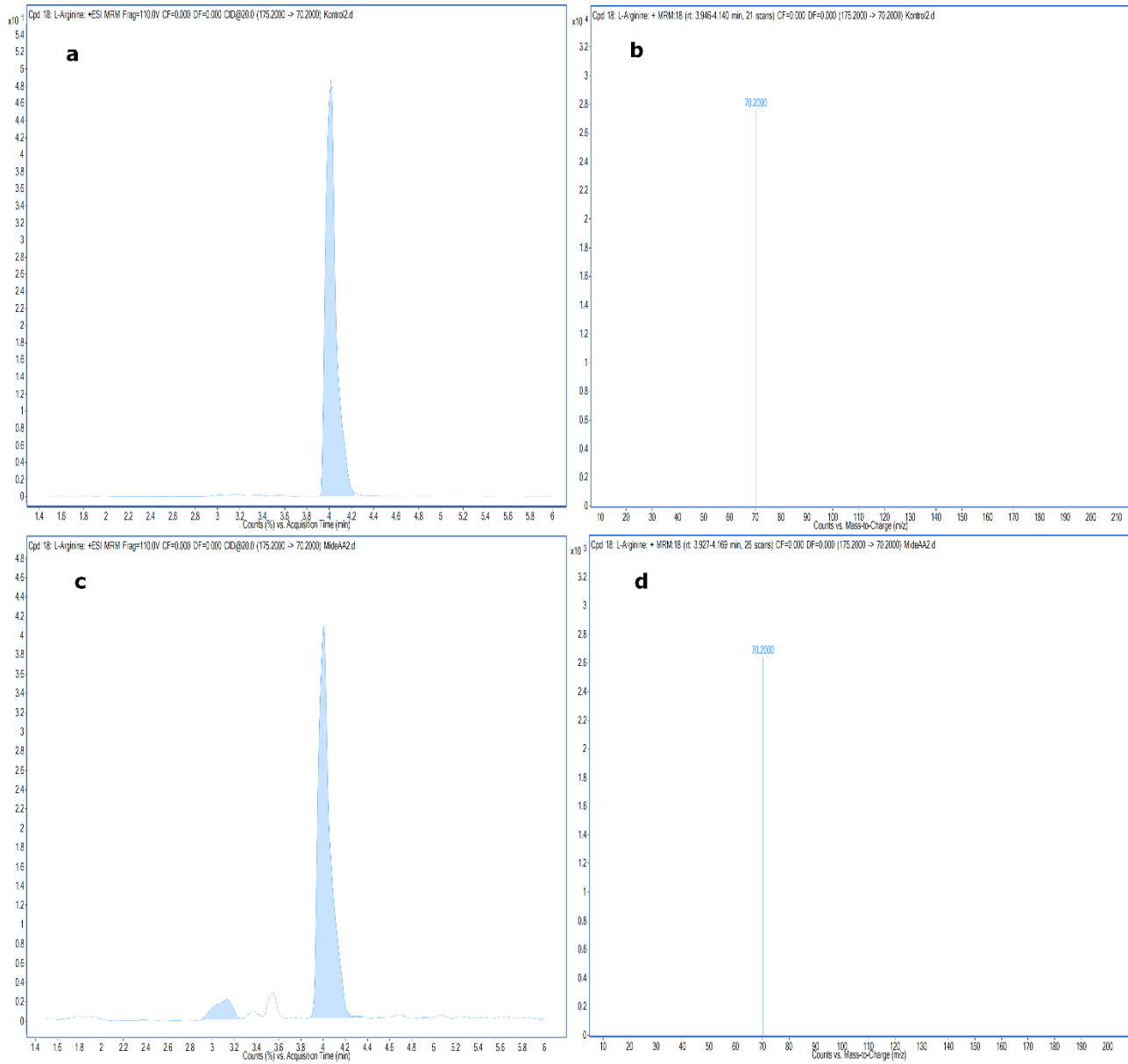


Figure 4: Typical chromatograms and product ion mass spectrums for L-arginine: a) The chromatogram BS of the group, b) the mass spectrum of BS the group, c) the chromatogram of AS the group, and d) the mass spectrum of AS group.

A comparative analysis of plasma amino acid levels between the BS and AS groups revealed significant differences. According to the *t*-test analysis results, plasma concentrations of L-asparagine, L-alanine,

gamma-aminobutyric acid (4-aminobutanoate), and L-glutamic acid (L-glutamate) exhibited a noteworthy increase in the AS group compared to the BS group (Figure 5a-d).

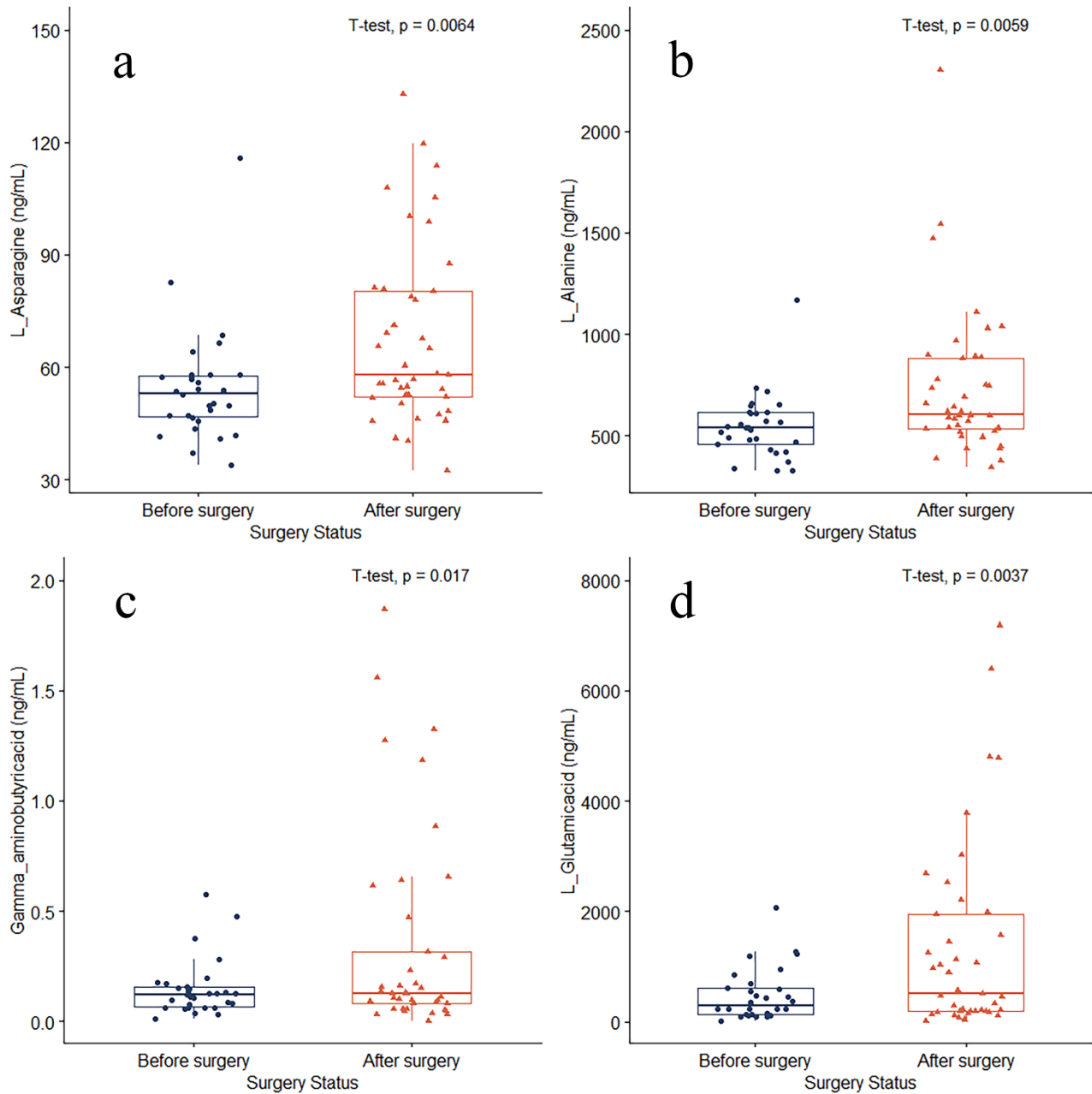


Figure 5: Box plots graphs showing differences in amino acid levels a) L-asparagine, b) L-alanine, c) gamma-aminobutyric acid, d) L-glutamic acid, e) L-histidine, f) 3-methyl-L-histidine, g) L-tyrosine, and h) 3-aminoisobutyric acid.

Among the amino acids analyzed, four demonstrated statistically significant differences in plasma concentrations following gastrectomy. These amino acids included L-histidine, 3-methyl-L-histidine, L-

tyrosine, and 3-aminoisobutyric acid. Notably, the plasma levels of these amino acids exhibited a significant increase after a three-month period following the surgical procedure (Figure 6a-d).

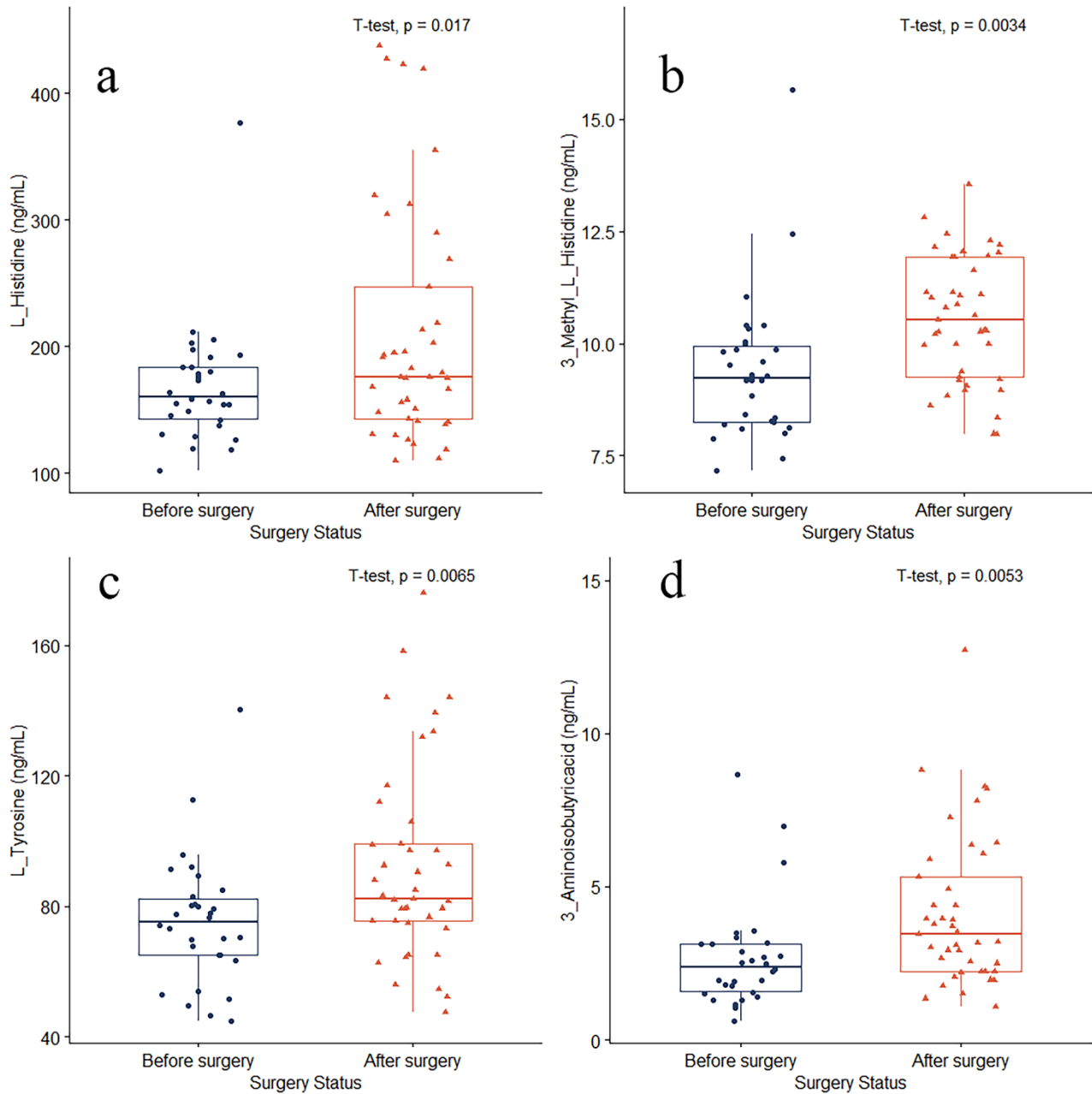


Figure 6: Box plots graphs showing differences in amino acid levels a) L-histidine, b) 3-methyl-L-histidine, c) L-tyrosine, and d) 3-aminoisobutyric acid.

Furthermore, significant changes were observed in plasma concentrations of glycine, L-cystathionine, L-cystine, and L-lysine following TG, particularly after a three-month duration. Notably, the plasma levels

of these amino acids demonstrated a distinct increase, highlighting their altered metabolic profiles in response to the surgical intervention (Figure 7).

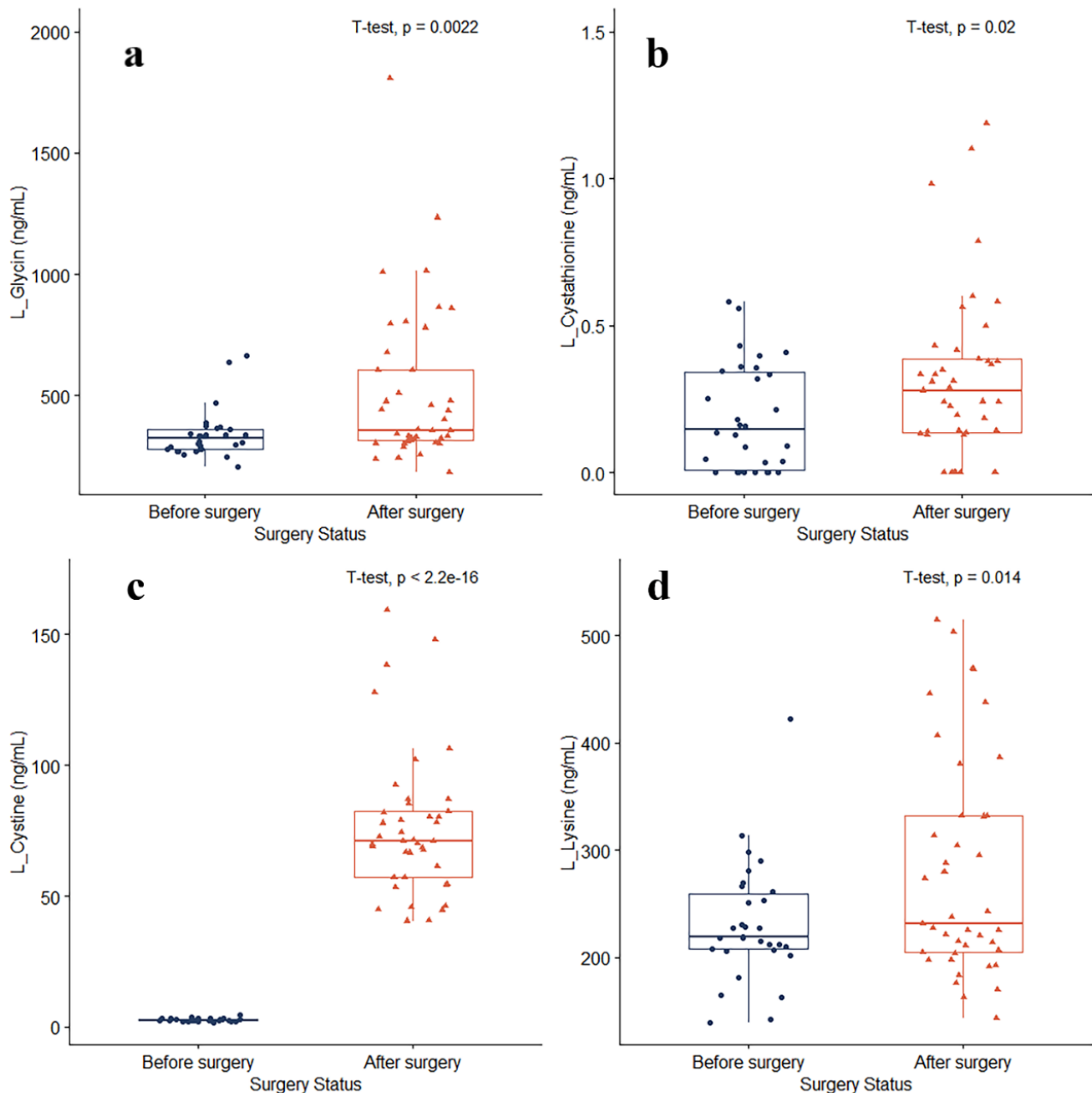


Figure 7: Box plots graphs showing differences in amino acid levels: a) glycine, b) L-cystathionine, c) L-cystine, and d) L-lysine.

3.3. PCA (Principal Component Analysis)

PCA was performed on 34 amino acid variables. Eight principal components with eigenvalues of 1 or above were extracted. The eight principal components explained 78.0% of the total variance. Table 6 shows the eigenvalues and variance ratios of the eight principal components. The first principal component had the largest eigenvalue (15.558) and explained 40.9% of the total variance. The second principal component had the second largest eigenvalue (3.492) and explained 9.9% of the total variance. The third principal component had the third largest

eigenvalue (2.926) and explained 7.7% of the total variance. The remaining five principal components explained 19.5% of the total variance.

Table 7 shows the results of the Kaiser-Meyer-Olkin (KMO) test and the Bartlett test. The Kaiser-Meyer-Olkin Measure and Bartlett's test of sphericity were used to assess sampling adequacy. Kaiser-Meyer-Olkin Measure was 0.748, and Bartlett's test of sphericity was 306 (df 703; $p < 0.001$), suggesting acceptable sample adequacy.

Table 6: PCA results (Total Variance Explained).

Component	Total Variance Explained								
	Initial Eigenvalues			Extraction Sums of Squared Loadings			Rotation Sums of Squared Loadings		
	Total	% of Variance	Cumulative %	Total	% of Variance	Cumulative %	Total	% of Variance	Cumulative %
1	15.558	40.943	40.943	15.558	40.943	40.943	14.784	38.905	38.905
2	3.492	9.189	50.131	3.492	9.189	50.131	2.785	7.330	46.235
3	2.926	7.701	57.832	2.926	7.701	57.832	2.343	6.166	52.401
4	2.440	6.421	64.253	2.440	6.421	64.253	2.040	5.369	57.770
5	1.604	4.221	68.474	1.604	4.221	68.474	2.037	5.360	63.130
6	1.300	3.420	71.894	1.300	3.420	71.894	2.037	5.359	68.490
7	1.227	3.228	75.123	1.227	3.228	75.123	1.868	4.916	73.406
8	1.100	2.894	78.017	1.100	2.894	78.017	1.752	4.611	78.017
9	0.965	2.540	80.557						
10	0.942	2.479	83.036						
11	0.808	2.127	85.163						
12	0.727	1.912	87.075						
13	0.653	1.718	88.793						
14	0.516	1.358	90.151						
15	0.478	1.259	91.410						
16	0.434	1.142	92.552						
17	0.393	1.034	93.586						
18	0.329	0.867	94.453						
19	0.314	0.827	95.280						
20	0.304	0.800	96.080						
21	0.246	0.646	96.727						
22	0.217	0.570	97.297						
23	0.195	0.513	97.810						
24	0.151	0.396	98.207						
25	0.131	0.345	98.551						
26	0.106	0.278	98.829						
27	0.085	0.225	99.054						
28	0.065	0.170	99.224						
29	0.059	0.156	99.380						
30	0.047	0.124	99.505						
31	0.045	0.117	99.622						
32	0.037	0.098	99.720						
33	0.031	0.081	99.801						
34	0.029	0.075	99.876						
35	0.020	0.053	99.930						
36	0.013	0.034	99.964						
37	0.008	0.021	99.985						
38	0.006	0.015	100.000						

Extraction Method: Principal Component Analysis.

Table 7: The Kaiser–Meyer–Olkin and Bartlett test results of PCA analysis.

KMO and Bartlett's Test		
Kaiser-Meyer-Olkin Measure of Sampling Adequacy.		0.748
Bartlett's Test of Sphericity	Approx. Chi-Square	3060.971
	df	703
	Sig.	0.000

3.4. Correlation Matrix

Utilizing correlation matrix (R, Spearman) analysis, the interrelationship among plasma concentrations of amino acids over time following TG was investigated. Notably, a strong positive correlation coefficient exceeding 0.8 was observed between the branched-chain amino acids (BCAAs) L-leucine, L-isoleucine, and L-valine. These amino acids demonstrated a concurrent increase in their plasma levels after surgery. Additionally, plasma L-histidine levels

exhibited a similar pattern of increase alongside L-ornithine, L-leucine, and L-isoleucine. Conversely, a correlation coefficient greater than 0.8 was found between L-tyrosine levels and L-lysine, L-methionine, L-valine, and L-leucine. Furthermore, Spearman correlation matrix analysis revealed a strong positive correlation among plasma levels of L-ornithine, glycine, L-phenylalanine, and ethanolamine (Figure 8).

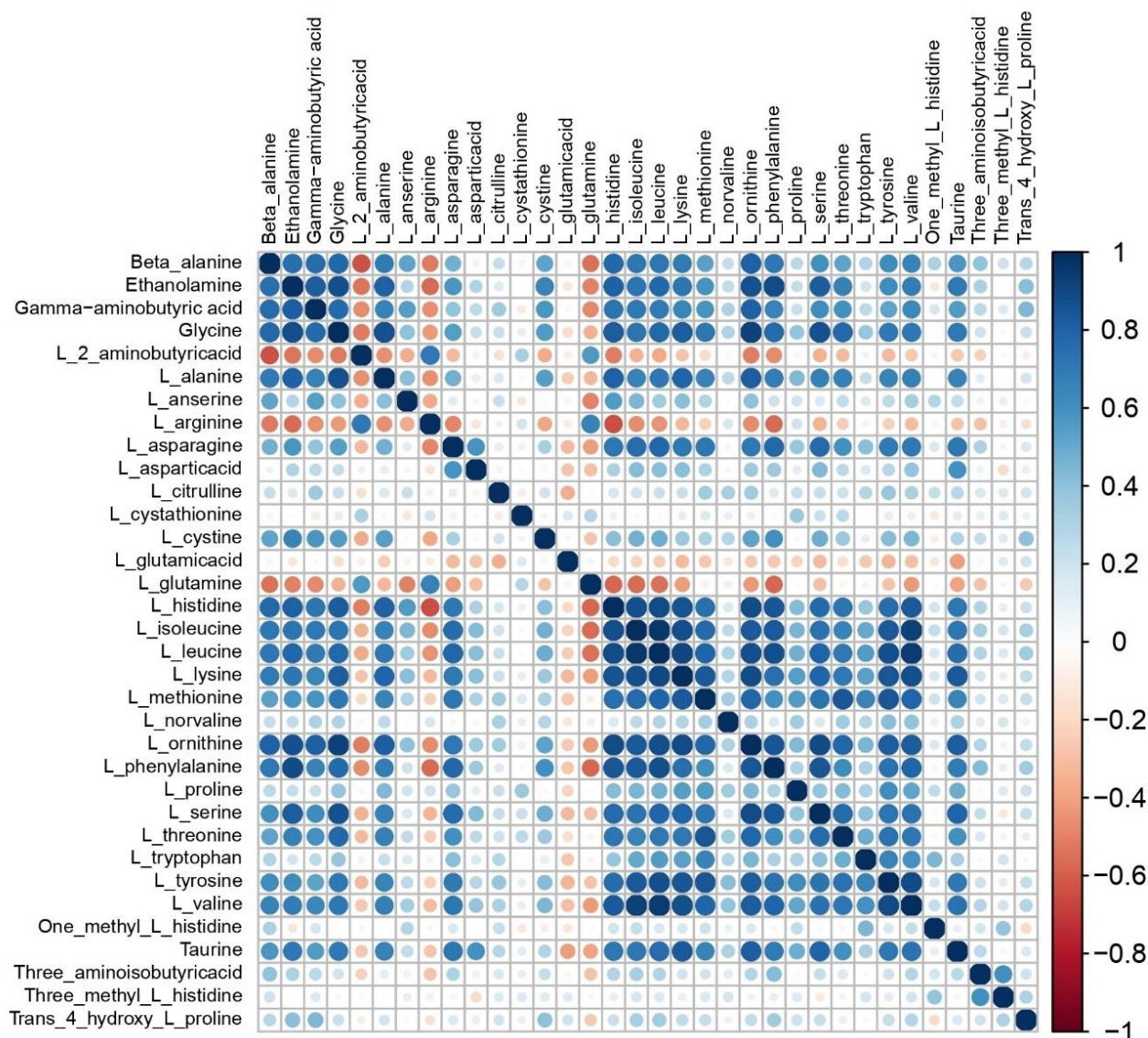


Figure 8: Spearman correlation matrix of plasma free amino acids levels. Positive and negative correlations are indicated by blue and red colors, respectively.

3.5. Metabolic Pathway Analysis

The metabolic pathways that the metabolic changes could impact were identified through pathway analysis. Using the MetaboAnalyst 4.0 software, the 20 amino acids listed in Table 8 were analyzed in detail to determine their metabolic pathways. Figure 9 displays the relevant pathways and their respective effect values. According to the data obtained from MetaboAnalyst 4.0, it was observed that 25 different metabolic pathways may be affected due to the significant difference observed in 20 amino acids. Amino acids that were significantly altered, involved in the pathways of which have $-\log p$ values higher

than 2 were discussed below (Significantly changed amino acids / total metabolites in an individual pathway): 4/8 valine, leucine, and isoleucine biosynthesis, 5/36 arginine and proline metabolism, 4/28 alanine, aspartate and glutamate metabolism, 3/14 arginine biosynthesis, 3/16 histidine metabolism, 3/28 glutathione metabolism, 3/33 glycine, serine and threonine metabolism, 3/33 cysteine and methionine metabolism, 3/40 valine, leucine and isoleucine degradation, 2/15 butanoate metabolism, 1/4 phenylalanine, tyrosine and tryptophan biosynthesis.

Table 8: Metabolic pathway analysis of amino acids whose concentration changed significantly after TG.

Pathway Name	Match Status*	<i>p</i>	$-\log(p)$
Valine, leucine, and isoleucine biosynthesis	4/8	1.0302E-6	5.9871
Arginine and proline metabolism	5/36	4.3297E-5	4.3635
Alanine, aspartate and glutamate metabolism	4/28	2.5837E-4	3.5878
Arginine biosynthesis	3/14	4.9883E-4	3.302
Histidine metabolism	3/16	7.5577E-4	3.1216
Glutathione metabolism	3/28	0.004033	2.3944
Glycine, serine and threonine metabolism	3/33	0.0064644	2.1895
Cysteine and methionine metabolism	3/33	0.0064644	2.1895
Valine, leucine and isoleucine degradation	3/40	0.011095	1.9549
Butanoate metabolism	2/15	0.013189	1.8798
Phenylalanine, tyrosine, and tryptophan biosynthesis	1/4	0.047432	1.3239

* Significantly changed amino acids / total metabolites in an individual pathway.

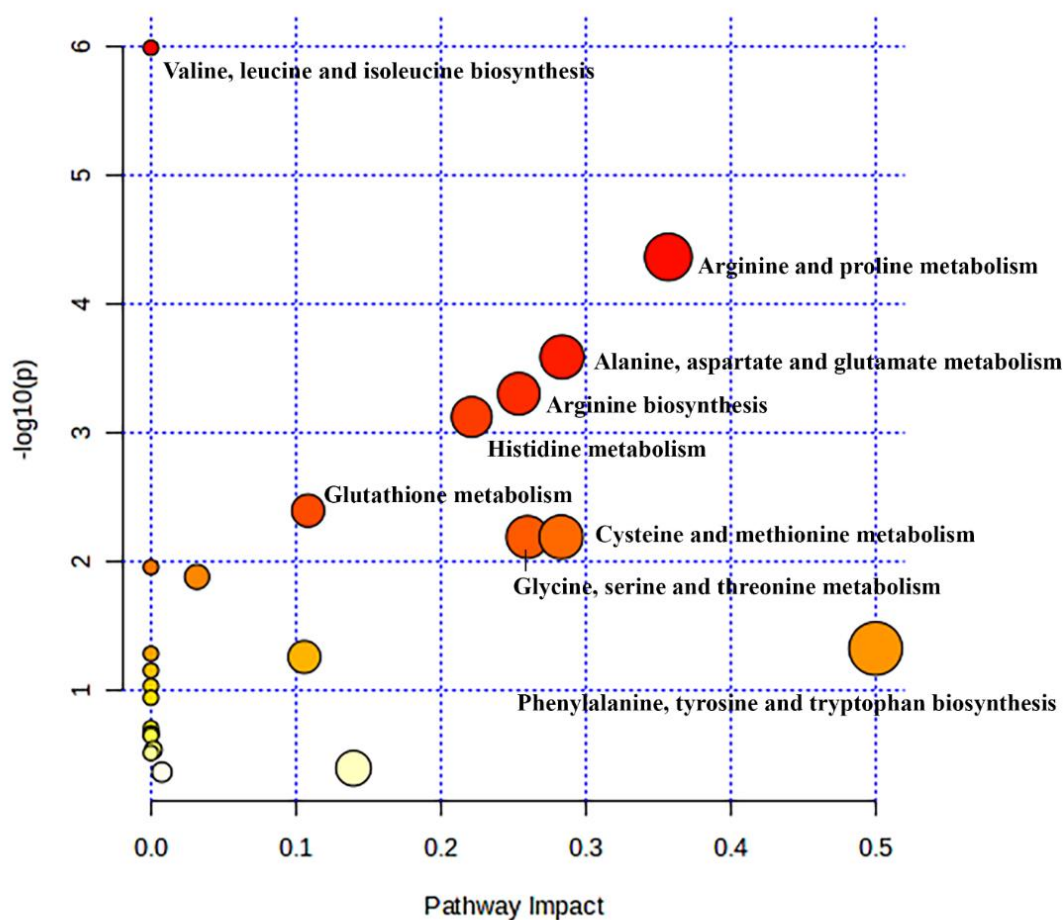


Figure 9: Impact analysis for pathways created by MetaboAnalyst online: main pathways altered in the BS group vs the AS group.

4. DISCUSSION

Understanding the interaction between amino acids and molecular pathways may be useful for optimizing pharmaceutical and surgical treatment methods and reducing mortality (18). The study provides important insights into the changes in amino acid profiles in patients with stage II gastric cancer after TG. The study suggests that negative symptoms (overall morbidity, \geq grade 3 and local complications, intraabdominal infection, intestinal obstruction, abnormal food passage, disturbed nutrition intake,

compromised digestion and absorption processes, and deficiencies in essential micronutrients) can alter PFAA levels in 3 months post-gastrectomy.

Understanding the specific alterations in PFAA profiles is crucial for several reasons. First, it can shed light on the underlying mechanisms responsible for postoperative nutritional deficiencies and metabolic changes, enabling the development of targeted interventions to mitigate these issues. Second, it may help identify potential biomarkers for

assessing the nutritional status and prognosis of gastric cancer patients postoperatively.

The results of the PCA analysis suggest that the eight principal components can be used to represent the 34 amino acid variables. The first principal component is likely to be related to the overall hydrophobicity of the amino acids. In contrast, the second principal component is expected to be associated with the overall polarity of the amino acids. The third principal component is likely to be related to the overall charge of the amino acids. The remaining five principal components are likely to be related to other properties of the amino acids. The PCA analysis provides a way to reduce the dimensionality of the 34 amino acid variables to eight principal components. This can be useful for further analysis of the data.

The study revealed a significant increase in plasma concentrations of L-leucine ($p = 0.0302$), L-isoleucine ($p = 0.0001$), and L-valine ($p = 0.0007$) after gastrectomy. In contrast to these results, Tatar et al. (15) did not observe a significant difference in plasma levels of L-leucine, L-isoleucine, and L-valine one year after TG in men ($p > 0.05$). Another study revealed that long-term fundectomy statistically reduced plasma leucine and valine concentrations in pigs (14). Accordingly, it is seen that BCAAs concentrations, which increase due to the impaired function of the gastric-hypothalamic-pituitary axis in the first periods after TG, can decrease and reach normal levels within a year. It can be thought that, unlike TG, fundectomy may further reduce the plasma concentrations of these amino acids in the long term. The increase in BCAAs concentrations in the three months after TG may be a sign of pathology due to the increase in tissue repair in the surgical area, muscle catabolism, and prevention of trauma-induced cachexia (12,19,20). Additionally, the correlation matrix analysis found correlation values larger than 0.8 (R, Spearman) for leucine, isoleucine, and valine (Figure 8). The analysis showed that the plasma concentration of BCAA increased together for 3 months following TG. These findings suggested that the TG increases BCAA breakdown in muscles by affecting BCAA metabolism and highlight the need for clinical studies to determine whether BCAA supplementation can prevent organ damage in patients after TG.

Glutathione (GSH), synthesized using cysteine, glutamate, and glycine, is vital for activating T-lymphocytes and leukocytes and producing cytokines. Thereby it facilitates robust immune responses for the body in the face of immunological challenges. Maintaining adequate GSH concentrations is crucial for the immune system, less weight loss, regulation of gastrointestinal hormones, and inflammation (21,22). In this study, plasma concentrations of L-glutamic acid (glutamate) ($p = 0.0037$), glycine ($p = 0.0021$), and L-cystine ($p = 2.2 \times 10^{-6}$) increased significantly, while the decrease in L-glutamine level was not statistically significant. (Table 5) In a previous study in men, TG did not considerably alter L-glutamic acid, glycine, L-

cystine, and L-glutamine plasma concentrations (15).

In contrast to the results, prolonged fundectomy decreased both glycine and glutamine concentrations (14). On the other hand, long-term fundectomy increased glutamate and cystine concentrations, which is parallel to the study. According to these results, it is estimated that the release of L-glutamate, glycine, and L-cystine from the gastric mucosa increases to reduce weight loss and inflammation in the first 3 months of TG. It can be thought that L-glutamine is also consumed for glutamate synthesis. In 1 year, the concentrations of these amino acids may have reached normal levels with the use of GSH synthesized from these amino acids, adequate nutrition, and the end of weight loss and inflammation. Consequently, supplementation with L-glutamine may be recommended to increase intracellular levels of these amino acids, thereby maximizing glutathione synthesis.

L-lysine plays a role in regulating nitric oxide generation from arginine and acts as a crucial precursor for energy production and protein synthesis. L-arginine serves as a precursor for synthesizing various essential amino acids, including nitric oxide, L-proline, L-ornithine, L-glutamate, and L-citrulline. In addition to its role as a precursor, L-arginine plays a critical role in tissue repair and wound healing processes, facilitating the regeneration and restoration of damaged tissues (20,23). In this study, at the end of 3 months, L-arginine ($p = 4.1 \times 10^{-7}$) concentration decreased statistically, while L-lysine ($p = 0.0135$), L-ornithine ($p = 0.0009$), and L-glutamate ($p = 0.0037$) increased. In parallel with this study, fundectomy significantly decreased L-arginine levels and increased glutamate over a 1-year period. However, unlike the study, L-arginine, L-lysine, L-ornithine, and L-glutamate concentrations did not change significantly at the end of 1 year following TG. This reduction in the first period of TG may be due to the use of L-arginine in the regeneration of damaged tissues and protein synthesis.

Additionally, L-arginine may have decreased after TG to produce L-lysine, L-ornithine, and L-glutamate. It has been reported that plasma nitric oxide levels increase after gastrectomy (24). This may explain the increase in L-lysine production for the increased energy needs due to malnutrition after gastrectomy.

In the study, L-alanine, L-asparagine, L-histidine, 3-methyl-L-histidine, and L-methionine plasma levels increased significantly in the 3 months after gastrectomy (Table 5). In previous studies, while histidine and alanine did not change considerably in the first year after fundectomy, the plasma concentration of methionine decreased significantly, unlike our study. In another study, like this study, although an increase in alanine and histidine plasma concentrations was observed 1 year after TG, this change was not significant. L-asparagine has a suppressive effect on apoptosis (25). L-alanine and L-methionine improve the immune system (20,26,27). L-histidine is a crucial amino acid that

serves as a substrate for histamine synthesis in specific immune cells, including macrophages, platelets, dendritic cells, and T lymphocytes. 3-methyl-L-histidine is an amino acid that increases muscle and tissue destruction (28,29). Significant changes in these amino acids indicate that TG affects tissue regeneration and the immune system.

5. CONCLUSION

Total gastrectomy statistically changed the concentrations of 20 amino acids and affected 12 metabolic pathways. The effect of total gastrectomy on amino acid profiles may have some consequences for patients with stage II gastric cancer. First, the changes in amino acid profiles may lead to impaired metabolic functioning, which could increase the risk of complications such as malnutrition, anemia, and infection. Second, the changes in amino acid profiles may impair the immune response, which could increase the risk of cancer recurrence. Third, the changes in amino acid profiles may lead to fatigue, weakness, and other symptoms that can negatively impact the quality of life. However, contrary to these expectations, the findings support that total gastrectomy has a positive effect on the immune system, tissue repair, and energy production. It is conceivable that L-arginine supplementation after gastrectomy may prevent the risk of cancer recurrence, the possibility of infection, and malnutrition. By maintaining optimal levels of L-arginine, patients' immune function, tissue healing, and overall well-being can be improved after surgery. All these results need to be supported by new and more comprehensive studies. The study showed that assessing amino acid profiles may help improve metabolic functioning, immune response, and quality of life in these patients. Investigating the effects of different surgical approaches on amino acid metabolism can contribute to optimizing surgical strategies and improving long-term outcomes for patients.

6. ACKNOWLEDGEMENTS

The authors are grateful to Atatürk University and Erzincan Binali Yıldırım University for their support of this study.

7. ETHICAL STATEMENT

Ethical approval was obtained from the Non-Interventional Clinical Trials Ethics Committee, Atatürk University, on March 29, 2024, under the permit number B.30.2.ATA.0.01.00/244.

8. DATA AVAILABILITY STATEMENT

The data that support the findings of this study are available from the corresponding author upon reasonable request.

9. CONFLICT OF INTEREST

The authors declare that they have no conflicts of interest to disclose.

10. REFERENCES

- Goh YM, Gillespie C, Couper G, Paterson-Brown S. Quality of life after total and subtotal gastrectomy for gastric carcinoma. *Surg* [Internet]. 2015 Oct 1;13(5):267–70. Available from: [<URL>](#).
- Sexton RE, Al Hallak MN, Diab M, Azmi AS. Gastric cancer: A comprehensive review of current and future treatment strategies. *Cancer Metastasis Rev* [Internet]. 2020 Dec 7;39(4):1179–203. Available from: [<URL>](#).
- Svedlund J, Sullivan M, Liedman B, Lundell L. Long term consequences of gastrectomy for patients' quality of life: The impact of reconstructive techniques. *Am J Gastroenterol* [Internet]. 1999 Feb;94(2):438–45. Available from: [<URL>](#).
- Schölmerich J. Postgastrectomy syndromes—diagnosis and treatment. *Best Pract Res Clin Gastroenterol* [Internet]. 2004 Oct 1;18(5):917–33. Available from: [<URL>](#).
- Poitou Bernert C, Ciangura C, Coupaye M, Czernichow S, Bouillot JL, Basdevant A. Nutritional deficiency after gastric bypass: Diagnosis, prevention and treatment. *Diabetes Metab* [Internet]. 2007 Feb 1;33(1):13–24. Available from: [<URL>](#).
- Mayers JR, Wu C, Clish CB, Kraft P, Torrence ME, Fiske BP, et al. Elevation of circulating branched-chain amino acids is an early event in human pancreatic adenocarcinoma development. *Nat Med* [Internet]. 2014 Oct 28;20(10):1193–8. Available from: [<URL>](#).
- Öztürk Er E, Erarpat S, Bodur S, Günkara ÖT, Özbek B, Bakırdere S. Accurate determination of amino acids by quadruple isotope dilution-reverse phase liquid Chromatography-Tandem mass spectrometry after derivatization with 2-Naphthoyl chloride. *J Chromatogr A* [Internet]. 2022 Mar 29;1667:462870. Available from: [<URL>](#).
- Mondanelli G, Iacono A, Carvalho A, Orabona C, Volpi C, Pallotta MT, et al. Amino acid metabolism as drug target in autoimmune diseases. *Autoimmun Rev* [Internet]. 2019 Apr 1;18(4):334–48. Available from: [<URL>](#).
- Rondanelli M, Opizzi A, Antonello N, Boschi F, Iadarola P, Pasini E, et al. Effect of essential amino acid supplementation on quality of life, Amino acid profile and strength in institutionalized elderly patients. *Clin Nutr* [Internet]. 2011 Oct 1;30(5):571–7. Available from: [<URL>](#).
- Manig F, Kuhne K, von Neubeck C, Schwarzenbolz U, Yu Z, Kessler BM, et al. The why and how of amino acid analytics in cancer diagnostics and therapy. *J Biotechnol* [Internet]. 2017 Jan 20;242:30–54. Available from: [<URL>](#).
- Bi X, Henry CJ. Plasma-free amino acid profiles are predictors of cancer and diabetes development. *Nutr Diabetes* [Internet]. 2017 Mar 13;7(3):e249. Available from: [<URL>](#).

12. Atila A, Alay H, Yaman ME, Akman TC, Cadirci E, Bayrak B, et al. The serum amino acid profile in COVID-19. *Amino Acids* [Internet]. 2021 Oct 4;53(10):1569–88. Available from: [<URL>](#).
13. Erawijantari PP, Mizutani S, Shiroma H, Shiba S, Nakajima T, Sakamoto T, et al. Influence of gastrectomy for gastric cancer treatment on faecal microbiome and metabolome profiles. *Gut* [Internet]. 2020 Aug 1;69(8):1404–15. Available from: [<URL>](#).
14. Tataru MR, Śliwa E, Krupski W, Worzakowska M. 3-Hydroxy-3-methylbutyrate administration diminishes fundectomy-induced osteopenia of the lumbar spine in pigs. *Nutrition* [Internet]. 2008 Jul 1;24(7–8):753–60. Available from: [<URL>](#).
15. Tataru MR, Krupski W, Szpetnar M, Dąbrowski A, Bury P, Szabelska A, et al. Effects of total gastrectomy on plasma silicon and amino acid concentrations in men. *Exp Biol Med* [Internet]. 2015 Dec 2;240(12):1557–63. Available from: [<URL>](#).
16. Aquilani R, Maestri R, Boselli M, Achilli MP, Arrighi N, Bruni M, et al. The relationship between plasma amino acids and circulating albumin and haemoglobin in postabsorptive stroke patients. Clelland JD, editor. *PLoS One* [Internet]. 2019 Aug 14;14(8):e0219756. Available from: [<URL>](#).
17. Package “ggpubr” type package title “ggplot2” based publication ready plots [Internet]. [cited 2024 May 18]. Available from: [<URL>](#).
18. Gwin JA, Church DD, Wolfe RR, Ferrando AA, Pasiakos SM. Muscle Protein Synthesis and Whole-Body Protein Turnover Responses to Ingesting Essential Amino Acids, Intact Protein, and Protein-Containing Mixed Meals with Considerations for Energy Deficit. *Nutrients* [Internet]. 2020 Aug 15;12(8):2457. Available from: [<URL>](#).
19. Holeček M. Branched-chain amino acids in health and disease: metabolism, alterations in blood plasma, and as supplements. *Nutr Metab (Lond)* [Internet]. 2018 Dec 3;15(1):33. Available from: [<URL>](#).
20. Wu G. Amino acids: Metabolism, functions, and nutrition. *Amino Acids* [Internet]. 2009 May 20;37(1):1–17. Available from: [<URL>](#).
21. Wu G, Lupton JR, Turner ND, Fang YZ, Yang S. Glutathione metabolism and its implications for health. *J Nutr* [Internet]. 2004 Mar 1;134(3):489–92. Available from: [<URL>](#).
22. Cheng X, Xu HD, Ran HH, Liang G, Wu FG. Glutathione-depleting nanomedicines for synergistic cancertherapy. *ACS Nano* [Internet]. 2021 May 25;15(5):8039–68. Available from: [<URL>](#).
23. Kumar M, Ji B, Babaei P, Das P, Lappa D, Ramakrishnan G, et al. Gut microbiota dysbiosis is associated with malnutrition and reduced plasma amino acid levels: Lessons from genome-scale metabolic modeling. *Metab Eng* [Internet]. 2018 Sep 1;49:128–42. Available from: [<URL>](#).
24. Nagahama S, Korenaga D, Honda M, Inutsuka S, Sugimachi K. Assessment of the intestinal permeability after a gastrectomy and the oral administration of anticancer drugs in rats: Nitric oxide release in response to gut injury. *Surgery* [Internet]. 2002 Jan 1;131(1):S92–7. Available from: [<URL>](#).
25. Luise D, Chalvon-Demersay T, Correa F, Bosi P, Trevisi P. Review: A systematic review of the effects of functional amino acids on small intestine barrier function and immunity in piglets. *animal* [Internet]. 2023 Jun 1;17:100771. Available from: [<URL>](#).
26. Shynkevych VI, Kolomiets S V., Kaidashev IP. Effects of l-arginine and l-ornithine supplementations on the treatment of chronic periodontitis: A preliminary randomized short-term clinical trial. *Heliyon* [Internet]. 2021 Nov 1;7(11):e08353. Available from: [<URL>](#).
27. O’Riordain M. Effect of glutamine on immune function in the surgical patient. *Nutrition* [Internet]. 1996 Dec 1;12(12):S82–4. Available from: [<URL>](#).
28. Chinkes DL. Methods for measuring tissue protein breakdown rate in vivo. *Curr Opin Clin Nutr Metab Care* [Internet]. 2005 Sep;8(5):534–7. Available from: [<URL>](#).
29. Demopoulos C, Antonopoulou S, Theoharides TC. COVID-19, microthromboses, inflammation, and platelet activating factor. *BioFactors* [Internet]. 2020 Nov 9;46(6):927–33. Available from: [<URL>](#).



Synthesis of P-N Type Schiff Bases and Their Secondary Amines: Investigation of the Antioxidant Properties of the Synthesized Molecules

Irem Akgul¹ , Merve Dogan¹ , Ozgur Yilmaz^{1*} 

¹Department of Chemistry, Faculty of Sciences, Mersin University, 33343 Mersin, Turkey.

Abstract: In this study, P-N type Schiff bases (imino-phosphine) and their secondary amine (amino-phosphine) derivatives were synthesized. After the successful synthesis of Schiff bases and the relevant secondary amines obtained from the reduction of Schiff bases, the antioxidant activities of all synthesized molecules were examined by the DPPH (2,2-diphenyl-1-picrylhydrazyl) and ABTS (2,2'-azino-bis(3-ethylbenzothiazoline-6-sulfonic acid)) methods and IC₅₀ values were calculated. Secondary amines (amino-phosphine derivatives **4** and **7**) obtained by reduction of Schiff bases (imino-phosphine derivatives **3** and **6**) were found to exhibit high DPPH free radical scavenging activity. At the same time, all synthesized molecules demonstrated very high ABTS cationic radical scavenging activity. Most of the molecules showed better antioxidant activity than the BHT and BHA molecules used as positive controls. The structures of all synthesized molecules were characterized by ¹H-NMR, ¹³C-NMR, GC-MS, and FT-IR.

Keywords: Schiff bases, Secondary amines, Imino- and amino-phosphine, DPPH, ABTS, Antioxidant activity.

Submitted: July 25, 2024. **Accepted:** October 16, 2024.

Cite this: Akgul I, Dogan M, Yilmaz O. Synthesis of P-N Type Schiff Bases and Their Secondary Amines: Investigation of the Antioxidant Properties of the Synthesized Molecules. JOTCSA. 2024;11(4): 1623-8.

DOI: <https://doi.org/10.18596/jotcsa.1522459>

***Corresponding author's E-mail:** yilmazozgur@mersin.edu.tr

1. INTRODUCTION

Schiff bases and secondary amines obtained by their reduction are a very important class of molecules in the field of organic chemistry because they have many biological activities, such as antibacterial, antifungal, antioxidant, anti-tumor, anti-HIV, and anti-inflammatory (1–12). In addition to these important biological properties, these molecules are also important because of their widespread use as intermediates in the synthesis of a variety of natural products (13–17). There are also studies in the literature showing that these molecule derivatives catalyze many reactions, such as Heck and Suzuki coupling, especially P-N type ligands in imino- and amino-phosphine structures (18,19). Although there are many articles on the catalytic activity of Schiff bases and secondary amine structures, there are a limited number of studies discussing their biological activity. However, in these studies, it is understood that these molecules also have high biological activity. All the above characteristics increase the number of studies involving the synthesis of new Schiff bases and related secondary amines and the investigation

of the biological and catalytic properties of the resulting molecules.

In this article, new Schiff bases with the imino-phosphine structure were synthesized from the reaction of 4-aminoindan and 5-aminoindan molecules with 2-(diphenylphosphino)benzaldehyde. The corresponding amino-phosphine derivatives were also obtained by the reduction reaction of these molecules. The structures of all synthesized molecules were elucidated by NMR, FTIR, and GC-MS methods, and their antioxidant activities were investigated by DPPH and ABTS methods. The structure-activity relationship has been discussed based on molecular structures with the same skeleton but differing in positional substitutions.

2. EXPERIMENTAL SECTION

2.1. Materials

All reagents were obtained by Sigma-Aldrich or Merck. Bruker Ultrashield Plus Biospin Avance III 400 MHz NaNoBay FT-NMR, Chebios Optimum-One UV-Vis spectrophotometer, and Perkin Elmer Spectrum-100 were used for ¹H and ¹³C NMR

spectra, antioxidant activities, and FT-IR spectra, respectively.

2.2. General Method for The Synthesis of Molecules

2.2.1. Synthesis of the schiff bases

0.15 g (1.13 mmol, 1 eq.) 5-aminoindan (**1**) or 4-aminoindan (**5**) was dissolved with MeOH (8 mL) and then 0.39 g (1.35 mmol, 1.2 eq.) 2-(Diphenylphosphino)benzaldehyde (**2**) was added. The resulting solutions were stirred at room temperature until the TLC analysis revealed the consumption of the starting material (maximum 2 h). The solvent was evaporated, and products (**3** or **6**) were purified by crystallization (2).

2.2.2. Synthesis of secondary amines

1 mmol of the synthesized Schiff bases (**3** and **6**) was taken and dissolved in 20 mL of methanol, and 2 mmol of NaBH₄ was slowly added and mixed for 3 hours. The solvent was removed under vacuum after the reaction was confirmed by thin-layer chromatography. The residue was washed with 3x10 mL of methylene chloride with the addition of 10 mL of water. After the collection of the organic phases, they were dried with sodium sulfate. After the removal of the solvent, the secondary amine derivatives were obtained (**4** or **7**) (2).

2.3. Antioxidant Activities

2.3.1. DPPH free radical scavenging activity

The 2,2-diphenyl-1-picrylhydrazyl (DPPH) radical scavenging assay was used to measure antioxidant activity. Butylated hydroxytoluene (BHT) and butylated hydroxyanisole (BHA) were used as reference test materials. At the beginning, the concentrations (6.75 - 400 µg/mL) of all the synthesized compounds and the reference test materials were prepared in EtOH. Then, 1 mL of each sample was added to 1 mL of 1 x 10⁻⁴ M DPPH solution, which was prepared as freshly prepared, and they were incubated in the dark for half an hour at room temperature. The absorbance of each sample was measured at 517 nm at the end of the incubation period. The scavenging activity was calculated as a percentage according to the formula

given below (Equation 1). The IC₅₀, which is the concentration necessary for 50% removal of DPPH free radicals, was calculated (1,2,20).

$$\% \text{ DPPH Scavenging} = (A_0 - A_s / A_0) \times 100 \quad (1)$$

(A₀ = Absorbance of the control; A_s = Absorbance of the sample at 517 nm)

2.3.2. ABTS cation radical scavenging activity

The ABTS scavenging activity of the synthesized molecules was determined as described by Re et al. Briefly, ABTS radicals were generated by a reaction of 2 mM ABTS in H₂O with 2.45 mM potassium persulfate (K₂S₂O₈), and it was stored for 2 h at room temperature in the dark. This solution was diluted in 0.1 M sodium phosphate buffer (pH=7.4) to an absorbance of 0.900 ± 0.100 at 734 nm. Subsequently, 1 mL of ABTS^{•+} solution was added to 3 mL of each synthesized molecule at a concentration of 400 µg/mL, and the absorbances were read at 734 nm after 30 min. Equation 2 was used to calculate the results as percentages. Different concentrations of each active molecule were prepared to calculate IC₅₀ values after determining the active compounds (21).

$$\% \text{ ABTS Scavenging activity} = (A_0 - A_s / A_0) \times 100 \quad (2)$$

(A₀ = Absorbance of the control; A_s = Absorbance of the sample at 734 nm)

3. RESULTS AND DISCUSSION

For the synthesis of Schiff bases, 5-aminoindan (**1**) and 4-aminoindan (**5**) were chosen as starting compounds. By separately reacting these amine compounds with 2-(Diphenylphosphino)benzaldehyde (**2**) in methanol at 40 °C, the target Schiff bases (imino-phosphine derivatives) (**3**) and (**6**) were synthesized in high yields (Figure 1). After purification by crystallization, the Schiff bases were reduced to the corresponding secondary amines (amino-phosphine derivatives) (**4**) and (**7**) by reaction with NaBH₄.

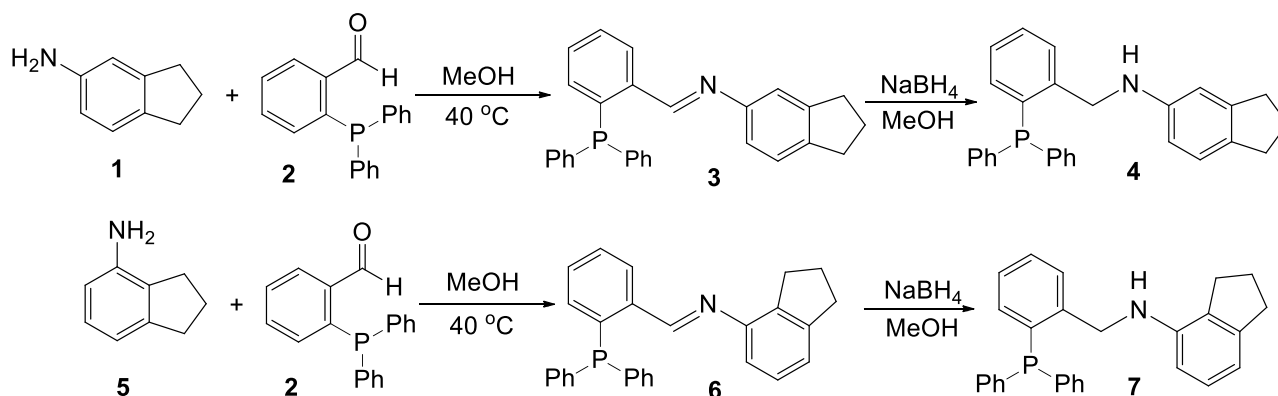


Figure 1: Synthesis of Schiff bases (**3** and **6**) and their related secondary amines (**4** and **7**).

After successful synthesis, the structures of all synthesized molecules were elucidated using ¹H-NMR, ¹³C-NMR, FTIR spectroscopy, and GC-MS. ¹H-NMR spectra of the synthesized Schiff bases (**3** and

6) show that aromatic protons appear in the range of δ 8.13-6.22 ppm in accordance with the literature (1,2). The specific imine (-N=CH-) protons of the Schiff bases (iminophosphine)

resonated as a doublet in the range δ 9.05-9.00 (18). It is seen that the three $-CH_2$ groups in the structure are only affected by each other in accordance with the structure and resonate as triplet and quintet, respectively (2). In the NMR spectra of molecules **4** and **7** synthesized by reducing the $-N=CH-$ group in molecules **3** and **6**, the signals belonging to the $-N-CH_2-$ group resonated as a singlet in the range δ 4.54-4.47 ppm (2). 1H -NMR spectra of all molecules are in agreement with the structure. In addition to the 1H -NMR spectra, ^{13}C -NMR, FTIR, and GCMS measurements also support the successful and pure preparation of the molecules.

DPPH scavenging activity

After the successful completion of the target molecules, it was aimed to determine the antioxidant activities of all molecules. Radicals, which are known to be continuously produced in the

human body for various reasons, can cause cell destruction and many diseases, such as cardiovascular disease. These radicals can be kept under control by antioxidants (20,22). Therefore, it is of great importance to obtain new molecules with high antioxidant properties. In light of this information, firstly, the radical scavenging properties of the synthesized molecules were investigated by the DPPH (2,2-diphenyl-1-picrylhydrazil) method, which is widely used in the literature. 800 μ g/mL was determined as the highest concentration, and solutions of the synthesized molecules at this dose were prepared. In preliminary experiments at the highest dose, it was determined that **4** and **7** molecules showed high radical scavenging activity. In order to calculate the IC_{50} values of these molecules, lower dose solutions were prepared, the measurements were repeated (Figure 2), and IC_{50} values were determined (Table 1).

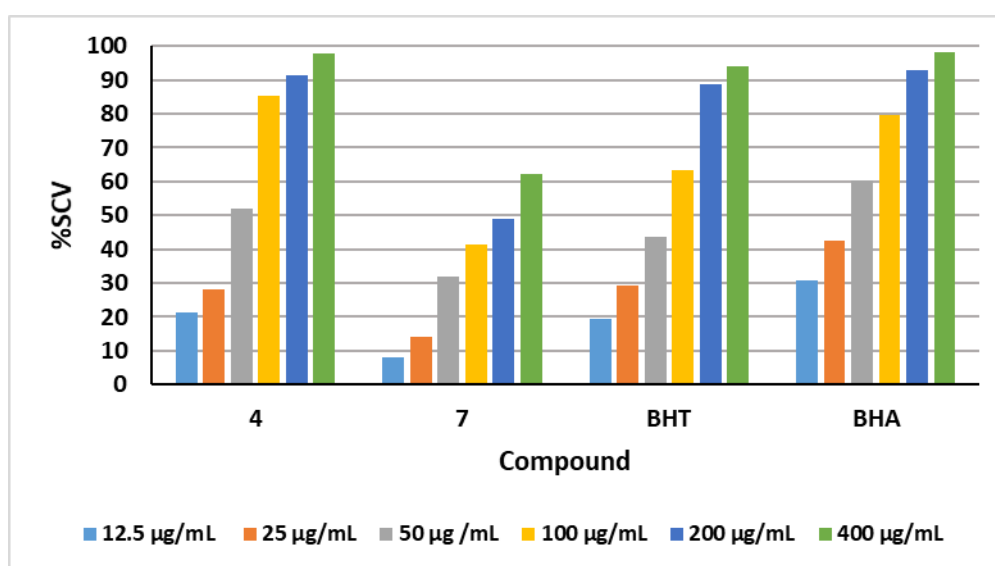


Figure 2: DPPH scavenging activities of each molecule for each concentration.

When the results obtained are evaluated, it is seen that the secondary amine derivatives (aminophosphines **4** and **7**) have much higher radical scavenging activity compared to Schiff bases (iminophosphines **3** and **6**). It is clearly understood that this result is due to the $-NH$ groups present in the secondary amines obtained after the reduction of Schiff bases. On the other hand, the antioxidant activities of molecules **4** (synthesized via 5-

aminoindanes) and **7** (synthesized via 4-aminoindanes), which have different positions but similar molecular structures, were found to be significantly different. This result showed that besides the side groups, different positions of the same groups can also change the antioxidant activity to a high extent. As a result, DPPH scavenging activity changes in the order of BHT>**4**>BHA>**7**.

Table 1: IC_{50} values of synthesized molecules for DPPH scavenging activities.

Compound	4	7	BHT	BHA
IC_{50} values (μg/mL)	51.3	262.6	40.9	86.8
Equation	$y = 0.7426x + 11.867$ $R^2 = 0.994$	$y = 0.1131x + 20.304$ $R^2 = 0.8751$	$y = 0.5766x + 26.396$ $R^2 = 0.9305$	$y = 0.3475x + 19.825$ $R^2 = 0.9578$

ABTS scavenging activity

The reaction between ABTS and potassium persulfate produces the radical cation ABTS, which, with water, produces a blue solution. This solution gives absorbance at 734 nm, and the antioxidant activity of molecules is measured according to the

decrease in absorbance. While the DPPH method is generally based on the transfer of hydrogen atoms, the ABTS method is based on the transfer of electrons (21,23,24).

The solutions prepared for the DPPH method were also used for this method. Preliminary measurements at the highest concentration (800 µg/mL) showed that all molecules had very high

ABTS activity. Measurements were repeated for solutions prepared at lower concentrations (Figure 3), and IC₅₀ values were calculated using the equations obtained (Table 2).

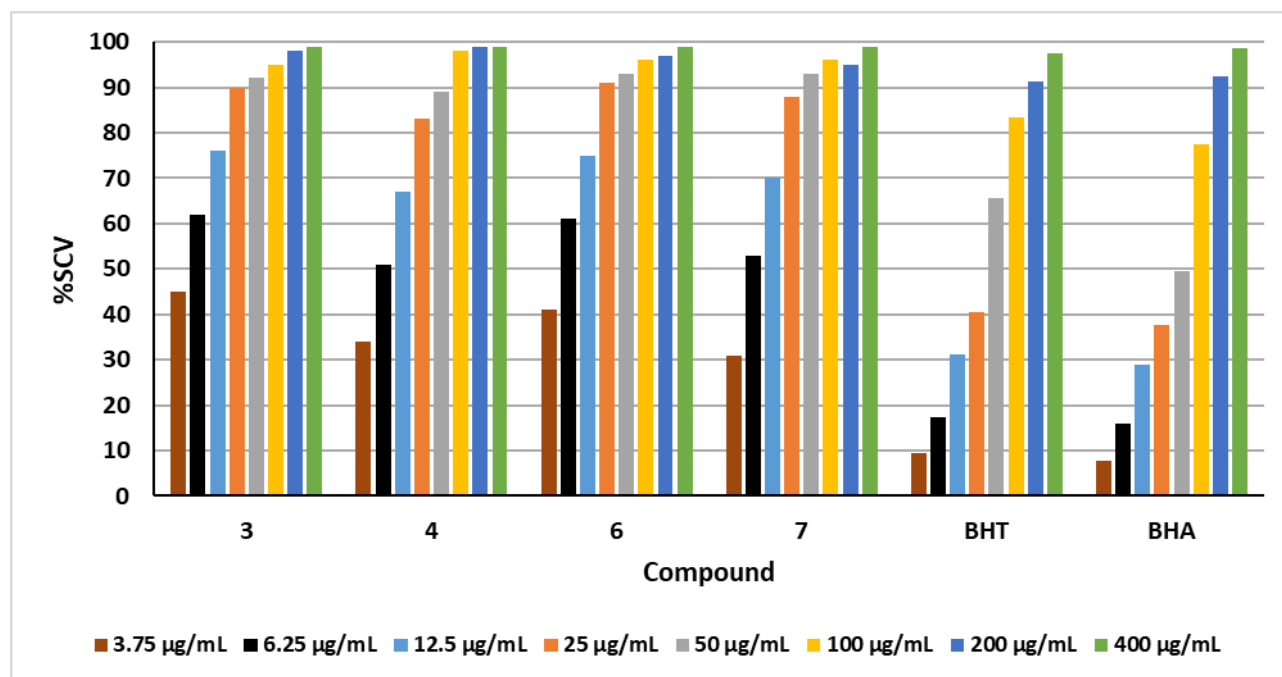


Figure 3: ABTS scavenging activities of each molecule for each concentration.

The results showed that all synthesized molecules had much better ABTS activity than the positive controls. At first glance, it is clear that these high activities are due to the triphenylphosphine group in

all molecules. According to the ABTS activities in the order of **3>6>7>4> BHT>BHA**, Schiff bases have higher ABTS activity compared to secondary amines.

Table 2: IC₅₀ values of synthesized molecules for ABTS scavenging activities.

Compound	3	4	6	7	BHT	BHA
IC ₅₀ values (µg/mL)	1.12	1.96	1.34	1.93	4.10	4.41
Equation	$y = 12.2x + 36.4$ $R^2 = 0.9517$	$y = 14.2x + 22.2$ $R^2 = 0.9785$	$y = 13.4x + 32$ $R^2 = 0.9486$	$y = 15.9x + 19.3$ $R^2 = 0.9657$	$y = 14.714x - 10.457$ $R^2 = 0.9783$	$y = 14.2x - 12.6$ $R^2 = 0.9632$

(E)-N-(2-(diphenylphosphino)benzylidene)-2,3-dihydro-1H-inden-5-amine (3, C₂₈H₂₄NP)

¹H NMR (400 MHz, CDCl₃) δ 9.00 (d, *J* = 5.2 Hz, 1H, -CH=N-), 8.13 (ddd, *J* = 7.7, 3.9, 1.2 Hz, 1H, Ph-H), 7.36 (t, *J* = 7.5 Hz, 1H, Ph-H), 7.30 – 7.19 (m, 11H, Ph-H), 7.05 (d, *J* = 8.0 Hz, 1H, Ph-H), 6.84 (ddd, *J* = 7.7, 4.7, 0.9 Hz, 1H, Ph-H), 6.70 – 6.64 (m, 2H, Ph-H), 2.78 (td, *J* = 7.4, 2.4 Hz, 4H, -2CH₂), 2.03 – 1.94 (p, *J* = 7.5, 2H, -CH₂) ppm. ¹³C NMR (101 MHz, CDCl₃) δ 157.9 (CH=N), 157.7 (PhC), 150.2 (PhC), 145.1 (PhC), 142.1 (PhC), 139.6 (PhC), 139.4 (PhC), 138.5 (PhC), 138.3 (PhC), 136.6 (PhC), 136.5 (PhC), 134.2 (PhC), 134.0 (PhC), 133.5 (PhC), 130.6 (PhC), 128.9 (PhC), 128.9 (PhC), 128.7 (PhC), 128.6 (PhC), 127.9 (PhC), 127.9 (PhC), 124.5 (PhC), 119.3 (PhC), 116.7 (PhC), 32.8 (-CH₂), 32.4 (-CH₂), 25.6 (-CH₂) ppm. FTIR (KBr): = 3051, 2948, 2837, 1596, 1579, 1482, 1432, 741, 693 cm⁻¹. GC-MS: 405.2 (M⁺), 290.1, 261.1, 183.0, 107.0, 51.0.

N-(2-(diphenylphosphino)benzyl)-2,3-dihydro-1H-inden-5-amine (4, C₂₈H₂₆NP)

¹H NMR (400 MHz, CDCl₃) δ 7.49 (dd, *J* = 7.1, 4.0 Hz, 1H), 7.42 – 7.25 (m, 11H, Ph-H), 7.21 – 7.13 (m, 1H, Ph-H), 6.96 – 6.88 (m, 2H, Ph-H), 6.30 (d, *J* = 1.8 Hz, 1H, Ph-H), 6.22 (dd, *J* = 8.0, 2.2 Hz, 1H, Ph-H), 4.47 (s, 2H, -NCH₂), 3.83 (bs, 1H, -NH) 2.76 (t, *J* = 7.3 Hz, 4H, -2CH₂), 1.98 (sext, *J* = 7.3 Hz, 2H, -CH₂) ppm. ¹³C NMR (101 MHz, CDCl₃) δ 146.5 (PhC), 145.1 (PhC), 143.8 (PhC), 143.6 (PhC), 136.5 (PhC), 136.4 (PhC), 134.0 (PhC), 133.8 (PhC), 133.5 (PhC), 133.0 (PhC), 129.0 (PhC), 128.8 (PhC), 128.6 (PhC), 128.5 (PhC), 128.1 (PhC), 128.1 (PhC), 127.3 (PhC), 124.5 (PhC), 111.3 (PhC), 109.0 (PhC), 53.3 (-NCH₂), 33.1 (-CH₂), 31.9 (-CH₂), 25.6 (-CH₂) ppm. FTIR (KBr): = 3411, 3051, 2920, 2842, 1613, 1584, 1499, 1433, 906, 742, 694 cm⁻¹. GC-MS: 407.1 (M⁺) not appeared, 223.1, 205.1, 149.0, 104.0, 32.0.

(E)-N-(2-(diphenylphosphino)benzylidene)-2,3-dihydro-1H-inden-4-amine (6, C₂₈H₂₄NP)

¹H NMR (400 MHz, CDCl₃) δ 9.05 (d, *J* = 5.2 Hz, 1H, -CH=N-), 8.24 (ddd, *J* = 7.7, 3.9, 1.0 Hz, 1H, Ph-H), 7.44 (t, *J* = 7.6 Hz, 1H, Ph-H), 7.38 – 7.26 (m, 11H, Ph-H), 7.10 – 7.00 (m, 2H, Ph-H), 6.91 (ddd, *J* = 7.6, 4.6, 1.0 Hz, 1H, Ph-H), 6.47 (d, *J* = 7.2 Hz, 1H, Ph-H), 2.89 (t, *J* = 7.4 Hz, 2H, -CH₂), 2.73 (t, *J* = 7.3 Hz, 2H, -CH₂), 1.98 (p, *J* = 7.5 Hz, 2H, -CH₂) ppm. **¹³C NMR (101 MHz, CDCl₃)** δ 158.8 (CH=N), 158.6 (PhC), 148.4 (PhC), 145.3 (PhC), 139.7 (PhC), 139.5 (PhC), 138.5 (PhC), 138.3 (PhC), 137.2 (PhC), 136.5 (PhC), 136.4 (PhC), 134.2 (PhC), 134.0 (PhC), 133.4 (PhC), 130.7 (PhC), 128.9 (PhC), 128.9 (PhC), 128.7 (PhC), 128.6 (PhC), 127.9 (PhC), 127.9 (PhC), 127.0 (PhC), 121.6 (PhC), 116.3 (PhC), 33.1 (-CH₂), 30.4 (-CH₂), 25.1 (-CH₂) ppm. **FTIR (KBr):** = 3053, 2944, 2842, 1618, 1579, 1467, 1432, 1121, 742, 693 cm⁻¹. **GC-MS:** 405.2 (M⁺) not appeared, 290.1, 261.1, 183.0, 107.0, 51.0

N-(2-(diphenylphosphino)benzyl)-2,3-dihydro-1H-inden-4-amine (7, C₂₈H₂₆NP)

¹H NMR (400 MHz, CDCl₃) δ 7.52 – 7.46 (m, 1H, Ph-H), 7.37 – 7.27 (m, 11H, Ph-H), 7.19 (t, *J* = 7.7 Hz, 1H, Ph-H), 7.00 – 6.89 (m, 2H, Ph-H), 6.60 (d, *J* = 7.4 Hz, 1H, Ph-H), 6.30 (d, *J* = 8.0 Hz, 1H, Ph-H), 4.55 (s, 2H, -NCH₂), 3.75 (s, 1H, -NH), 2.85 (t, *J* = 7.5 Hz, 2H, -CH₂), 2.35 (t, *J* = 7.4 Hz, 2H, -CH₂), 1.99 (sext, *J* = 7.3 Hz, 2H, -CH₂) ppm. **¹³C NMR (101 MHz, CDCl₃)** δ 144.5 (PhC), 144.0 (PhC), 143.8 (PhC), 143.5 (PhC), 136.5 (PhC), 136.5 (PhC), 135.8 (PhC), 135.6 (PhC), 134.0 (PhC), 133.8 (PhC), 130.9 (PhC), 129.1 (PhC), 128.8 (PhC), 128.7 (PhC), 128.6 (PhC), 128.5 (PhC), 128.3 (PhC), 128.2 (PhC), 128.1 (PhC), 127.4 (PhC), 113.5 (PhC), 107.6 (PhC), 71.8 (-NCH₂), 33.3 (-CH₂), 29.0 (-CH₂), 24.5 (-CH₂) ppm. **FTIR (KBr):** = 3341, 3054, 2922, 2845, 1592, 1472, 1434, 1180, 1116, 907, 721, 693 cm⁻¹. **GC-MS:** 407.1 (M⁺) not appeared, 223.1, 205.1, 149.0, 104.0, 57.1.

4. CONCLUSION

New Schiff bases (iminophosphine) were synthesized by utilizing the reactions between 4-aminoindan or 5-aminoindan and 2-(Diphenylphosphino)benzaldehyde, and secondary amines (aminophosphine) were obtained with high yields by reduction of synthesized Schiff bases. The antioxidant activities of these newly synthesized molecules were examined by using DPPH and ABTS methods. When the antioxidant activity results are discussed, it was observed that only the secondary amine derivatives have DPPH activity, while all synthesized molecules have very high ABTS activity. The significant difference in DPPH activities between molecules 4 and 7, which have the same groups in different positions, indicated that not only positional variations but also the side groups significantly affect biological activity. The structural similarity of the synthesized molecules enabled a discussion of the structure-activity relationship.

5. CONFLICT OF INTEREST

The authors declare no conflict of interest.

6. ACKNOWLEDGMENTS

This research was supported by a grant from TÜBİTAK 2209-A Project (1919B012304506).

7. REFERENCES

1. Yılmaz Ö. Synthesis of new Schiff bases; Investigation of their in situ catalytic activity for Suzuki C-C coupling reactions and antioxidant activities. J Chinese Chem Soc [Internet]. 2021 May 8;68(5):917–28. Available from: [<URL>](#).
2. Erdoğan H, Yılmaz Ö, Çevik PK, Doğan M, Özen R. Synthesis of schiff bases and secondary amines with indane skeleton; evaluation of their antioxidant, antibiotic, and antifungal activities. Chem Biodivers [Internet]. 2023 Sep 5;20(9):e202300684. Available from: [<URL>](#).
3. Shebl M, Adly OMI, Abdelrhman EM, El-Shetary BA. Binary and ternary copper(II) complexes of a new Schiff base ligand derived from 4-acetyl-5,6-diphenyl-3(2H)-pyridazinone: Synthesis, spectral, thermal, antimicrobial and antitumor studies. J Mol Struct [Internet]. 2017 Oct 5;1145:329–38. Available from: [<URL>](#).
4. Salvatore RN, Yoon CH, Jung KW. Synthesis of secondary amines. Tetrahedron [Internet]. 2001 Sep 10;57(37):7785–811. Available from: [<URL>](#).
5. Fiore AM, Romanazzi G, Dell'Anna MM, Latronico M, Leonelli C, Mali M, et al. Mild and efficient synthesis of secondary aromatic amines by one-pot stepwise reductive amination of arylaldehydes with nitroarenes promoted by reusable nickel nanoparticles. Mol Catal [Internet]. 2019 Oct 1;476:110507. Available from: [<URL>](#).
6. Molaei H, Moghadam M, Mirkhani V, Tangestaninejad S, Mohammadpoor-Baltork I, Kajani AA, et al. Synthesis of chiral palladium oxazolidine and imine complexes: Investigation the oxazolidine-imine conversion by DFT method. Polyhedron [Internet]. 2019 Mar 1;160:130–8. Available from: [<URL>](#).
7. Huttunen KM, Raunio H, Rautio J. Prodrugs—from Serendipity to Rational Design. Koulou M, editor. Pharmacol Rev [Internet]. 2011 Sep 1;63(3):750–71. Available from: [<URL>](#).
8. Wang YY, Xu FZ, Zhu YY, Song B, Luo D, Yu G, et al. Pyrazolo[3,4-d]pyrimidine derivatives containing a Schiff base moiety as potential antiviral agents. Bioorg Med Chem Lett [Internet]. 2018 Sep 15;28(17):2979–84. Available from: [<URL>](#).
9. Prasanna Kumar BN, Mohana KN, Mallesha L. Synthesis and antiproliferative activity of some new fluorinated Schiff bases derived from 1,2,4-triazoles. J Fluor Chem [Internet]. 2013 Dec

1;156:15–20. Available from: [<URL>](#).

10. Al Zoubi W, Al-Hamdani AAS, Kaseem M. Synthesis and antioxidant activities of Schiff bases and their complexes: A review. *Appl Organomet Chem* [Internet]. 2016 Oct 14;30(10):810–7. Available from: [<URL>](#).

11. Sztanke K, Maziarka A, Osinka A, Sztanke M. An insight into synthetic Schiff bases revealing antiproliferative activities in vitro. *Bioorg Med Chem* [Internet]. 2013 Jul 1;21(13):3648–66. Available from: [<URL>](#).

12. Gungor E, Celen S, Azaz D, Kara H. Two tridentate Schiff base ligands and their mononuclear cobalt (III) complexes: Synthesis, characterization, antibacterial and antifungal activities. *Spectrochim Acta Part A Mol Biomol Spectrosc* [Internet]. 2012 Aug 1;94:216–21. Available from: [<URL>](#).

13. Huang B, Tian H, Lin S, Xie M, Yu X, Xu Q. Cu(I)/TEMPO-catalyzed aerobic oxidative synthesis of imines directly from primary and secondary amines under ambient and neat conditions. *Tetrahedron Lett* [Internet]. 2013 May 29;54(22):2861–4. Available from: [<URL>](#).

14. Xu H, Shi JL, Hao H, Li X, Lang X. Visible light photocatalytic aerobic oxidative synthesis of imines from alcohols and amines on dye-sensitized TiO₂. *Catal Today* [Internet]. 2019 Sep 1;335:128–35. Available from: [<URL>](#).

15. Chen D, Wang Y, Klankermayer J. Enantioselective hydrogenation with chiral frustrated lewis pairs. *Angew Chemie Int Ed* [Internet]. 2010 Dec 3;49(49):9475–8. Available from: [<URL>](#).

16. Segobia DJ, Trasarti AF, Apesteguía CR. Selective one-pot synthesis of asymmetric secondary amines via N-alkylation of nitriles with alcohols. *J Catal* [Internet]. 2019 Dec 1;380:178–85. Available from: [<URL>](#).

17. Neelapapu R, Petukhov PA. A one-pot selective synthesis of N-Boc protected secondary amines: tandem direct reductive amination/N-Boc protection. *Tetrahedron* [Internet]. 2012 Sep

2;68(35):7056–62. Available from: [<URL>](#).

18. Yılmaz MK, Güzel B. Iminophosphine palladium(II) complexes: synthesis, characterization, and application in Heck cross-coupling reaction of aryl bromides. *Appl Organomet Chem* [Internet]. 2014 Jul 29;28(7):529–36. Available from: [<URL>](#).

19. Yılmaz MK. Palladium(II) complexes with new bidentate phosphine-imine ligands for the Suzuki C–C coupling reactions in supercritical carbon dioxide. *J Supercrit Fluids* [Internet]. 2018 Aug 1;138:221–7. Available from: [<URL>](#).

20. Bursal E, Aras A, Kılıç Ö, Taslimi P, Gören AC, Gülçin İ. Phytochemical content, antioxidant activity, and enzyme inhibition effect of *Salvia eriophora* Boiss. & Kotschy against acetylcholinesterase, α -amylase, butyrylcholinesterase, and α -glycosidase enzymes. *J Food Biochem* [Internet]. 2019 Mar 1;43(3):e12776. Available from: [<URL>](#).

21. Yılmaz Ö, Çevik PK, Yılmaz MK. Synthesis of new substituted diamides. Investigation of their antioxidant and antibacterial properties. *Russ J Bioorganic Chem* [Internet]. 2021 Mar 26;47(2):543–51. Available from: [<URL>](#).

22. Güzel S, Özay Y, Kumaş M, Uzun C, Özkorkmaz EG, Yıldırım Z, et al. Wound healing properties, antimicrobial and antioxidant activities of *Salvia kronenburgii* Rech. f. and *Salvia euphratica* Montbret, Aucher&Rech. f. var. *euphratica* on excision and incision wound models in diabetic rats. *Biomed Pharmacother* [Internet]. 2019 Mar 1;111:1260–76. Available from: [<URL>](#).

23. Gülçin İ. Antioxidant activity of eugenol: A structure–activity relationship study. *J Med Food* [Internet]. 2011 Sep 21;14(9):975–85. Available from: [<URL>](#).

24. Gülçin İ, Huyut Z, Elmastaş M, Aboul-Enein HY. Radical scavenging and antioxidant activity of tannic acid. *Arab J Chem* [Internet]. 2010 Jan 1;3(1):43–53. Available from: [<URL>](#).



Edaravone's Hepatoprotective Effects Against Oxidative Stress in Valproic Acid-induced Rat Model

Neziha Hacıhasanoğlu Çakmak^{1*}, Refiye Yanardag²

¹Istanbul Medipol University, Vocational School of Health Services, Medical Laboratory Techniques, Beykoz 34810 Istanbul, Türkiye.

²Istanbul University-Cerrahpaşa, Faculty of Engineering, Department of Chemistry, Avcılar 34320 Istanbul, Turkey.

Abstract: In this experimental study, the effect of edaravone (EDA) on liver damage caused by valproic acid (VPA) was investigated. The antioxidant, oxidative stress, and inflammation indicators such as glutathione (GSH), total lipid (TL), sialic acid (SA), aspartate (AST) and alanine transaminase (ALT), alkaline phosphatase (ALP), gamma-glutamyl transferase (GGT), catalase (CAT), superoxide dismutase (SOD), glutathione peroxidase (GPx), glutathione reductase (GR) and glutathione-S-transferase (GST) were examined. Male Sprague Dawley rats were used in the experiment and randomly divided into 4 groups. The experiment lasted for 7 days. Group I: control group rats; Group II: rats receiving 0.5 g/kg VPA intraperitoneally daily. Group III: rats receiving 30 mg/kg EDA intraperitoneally daily. Group IV: rats receiving 0.5 g/kg VPA and 30 mg/kg EDA intraperitoneally daily (at the same time). On day 8, all animals were sacrificed under anesthesia, and liver tissues were removed. VPA caused the decreases in GSH, CAT, SOD, GPx, GR, and GST values and the increases in AST, ALT, ALP, GGT, sialic acid, and total lipid values. EDA reversed the in all values. These results suggest that EDA administration potentially reduces liver injury in VPA-induced hepatotoxicity.

Keywords: Liver, Edaravone, Valproic acid, Oxidative stress, Antioxidant.

Submitted: September 11, 2024. **Accepted:** October 15, 2024.

Cite this: Hacıhasanoğlu Çakmak N, Yanardag R. Edaravone's Hepatoprotective Effects Against Oxidative Stress in Valproic Acid-induced Rat Model. JOTCSA. 2024;11(4): 1629-40.

DOI: <https://doi.org/10.18596/jotcsa.1548185>

***Corresponding author's E-mail:** ncakmak@medipol.edu.tr

1. INTRODUCTION

Epilepsy is one of the most common neurological problems, occurring in 1-2% of people worldwide, although it is particularly prevalent among young people (1). Anti-epileptic drugs (AEDs) are primarily used to treat epilepsy. AEDs are widely used as long-term adjunctive therapy or as monotherapy for other indications. AEDs include drugs that are highly susceptible to interactions (2,3). Valproic acid (2-propylpentanoic acid, VPA) is one of the oldest and most frequently prescribed drugs for epilepsy, bipolar disorder, migraine prophylaxis, schizoaffective disorders, addiction diseases and neuropathic pain (4,5). VPA activity is mediated by an increase in the synthesis and release of γ -aminobutyric acid and blockade of voltage-sensitive sodium channels (6,7). VPA is used as a neuroprotector in cases of Alzheimer's disease (8), migraine (9), and bipolar disorders for multiple tumors, neurodegenerative diseases such as Huntington's disease, Parkinson's disease, Duchenne

progressive dystrophy, etc., and human immunodeficiency syndrome (10,11). Epidemiological studies suggest that VPA can cause hepatotoxicity (12), pancreatitis (13), and teratogenicity (5). The mechanism that causes liver damage has not been fully elucidated; hepatotoxicity may be due to reasons such as the development of oxidative stress, increased apoptosis, and microvesicular liver steatosis (14,15).

An increase in the amount of reactive oxygen characterizes oxidative stress. Disruption of the balance between reactive oxygen species (ROS) and antioxidant mechanisms leads to physiologic and biochemical dysfunctions (16,17). Antioxidants play an important role in disease prevention due to their reactive oxygen species scavenging activity (18). Edaravone (3-methyl-1-phenyl-2-pyrazolin-5-one) is a novel free radical scavenger with potent antioxidant properties and is used in patients with acute brain infarction. Several studies have shown that it prevents cell damage caused by oxidative

stress by capturing hydroxyl radicals and scavenging ROS (19,20). EDA is a lipophilic molecule, and mainly non-enzymatic peroxidation is a new antioxidant moving by inhibiting lipoxygenase activity *in vitro* (21-23). In addition to edaravone's antioxidizing activity, it has anti-inflammatory, anti-apoptotic, and anti-necrotic effects (24).

This study aimed to investigate the potential protective effect of EDA, which has antioxidant properties, against VPA-induced liver injury.

2. EXPERIMENTAL SECTION

2.1. Chemicals

VPA and EDA were obtained from Merck (Darmstadt, Germany). All other chemicals used in the experiments were of analytical purity and were purchased from Merck (Darmstadt, Germany), Sigma-Aldrich (St. Louis, MO, USA), and Fluka (Buchs, Switzerland).

2.2. Laboratory Animals and Experimental Design

All the experimental procedures were approved by the Istanbul University Local Ethics Committee on Animal Research (2010/54-the ethic committee number).

Thirty-eight Sprague Dawley rats (2.5-3 months old, male) were randomly divided into 4 groups. The animals were housed in the standard cage with optimal temperature (20 °C±2) and light/dark (12 h light/12 h dark) conditions. Group I: control rats (n=8). Group II: rats receiving intraperitoneal 0.5 g/kg VPA daily for 7 days (n=10). Group III: rats receiving 30 mg/kg EDA intraperitoneally daily for 7 days (n=10). Group IV: rats receiving 0.5 g/kg VPA, intraperitoneally 30 mg/kg EDA administration daily for 7 days (n=10) (at the same time). All rats were sacrificed under anesthesia 16 hours after VPA and EDA administration. On day 8, liver tissues were taken. Liver homogenates (10% w/v) were prepared in physiological saline (NaCl, 0.9%).

2.3. Biochemical Analysis

Biochemical analyses were performed on blood, serum, and liver homogenates according to the methods specified below.

2.3.1. Estimation of Glutathione (mg % GSH)

Glutathione (GSH) levels were determined by the method using metaphosphoric acid and 5,5'-dithiobis-2-nitrobenzoic acid (DTNB) (25).

2.3.2. Estimation of Total Lipid (mg % Lipid)

The sulfophosphovanillin method was used for the determination of total lipids in serum. This method is based on the principle of pink coloration of lipids with vanillin in sulfuric and phosphoric acid medium. The color intensity was determined in a spectrophotometer at 532 nm (26).

2.3.3. Estimation of Sialic Acid (mmol sialic acid/L)

Sodium periodate was used to oxidize sialic acid (SA) in concentrated phosphoric acid. Next, TBA was combined with the product of periodate oxidation. A

pink chromophore was obtained, which was then extracted into cyclohexanone (27).

2.3.4. Estimation of Aspartate Transaminase (U/ g protein)

Aspartate transaminase (AST) activities were measured by converting L-glutamic acid to oxaloacetic acid, and the color was given by 2,4 dinitrophenyl hydrazine in the medium. The color obtained was measured with a spectrophotometer at 546 nm (28).

2.3.5. Estimation of Alanine Transaminase (U/ g protein)

Alanine transaminase (ALT) activities were measured by converting L-alanine to pyruvic acid and the color given by 2,4 dinitrophenyl hydrazine in the medium. The color obtained was measured with a spectrophotometer at 546 nm (28).

2.3.6. Estimation of Alkaline Phosphatase (U/ g protein)

Alkaline phosphatase (ALP) activities were determined at 405 nm according to the two-point method (29).

2.3.7. Estimation of Gamma-glutamyl Transferase (U/ g protein)

Gamma-glutamyl transferase (GGT) activity is based on the determination of the amount of p-nitroaniline formed as a result of the reaction by reading it in a spectrophotometer (30).

2.3.8. Estimation of Catalase (U /mg protein)

Catalase (CAT) activities were determined based on the reduction of hydrogen peroxide (H₂O₂) to water (H₂O) (31). The decrease in absorbance was measured spectrophotometrically at 240 nm.

2.3.9. Estimation of Superoxide Dismutase (U /g protein)

Superoxide dismutase (SOD) activities were measured as the ability to increase the rate of photooxidation of riboflavin-sensitized o-dianisidine (32).

2.3.10. Estimation of Glutathione Peroxidase (U /g protein)

Glutathione peroxidase (GPx) activities were determined according to the Wendel method, in which the conversion of GSH to GSSG was measured (33).

2.3.11. Estimation of Glutathione Reductase (U /g protein)

Glutathione reductase (GR) activity is based on calculating of the proportion of NADPH oxidized during the reduction of oxidized glutathione (GSSG) by GR at 340 nm (33).

2.3.12. Estimation of Glutathione-S-Transferase (U / mg tissue)

Glutathione-S-transferase (GST) activity was assayed by determining the amount of product obtained by conjugation of GSH with 1-chloro-2,4-dinitrobenzene (CDNB) (34).

2.3.13. Estimation of Proteins

Lowry et al., developed the method to determine the amount of protein in liver tissue (35).

2.4. Statistics

Statistical analysis of biochemical results was calculated with GraphPad Prism 9.0 (GraphPad Software, San Diego, California, USA). Values are shown as mean \pm standard deviation (SD). Unpaired t-test and analysis of variance (ANOVA) followed by Tukey multiple comparison analyses were used for the results. A value of $P < 0.05$ was considered statistically significant.

3. RESULTS AND DISCUSSION

In this study, VPA administration caused a decrease in GSH levels ($p < 0.01$) and an increase in total lipid ($p < 0.0001$) and SA ($p < 0.01$) levels compared to the control group. In addition, GSH levels ($p < 0.001$) increased and total lipid ($p < 0.0001$) and sialic acid

levels ($p < 0.01$) decreased in the VPA+ EDA treated group compared to the VPA (Figure 1).

In our study, there was a significant increase in AST ($p < 0.0001$), ALT ($p < 0.0001$), ALP ($p < 0.0001$) and GGT ($p < 0.001$) activities in the VPA group compared to the control group. However, there was a significant decrease in AST ($p < 0.0001$), ALT ($p < 0.0001$), ALP ($p < 0.0001$) and GGT ($p < 0.01$) activities in the VPA+EDA group compared to the VPA group (Figure 2).

The present study showed that the administration of VPA was associated with a decrease in the activities of CAT ($p < 0.001$), SOD ($p < 0.01$), GPx ($p < 0.05$), GR ($p < 0.001$), GST ($p < 0.0001$) compared to the control group. VPA+EDA group caused a significant increase in CAT ($p < 0.01$), SOD ($p < 0.01$), GPx ($p < 0.001$), GR ($p < 0.01$) and GST ($p < 0.05$) activities compared to VPA group (Figure 3).

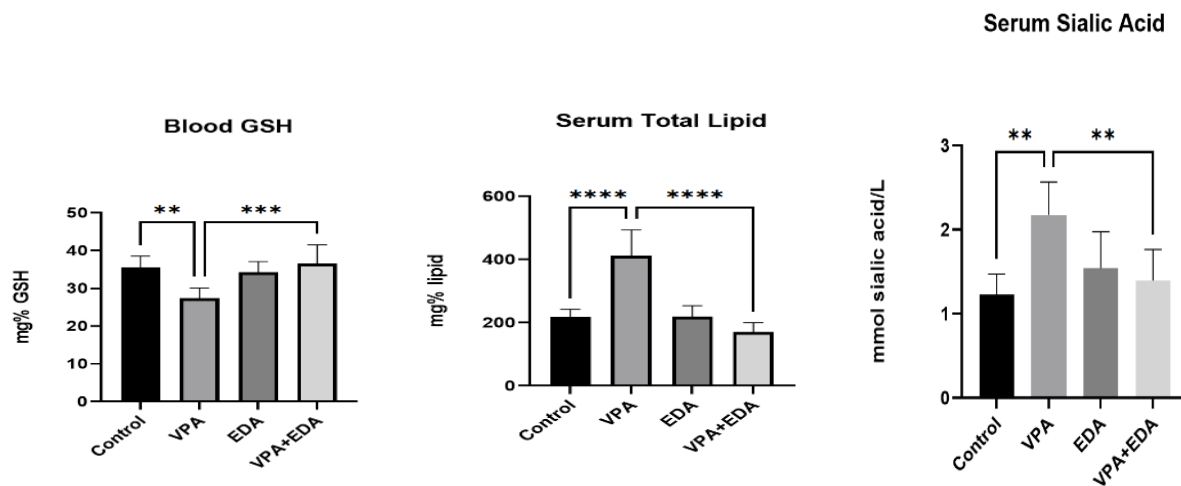


Figure 1: Blood GSH, serum total lipid and serum sialic acid levels.

The columns represent mean \pm SD. VPA: Valproic acid group, EDA: Edaravone group, VPA+EDA: Valproic acid+Edaravone, GSH: Glutathione.

** represent $p < 0.01$, *** represent $p < 0.001$, **** represent $p < 0.0001$

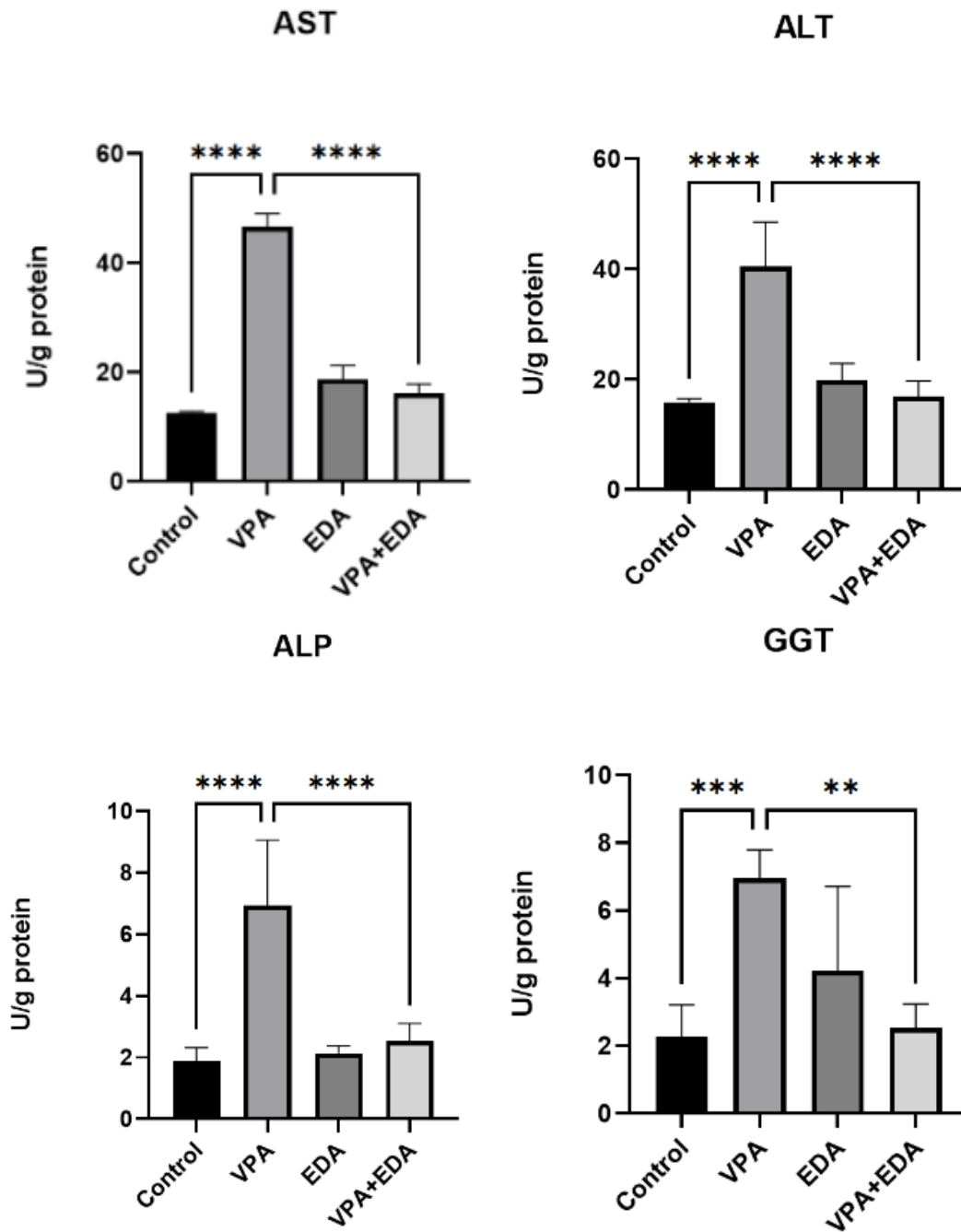


Figure 2: Liver AST, ALT, ALP and GGT activities of the groups.

The columns represent mean \pm SD. VPA: Valproic acid group, EDA: Edaravone group, VPA+EDA: Valproic acid+Edaravone, AST: Aspartate transaminase, ALT: Alanine transaminase, ALP: Alkaline phosphatase, GGT: Gamma-glutamyl transferase.

** represent $p < 0.01$, *** represent $p < 0.001$, **** represent $p < 0.0001$

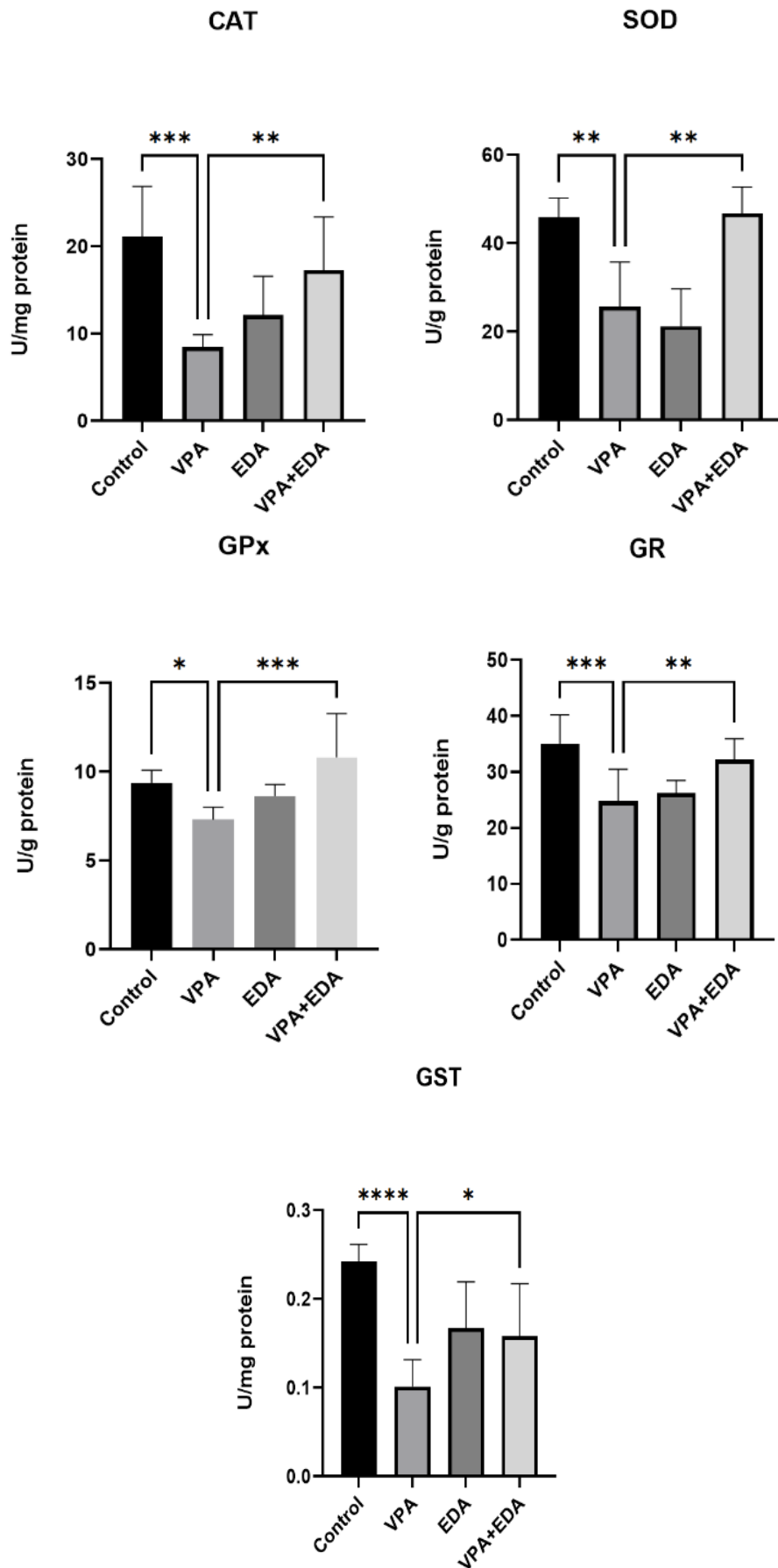


Figure 3: Liver CAT, SOD, GPx, GR and GST activities of the groups

The columns represent mean \pm SD. VPA: Valproic acid group, EDA: Edaravone group, VPA+EDA: Valproic acid+Edaravone, CAT: Catalase, SOD: Superoxide dismutase, GPx: Glutathione peroxidase, GR: Glutathione reductase, GST: Glutathione-S-transferase.

*represent p < 0.05, ** represent p < 0.01, *** represent p < 0.001, **** represent p < 0.0001

VPA is prescribed as a first-line antiepileptic drug due to its high efficacy and low cost and is one of the most common causes of acute liver failure (36,37). Therefore, VPA has been used since the 1960s to treat seizures and mood disorders and to treat many diseases, such as migraine (38). Hepatocyte damage is a common effect after VPA administration and can sometimes lead to irreversible, fatal liver failure. However, oxidative stress is generally considered critical for hepatocyte damage (39). Superoxide radicals, hydroxyl radicals, and hydrogen peroxide radicals cause an increase in ROS in the body, and this increase in ROS disrupts the antioxidant and oxidant balance in the body. Many organs and tissues in the body are adversely affected by this (17, 40). Free radicals impair cell functions and can cause cell death by destroying membrane lipids and proteins (41).

Antioxidants play an important role in disease prevention due to their reactive oxygen species scavenging activity (18). The production of reactive metabolites and ROS can affect GSH balance (42). GSH is an important cell protective biomolecule against synthetic activated cytotoxicity by electrophilic compounds and through glutathione-S-transferase (GST) conjugation (43). GSH is also an important antioxidant agent capable of immediate enzymatic (glutathione peroxidase, GPx) -mediated formation of ROS hydrogen peroxide and lipid hydroperoxides (44). ROS are also removed by antioxidant enzymes such as catalase (CAT), superoxide dismutase (SOD), and reduced GSH. Antioxidants play an important role in disease prevention due to their ROS scavenging activity (45,46).

Edaravone is a free radical scavenger previously approved in Japan for the treatment of patients with acute ischemic stroke, and EDA has also been approved for the treatment of amyotrophic lateral sclerosis due to its neuroprotective effect (23,47). The radical scavenging activity of EDA is mediated by an electron-donating mechanism on a wide range of radical species (48-51). However, the antioxidant mechanisms of EDA are not fully understood. Accordingly, it is hypothesized that EDA may manage oxidative stress by regulating ROS-NOX signaling pathways.

It has been reported that GSH concentration in liver tissue was significantly reduced in VPA group compared to control group (52-54). In another study, it was reported that the amount of GSH decreased in the VPA group compared to the control group (55). In addition, Oktay et al. reported that there was no significant change in GSH level in the VPA group compared to the control group (56). In our study, we found that GSH levels decreased with VPA compared to the control group. Alzoubi et al. reported an increase in GSH levels using EDA in the treatment of memory impairment caused by chronic L-methionine administration (57). In the study investigating the protective effect of EDA on cyclophosphamide-induced oxidative stress and neurotoxicity in rats, it was reported that the amount of GSH increased with EDA (58). EDA increased GSH

levels in a study on oxidative stress and allergic airway inflammation (59). In our study, GSH levels were significantly increased in the VPA + EDA group compared to the VPA group.

Dyslipidemia is implicated in the development of cardiovascular diseases. In particular, high total cholesterol and low-density lipoprotein cholesterol (LDL-C) levels as well as low high-density lipoprotein cholesterol (HDL-C) are associated with cardiovascular mortality. VPA is well known to cause weight gain and insulin resistance and to increase triglyceride levels (60). Different effects of VPA on total cholesterol have been described in previous studies. Nikolaos et al. reported that VPA decreased total cholesterol levels, while Erminio et al. reported that VPA increased cholesterol levels (61,62). According to another study, a decrease in total cholesterol and low-density lipoprotein levels was observed in pediatric groups given VPA (63). In our study, we found that total lipid levels in serum increased with VPA compared to the control group. Experimental studies show that antioxidants have protective effects on atherosclerosis and endothelial damage. Dietary antioxidants have been reported to protect endothelial function (64,65) and prevent atherosclerosis in cholesterol-fed rabbits (66). Xi et al. have reported that mice given high doses of cholesterol in their diet and given EDA at the same time for 4 weeks had smaller atherosclerosis lesions (67). In our study, total lipid levels in serum decreased with EDA administration to the VPA group.

SA levels have been reported to increase during inflammatory processes, probably due to increased levels of acute phase glycoproteins, hypertriglyceridemia, and atherosclerosis (68-72). Various studies have reported that SA is a marker for inflammatory diseases. Increased SA levels reflect the body's self-protection (68-72). In our study, VPA administered to rats caused a significant increase in sialic acid levels in serum. Oktay et al. reported that administration of VPA+EDA group SA levels decreased when compared to the VPA group (56). EDA administration has been reported to cause a significant decrease in SA levels in pancreatic functions compared to VPA animals (73). In our study, it was observed that SA levels, which were increased by EDA administration to the VPA group, decreased.

Abdelkader et al., (2020) reported that VPA administration caused a significant increase in ALT, AST, ALP, and GGT activities in serum, which are considered to be an indicator of hepatocellular damage (53). Various studies have shown that VPA administration causes liver damage and significantly increases serum ALT, AST, and ALP levels compared to the control group (54,74). Koroglu et al. showed that administration of VPA group serum ALT levels significantly decreased when compared to the control group. There was no significant difference among the groups in terms of serum AST and GGT levels (75). In our study, VPA caused a significant increase in AST, ALT, ALP, and GGT activities in liver tissue. Hassanein et al. reported that the administration of VPA+EDA group AST, ALT, and ALP levels decreased

when compared to the VPA group (76). In our study, VPA+EDA group AST, ALT, ALP and GGT values decreased compared to VPA group.

Reactive oxygen species formed in the body are also removed by antioxidant enzymes. Antioxidants play an important role in the prevention of diseases due to their ROS scavenging activities (45,46). VPA administration has been reported to significantly decrease CAT in the autistic groups compared with the healthy groups (77). It has been reported that the activities of SOD were decreased in the liver of VPA-treated rats compared to the control group (75). In our study, CAT and SOD enzyme activities were lower in the VPA group compared to the control group. Sheng-Rui Fan et al. showed that administration of EDA group CAT and SOD levels increased when compared to the VPA group (78). EDA administration has been reported to cause a significant increase in SOD levels in heart functions compared to VPA animals (79). All these studies (78,79) support our findings that CAT and SOD values increased in rats administered VPA+ EDA.

There are conflicting results in GPx activities. CE reported decreased GPx activity in erythrocytes of patients treated with VPA, and Cotariu et al. reported decreased GPx activity in rats treated with intraperitoneal VPA (80,81). In contrast to these results, Hamed et al., Cengiz et al., and Kurekci et al. found an increase in GPx activity in VPA-treated patients (82-84). In our study, a decrease in GPx activity was observed in the VPA group. The decrease in GPx levels may indicate that the antioxidant capacity, which is effective in preventing various damages caused by VPA metabolism and its side effects, has decreased. It has been reported that EDA administration caused a significant increase in GPx activity in the VPA group (85). In our study, a decrease in GPx activity and GSH levels was observed in the VPA group and a significant increase in GSH and GPx activities in the VPA + EDA group.

GR is one of the antioxidant enzymes (86) and Oztaylan et al. investigated the effect of VPA on the lens and reported that the amount of GR increased with VPA administration (87). Turkyilmaz et al. reported that GR activity decreased in VPA-induced brain injury (55). In another study, it was reported that GR activity decreased in the VPA group compared to the control group (88). In this study, we found that GR activity in liver tissue was significantly decreased in the VPA group. Hassan et al. reported an increase in GR, one of the antioxidant enzymes, in heart tissue when EDA was given for protection against isoproterenol (ISO) (89). Bayrak et al. reported that glutathione reductase activities decreased insignificantly in the VPA group in lung tissue, whereas GR activity increased significantly in the EDA group (85). In our study, VPA+EDA group GR values increased compared to the VPA group.

Tong et al. found an increase in α -GST levels, a marker of hepatocyte damage, in serum 4 days after VPA treatment (90), while Chaudhary et al. found a decrease in GST activity in the cerebellum and cerebral cortex (91). In another study, in valproic

acid-induced brain injury, GST decreased in the VPA group compared to the control group (55). It was reported that a decrease in GST levels in a rat model study of VPA-induced autism spectrum disorder (92). We found a significant decrease in GST activity in liver tissue in the VPA group compared to the control group. EDA administration has been reported to cause a significant increase in GST levels in heart functions compared to VPA animals (79). In another study, GST activity increased in the VPA+EDA group compared to the VPA group (89). Lu et al. reported an increase in GST levels in the VPA+EDA group compared to the EDA group (92). We found a significant decrease in GST activity in liver tissue VPA+ EDA group compared to the VPA group.

4. CONCLUSION

VPA is a widely used anti-antiepileptic. Although it has beneficial effects, there are many systems and organs that are affected due to its serious side effects. The liver is the organ most exposed to and affected by toxicity and free radical species. Protecting this tissue is a vital goal for all research. For this purpose, EDA was chosen as a preservative because its protective effects have been shown in previous studies and it is a good antioxidant. The biochemical results obtained from this study support the protective effects of EDA on liver tissue exposed to VPA.

5. CONFLICT OF INTEREST

There are no conflicts to declare.

6. REFERENCES

1. Hauser WA. The prevalence and incidence of convulsive disorders in children. *Epilepsia* [Internet]. 1994 Apr 5;35(s2):S1-6. Available from: [<URL>](#).
2. Johannessen Landmark C. Antiepileptic drugs in non-epilepsy disorders. *CNS Drugs* [Internet]. 2008 Aug 29;22(1):27-47. Available from: [<URL>](#).
3. Johannessen Landmark C, Larsson PG, Rytter E, Johannessen SI. Antiepileptic drugs in epilepsy and other disorders—A population-based study of prescriptions. *Epilepsy Res* [Internet]. 2009 Nov 1;87(1):31-9. Available from: [<URL>](#).
4. García-Morales I, Sancho Rieger J, Gil-Nagel A, Herranz Fernández JL. Antiepileptic drugs. *Neurologist* [Internet]. 2007 Nov;13(6):S20-8. Available from: [<URL>](#).
5. Jentink J, Loane MA, Dolk H, Barisic I, Garne E, Morris JK, et al. Valproic acid monotherapy in pregnancy and major congenital malformations. *N Engl J Med* [Internet]. 2010 Jun 10;362(23):2185-93. Available from: [<URL>](#).
6. Rahman M, Awosika AO, Nguyen H. Valproic acid StatPearls . 2024. Available from: [<URL>](#).
7. Mishra MK, Kukal S, Paul PR, Bora S, Singh A, Kukreti S, et al. Insights into structural modifications of valproic acid and their pharmacological profile.

Molecules [Internet]. 2021 Dec 24;27(1):104. Available from: [<URL>](#).

8. Zhang XZ, Li XJ, Zhang HY. Valproic acid as a promising agent to combat Alzheimer's disease. Brain Res Bull [Internet]. 2010 Jan 15;81(1):3-6. Available from: [<URL>](#).

9. Brown BL, Craycraft LK, Justice SB. Valproic acid in the treatment of migraines. Adv Emerg Nurs J [Internet]. 2020 Oct 1;42(4):243-53. Available from: [<URL>](#).

10. Shnayder NA, Grechkina V V., Khasanova AK, Bochanova EN, Dontceva EA, Petrova MM, et al. Therapeutic and toxic effects of valproic acid metabolites. Metabolites [Internet]. 2023 Jan 16;13(1):134. Available from: [<URL>](#).

11. Yee CS, Vázquez GH, Hawken ER, Biorac A, Tondo L, Baldessarini RJ. Long-term treatment of bipolar disorder with valproate: Updated systematic review and meta-analyses. Harv Rev Psychiatry [Internet]. 2021 May 1;29(3):188-95. Available from: [<URL>](#).

12. Meseguer ES, Elizalde MU, Borobia AM, Ramírez E. Valproic acid-induced liver injury: A case-control study from a prospective pharmacovigilance program in a tertiary hospital. J Clin Med [Internet]. 2021 Mar 10;10(6):1153. Available from: [<URL>](#).

13. Nørgaard M, Jacobsen J, Ratanajamit C, Jepsen P, McLaughlin JK, Pedersen L, et al. Valproic acid and risk of acute pancreatitis: A population-based case-control study. 2006;13(2):113-7. Available from: [<URL>](#).

14. Salimi A, Alyan N, Akbari N, Jamali Z, Pourahmad J. Selenium and L-carnitine protects from valproic acid-Induced oxidative stress and mitochondrial damages in rat cortical neurons. Drug Chem Toxicol [Internet]. 2022 May 4;45(3):1150-7. Available from: [<URL>](#).

15. Gayam V, Mandal AK, Khalid M, Shrestha B, Garlapati P, Khalid M. Valproic acid induced acute liver injury resulting in hepatic encephalopathy- a case report and literature review. J Community Hosp Intern Med Perspect [Internet]. 2018 Sep 3;8(5):311-4. Available from: [<URL>](#).

16. Rodriguez C, Mayo JC, Sainz RM, Antolín I, Herrera F, Martín V, et al. Regulation of antioxidant enzymes: A significant role for melatonin. J Pineal Res [Internet]. 2004 Jan 11;36(1):1-9. Available from: [<URL>](#).

17. Gunata M, Parlakpinar H, Acet HA. Melatonin: A review of its potential functions and effects on neurological diseases. Rev Neurol (Paris) [Internet]. 2020 Mar 1;176(3):148-65. Available from: [<URL>](#).

18. Kabuto H, Hasuike S, Minagawa N, Shishibori T. Effects of bisphenol A on the metabolisms of active oxygen species in mouse tissues. Environ Res [Internet]. 2003 Sep 1;93(1):31-5. Available from: [<URL>](#).

19. Green A, Ashwood T. Free radical trapping as a therapeutic approach to neuroprotection in stroke: Experimental and clinical studies with NXY-059 and free radical scavengers. Curr Drug Target -CNS Neurol Disord [Internet]. 2005 Apr 1;4(2):109-18. Available from: [<URL>](#).

20. Saini AK, Patel RJ, Sharma SS, H. S. AK. Edaravone attenuates hydroxyl radical stress and augmented angiotensin II response in diabetic rats. Pharmacol Res [Internet]. 2006 Jul 1;54(1):6-10. Available from: [<URL>](#).

21. Abe K, Yuki S, Kogure K. Strong attenuation of ischemic and postischemic brain edema in rats by a novel free radical scavenger. Stroke [Internet]. 1988 Apr;19(4):480-5. Available from: [<URL>](#).

22. Nishi H, Watanabe T, Sakurai H, Yuki S, Ishibashi A. Effect of MCI-186 on brain edema in rats. Stroke [Internet]. 1989 Sep;20(9):1236-40. Available from: [<URL>](#).

23. Watanabe K, Tanaka M, Yuki S, Hirai M, Yamamoto Y. How is edaravone effective against acute ischemic stroke and amyotrophic lateral sclerosis? J Clin Biochem Nutr [Internet]. 2018 Jan 1;62(1):20-38. Available from: [<URL>](#).

24. Kikuchi K, Tanchaen S, Takeshige N, Yoshitomi M, Morioka M, Murai Y, et al. The efficacy of edaravone (Radicut), a free radical scavenger, for cardiovascular disease. Int J Mol Sci [Internet]. 2013 Jul 4;14(7):13909-30. Available from: [<URL>](#).

25. Beutler E. Glutathione in red blood cell metabolism. A manual biochem methods. Ann Intern Med [Internet]. 1975;83(6):919. Available from: [<URL>](#).

26. Frings CS, Fendley TW, Dunn RT, Queen CA. Improved determination of total serum lipids by the sulfo-phospho-vanillin reaction. Clin Chem [Internet]. 1972 Jul 1;18(7):673-4. Available from: [<URL>](#).

27. Warren L. The thiobarbituric acid assay of sialic acids. J Biol Chem [Internet]. 1959;234(8):1971-5. Available from: [<URL>](#).

28. Reitman S, Frankel S. A colorimetric method for the determination of serum glutamic oxalacetic and glutamic pyruvic transaminases. Am J Clin Pathol [Internet]. 1957 Jul 1;28(1):56-63. Available from: [<URL>](#).

29. Walter K, Schütt C. Acid and alkaline phosphatase in serum. In: Urlich Bergmeyer H, editor. Methods Enzym Anal [Internet]. 1974. p. 856-60. Available from: [<URL>](#).

30. Szasz G. A kinetic photometric method for serum γ -Glutamyl transpeptidase. Clin Chem [Internet]. 1969 Feb 1;15(2):124-36. Available from: [<URL>](#).

31. Aebi H. Catalase *in vitro*. Methods Enzymol [Internet]. 1984; 105: 121-6. Available from: [<URL>](#).





32. Mylroie AA, Collins H, Umbles C, Kyle J. Erythrocyte superoxide dismutase activity and other parameters of copper status in rats ingesting lead acetate. *Toxicol Appl Pharmacol* [Internet]. 1986 Mar 15;82(3):512–20. Available from: [<URL>](#).
33. Wendel A. Glutathione peroxidase. *Methods Enzymol*; 1981.77: 325–33. Available from: [<URL>](#).
34. Habig WH, Jakoby WB. Assays for differentiation of glutathione S-Transferases. *Methods Enzymol*. [Internet] Academic Press; 1981. 77: 398–405. Available from: [<URL>](#).
35. Lowry O, Rosebrough N, Farr A, Randall R. Protein measurement with the folin phenol reagent. *J Biol Chem* [Internet]. 1951;193(1):265–75. Available from: [<URL>](#).
36. Andrade RJ, Chalasani N, Björnsson ES, Suzuki A, Kullak-Ublick GA, Watkins PB, et al. Drug-induced liver injury. *Nat Rev Dis Prim* [Internet]. 2019 Aug 22;5(1):58. Available from: [<URL>](#).
37. Shah J, Lingiah V, Pysropoulos N, Galan M. Acute liver injury in a patient treated with rosuvastatin: A rare adverse effect. *Gastroenterol Res* [Internet]. 2019;12(5):263–6. Available from: [<URL>](#).
38. Zhou L, Chen L, Zeng X, Liao J, Ouyang D. Ginsenoside compound K alleviates sodium valproate-induced hepatotoxicity in rats via antioxidant effect, regulation of peroxisome pathway and iron homeostasis. *Toxicol Appl Pharmacol* [Internet]. 2020 Jan 1;386:114829. Available from: [<URL>](#).
39. Chang TKH, Abbott FS. Oxidative stress as a mechanism of valproic acid-associated hepatotoxicity. *Drug Metab Rev* [Internet]. 2006 Jan 9;38(4):627–39. Available from: [<URL>](#).
40. Murphy MP. How mitochondria produce reactive oxygen species. *Biochem J* [Internet]. 2009 Jan 1;417(1):1–13. Available from: [<URL>](#).
41. Cagin YF, Parlakpınar H, Polat A, Vardi N, Atayan Y, Erdogan MA, et al. The protective effects of apocynin on ionizing radiation-induced intestinal damage in rats. *Drug Dev Ind Pharm* [Internet]. 2016 Feb 1;42(2):317–24. Available from: [<URL>](#).
42. Graf W, Oleinik O, Glauser T, Maertens P, Eder D, Pippenger C. Altered antioxidant enzyme activities in children with a serious adverse experience related to valproic acid therapy. *Neuropediatrics* [Internet]. 1998 Aug 12;29(04):195–201. Available from: [<URL>](#).
43. Reed DJ. Glutathione: Toxicological implications. *Annu Rev Pharmacol Toxicol* [Internet]. 1990 Apr 1;30(1):603–31. Available from: [<URL>](#).
44. Meister A. Selective modification of glutathione metabolism. *Science* (80-) [Internet]. 1983 Apr 29;220(4596):472–7. Available from: [<URL>](#).
45. Bindhumol V, Chitra KC, Mathur PP. Bisphenol A induces reactive oxygen species generation in the liver of male rats. *Toxicology* [Internet]. 2003 Jun 30;188(2–3):117–24. Available from: [<URL>](#).
46. Kabuto H, Amakawa M, Shishibori T. Exposure to bisphenol A during embryonic/fetal life and infancy increases oxidative injury and causes underdevelopment of the brain and testis in mice. *Life Sci* [Internet]. 2004 Apr 30;74(24):2931–40. Available from: [<URL>](#).
47. Bailly C, Hecquet PE, Kouach M, Thuru X, Goossens JF. Chemical reactivity and uses of 1-phenyl-3-methyl-5-pyrazolone (PMP), also known as edaravone. *Bioorg Med Chem* [Internet]. 2020 May 15;28(10):115463. Available from: [<URL>](#).
48. Yamamoto Y, Kuwahara T, Watanabe K, Watanabe K. Antioxidant activity of 3-methyl-1-phenyl-2-pyrazolin-5-one. *Redox Rep* [Internet]. 1996 Oct 13;2(5):333–8. Available from: [<URL>](#).
49. Ohara K, Fujii A, Ichimura Y, Sato K, Mukai K. Kinetic study of radical-scavenging and vitamin E-regenerating actions of edaravone (3-Methyl-1-phenyl-2-pyrazolin-5-one). *Bull Chem Soc Jpn* [Internet]. 2006 Mar 1;79(3):421–6. Available from: [<URL>](#).
50. Hu C, Nydes M, Shanley KL, Morales Pantoja IE, Howard TA, Bizzozero OA. Reduced expression of the ferroptosis inhibitor glutathione peroxidase-4 in multiple sclerosis and experimental autoimmune encephalomyelitis. *J Neurochem* [Internet]. 2019 Feb 3;148(3):426–39. Available from: [<URL>](#).
51. Ferretti G, Bacchetti T. Peroxidation of lipoproteins in multiple sclerosis. *J Neurol Sci* [Internet]. 2011 Dec 15;311(1–2):92–7. Available from: [<URL>](#).
52. Hussein AM, Awadalla A, Abbas KM, Sakr HF, Elghaba R, Othman G, et al. Chronic valproic acid administration enhances oxidative stress, upregulates IL6 and downregulates Nrf2, Glut1 and Glut4 in rat's liver and brain. *Neuroreport* [Internet]. 2021 Jul 7;32(10):840–50. Available from: [<URL>](#).
53. Abdelkader NF, Elyamany M, Gad AM, Assaf N, Fawzy HM, Elesawy WH. Ellagic acid attenuates liver toxicity induced by valproic acid in rats. *J Pharmacol Sci* [Internet]. 2020 May 1;143(1):23–9. Available from: [<URL>](#).
54. Khodayar MJ, Kalantari H, Khorsandi L, Ahangar N, Samimi A, Alidadi H. Taurine attenuates valproic acid-induced hepatotoxicity via modulation of RIPK1/RIPK3/MLKL-mediated necroptosis signaling in mice. *Mol Biol Rep* [Internet]. 2021 May 25;48(5):4153–62. Available from: [<URL>](#).
55. Turkeyilmaz IB, Altas N, Arisan I, Yanardag R. Effect of vitamin B₆ on brain damage in valproic acid induced toxicity. *J Biochem Mol Toxicol* [Internet]. 2021 Sep 26;35(9):e22855. Available from: [<URL>](#).
56. Oktay S, Alev B, Tunali S, Emekli-Alturfan E, Tunali-Akbay T, Koc-Ozturk L, et al. Edaravone ameliorates the adverse effects of valproic acid toxicity in small intestine. *Hum Exp Toxicol*

- [Internet]. 2015 Jun 10;34(6):654–61. Available from: [<URL>](#).
57. Alzoubi KH, Aburashed ZO, Mayyas F. Edaravone protects from memory impairment induced by chronic L-methionine administration. *Naunyn Schmiedeberg Arch Pharmacol* [Internet]. 2020 Jul 27;393(7):1221–8. Available from: [<URL>](#).
58. Singh S, Kumar A. Protective effect of edaravone on cyclophosphamide induced oxidative stress and neurotoxicity in rats. *Curr Drug Saf* [Internet]. 2019 Sep 17;14(3):209–16. Available from: [<URL>](#).
59. Zhu G, Zeng Y, Peng W, Lu C, Cai H, Abuduxukuer Z, et al. Edaravone alleviated allergic airway inflammation by inhibiting oxidative stress and endoplasmic reticulum stress. *Eur J Pharmacol* [Internet]. 2024 Jan 5;966:176317. Available from: [<URL>](#).
60. Yamamoto Y, Terada K, Takahashi Y, Imai K, Kagawa Y, Inoue Y. Influence of antiepileptic drugs on serum lipid levels in adult epilepsy patients. *Epilepsy Res* [Internet]. 2016 Nov 1;127:101–6. Available from: [<URL>](#).
61. Nikolaos T, Stylianos G, Chryssoula N, Irini P, Christos M, Dimitrios T, et al. The effect of long-term antiepileptic treatment on serum cholesterol (TC, HDL, LDL) and triglyceride levels in adult epileptic patients on monotherapy. *Med Sci Monit* [Internet]. 2004;10(4):MT50–2. Available from: [<URL>](#).
62. Erminio C, Ferini-Strambi L, Calori G, Zamboni M, Iannaccone S, Smirne S. Effect of chronic antiepileptic treatment on biochemical parameters. *Clin Neuropharmacol* [Internet]. 1994;17(2):199–203. Available from: [<URL>](#).
63. Guo H, Dong N, Chen F, Zeng Y, Hu Y, Xia Y, et al. Effect of long-term valproic acid therapy on lipid profiles in paediatric patients with epilepsy: A meta-analysis. *Epileptic Disord* [Internet]. 2022 Oct 3;24(5):822–30. Available from: [<URL>](#).
64. Keaney JF, Gaziano JM, Xu A, Frei B, Curran-Celentano J, Shwaery GT, et al. Dietary antioxidants preserve endothelium-dependent vessel relaxation in cholesterol-fed rabbits. *Proc Natl Acad Sci* [Internet]. 1993 Dec 15;90(24):11880–4. Available from: [<URL>](#).
65. Keaney JF, Xu A, Cunningham D, Jackson T, Frei B, Vita JA. Dietary probucol preserves endothelial function in cholesterol-fed rabbits by limiting vascular oxidative stress and superoxide generation. *J Clin Invest* [Internet]. 1995 Jun 1;95(6):2520–9. Available from: [<URL>](#).
66. Lamb DJ, Reeves GL, Taylor A, Ferns GA. Dietary copper supplementation reduces atherosclerosis in the cholesterol-fed rabbit. *Atherosclerosis* [Internet]. 1999 Sep 1;146(1):33–43. Available from: [<URL>](#).
67. Xi H, Akishita M, Nagai K, Yu W, Hasegawa H, Eto M, et al. Potent free radical scavenger, edaravone, suppresses oxidative stress-induced endothelial damage and early atherosclerosis. *Atherosclerosis* [Internet]. 2007 Apr 1;191(2):281–9. Available from: [<URL>](#).
68. Varki A. Sialic acids in human health and disease. *Trends Mol Med* [Internet]. 2008 Aug 1;14(8):351–60. Available from: [<URL>](#).
69. Succari M, Foglietti MJ, Percheron F. Perchlorosoluble glycoproteins and myocardial infarct: modifications of the carbohydrate moiety (author's transl. *Pathol Biol* [Internet]. 1982 Mar 1;30(3):151–4. Available from: [<URL>](#).
70. Crook M, Tutt P. Serum sialic acid concentration in patients with hypertriglyceridaemia showing the Frederickson's IIB phenotype. *Clin Sci* [Internet]. 1992 Nov 1;83(5):593–5. Available from: [<URL>](#).
71. Rastam L, Lindberg G, Folsom AR, Burke GL, Nilsson-Ehle P, Lundblad A. Association between serum sialic acid concentration and carotid atherosclerosis measured by B-mode ultrasound. *Int J Epidemiol* [Internet]. 1996;25(5):953–8. Available from: [<URL>](#).
72. Crook M, Haq M, Haq S, Tutt P. Plasma sialic acid and acute-phase proteins in patients with myocardial infarction. *Angiology* [Internet]. 1994 Aug 1;45(8):709–15. Available from: [<URL>](#).
73. Oktay S, Alev-Tüzüner B, Tunalı S, Ak E, Emekli-Alturfan E, Tunalı-Akbay T, et al. Investigation of the effects of edaravone on valproic acid induced tissue damage in pancreas. *Marmara Pharm J* [Internet]. 2017 Jun 20;21(3):570–7. Available from: [<URL>](#).
74. Kandemir FM, Ileriturk M, Gur C. Rutin protects rat liver and kidney from sodium valproate-induced damage by attenuating oxidative stress, ER stress, inflammation, apoptosis and autophagy. *Mol Biol Rep* [Internet]. 2022 Jul 29;49(7):6063–74. Available from: [<URL>](#).
75. Koroglu OF, Gunata M, Vardi N, Yildiz A, Ates B, Colak C, et al. Protective effects of naringin on valproic acid-induced hepatotoxicity in rats. *Tissue Cell* [Internet]. 2021 Oct 1;72:101526. Available from: [<URL>](#).
76. Hassanein EHM, Mohamed WR, Hussein RM, Arafa ESA. Edaravone alleviates methotrexate-induced testicular injury in rats: Implications on inflammation, steroidogenesis, and Akt/p53 signaling. *Int Immunopharmacol* [Internet]. 2023 Apr 1;117:109969. Available from: [<URL>](#).
77. Seyedinia SA, Tarahomi P, Abbarin D, Sedaghat K, Rashidy-Pour A, Yaribeygi H, et al. Saffron and crocin ameliorate prenatal valproic acid-induced autistic-like behaviors and brain oxidative stress in the male offspring rats. *Metab Brain Dis* [Internet]. 2023 Oct 11;38(7):2231–41. Available from: [<URL>](#).
78. Fan SR, Ren TT, Yun MY, Lan R, Qin XY. Edaravone attenuates cadmium-induced toxicity by inhibiting oxidative stress and inflammation in ICR mice. *Neurotoxicology* [Internet]. 2021 Sep 1;86:1–9. Available from: [<URL>](#).

79. Emekli Alturfan E, Alev B, Tunali S, Oktay S, Tunali AT, Ozturk L, et al. Effects of Edaravone on Cardiac Damage in Valproic Acid Induced Toxicity. *Ann Clin Lab Sci* [Internet]. 2015;45(2):166–72. Available from: [<URL>](#).
80. Pippenger CE. Valproate therapy depresses GSH-Px and superoxide dismutase enzyme activity. A possible mechanism for VPA induced idiosyncratic drug toxicity. *Clin Chem* [Internet]. 1989;35:1173-. Available from: [<URL>](#).
81. Cotariu D, Evans S, Zaidman JL, Marcus O. Early changes in hepatic redox homeostasis following treatment with a single dose of valproic acid. *Biochem Pharmacol* [Internet]. 1990 Aug 1;40(3):589–93. Available from: [<URL>](#).
82. Hamed SA, Abdellah MM, El-Melegy N. Blood levels of trace elements, electrolytes, and oxidative stress/antioxidant systems in epileptic patients. *J Pharmacol Sci* [Internet]. 2004;96(4):465–73. Available from: [<URL>](#).
83. Cengiz M, Yüksel A, Seven M. The effects of carbamazepine and valproic acid on the erythrocyte glutathione, glutathione peroxidase, superoxide dismutase and serum lipid peroxidation in epileptic children. *Pharmacol Res* [Internet]. 2000 Apr 1;41(4):423–5. Available from: [<URL>](#).
84. Kürekçi AE, Alpay F, Tanindi Ş, Gokçay E, Ozcan O, Akin R, et al. Plasma trace element, plasma glutathione peroxidase, and superoxide dismutase levels in epileptic children receiving antiepileptic drug therapy. *Epilepsia* [Internet]. 1995 Jun 28;36(6):600–4. Available from: [<URL>](#).
85. Bayrak BB, Yilmaz S, Hacıhasanoglu Cakmak N, Yanardag R. The effects of edaravone, a free-radical scavenger in lung injury induced by valproic acid demonstrated via different biochemical parameters. *J Biochem Mol Toxicol* [Internet]. 2021 Sep 26;35(9):e22847. Available from: [<URL>](#).
86. Tabassum H, Parvez S, Rehman H, Dev Banerjee B, Siemen D, Raisuddin S. Nephrotoxicity and its prevention by taurine in tamoxifen induced oxidative stress in mice. *Hum Exp Toxicol* [Internet]. 2007 Jun 1;26(6):509–18. Available from: [<URL>](#).
87. Öztaylan Y, Türkyılmaz İ, Yanardağ R. The effects of alpha lipoic acid on lens injury in rats administered with valproic acid. *J Istanbul Fac Med* [Internet]. 2022 Aug 17;85(4):557–63. Available from: [<URL>](#).
88. Chaudhary S, Parvez S. An *in vitro* approach to assess the neurotoxicity of valproic acid-induced oxidative stress in cerebellum and cerebral cortex of young rats. *Neuroscience* [Internet]. 2012 Dec 6;225:258–68. Available from: [<URL>](#).
89. Hassan MQ, Akhtar MS, Akhtar M, Ali J, Haque SE, Najmi AK. Edaravone protects rats against oxidative stress and apoptosis in experimentally induced myocardial infarction: Biochemical and ultrastructural evidence. *Redox Rep* [Internet]. 2015 Nov 2;20(6):275–81. Available from: [<URL>](#).
90. Tong V, Teng XW, Chang TKH, Abbott FS. Valproic acid I: Time course of lipid peroxidation biomarkers, liver toxicity, and valproic acid metabolite levels in rats. *Toxicol Sci* [Internet]. 2005 Aug 1;86(2):427–35. Available from: [<URL>](#).
91. Chaudhary S, Ganjoo P, Raiusddin S, Parvez S. Nephroprotective activities of quercetin with potential relevance to oxidative stress induced by valproic acid. *Protoplasma* [Internet]. 2015 Jan 8;252(1):209–17. Available from: [<URL>](#).
92. Lu XY, Li MQ, Li YT, Yao JY, Zhang LX, Zeng ZH, et al. Oral edaravone ameliorates behavioral deficits and pathologies in a valproic acid-induced rat model of autism spectrum disorder. *Neuropharmacology* [Internet]. 2024 Nov 1;258:110089. Available from: [<URL>](#).



Using of Benzotriazolium Iodide Ionic Liquids for Extractive Desulfurization of Model Diesel Oil

Assim A. Sabah^{1*} , Safa Aldeen A. Sulyman¹ , Ahmed A. Aldabagh¹ , Arqam K. Ayoob¹ ,
Mohammed Alsultan¹ , Rowaa T. Hameed¹ 

¹Department of Science, College of Basic Education, University of Mosul, Mosul, Iraq.

Abstract: Benzotriazolium-based ionic salts have been prepared with an alkyl group (methyl and allyl), with iodine anion, the prepared compound ([diMBt]I (1), [AMBt]I (2) and [AMBt]I₃ (3) structure have determined by single crystal x-ray and they used for desulfurization of sulfur from model diesel oil in order to obtain reduced sulfur fuel with more environmental friendly properties. The prepared compounds were characterized using several techniques, and their efficiency in removing sulfur from the sample oil was evaluated. The results showed that the removal efficiency was acceptable and could be improved in future research.

Keywords: Ionic liquids, Benzotriazolium base, Desulfurization.

Submitted: December 14, 2023. **Accepted:** October 7, 2024.

Cite this: Sabah AA, Sulyman SAA, Aldabagh AA, Ayoob AK, Alsultan M, Hameed RT. Using of Benzotriazolium Iodide Ionic Liquids for Extractive Desulfurization of Model Diesel Oil. JOTCSA. 2024;11(4): 1641-50.

DOI: <https://doi.org/10.18596/jotcsa.1404722>

***Corresponding author's E-mail:** assimsabah@uomosul.edu.iq

1. INTRODUCTION

Liquids with just ions are generally referred to as anionic liquids. Nevertheless, any salt that is heated to the point of melting, like sodium chloride, is an ionic liquid with a very high melting point of 803°C. This term has another definition that differentiates it from the traditional definition of molten salts. Melted salts are typically considered extremely corrosive, highly viscous, and have a high melting point; however, ionic liquids are liquid at temperatures below 100°C and have a relatively low viscosity. The melting point temperature of 100°C is the relatively sharp boundary that separates molten salts from ionic liquids (1-3).

In theory, there are one trillion different types of ionic liquids. Ionic liquids are available for chemists to select from based on what their work requires. Organic solvents and ionic liquids are not the same thing. Gases cannot be formed from their evaporation. Thus, ionic liquids cannot produce new air pollution or hazardous gases in chemical experiments. Ionic liquids have been of interest to chemists because they are recyclable multiple times. Therefore, the design, development, and application of chemical products and processes aimed at

minimizing or completely doing away with using and producing substances harmful to the environment and human health is known as "green chemistry" (4-6).

Ionic liquids have many potential uses in the energy sector, from nuclear applications to the petroleum industry. Ionic liquids can potentially address several unresolved problems in the industry, including waste minimization, recycling, and recovering helpful hydrocarbon fuels from refractory sources. Although many of these ideas have been demonstrated in the lab, there have not been many reports or widespread attempts to scale them up to industrial proportions (3,7-9).

The increase in harmful emissions to the atmosphere is one of the effects of industrialized countries' rapid development. Elevated sulfur oxide levels are a primary historical source of air pollution because they can be converted to sulfuric acid when combined with water vapor. This is why high sulfur oxide levels cause unwanted acid rain. The combustion of fossil fuels containing sulfur is the primary source of these pollutant emissions, and environmental regulation efforts are concentrated on reducing emissions from transportation exhaust gases (10-12).

This work aims to determine how well benzotriazolium iodide de-sulfurizes model diesel oil.

2. MATERIAL AND METHODS

2.1. Preparation of Benzotriazolium iodide Salts (13-17)

1,3-dimethyl benzotriazolium iodide salt **[diMBt]I (1)**: The preparation of this compound involved dissolving 0.01 mol, 1.19 g of Benzotriazole in 10 mL of ethanol and adding 0.01 mol, 0.62 mL of methyl iodide to the mixture in a 50 mL round-bottom flask. Next, 10 mL of 10% KOH was added to the mixture. Refluxing the mixture lasted for one hour. The mixture was refluxed for one hour with five milliliters of methyl iodide added. The mixture was extracted three times with an equal volume of regular hexane to eliminate the extra methyl iodide. The solution was then set aside for a day. Diethyl ether was used to extract yellow crystals, filter them, and repeatedly wash them.

1-allyl -3-methyl benzotriazolium iodide salt **[AMBt]I (2)** It was prepared using the same method as in **(1)**, with the exception that, in order to produce brown-yellow crystals, the solution mixture was supplemented with 5 milliliters of allyl chloride in the second step rather than methyl iodide. Compounds **(1)** and **(2)** were characterized by NMR spectroscopy, mass spectroscopy, and other spectroscopic methods such as infrared spectroscopy. The results of these measurements are given in the attached supplementary file. With DMSO-d₆ as the solvent and 20°C, the proton nuclear magnetic resonance was measured using a BRUKER AVANCE DPX 400 MHz instrument. The Trio-1000 Mass Spectrometer was used to perform these measurements.

1-allyl -3-methyl benzotriazolium triiodide salt **[AMBt]I₃ (3)** was accidentally created while the second compound was being prepared, as its precipitated crystals were separated using the same preparation technique from the second compound's remaining solution.

2.2. X-Ray Diffraction

On a (Bruker D8) diffractometer, 1.5 kW graphite monochromated Mo radiations and an APEX CCD detector were used to gather single crystal X-ray data. The crystal's distance from the detector was 5.985 cm. During the data collection process, exposure times of 10 seconds per frame and scan widths of 0.3° were employed.

The crystals' faces were indexed for a numerical absorption correction, and their separations from the center were measured. Three ω scans with varying φ values were used to collect the data, which produced data with an average completeness of 90.2-99.7% in the 2.33 to 33.04° range. The SAINT v7.45a (150) was integrated with the frames. Using SADABS V2008-1 (151), a numerical absorption correction

based on the crystal's size and shape was performed. The structure was solved and improved using X-SEED, a graphical interface for SHELX (18,19).

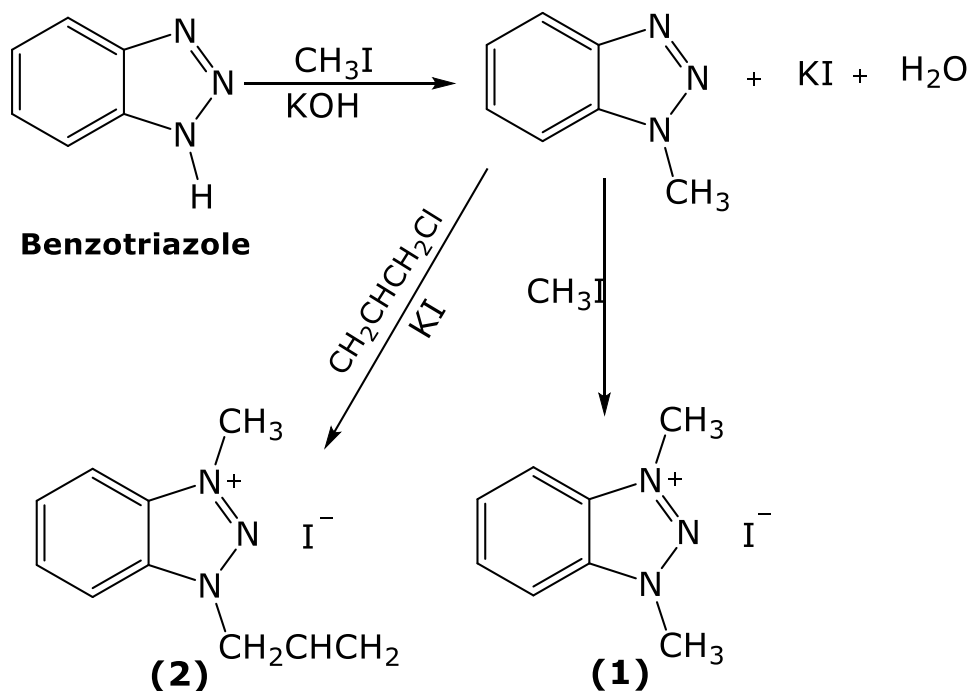
2.3. Desulfurization of Fuel

The model diesel oil was made by dissolving dibenzothiophene (DBT) by weight in n-hexane, resulting in a concentration of 3000 parts per million of DBT. In order to identify the best compound and conduct additional testing with a different concentration, time, and concentration, all of the prepared compounds were tested for extractive desulfurization using model fuel with the same concentration and time (10 g of model fuel, with 0.05 g of the compound dissolved in 5 ml of DMSO, 30 min of extraction). A flame ionization detector is used in gas chromatography (GC-FID). (CARLO ERBA STRUMENT-AZIONE 4200) It was used to perform the gas chromatography. The temperatures of the program are as follows: The temperature of the injector is 295°C, the detector is 273°C, and the oven is 130°C for two minutes before ramping up to 175°C for ten minutes. Details of gas flow rates: "Water:1kg/cm². Cosmetics (air): 1 kg/cm Helium: 2 kg/cm², air: 1.5 kg/cm². Column characteristics: Call sign: SE-30, 30 m in length, 0.53 mm in diameter, and 1.2 μ m in film thickness" (20,21).

3. RESULT AND DISCUSSION

The outcome is dependent on the reaction process, which involves adding methyl (allyl) group to the second nitrogen atom in Benzotriazole and then substituting the methyl group on nitrogen, as illustrated in scheme 1.

¹H-NMR of **[diMBt]I (1)**: DMSO-d₆ was used as a solvent to measure the proton nuclear magnetic resonance (NMR) spectra. The singlet signal at (4.63 ppm) with integration (6.11) is associated with two methyl groups on the 1 and 3 positions of the nitrogen atom. The four protons of the benzene aromatic ring in the benzotriazole are represented by the multiple signals in (7.99 - 8.37 ppm) with integrations of (4.20). The main mass fragments are *m/z*: 133 (100.0%), 132 (20%), 119 (10%). **[AMBt]I (2)**: singlet signal at (2.10 ppm) with integration (2.95) is associated with nitrogen atom methyl groups. The doublet signal in (4.64 ppm) with integrations of 1.84, its chemical shift, and its integration are associated with the protons in the allyl group's terminal (CH₂) group. The protons in the allyl group with the nitrogen atom in the benzotriazole's attached (CH₂) groups are responsible for the second doublet signals in (5.71 ppm) with integrations (1.78). With integrations of 1.04, the multiple signals in (5.46-5.55 ppm) correspond to the proton of (CH) in the allyl group. The four protons of the multiple signals in (8.00-8.02 ppm) and (8.34-8.39 ppm) with integrations of (1.80) and (1.85), respectively, belong to benzotriazole's aromatic ring.



3.1. Characterizations of Salts

The yellow crystals of compound **(1)** [diMBt]I, have been studied using a single crystal X-ray. An orthorhombic crystal system with a P_{nma} space group is present in the crystal size (0.52x 0.51x 0.40

mm³). A perspective drawing of compound **(1)** and the atom-numbering system are displayed in Figure 1. 50% of the time, displacement ellipsoids are depicted, and H atoms are displayed as tiny spheres with arbitrary radii.

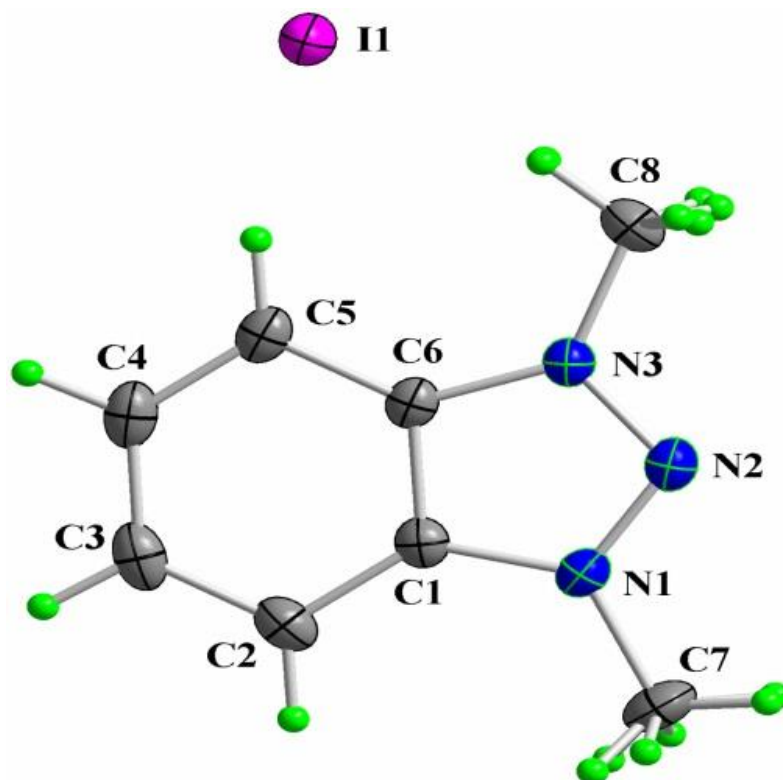


Figure 1: Crystal structure of compound **(1)** [diMBt]I.

Planar organic ions are those that are situated on the crystallographic mirror plane. 50% occupancy results in disordered methyl hydrogen. The positively charged portion of the corresponding cation is not directly connected to the anion I⁻. Instead, I⁻ holds

cations together via C-H...I1 (2.93 Å) and C(3)-H(3)...I1i (2.95 Å) are examples of I-hydrogen bonds. These findings are in good agreement with the literature (17,22). Table 1 contains a list of the crystal data.

Table 1: Crystal data of compound **(1)** [diMBt]I.

Empirical formula	(C ₈ H ₁₀ N ₃) ⁺ · I ⁻	Index ranges	-13 ≤ h ≤ 13, -9 ≤ k ≤ 9, -26 ≤ l ≤ 26
Formula weight	275.09	Reflections collected	16404
Temperature	153(2) K	Independent reflections	1922 [R(int) = 0.0606]
Wavelength	0.71073 Å	Completeness to theta = 32.00°	99.7 %
Crystal system	Orthorhombic	Absorption correction	multi-scan
Space group	P _{nma}	Max. and min. transmission	0.3597 and 0.2858
Unit cell dimensions	a = 8.8972(4) Å α = 90° b = 6.4646(3) Å β = 90° c = 17.0708(7) Å γ = 90°	Refinement method	Full-matrix least-squares on F ²
Volume	981.86(8) Å ³	Data/restraints/parameters	1922 / 0 / 76
Z	4	Goodness-of-fit on F²	1.005
Density (calculated)	1.861 Mg/m ³	Final R indices [I > 2σ(I)]	R1 = 0.0322, wR2 = 0.0773
Absorption coefficient	3.213 mm ⁻¹	R indices (all data)	R1 = 0.0418, wR2 = 0.0816
F(000)	528	Extinction coefficient	0.0398(18)
Crystal size	0.52 × 0.51 × 0.40 mm ³	Largest diff. Peak and hole	1.310 and -1.612 e.Å ⁻³

The Brown-yellow crystals of compound **(2)** [AMBt]I have been studied using a single crystal X-ray. Compound **(2)** crystallizes in the Triclinic space group P-1. A crystal size (0.39 × 0.40 × 0.10 mm³) was measured, and the substitution of methyl and

allyl groups on the 1,3 position on nitrogen atoms was clarified (14). Figure 2 shows the crystal structure of compound **(2)**. The crystal data are listed in Table 2.

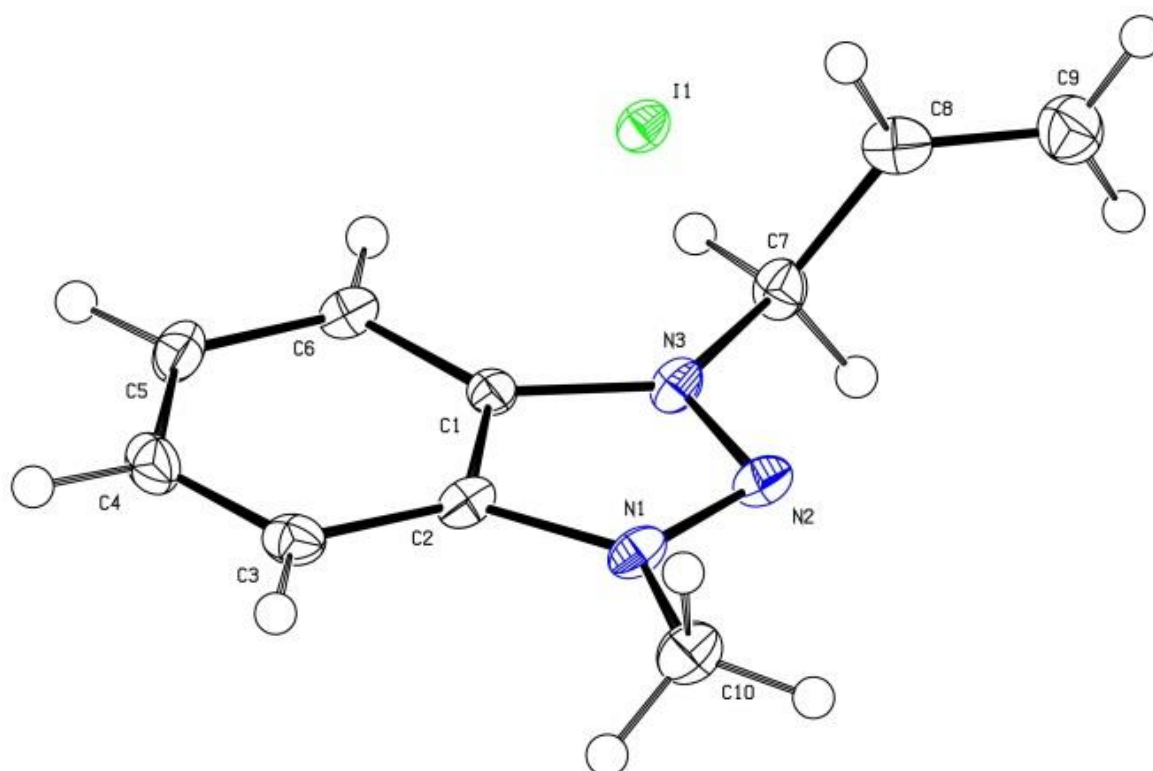
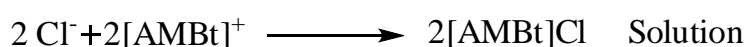
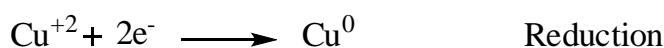
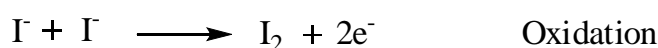
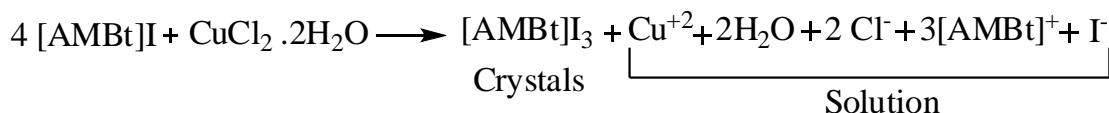
**Figure 2:** Crystal structure of compound **(2)** [AMBt]I.

Table 2: Crystal data of compound **(2)** [AMBt]I.

Empirical formula	(C ₁₀ H ₁₂ N ₃) ⁺ · I ⁻	Index ranges	2.33 to 28.31°.
Formula weight	301.13	Reflections collected	-10<=h<=10, -10<=k<=10, -13<=l<=13
Temperature	100(2) K	Independent reflections	7816
Wavelength	0.71073 Å	Completeness to theta = 32.00°	2798 [R(int) = 0.0894]
Crystal system	Triclinic	Absorption correction	Semi-empirical from equivalents
Space group	P -1	Max. and min. transmission	0.972 and 0.409
Unit cell dimensions	a = 7.8839(12) Å a = 114.093(2)° b = 8.2265(14) Å β = 104.033(15)° c = 9.9957(17) Å γ = 92.201(13)°	Refinement method	Full-matrix least-squares on F ²
Volume	567.20(16) Å ³	Data/restraints/parameters	2798 / 0 / 128
Z	2	Goodness-of-fit on F²	0.955
Density (calculated)	1.763 Mg/m ³	Final R indices [I>2sigma(I)]	R1 = 0.0349, wR2 = 0.0641
Absorption coefficient	2.790 mm ⁻¹	R indices (all data)	R1 = 0.0399, wR2 = 0.0661
F(000)	292	Extinction coefficient	1.581 and -1.354e.Å ⁻³
Crystal size	0.39 x 0.40 x 0.10 mm ³	Largest diff. peak and hole	2.33 to 28.31°.

The unexpected result is the preparation of the novel organic salt [AMBt]I₃ (**3**) isolated as a brown crystal through the preparation of the complex salt of the formula [AMBt]₂[CuCl₂I₂] of complex salt in the

attempt to prepare copper (II) chloride with the organic salt number (2) [AMBt]I. The suggested mechanism is shown in the equations below:



A single crystal x-ray characterized this new organic salt [AMBt]I₃ (**3**). A perspective drawing of compound (**3**) is shown in Figure 3. All the bond

lengths and angles are in the normal range and similar to those in the literature data (23,24).

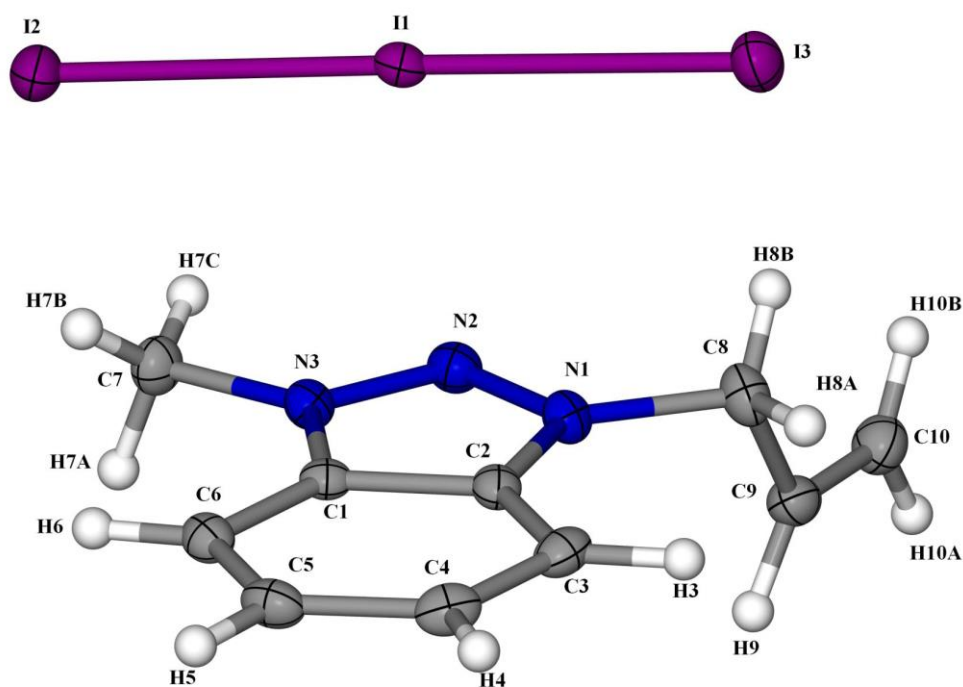


Figure 3: The crystal structure of compound **(3)** [AMBt] I_3 .

Different views of a fragment of the crystal structure of compound **(3)** [AMBt] I_3 are shown in Figure 4. Due to its large size, the linear triiodide anion is ideal for forming numerous weak C-H hydrogen bonds and

interacting with the electropositive phenyl rings of the cations. The overall positive charge of the cation is spread out over the hydrogen atoms.

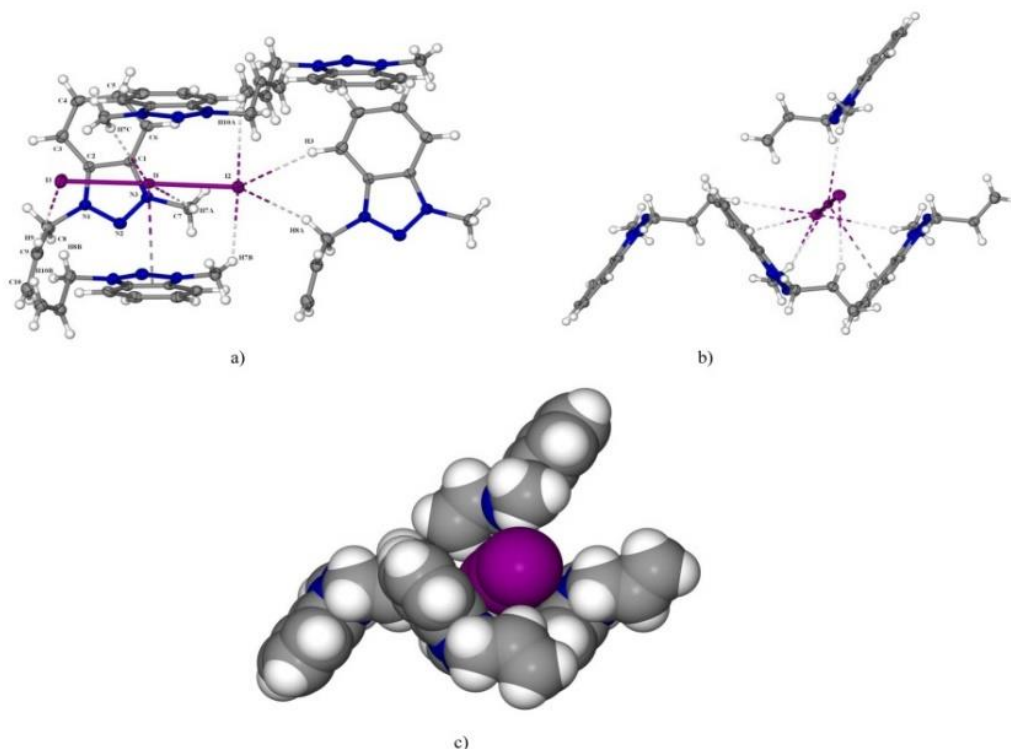


Figure 4: Different views of the crystal structure of the compound **(3)** [AMBt] I_3 .

Five cations surround every tri-iodide anion. The I_3^- ions are encircled by the organic molecules, creating a structure resembling a cage. The terminal I atom of the long bond (I_2) in the tri-iodide anion (I_1-I_2 , 2.9451(5) Å; I_1-I_3 , 2.8822(5) Å) accepts more

hydrogen bonds from the cations than the other I atoms in the anion. The H atoms are depicted as spheres with arbitrary radii, and displacement ellipsoids are drawn with a 50% probability. Table 3 contains a list of the crystal data.

Table 3: Crystal data of compound (3) [AMBt]I₃.

Empirical formula	C ₁₀ H ₁₂ I ₃ N ₃	Theta range for data collection	2.33 to 27.10°.
Formula weight	554.93	Index ranges	-12<=h<=12, -17<=k<=18, -14<=l<=15
Temperature	100(2) K	Reflections collected	10767
Wavelength	0.71073 Å	Independent reflections	3327 [R(int) = 0.0226]
Crystal system	Monoclinic	Absorption correction	Semi-empirical from equivalents
Space group	P21/n	Max. and min. transmission	0.8365 and 0.5773
Unit cell dimensions	a = 9.5684(13) Å α = 90° b = 14.2827(19) Å β = 111.566(2)° c = 11.9163(16) Å γ = 90°	Refinement method	Full-matrix least-squares on F ²
Volume	1514.5(4) Å ³	Data/restraints/parameters	3327 / 0 / 193
Z	4	Goodness-of-fit on F²	1.078
Density (calculated)	2.434 Mg/m ³	Final R indices [I > 2σ(I)]	R1 = 0.0199, wR2 = 0.0407
Absorption coefficient	6.173 mm ⁻¹	R indices (all data)	R1 = 0.0274, wR2 = 0.0423
F(000)	1008	Largest diff. Peak and hole	0.547 and -0.620 e.Å ⁻³
Crystal size	0.10 x 0.10 x 0.03 mm ³		

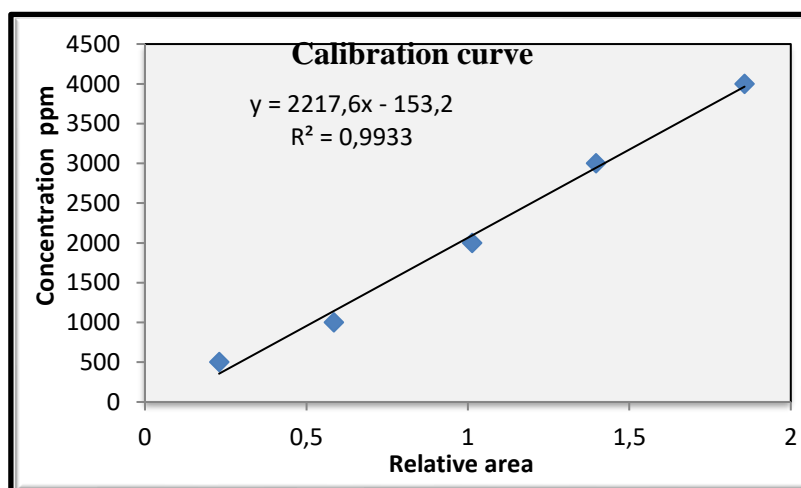
3.2. The Desulfurization of Model Diesel Oil

Model diesel oil has undergone treatment multiple times at various concentrations following the creation of a calibration curve using the gas chromatography method (25,26). As indicated in Table 4 Diagram 1,

the calibration curve diagram was created using the relationship between the concentration of the standard solution and the ratio of the standard Dibenzothiophene (DBT) peak's area over the celebrant's Hexadecane (C₁₆) peak's area.

Table 4: The relative area of (DBT) over (C₁₆) and the concentration of a standard solution.

Conc. ppm X1000	DBT / C ₁₆	C ₁₆ %	DBT %
4	1.8568	207314	384958
3	1.3963	226161	315797
2	1.0131	141492	143349
1	0.5847	135207	79067
0.5	0.2294	133305	30586

**Diagram 1:** Calibration curve of standard solution.

The prepared compounds (1-3) were all tested in the extraction process for 30 minutes at the same concentration (0.05g), which was the process' ideal condition. The outcomes are shown in Table 5. In

order to achieve the highest extraction efficiency, the optimal conditions for the extractive sulfur extraction process were predetermined and included 30 minutes at 25°C and a weight of ionic salts 0.05 g.

Table 5: The removal of sulfur % for 30 min and 0.05g extractive treatment.

No.	DBT %	C16 %	DBT/C16	DBT conc. ppm	S removal %
1	79602	138832	0.5734	1206.0249	22.4122
2	116492	182211	0.6393	1344.7557	13.4872
3	67591	125265	0.5396	1134.9612	26.9840

The extraction efficiency is good compared to previous studies (27, 28), with the observation that less salt is used; adding more weight will improve the extraction efficiency and the sulfur removal process. In conformity with the literature (15,27,28), it is also mentioned that the ionic liquids utilized are less effective than those that do contain Lewis acids, such as ferric chloride or other Lewis acids (28,29). Increasing the percentage of Lewis acids is anticipated to improve the extraction process' efficiency (30,31). The results indicate this. The rate at which sulfur is removed increases as iodine ions rise.

4. CONCLUSION

The prepared compounds have varying desulfurization efficiencies because the different anion or cation interacts differently with the organosulfur compounds in diesel oil. Because of the significant tri-iodide anion, salt (**3**) produced the best desulfurization.

5. ACKNOWLEDGMENT

We appreciate the University of Mosul funding this work and the University of Liverpool's Department of Chemistry for allowing us to conduct the required research and utilize departmental data.

6. REFERENCES

- Seddon KR. Ionic liquids for clean technology. *J Chem Technol Biotechnol* [Internet]. 1997;68(4):351–6. Available from: [<URL>](#).
- Wasserscheid P, Welton T. Ionic liquids in synthesis [Internet]. Wasserscheid P, Welton T, editors. Vol. 1, *Ionic Liquids in Synthesis: Second Edition*. Wiley; 2007. 1–721 p. Available from: [<URL>](#).
- Singh SK, Savoy AW. Ionic liquids synthesis and applications: An overview. *J Mol Liq* [Internet]. 2020 Jan 1;297:112038. Available from: [<URL>](#).
- Manahan SE. Green chemistry and the ten commandments of sustainability. *ChemChar Res*. 2006;
- Fonseca GS, Umpierre AP, Fichtner PFP, Teixeira SR, Dupont J. The use of imidazolium ionic liquids for the formation and stabilization of Ir⁰ and Rh⁰ nanoparticles: Efficient catalysts for the hydrogenation of arenes. *Chem – A Eur J* [Internet]. 2003 Jul 21;9(14):3263–9. Available from: [<URL>](#).
- Ren F, Wang J, Xie F, Zan K, Wang S, Wang S. Applications of ionic liquids in starch chemistry: A review. *Green Chem* [Internet]. 2020 Apr 6;22(7):2162–83. Available from: [<URL>](#).
- Schmidt R. [bmim]AlCl₄ Ionic Liquid for Deep Desulfurization of Real Fuels. *Energy & Fuels* [Internet]. 2008 May 1;22(3):1774–8. Available from: [<URL>](#).
- Shiraishi Y, Hirai T. Desulfurization of vacuum gas oil based on chemical oxidation followed by liquid–liquid extraction. *Energy & Fuels* [Internet]. 2004 Jan 1;18(1):37–40. Available from: [<URL>](#).
- Welton T. Ionic liquids: A brief history. *Biophys Rev* [Internet]. 2018 Jun 26;10(3):691–706. Available from: [<URL>](#).
- Arce A, Francisco M, Soto A. Evaluation of the polysubstituted pyridinium ionic liquid [hmmpy][Ntf₂] as a suitable solvent for desulfurization: Phase equilibria. *J Chem Thermodyn* [Internet]. 2010 Jun 1;42(6):712–8. Available from: [<URL>](#).
- Isosaari P, Srivastava V, Sillanpää M. Ionic liquid-based water treatment technologies for organic pollutants: Current status and future prospects of ionic liquid mediated technologies. *Sci Total Environ* [Internet]. 2019 Nov 10;690:604–19. Available from: [<URL>](#).
- Ehsan Kianfar, Sajjad Mafi. Ionic liquids: Properties, application, and synthesis. *Fine Chem Eng* [Internet]. 2020 Dec 31;22–31. Available from: [<URL>](#).
- Earle MJ, McCormac PB, Seddon KR. Regioselective alkylation in ionic liquids. *Chem Commun* [Internet]. 1998 Jan 1;1998(20):2245–6. Available from: [<URL>](#).
- Buttrus NH, Sabah AA, Taqa AA, Englert U. 3-Allyl-1-methyl-1*H*-benzotriazol-3-ium iodide. *Acta Crystallogr Sect E Struct Reports Online* [Internet]. 2012 Sep 15;68(9):o2735–o2735. Available from: [<URL>](#).
- Sabah AA. Extractive desulfurization using piperidinium based ionic liquids with Lewis acids. *J Turkish Chem Soc Sect A Chem* [Internet]. 2021 Nov 30;8(4):1057–88. Available from: [<URL>](#).
- Sabah A. Extractive desulfurization of model oil using 1-methyl-4-ethyl pyridinium iodide ionic liquids with some Lewis acids. *Egypt J Chem* [Internet].

2021 Oct 30;65(5):147–52. Available from: [<URL>](#).

17. Boche G, Andrews P, Harms K, Marsch M, Rangappa KS, Schimeczek M, et al. Crystal and electronic structure of stable nitrenium ions. A comparison with structurally related carbenes. *J Am Chem Soc* [Internet]. 1996 Jan 1;118(21):4925–30. Available from: [<URL>](#).

18. Barbour LJ. X-Seed — A software tool for supramolecular crystallography. *J Supramol Chem* [Internet]. 2001 Jul 1;1(4–6):189–91. Available from: [<URL>](#).

19. Hübschle CB, Sheldrick GM, Dittrich B. *ShelXle*: a Qt graphical user interface for *SHELXL*. *J Appl Crystallogr* [Internet]. 2011 Dec 1;44(6):1281–4. Available from: [<URL>](#).

20. Shiraishi Y, Tachibana K, Hirai T, Komasa I. A novel desulfurization process for fuel oils based on the formation and subsequent precipitation of *S*-alkylsulfonium salts. 3. Denitrogenation behavior of light oil feedstocks. *Ind Eng Chem Res* [Internet]. 2001 Jul 1;40(15):3390–7. Available from: [<URL>](#).

21. Sabah AA, Assim YF, Ahmed AS, Alhassan OK, Huseen AS, Jasim BH, et al. Extractive desulfurization of model diesel oil by using novel indolium based ionic liquids. *Int J Enhanc Res Sci Technol Eng* [Internet]. 2017;6(12):32–9. Available from: [<URL>](#).

22. Lee KM, Lee CK, Lin IJB. First example of interdigitated U-shape benzimidazolium ionic liquid crystals. *Chem Commun* [Internet]. 1997 Jan 1;9):899–900. Available from: [<URL>](#).

23. Yang Y, Zhang ZQ, Ding JM, Wang SM, Ju YC. Crystal structure of tetrapyrindinecopper(II) bis(triiodide), [Cu(C₅H₅N)₄][I₃]₂. *Zeitschrift für Krist - New Cryst Struct* [Internet]. 2011 Jan 1;226(2):185–6. Available from: [<URL>](#).

24. Chen L. Crystal structure of bis(pyridin-2-yl)disulfide hydrotriiodide, [C₁₀H₉N₂S₂][I₃]. *Zeitschrift*

für Krist - New Cryst Struct [Internet]. 2006 Apr 1;221(1–4):443–4. Available from: [<URL>](#).

25. Gutowski KE, Cocalia VA, Griffin ST, Bridges NJ, Dixon DA, Rogers RD. Interactions of 1-Methylimidazole with UO₂(CH₃CO₂)₂ and UO₂(NO₃)₂: Structural, spectroscopic, and theoretical evidence for imidazole binding to the uranyl ion. *J Am Chem Soc* [Internet]. 2007 Jan 1;129(3):526–36. Available from: [<URL>](#).

26. Tanaka R, Matsushita N. Crystal structure of bis(1-ethylpyridinium) dioxonium hexacyanidoferrate(II). *Acta Crystallogr Sect E Crystallogr Commun* [Internet]. 2017 Feb 1;73(2):219–22. Available from: [<URL>](#).

27. Sabah AA. Synthesis and characterization of some transition metals complex salts of pyridinium iodide ionic liquids: Application on extractive desulfurization. *J Turkish Chem Soc Sect A Chem* [Internet]. 2021 Aug 31;8(3):763–74. Available from: [<URL>](#).

28. Zaidan SW, Ameen AM, Sabah AA. Application on Extractive desulfurization using substituted pyrimidine ionic salt and its some transition metals complex salts. *Coll Basic Educ Res J* [Internet]. 2023;19(3):638–51. Available from: [<URL>](#).

29. Li F tang, Liu Y, Sun Z min, Chen L ju, Zhao D shun, Liu R hong, et al. Deep extractive desulfurization of gasoline with xEt₃NHCl·FeCl₃ ionic liquids. *Energy & Fuels* [Internet]. 2010 Aug 19;24(8):4285–9. Available from: [<URL>](#).

30. Ban LL, Liu P, Ma CH, Dai B. Deep extractive desulfurization of diesel fuels by FeCl₃/ionic liquids. *Chinese Chem Lett* [Internet]. 2013 Aug 1;24(8):755–8. Available from: [<URL>](#).

31. Ko NH, Lee JS, Huh ES, Lee H, Jung KD, Kim HS, et al. Extractive desulfurization using Fe-containing ionic liquids. *Energy & Fuels* [Internet]. 2008 May 1;22(3):1687–90. Available from: [<URL>](#).



Study of Chromophores Potential in Binahong Leaf Extracts for Solar Cell Development

I Gusti Made Sanjaya^{1*} , Pirim Setiarso¹ 

¹Universitas Negeri Surabaya, Department of Chemistry, Surabaya, 60231, Indonesia.

Abstract: Solar cell material from organic chromophores is interesting to develop because it has adjustable electronic and optical properties, the material is relatively cheap, the manufacturing method is simple, environmentally friendly, and easy to recycle. This research aims to study the potential of leaf extract from binahong as a raw material for the development of organic solar cells in terms of its chromophore. The study was carried out through an analysis of leaf extracts from binahong with red stems and leaf extracts from binahong with green stems with the help of a UV-VIS spectrophotometer instrument and a Shimadzu LCMS – 8040 LC/MS instrument. The compounds identified from each extract through their LCMS chromatograms were then characterized computationally using gamess applications with the DFT method and 6.31G* basis set. The results showed that the leaf extract from binahong with red stems had a different color and band gap than the leaf extract from binahong with green stems. This is because the red-stemmed binahong leaf extract has an excess of 3 compounds, namely kaempferol-3-(6"-malonyl glucoside), prodelphinidin B1, and prodelphinidin C2. The LCMS chromatogram showed that there were 55 bioactive compounds identified in the leaf extract from binahong with red stems and 52 compounds identified in the leaf extract from binahong with green stems. Of all these compounds, the majority, namely 44 compounds in the leaf extract from binahong leaves with red stems and 42 compounds in the leaf extract from binahong with green stems, are chromophores that have the potential to be used as raw materials for developing solar cells.

Keywords: Binahong, solar cell, organic, band gap.

Submitted: December 11, 2022. **Accepted:** October 5, 2024.

Cite this: Sanjaya IGM, Setiarso P. Study of Chromophores Potential in Binahong Leaf Extracts for Solar Cell Development. JOTCSA. 2024;11(4): 1651-8.

DOI: <https://doi.org/10.18596/jotcsa.1217367>

***Corresponding author's E-mail:** igmasanjaya@unesa.ac.id

1. INTRODUCTION

The rapid increase in energy consumption due to population growth and modernization which is not matched by rapid energy production due to limited primary energy sources, has triggered a global energy crisis (1). This also causes an increase in the amount of carbon in the air which contributes greatly to air pollution and an increase in global temperatures which is the main cause of the greenhouse effect (2). To solve this, it is necessary to develop new energy sources that are oriented towards renewable and environmentally friendly energy sources or clean energy (3).

Sources of clean energy that are much looked at and are being intensively studied include solar cells (4). This is related to abundant sunlight that has not been utilized optimally yet (5). It should be noted that the average exposure to sunlight reaches 12 hours more per day (4,422 hours per year) for the tropics (6),

which is equivalent to energy above 120 W/m² (7). The solar cell works by converting light energy or photons from the sun into electrical energy. Of course, as one of the most important sources of sustainable electricity that is fossil-free and environmentally friendly, the realization of highly efficient solar energy is urgently needed.

Silicon-based solar cells with an optimum band gap of 1.12 eV, which dominate the market and are used worldwide, can use at most about 30% of the sun's energy to be converted into electricity (8,9). This happens because of the spectral mismatch between the solar spectrum (photons) and the absorption properties of the material. For example, photons with an energy higher than the band gap that is absorbed exhibits excess energy lost due to thermalization. Meanwhile, photons with lower energy than the band gap are not absorbed and their energy is not used for the generation of charge carriers. Another limiting factor is due to the recombination of charge carriers.

Solar cells developed with silicon-based inorganic materials, apart from having high production costs and low efficiency (10), also have the potential to pollute the environment (11). Therefore, attention is diverted to solar cells made from organic materials called organic solar cells.

The use of organic materials as raw materials for solar cells has attracted a lot of attention because of their promising properties. Organic solar cells have adjustable electronic and optical properties, relatively inexpensive materials, simple manufacturing methods, low material toxicity, environmental friendliness and easy recycling (12,13). The organic materials used to develop organic solar cells are materials that can be conductors or semiconductors. These materials have chromophores in the form of functional groups which are generally in the form of conjugated bonds (alternating single and double bonds). Such bonding results in a delocalization of the electrons along the chain. The conjugated n bonds of these organic compounds have received great attention during the last three decades due to their advanced technological applications in the field of photodiodes (14,15), solar cell (16,17), and molecular electronics (18,19) in addition to its adjustable electronic devices, optical properties and stability properties (20).

Organic materials used as raw materials for making organic solar cells are generally obtained from plants that have parts such as roots, stems, leaves, flowers or fruit that are colored (21). Plants of this kind that are easy to grow and have the potential to be used as raw materials for making organic solar cells, include binahong.

Binahong, with the Latin name *Anredera cordifolia*, is really important to study as a promising potential raw material for the development of organic solar cells, because binahong, which is a vine, is very easy to grow in various locations with fruit, leaves or stems producing quite strong colors. This causes binahong to be estimated to have the potential to produce efficient solar cells because the stronger the color, the higher the efficiency of the solar cell (22).

The study of the binahong plant as a source of chromophore in the development of organic solar cells this time starts from the extract of the leaves, which besides the fruit, are also thought to contain organic compounds that have conjugated double bonds (23). Potentially important compounds in the development of organic solar cells from third generation solar cells and organic-inorganic combination solar cells from fourth generation solar cells (24).

Because the binahong plant generally grows with red stems and green stems, the chromophore potential of the leaf extract of the red-trunked binahong plant and the leaf extract of the binahong plant with green stems is currently being studied as a raw material for making organic solar cells. To ensure the possibility of each of these extracts being used as a raw material for solar cell development, the band gap is checked with a UV-VIS spectrophotometer. Further-

more, to detect the compounds contained in each binahong leaf extract, analysis is carried out using LCMS. As for predicting these compounds as potential chromophores for the development of organic solar cells, chemical computations are carried out with the B3LYP function, the DFT method, and the 6.31G* basis set where the results are then compared with the TiO_2 conduction band energy and the energy of the LUMO redox couple of I^-/I_3^- .

2. EXPERIMENTAL SECTION

2.1. Materials

The main research material was binahong leaves from the red-stemmed binahong plant and from the green-stemmed binahong plant which were harvested from the environment in East Java, besides aquadest. The instruments used are a rotary evaporator, UV-VIS spectrophotometer, Shimadzu LCMS - 8040 LC/MS, and a Zeon computer with games applications to perform chemical computations and Avogadro to virtualize molecules and create input files.

2.2. Method

2.2.1. Preparation of binahong leaf extract

Each binahong leaf extract was obtained by extracting the dried binahong leaves with water solvent using a rotary evaporator. Each extract obtained was divided into two. A part of the extract was measured for its spectrum with a UV-VIS spectrophotometer to determine the band gap (25). The other part of the extract was analyzed with the help of the Shimadzu LCMS - 8040 LC/MS to determine the compounds contained in each of the binahong leaf extracts (26).

2.2.2. Determination of chromophores in extracts that have potential as raw materials for solar cells

The potential of the compounds contained in binahong leaf extract as a raw material for solar cells was determined through chemical computation. Molecular models of the compounds detected in the LCMS chromatograms were made by redrawing the molecules and then optimizing their geometries using the Avogadro application. The molecular model has then degenerated into a games application input file with the B3LYP function, the DFT method, and a 6.31G* basis set using the games input generator in the Avogadro application. Furthermore, a chemical computation process was carried out using the games application to obtain information on the HOMO, LUMO, and bandgap energies of each molecular model of the compounds detected in the binahong leaf extract. The LUMO energy was then compared with the TiO_2 conduction band energy and the HOMO energy was compared with the LUMO redox couple of I^-/I_3^- energy to find the potential of the compounds in each binahong leaf extract as chromophores for the development of organic solar cells.

3. RESULTS AND DISCUSSION

3.1. Results

The binahong leaf extract produced from the red-trunked binahong plant and the green-trunked

binahong plant extracted using distilled water is shown in Figure 1. Measurement of light absorption of each binahong leaf extract with a UV-VIS spectrophotometer produced spectra as shown in Figure 2. Figure 3 shows the chromatogram of the extracts of binahong leaves with red stems and

binahong leaves with green stems produced using the Shimadzu LCMS – 8040 LC/MS instrument.



Figure 1: Extracts of leaves from binahong with red stems (left) and binahong with green stems (right).

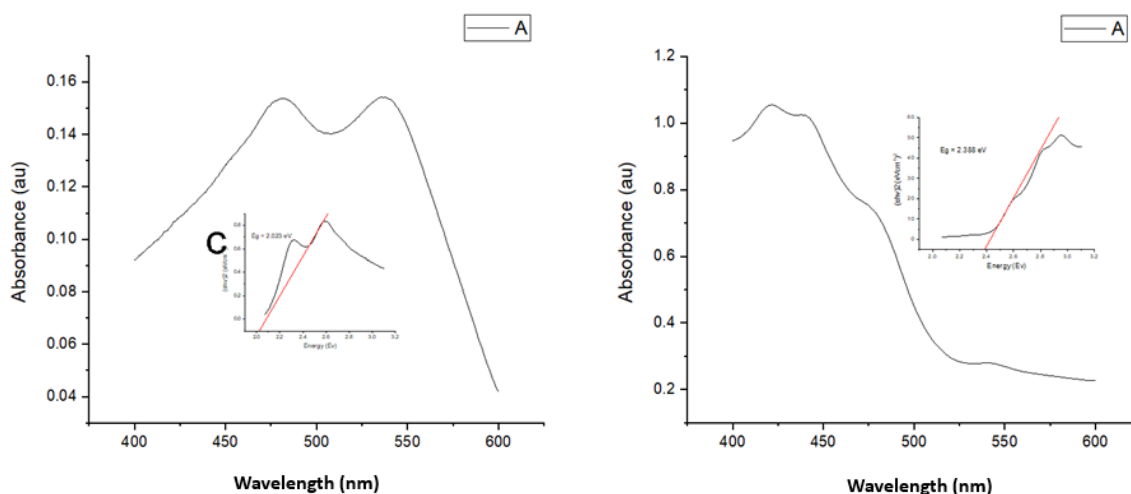


Figure 2: UV-VIS spectra of leaf extracts from binahong with red stems (left) and binahong with green stems (right).

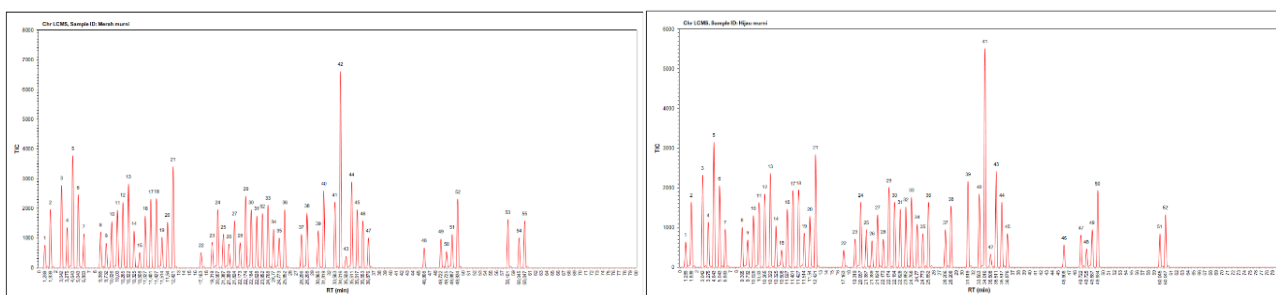


Figure 3: LCMS Chromatogram results of binahong leaf extracts with red stems (left) and green stems (right).

The details of the compounds identified through each chromatogram and the computational results of the HOMO, LUMO, and band gap energies of each

molecule using the games application with the DFT method and 6.31G* basis set are shown in Table 1.

Table 1: List of compounds and computational results for each molecule contained in binahong leaf extract.

No.	Red Binahong	Green Binahong	HOMO Energy (eV)	LUMO Energy (eV)	Band Gap (eV)
1	benzoic acid	benzoic acid	-6.9906	-1.2136	5.7770
2	p-coumaric acid	p-coumaric acid	-5.8967	-1.5402	4.3565
3	gallic acid	gallic acid	-5.8967	-0.9687	4.9280
4	esculetin	esculetin	-5.7770	-1.5837	4.1933
5	caffeic acid	caffeic acid	-5.7361	-1.5211	4.2150
6	ferulic acid	ferulic acid	-5.8423	-1.5402	4.3021
7	spathulenol	spathulenol	-6.1253	0.8816	7.0069
8	apigenin	apigenin	-5.8178	-1.6000	4.2178
9	naringenin	naringenin	-5.9185	-1.3252	4.5933
10	7-O-methyl-cryptostrobin	7-O-methyl-cryptostrobin	-5.6790	-0.8980	4.7810
11	demethoxymatteucinol	demethoxymatteucinol	-5.6436	-0.8626	4.7810
12	luteolin	luteolin	-5.7661	-1.5755	4.1905
13	kaempferol	kaempferol	-5.6191	-1.2572	4.3620
14	fisetin	fisetin	-5.7416	-1.1592	4.5824
15	phytol	phytol	-6.1933	0.6993	6.8926
16	desmosflavone	desmosflavone	-5.6028	-1.7470	3.8558
17	ellagic acid	ellagic acid	-6.1525	-1.8395	4.3130
18	quercetin	quercetin	-5.6436	-1.2789	4.3647
19	myricetin	myricetin	-5.6083	-1.2436	4.3647
20	4,7-dihydroxy-5-methoxy-6-methyl-8-formylflavan	4,7-dihydroxy-5-methoxy-6-methyl-8-formylflavan	-5.7008	-1.4095	4.2912
21	chlorogenic acid	chlorogenic acid	-5.7552	-1.6490	4.1062
22	β -sitosterol	β -sitosterol	-0.8408 (α) / -6.0681 (β)	0.9306 (α) / -0.8408 (β)	1.7715 (α) / 5.2273 (β)
23	β -amyrin	β -amyrin	-5.7933	0.7538	6.5470
24	6- β -D-glucopyranosyl-4',5,7-trihydroxyflavone	6- β -D-glucopyranosyl-4',5,7-trihydroxyflavone	-5.6981	-1.5891	4.1089
25	vitexin	vitexin	-5.8586	-1.6272	4.2314
26	apigetrin	apigetrin	-5.9021	-1.6980	4.2041
27	larreagenin A	larreagenin A	-5.9402	0.1578	6.0981
28	astragalin	astragalin	-6.0028	-1.4612	4.5416
29	quercetin-3-O-rhamnoside	quercetin-3-O-rhamnoside	-5.8722	-1.1456	4.7266
30	fisetin-4'-glucoside	fisetin-4'-glucoside	-5.5865	-1.5592	4.0273
31	luteolin-7-glucoside	luteolin-7-glucoside	-5.9212	-1.6980	4.2232
32	diosmetin-7-O- β -Dglucopyranoside	diosmetin-7-O- β -Dglucopyranoside	-1.6925 (α) / -5.8015 (β)	-1.1565 (α) / -1.6925 (β)	0.5361 (α) / 4.1089 (β)
33	kaempferol-3-(2''-acetylramnoside)	kaempferol-3-(2''-acetylramnoside)	-1.5075 (α) / -5.5266 (β)	-0.9769 (α) / -1.5075 (β)	0.5306 (α) / 4.0191 (β)
34	kaempferol-3-(3''-acetylramnoside)	kaempferol-3-(3''-acetylramnoside)	-5.5946	-1.2789	4.3157
35	kaempferol-3-(4''-acetylramnoside)	kaempferol-3-(4''-acetylramnoside)	-1.6925 (α) / -5.5729 (β)	-1.2898 (α) / -1.6925 (β)	0.4027 (α) / 3.8803 (β)
36	isorhamnetin-3-O- β -Dgalactopyranoside	isorhamnetin-3-O- β -Dgalactopyranoside	-1.5919 (α) / -5.5620 (β)	-1.3769 (α) / -1.5919 (β)	0.2150 (α) / 3.9701 (β)
37	kaempferol-3-(2'',4''-diacetylramnoside)	kaempferol-3-(2'',4''-diacetylramnoside)	-5.3824	-1.3987	3.9837
38	kaempferol-3-(3'',4''-diacetylramnoside)	kaempferol-3-(3'',4''-diacetylramnoside)	-5.8504	-1.5102	4.3402
39	kaempferol-3-(6''-malonyl glucoside)	-	-1.5021 (α) / -5.5130 (β)	-1.0694 (α) / -1.5021 (β)	0.4327 (α) / 4.0109 (β)
40	quercetin-3-Omalonylglucoside	quercetin-3-Omalonylglucoside	-1.5510 (α) / -5.3579 (β)	-1.1021 (α) / -1.5510 (β)	0.4490 (α) / 3.8069 (β)
41	naringin	naringin	-6.0355	-1.2436	4.7919
42	kaempferol 3-(5''-feruloylapioside)	kaempferol 3-(5''-feruloylapioside)	-5.6627	-1.6000	4.0627
43	kaempferol 3-(6''-caffeoylglucoside)	kaempferol 3-(6''-caffeoylglucoside)	-1.6789 (α) / -5.5212 (β)	-1.3034 (α) / -1.6789 (β)	0.3755 (α) / 3.8422 (β)

44	quercetin-3-glucoside-7-rhamnoside	quercetin-3-glucoside-7-rhamnoside	-3.6273	-2.5960	1.0313
45	rutin	rutin	-5.8123	-1.6735	4.1388
46	prodelphinidin B1	-	-5.2926	-0.0190	5.2736
47	myricetin 3-rutinoside	myricetin 3-rutinoside	-5.8668	-1.6980	4.1688
48	momordin Ic	momordin Ic	-5.7851	-0.3646	5.4205
49	boussingoside A2	boussingoside A2	-4.8355	-2.3184	2.5170
50	momordin Ia	momordin Ia	-5.8559	0.0136	5.8695
51	boussingoside E	boussingoside E	-5.9076	-0.1388	5.7688
52	quinoasaponin 9	quinoasaponin 9	-5.8178	-0.1170	5.7008
53	prodelphinidin C2	-	-7.3090	3.2082	10.5172
54	momordin Iic	momordin Iic	-3.9164	4.2966	8.2130
55	momordin Iia	momordin Iia	-7.4483	3.9731	11.4214

3.2. Discussion

Figure 1 shows the leaf extract of the red-stemmed binahong plant which is red in color, is different from the leaf extract of the green-stemmed binahong plant which is greenish-yellow in color. In addition,

there is also a difference in the band gap between the two types of extracts based on the results of the respective UV-VIS spectral measurements in Figure 2 which can be rewritten in Table 2.

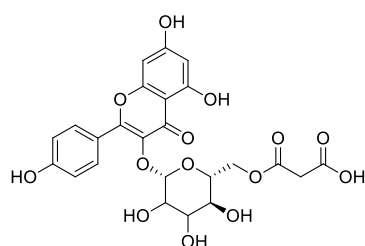
Table 2: Band gap of binahong leaf extract.

No.	Sample	Band Gap (eV)
1	Leaf extract from red-stemmed binahong	2.023
2	Leaf extract from binahong has green stems	2.388

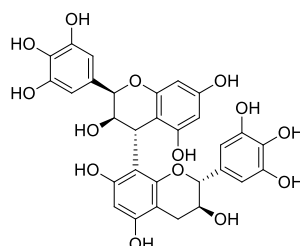
Even so, the difference in the band gap still exists in the band gap area which has efficiency in converting power from sunlight (27).

The color difference produced in the red-stemmed binahong leaf extract and the green-stemmed binahong leaf extract in Figure 1 occurs because there are differences in the content of bioactive

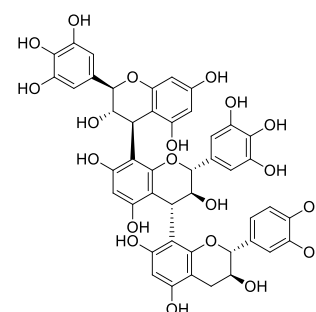
compounds in each extract (28,29). As shown in table 1 which details the chromatogram results from Figure 2, there are 3 compounds that cause color differences in the red-stemmed binahong leaf extract from the green-stemmed binahong leaf extract, namely kaempferol-3-(6"-malonyl glucoside), prodelphinidin B1, and prodelphinidin C2.



kaempferol-3-(6''-malonyl glucoside)



prodelphinidin B1



prodelphinidin C2

Figure 4: Three compounds that differentiate the red-stemmed binahong leaf extract from the green-trunked binahong leaf extract.

Table 1 shows that the bioactive compounds contained in leaf extracts from red-stemmed binahong and leaf extracts from green-stemmed binahong are generally semiconductors with energy band gaps ranging from 1.0313 eV to 11.4214 eV. Semiconductors from bioactive compounds that have an energy gap above the standard silicon energy gap, namely 1.12 eV, work outdoors in bright light.

Based on an understanding of the DSSC chart (30) and an understanding of the optimal electron donor-acceptor pair that can be selected based on an understanding of the TiO₂ conduction band as a standard, namely -4.05 eV (31,32), then the LUMO energy of the chromophore in binahong leaf extract

that must be sought is the one with a more positive value than the TiO₂ conduction band. This is based on the assumption that the excited state of the chromophore is in the LUMO state. This state is related to the ability of the chromophore molecule to inject electrons from its excited state into the TiO₂ conduction band. For HOMO from the chromophore of binahong leaf extract, it is necessary to find a molecule that has a HOMO energy that is more negative than the energy of the LUMO redox couple of I⁻/I₃⁻ = -4,85 eV (33-35).

Based on the computation of the HOMO, LUMO, and band gap in Table 1, ignoring molecules that have two types of band gaps energy, there are 44

compounds in the leaf extract from the red stemmed binahong and 42 compounds in the leaf extract from the green stemmed binahong which have the possibility of being new chromophores for interest in the development of organic solar cells.

4. CONCLUSION

The leaf extract from binahong with red stems has a different color than the color of the leaf extract from binahong with green stems, as well as the band gap. The causes of these differences were the compounds kaempferol-3-(6"-malonyl glucoside), prodelfinidin B1, and prodelfinidin C2 which were only present in leaf extracts from red-trunked binahong, not found in leaf extracts from green-trunked binahong. The LCMS chromatogram showed that there were 55 bioactive compounds identified in the leaf extract from binahong with red stems and 52 compounds identified in the leaf extract from binahong with green stems. Of all these compounds, the majority, namely 44 compounds in the leaf extract from the red-stemmed binahong and 42 compounds in the leaf extract from the green-stemmed binahong, are chromophores that have the potential to be used as raw materials for the development of organic solar cells. Based on this and the results of the band gap measurements, each binahong leaf extract has the potential to be used as a raw material for solar cell development.

5. ACKNOWLEDGMENT

We are grateful to State University of Surabaya for providing research grants and facilitating the implementation of this research.

6. REFERENCES

- International Energy Agency. World energy outlook 2021. 2021;
- Perera F. Pollution from fossil-fuel combustion is the leading environmental threat to global pediatric health and equity: Solutions exist. *Int J Environ Res Public Health* [Internet]. 2017 Dec 23;15(1):16. Available from: [<URL>](#).
- International Energy Agency. Net zero by 2050 a roadmap for the global energy sector. 2021; Available from: [<URL>](#).
- Gielen D, Boshell F, Saygin D, Bazilian MD, Wagner N, Gorini R. The role of renewable energy in the global energy transformation. *Energy Strateg Rev* [Internet]. 2019 Apr 1;24:38–50. Available from: [<URL>](#).
- Handayani NA, Ariyanti D. Potency of solar energy applications in Indonesia. *Int J Renew Energy Dev* [Internet]. 2012 Jul 1;1(2):33–8. Available from: [<URL>](#).
- Anonymous. Durasi penyinaran matahari [Internet]. [cited 2022 Apr 13]. Available from: [<URL>](#).
- Hamdi S. Mengenal lama penyinaran matahari sebagai salah satu parameter klimatologi. *Ber Dirgant* [Internet]. 2014;15(1):7–16. Available from: [<URL>](#).
- Shockley W, Queisser H. Detailed balance limit of efficiency of p–n junction solar cells. In: *Renewable Energy* [Internet]. Routledge; 2018. p. 35–54. Available from: [<URL>](#).
- Tiedje T, Yablonovitch E, Cody GD, Brooks BG. Limiting efficiency of silicon solar cells. *IEEE Trans Electron Devices* [Internet]. 1984 May;31(5):711–6. Available from: [<URL>](#).
- NREL. Best research-cell efficiency chart [Internet]. [cited 2024 Sep 13]. Available from: [<URL>](#).
- Almosni S, Delamarre A, Jehl Z, Suchet D, Cojocaru L, Giteau M, et al. Material challenges for solar cells in the twenty-first century: Directions in emerging technologies. *Sci Technol Adv Mater* [Internet]. 2018 Dec 31;19(1):336–69. Available from: [<URL>](#).
- Zhou Y, Fuentes-Hernandez C, Khan TM, Liu JC, Hsu J, Shim JW, et al. Recyclable organic solar cells on cellulose nanocrystal substrates. *Sci Rep* [Internet]. 2013 Mar 25;3(1):1536. Available from: [<URL>](#).
- Zhong S, Yap BK, Zhong Z, Ying L. Review on Y6-based semiconductor materials and their future development via machine learning. *Crystals* [Internet]. 2022 Jan 24;12(2):168. Available from: [<URL>](#).
- Greenham NC, Moratti SC, Bradley DDC, Friend RH, Holmes AB. Efficient light-emitting diodes based on polymers with high electron affinities. *Nature* [Internet]. 1993 Oct 14;365(6447):628–30. Available from: [<URL>](#).
- Friend RH, Gymer RW, Holmes AB, Burroughes JH, Marks RN, Taliani C, et al. Electroluminescence in conjugated polymers. *Nature* [Internet]. 1999 Jan 14;397(6715):121–8. Available from: [<URL>](#).
- Schmidt-Mende L, Fechtenkötter A, Müllen K, Moons E, Friend RH, MacKenzie JD. Self-organized discotic liquid crystals for high-efficiency organic photovoltaics. *Science* (80-) [Internet]. 2001 Aug 10;293(5532):1119–22. Available from: [<URL>](#).
- Dance ZEX, Ahrens MJ, Vega AM, Ricks AB, McCamant DW, Ratner MA, et al. Direct observation of the preference of hole transfer over electron transfer for radical Ion pair recombination in donor–bridge–acceptor molecules. *J Am Chem Soc* [Internet]. 2008 Jan 1;130(3):830–2. Available from: [<URL>](#).
- Palma M, Levin J, Lemaun V, Liscio A, Palermo V, Cornil J, et al. Self-organization and nanoscale electronic properties of azatriphenylene-based architectures: A scanning probe microscopy study. *Adv Mater* [Internet]. 2006 Dec 18;18(24):3313–7. Available from: [<URL>](#).

19. Chen X, Jeon YM, Jang JW, Qin L, Huo F, Wei W, et al. On-wire lithography-generated molecule-based transport junctions: A new testbed for molecular electronics. *J Am Chem Soc* [Internet]. 2008 Jul 1;130(26):8166–8. Available from: [<URL>](#).
20. Forrest SR. The path to ubiquitous and low-cost organic electronic appliances on plastic. *Nature* [Internet]. 2004 Apr 29;428(6986):911–8. Available from: [<URL>](#).
21. Etienne T, Chbib L, Michaux C, Perpète EA, Assfeld X, Monari A. All-organic chromophores for dye-sensitized solar cells: A theoretical study on aggregation. *Dye Pigment* [Internet]. 2014 Feb 1;101:203–11. Available from: [<URL>](#).
22. Ayalew WA, Ayele DW. Dye-sensitized solar cells using natural dye as light-harvesting materials extracted from *Acanthus sennii chiovenda* flower and *Euphorbia cotinifolia* leaf. *J Sci Adv Mater Devices* [Internet]. 2016 Dec 1;1(4):488–94. Available from: [<URL>](#).
23. Cahyani N, Sanjaya IGM. Potensi senyawa betalain pada ekstrak biji binahong berbatang merah (*Anredera cordifolia*) sebagai fotosensitizer dye sensitized solar cell (DSSC). *Al-Kimia* [Internet]. 2021 Dec 31;9(2):103–14. Available from: [<URL>](#).
24. Luceño-Sánchez JA, Díez-Pascual AM, Peña Capilla R. Materials for photovoltaics: State of art and recent developments. *Int J Mol Sci* [Internet]. 2019 Feb 23;20(4):976. Available from: [<URL>](#).
25. Setiawan IN, Giriantari IAD, Ariastina WG, Swamardika IBA. Effect of solvents on natural dyes extraction from mangosteen waste for dye sensitized solar cell application. *Int J Eng Emerg Technol* [Internet]. 2018;3(2):129–32. Available from: [<URL>](#).
26. Dwitiyanti YH, Elya B, Bahtiar A. Impact of solvent on the characteristics of standardized binahong Leaf (*Anredera cordifolia* (ten.) steenis). *Pharmacogn J* [Internet]. 2019 Dec 1;11(6s):1463–70. Available from: [<URL>](#).
27. Jarosz G, Marczyński R, Signerski R. Effect of band gap on power conversion efficiency of single-junction semiconductor photovoltaic cells under white light phosphor-based LED illumination. *Mater Sci Semicond Process* [Internet]. 2020 Mar 1;107:104812. Available from: [<URL>](#).
28. Pawar N, Shinde M, Junna L. Stabilization of food colourant and antimicrobial activity in fruit extracts of *Basella rubra* L. *Int J Pharmacogn Phytochem Res* [Internet]. 2018;10(1):43–7. Available from: [<URL>](#).
29. Masniah, Manurung J. Phytochemicals screening and activities of binahong (*Anredera cordifolia* [TEN.] steenis) leaves and beetroots (*Beta vulgaris* L.) in increasing swimming endurance in mice. *Asian J Pharm Clin Res* [Internet]. 2019 Mar 14;12(4):235–7. Available from: [<URL>](#).
30. Kislenko SA, Amirov RK, Popel' OS, Samoilov IS. Dye-sensitized solar cells: Present state and prospects for future development. *Therm Eng* [Internet]. 2010 Nov 26 [cited 2024 Dec 1];57(11):969–75. Available from: [<URL>](#).
31. Fujisawa J ichi, Eda T, Hanaya M. Comparative study of conduction-band and valence-band edges of TiO₂, SrTiO₃, and BaTiO₃ by ionization potential measurements. *Chem Phys Lett* [Internet]. 2017 Oct 1;685:23–6. Available from: [<URL>](#).
32. Bledowski M, Wang L, Ramakrishnan A, Khavryuchenko O V., Khavryuchenko VD, Ricci PC, et al. Visible-light photocurrent response of TiO₂-polyheptazine hybrids: evidence for interfacial charge-transfer absorption. *Phys Chem Chem Phys* [Internet]. 2011 Nov 29;13(48):21511. Available from: [<URL>](#).
33. Wazzan NA. A DFT/TDDFT investigation on the efficiency of novel dyes with ortho-fluorophenyl units (A1) and incorporating benzotriazole / benzothiadiazole / phthalimide units (A2) as organic photosensitizers with D–A2–π–A1 configuration for solar cell applications. *J Comput Electron* [Internet]. 2019 Jun;18(2):375–95. Available from: [<URL>](#).
34. Feldt S. Alternative Redox Couples for Dye-Sensitized Solar Cells [Internet]. [Uppsala, Sweden]: Digital Comprehensive Summaries of Uppsala Dissertations from the Faculty of Science and Technology; 2013. Available from: [<URL>](#).
35. Iftikhar H, Sonai GG, Hashmi SG, Nogueira AF, Lund PD. Progress on electrolytes development in dye-sensitized solar cells. *Materials* [Internet]. 2019 Jun 21;12(12):1998. Available from: [<URL>](#).

